



# Towards a complete understanding of neutrino-nucleus interactions with the T2K near detector upgrade

Jaafar Chakrani

## ► To cite this version:

Jaafar Chakrani. Towards a complete understanding of neutrino-nucleus interactions with the T2K near detector upgrade. High Energy Physics - Experiment [hep-ex]. Institut Polytechnique de Paris, 2023. English. NNT : 2023IPPAX059 . tel-04461663

**HAL Id: tel-04461663**

**<https://theses.hal.science/tel-04461663>**

Submitted on 16 Feb 2024

**HAL** is a multi-disciplinary open access archive for the deposit and dissemination of scientific research documents, whether they are published or not. The documents may come from teaching and research institutions in France or abroad, or from public or private research centers.

L'archive ouverte pluridisciplinaire **HAL**, est destinée au dépôt et à la diffusion de documents scientifiques de niveau recherche, publiés ou non, émanant des établissements d'enseignement et de recherche français ou étrangers, des laboratoires publics ou privés.



# Towards a complete understanding of neutrino-nucleus interactions with the upgraded T2K near detector

Thèse de doctorat de l'Institut Polytechnique de Paris  
préparée à l'École polytechnique

École doctorale n°626 Dénomination (EDIPP)  
Spécialité de doctorat : Physique des particules

Thèse présentée et soutenue à Palaiseau, le 5 septembre 2023, par

**JAAFAR CHAKRANI**

Composition du Jury :

Andrea Giuliani Directeur de Recherche, Laboratoire de Physique des 2 infinis Irène Joliot-Curie	Président, Rapporteur & Examinateur
Alessandra Tonazzo Professeure, Laboratoire Astroparticules et Cosmologie	Rapporteuse & Examinatrice
Sara Bolognesi Chercheuse, IRFU-CEA Saclay	Examinatrice
Jamie Dawson Chargée de Recherche, Laboratoire Astroparticules et Cosmologie	Examinatrice
Federico Sánchez Nieto Professeur, Université de Genève	Examinateur
Margherita Buizza Avanzini Chargée de Recherche, Laboratoire Leprince-Ringuet	Directrice de thèse





To my family...



# Acknowledgements

My experience as a PhD student comes to an end with this section, and it has been amazing! I would like to take the time in these few lines to thank the various people that helped throughout this endeavor.

It was during my masters that Michel Gonin introduced me to the neutrino group of LLR and particularly to my marvelous PhD director Margherita Buizza Avanzini, and for this I am extremely grateful to him. Margherita has been an exceptional guide and mentor since I first met her during my two-month internship, and it is thanks to her that my PhD experience has been an exciting learning adventure. Her empathy and thoughtfulness, as well as the trust she put in me to pursue my interests within the T2K collaboration, have allowed me to grow as a researcher. The uncertain times during the peak of the pandemic were made easy thanks to her constant presence and availability. She always took the time to hear my ideas and answer my questions while guiding me to utilize my time and effort in the best possible ways. Her scientific curiosity is now deeply imprinted on me. Sharing the office once we could work onsite enabled many stimulating discussions that helped me gain a deeper understanding of neutrino physics. I simply could not have hoped for a better PhD director. She will always be a mentor to me, and I will be eternally indebted to her for my career as a physicist.

All the work presented in this manuscript was performed within the T2K collaboration, and as such, none of it would have been possible without the many T2K collaborators since the start of the experiment.

Stephen Dolan was one of the first colleagues I got a chance to work with, beginning with my internship with him at CERN the summer prior to my PhD. He truly set an example for me of what a researcher is like with his scientific rigor and methodical approach in the various topics, and inspired me to go even further in the field of neutrino physics. I would like to express my sincere thanks to him for his help in the wide range of subjects we discussed, as well as his continued support and kindness.

I had the chance to be involved within multiple T2K working groups convened by inspiring and passionate people to whom I would like to express my gratitude. I started within the ND Upgrade Physics & Performance group with Stephen, Laura Munteanu and Sara Bolognesi, who never failed to encourage me and suggest new ideas to explore. The NIWG group with Stephen, Luke Pickering and Kevin McFarland gave me the opportunity to contribute to the T2K interaction model and provided a space for rich discussions with many experts, especially

## Acknowledgements

---

on neutrino event generators.

I also had the chance to discover the hardware side of the T2K experiment with the Super-FGD in the electronics group convened by Christopher Mauger and Olivier Drapier. Olivier, only a few steps from my office, was always available to answer in a very intuitive manner my many beginner questions related to this topic and helped me get started. The work on the Super-FGD front-end boards was carried out with an extremely talented team of engineers at LLR and the University of Geneva. I would like to specifically thank Frank Gastaldi, with whom I spent long hours trying to understand issues related to our test bench, Sébastien Cap, who always made time in his extremely busy schedule to respond to my questions and to help debug electronics issues, and without whom these boards would simply not exist, and also Yannick Favre, Jérôme Nanni and the rest of the LLR and UniGe technical staff.

My projects led me to the T2K oscillation analysis group, starting from the ND group with Ciro Riccio, Tristan Doyle, Joe Walsh and Laura who were present at all times to explain the subtleties of the near-detector analysis. The newly formed GUNDAM group, especially with Adrien Blanchet, provided me with an amazing opportunity to develop my coding skills. The GUNDAM validations were a big challenge, but thanks to the strong support of the ND group, and particularly Laura, we were able to steadily advance. The P-Theta group, convened by Mathieu Guigue and Lukas Berns, welcomed me with open arms to carry out my studies and provided me with all the tools, the explanations and the suggestions, and for this I would like to thank them.

I also encountered other T2K graduate students with whom I shared similar topics (and struggles!), like Viet Nguyen, Eric Chong, Lorenzo Giannessi, Vlada Yevarouskaya, Jordan McElwee, Anna Ershova, and many others. Seeing them in the few in-person collaboration meetings or conferences was always a great pleasure!

The neutrino group of LLR provided great support throughout my thesis. I would like to express my gratitude to Benjamin Quilain for taking the time to exchange ideas especially during my last PhD projects, and to Thomas Mueller and Pascal Paganini for their availability and kindness to chat about various physics and non-physics topics. Additionally, it was always a great pleasure to share a lot of fun moments with the other young members of the group: Antoine Beauchêne, Andrew Santos, Alberto Giampaolo, Laura Bernard, Brice Douet, Amelie Koch, Viet Nguyen, Rudolph Rogly, Mathieu Ferrey, and Christine Quach. Other members of the lab have also been a great support, especially Emilie Maurice and Frédéric Fleuret, and of course the IT and HR staff who give us the luxury to solely focus on research.

I would like to express my sincere gratitude to the members of the jury Sara Bolognesi, Jamie Dawson, Andrea Giuliani, Federico Sánchez Nieto, and Alessandra Tonazzo for their extremely valuable feedback and insightful discussions.

Lastly, I am blessed with the company of many people that constantly support me outside of the lab. Thank you to Simo, Taha, and Amine for our regular hangouts in the weekdays, to Yasser for the occasional drinks and all-you-can-eat sushi restaurants, to Mahmoud for the

## Acknowledgements

---

beach trips, to Hamza and Youssef for keeping in touch from across the Atlantic, and most importantly to Kira for her endless grace and support throughout this adventure. Finally, I would like to thank my mom Khadija, my dad Hamid and my brother Faris for always believing in me, for their constant presence even though we are on different continents, for their encouragements to explore the world, and for all the love and care that allowed me to become who I am today.

*Palaiseau, September 6, 2023*

J. C.



# Abstract

The goal of the T2K experiment is to study the oscillations of muon neutrinos and antineutrinos. These neutrinos are produced at J-PARC on the east coast of Japan and measured at Super-Kamiokande, 300 km away, to determine their mixing parameters, and particularly the CP-violating phase. One of the dominant systematic uncertainties in these measurements is related to the poor knowledge of the nuclear physics of neutrino interactions with the target nuclei. This is among the reasons why a suite of “near” detectors like ND280 is located close to the beam production point, allowing us to better understand the mechanisms of neutrino scattering. T2K is currently upgrading ND280 for more refined neutrino interaction measurements. Its installation, along with an upgrade of the beam power, are taking place this year and will constitute the start of a second phase of data taking until 2027.

Modeling neutrino interactions is a key step in any oscillation analysis. This often relies on crude assumptions and ad-hoc models that are not satisfactory to explain the observed data. A sophisticated way of describing the ground nuclear state in neutrino charged-current quasielastic interactions is based on the spectral function (SF) model, recently adopted by T2K, which is built from the well-established nuclear shell model and electron scattering data. We present a new parametrization of the systematic uncertainties related to this model and show how these allow for a good model tuning and improved agreement with a variety of cross section measurements. This parametrization consequently became part of the T2K oscillation analysis.

The heart of the near detector upgrade is the SFGD, a 3D fine-grained plastic scintillator detector. Its unprecedented granularity will open the door to a precise probing of the complex physics behind the dominant systematic uncertainties with its capabilities of full polar angle acceptance, lower proton tracking threshold, and reconstruction of neutron kinematics. The readout of its channels requires a complex chain of electronics which is discussed in this thesis, with a focus on the exhaustive testing of its front-end boards.

The upgrade era will open the door to an improved understanding of neutrino interaction physics, but there are multiple challenges to overcome to achieve this. One of these is related to the computational difficulties in fitting large data samples with high-dimensional models. This thesis discusses a new optimized framework called GUNDAM, with a focus on its validation by reproducing the latest analyses. GUNDAM is now becoming part of the main T2K software. The ability of the SFGD to reconstruct low-momentum hadrons allows us to use more sophisticated observables. In this thesis, we design a near-detector analysis within GUNDAM exploiting new variables particularly sensitive to the nuclear effects that impact oscillation



## Abstract

---

measurements. We quantify the expected precision in the tuning of the interaction model, and notably in the SF model parameters introduced previously which show a strong reduction in their uncertainties when adding the new SFGD samples.

Furthermore, we present the expected constraints on the oscillation parameters in this new period of data taking with this improved modeling. We show how the CP-violating phase could be constrained depending on the neutrino mass ordering and the values of the other mixing angles, and highlight the increasing role of the systematic uncertainties by the end of this period. In particular, if the mass ordering is known, CP-symmetry could be excluded at  $3\sigma$  for certain values of the mixing angles only if the systematic uncertainties are further improved. We also evaluate the expected resolution on the remaining unknown mixing parameters and assess the weak sensitivity of T2K to the mass ordering. We conclude with a discussion on ways of how to fully leverage the power of the upgrade to improve the oscillation measurements.

# Résumé

L'expérience T2K étudie les oscillations des neutrinos et des antineutrinos. Ceux-ci sont produits à J-PARC et détectés à Super-Kamiokande 300 km plus loin pour déterminer les paramètres de mélange, et surtout la phase de violation CP. La source principale des incertitudes systématiques dans ces mesures est liée à la méconnaissance de la physique nucléaire qui régit l'interaction du neutrino avec un noyau du détecteur. C'est pour cela qu'un ensemble de détecteurs proches, comme ND280, est situé près de la source des neutrinos afin de mieux comprendre leurs mécanismes de diffusion. T2K est en train de mettre à niveau ND280 pour raffiner ses mesures des interactions neutrino-noyau. Son installation et la mise à niveau du faisceau sont en cours et constitueront le début d'une seconde phase de prise de données jusqu'en 2027.

La modélisation des interactions neutrino-noyau est une étape clé dans toute analyse d'oscillation. Elle est fondée sur des hypothèses parfois grossières qui ne permettent souvent pas d'expliquer les données observées. L'un des modèles raffinés pour décrire les interactions quasi-élastiques est le modèle à fonction spectrale (SF), récemment adopté par T2K, qui est fondé sur le modèle des couches nucléaires et des données de diffusion des électrons. Nous présentons une nouvelle paramétrisation de ses incertitudes, et démontrons l'amélioration de ses prédictions pour plusieurs données de sections efficaces. Par conséquent, cette paramétrisation a été utilisée dans l'analyse d'oscillation de T2K.

La mise à niveau du ND280 est centrée autour du SFGD, un détecteur 3D de 2 millions de cubes de plastique scintillateur. Sa granularité fine permettra d'explorer la physique derrière les erreurs systématiques dans les mesures d'oscillation avec une précision inédite, notamment grâce à son acceptance isotrope, son bas seuil de détection de protons et sa capacité à mesurer la cinématique des neutrons. La lecture de ses données requiert une chaîne complexe d'électronique discutée dans cette thèse avec un accent sur les tests exhaustifs des cartes électroniques.

T2K entrera dans une nouvelle ère d'études de la physique des interactions neutrino-noyau avec cette mise à niveau. Cependant, plusieurs défis doivent être surmontés. D'abord, les ressources de calcul nécessaires ne cesseront d'augmenter pour le fonctionnement des algorithmes d'ajustement quand la statistique des échantillons est plus importante et la dimensionnalité des modèles est plus élevée. Cette thèse présente un nouveau logiciel, GUNDAM, conçu pour adresser ce problème. Nous nous focalisons sur sa validation en reproduisant les deux dernières analyses d'oscillations de T2K. Ainsi, GUNDAM deviendra l'un des outils principaux de T2K.

## Résumé

---

La capacité du SFGD à mesurer les hadrons à basse impulsion permet de définir de nouvelles observables. Nous concevons dans GUNDAM une analyse des données du détecteur proche en exploitant de nouvelles variables particulièrement sensibles aux effets nucléaires impactant les mesures d'oscillations. Les contraintes attendues sur les incertitudes liées au modèle d'interaction, et particulièrement le modèle SF, sont quantifiées et montrent une réduction importante grâce au SFGD.

De plus, nous présentons la sensibilité attendue de la mesure des paramètres d'oscillation avec cette nouvelle période de prise de données avec cette modélisation améliorée. Nous montrons comment la phase de violation CP pourrait être contrainte en fonction des autres paramètres de mélange, et soulignons le rôle croissant des incertitudes systématiques à la fin de cette période. En particulier, si la hiérarchie des masses est connue, la symétrie CP pourrait être exclue à  $3\sigma$  pour certaines valeurs des paramètres de mélange uniquement si les incertitudes systématiques peuvent être réduites. Nous évaluons aussi la résolution sur les autres paramètres et concluons avec une discussion sur comment mieux exploiter le SFGD pour améliorer les mesures d'oscillation.

# Contents

<b>Acknowledgements</b>	<b>i</b>
<b>Abstract (English/Français)</b>	<b>v</b>
<b>List of Figures</b>	<b>xv</b>
<b>List of Tables</b>	<b>xxix</b>
<b>Introduction</b>	<b>1</b>
<b>I Neutrinos and T2K</b>	<b>3</b>
<b>1 Neutrinos in the Standard Model and beyond</b>	<b>5</b>
1.1 A brief history of neutrino discovery . . . . .	5
1.1.1 Mysterious $\beta$ decays . . . . .	5
1.1.2 First detections . . . . .	6
1.1.3 Subsequent discoveries . . . . .	6
1.2 Neutrinos and the Standard Model . . . . .	7
1.2.1 Standard Model of particle physics . . . . .	7
1.2.2 Electroweak Lagrangian . . . . .	8
1.2.3 Neutrino mass problem . . . . .	14
1.2.4 Experimental measurements and constraints . . . . .	16
1.3 Neutrino oscillations . . . . .	19
1.3.1 A brief history of neutrino oscillation discovery . . . . .	19
1.3.2 General three-flavor neutrino oscillation probability . . . . .	24
1.3.3 Discussion . . . . .	29
1.3.4 Neutrino oscillations in matter . . . . .	35
1.4 Experimental status . . . . .	40
1.4.1 Open questions in the PMNS paradigm . . . . .	40
1.4.2 Solar sector . . . . .	41
1.4.3 Atmospheric sector . . . . .	42
1.4.4 Measurement of $\theta_{13}$ . . . . .	43
1.4.5 Measurement of $\delta_{\text{CP}}$ . . . . .	43
	ix

## Contents

---

<b>2</b>	<b>T2K experiment</b>	<b>47</b>
2.1	Beamline . . . . .	48
2.1.1	Primary beamline . . . . .	48
2.1.2	Secondary beamline . . . . .	49
2.1.3	Off-axis angle . . . . .	50
2.1.4	Neutrino flux prediction . . . . .	52
2.2	Near detectors . . . . .	53
2.2.1	INGRID . . . . .	55
2.2.2	ND280 . . . . .	55
2.2.3	WAGASCI/BabyMIND . . . . .	60
2.2.4	ND280 upgrade . . . . .	61
2.3	Far detector: Super-Kamiokande . . . . .	61
2.4	Physics results . . . . .	64
2.4.1	Data . . . . .	64
2.4.2	Oscillation measurements . . . . .	64
2.4.3	Cross-section measurements . . . . .	64
<b>II</b>	<b>Neutrino scattering</b>	<b>67</b>
<b>3</b>	<b>Modeling neutrino-nucleus interactions</b>	<b>69</b>
3.1	Neutrino-nucleon scattering . . . . .	69
3.1.1	Quasielastic interactions . . . . .	70
3.1.2	Single-pion production . . . . .	74
3.1.3	Deep inelastic scattering . . . . .	77
3.2	Neutrino-nucleus scattering . . . . .	78
3.2.1	Impulse approximation . . . . .	78
3.2.2	Nuclear ground state . . . . .	78
3.2.3	Beyond the impulse approximation . . . . .	82
3.3	Neutrino event generators . . . . .	88
3.4	Neutrino energy reconstruction . . . . .	89
3.4.1	Kinematic method . . . . .	89
3.4.2	Calorimetric method . . . . .	90
3.4.3	Impact on oscillation measurements . . . . .	91
<b>4</b>	<b>Uncertainties in the charged-current quasielastic interactions</b>	<b>93</b>
4.1	Cross-section measurements . . . . .	94
4.1.1	Extracting a cross section . . . . .	94
4.1.2	CC0 $\pi$ measurements on carbon and oxygen . . . . .	96
4.2	Systematic uncertainties . . . . .	98
4.2.1	Event reweighting . . . . .	98
4.2.2	Novel shell-model uncertainties . . . . .	99
4.2.3	Additional CC0 $\pi$ uncertainties . . . . .	107

4.3	Fits to cross-section measurements . . . . .	110
4.3.1	Fit method . . . . .	112
4.3.2	Fit results . . . . .	115
4.4	Implications for oscillation analyses . . . . .	123
<b>III</b>	<b>Upgraded near detectors</b>	<b>129</b>
<b>5</b>	<b>T2K near detector upgrade</b>	<b>131</b>
5.1	Limitations of the current ND280 . . . . .	131
5.2	Subdetectors . . . . .	133
5.2.1	Super-FGD . . . . .	133
5.2.2	High-angle time projection chambers . . . . .	139
5.2.3	Time-of-flight detector . . . . .	142
5.3	Tests and prototypes . . . . .	143
5.3.1	Super-FGD prototypes . . . . .	144
5.3.2	Beam tests of the high-angle time projection chambers . . . . .	146
5.3.3	Performance of the time-of-flight detector . . . . .	147
5.4	Expected physics performance . . . . .	148
5.4.1	Muons . . . . .	148
5.4.2	Protons . . . . .	149
5.4.3	Neutrons . . . . .	149
5.4.4	New observables . . . . .	152
<b>6</b>	<b>Electronics of the Super-FGD</b>	<b>155</b>
6.1	Architecture of the electronics in the Super-FGD . . . . .	155
6.1.1	From the neutrino interaction to the front-end boards . . . . .	155
6.1.2	From the front-end boards to the data . . . . .	157
6.2	Performance tests of the FEB . . . . .	160
6.2.1	Overview . . . . .	160
6.2.2	Analog calibration . . . . .	163
6.2.3	Linearity . . . . .	170
6.2.4	Channel-to-channel cross talk . . . . .	173
6.2.5	Timing . . . . .	177
6.3	Tests in a magnetic field . . . . .	182
6.4	Other ongoing tests . . . . .	189
6.4.1	Integration tests . . . . .	189
6.4.2	FEB functional tests . . . . .	190
<b>IV</b>	<b>Oscillation measurements</b>	<b>191</b>
<b>7</b>	<b>T2K oscillation analysis</b>	<b>193</b>
7.1	Overview . . . . .	193

## Contents

---

7.2	Data selection . . . . .	196
7.2.1	Monte-Carlo simulations . . . . .	197
7.2.2	Near-detector selection . . . . .	197
7.2.3	Far-detector selection . . . . .	199
7.3	Systematic uncertainties . . . . .	201
7.3.1	Flux . . . . .	201
7.3.2	Detector response . . . . .	202
7.3.3	Neutrino interactions . . . . .	207
7.4	Fitting frameworks . . . . .	212
7.4.1	Likelihoods . . . . .	215
7.4.2	Fitting tools . . . . .	218
7.5	Results of the 2022 oscillation analysis . . . . .	220
7.5.1	Near-detector analysis . . . . .	220
7.5.2	Far-detector analysis . . . . .	227
7.5.3	Impact of alternative neutrino interaction models . . . . .	234
7.6	Summary . . . . .	235
<b>8</b>	<b>GUNDAM: a new fitting framework</b>	<b>237</b>
8.1	Overview . . . . .	237
8.2	Reproducing the 2020 oscillation analysis . . . . .	239
8.2.1	Prefit event rates . . . . .	239
8.2.2	Varied event rates . . . . .	240
8.2.3	Likelihood scans . . . . .	243
8.2.4	Fits . . . . .	244
8.3	Reproducing the 2022 oscillation analysis . . . . .	252
8.4	Ongoing developments and prospects . . . . .	256
<b>9</b>	<b>T2K future sensitivity</b>	<b>259</b>
9.1	New samples with the upgraded near detector . . . . .	259
9.1.1	Simulating the upgrade . . . . .	259
9.1.2	Observables . . . . .	260
9.1.3	Event rates . . . . .	262
9.2	Impact on the near-detector fit . . . . .	263
9.2.1	Assumptions . . . . .	263
9.2.2	Results . . . . .	266
9.3	Sensitivity to constrain oscillation parameters . . . . .	274
9.3.1	FGD1+2-only near-detector configuration . . . . .	274
9.3.2	Towards the use of constraints from the near-detector upgrade . . . . .	287
9.4	Prospects . . . . .	292
	<b>Conclusion</b>	<b>295</b>
<b>A</b>	<b>Projected constraints on other flux and cross-section uncertainties</b>	<b>299</b>

	<b>Contents</b>
<b>B Three-variable correlations</b>	<b>305</b>
<b>References</b>	<b>307</b>





# List of Figures

1.1	Summary of the elementary particles and their interaction mediators in the Standard Model. Adapted from Reference [9]. . . . .	8
1.2	Feynman diagrams for CC interactions described by Equation (1.7). . . . .	11
1.3	Feynman diagrams for NC interactions described by Equations (1.11) and (1.12). . . . .	12
1.4	Left: schematic representation of the Wu experiment. It measured the rate of decay $e^-$ in two mirrored setups with respect to the spin $\vec{s}$ of the $^{60}\text{Co}$ nucleus. Right: Results of the experiment from Reference [16], comparing the rate when counting the electrons emitted in the opposite direction of $\vec{s}$ ( $\times$ ) and in the same direction ( $\bullet$ ). The asymmetry decreases as a function of time due to the increase of the temperature which randomizes the spin direction. . . . .	17
1.5	Measurement of the hadron cross sections around the Z resonance at the LEP compared to different scenarios of $N_\nu = 2, 3, 4$ . Figure from Reference [17]. . . . .	18
1.6	Feynman diagrams for double beta decays for two initial state neutrons ( $udd$ ) decaying into protons ( $uud$ ). Neutrinoless double beta decay (right) would occur if neutrinos are Majorana particles (i.e. $\nu = \bar{\nu}$ ). . . . .	19
1.7	The predicted solar neutrino flux in $\text{cm}^{-2}\text{s}^{-1}\text{MeV}^{-1}$ for continuum sources and $\text{cm}^{-2}\text{s}^{-1}$ for line sources along with the theoretical errors (left) produced by the different reactions in the $pp$ -chain (right). Figure from Reference [23]. . . . .	21
1.8	Results of the SNO experiment. Figure from Reference [24]. . . . .	21
1.9	Left: schematic representation of the different neutrino directions measured in Super-Kamiokande, from Reference [35]. Right: atmospheric shower produced by a cosmic ray. . . . .	23
1.10	Zenith angle distributions of $\nu_e$ -like (top) and $\nu_\mu$ -like (bottom) events for sub-GeV (left) and multi-GeV (right) data set, separated by regions in the reconstructed charged lepton momentum. The multi-GeV $\nu_\mu$ -like samples are shown separately for fully contained and partially contained events. The hatched region shows the Monte Carlo expectation for no oscillations normalized to the data live-time with statistical errors. The bold line is the best-fit expectation for $\nu_\mu \leftrightarrow \nu_\tau$ oscillations with the overall flux normalization fitted as a free parameter. Figure from Reference [34]. . . . .	23
1.11	Left: location of KamLAND and nuclear reactors (blue circles), from Reference [38]. Right: survival probability of electron antineutrinos as a function of the ratio $L_0/E_{\bar{\nu}_e}$ , from Reference [37]. . . . .	24

## List of Figures

---

1.12	Comparison of a plane wave (left) and a Gaussian wave packet (right) in space.	27
1.13	Muon neutrino oscillation probabilities in vacuum using global best-fit values of oscillation parameters shown in Table 1.3 for large (left) and small (right) $L/E$ .	32
1.14	Feynman diagrams for CC interactions of electron (anti)neutrinos with electrons (left and center) and NC interactions of all (anti)neutrino flavors with $X = n, p, e^-$ (right).	35
1.15	Variation of $\sin^2 2\vartheta_m$ (left) and the effective masses $m_{m,i}^2$ assuming $m_1^2 = 0$ and $m_2^2 = 10^{-5} \text{ eV}^2$ (right) as a function of $\kappa$ for values of $\sin^2 2\vartheta$ ranging from 0.01 (pink) to 0.4 (cyan).	39
1.16	Illustration of the normal (left) and inverted (right) mass orderings. The flavor share of each mass state is also displayed.	41
1.17	Left: electron and muon neutrino disappearance probability in vacuum. Right: electron antineutrino disappearance probability in vacuum for the normal and inverted orderings.	42
1.18	Latest constraints at 90% C.L. on the atmospheric parameters in normal ordering from the T2K [61], Super-Kamiokande [63], MINOS+ [60], NOvA [62] and IceCube [64] experiments.	43
1.19	Latest constraints at 68% and 90% C.L. on $\delta_{CP}$ and $\sin^2 \theta_{13}$ from the T2K experiment with (magenta) and without (cyan) constraints from reactor experiments on $\theta_{13}$ from Reference [12].	45
1.20	Latest constraints at 90% C.L. on $\delta_{CP}$ and $\sin^2 \theta_{23}$ in normal (left) and inverted (right) ordering from the T2K [61], Super-Kamiokande [63] and NOvA [62] experiments.	45
2.1	Overview of the T2K experiment.	48
2.2	Overview of the T2K neutrino beamline.	49
2.3	Side view of the secondary beamline. In this view, protons travel from the left to the right.	50
2.4	Breakdown of the neutrino flux at ND280 in the FHC (left) and RHC (right) modes. Figure from Reference [78].	52
2.5	Left: neutrino energy from two-body pion decay as a function of the pion momentum for different values of the off-axis angle $\theta_{OA}$ . Right: T2K neutrino flux for different off-axis angles (bottom) and the corresponding muon neutrino disappearance probability which is maximal at 600 MeV. Right panel from Reference [77].	53
2.6	Breakdown of the neutrino flux at ND280 in the FHC (left) and RHC (right) modes. Figure from Reference [78].	54
2.7	The T2K near detector complex (left) and an exploded view of the ND280 off-axis detector (right). Figure from Reference [86].	55
2.8	Illustrations of the INGRID setup.	56
2.9	Left: tracking planes and iron plates of an INGRID module. Right: veto planes surrounding the INGRID module.	56

2.10	Example of an ND280 event display showing a highly inelastic neutrino interaction in FGD1 producing multiple tracks, and an unrelated muon track (likely a cosmic muon) going through the PØD and the tracker. The beam direction is from the left to the right. . . . .	57
2.11	Left: schematic view of a TPC of ND280. Right: illustration of the principle of the standard bulk MicroMegas (not to scale). Left panel from Reference [86]. . . . .	59
2.12	Left: setup of the WAGASCI-BabyMIND detector. Right: exploded view of the proton module. . . . .	61
2.13	Schematic illustration of Super-Kamiokande. Figure from Reference [97]. . . . .	62
2.14	Distribution of the particle identification (PID) parameter used to discriminate between electron-like and muon-like Čerenkov rings. Figure from Reference [53]. . . . .	63
2.15	History of the delivered protons on target (POT) and the beam power since the start of the T2K experiment. . . . .	64
3.1	Muon neutrino cross section on hydrocarbon as a function of the neutrino energy, broken down by interaction mode and compared to the energy spectrum from neutrino experiments. . . . .	70
3.2	Example of Feynman diagrams for $\nu_\mu$ and $\bar{\nu}_\mu$ CCQE interactions. . . . .	72
3.3	Example of Feynman diagrams for $\nu_\mu$ and $\bar{\nu}_\mu$ CC single-pion production via intermediate $\Delta(1232)$ resonances. . . . .	75
3.4	Non-resonant pion production Feynman diagrams. Figure from [151]. . . . .	76
3.5	Feynman diagram of a CCDIS interaction with a nucleon. . . . .	77
3.6	Left: comparison of the spectral-function distributions between the relativistic Fermi gas (RFG), the local Fermi gas (LFG) and the Benhar Spectral Function (SF) models for carbon using the NEUT event generator. The SF model captures the complex nuclear structure, featuring the sharp $p$ -shell at $E_m \sim 18$ MeV and the diffuse $s$ -shell around $E_m \sim 35$ MeV. Right: comparison of the missing-momentum distribution between the three models. . . . .	82
3.7	Double differential cross section of the quasielastic peak for electron scattering on carbon $\frac{d\sigma}{d\omega d\Omega_e}$ from various experimental data. As a reference, the dotted blue lines and the purple long-dashed lines correspond to the RFG model and the SF model respectively in the IA formalism without any FSI corrections. The solid red and short-dashed orange lines show the result of the corrected SF-model cross section according to Equation (3.13), the former using the LDA-based Pauli blocking of Equation (3.9) while the latter uses the step-function Pauli blocking of Equation (3.8). The panels are labeled according to the beam energy, the scattering angle, and the values of $ \vec{q} $ and $Q^2$ respectively. Figure from Reference [167] . . . . .	84

## List of Figures

---

3.8	Comparison of various models with the MiniBooNE CCQE-like cross-section measurement on carbon of Reference [170]. A good agreement with the data is only achieved with a significantly high value of $M_A$ at tension with bubble chamber data, or when taking into account 2p2h contributions. Figure from Reference [171]. . . . .	85
3.9	Diagrams of coupling to a pair of correlated nucleons, also called the nucleon-nucleon correlations in the 2p2h processes. The SF model takes this contribution into account in its SRC prediction. . . . .	86
3.10	Diagrams of the meson exchange currents of 2p2h processes. Solid (dashed) lines denote nucleons (pions), whereas double lines represent $\Delta(1232)$ . The top row corresponds to the so-called contact term and the pion-in-flight diagrams, the middle row to the pion-pole diagrams, and the bottom row to the coupling to a delta resonance. Adapted from Reference [172]. . . . .	86
3.11	Cross section of 2p2h on carbon as a function of the neutrino energy from the Nieves et al. (black) and the Martini et al. (red) models for neutrinos (filled circles) and antineutrinos (empty circles). Figure from Reference [175]. . . . .	87
3.12	Resolution and bias of the neutrino energy estimator $E_\nu^{\text{QE}}$ for all CC events (left) and for CC0 $\pi$ events (right) with the contributions from the different interaction modes using the T2K neutrino flux with the NEUT event generator. . . . .	90
3.13	Left: resolution and bias of the neutrino energy estimator $E_\nu^{\text{QE}}$ for CCQE events when using RFG, LFG and SF models. Right: resolution and bias of $E_\nu^{\text{cal}}$ for all CC events with the contributions from events with (blue) and without (red) neutrons in the final state using the MINERvA flux (shown in Figure 3.1) with the NEUT event generator. . . . .	91
4.1	Distribution of the true and reconstructed muon momentum in ND280. . . . .	95
4.2	Schematic representation of the single-transverse variables. Figure from Reference [224]. . . . .	97
4.3	NEUT prediction of the two-dimensional distribution of the missing energy and the missing momentum for carbon (left) and oxygen (right). The brightness of the color represents the probability of finding an initial-state nucleon with a particular removal energy and momentum state. The white lines indicate the cuts used to separate the MF region (low $E_m, p_m$ ) from the SRC region (high $E_m, p_m$ ) in NuWro (dashed) and NEUT (full). . . . .	100
4.4	Distribution of the missing momentum within each shell for carbon. . . . .	101
4.5	Impact of the shell normalization parameter $N_{\text{shell}}$ on the total CCQE cross section for each shell in carbon (left) and oxygen (right). The dashed horizontal lines indicate the $\pm 10\%$ variations, chosen to correspond to the $1\sigma$ error for these parameters. . . . .	102
4.6	Variations of the shell normalizations from $-1.5\sigma$ to $+1.5\sigma$ in $E_m$ (left) and the impact on $\delta p_T$ (right) compared to the nominal distributions (black). . . . .	102

4.7	Distributions of the missing momentum from the NEUT SF inputs (black) compared to electron scattering measurements (blue and red) made for different nucleon and lepton kinematics for carbon in the $p$ -shell (left) and the $s$ -shell (right). The data is from Reference [226] . . . . .	104
4.8	Impact of varying the $p$ -shell shape uncertainty from $-2\sigma$ (pink) to $2\sigma$ (cyan) on $\cos\theta_\mu$ (left) and on $\delta p_T$ (right) compared to nominal distributions (black) for carbon. . . . .	104
4.9	Distribution of the missing momentum in the SF model in NEUT (left) and in NuWro (right) for carbon with the MF and SRC contributions. . . . .	105
4.10	Impact of varying the PB threshold from $-1.5\sigma$ (cyan) to $+1.5\sigma$ (pink) on the pre-FSI nucleon momentum (top), $\cos\theta_\mu$ (bottom left) and on the muon momentum in the forward region for $\cos\theta_\mu > 0.9$ (bottom right) compared to the NEUT nominal distributions (black). . . . .	106
4.11	Comparison of the two-dimensional distributions predicted by NuWro of $(q_0,  \vec{q} )$ with (top right) and without (top left) applying the OP-based FSI correction, as well as their ratio (bottom). . . . .	108
4.12	Impact of applying OP correction from 0%, i.e. nominal, (black) to 100% (orange) on $\cos\theta_\mu$ (left) and on the muon momentum in the forward region for $\cos\theta_\mu > 0.9$ (right). . . . .	108
4.13	Correlations between the three parameters of the Rein – Sehgal model obtained from fits to ANL [145] and BNL [146] data. . . . .	110
4.14	Two-dimensional distribution of energy and momentum transfer (left) and the neutrino energy bias broken down by $\Delta$ -like and non- $\Delta$ -like contributions (right) as predicted by the 2p2h Nieves et al. model implemented in NEUT. . . . .	112
4.15	Left: manifestation of Peelle's pertinent puzzle when fitting the MINERvA $\delta p_T$ data by minimizing the chi-square given by Equation (4.3). Right: the bin-to-bin correlation matrix in the $\delta p_T$ measurement of MINERvA. . . . .	113
4.16	Prefit (red) and postfit (blue) distributions of $p_\mu$ in bins of $\cos\theta_\mu$ from the fit to T2K CC0 $\pi$ joint measurement of lepton kinematics on carbon and oxygen. The usual chi-squares as well as the number of bins are quoted in the legend. The NS chi-square $\chi^2_{\text{NS}}$ used in the minimization is reported in Table 4.3. . . . .	116
4.17	Prefit (red) and postfit (blue) values and constraints on the uncertainties from the fit to T2K CC0 $\pi$ joint measurement of lepton kinematics on carbon and oxygen. . . . .	117
4.18	Postfit correlation matrix from the fit to T2K CC0 $\pi$ joint measurement of lepton kinematics on carbon and oxygen. . . . .	117
4.19	Neutrino energy distribution from the T2K beam for the CC0 $\pi$ 0 $p$ (blue) and CC0 $\pi$ $Np$ (red) topologies. . . . .	119
4.20	Prefit (red) and postfit (blue) distributions of $\delta p_T$ from fitting the T2K CC0 $\pi$ $Np$ data only. The usual chi-squares as well as the number of bins are quoted in the legend. The NS chi-square $\chi^2_{\text{NS}}$ used in the minimization is reported in Table 4.3. . . . .	120

## List of Figures

---

4.21	Prefit (red) and postfit (blue) distributions of $p_\mu$ in bins of $\cos\theta_\mu$ from fitting T2K CC0 $\pi$ 0 $p$ data only. The usual chi-squares as well as the number of bins are quoted in the legend. The NS chi-square $\chi^2_{\text{NS}}$ used in the minimization is reported in Table 4.3. . . . .	121
4.22	Prefit (red) and postfit (blue) values and constraints on the uncertainties from the fit to T2K CC0 $\pi$ 0 $p$ measurement of lepton kinematics and CC0 $\pi$ $Np$ measurement of $\delta p_T$ on carbon. . . . .	122
4.23	Postfit correlation matrices from the fit to T2K CC0 $\pi$ 0 $p$ measurement of lepton kinematics (top left) and CC0 $\pi$ $Np$ measurement of $\delta p_T$ (top right), as well as the simultaneous fit (bottom). . . . .	122
4.24	Left: prefit (red) and postfit (blue) distributions from the fit to MINERvA CC0 $\pi$ $Np$ measurement of $\delta p_T$ on carbon. The usual chi-squares as well as the number of bins are quoted in the legend. The NS chi-square $\chi^2_{\text{NS}}$ used in the minimization is reported in Table 4.3. Right: postfit correlation matrix between the parameters for the same fit. . . . .	124
4.25	Prefit (red) and postfit (blue) values and constraints on the uncertainties from the fit to MINERvA CC0 $\pi$ $Np$ measurement of $\delta p_T$ on carbon. . . . .	124
4.26	Prefit (red) and postfit (blue) constraints on the true neutrino energy (top) and the bias of $E_\nu^{\text{QE}}$ (bottom) for carbon from the fit to the T2K CC0 $\pi$ joint measurement of lepton kinematics on carbon and oxygen. The plots on the left show the overall constraint on the cross section, while the plots on the right indicate the constraint on the shape of the distribution. . . . .	127
5.1	Reconstruction efficiency of the muon as a function of the cosine of its angle with respect to the neutrino direction in the CC0 $\pi$ selection (left) and of the proton as a function of its momentum in the CC0 $\pi$ $Np$ selection (right) in the current ND280 (blue) compared to the NEUT-predicted distributions (green). . . . .	132
5.2	Two-dimensional distributions of the reconstructed momentum and angle of the charged lepton from $\nu_\mu$ interactions at ND280 (left) and $\nu_e$ interactions at Super-Kamiokande (right). . . . .	133
5.3	Illustrations of the near detector upgrade in an exploded view (top) and within the ND280 basket where one of the ToF panels is not shown to display the inner components of the detector (bottom). The neutrino beam comes from the left to the right. . . . .	134
5.4	Comparison of the XY bars used the FGDs (left) and the novel concept of cubes in the Super-FGD (right). Figure from Reference [242]. . . . .	136
5.5	Schematic representation of the Super-FGD. Figure from Reference [243]. . . . .	136
5.6	Left: the three two-dimensional views of a neutrino interaction the Super-FGD. Right: the reconstructed tracks in three dimensions. Figure from Reference [241]	136
5.7	Preassembly of the Super-FGD layers with fishing lines. Credits: M. Khabibullin.	138
5.8	Assembly operation of the Super-FGD cubes into the mechanical box. . . . .	138
5.9	Light guide plate for the gain calibration of the Super-FGD electronics. . . . .	138

5.10 Super-FGD with its cabled photosensor boards. . . . .	139
5.11 Illustration of the HA-TPC design. Figure from Reference [243]. . . . .	141
5.12 Left: standard bulk Micromegas used in the existing TPCs. Right: resistive Micromegas with the additional insulating layer. Figure from Reference [243]. . .	141
5.13 Exploded view of an ERAM module with its mechanical structure and readout electronics. Adapted from Reference [243]. . . . .	141
5.14 Left: printed circuit board with the 8 photosensors (top) and its setup on one end of the scintillator bar (bottom). Right: picture of the assembled ToF panels. Figure from Reference [247]. . . . .	143
5.15 Pictures of the $24 \times 8 \times 48$ prototype (left) and the US-Japan prototype (right). .	145
5.16 Event display from the three readout planes of a stopping proton (top) and a photon interaction (bottom). Figure from Reference [249]. . . . .	145
5.17 Energy loss along the beam direction (left) and the average energy deposit (right) for protons, pions and muons at 800 MeV/c. Figure from Reference [249]. . . .	145
5.18 The total neutron-CH cross section as a function of the neutron kinetic energy, where the black (red) vertical bars represent the total (statistical) uncertainty. Figure from Reference [251]. . . . .	146
5.19 Spatial resolution (left) and energy loss resolution (right) as a function of the drift distance for the tested particles. Figure from Reference [252]. . . . .	147
5.20 Left: setup to test the timing resolution from a single ToF bar. Right: timing resolution obtained from the photosensors at each end of the bar separately (blue and orange) and their weighted average (green). . . . .	148
5.21 Top: reconstruction efficiency of the muon as a function of the cosine of its angle with respect to the neutrino direction (left) and of the proton as a function of its momentum (right) for the current (blue) and the upgraded (black) ND280, compared to the NEUT-predicted distributions (green). Bottom: two-dimensional distributions of the reconstructed momentum and angle of the charged lepton from $\nu_\mu$ interactions at the current (left) and upgraded (right) ND280. . . . .	150
5.22 Two-dimensional distributions of the true vs. reconstructed momentum for various particles in ND280 and as expected in the upgrade. . . . .	151
5.23 Schematic illustration of the measurement of the neutron kinematics using their time-of-flight. Figure from Reference [255]. . . . .	151
5.24 Distribution of $\delta p_T$ for neutrinos (left) and antineutrinos (right) in the $CC0\pi Np$ topology, broken down by the type of contribution. Figure from Reference [240].	152
5.25 Left: distribution of $\delta\alpha_T$ for the $CC0\pi Np$ neutrino interactions at the truth level (shaded) where the contribution from events with (red shade) and without FSI (blue shade) is highlighted, compared to the current ND280 (red line) and the Super-FGD (blue line). Right: $E_{\text{vis}}$ (full) and $E_{\text{vis}}^{\text{QE}}$ (dashed) bias to estimate the true neutrino energy $E_\nu$ , with the impact of a global $\pm 10$ MeV shift to the removal energy. Figure from Reference [240]. . . . .	153



## List of Figures

---

6.1	Left: zoomed-in picture of the Hamamatsu MPPC S13360-1325CS used in the Super-FGD. The pixelized area is of size $1.3 \times 1.3 \text{ mm}^2$ . Right: picture of the MPPC64 board ( $83.8 \times 83.8 \text{ mm}^2$ ) designed for the Super-FGD which contains 64 of the MPPCs displayed in the left panel. Credits: T. Kutter. . . . .	156
6.2	Schematic illustration of the Super-FGD electronics. . . . .	157
6.3	Top: picture of the top side of the FEB. Bottom: simplified diagram of a CITIROC channel. . . . .	158
6.4	Schematic illustrations of the MIB (left) and a crate with two FEBs (right). . . .	159
6.5	Setup for single-channel injection tests with a pulsed LED and an MPPC (top) or with a filtered pulse from a waveform generator (bottom). . . . .	162
6.6	Left: high-pass RC circuit used with the pulse generator such that $R = 50 \text{ } \Omega$ and $C = 100 \text{ pF}$ . Right: the leading edge of the waveform generator with a characteristic time of 10 ns (blue) and the corresponding RC circuit output (red). . . . .	162
6.7	Example of the distribution of the amplitude recorded in a single channel receiving a signal from an MPPC with LED light injection in the raw HG ADC counts (left) and in p.e. units after calibration (right). An excellent peak-to-valley ratio is achieved thanks to the low noise obtained with the FEB design. . . . .	163
6.8	Example of the HG amplitude distribution for different values of the HG gain in one channel. . . . .	166
6.9	Example of linear fits to the photoelectron peak positions for different values of the HG gain in one channel. The pedestal is obtained at the intersection of the lines, which corresponds to the amplitude of the 0 photoelectron position. . . .	166
6.10	Stacked histogram of the pedestal position for all the 256 channels. . . . .	167
6.11	Stacked histogram of the HG ADC Count to photoelectron ratio for all the 256 channels with different values of the HG gain. . . . .	168
6.12	HG versus LG amplitudes for all the 256 channels. . . . .	169
6.13	Left: stacked histogram of the LG to HG ratio for all the 256 channels (preamplifier settings: HG 55 and LG 61). Right: stacked histogram of the amplitude of the HG saturation across all the 256 channels. The saturation can also be distinguished for the CITIROCs separately in Figure 6.12. . . . .	169
6.14	Data rate of the FEB as a function of the threshold set on the ASIC for channel 0 with the MPPC dark noise. . . . .	170
6.15	Example of the measured mapping between the injected amplitude and the measured ADC count in the HG (top) and the LG (bottom) in a single channel for different preamplifier gain values. Credits: L. Giannessi. . . . .	171
6.16	The maximum linear response point in ADC counts for different gain settings in the HG (blue) and the LG (orange), averaged over the 256 channels of the FEB. . . .	172
6.17	Amplitude observed in channel 1 when $\sim 1200$ p.e. charge is injected in channel 0 (red) compared to when no light is injected, i.e. pedestal (blue). . . . .	174
6.18	Channel-to-channel cross talk matrix for MIBv1 (top) and MIBv2 (bottom). A charge of $\sim 1200$ p.e. is injected in the injection channel. . . . .	175

6.19	Layout of parts of the MIB that might be responsible for the cross talk (MIBv1). Top: two traces on adjacent layers with no separation layer. Bottom: traces on the same layer around the 400-pin MIB-to-FEB connector. . . . .	176
6.20	Distributions of the timing difference between two successive rising edges in one channel of the FEB, with the period of the signal $\Delta T_{\text{gen}}$ as set on the pulse generator, and the mean of the distribution $\Delta T_{\text{mes}}$ as the measured timing dif- ference. . . . .	178
6.21	Sketch of the setup used to measure the timing difference between the channels.	179
6.22	Timing difference between the channel 0 and the other 31 channels of the ASIC 0 as simulated by the FPGA programming software (dashed) and measured from the FEB data (full) for the version of the FPGA firmware where the timing trigger lines are not matched (pink) and when matched within $\pm 150$ ps (cyan). . . . .	180
6.23	Timing difference between the channel 0 and the other 255 channels of the FEB as measured from the data (full) and simulated by the FPGA programming software (dashed) with the firmware where timing trigger lines are matched within $\pm 150$ ps. . . . .	181
6.24	Points of probe with the oscilloscope on the FEB. P1 and P2 correspond to a probe at the input of the CITIROC, P3 and P4 to its output, which is also the input to the level shifters, and P5 and P6 to their output. The signals flow from the left (where the MIB is connected) to the right. . . . .	183
6.25	The signals probed with the oscilloscope both at P1 and P2 (top), as well as P3 and P4 (bottom) for channels 169 and 185. . . . .	183
6.26	Picture of the FEB setup in the MNP17 magnet at CERN. . . . .	184
6.27	Different FEB configurations tested in the MNP17 magnet (pink). The top row corresponds to the magnetic field that will be experienced by the FEBs in the Super-FGD setup within the UA1 magnet, while the bottom two configurations are tested as well although they do not reflect any considered Super-FGD setting.	185
6.28	Examples of HG amplitude distributions for a few channels in linear (left) and logarithmic (right) scales compared between the reference 0 T field (red) and the other tested configurations (blue) shown in Figure 6.27. Note that the light source used in this test does not provide a uniform light distribution on all the four MPPC64 channels. . . . .	187
6.29	Linearity of the FEB channel 96 in the HG (left) and the LG (right) amplitudes for the ND280 nominal 0.2 T (top row) as well as 0.4 T field (middle row) in the $\pm x$ -axis configuration, and the $y$ - and $z$ -axis settings at 0.4 T (bottom row) for different gain settings of the CITIROC HG and LG preamplifiers. . . . .	188
6.30	Picture of the first fully populated crate with all the electronic boards in the VST.	190
7.1	Impact of varying $\delta_{\text{CP}}$ on the observed $\nu_e$ (left) and $\bar{\nu}_e$ (right) event rate at Super- Kamiokande as a function of the true neutrino energy $E_\nu$ assuming normal ordering. . . . .	194

## List of Figures

---

7.2	Impact of varying $\Delta m_{32}^2$ (left) and $\theta_{23}$ (right) from the T2K best fit values (black) to the corresponding 90% C.L. limits values (red and cyan) on the observed $\nu_\mu$ event rate at Super-Kamiokande as a function of the true neutrino energy. . . .	195
7.3	One-dimensional projection on the prefit muon momentum distribution in the FHC FGD1 $\nu_\mu$ CC0 $\pi$ 0 $p$ 0 $\gamma$ (left) and the FHC FGD2 $\nu_\mu$ CC0 $\pi$ 0 $p$ 0 $\gamma$ (right) samples. . . .	200
7.4	Left: two-dimensional distribution of the events in the FHC 1R $\mu$ sample in the reconstructed neutrino energy $E_\nu^{\text{reco}}$ based on the CCQE assumption given by Equation (3.15) and the reconstructed charged lepton angle. Right: two-dimensional distribution of the events in the FHC 1Re sample in the reconstructed charged lepton momentum and its angle. . . . .	202
7.5	Prefit correlation matrix of the 100 flux parameters. Each parameter corresponds to a normalization in a bin of the true neutrino as given by Table 7.3. . . . .	204
7.6	Correlation matrix between the 552 “ObsNorm” parameters of the uncertainty on the ND280 response. . . . .	205
7.7	Prefit correlation matrix of the pion FSI parameters. . . . .	212
7.8	One-dimensional projection on the postfit muon momentum distribution in the FHC FGD1 $\nu_\mu$ CC0 $\pi$ 0 $p$ 0 $\gamma$ (left) and the FHC FGD2 $\nu_\mu$ CC0 $\pi$ 0 $p$ 0 $\gamma$ (right) samples. . . .	220
7.9	Prefit (red) and postfit (black) values and constraints on flux and cross-section parameters. . . . .	221
7.10	Prefit (left) and postfit (right) correlation matrices of the flux and cross-section parameters. . . . .	222
7.11	Postfit correlation matrix of the cross-section parameters. . . . .	222
7.12	Comparison between the BANFF postfit and the results of fitting the joint T2K cross-section measurement on oxygen and carbon in the CC0 $\pi$ (top) and the T2K cross-section measurement on carbon in the CC0 $\pi$ 0 $p$ and the CC0 $\pi$ N $p$ topologies (bottom) as described in Chapter 4. . . . .	225
7.13	Distribution of the pseudo-experiment postfit negative log-likelihoods (or $\Delta\chi^2$ ) compared to the data postfit negative log-likelihood (vertical red line). The fraction of the pseudo-experiments above the red line gives the $p$ -value. . . . .	228
7.14	Impact of the near-detector tuning and constraints on the distribution the reconstructed neutrino energy in the FHC mode for the 1R $\mu$ (left) and the 1Re samples. The oscillation parameters are evaluated close to the T2K best fit values from the previous analysis. . . . .	230
7.15	Fixed- $\Delta\chi^2$ two-dimensional confidence level contours in $\Delta m_{32}^2$ ( $ \Delta m_{31}^2 $ for inverted ordering) vs. $\sin^2 \theta_{23}$ for normal (cyan) and inverted (magenta) ordering with (right) and without (left) reactor constraints of Reference [12]. . . . .	233
7.16	One-dimensional negative log-likelihood in $\delta_{\text{CP}}$ for normal (blue) and inverted (orange) ordering using reactor constraints of Reference [12], and the shaded regions correspond to confidence levels obtained with the Feldman – Cousins method. . . . .	233
7.17	Postfit CCQE parameters from a near-detector fit with BANFF to the simulated data corresponding to the HF+CRPA model. . . . .	235

8.1	Simplified structure of GUNDAM. Credits: A. Blanchet. . . . .	238
8.2	One example of the 712 likelihood scan comparisons of the statistical part $-2\log\mathcal{L}_{\text{stat}}$ (left) and the penalty term $-2\log\mathcal{L}_{\text{sys}}$ (center) separately, as well as the total likelihood $-2\log\mathcal{L}_{\text{tot}}$ (right) for the $M_A^{\text{QE}}$ parameter. . . . .	243
8.3	Flux parameters compared between BANFF and GUNDAM for the OA2020 Asimov fit. . . . .	245
8.4	Cross-section parameters compared between BANFF and GUNDAM for the OA2020 Asimov fit. Parameters with no GUNDAM postfit errors are fixed in the fits. . . . .	246
8.5	Illustration of extending a weight function $f(\lambda)$ beyond its physical boundaries $[a, b]$ (red) to $f_{\text{mirr}}(\lambda)$ defined on a larger interval $[2a - b, 2b - a]$ by mirroring as shown in Equation (8.2) (blue). The cubic spline interpolation used in the fit is also displayed (black). . . . .	247
8.6	Flux parameters compared between BANFF and GUNDAM for the OA2020 data fit. . . . .	248
8.7	Cross-section parameters compared between BANFF and GUNDAM for the OA2020 data fit. Parameters with no GUNDAM postfit errors are fixed in the fits. . . . .	249
8.8	One-dimensional sensitivity $\Delta\chi^2$ in $\Delta m_{32}^2$ (top left), $\sin^2\theta_{23}$ (top right) and $\delta_{\text{CP}}$ (bottom) for normal (full) and inverted (dashed) ordering at the Asimov Set A20 point compared between BANFF (blue) and GUNDAM (red) using the near-detector data fit constraints of OA2020. . . . .	251
8.9	Two-dimensional sensitivity $\Delta\chi^2$ in the disappearance oscillation parameters for normal (left) and inverted (right) ordering at Asimov Set A20 point compared between BANFF (blue) and GUNDAM (red) using the near-detector data fit constraints of OA2020. . . . .	251
8.10	Two-dimensional sensitivity $\Delta\chi^2$ in the appearance oscillation parameters for normal (left) and inverted (right) ordering at the Asimov Set A20 point compared between BANFF (blue) and GUNDAM (red) using the near-detector data fit constraints of OA2020. . . . .	252
8.11	Subset of the cross-section parameters compared between BANFF (blue) and GUNDAM (red) for the OA2020 fit to the Martini et al. alternative model. . . . .	253
8.12	Cross-section parameters compared between BANFF and GUNDAM for the OA2020 data fit. Parameters with no GUNDAM postfit errors are fixed in the fits. . . . .	254
8.13	Two-dimensional distribution of the MCMC steps after burn-in in MaCh3 for the oxygen Pauli blocking $\bar{\nu}$ (in $1\sigma$ units) and optical potential, compared to the best fit points and the elliptical representation of the covariance found by BANFF ( $\blacktriangledown$ , dotted) and GUNDAM ( $\star$ , full). . . . .	255
8.14	One-dimensional sensitivity $\Delta\chi^2$ in $\Delta m_{32}^2$ (top left), $\sin^2\theta_{23}$ (top right) and $\delta_{\text{CP}}$ (bottom) for normal (full) and inverted (dashed) ordering at the Asimov Set A22 point compared between BANFF and GUNDAM using the near-detector data fit constraints of OA2022. . . . .	256
8.15	Left: $\Delta m_{32}^2$ contour as shown in Figure 8.14, with the covariance matrix bug in BANFF. Right: $\Delta m_{32}^2$ contours when the BANFF covariance matrix is corrected by flipping the sign of the correlations with the mirrored parameters. . . . .	257

## List of Figures

---

8.16	One-dimensional $\Delta m_{32}^2$ contour with the covariance matrix bug fix for BANFF and where GUNDAM postfit values of oxygen Pauli blocking and optical potential parameters are replaced by the BANFF ones. . . . .	257
9.1	Two-dimensional distributions of the reconstructed $(\delta p_T, E_{\text{vis}})$ in the CC0 $\pi$ samples with a reconstructed nucleon within the Super-FGD in the FHC (left) and RHC (right) beam mode, each with $1.13 \times 10^{21}$ POT. . . . .	261
9.2	Projected beam power and delivered POT in the upcoming phase of T2K data taking. . . . .	263
9.3	Statistical negative log-likelihood scan typically obtained for a parameter in an Asimov fit when using the Poisson likelihood (black) of Equation (7.5), the Barlow – Beeston likelihood (blue) of Equation (7.6), and the modified Barlow – Beeston likelihood to account for the detector smearing (red) used in this sensitivity study for the Super-FGD samples. . . . .	266
9.4	Expected constraints on CCQE-related uncertainties for the FGD1+2 only (dashed), SFGD+FGD1+2 $\mu$ only (dotted) and SFGD+FGD1+2 $\mu + N$ (full) configurations described in Section 9.2.1. . . . .	267
9.5	Expected constraints on CCQE- and 2p2h-related uncertainties for the FGD1+2 only (dashed), SFGD+FGD1+2 $\mu$ only (dotted) and SFGD+FGD1+2 $\mu + N$ (full) configurations described in Section 9.2.1. . . . .	268
9.6	Expected constraints on ND280 flux uncertainties for the FGD1+2 only (dashed), SFGD+FGD1+2 $\mu$ only (dotted) and SFGD+FGD1+2 $\mu + N$ (full) configurations described in Section 9.2.1. . . . .	272
9.7	Postfit covariance matrix of the flux parameters when using in the FGD1+2-only (left) and the SFGD+FGD1+2 (right) configuration when the added POT is $1 \times 10^{21}$ . . . . .	273
9.8	Principle components of the postfit flux correlation matrices shown in Figure 9.7. . . . .	273
9.9	Impact of the statistical fluctuations in the marginalization using independently generated sets for the systematic parameters with $N_{\text{marg}} = 100,000$ (left) and $N_{\text{marg}} = 300,000$ (right) on the $\delta_{\text{CP}}$ sensitivity at the Set A22 Asimov point using the expected statistics in 2027 (see Table 9.1). . . . .	278
9.10	Evolution of the $\Delta m_{32}^2$ contours in the normal ordering at the Asimov Set A22 for the projected POT shown in Table 9.1 using the systematic uncertainties of the 2022 oscillation analysis, constrained with the FGD1+2-only configuration at each value of the delivered POT. The dashed line indicate the $1\sigma$ C.L. (i.e. $\Delta\chi^2 = 1$ ) used to extract the resolution. . . . .	280
9.11	Resolution on $\Delta m_{32}^2$ in the normal ordering at the Set A22 (left) and the Set B22 (right) for the projected POT shown in Table 9.1 compared between when considering only statistical uncertainties (dotted) and when using the systematic uncertainties of the 2022 oscillation analysis constrained with the FGD1+2-only configuration at each value of the delivered POT (full). . . . .	280

9.12	Evolution of the $\sin^2 \theta_{23}$ contours in the normal ordering at the Set A22 (left) and the Set B22 (right) for the projected POT shown in Table 9.1 using the systematic uncertainties of the 2022 oscillation analysis, constrained with the FGD1+2-only configuration at each value of the delivered POT. The dashed line indicate the $1\sigma$ C.L. (i.e. $\Delta\chi^2 = 1$ ) used to extract the resolution. . . . .	281
9.13	Resolution on $\sin^2 \theta_{23}$ in the normal ordering at the Set A22 (left) and the Set B22 (right) for the projected POT shown in Table 9.1 compared between when considering only statistical uncertainties (dotted) and when using the systematic uncertainties of the 2022 oscillation analysis constrained with the FGD1+2-only configuration at each value of the delivered POT (full). . . . .	281
9.14	90% C.L. contours in $(\sin^2 \theta_{23}, \Delta m_{32}^2)$ in the normal ordering at the Set A22 (left) and the Set B22 (right) for the delivered POT in 2022 (red), 2025 (orange) and 2027 (cyan) as shown in Table 9.1 compared between when considering only statistical uncertainties (dotted) and when using the systematic uncertainties of the 2022 oscillation analysis constrained with the FGD1+2-only configuration at each value of the delivered POT (full). . . . .	282
9.15	Left: evolution of the $\delta_{\text{CP}}$ contours in the normal ordering at the Asimov Set A22 for the projected POT shown in Table 9.1 using the systematic uncertainties of the 2022 oscillation analysis constrained with the FGD1+2-only configuration at each value of the delivered POT, where the dashed line indicate the CP-conserving values of $\delta_{\text{CP}}$ . Right: $\Delta\chi^2$ to exclude CP violation as a function of the delivered POT when considering only statistical uncertainties (dotted) and when using the systematic uncertainties of the 2022 oscillation analysis constrained with the FGD1+2-only configuration at each value of the delivered POT (full). . . . .	283
9.16	Sensitivity to exclude CP conservation as a function of the true value of $\delta_{\text{CP}}$ when the true mass ordering is normal if it is <i>known</i> (left) or <i>unknown</i> (right) for the statistics-only case and for the systematic uncertainties of the 2022 oscillation analysis constrained with the FGD1+2-only configuration at the current (red) and the 2027 (cyan) values of the delivered POT. This is evaluated for three values of $\sin^2 \theta_{23}$ from the current T2K 90% C.L. constraints: 0.44 (top), 0.5 (middle) and 0.6 (bottom). . . . .	285
9.17	Sensitivity to exclude the inverted ordering assuming a true normal ordering as a function of the projected POT shown in Table 9.1 when using the systematic uncertainties of the 2022 oscillation analysis constrained with the FGD1+2-only configuration at each value of the delivered POT assuming a true value of $\delta_{\text{CP}}$ at 0 (dotted) and $-\pi/2$ (full) for three values of $\sin^2 \theta_{23}$ from the current T2K 90% C.L. constraints: 0.44 (orange), 0.5 (cyan) and 0.6 (red). . . . .	286
9.18	Expected constraints on CCQE-related uncertainties in the SFGD+FGD1+2 $\mu + N$ configuration without (full) and with (dashed) the carbon-oxygen correlations. . . . .	289

## List of Figures

---

A.1	Expected constraints on CCRES-related uncertainties for the FGD1+2 only (dashed), SFGD+FGD1+2 $\mu$ only (dotted) and SFGD+FGD1+2 $\mu + N$ (full) configurations described in Section 9.2.1. . . . .	300
A.2	Expected constraints on CCDIS-related and other uncertainties for the FGD1+2 only (dashed), SFGD+FGD1+2 $\mu$ only (dotted) and SFGD+FGD1+2 $\mu + N$ (full) configurations described in Section 9.2.1. . . . .	301
A.3	Expected constraints on Super-Kamiokande flux uncertainties for the FGD1+2 only (dashed), SFGD+FGD1+2 $\mu$ only (dotted) and SFGD+FGD1+2 $\mu + N$ (full) configurations described in Section 9.2.1. . . . .	302
A.4	Expected constraints on ND280 (top) and Super-Kamiokande (bottom) flux uncertainties for the FGD1+2 only (dashed), SFGD+FGD1+2 $\mu$ only (dotted) and SFGD+FGD1+2 $\mu + N$ (full) configurations described in Section 9.2.1. . . . .	303

# List of Tables

1.1	Summary of quantum numbers for the leptons in the electroweak theory. . . .	9
1.2	Vector and axial coefficients that appear in the NC Lagrangian of Equation (1.12) for $l \in \{e, \mu, \tau\}$ . . . . .	12
1.3	Summary of the best fit values of oscillation parameters from global data [43]. .	32
1.4	Comparison between the T2K and NOvA experiments. . . . .	45
2.1	Decay modes that produce neutrinos in the FHC mode with the corresponding branching ratios [77]. . . . .	51
2.2	Summary of the T2K cross-section measurements. T2K reports either the total ( $\sigma$ ), single differential ( $\frac{d\sigma}{dX}$ ) or double differential ( $\frac{d^2\sigma}{dXdY}$ ) cross section in given observables. Unless mentioned otherwise in the table, the measurement is performed with the $2.5^\circ$ off-axis neutrino beam. . . . .	66
4.1	Energy levels with their widths for the different shells as in NEUT. Last column represents the relative prior uncertainty set on the corresponding shell normalization parameter, which all have central value set to 0. . . . .	100
4.2	Summary of the parameters described in Section 4.2 and their prior uncertainties.	111
4.3	Summary of the prefit and postfit NS chi-square $\chi^2_{\text{NS}}$ used in the minimization (top) as well as the usual $\chi^2$ given by Equation (4.3) (bottom) for the different fits along with the corresponding number of bins. . . . .	125
6.1	Variation in percentage at 0.2 and 0.4 T fields of the average consumed current on the low-voltage (12 V) power supply as recorded by a sensing chip on the FEB with respect to the reference 0 T field (1.79 A) case for the different configurations shown in Figure 6.27. . . . .	186
7.1	Summary of the collected data used in the 2022 oscillation analysis in units of $10^{19}$ POT at both ND280 and Super-Kamiokande, separated by the beam mode.	196
7.2	Summary of the 22 samples of the 2022 oscillation analysis with the data and prefit MC event rates as well as their ratio. . . . .	200
7.3	Binning used to define the flux uncertainty parameters as a function of the beam mode and the neutrino type. . . . .	203



## List of Tables

---

7.4	Summary of the systematic uncertainty sources related to the response of ND280 for FHC samples and the corresponding integrated relative errors in % for each source. Table adapted from Reference [268]. . . . .	206
7.5	Shifts applied to the charged-lepton momentum to correct for the Coulomb effect. . . . .	210
7.6	Summary of the CCQE and 2p2h uncertainties and their related priors. . . . .	213
7.7	Summary of the non-QE uncertainties and their related priors. . . . .	214
7.8	Comparison between the fitters used in the two T2K analysis streams. . . . .	220
7.9	Sampling distributions used for the marginalized oscillation parameters. $\Delta m^2$ refers to $\Delta m_{32}^2$ in the normal mass ordering and to $ \Delta m_{31}^2 $ in the inverted ordering. $\mathcal{U}(a, b)$ denotes a uniform distribution over the interval $[a, b]$ , while $\mathcal{N}(\mu, \sigma)$ corresponds to a Gaussian distribution of mean $\mu$ and variance $\sigma^2$ . . .	229
7.10	Fixed $\Delta\chi^2$ values to define confidence intervals. . . . .	229
7.11	Best fit values of the oscillation parameters in the normal and inverted ordering when using T2K data only and when combining it with the reactor constraints from Reference [12], along with the negative log-likelihood values. $\Delta m^2$ refers to $\Delta m_{32}^2$ in the normal mass ordering and to $ \Delta m_{31}^2 $ in the inverted ordering. . .	232
7.12	Predicted event rate in each of the far detector samples at the T2K best fit values of the systematic parameters as well as of the oscillation parameters shown in Table 7.11 for different values of the phase $\delta_{CP}$ , compared to the measured event rate. . . . .	232
8.1	Four examples of the 18 prefit event rate tables comparing BANFF and GUNDAM per sample, broken down by weight type. . . . .	241
8.2	One example of the 712 tables comparing the event rate in each sample at $-3\sigma$ , $-1\sigma$ , $1\sigma$ and $3\sigma$ for the $M_A^{\text{QE}}$ parameter, as well as the relative difference in the last column at $-1\sigma$ . . . . .	242
8.3	Reference A20 point of the oscillation parameters used in the Asimov fits with P-Theta to compare BANFF and GUNDAM. . . . .	250
8.4	Comparison of the postfit statistical, penalty and total likelihood $-2\log\mathcal{L}$ between BANFF and GUNDAM. . . . .	253
9.1	Summary of the projected POT delivered in the second phase of T2K data taking until 2027. . . . .	264
9.2	Comparison between the expected event rates in the current FGDs and the Super-FGD for $1.13 \times 10^{21}$ POT in the FHC mode. . . . .	264
9.3	Comparison between the expected event rates in the current FGDs and the Super-FGD for $1.13 \times 10^{21}$ POT in the RHC mode. Note that the FGDs do not have the ability to tag neutrons. . . . .	264
9.4	Estimated uncertainty on the Super-FGD samples related to the detector response. . . . .	265
9.5	Reference points of the oscillation parameters used in the Asimov fits with P-Theta to evaluate the sensitivity. . . . .	277

9.6	Predicted event rate in each of the six far detector samples at the Asimov Set A22 with the additional POT per year as shown in Table 9.1. . . . .	277
9.7	Predicted event rate in each of the six far detector samples at the Asimov Set B22 with the additional POT per year as shown in Table 9.1. . . . .	277
9.8	Chosen $N_{\text{marg}}$ for each value of the additional considered POT (see Table 9.1). .	278
9.9	Impact of the systematic uncertainties on the event rates in the six Super-Kamiokande samples in % for the different POT and configurations in the near-detector fit, broken down by the uncertainties constrained and unconstrained with the near-detector data as well as the Super-Kamiokande detector response uncertainty. The statistical uncertainties evaluated with the event rates at the Set A22 (see Table 9.6) are also shown for reference. . . . .	291
9.10	Impact of the near-detector-unconstrained systematic uncertainties on the event rates in the six Super-Kamiokande samples in %. Their values are the same across the different POT values and near-detector-fit configurations. . . . .	292



# Introduction

Although one of the most abundant elementary particles in the Universe, neutrinos are among the most elusive ones as they only seldom interact with matter. They may also hold the key to explaining why our Universe is made up of matter instead of antimatter. Their existence was first postulated as early as 1930, but it took decades to experimentally detect their three flavors. Along the way, multiple puzzles and anomalies related to neutrinos appeared and highlighted our lack of understanding of this particle's nature. Many of them could be elegantly explained by the oscillation phenomenon, by which neutrinos experience flavor transition as they travel. This phenomenon was only confirmed experimentally in 1998, paving the way for a new probe of the matter-antimatter asymmetry in the Universe. Indeed, if neutrinos and antineutrinos oscillate differently, this would be a manifestation of a violation of the charge-parity (CP) symmetry in the lepton sector. Such a CP violation was already observed in the quark sector, but is by no means enough to fully explain the matter-dominated Universe.

In order to exploit this oscillation phenomenon to study the CP symmetry, a well-understood source of neutrinos is an absolute necessity. This is why the experiments that are most sensitive to this effect use accelerators to produce an intense muon neutrino beam at a relatively well determined energy. This is the case of the T2K experiment and its accelerated protons at J-PARC, which impinge on a graphite target to produce hadrons that decay into  $\bar{\nu}_\mu$ . Meanwhile, 300 km away is located Super-Kamiokande, the far detector of the experiment that measures the disappearance of  $\bar{\nu}_\mu$  and the appearance of  $\bar{\nu}_e$ . The precise measurements of these oscillations require, in addition to the well-known neutrino beam, a good control over the systematic errors that can produce significant biases in the results. This is particularly the case of the systematic uncertainties related to the complex nuclear physics of how neutrinos interact with nuclei. This is the reason why accelerator-based experiments use a set of near detectors that can measure neutrino interactions close to the neutrino source with large statistics and thus constrain such systematic uncertainties.

A better understanding of neutrino-nucleus interactions can be achieved by further theoretical model developments, but these are always accompanied by tests against actual neutrino interaction measurements which allow us to identify their shortcomings. More detailed and high-statistics measurements are the key to discriminate between models and motivate further developments. Consequently, the T2K collaboration is upgrading its near detector to increase its capabilities to measure with great precision the particles produced in neutrino interactions.

## Introduction

---

Innovative detector designs come with a wide range of challenges that need to be overcome in order to utilize their capabilities to their fullest.

This thesis walks through the different projects to which I contributed within the T2K collaboration.

Part I provides a broad overview of neutrino physics and the T2K experiment. In particular, Chapter 1 describes the Standard Model of particle physics and how neutrinos fit in its framework, and details the standard paradigm of three-flavor oscillations. In Chapter 2, we review the T2K experiment, its beamline, and its various subdetectors.

Part II of this thesis is dedicated to neutrino interactions. Chapter 3 summarizes how the different neutrino-nucleus scattering channels are modeled while Chapter 4 describes a study I carried out to define new uncertainties for the Benhar Spectral Function model of charged-current quasielastic interactions and check their impact against various cross-section measurements.

Part III of this thesis concerns the T2K near-detector upgrade: Chapter 5 describes its new subdetectors, their novel technologies and the expected performances, whereas Chapter 6 focuses on the electronics of the Super-FGD and particularly the comprehensive tests of the front-end boards on which I worked.

Part IV of this thesis is focused on the measurement of the oscillation parameters. Chapter 7 presents an overview of the steps in the T2K oscillation analysis and describes the results of latest constraints on the oscillation parameters. Chapter 8 introduces a new fitting software developed for the near-detector part of the oscillation analysis and its extensive validations. Finally, Chapter 9 focuses on the future sensitivities to constrain the systematic uncertainties particularly with the improved performances after the near-detector upgrade, and the potential impact this may have on the oscillation parameters.

# Neutrinos and T2K Part I



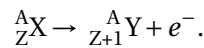
# 1 Neutrinos in the Standard Model and beyond

This chapter presents an overview of neutrino physics, from its historical milestones to the current status, with a focus on the neutrino oscillation phenomenon.

## 1.1 A brief history of neutrino discovery

### 1.1.1 Mysterious $\beta$ decays

In his famous letter addressed to the participants of the nuclear physics conference in Tübingen, W. Pauli postulated the existence of the neutrino in 1930 [1]. At that time, protons and electrons were considered to be the elementary particles which form nuclei. But this was known to be an incomplete picture since the beta decay measurements by J. Chadwick in 1914 [2]. Such decay corresponds to the radioactive disintegration of a nucleus  ${}^A_ZX$  into  ${}^A_{Z+1}Y$  in which an electron is emitted according to the following reaction:



By energy conservation in this two-body process, the electron energy can be expressed in the rest frame of the nucleus  ${}^A_ZX$  as a function of the masses  $M_X$ ,  $M_Y$  and  $M_e$  of respectively  ${}^A_ZX$ ,  ${}^A_{Z+1}Y$  and the electron as:

$$E_e = \frac{M_X^2 - M_Y^2 + M_e^2}{2M_X}.$$

While the electron energy spectrum from  $\beta$  decays would be expected to be at this well-defined and fixed value  $E_e$ , Chadwick rather found it to be a continuous spectrum where the maximal energy corresponded to  $E_e$ . In his letter, Pauli attempted to explain these mysterious findings by the existence of an additional particle produced in this decay, making it a three-body process where the electron energy spectrum would indeed be expected to be continuous with an endpoint at  $E_e$ . This particle, which would later be known as the neutrino, would necessarily be of spin 1/2, electromagnetically neutral, and extremely light, thus hard to measure.



### 1.1.2 First detections

As he theorized its existence, Pauli soon realized the possible consequences and (supposedly) stated: “I have done a terrible thing, I have postulated a particle that cannot be detected”. It was long thought that detecting this particle was an impossible task until the 1940s, with the development of nuclear reactors that would provide an intense source of neutrinos. C. Cowan and F. Reines took up this challenge and proposed an experiment that could demonstrate their existence through the inverse beta decay [3]:

$$\bar{\nu}_e + p \rightarrow e^+ + n.$$

It consisted of two tanks of water mixed with cadmium chloride  $\text{CdCl}_2$ , placed near the Savannah River Plant and sandwiched between three liquid scintillator detectors. The characteristic signal of the inverse beta decay process would be the coincidence of two signals: the positron annihilation  $e^+ + e^- \rightarrow 2\gamma$  which produces two photons of a characteristic energy of 511 keV, and the neutron capture on cadmium which emits a photon with a 5  $\mu\text{s}$  delay. Sure enough, on June 14th, 1956, and after months of data taking, Cowen and Reines sent a telegram to Pauli confirming that they had “definitely detected neutrinos” [4]. This discovery was later crowned with the Nobel Prize of physics in 1995.

### 1.1.3 Subsequent discoveries

Cowen and Reines’ results were only the start of experimental neutrino physics, and the understanding of neutrino properties progressed rapidly.

Following this discovery of the electron (anti)neutrino, L. Lederman, M. Schwartz and J. Steinberger [5] produced the first neutrino beam from accelerated protons fired on a target and discovered in 1962 at the Brookhaven National Laboratory a second type of neutrinos, named muon neutrinos  $\nu_\mu$ , which produce muons in contrast with electron antineutrinos that produce positrons in inverse beta decays.

In the mid-1970s, a third generation of leptons was unexpectedly discovered at the Stanford Linear Accelerator Complex (SLAC) [6] which hinted at the existence of a third neutrino type: the tau neutrino  $\nu_\tau$ . Measurements of the  $Z^0$  boson decay with Large Electron Positron collider at CERN (see Figure 1.5) as well as with the Mark II experiment at SLAC were an indirect evidence of the existence of three neutrino species in the 1990s [7]. Direct measurements of tau neutrinos later came with the DONUT experiment at Fermilab in 2000 [8].

## 1.2 Neutrinos and the Standard Model

### 1.2.1 Standard Model of particle physics

#### Overview

The Standard Model of particle physics describes our best understanding of the fundamental constituents of matter and their interactions. It is a quantum field theory which unifies the weak, strong and electromagnetic forces based on special relativity and quantum mechanics.

As summarized in Figure 1.1, it contains two types of particles: *fermions*, of half-integer spin which make up matter, and *bosons*, of integer spin which mediate interactions. Among the fermions, it includes six quarks, denoted by the letters  $u$ ,  $d$ ,  $c$ ,  $s$ ,  $t$  and  $b$ , as well as three generations (or *flavors*) of charged leptons: the electron  $e$ , the muon  $\mu$ , and the tau  $\tau$ . Each of the charged leptons is associated with a neutral lepton, the neutrino, denoted by  $\nu_e$ ,  $\nu_\mu$  and  $\nu_\tau$ . Additionally, each of these twelve fermions  $f$  has an equivalent antiparticle  $\bar{f}$ .

For instance, quarks participate in all of the three interactions of the Standard Model. In Nature, they are always found bound within systems held together by the strong force. They can form *mesons*, usually in two-quark systems such as pions (e.g.  $u\bar{d}$  for  $\pi^+$ ), or *baryons* in three-quark systems as is the case for nucleons ( $uud$  for protons and  $udd$  for neutrons).

#### Formulation

The Standard Model is a gauge theory where quantum fields represent particles and satisfy symmetries described by the local symmetry group  $SU_C(3) \times SU_L(2) \times U_Y(1)$ . It aggregates the three Standard Model interactions:

- $SU_C(3)$  describes quantum chromodynamics (QCD), or the strong interactions. This only involves particles with an associated *color*, namely the quarks and the gluons. The eight generators of the group are  $T_a = \lambda_a/2$  and correspond to the eight massless gluons that mediate the strong interaction, where  $\lambda_a$  are Gell-Mann matrices.
- $SU_L(2) \times U_Y(1)$  describes the electroweak interactions. There are four generators corresponding to this group: three  $SU_L(2)$  generators defined with Pauli matrices  $\sigma_i$  as  $I_i = \sigma_i/2$  which correspond to the  $W^i$ ,  $i = 1, 2, 3$  bosons, and one generator for  $U_Y(1)$  associated with the  $B$  gauge boson.

The evolution of quantum fields under these symmetries is described with a Lagrangian  $\mathcal{L}$  in a flat Minkowski spacetime. The gauge invariance, the Lorentz structure and renormalizability (e.g. absence of higher powers of fields) are what determines the couplings between bosons and fermions as well as their self-interactions. In the following, we will mainly focus on the lepton sector and the electroweak interactions.

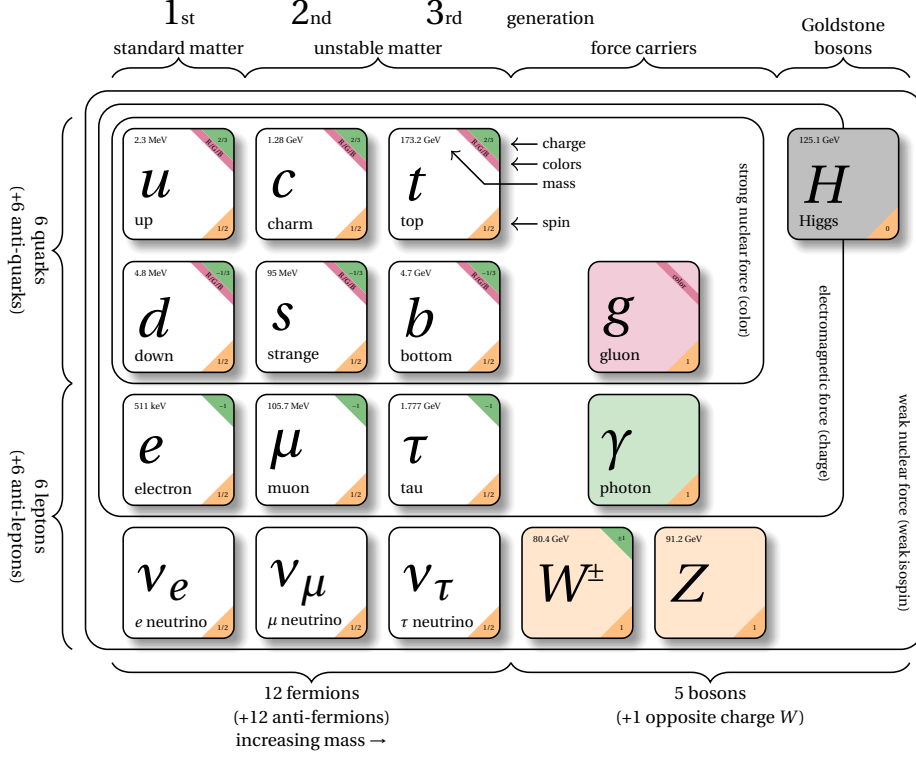


Figure 1.1: Summary of the elementary particles and their interaction mediators in the Standard Model. Adapted from Reference [9].

### 1.2.2 Electroweak Lagrangian

The electroweak Lagrangian is commonly expressed as:

$$\mathcal{L}_{EW} = \mathcal{L}_{YM} + \mathcal{L}_{Higgs} + \mathcal{L}_{Yukawa}. \quad (1.1)$$

In the following paragraphs, we review the construction of the different terms of this Lagrangian, which describes the couplings between the different leptons and the gauge bosons as well as the mechanisms by which they acquire mass.

#### Representation of leptons

A key characteristic of the weak force is the *chirality*, or *handedness*, of a fermion field  $f$ , which is a Lorentz-invariant quantum-mechanical property related to spin. In the simple case of a massless (or highly-energetic) fermion, the chirality corresponds to the helicity of the particle, that is the sign of the projection of its spin vector onto its momentum. There is however no straightforward relationship between chirality and helicity for massive particles.

## 1.2 Neutrinos and the Standard Model

Lepton	Electric charge $Q$	Isospin $I_3$	Hypercharge $Y$
$\nu_{lL}$	0	1/2	-1
$l_L$	-1	-1/2	-1
$l_R$	-1	0	-2

Table 1.1: Summary of quantum numbers for the leptons in the electroweak theory.

It was observed experimentally that left- and right-handed leptons behave differently under the weak interaction (see Section 1.2.4). Therefore, two different representations are used to account for these findings which project the lepton field  $L$  into left- and right-handed components  $L_L = P_L L$  and  $L_R = P_R L$  respectively, where:

$$P_L = \frac{1 - \gamma^5}{2} \quad \text{and} \quad P_R = \frac{1 + \gamma^5}{2}. \quad (1.2)$$

$\gamma^5$  is defined as  $\gamma^5 = i\gamma^0\gamma^1\gamma^2\gamma^3$ , which includes the product of the four gamma (or Dirac) matrices  $\gamma^\mu$ .

To account for the aforementioned experimental observation, the projections  $L_L$  and  $L_R$  do not correspond to the same representations. The left-handed lepton fields are represented as doublets of  $SU(2)$  whereas the right-handed ones as singlets. This is expressed as:

$$L_L = \begin{bmatrix} \nu_{lL} \\ l_L \end{bmatrix} \quad \text{and} \quad L_R = [l_R] \quad (1.3)$$

where  $l = e, \mu, \tau$  corresponds to the lepton flavor.

The electroweak theory is described by the product of the group  $SU_L(2)$ , characterized by the components of the *weak isospin*  $I_i$ , and the group  $U_Y(1)$ , characterized by the *hypercharge*  $Y$ . This is summarized in Table 1.1. By convention, the Gell-Mann – Nishijima relation links the third weak isospin component and the hypercharge to the electric charge  $Q$  by:

$$Q = I_3 + \frac{Y}{2}. \quad (1.4)$$

### Yang-Mills Lagrangian

The first term in Equation (1.1) is the *Yang-Mills* Lagrangian of the electroweak symmetry group  $SU_L(2) \times U_Y(1)$  which ensures the local gauge invariance. It can be written as<sup>1</sup>:

$$\mathcal{L}_{\text{YM}} = -\frac{1}{4}F_{\mu\nu}^i F_i^{\mu\nu} - \frac{1}{4}B_{\mu\nu} B^{\mu\nu} + \bar{L}_L i\gamma^\mu D_\mu L_L + \bar{L}_R i\gamma^\mu D_\mu L_R \quad (1.5)$$

<sup>1</sup>The formulae in this chapter use the Einstein summation convention, where Latin letters take values from 1 to 3 for the space coordinates and Greek letters from 0 to 3 for the time and space coordinates.

## Chapter 1. Neutrinos in the Standard Model and beyond

---

where:

- $B_{\mu\nu} = \partial_\mu B_\nu - \partial_\nu B_\mu$  is the gauge tensor constructed with the gauge field  $B$  associated with  $U_Y(1)$ ,
- $F_{\mu\nu}^i = \partial_\mu W_\nu^i - \partial_\nu W_\mu^i - g\epsilon_{ijk}W_\mu^jW_\nu^k$  is the gauge tensor constructed with the gauge fields  $W^i$ ,  $i = 1, 2, 3$  associated with the generators of  $SU_L(2)$ ,  $\epsilon_{ijk}$  its structure functions (called *Levi-Civita tensor*), and  $g$  the  $SU_L(2)$  coupling constant,
- $D_\mu$  is the covariant derivative defined as  $D_\mu = \partial_\mu + igI_iW_\mu^i + ig'\frac{1}{2}Y(L)B_\mu$  where  $I_i = \sigma_i/2$  are the  $SU_L(2)$  generators,  $Y(L)$  is the  $U_Y(1)$  generator whose values are shown in Table 1.1, and  $g'$  is the  $U_Y(1)$  coupling constant.

When using the chiral properties of leptons shown in Equation (1.3), Equation (1.5) can be conveniently simplified as:

$$\mathcal{L}_{\text{YM}} = \mathcal{L}_{\text{kin}} + \mathcal{L}_{\text{CC}} + \mathcal{L}_{\text{NC}} + \mathcal{L}_{\text{EM}}. \quad (1.6)$$

The first term here  $\mathcal{L}_{\text{kin}} = i\bar{L}_L\gamma^\mu\partial_\mu L_L + i\bar{l}_R\gamma^\mu\partial_\mu l_R$  is defined as the kinetic term.

The second term  $\mathcal{L}_{\text{CC}}$  contains only the Yang-Mills Lagrangian parts that include the  $W^1$  and  $W^2$  fields:

$$\mathcal{L}_{\text{CC}} = gW_\mu^1\bar{L}_L\gamma^\mu I_1 L_L + gW_\mu^2\bar{L}_L\gamma^\mu I_2 L_L$$

This yields, using the expressions of Pauli matrices:

$$\mathcal{L}_{\text{CC}} = -\frac{g}{\sqrt{2}} \left[ \frac{W_\mu^1 - iW_\mu^2}{\sqrt{2}} \right] \bar{\nu}_{lL}\gamma^\mu l_L - \frac{g}{\sqrt{2}} \left[ \frac{W_\mu^1 + iW_\mu^2}{\sqrt{2}} \right] \bar{l}_L\gamma^\mu \nu_{lL}.$$

We can see that the  $W^1$  and  $W^2$  can be related to the experimentally observed bosons  $W^\pm$ , which mediate the coupling between the charged leptons and neutrinos, by the following linear relation:

$$W^\pm = \frac{W^1 \mp iW^2}{\sqrt{2}},$$

which allows us to write:

$$\mathcal{L}_{\text{CC}} = -\frac{g}{\sqrt{2}} W_\mu^+ \bar{\nu}_{lL}\gamma^\mu l_L - \frac{g}{\sqrt{2}} W_\mu^- \bar{l}_L\gamma^\mu \nu_{lL}. \quad (1.7)$$

This Lagrangian describes the so-called *charged-current* (CC) weak interaction. Similar terms can be derived for CC interactions between quarks of the same doublet, and Figure 1.2 shows Feynman diagrams corresponding to these interactions.

Finally, the last two terms in Equation (1.6) contain the dependence on the  $W^3$  and  $B$  fields as

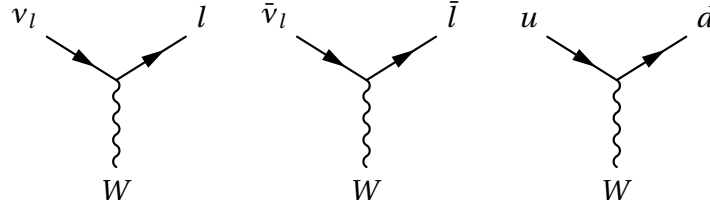


Figure 1.2: Feynman diagrams for CC interactions described by Equation (1.7).

follows:

$$\begin{aligned} \mathcal{L}_{\text{NC}} + \mathcal{L}_{\text{EM}} = & \frac{g}{2} W_\mu^3 [\bar{\nu}_{lL} \gamma^\mu \nu_{lL} - \bar{l}_L \gamma^\mu l_L] \\ & + \frac{g'}{2} B_\mu [-(\bar{\nu}_{lL} \gamma^\mu \nu_{lL} + \bar{l}_L \gamma^\mu l_L) - 2\bar{l}_R \gamma^\mu l_R]. \end{aligned} \quad (1.8)$$

It can be seen that neither  $W^3$  nor  $B$  can be interpreted as photon fields since they couple to electromagnetically neutral fields (neutrinos) with the terms  $W_\mu^3 \bar{\nu}_{lL} \gamma^\mu \nu_{lL}$  and  $B_\mu \bar{\nu}_{lL} \gamma^\mu \nu_{lL}$ . But we can apply a rotation of an angle  $\theta_W$ , called *Weinberg angle*, in the space of the two fields  $W^3$  and  $B$  that would define the photon field  $A_\mu$  which appears in the electromagnetic Lagrangian  $\mathcal{L}_{\text{EM}}$ , and inevitably the  $Z^0$  field in the *neutral current* (NC) Lagrangian  $\mathcal{L}_{\text{NC}}$ :

$$\begin{aligned} B_\mu &= A_\mu \cos \theta_W - Z_\mu \sin \theta_W, \\ W_\mu^3 &= A_\mu \sin \theta_W + Z_\mu \cos \theta_W. \end{aligned}$$

By replacing  $W_\mu^3$  and  $B_\mu$  in Equation (1.8), we obtain:

$$\begin{aligned} \mathcal{L}_{\text{EM}} = & \left( \frac{g'}{2} \cos \theta_W - \frac{g}{2} \sin \theta_W \right) A_\mu \bar{\nu}_{lL} \gamma^\mu \nu_{lL} \\ & + \left( \frac{g}{2} \sin \theta_W + \frac{g'}{2} \cos \theta_W \right) A_\mu \bar{l}_L \gamma^\mu l_L \\ & + g' \cos \theta_W A_\mu \bar{l}_R \gamma^\mu l_R. \end{aligned} \quad (1.9)$$

We can impose the condition that the term that couples  $A_\mu$  to neutral fields in the first line of Equation (1.9) to be vanishing. Additionally, in the second and third lines of Equation (1.9) we can identify the coupling constant between the photon and the charged lepton fields with the electromagnetic coupling, given by the elementary electric charge  $e$ . This gives us the following equations:

$$\begin{aligned} \frac{g'}{2} \cos \theta_W - \frac{g}{2} \sin \theta_W &= 0, \\ \frac{g}{2} \sin \theta_W + \frac{g'}{2} \cos \theta_W &= e, \\ g' \cos \theta_W &= e. \end{aligned} \quad (1.10)$$

## Chapter 1. Neutrinos in the Standard Model and beyond

Lepton	$C_V$	$C_A$
$\nu_l$	$\frac{1}{2}$	$\frac{1}{2}$
$l$	$-\frac{1}{2} + 2\sin^2\theta_W$	$-\frac{1}{2}$

Table 1.2: Vector and axial coefficients that appear in the NC Lagrangian of Equation (1.12) for  $l \in \{e, \mu, \tau\}$ .

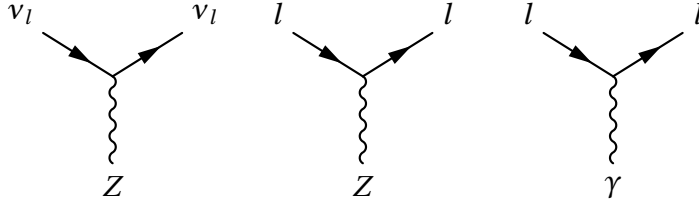


Figure 1.3: Feynman diagrams for NC interactions described by Equations (1.11) and (1.12).

Therefore, the electromagnetic Lagrangian  $\mathcal{L}_{\text{EM}}$  becomes:

$$\mathcal{L}_{\text{EM}} = eA_\mu \bar{l}_L \gamma^\mu l_L + eA_\mu \bar{l}_R \gamma^\mu l_R. \quad (1.11)$$

On the other hand, the NC Lagrangian, which is obtained by isolating the terms that depend on  $Z_\mu$ , can be rewritten, when using Equation (1.10), as:

$$\mathcal{L}_{\text{NC}} = \frac{g}{2\cos\theta_W} Z_\mu \left[ \bar{\nu}_l \gamma^\mu (C_V^{\nu_l} - C_A^{\nu_l} \gamma^5) \nu_l + \bar{l} \gamma^\mu (C_V^l - C_A^l \gamma^5) l \right] \quad (1.12)$$

where we reintroduce the expressions of the projectors  $P_L$  and  $P_R$  from Equation (1.2) and make the vector and axial coefficients  $C_V$  and  $C_A$  respectively appear. These coefficients depend on the corresponding lepton and their expressions are summarized in Table 1.2. The Feynman diagrams for the NC and electromagnetic interactions are displayed in Figure 1.3.

The  $Z^0$  and  $W^\pm$  bosons were experimentally discovered in the Super Proton Synchrotron (SPS) at CERN only in 1983 [10, 11]. In fact, due to their relatively large mass (discussed below), their discovery would have to wait until a sufficiently powerful beam of particles could be built. With the collision of protons and antiprotons, the UA1 and UA2 experiments recorded clear signals of these gauge bosons, particularly through their decays  $W \rightarrow e\nu$ ,  $Z^0 \rightarrow e^+e^-$  and  $Z^0 \rightarrow \mu^+\mu^-$ .

### Masses of the gauge bosons

Within the Yang-Mills Lagrangian, the gauge bosons are massless. In fact, no explicit mass term of the form  $M_X^2 X_\mu X^\mu$  for a gauge boson field  $X$  can be allowed in the Lagrangian as it would not respect the gauge invariance. However, while we know that the photon is indeed massless,

we also know that the bosons  $W^\pm$  and  $Z^0$  are massive, and their masses are measured to be  $M_W = 80.377 \pm 0.013 \text{ GeV}/c^2$  and  $M_Z = 91.1876 \pm 0.0021 \text{ GeV}/c^2$  respectively [12].

In 1964, Brout, Englert [13] and Higgs [14] proposed a *spontaneous symmetry breaking* of the  $SU_L(2) \times U_Y(1)$  group. It is a mechanism through which masses of the weak bosons are generated by including a scalar field doublet  $\Phi$  of  $SU_L(2) \times U_Y(1)$ :

$$\Phi = \begin{bmatrix} \phi^+ \\ \phi_0 \end{bmatrix}.$$

It is composed of two complex scalar fields, a positively charged one  $\phi^+$  with  $I_3 = 1/2$ , and neutral one  $\phi_0$  with  $I_3 = -1/2$ . The Gell-Mann – Nishijima relation (1.4) consequently fixes its hypercharge to  $Y = 1$ .

The evolution of this scalar field is described by the Higgs Lagrangian  $\mathcal{L}_{\text{Higgs}}$ , the second term of Equation (1.1), which is expressed as:

$$\mathcal{L}_{\text{Higgs}} = (D_\mu \Phi)^\dagger (D^\mu \Phi) - V(\Phi) \quad (1.13)$$

where the kinetic term induces the coupling between  $\Phi$  and the electroweak boson fields, and  $V$  is the potential given by:

$$V(\Phi) = \mu^2 \Phi^\dagger \Phi + \lambda (\Phi^\dagger \Phi)^2$$

with  $\lambda > 0$ . It can be noted that this potential is symmetric under  $SU_L(2) \times U_Y(1)$ .

The vacuum expectation value  $\langle \Phi \rangle$  of the field  $\Phi$  corresponds to a state at the minimum of the potential  $V$ . This is reached, when  $\mu^2 < 0$ , for  $\Phi^\dagger \Phi = v^2/2$  where  $v$  is defined by  $v^2 = -\mu^2/\lambda$ . In this case, we can, up to a rotation, take the ground state of  $\Phi$  to be:

$$\langle \Phi \rangle = \frac{1}{\sqrt{2}} \begin{bmatrix} 0 \\ v \end{bmatrix}.$$

The Higgs Lagrangian, as defined in Equation (1.13), satisfies  $SU_L(2) \times U_Y(1)$  symmetry, but its solution that minimizes the potential  $V$  breaks it, as it is no longer invariant under  $SU_L(2) \times U_Y(1)$ . This is the spontaneous symmetry breaking. The variation of the field  $\Phi$  around its ground state  $\langle \Phi \rangle$ , can be parameterized by a scalar field  $H$ , called the *Higgs field*, as:

$$\Phi(x) = \frac{1}{\sqrt{2}} \begin{bmatrix} 0 \\ v + H(x) \end{bmatrix}. \quad (1.14)$$

By developing the kinetic term of the Higgs Lagrangian in Equation (1.13), we find:

$$(D_\mu \Phi)^\dagger D^\mu \Phi = \frac{1}{2} \partial_\mu H \partial^\mu H + \left[ \left( \frac{g v}{2} \right)^2 W_\mu^+ W^{\mu-} + \frac{1}{2} \frac{(g^2 + g'^2) v^2}{4} Z_\mu Z^\mu \right] \left( 1 + \frac{H}{v} \right)^2$$



## Chapter 1. Neutrinos in the Standard Model and beyond

---

where we can see that the  $W^\pm$  and  $Z^0$  gauge bosons have acquired masses defined as:

$$M_W^2 = \frac{g^2 v^2}{4} \quad \text{and} \quad M_Z^2 = \frac{(g^2 + g'^2) v^2}{4} = \frac{M_W^2}{\cos^2 \theta_W}$$

respectively.

### Masses of the charged leptons

We have seen thus far that the Yang-Mills term of the electroweak Lagrangian describes the evolution of massless leptons with massless gauge bosons. We have also discussed how adding the Higgs term provides a mechanism by which the bosons can become massive. In this paragraph, we will briefly mention how the charged leptons also acquire mass.

Yet again, the constraint is to add terms to the electroweak Lagrangian that are invariant under  $SU_L(2) \times U_Y(1)$  symmetry. A direct mass term with a bilinear form (Dirac-like) in the lepton field  $L$  such as<sup>2</sup>  $M_L \bar{L}L = M_L (\bar{L}_L L_R + \bar{L}_R L_L)$  breaks  $SU_L(2)$  symmetry because  $L_L$  is a doublet whereas  $L_R$  is a singlet. This can be overcome by introducing a coupling, called *Yukawa coupling*, with the scalar field  $\Phi$  of the form:

$$\mathcal{L}_{\text{Yukawa}} = g_L \bar{L}_L \Phi L_R + \text{h.c.}$$

where  $g_L$  denotes the corresponding coupling constant. The spontaneous symmetry breaking expressed in Equation (1.14) gives:

$$\begin{aligned} \mathcal{L}_{\text{Yukawa}} &= \frac{g_L v}{\sqrt{2}} \bar{l}_L l_R + \frac{g_L}{\sqrt{2}} \bar{l}_L l_R H + \text{h.c.} \\ &= \frac{g_L v}{\sqrt{2}} \bar{l}l + \frac{g_L}{\sqrt{2}} \bar{l}l H \end{aligned}$$

using the fact that  $(\bar{l}_L l_R)^\dagger = \bar{l}_R l_L$  and  $\bar{l}l = \bar{l}_L l_R + \bar{l}_R l_L$ . The charged lepton mass is therefore obtained as  $M_l = -g_L v / \sqrt{2}$ .

In this way, the charged leptons acquire mass through the spontaneous symmetry breaking described by the Higgs mechanism, and by coupling with the scalar field  $\Phi$ . The quark masses are introduced by a similar process. This consequently concludes our description of the electroweak theory in the Standard Model.

### 1.2.3 Neutrino mass problem

As described in the previous paragraphs, the electroweak Lagrangian includes the masses of the charged leptons and gauge bosons as observed in Nature, but not for the neutrinos. This is due to the fact that it only accounts for left(right)-handed (anti)neutrinos, thus making it

---

<sup>2</sup>Using  $\bar{L}_L = \bar{L} P_R$  and  $P_R L_L = 0$ .

impossible to acquire a mass in the same manner as their charged partners.

However, the observation of neutrino oscillations, which will be detailed in Section 1.3, is the definite proof that these particles are actually massive, albeit with a very small mass (see Section 1.2.4). There are multiple extensions to the Standard Model that can account for this observation.

### Dirac neutrinos

With the same mechanism that generates mass for quarks and charged leptons in the Standard Model, it is possible to give neutrinos a mass. This would require introducing right-handed neutrino singlets  $\nu_{lR}$  of  $SU_L(2) \times U_Y(1)$ , in addition to what was shown in Equation (1.3). These are singlet, i.e. of  $I_3 = 0$ , neutral fields ( $Q = 0$ ), and of hypercharge  $Y = 0$  as given by the Gell-Mann – Nishijima formula (1.4). Therefore, they are not sensitive to any of the Standard Model forces, and usually called *sterile* neutrinos.

As with the charged leptons, thanks to the spontaneous symmetry breaking and a coupling to the Higgs field, we can add a Dirac mass term of the form  $\mathcal{L}_{\text{Dirac}}^m = M_{\nu_l}^D (\bar{\nu}_{lL} \nu_{lR} + \bar{\nu}_{lR} \nu_{lL}) = M_{\nu_l}^D \bar{\nu}_l \nu_l$ .

Since this right-handed (sterile) neutrino does not interact with the other particles of the Standard Model, the only way to observe it would be through gravitation. Another limitation of this approach is that it gives neutrinos the same features as the other charged lepton masses and does not explain the difference of many orders of magnitude between the charged lepton and neutrino masses, unlike the quark sector, which could hint to a different mechanism of mass generation.

### Majorana neutrinos

An alternative approach to extend the Standard Model and account for neutrino masses is to consider that neutrinos are *Majorana* particles, namely that they are their own antiparticle.

In this picture, left- and right-handed neutrino fields are not independent, but rather related by the particle – antiparticle conjugation transformation, expressed as  $\nu_{lL} = (\nu_{lR})^C$ . The mass term in the Lagrangian can thus be of the form  $\mathcal{L}_{\text{Majorana}}^m = \frac{M_{\nu_l}^M}{2} \left( \bar{\nu}_{lL} (\nu_{lL})^C + (\nu_{lL})^C \bar{\nu}_{lL} \right)$ .

Assuming that neutrinos are Majorana particles, the *see-saw mechanism* allows us to describe the smallness of neutrino masses. This requires both the Majorana and Dirac mass terms in the Lagrangian, with the associated masses  $M_M$  and  $M_D$  respectively, which can give masses to the left- and right-handed neutrinos. In this picture, the mass of the left-handed neutrino is found to be  $\frac{M_D^2}{M_M}$ , and that of the right-handed neutrino  $M_M$ , where  $M_D$  is assumed to be of the same order of magnitude as the other fermions. In this picture, the heavier is the right-handed neutrino, the lighter the left-handed neutrino. Typically,  $M_R$  is assumed to be at

## Chapter 1. Neutrinos in the Standard Model and beyond

---

the Grand Unification Theory scale in order for the neutrino masses to be in agreement with the experimental observations.

Ongoing measurements of the so-called neutrinoless beta decay (see Section 1.2.4) are attempting to determine whether neutrinos are Dirac or Majorana particles. So far, only upper limits are established on the existence of such decays.

### 1.2.4 Experimental measurements and constraints

Together with the theoretical developments of the Standard Model during the 20th century, multiple experiments have been running to detect the predicted particles and measure their properties. In this section, we briefly review key experiments that are particularly relevant for neutrino physics.

#### Neutrino chirality

Until the 1950s, spatial parity was thought to be a conserved physical property, that is, a physical process cannot be different from its mirrored image. In 1956, T. D. Lee and C. N. Yang [15] suggested for the first time that this symmetry could be violated by the weak interactions. Less than a year later, C. S. Wu confirmed this hypothesis by measuring the beta decay of a polarized  $^{60}\text{Co}$  nucleus [16].

Wu's experiment consisted of observing the angular distribution of the electrons emitted in this beta decay process  $^{60}\text{Co} \rightarrow ^{60}\text{Ni} + e^- + \bar{\nu}_e$  at very low temperatures ( $\sim 10^{-3}\text{K}$ ). At these temperatures, the  $^{60}\text{Co}$  nuclei can be polarized and their spins aligned. If parity is conserved, the angular distribution of the emitted electrons would be symmetrical with respect to the direction of polarization.

As displayed in Figure 1.4, Wu found that if the beta decay occurs, its mirror image is significantly suppressed. This showed that the electrons produced in this decay have a negative helicity, which means that the antineutrino produced along has a positive helicity. As mentioned previously, since the helicity and chirality are the same for a highly energetic (or nearly massless) particle, this indicated that only right-handed antineutrinos can be produced in the weak interactions, which is known as *parity violation*.

#### Number of neutrinos

After the first discoveries of the  $W^\pm$  and  $Z^0$  bosons [10, 11], the increasingly precise measurements of  $Z^0$  decays rendered constraining the number of neutrinos possible. Indeed, as shown in the NC Lagrangian of Equation (1.12), the  $Z^0$  boson can decay into both quarks and charged leptons, which can be easily observed experimentally, and neutrinos. The total decay rate  $\Gamma_{\text{tot}}$ , also called the *width of the resonance*, has therefore two contributions: a “visible”

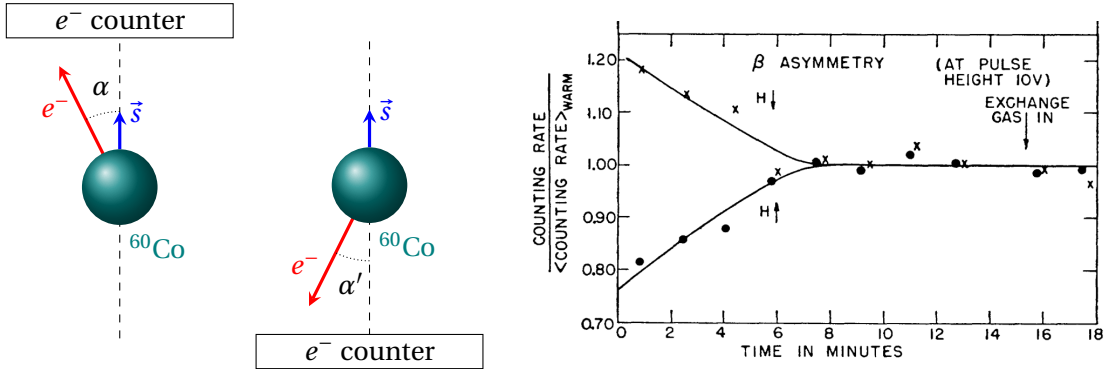


Figure 1.4: Left: schematic representation of the Wu experiment. It measured the rate of decay  $e^-$  in two mirrored setups with respect to the spin  $\vec{s}$  of the  $^{60}\text{Co}$  nucleus. Right: Results of the experiment from Reference [16], comparing the rate when counting the electrons emitted in the opposite direction of  $\vec{s}$  ( $\times$ ) and in the same direction ( $\bullet$ ). The asymmetry decreases as a function of time due to the increase of the temperature which randomizes the spin direction.

contribution  $\Gamma_{\text{vis}}$  coming from the charged particles, and an “invisible” contribution  $\Gamma_{\text{inv}}$  from the undetected particles. By measuring the total width of the resonance, and assuming that the decay  $Z^0 \rightarrow \nu\bar{\nu}$  occurs at the same width  $\Gamma_\nu$  for all neutrino flavors (as expected by Equation (1.12)), the dependence on the number of neutrinos can be obtained with the relation  $\Gamma_{\text{tot}} = \Gamma_{\text{vis}} + \Gamma_{\text{inv}} = \Gamma_{\text{vis}} + N_\nu \Gamma_\nu$ .

This way, ALEPH, DELPHI, L3 and OPAL experiments at the Large Electron Positron (LEP) collider [17] provided strong constraints on the number of neutrinos as shown in Figure 1.5. This gives only a partial answer to the question of the number of neutrinos. The fact that these neutrinos come from  $Z^0$  weak decay mean that this measurement is only sensitive to active neutrinos. Furthermore, this decay cannot kinematically occur if the neutrino masses are larger than  $M_Z/2$ . Therefore, constraints on  $N_\nu$  from these experiments only apply to active neutrinos with a mass below  $M_Z/2$ . As we will briefly mention below, other constraints on the number of neutrinos can be obtained from cosmological surveys which apply regardless whether the neutrinos are active or sterile [18], but these remain highly dependent on the underlying cosmological model.

### Neutrino mass

Since Pauli has first predicted their existence, it was known that neutrinos are expected to have a very small mass due to the shape of the beta decay energy spectrum. Experimentally, there are three main ways to probe their mass: astrophysical and cosmological observations, neutrinoless double beta decay, and direct kinematic measurements.

Neutrinos, among the most abundant particles in the Universe, have a significant contribution to the energy density at very early times of the Universe formation in the hot big bang model. More specifically, the fluctuations of the cosmological density heavily depend on the sum of

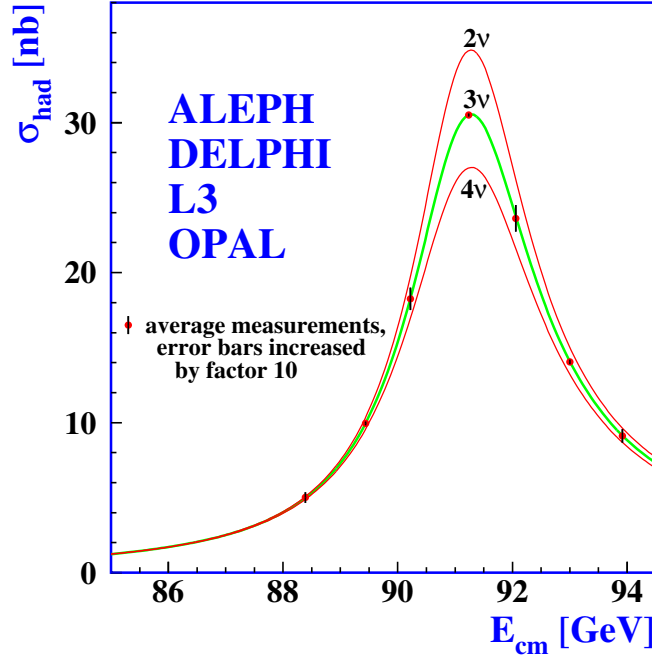


Figure 1.5: Measurement of the hadron cross sections around the Z resonance at the LEP compared to different scenarios of  $N_\nu = 2, 3, 4$ . Figure from Reference [17].

neutrino masses  $\Sigma M_\nu$ , and its impact can be visible in the cosmic microwave background (CMB) [19], which represents the Universe at the age of 380,000 years after the big bang. The increasingly precise cosmological surveys that map the non-statistical fluctuations of the energy and temperature distributions in the CMB can provide the strongest constraints on  $\Sigma M_\nu$ . For instance, the Planck experiment, a space-based observatory, provided an upper limit of  $\Sigma M_\nu < 0.12 \text{ eV}$  (95% C.L.) in 2018 [18]. Combining these measurements with other astrophysical and cosmological observations, such as the large scale structure of the Universe and Type Ia supernova luminosity distances, can also yield even more constraining bounds by breaking degeneracies between the many cosmological parameters [20].

On the other hand, neutrinoless double beta decay experiments probe the Majorana nature of neutrinos. In Nature, nuclei can undergo beta decays where one of their protons (neutrons) is transformed to neutron (proton), accompanied by the emission of a positron (electron) and an electron (anti)neutrino through the weak interaction. This occurs so that the nucleus can have a more stable proton-to-neutron ratio. Some special nuclei can only undergo a *double* beta decay, where for instance two neutrons turn into protons simultaneously, producing two decay electrons as shown in the left Feynman diagram of Figure 1.6. It is a rare process as it requires two coinciding weak interactions, with a typical half life of more than  $10^{19}$  years. If neutrinos are Majorana particles, *neutrinoless* double beta decay can actually occur as displayed in the right diagram of Figure 1.6. The half-life time measurement of this process is the subject of multiple ongoing experiments for different nuclear isotopes. It is also sensitive to the neutrino mass, and the upper bounds that are currently obtained are around  $\sim 0.1 - 0.2 \text{ eV}$  [12].

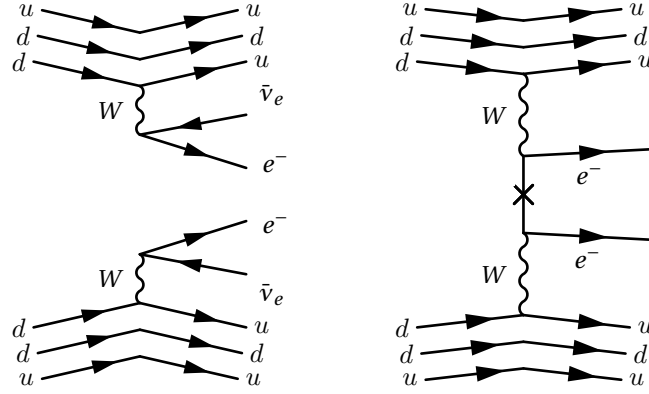


Figure 1.6: Feynman diagrams for double beta decays for two initial state neutrons ( $udd$ ) decaying into protons ( $uud$ ). Neutrinoless double beta decay (right) would occur if neutrinos are Majorana particles (i.e.  $\nu = \bar{\nu}$ ).

Finally, the kinematics of (single) beta decays provide the most direct way to assess the neutrino mass. Unlike cosmological constraints which heavily depend on the underlying cosmological assumptions, and neutrinoless double beta decay which depends on the Majorana nature of the neutrino, high precision measurements of the beta decay spectrum can directly constrain the neutrino mass by examining the energy of the emitted electrons. For instance, in 2022, the KATRIN experiment has reported an upper limit on the effective<sup>3</sup> electron neutrino mass of  $M_{\nu_e}^{\text{eff}} < 0.8$  eV (90% C.L.) using tritium decay  ${}^3\text{H} \rightarrow {}^3\text{He} + e^- + \bar{\nu}_e$  [21].

## 1.3 Neutrino oscillations

### 1.3.1 A brief history of neutrino oscillation discovery

Following the experimental discovery of neutrinos, multiple experiments attempted to utilize their unique properties to probe previously-inaccessible physics. Indeed, their weakly-interacting nature, with a small interaction cross section, make them the perfect messenger to directly inform us about their source, unlike other radiation types, since they can pass through matter without significant alteration. In this section, we review three sources in particular that were studied with neutrinos: nuclear reactions inside the Sun, atmospheric showers resulting from the collision of cosmic rays with nuclei in Earth's upper atmosphere, and neutrinos produced in nuclear reactors.

<sup>3</sup>As will be discussed in the next section, flavor states of neutrinos do not have a definite mass, but we can define an *effective* mass for a given flavor as a combination of the masses of neutrino mass states, such as:  $M_{\nu_e}^{\text{eff}} = \sqrt{\sum_i |U_{ei}|^2 m_i^2}$  using the notations of the next section.

### Solar neutrinos

In the 1960s, R. Davis and J. Bahcall wanted to measure the incoming neutrino flux from nuclear reactions beyond the surface of the Sun. J. Bahcall had developed the *standard solar model* which predicts the solar neutrino spectrum [22]. It models the cycles of nuclear fusion in the core of the Sun that prevent it from collapsing under its own gravitational force. These include a variety of processes such as those happening in the *pp-chain* which is shown in Figure 1.7.

To compare the predictions of this model, they set up the Homestake experiment [25], measuring the electron neutrinos from the Sun through their inverse beta decay on calcium. The results of this experiment suggested that the measured electron neutrino flux was two to three times smaller than Bahcall's prediction [26]. It was thought to come either from a systematic uncertainty that was not accounted for in the experiment, or flaws in the standard solar model. Further developments of this model over several decades still could not explain this discrepancy, and several other experiments in the 1990s [27–29] confirmed the flux deficit which became known as the *solar neutrino problem*.

A solution to this problem had been first proposed by B. Pontecorvo as early as 1957 [30] and further elaborated by Z. Maki, M. Nakagawa and S. Sakata in 1962 [31]. It suggested that neutrinos could oscillate between flavors as they propagate, leading to a conserved total neutrino flux but a smaller electron neutrino contribution, the other neutrino flavors being undetected due to experimental limitations. However, while this process, which is now called *neutrino oscillations*, gave good explanations to the solar neutrino problem, other solutions were also plausible, such as possible neutrino decays beyond the Standard Model.

First confirmations of this theory came with the *Super-Kamiokande* experiment in 1992 for atmospheric neutrinos (see next Section) and the *Sudbury Neutrino Observatory* (SNO) for solar neutrinos. The SNO experiment used a spherical water Čerenkov detector containing 1,000 tons of pure heavy water ( $D_2O$ ) placed in an underground mine in Canada, with photomultipliers on its inner surface to detect light emissions. It targeted the neutrinos issued from the  $^8B$  ray (see Figure 1.7), and measured their interactions in three detection channels, one of them is sensitive to electron neutrinos only, while the two others are sensitive for all neutrino flavors:

- CC interactions of electron neutrinos with the deuterium  $\nu_e + d \rightarrow p + p + e^-$ . This is sensitive only to electron neutrinos because of the energy spectrum of the solar neutrino flux is below the masses of the muon and tau leptons, and therefore they cannot be produced by such interaction.
- NC interactions of all neutrino flavors with deuterium  $\nu_l + d \rightarrow \nu_l + p + n$ . The produced neutron is captured by deuterium, emitting a gamma ray of  $\sim 6$  MeV. This interaction is equally sensitive to all neutrino flavors.
- Interactions with electrons of heavy water atoms  $\nu_l + e^- \rightarrow \nu_l + e^-$ , called elastic scatter-

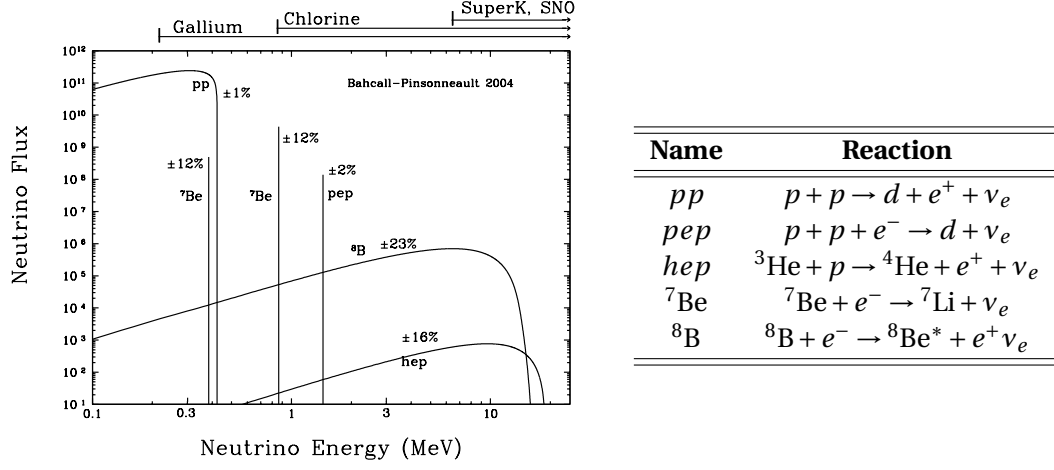


Figure 1.7: The predicted solar neutrino flux in  $\text{cm}^{-2}\text{s}^{-1}\text{MeV}^{-1}$  for continuum sources and  $\text{cm}^{-2}\text{s}^{-1}$  for line sources along with the theoretical errors (left) produced by the different reactions in the  $pp$ -chain (right). Figure from Reference [23].

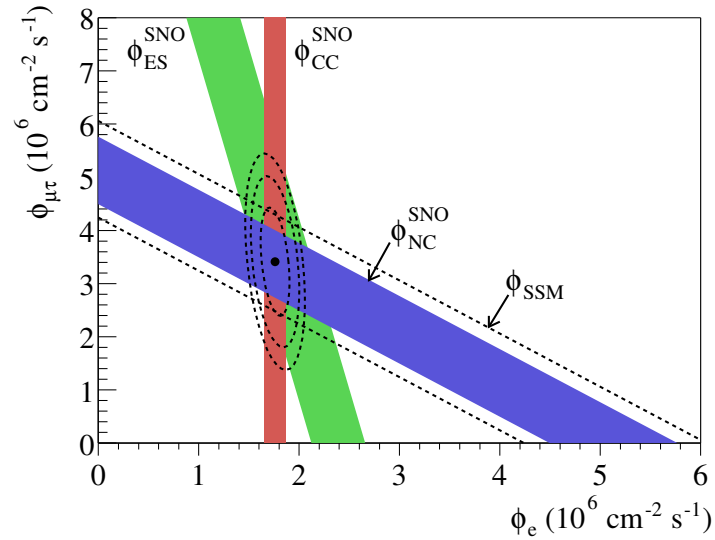


Figure 1.8: Results of the SNO experiment. Figure from Reference [24].



## Chapter 1. Neutrinos in the Standard Model and beyond

---

ing (ES). This channel is dominated by electron neutrinos because it can occur in two ways: through CC interaction which occurs for electron neutrinos only, and through NC interaction for all flavors.

If there were no flavor transitions, the measured neutrino fluxes from the three detection channels should be equal, as only electron neutrinos would be coming from the Sun. However, as displayed in Figure 1.8, the SNO experiment observed the three different flavors. In addition to that, the flux measurement from the NC channel, which is equally sensitive to all neutrino flavors, is in very good agreement with the standard solar model [24]. This demonstrates that the deficit previously observed in the electron neutrino flux is indeed due to the neutrino flavor conversion.

### Atmospheric neutrinos

In the late 1980s, around the same time when anomalies were observed and confirmed for solar neutrinos, the Kamiokande-II [32] and IMB [33] experiments also reported deficits in the flux of the muon neutrinos produced from the hadronic decays of the product of cosmic ray interactions with the atmosphere, while the electron neutrino flux well matched the predictions. This too was named the *atmospheric neutrino problem*.

Atmospheric neutrinos come primarily from the decay of pions  $\pi^+ \rightarrow \nu_\mu + \mu^+$  into muon neutrinos of energies typically above 0.1 GeV. The muons from this interaction can also decay into electron and muon neutrinos as given by:  $\mu^+ \rightarrow e^+ + \nu_e + \bar{\nu}_\mu$ , and the expected ratio between muon and electron neutrinos is roughly  $(\nu_\mu + \bar{\nu}_\mu) : (\nu_e + \bar{\nu}_e) \approx 2 : 1$ . Additionally, as neutrinos were assumed to be massless, this flux was expected to be independent of the zenith angle  $\Theta$  (see Figure 1.9), at least for multi-GeV neutrinos where their mass, if any, can be certainly neglected. Therefore, this ratio should remain the same both for upward (i.e.  $\cos\Theta < 0$ ) and downward ( $\cos\Theta > 0$ ) going neutrinos.

The Kamiokande-II Collaboration observed a muon to electron neutrino ratio of  $\sim 1.2$  instead, a value that is very different from the expectations which could not be explained by any of the systematic uncertainties in the experiment [32]. This was later confirmed by the Super-Kamiokande experiment where the asymmetry was observed with over  $6\sigma$  significance between upward going and downward going muon neutrinos [34], as shown in Figure 1.10. More specifically, approximately half of the upward going muon neutrinos that travel around 10,000 km (see Figure 1.9) *disappeared* in comparison with the downward going muon neutrinos that travel around 20 km. Furthermore, it also showed that this disappearance could be explained by the  $\nu_\mu \leftrightarrow \nu_\tau$  oscillations since no excess was observed in the electron neutrino samples [34].

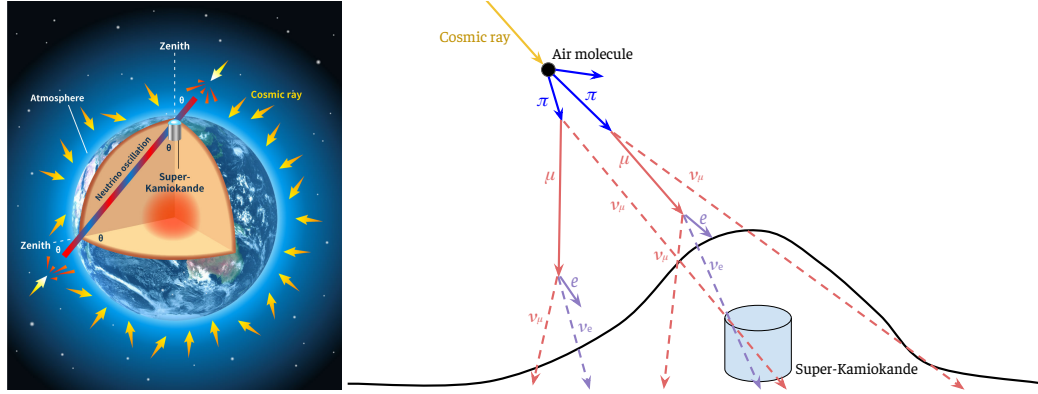


Figure 1.9: Left: schematic representation of the different neutrino directions measured in Super-Kamiokande, from Reference [35]. Right: atmospheric shower produced by a cosmic ray.

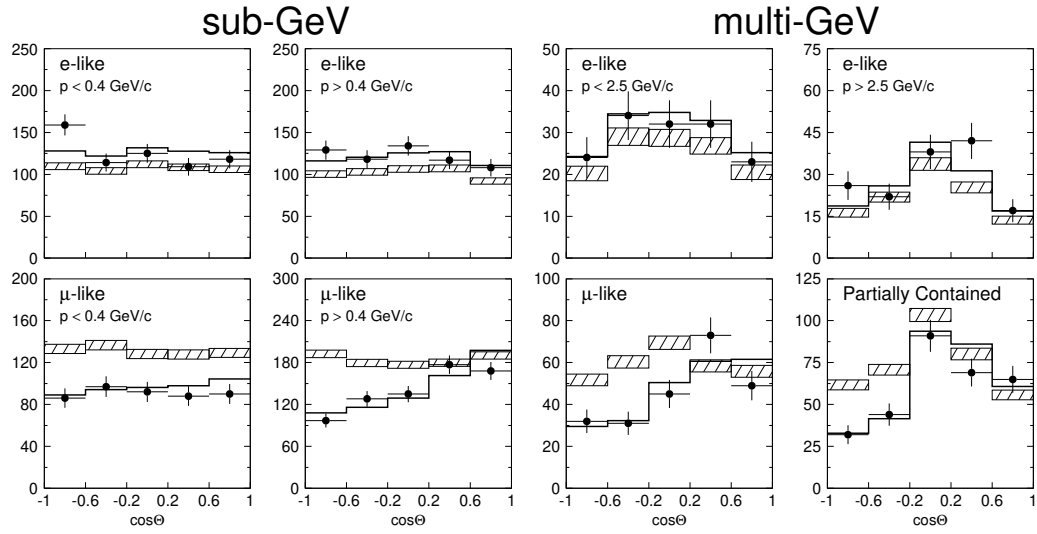


Figure 1.10: Zenith angle distributions of  $\nu_e$ -like (top) and  $\nu_\mu$ -like (bottom) events for sub-GeV (left) and multi-GeV (right) data set, separated by regions in the reconstructed charged lepton momentum. The multi-GeV  $\nu_\mu$ -like samples are shown separately for fully contained and partially contained events. The hatched region shows the Monte Carlo expectation for no oscillations normalized to the data live-time with statistical errors. The bold line is the best-fit expectation for  $\nu_\mu \leftrightarrow \nu_\tau$  oscillations with the overall flux normalization fitted as a free parameter. Figure from Reference [34].

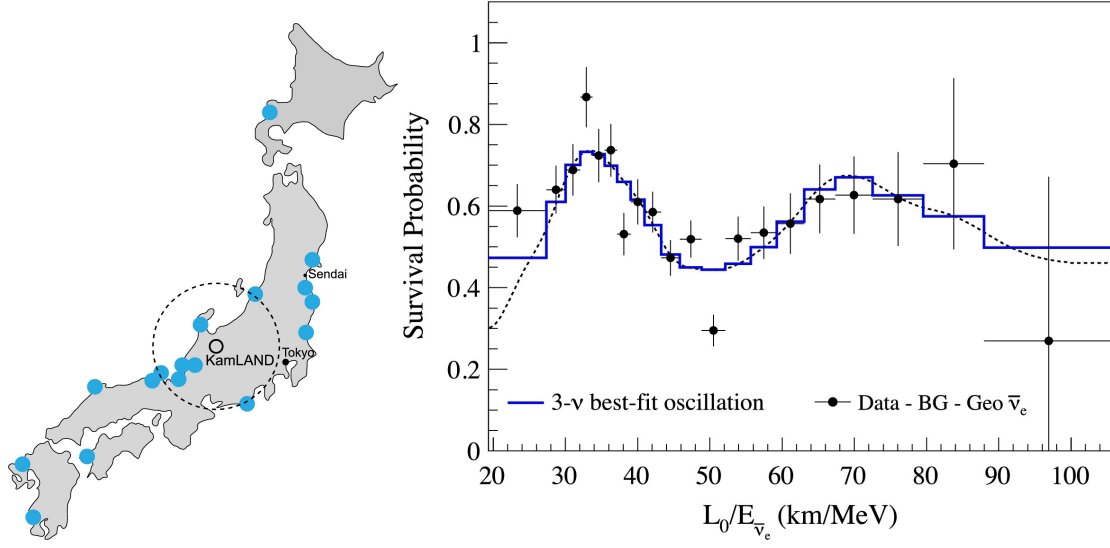


Figure 1.11: Left: location of KamLAND and nuclear reactors (blue circles), from Reference [38]. Right: survival probability of electron antineutrinos as a function of the ratio  $L_0/E_{\bar{\nu}_e}$ , from Reference [37].

### Reactor neutrinos

Following the strong evidence in favor of neutrino oscillations from SNO and Super-Kamiokande, the KamLAND experiment further confirmed this with neutrinos coming from nuclear reactors. With 1000 tons of pure liquid scintillator (similar to SNO), it measured the electron antineutrinos produced by inverse beta decays in more than 50 reactors around Japan, with a mean distance of  $L_0 \sim 180$  km. Consequently, not only did it measure a deficit in the  $\bar{\nu}_e$  flux [36], but it also observed an energy dependence in this deficit [37]. The left panel of Figure 1.11 shows the survival probability, i.e. the ratio of observed over expected event rate without oscillations, of electron antineutrinos as a function of the mean distance from nuclear reactors  $L_0$  over the electron antineutrino energy  $E_{\bar{\nu}_e}$ .

### 1.3.2 General three-flavor neutrino oscillation probability

In the standard neutrino oscillation formalism, the flavor states of neutrinos, denoted by  $|\nu_\alpha\rangle$  with  $\alpha = e, \mu, \tau$ , are a linear combination of their mass states  $|\nu_i\rangle$ ,  $i = 1, 2, 3$ , described by the so-called Pontecorvo – Maki – Nakagawa – Sakata (PMNS) unitary matrix  $U$  as:

$$|\nu_\alpha\rangle = \sum_i U_{\alpha i}^* |\nu_i\rangle, \quad \text{or equivalently} \quad |\nu_i\rangle = \sum_\alpha U_{\alpha i} |\nu_\alpha\rangle. \quad (1.15)$$

The neutrino mass states are by definition eigenvectors of the free Hamiltonian  $\mathcal{H}_{\text{free}}$  when neutrinos propagate in vacuum, satisfying  $\mathcal{H}_{\text{free}} |\nu_i\rangle = E_i |\nu_i\rangle$  where  $E_i$  is the energy of the

mass state  $|\nu_i\rangle$ . The Schrödinger equation describes the evolution of the mass states as:

$$i \frac{\partial}{\partial t} |\nu_i(t, \vec{x})\rangle = E_i |\nu_i(t, \vec{x})\rangle = -\frac{1}{2m_i} \nabla^2 |\nu_i(t, \vec{x})\rangle. \quad (1.16)$$

#### Plane wave solution

The plane wave solution of Equation (1.16) is written as:

$$|\nu_i(t, \vec{x})\rangle = e^{-i(E_i t - \vec{p}_i \cdot \vec{x})} |\nu_i\rangle \quad (1.17)$$

where we denote the initial condition of  $|\nu_i(t, \vec{x})\rangle$  at  $(t, \vec{x}) = (0, \vec{0})$  by  $|\nu_i\rangle$ , and  $\vec{p}_i$  is the momentum of the state  $|\nu_i(t, \vec{x})\rangle$  which satisfies the *dispersion* relation:

$$E_i^2 = p_i^2 + m_i^2. \quad (1.18)$$

To simplify the notations, we can define the phase  $\varphi_i$  of the plane wave as:

$$\varphi_i(t, \vec{x}) = E_i t - \vec{p}_i \cdot \vec{x}.$$

Therefore, the time evolution for the flavor state  $|\nu_\alpha(t, \vec{x})\rangle$  can be obtained using Equation (1.15):

$$\begin{aligned} |\nu_\alpha(t, \vec{x})\rangle &= \sum_i U_{\alpha i}^* e^{-i\varphi_i(t, \vec{x})} |\nu_i\rangle \\ &= \sum_i \sum_\beta U_{\alpha i}^* U_{\beta i} e^{-i\varphi_i(t, \vec{x})} |\nu_\beta\rangle, \end{aligned}$$

where we also denote by  $|\nu_\beta\rangle$  the initial condition of  $|\nu_\beta(t, \vec{x})\rangle$ , with  $\beta = e, \mu, \tau$ .

The probability for a flavor state  $\nu_\alpha$  to evolve into a flavor state  $\nu_\beta$  at the spacetime coordinate  $(T, \vec{L})$  is then given by:

$$P(\nu_\alpha \rightarrow \nu_\beta; T, \vec{L}) = |\langle \nu_\beta(t, \vec{x}) | \nu_\alpha \rangle|^2 = \sum_{i,j} U_{\alpha i}^* U_{\beta i} U_{\alpha j} U_{\beta j}^* e^{-i\varphi_{ij}}. \quad (1.19)$$

where  $\varphi_{ij}$  is the phase difference defined by  $\varphi_{ij} = \varphi_i(T, \vec{L}) - \varphi_j(T, \vec{L})$ . It is commonly called the *disappearance* probability when  $\alpha = \beta$ , and the *appearance* probability for  $\alpha \neq \beta$ .

In the trivial case when  $T = 0$  and  $\vec{L} = \vec{0}$ , we find that the probability is  $P(\nu_\alpha \rightarrow \nu_\beta; 0, \vec{0}) = \delta_{\alpha\beta}$  as we expect, using the unitarity of the PMNS matrix.

Let us now express the phase difference<sup>4</sup>:

$$\varphi_{ij} = (E_i - E_j) T - (\vec{p}_i - \vec{p}_j) \cdot \vec{L}. \quad (1.20)$$

<sup>4</sup>It is common, in order to quickly derive the oscillation probability, to assume that the different mass states have the same energy. Here we choose not to make this assumption which does not hold in general.

## Chapter 1. Neutrinos in the Standard Model and beyond

---

The first approximation that we will make is that all massive neutrino momenta  $\vec{p}_i$  are aligned with  $\vec{L}$ . Indeed, in oscillation experiments, neutrinos travel a macroscopic distance between production and detection, and the transverse component can be neglected. Small deviations from this assumption can be shown to have a negligible impact on the final result (see e.g. Section 8.1.3 in Reference [39]). The phase difference becomes:

$$\varphi_{ij} = (E_i - E_j) T - (p_i - p_j) L. \quad (1.21)$$

The energy and momenta of the neutrino mass states can be fully determined by their production process. In the case of the T2K experiment, as will be seen in Chapter 2, neutrinos are produced by the pion decay as:  $\pi^+ \rightarrow \mu^+ + \nu_\mu$ . The energy and momentum of the produced mass state neutrinos can be obtained directly from the kinematics of the muon and the pion.

As shown in Section 1.2.4, neutrinos are expected to have masses smaller than 1 eV, and can thus be assumed to be ultrarelativistic for oscillation experiments where neutrino energies are of the order of 1 GeV.

In the first order in this approximation, when neutrinos are assumed to be massless, all the mass states have the same energy and momentum  $\bar{E} = \bar{p}$  obtained by energy-momentum conservation in the rest frame of the decaying pion as a function of the muon and pion masses  $M_\mu$  and  $M_\pi$  respectively:

$$\bar{E} = \bar{p} = \frac{M_\pi^2 - M_\mu^2}{2M_\pi}. \quad (1.22)$$

In general, we can derive the energy and momentum for the produced mass state  $\nu_i$  from the pion decay in the rest frame of  $\pi^+$  [40, 41]:

$$\begin{aligned} p_i^2 &= \frac{M_\pi^2}{4} \left(1 - \frac{M_\mu^2}{M_\pi^2}\right)^2 - \frac{m_i^2}{2} \left(1 + \frac{M_\mu^2}{M_\pi^2}\right) + \frac{m_i^4}{4M_\pi^2}, \\ E_i^2 &= \frac{M_\pi^2}{4} \left(1 - \frac{M_\mu^2}{M_\pi^2}\right)^2 + \frac{m_i^2}{2} \left(1 - \frac{M_\mu^2}{M_\pi^2}\right) + \frac{m_i^4}{4M_\pi^2}. \end{aligned}$$

We can see that this adds high order corrections to the energy and momentum of the mass state in the massless neutrino limit of Equation (1.22). In the leading order with respect to the neutrino mass, we can write this as:

$$\begin{aligned} p_i &\approx \bar{E} - \xi \frac{m_i^2}{2\bar{E}}, \\ E_i &\approx \bar{E} + (1 - \xi) \frac{m_i^2}{2\bar{E}}. \end{aligned} \quad (1.23)$$

where  $\xi$  is a quantity that characterizes the neutrino production process. In our case where

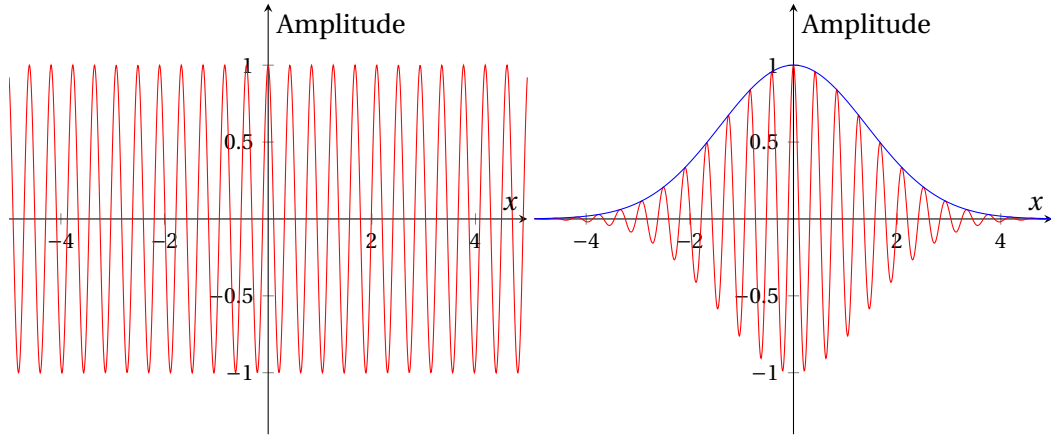


Figure 1.12: Comparison of a plane wave (left) and a Gaussian wave packet (right) in space.

the pion decays into a muon and neutrino, it corresponds to:  $\xi = \frac{1}{2} \left( 1 + \frac{M_\mu^2}{M_\pi^2} \right) \approx 0.8$ .

We can now express the phase difference from Equation (1.21) as:

$$\varphi_{ij} = (1 - \xi) \frac{\Delta m_{ij}^2}{2\bar{E}} T + \xi \frac{\Delta m_{ij}^2}{2\bar{E}} L \quad (1.24)$$

where  $\Delta m_{ij}^2 = m_i^2 - m_j^2$  is the *squared mass splitting*. In neutrino oscillation experiments, the propagation distance is well known, but the travel time is not measured. To reach the final oscillation probability formula, we need to express  $T$  in terms of the distance  $L$ . Up until this point, we considered a plane wave solution to the Schrödinger equation. By definition, a plane wave extends over all the spacetime, while the production and the detection processes of neutrinos are localized in space. In the next part, we see how the neutrinos can be treated as wave packets which will allow us to link the travel time and the distance.

### Wave packet approach

Localized processes are described by wave packets. A wave packet is a superposition of plane waves with momenta in a region of width  $\sigma_p$  around a reference momentum  $\vec{p}_0$ . These plane waves have a constructive interference in a spatial region of width  $\sigma_x$  around a point  $\vec{x}_0$ , and outside of this region, the interference is destructive as displayed in Figure 1.12. The widths in position and momentum spaces are related by the Heisenberg uncertainty relation:

$$\sigma_x \sigma_p \geq \frac{1}{2}. \quad (1.25)$$

In this approach, the plane wave solution to the Schrödinger equation shown in Equation (1.17) is modified to account for these features as  $|\nu_i(t, \vec{x})\rangle = \Psi_i(t, \vec{x}) |\nu_i\rangle$  where the wave packet  $\Psi_i$

## Chapter 1. Neutrinos in the Standard Model and beyond

---

can be expressed as:

$$\Psi_i(\vec{x}, t) = \int \frac{d^3 p}{(2\pi)^3} f_i(\vec{p}) e^{-i(E_i(p)t - \vec{p} \cdot \vec{x})}. \quad (1.26)$$

$f_i$  describes the momentum distribution, and the dispersion relation that allows this wave packet to satisfy the Schrödinger equation is:

$$E_i^2(p) = p^2 + m_i^2. \quad (1.27)$$

At the source, the shape of the wave packet is defined by the neutrino production process and its momentum uncertainty. For ultrarelativistic neutrinos, we can safely assume that  $\sigma_{p_i}^P \ll p_i$ . Therefore, we can approximate the wave packet by a sharply peaked Gaussian wave function around a central momentum  $p_i$  given by:

$$f_i^P(p) \propto \exp \left[ -\frac{(p - p_i)^2}{4\sigma_{p_i}^{P^2}} \right].$$

Since we can neglect the spreading  $\sigma_{p_i}^P$ , we can find from Equation (1.26) that the wave packet at production  $\Psi_i^P$  is:

$$\Psi_i^P(\vec{x}, t) \propto \exp \left[ -\frac{(x - v_i t)^2}{4\sigma_x^{P^2}} \right] e^{-i(E_i t - p_i x)} \quad (1.28)$$

where  $\sigma_x^P$  is the spatial uncertainty in the production process related to  $\sigma_p^P$  by  $\sigma_x^P \sigma_p^P = 1/2$ . The small momentum spread allows us to approximate the energy to the first order by:

$$E_i(p) \approx E_i + v_i(p - p_i).$$

and  $v_i$  is the group velocity of the wave packet defined by:

$$v_i = \left. \frac{\partial E_i(p)}{\partial p} \right|_{p_i} = \frac{p_i}{E_i} \approx 1 - \frac{m_i^2}{2E_i^2}. \quad (1.29)$$

where we applied the relations given by Equation (1.23).

Equation (1.28) shows that the wave function is a plane wave with a Gaussian envelope of  $\sigma_x$  width. This highlights an important feature that allows oscillations to occur called *coherence*: the amplitude is strongly suppressed as soon as  $|x - v_i t| \gtrsim \sigma_x^P$ .

Similarly, we can obtain the expression of the wave packet for the detection process that depends on the spatial detection uncertainty  $\sigma_x^D$ . The oscillation probability after a travel distance  $L$  and time  $T$  obtained with the plane wave solution in Equation (1.19) becomes in the wave packet approach:

$$P(\nu_\alpha \rightarrow \nu_\beta; T, L) \propto \sum_{i,j} U_{\alpha i}^* U_{\beta i} U_{\alpha j} U_{\beta j}^* e^{-i\varphi_{ij}(T,L)} \times \exp \left[ -\frac{(L - v_i T)^2 + (L - v_j T)^2}{4\sigma_x^2} \right]$$

where  $\sigma_x$  is the combined uncertainty in the production and detection processes  $\sigma_x^2 = \sigma_x^{P^2} + \sigma_x^{D^2}$ . As mentioned previously, the travel time is not measured in oscillation experiments, so we can integrate over it and get:

$$P(\nu_\alpha \rightarrow \nu_\beta; L) = \int P(\nu_\alpha \rightarrow \nu_\beta; T, L) dT$$

$$= \sum_i |U_{\alpha i}|^2 |U_{\beta i}|^2 + 2\Re \left\{ \sum_{i>j} \mathcal{N}_{ij} U_{\alpha i}^* U_{\beta i} U_{\alpha j} U_{\beta j}^* \exp \left[ -2\pi i \frac{L}{L_{ij}^{\text{osc}}} - \left( \frac{L}{L_{ij}^{\text{coh}}} \right)^2 \right] \right\}. \quad (1.30)$$

This is the general oscillation probability for a produced neutrino  $\nu_\alpha$  to be found as  $\nu_\beta$  after a travel distance  $L$ , where we define the following quantities:

- The oscillating phase, i.e. the imaginary part in the exponential, can be expressed in terms of the oscillation length:

$$L_{ij}^{\text{osc}} = \frac{4\pi \bar{E}}{\Delta m_{ij}^2} \quad (1.31)$$

- The coherence length, which appears in the real part in the exponential and can suppress the oscillation amplitude, is defined as:

$$L_{ij}^{\text{coh}} = \frac{4\sqrt{2}\sigma_x \bar{E}^2}{|\Delta m_{ij}^2|} \quad (1.32)$$

- $\mathcal{N}_{ij} = \exp \left[ -2\pi^2 (1 - \xi)^2 \left( \frac{\sigma_x}{L_{ij}^{\text{osc}}} \right)^2 \right]$  is the norm factor ensuring  $\sum_\beta P(\nu_\alpha \rightarrow \nu_\beta; L) = 1$ .

#### 1.3.3 Discussion

##### Coherence

As shown in Equation (1.32), the coherence length is proportional to the combined spatial uncertainty on the neutrino production and detection processes. In order for oscillations to be observed, two conditions need to be satisfied:

1. The first condition arises from the normalization factor  $\mathcal{N}_{ij}$ , which describes the localization of the wave packet with respect to the oscillation length, and is  $\sigma_x \ll L_{ij}^{\text{osc}}$ . This is equivalent, in terms of momentum width  $\sigma_p$ , to  $|p_i - p_j| \ll \sigma_p$  using Equations (1.23) and (1.25). This means that, in order for the oscillations to be observed, the uncertainty should not allow to distinguish between the momenta of the mass states.
2. The second condition appears in the exponential of Equation (1.30) and corresponds to  $L_{ij}^{\text{coh}} \ll L$ . This can be understood in an intuitive way: each wave packet propagates with an average (group) velocity  $v_i$ , and the distance between two mass states at the



## Chapter 1. Neutrinos in the Standard Model and beyond

---

detection level can be expressed as  $\Delta x_{ij} = x_i - x_j = (\nu_i - \nu_j)L$  by taking here  $L = T$ . We can see, using Equation (1.29), that this condition is equivalent to  $\Delta x_{ij} \ll \sigma_x$ . Indeed, coherence is lost if the wave packet spatial resolution is too small as there would be no interference between the mass states. This shows that if the mass difference between two states is too large, or if the neutrino energy is too small, the decoherence can occur rather quickly during propagation.

These conditions are fully satisfied for accelerator neutrinos. Indeed, in the case of the T2K experiment, the spatial uncertainty can be estimated from the extent of the source and the detectors. The decay tunnel within which neutrinos are produced from pion decay is  $\sim 100$  m long. This dominates the spatial uncertainty as the detector resolution on the interaction position is typically of  $\sigma_x^D \sim 1$  cm, thus  $\sigma_x \approx \sigma_x^P \sim 100$  m. This can also be obtained from the fact that the production spatial uncertainty comes from the lifetime of the particles involved in the pion decay and is dominated by the shortest-lived one: the pion with a lifetime  $\tau_\pi \sim 10^{-8}$  s at rest. Since the pion decays in flight, the width can be expressed in the laboratory frame as  $\sigma_x^P \sim \gamma_\pi \tau_\pi$  using the Lorentz factor  $\gamma_\pi \sim 10$  for pions of energy  $\sim 1$  GeV, which gives  $\sigma_x^P \sim 100$  m. Given the measured values of  $\Delta m_{ij}^2$  (see Table 1.3,  $\Delta m_{12}^2 \sim 10^{-5}$  eV<sup>2</sup> and  $\Delta m_{13}^2 \sim 10^{-3}$  eV<sup>2</sup>) and the typical neutrino energy  $\bar{E} \sim 0.6$  GeV, we can see that the two conditions are satisfied with a large margin for a travel distance  $L \sim 100$  km.

On the scale of astrophysical and cosmological neutrino sources, these conditions are not always satisfied. Let us take solar neutrinos as an example. These neutrinos have energies around  $\bar{E} \sim 1$  MeV (see e.g. Figure 1.7) and propagate over a distance  $L \sim 10^{11}$  m. The spatial width of the production process, assumed at the atomic level, is estimated at  $\sigma_x^P \sim 10^{-11}$  m [42] and very small in comparison with the detection  $\sigma_x^D \sim 10^{-2}$  m. This gives a coherence length  $L_{ij}^{\text{coh}} \sim 10^7$  m, much smaller than the travel distance of solar neutrinos. Therefore, they lose all coherence when they reach Earth, and the flavor conversion that is observed in the solar neutrino flux can be mostly attributed to the matter effects as we will discuss below.

### Standard parametrization of the oscillation probability

Since the focus of this thesis is neutrinos produced in accelerators, we will neglect the decoherence effects and therefore use the following oscillation probability expression:

$$\begin{aligned}
 P(\nu_\alpha \rightarrow \nu_\beta) = & \delta_{\alpha\beta} - 4 \sum_{i>j} \Re \left( U_{\alpha i}^* U_{\beta i} U_{\beta j} U_{\alpha j}^* \right) \sin^2 \left( \frac{\Delta m_{ij}^2 L}{4E} \right) \\
 & + 2 \sum_{i>j} \Im \left( U_{\alpha i}^* U_{\beta i} U_{\beta j} U_{\alpha j}^* \right) \sin \left( \frac{\Delta m_{ij}^2 L}{2E} \right)
 \end{aligned} \tag{1.33}$$

where  $E$  is the neutrino energy and  $L$  is the propagation distance.

In this context, as displayed in Figure 1.16,  $\nu_1$  is commonly defined as the mass state with the

largest admixture of the electron flavor state,  $\nu_2$  as a more even mixture of the three flavors, and  $\nu_3$  composed mostly of muon and tau flavors.

For oscillation experiments, the PMNS matrix can be fully characterized by three mixing angles  $\theta_{12}$ ,  $\theta_{13}$  and  $\theta_{23}$ , and one phase  $\delta_{\text{CP}}$  as:

$$\begin{aligned}
 U &= \begin{bmatrix} 1 & 0 & 0 \\ 0 & c_{23} & s_{23} \\ 0 & -s_{23} & c_{23} \end{bmatrix} \begin{bmatrix} c_{13} & 0 & s_{13}e^{-i\delta_{\text{CP}}} \\ 0 & 1 & 0 \\ -s_{13}e^{i\delta_{\text{CP}}} & 0 & c_{13} \end{bmatrix} \begin{bmatrix} c_{12} & s_{12} & 0 \\ -s_{12} & c_{12} & 0 \\ 0 & 0 & 1 \end{bmatrix} \\
 &= \begin{bmatrix} c_{12}c_{13} & s_{12}c_{13} & s_{13}e^{-i\delta_{\text{CP}}} \\ -s_{12}c_{23} - c_{12}s_{23}s_{13}e^{i\delta_{\text{CP}}} & c_{12}c_{23} - s_{12}s_{23}s_{13}e^{i\delta_{\text{CP}}} & s_{23}c_{13} \\ s_{12}s_{23} - c_{12}c_{23}s_{13}e^{i\delta_{\text{CP}}} & -c_{12}s_{23} - s_{12}c_{23}s_{13}e^{i\delta_{\text{CP}}} & c_{23}c_{13} \end{bmatrix}
 \end{aligned} \tag{1.34}$$

where  $c_{ij} = \cos\theta_{ij}$  and  $s_{ij} = \sin\theta_{ij}$ .

As can be seen in Equation (1.33), oscillations are only possible if at least two of the three active neutrinos have non-vanishing mass, and if their masses are different. The dependence on the mass differences, rather than the absolute masses, shows that neutrino oscillations are only sensitive to the size of the mass differences and their sign, but not the absolute mass scale.

The frequency of oscillations in  $L/E$  is ruled by the inverse of the mass difference between the mass states. For instance, as shown in Table 1.3, our current knowledge of the squared mass differences show that  $|\Delta m_{21}^2| \ll |\Delta m_{32}^2|$ . The consequences of this is shown in Figure 1.13: for small  $L/E \sim 1 \text{ km/MeV}$  (right panel), as is the case for T2K, the oscillations are dominated by the effect of  $|\Delta m_{32}^2|$ , whereas for  $L/E \sim 100 \text{ km/MeV}$  (left panel) it is the low  $|\Delta m_{21}^2|$  frequency that drives the oscillations.

On the other hand, the amplitude of oscillations in  $L/E$  is governed by the values of the mixing angles in the PMNS matrix of Equation (1.34). Constraints from current experiments show that all of them are nonzero, while  $\theta_{13}$  is significantly smaller than  $\theta_{12}$  and  $\theta_{23}$  (see Table 1.3). This is why, for instance, the amplitude of the  $\nu_\mu \rightarrow \nu_e$  mixing in the right panel of Figure 1.13 is small in comparison with  $\nu_\mu \rightarrow \nu_{\mu,\tau}$ .

#### Charge-Parity symmetry

The parametrization of the PMNS matrix in Equation (1.34) shows a dependence on the phase  $\delta_{\text{CP}}$ , usually called *charge-parity violating phase* because it can affect neutrino and antineutrino oscillations differently. In fact, the action of the charge-parity (CP) and time

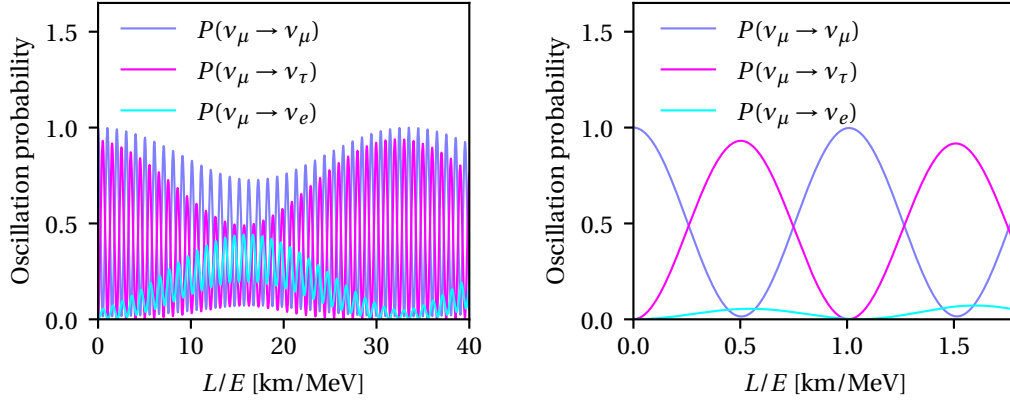


Figure 1.13: Muon neutrino oscillation probabilities in vacuum using global best-fit values of oscillation parameters shown in Table 1.3 for large (left) and small (right)  $L/E$ .

Oscillation parameter	Best fit $\pm 1\sigma$
$\sin^2 \theta_{12}$	$0.303^{+0.012}_{-0.012}$
$\theta_{12} [^\circ]$	$33.41^{+0.75}_{-0.72}$
$\sin^2 \theta_{23}$	$0.451^{+0.019}_{-0.016}$
$\theta_{23} [^\circ]$	$42.2^{+1.1}_{-0.9}$
$\sin^2 \theta_{13}$	$0.02225^{+0.00056}_{-0.00059}$
$\theta_{13} [^\circ]$	$8.58^{+0.11}_{-0.11}$
$\delta_{\text{CP}} [^\circ]$	$232^{+36}_{-26}$
$\Delta m_{21}^2 [10^{-5} \text{ eV}^2]$	$7.41^{+0.21}_{-0.20}$
$\Delta m_{31}^2 [10^{-3} \text{ eV}^2]$	$+2.507^{+0.026}_{-0.027}$

Table 1.3: Summary of the best fit values of oscillation parameters from global data [43].

reversing (T) symmetries on the oscillation probabilities can be summarized as:

$$\begin{aligned} P(\nu_\alpha \rightarrow \nu_\beta) &\xrightarrow{\text{CP}} P(\bar{\nu}_\alpha \rightarrow \bar{\nu}_\beta), \\ P(\nu_\alpha \rightarrow \nu_\beta) &\xrightarrow{\text{T}} P(\nu_\beta \rightarrow \nu_\alpha), \\ P(\nu_\alpha \rightarrow \nu_\beta) &\xrightarrow{\text{CPT}} P(\bar{\nu}_\beta \rightarrow \bar{\nu}_\alpha). \end{aligned}$$

In this thesis, CPT symmetry is assumed to be conserved, i.e.  $P(\nu_\alpha \rightarrow \nu_\beta) = P(\bar{\nu}_\beta \rightarrow \bar{\nu}_\alpha)$ . An important consequence of this assumption is that disappearance detection channels are not sensitive to CP violation, since  $P(\nu_\alpha \rightarrow \nu_\alpha) = P(\bar{\nu}_\alpha \rightarrow \bar{\nu}_\alpha)$ .

Therefore, CP symmetry conservation can only be probed by investigating the appearance channels and comparing the oscillation probabilities between neutrinos and antineutrinos. This asymmetry can be characterized by the quantity  $\Delta P_{\alpha\beta} = P(\nu_\alpha \rightarrow \nu_\beta) - P(\bar{\nu}_\alpha \rightarrow \bar{\nu}_\beta)$  which can be expressed as [44]:

$$\Delta P_{\alpha\beta} = \pm 16J \sin\left(\frac{\Delta m_{21}^2 L}{4E}\right) \sin\left(\frac{\Delta m_{31}^2 L}{4E}\right) \sin\left(\frac{\Delta m_{32}^2 L}{4E}\right)$$

where  $J = c_{12}s_{12}c_{23}s_{23}c_{13}^2s_{13}\sin\delta_{\text{CP}}$  is called the *Jarkslog invariant*, and the sign of  $\Delta P_{\alpha\beta}$  is positive (negative) if  $(\alpha, \beta, \gamma)$  is an even (odd) permutation of  $(e, \mu, \tau)$ . Therefore, it is clear that there would be no CP violating effect in neutrino oscillations unless all mixing angles and mass splittings are non-zero. If that is verified, then CP violation occurs as soon as  $\delta_{\text{CP}} \neq 0, \pi$ .

The search for CP violation in the lepton sector with neutrinos is of great interest as it can shed light on the matter – antimatter asymmetry in the Universe. Indeed, the baryonic matter asymmetry is quantified by:

$$\eta_B = \frac{n_B - n_{\bar{B}}}{n_\gamma} \sim 6 \times 10^{-10}$$

where  $n_B$ ,  $n_{\bar{B}}$  and  $n_\gamma$  are the number densities of baryons, antibaryons, and photons respectively. As early as 1967, A. Sakharov [45] proposed a set conditions that should be verified by a baryon generating interaction in order to explain the baryon asymmetry, among which CP violation is a critical element. Sakharov's CP-violation condition is actually required in the baryon sector, but as it was measured to be too small to explain the value of  $\eta_B$ , the lepton sector could be behind the baryon asymmetry. One popular mechanism to generate this is the baryogenesis via leptogenesis. In the leptogenesis, the right-handed Majorana neutrinos would decay and their couplings to the left-handed lepton doublets can violate the CP symmetry [46]. This lepton asymmetry is then translated into a baryon asymmetry by so-called sphaleron processes [47].

### Two-flavor oscillations

In many cases, especially for solar and atmospheric neutrinos, oscillation phenomena can be understood in a simple two-flavor picture. Indeed, neutrino mixing parameters involve two small quantities:

- $\Delta m_{21}^2 \ll |\Delta m_{32}^2|$ ,
- $\sin^2 \theta_{13} \ll \sin^2 \theta_{12} \sim \sin^2 \theta_{23}$ .

Therefore, in the limit of  $\sin^2 \theta_{13} \rightarrow 0$ , there are two regimes for oscillations defined by two scales. First, as shown for example in the right panel of Figure 1.13, the dominant effect for muon neutrinos when  $L/E \sim 1$  km/MeV (e.g. accelerator experiments) is the  $\nu_\mu \leftrightarrow \nu_\tau$  mixing driven by  $\Delta m_{32}^2$ . We can make the same observation for electron neutrino disappearance for  $L/E \gg 100$  km/MeV (e.g. solar neutrinos), where the very fast oscillations due to  $\Delta m_{32}^2$  are washed out due to the finite detector resolution, and only oscillations due to  $\Delta m_{21}^2$  can be observed.

In such cases, the  $2 \times 2$  mixing matrix between  $\nu_\alpha$  and  $\nu_\beta$  is parametrized by one angle  $\vartheta$  as:

$$U = \begin{bmatrix} \cos \vartheta & \sin \vartheta \\ -\sin \vartheta & \cos \vartheta \end{bmatrix}, \quad (1.35)$$

and the oscillation probability can be simply expressed as:

$$\begin{aligned} P(\nu_\alpha \rightarrow \nu_\beta) &= \sin^2 2\vartheta \sin^2 \left( \frac{\Delta m^2 L}{4E} \right), \quad \alpha \neq \beta, \\ P(\nu_\alpha \rightarrow \nu_\alpha) &= 1 - \sin^2 2\vartheta \sin^2 \left( \frac{\Delta m^2 L}{4E} \right) \end{aligned} \quad (1.36)$$

where  $\Delta m^2$  is the mass difference between the corresponding two mass states.

Let us take as an example the muon neutrino disappearance probability for the oscillation regime driven by  $\Delta m_{32}^2$ . With the parametrization of the PMNS matrix in Equation (1.34), it can be expressed as [44]:

$$P(\nu_\mu \rightarrow \nu_\mu) \approx 1 - 4c_{13}^2 s_{23}^2 (1 - c_{13}^2 s_{23}^2) \sin^2 \left( \frac{\Delta m_{32}^2 L}{4E} \right),$$

which can be identified with the two-flavor oscillation formula of Equation (1.36) for the effective mass splitting  $\Delta m_{\mu\mu}^2$  and the effective mixing angle  $\vartheta_{\mu\mu}$  such that:

$$P(\nu_\mu \rightarrow \nu_\mu) = 1 - \sin^2 2\vartheta_{\mu\mu} \sin^2 \left( \frac{\Delta m_{\mu\mu}^2 L}{4E} \right) \quad (1.37)$$

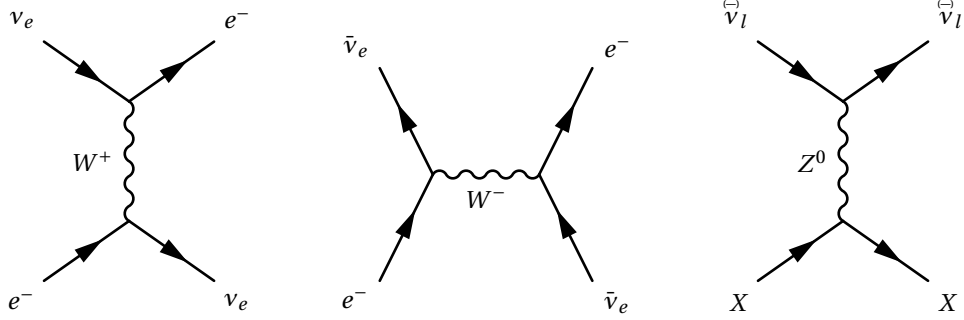


Figure 1.14: Feynman diagrams for CC interactions of electron (anti)neutrinos with electrons (left and center) and NC interactions of all (anti)neutrino flavors with  $X = n, p, e^-$  (right).

such that:

$$\sin^2 2\theta_{\mu\mu} = 4c_{13}^2 s_{23}^2 (1 - c_{13}^2 s_{23}^2) \approx \sin^2 2\theta_{23},$$

$$\Delta m_{\mu\mu}^2 \approx \Delta m_{32}^2,$$

where we use the smallness of  $\sin^2 \theta_{13}$  to neglect the terms proportional to it.

### 1.3.4 Neutrino oscillations in matter

Up until this point, we only considered neutrinos propagating in vacuum. In reality, they propagate in matter and can scatter on its constituents, namely electrons and nucleons. While we can safely ignore (incoherent) single scatterings due to the smallness of the neutrino cross section, interactions of the type:  $\nu_l + X \rightarrow \nu_l + X$  create a potential causing the so-called *coherent forward scattering*. This needs to be taken into consideration as it can have a significant effect on the oscillation pattern.

This type of interaction can occur for any neutrino or antineutrino flavor when it exchanges a  $Z^0$  boson with a nucleon or an electron of the medium, while only electron neutrinos can have a CC interaction with the electrons. This is shown in the Feynman diagrams of Figure 1.14.

#### Effective potentials

As usual, we can describe the neutrino propagation with a Hamiltonian. But this time, under these conditions, it should account for matter-induced effects. This can be expressed as  $\mathcal{H} = \mathcal{H}^{\text{free}} + \mathcal{H}^{\text{m}}$ .

The free Hamiltonian  $\mathcal{H}^{\text{free}}$  gives the evolution of neutrino mass states. In the space of mass states, it is a diagonal matrix with the energies of the mass states as eigenvalues, i.e.  $\text{diag}(E_1, E_2, E_3)$ . Therefore, in the space of flavor states, which is a rotation given by the PMNS

## Chapter 1. Neutrinos in the Standard Model and beyond

matrix  $U$  shown in Equations (1.15) and (1.34), we can write the free Hamiltonian as:

$$\mathcal{H}^{\text{free}} = U \text{diag}(E_1, E_2, E_3) U^\dagger.$$

On the other hand, the coherent forward scattering can be described as the presence of *effective* potentials due to interaction with matter. Let us denote the potential corresponding to a NC interaction  $\nu_l + X$  by  $V_{NC}(\nu_l + X)$  where  $X = n, p, e^-$  and a CC interaction by  $V_{CC}(\nu_l + e^-)$ . By developing the probability of interaction from the Feynman diagrams shown in Figure 1.14, we find that [39]:

$$\begin{aligned} V_{NC}(\nu_l + e^-) &= -\frac{\sqrt{2}}{2} G_F N_e, \\ V_{NC}(\nu_l + p) &= +\frac{\sqrt{2}}{2} G_F N_p, \\ V_{NC}(\nu_l + n) &= -\frac{\sqrt{2}}{2} G_F N_n, \\ V_{CC}(\nu_e + e^-) &= +\sqrt{2} G_F N_e. \end{aligned}$$

where  $G_F$  is the Fermi constant<sup>5</sup> and  $N_X$  is the number density of  $X = n, p, e^-$  in the medium. The potential for antineutrinos can be obtained by flipping the sign of the corresponding neutrino potential. Therefore, assuming that the medium is electrically neutral, i.e.  $N_p = N_e$ , the total potential  $V_l$  for a given neutrino  $\nu_l$  is:

$$\begin{aligned} V_\mu = V_\tau &= V_{NC}(\nu_l + e^-) + V_{NC}(\nu_l + p) + V_{NC}(\nu_l + p) \\ &= -\frac{\sqrt{2}}{2} G_F N_n \end{aligned}$$

and:

$$\begin{aligned} V_e &= V_{NC}(\nu_e + e^-) + V_{NC}(\nu_e + p) + V_{NC}(\nu_e + p) + V_{CC}(\nu_e + e^-) \\ &= -\frac{\sqrt{2}}{2} G_F N_n + \sqrt{2} G_F N_e. \end{aligned}$$

Therefore, the full Lagrangian can be expressed in the flavor state space as:

$$\mathcal{H} = U \begin{bmatrix} E_1 & 0 & 0 \\ 0 & E_2 & 0 \\ 0 & 0 & E_3 \end{bmatrix} U^\dagger + \begin{bmatrix} V_e & 0 & 0 \\ 0 & V_\mu & 0 \\ 0 & 0 & V_\tau \end{bmatrix}. \quad (1.38)$$

Since we are interested in effects on neutrino oscillation, any term proportional to the identity matrix  $\mathbf{1}_3$  would not have any impact. Therefore, if we assume that  $E_i \approx E + \frac{m_i^2}{2E}$  and denote  $V = V_e - V_\mu = V_e - V_\tau = +\sqrt{2} G_F N_e$ , we can subtract  $\left(E + \frac{m_1^2}{2E} + V_\mu\right) \times \mathbf{1}_3$  from Equation (1.38),

<sup>5</sup>The Fermi constant is defined by  $G_F = \frac{g^2}{2\sqrt{2}M_W^2}$ .

and obtain:

$$\mathcal{H} = \frac{1}{2E} U \begin{bmatrix} 0 & 0 & 0 \\ 0 & \Delta m_{21}^2 & 0 \\ 0 & 0 & \Delta m_{31}^2 \end{bmatrix} U^\dagger + \begin{bmatrix} V & 0 & 0 \\ 0 & 0 & 0 \\ 0 & 0 & 0 \end{bmatrix}. \quad (1.39)$$

The potential  $V$  is often expressed as a function of the medium density  $\rho$  as:

$$V = \sqrt{2} G_F N_e \approx 7.63 \times 10^{-14} \times Y_e \times \left[ \frac{\rho}{\text{g/cm}^3} \right] \text{ eV} \quad (1.40)$$

where  $Y_e$  is the electron relative number density and its value is usually  $\sim 1/2$ .

### Mikheyev – Smirnov – Wolfenstein effect

An important consequence of the additional potentials in the Hamiltonian is how they can have a sizeable enhancement of the flavor mixing amplitude in comparison with vacuum oscillations. This is known as the Mikheyev – Smirnov – Wolfenstein (MSW) effect [48, 49]. We can simply illustrate it in the two-flavor case for which we write the Hamiltonian from Equation (1.39) as:

$$\mathcal{H} = \frac{1}{2E} U \begin{bmatrix} 0 & 0 \\ 0 & \Delta m^2 \end{bmatrix} U^\dagger + \begin{bmatrix} V & 0 \\ 0 & 0 \end{bmatrix}.$$

We use the mixing matrix expressed in Equation (1.35), subtract again a diagonal term  $\frac{\Delta m^2 + V}{2} \times \mathbf{1}_2$  and define  $\kappa = \frac{2EV}{\Delta m^2}$ :

$$\begin{aligned} \mathcal{H} &= \frac{1}{4E} \begin{bmatrix} -\Delta m^2 \cos 2\vartheta + 2EV & \Delta m^2 \sin 2\vartheta \\ \Delta m^2 \sin 2\vartheta & \Delta m^2 \cos 2\vartheta - 2EV \end{bmatrix} \\ &= \frac{\Delta m^2}{4E} \begin{bmatrix} -\cos 2\vartheta + \kappa & \sin 2\vartheta \\ \sin 2\vartheta & \cos 2\vartheta - \kappa \end{bmatrix}. \end{aligned}$$

From this we can define a new effective mixing angle  $\vartheta_m$  as well as an effective mass splitting in matter such that:

$$\mathcal{H} = \frac{\Delta m^2}{4E} \begin{bmatrix} -\cos 2\vartheta + \kappa & \sin 2\vartheta \\ \sin 2\vartheta & \cos 2\vartheta - \kappa \end{bmatrix} = \frac{\Delta m_m^2}{4E} \begin{bmatrix} -\cos 2\vartheta_m & \sin 2\vartheta_m \\ \sin 2\vartheta_m & \cos 2\vartheta_m \end{bmatrix} \quad (1.41)$$

which satisfy:

$$\sin^2 2\vartheta_m = \frac{\sin^2 2\vartheta}{\sin^2 2\vartheta + (\cos 2\vartheta - \kappa)^2} \quad (1.42)$$

and:

$$\Delta m_m^2 = \Delta m^2 \times \sqrt{\sin^2 2\vartheta + (\cos 2\vartheta - \kappa)^2}. \quad (1.43)$$

With out loss of generality, we can assume that  $\Delta m^2 > 0$  for  $\vartheta \in [0, \frac{\pi}{2}]$ . Equations (1.42) and (1.43) allow us to understand the main features of matter effect on neutrino oscillations:



## Chapter 1. Neutrinos in the Standard Model and beyond

---

- When  $\kappa = 0$ , i.e. in the limit of no matter effects, we find our usual vacuum oscillation probabilities obtained in Equation (1.36).
- $\kappa \rightarrow \pm\infty$  corresponds to very dense matter or highly energetic (anti)neutrinos. In this case<sup>6</sup>,  $\sin^2 2\vartheta_m \rightarrow 0$ , and  $\vartheta_m \rightarrow \frac{\pi}{2}$  for neutrinos whereas  $\vartheta_m \rightarrow 0$  for antineutrinos. This implies that the electron neutrino becomes the heaviest mass state, whereas the electron antineutrino is the lightest one.
- The denominator of Equation (1.42) shows that there is a resonance in which matter effects can be maximal, called *MSW resonance*. Since  $\kappa$  is always positive for neutrinos and negative for antineutrinos, this resonance is seen only in the neutrino case as shown in the left panel of Figure 1.15 when  $\kappa_R = \cos 2\vartheta$ . The neutrino energy corresponding to this resonance is:

$$E_R = \frac{\Delta m^2 \cos 2\vartheta}{2V}. \quad (1.44)$$

and naturally depends on the electron density in the medium.

- Diagonalizing the Hamiltonian of Equation (1.41) yields the effective masses  $m_{m,i}^2 = \frac{1}{2}(m_1^2 + m_2^2 + 2EV \pm \Delta m_m^2)$ . The right panel of Figure 1.15 shows how these masses evolve as a function of  $\kappa$ . It can be observed that at the resonance, i.e.  $\kappa = \kappa_R$ , the effective mass difference  $\Delta m_m^2$  reaches its minimum  $\Delta m^2 \sin 2\vartheta$ , which is vanishing for  $\vartheta = 0, \frac{\pi}{2}$ .
- Since the sign of  $\kappa$  changes between neutrinos and antineutrinos, matter effects can have an impact that is similar to CP violation. This is only due to the fact that ordinary media are made of matter and not antimatter, and not because of intrinsic properties of the weak interaction. It is therefore crucial for oscillation experiments to correctly account for these effects to obtain unbiased measurements of the CP-violating phase  $\delta_{CP}$ .

### Solar neutrinos (revisited)

In media with varying densities along the direction of neutrino propagation, such as the Sun, the electron number density is naturally a function of the position  $N_e(\vec{x})$ . In this section, we will not provide an analytical derivation of the oscillation probabilities, which can be found in e.g. Reference [39], but rather have a qualitative discussion using the previous results by taking solar neutrinos as an example.

The density of the Sun monotonically decreases as a function of the distance from its center. Furthermore, as discussed in Section 1.3.1 and shown in Figure 1.7, the nuclear reactions at the core of the Sun ( $\rho \sim 150 \text{ g/cm}^3$ ) produce electron neutrinos with energy  $\lesssim 20 \text{ MeV}$ . At production, the high-energy neutrinos of this spectrum ( $E > 10 \text{ MeV}$ , typically produced by the  $^8\text{B}$  chain) [50] correspond to the heaviest mass state in the medium ( $\kappa \gg 1$ ), with the

---

<sup>6</sup>The sign of  $\tan 2\vartheta_m$  obtained from Equation (1.41) allows us to choose between the solutions  $\vartheta_m \rightarrow 0, \pi$ .

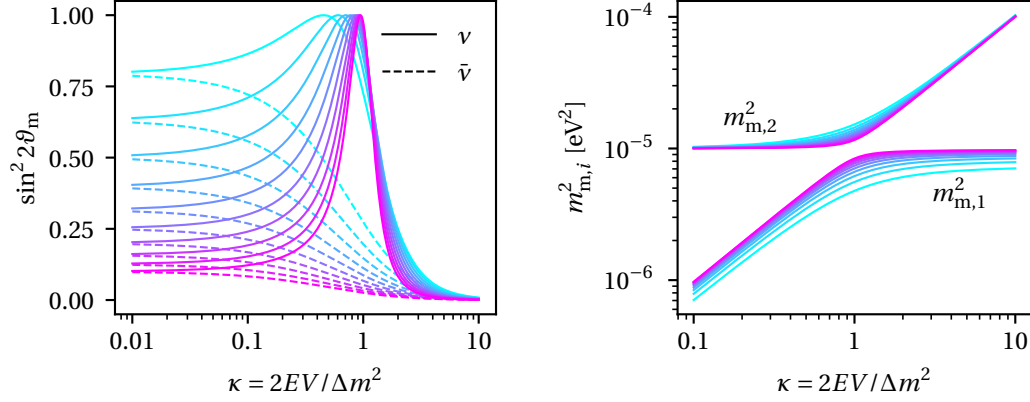


Figure 1.15: Variation of  $\sin^2 2\theta_m$  (left) and the effective masses  $m_{m,i}^2$  assuming  $m_1^2 = 0$  and  $m_2^2 = 10^{-5} \text{ eV}^2$  (right) as a function of  $\kappa$  for values of  $\sin^2 2\theta$  ranging from 0.01 (pink) to 0.4 (cyan).

mixing angle in the medium  $\theta_m \sim \frac{\pi}{2}$ . Under the assumption of *adiabatic* evolution, i.e. the density profile varies slowly in comparison to the oscillation length, neutrinos move towards the surface of the Sun and undergo, as the matter density decreases, the so-called *level crossing* at the MSW resonance where the flavor mixing is maximal, i.e.  $\theta_m \sim \frac{\pi}{4}$ , and the mass splitting is minimal<sup>7</sup>. Finally, by the time they cross the resonance and exit the Sun, the dominant flavor component of each mass state has changed, and neutrino propagation is described by vacuum oscillations with  $\theta_m \sim \theta$ .

### Accelerator neutrinos

For neutrinos artificially produced in accelerators and propagating in upper mantle of Earth, matter effects have a sub-leading contribution to neutrino oscillations that cannot be neglected. The electron appearance probability can be expressed as [51, 52]:

$$\begin{aligned}
 P(\nu_\mu \rightarrow \nu_e) \simeq & \sin^2 \theta_{23} \frac{\sin^2 2\theta_{13}}{(A-1)^2} \sin^2 [(A-1)\Delta_{31}] + \alpha^2 \cos^2 \theta_{23} \frac{\sin^2 2\theta_{12}}{A^2} \sin^2 (A\Delta_{31}) \\
 & + \alpha \frac{\cos \theta_{13} \sin 2\theta_{12} \sin 2\theta_{13} \sin 2\theta_{23} \cos \delta_{\text{CP}}}{A(1-A)} \cos \Delta_{31} \sin (A\Delta_{31}) \sin [(1-A)\Delta_{31}] \\
 & - \alpha \frac{\cos \theta_{13} \sin 2\theta_{12} \sin 2\theta_{13} \sin 2\theta_{23} \sin \delta_{\text{CP}}}{A(1-A)} \sin \Delta_{31} \sin (A\Delta_{31}) \sin [(1-A)\Delta_{31}]
 \end{aligned} \tag{1.45}$$

where  $\alpha = \Delta m_{21}^2 / \Delta m_{31}^2$ ,  $\Delta_{31} = \Delta m_{31}^2 L / 4E$ , and  $A = 2EV / \Delta m_{31}^2$ . The probability  $P(\bar{\nu}_\mu \rightarrow \bar{\nu}_e)$  is obtained by switching the sign of the CP-violating phase  $\delta_{\text{CP}}$  as well as the parameter  $A$  induced by matter effects. This expression is an expansion in  $\alpha$  and  $\sin \theta_{13}$  since they are known to be small. It is valid only for neutrino propagating in media of constant density with

<sup>7</sup>The adiabaticity assumption can be violated in this region since a smaller mass splitting means a larger oscillation length which can be comparable to the scale of density variations in the medium.

## Chapter 1. Neutrinos in the Standard Model and beyond

---

energies  $\sim 1$  GeV [52], which is well satisfied for accelerator-based oscillation experiments.

An important feature shown in this formula is the degeneracy between matter effects and CP-violation. Indeed, as mentioned previously, electron neutrinos and antineutrinos are subject to different potentials when propagating in matter. This matter-induced asymmetry between  $\nu_\mu \rightarrow \nu_e$  and  $\bar{\nu}_\mu \rightarrow \bar{\nu}_e$  depends on the sign of  $\Delta m_{31}^2$  and is a significant experimental challenge in the measurement of  $\delta_{\text{CP}}$ , but it also provides a way to access the sign of  $\Delta m_{31}^2$  that is still unknown.

When neglecting effects from propagation through matter, this probability can be simplified to the leading order as [53]:

$$P(\nu_\mu \rightarrow \nu_e) \approx \sin^2 2\theta_{13} \sin^2 \theta_{23} \sin^2 \left( \frac{\Delta m_{32}^2 L}{4E} \right) - \frac{\Delta m_{21}^2 L}{4E} 8J \sin^2 \left( \frac{\Delta m_{32}^2 L}{4E} \right), \quad (1.46)$$

where the sign of the term proportional to the Jarlskog invariant  $J$  is flipped for the antineutrino probability.

## 1.4 Experimental status

### 1.4.1 Open questions in the PMNS paradigm

Neutrino oscillations are of great interest as a strong probe of physics beyond the Standard Model. Precision measurement of this phenomenon can provide a path to answer outstanding questions in particle physics. For instance, a possible explanation for the generational resemblance between quarks and leptons could lie at an unattainable high energy scale in leptoquark unification [54]. Such theories can be examined and tested using neutrino oscillations.

The different neutrino oscillation parameters are known with different degrees of precision. The quantities  $\theta_{12}$ ,  $\theta_{13}$ ,  $\Delta m_{21}^2$  and  $|\Delta m_{31}^2|$  are well measured by different experiments and found to be consistent. However, it is still unknown until today whether  $\theta_{23}$  is in the upper octant ( $\theta_{23} > \frac{\pi}{4}$ ) or in the lower octant ( $\theta_{23} < \frac{\pi}{4}$ ).

Furthermore, while the sign of  $\Delta m_{21}^2$  has been determined with solar neutrinos, the mass ordering, i.e. whether  $\nu_3$  is the heaviest (*normal* ordering) or the lightest (*inverted* ordering), is still unknown. This is illustrated in Figure 1.16. It is thanks to matter effects that neutrino oscillation measurements can have an enhanced sensitivity to the sign of the mass splittings. Indeed, the large matter effects in the Sun, due to its dense core, allowed an unambiguous determination of the sign of  $\Delta m_{21}^2$ . On the other hand, the best sensitivity to the sign of  $\Delta m_{31}^2$  is obtained with atmospheric neutrinos as they can diagonally cross Earth. A non-negligible sensitivity to the mass ordering can also be achieved thanks to accelerator neutrinos since they propagate in matter as well, especially if the baseline is long.

The last open question in the PMNS paradigm concerns the CP-violating phase  $\delta_{\text{CP}}$ . As

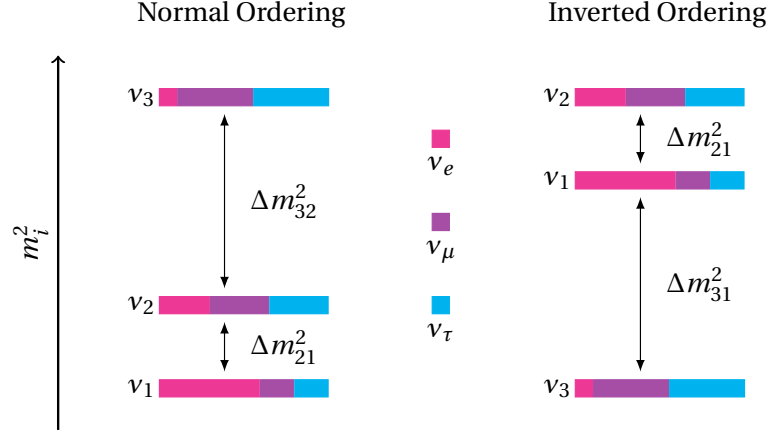


Figure 1.16: Illustration of the normal (left) and inverted (right) mass orderings. The flavor share of each mass state is also displayed.

mentioned in Section 1.3.4, the degeneracy with the mass ordering and other mixing angles makes its measurement challenging. In Chapter 9, we will see how the T2K experiment is sensitive to its values and the prospects of constraining it in the upcoming years.

### 1.4.2 Solar sector

The *solar mixing parameters* are  $\theta_{12}$  and  $\Delta m_{21}^2$ , and their measurement relies on the disappearance of electron (anti)neutrinos. To target this sector, the ratio  $L/E$  needs to be of the order of  $\sim 100$  km/MeV as shown in Figure 1.17. This is satisfied for the electron neutrinos produced in the Sun, and the inverse beta decay electron antineutrinos in nuclear reactors when the propagation distance is of  $\sim 100$  km.

Solar neutrinos have been detected through their interaction with water in the SNO [24], Kamiokande [55] and Super-Kamiokande [56] experiments. Borexino [57] used liquid scintillator to measure them between 2007 and 2021. Due to the high electron density in the Sun, solar neutrinos are significantly affected by the MSW effect, which explains their large disappearance. On the other hand, the KamLAND experiment provided precision measurements of this sector from reactor antineutrinos with a mean distance of  $\sim 180$  km (see Section 1.3.1) with negligible matter effects. The current knowledge of the solar parameters from these experiments is expressed as [43]:

$$\sin^2 \theta_{12} = 0.303^{+0.012}_{-0.012} \quad \text{and} \quad \Delta m_{21}^2 = 7.41^{+0.21}_{-0.20} \times 10^{-5} \text{ eV}^2.$$

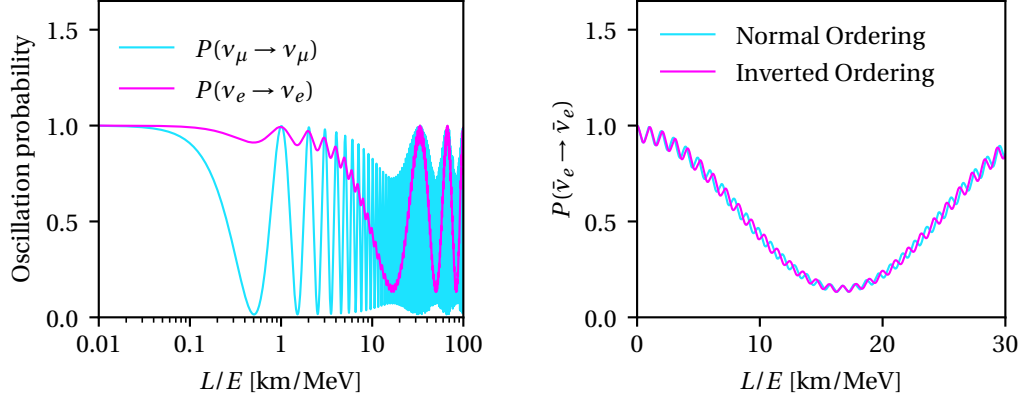


Figure 1.17: Left: electron and muon neutrino disappearance probability in vacuum. Right: electron antineutrino disappearance probability in vacuum for the normal and inverted orderings.

### 1.4.3 Atmospheric sector

The *atmospheric mixing parameters*  $\theta_{23}$  and  $\Delta m_{32}^2$  can be probed with the disappearance of muon (anti)neutrinos for  $L/E \sim 0.5$  km/MeV, as shown in Figure 1.17. This is achieved with atmospheric neutrinos, as the name suggests, but also with accelerator experiments. Atmospheric neutrinos provide a high-statistic measurement but with large uncertainties on the neutrino energy which ranges from  $\sim 0.1$  GeV to  $> 1$  TeV, and on the production process, mainly the pion decay  $\pi^+ \rightarrow \mu^+ \nu_\mu$  followed by  $\mu^+ \rightarrow e^+ \nu_e \bar{\nu}_\mu$ . They have been measured by Super-Kamiokande [56], ANTARES in the deep Mediterranean Sea [58], and IceCube using the South Pole ice [59]. On the other hand, accelerator experiments are able to provide a muon (anti)neutrino beam with a highly controlled energy spectrum. This is the case of the experiments MINOS(+) [60], T2K [61] and NOvA [62], which provide competitive constraints on these parameters as shown in Figure 1.18.

In fits to global neutrino data, the sensitivity to the mass ordering, i.e. the sign of  $\Delta m_{32}^2$ , is mainly driven by the high statistics of atmospheric neutrinos in Super-Kamiokande which favours normal ordering [43]. Experiments that can have an increased sensitivity are currently being built. For instance, JUNO [65] aims to determine the mass ordering by precisely measuring the  $\Delta m_{32}^2$ -induced  $\bar{\nu}_e$  oscillations, namely the fast oscillations in the right panel of Figure 1.17 from nuclear reactors using liquid scintillator. The challenge here is to have a detector that can reconstruct with high precision the neutrino energy to reach this sensitivity. Besides, the KM3NeT/ORCA experiment [66], the successor of ANTARES, is currently being deployed in the Mediterranean Sea and aims to measure atmospheric neutrinos. With the continued data taking of the ongoing experiments, and the start of these new experiments, the definite determination of the mass ordering may be reached by the end of the decade.

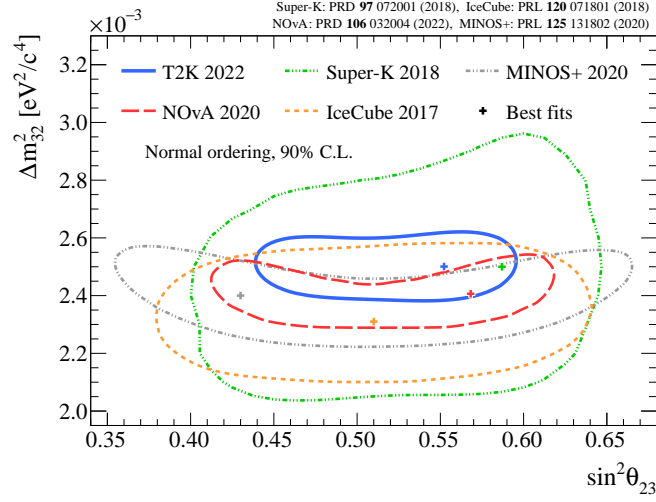


Figure 1.18: Latest constraints at 90% C.L. on the atmospheric parameters in normal ordering from the T2K [61], Super-Kamiokande [63], MINOS+ [60], NOvA [62] and IceCube [64] experiments.

#### 1.4.4 Measurement of $\theta_{13}$

$\theta_{13}$  is the last mixing angle that has been measured due to its relatively small value. Accelerator experiments are sensitive to its value mainly through electron neutrino appearance in their muon neutrino beams as shown in Equation (1.45). Indeed, T2K was the first experiment to show hints of a non-vanishing  $\theta_{13}$  with  $2.5\sigma$  in 2011 [67] and confirmed it in 2013 with  $7.3\sigma$  by detecting the oscillation  $\nu_\mu \rightarrow \nu_e$  [68]. NOvA also started constraining it using the same channel since 2015 [69]. But it is the reactor experiments that have now provided the best measurements of this parameter by probing the  $\bar{\nu}_e$  disappearance since the corresponding oscillation probability does not have the strong degeneracies with the atmospheric parameters or the CP-violating phase that accelerator experiments have. The main three reactor experiments that probed  $\theta_{13}$  are Daya Bay [70], RENO [71] and Double Chooz [72].  $\theta_{13}$  is currently the mixing angle determined with the highest precision [43]:

$$\sin^2 \theta_{13} = 0.02225^{+0.00056}_{-0.00059}.$$

#### 1.4.5 Measurement of $\delta_{\text{CP}}$

The confirmation of the non-vanishing value of the mixing angle  $\theta_{13}$  opened the door for neutrino oscillation physics to probe the CP symmetry in the lepton sector. The CP-violating phase  $\delta_{\text{CP}}$  is mainly probed by accelerator experiments through the appearance of electron (anti)neutrinos in a muon (anti)neutrino beam as shown in Equation (1.45), and particularly by looking at the difference between the neutrino and antineutrino oscillations.

As shown in Equation (1.45), its measurement is highly correlated with the mass ordering and

## Chapter 1. Neutrinos in the Standard Model and beyond

---

the parameters  $\Delta m_{32}^2$ ,  $\theta_{23}$  and  $\theta_{13}$ . Usually, accelerator experiments provide their oscillation measurements by jointly fitting data of the  $\bar{\nu}_\mu$  disappearance and the  $\bar{\nu}_e$  appearance channels. Therefore, the atmospheric parameters can be relatively well constrained by the disappearance of  $\nu_\mu$  and some of the degeneracy can be lifted. However, since  $\theta_{13}$  cannot be as well constrained by accelerator experiments as by the reactor ones, we can use their constraints to obtain an enhanced sensitivity to  $\delta_{\text{CP}}$ . This is displayed in Figure 1.19 where we can see how the constraints on  $\delta_{\text{CP}}$  is noticeably improved when including the reactor constraints.

Figure 1.20 shows the latest constraints on  $(\sin^2 \theta_{23}, \delta_{\text{CP}})$  from different experiments for both the normal and inverted ordering. As discussed previously, the mass ordering has a significant impact on the sensitivity to the CP-violating phase  $\delta_{\text{CP}}$  due to degeneracies in Equation (1.45). One way of lifting this degeneracy is performing joint fits with experiments with enhanced sensitivity to the mass ordering. This is the subject of ongoing studies as T2K is currently working on two joint fits:

- T2K + NOvA: Figure 1.20 shows a disagreement in the normal ordering between the two experiments, although without any large statistical significance. This motivated the two collaborations to perform a joint fit with both data sets. As shown in Table 1.4, there are design differences that can allow them to be complementary, particularly their baselines since NOvA's 810 km travel distance increases the sensitivity to the mass ordering.
- T2K + Super-Kamiokande: Atmospheric neutrinos measured by Super-Kamiokande are also an excellent way to alleviate the degeneracy between  $\delta_{\text{CP}}$  and the mass ordering. A joint analysis between T2K and Super-Kamiokande's atmospheric neutrinos can utilize their common detector to provide improved constraints on  $\delta_{\text{CP}}$ .

Within the upcoming years, a new generation of accelerator experiments will start taking neutrino oscillation data. Hyper-Kamiokande [73] is a larger version of the Super-Kamiokande detector with  $\sim 8$  times the fiducial mass and improved performances for its photomultiplier tubes, using the same T2K baseline of 295 km. On the other hand, US-based DUNE [74] will use a new technology of liquid argon time projection chambers and a high-power neutrino beam over a distance of  $\sim 1300$  km. Both experiments will aim to further probe CP violation and the mass ordering with significantly higher statistics and perform precision oscillation measurements.

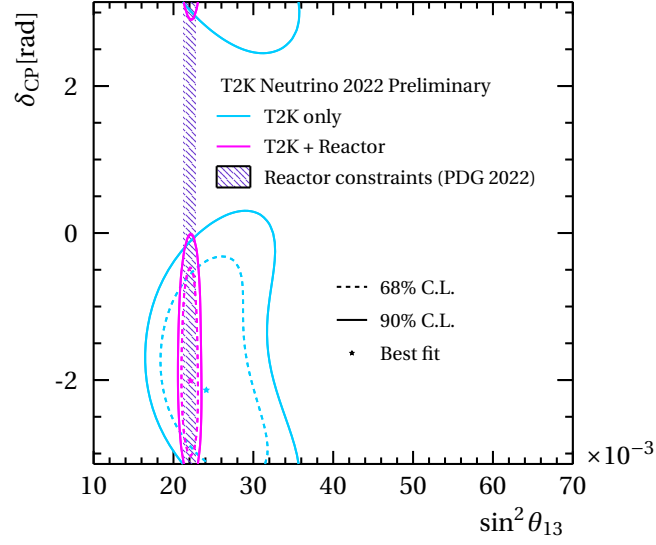


Figure 1.19: Latest constraints at 68% and 90% C.L. on  $\delta_{\text{CP}}$  and  $\sin^2 \theta_{13}$  from the T2K experiment with (magenta) and without (cyan) constraints from reactor experiments on  $\theta_{13}$  from Reference [12].

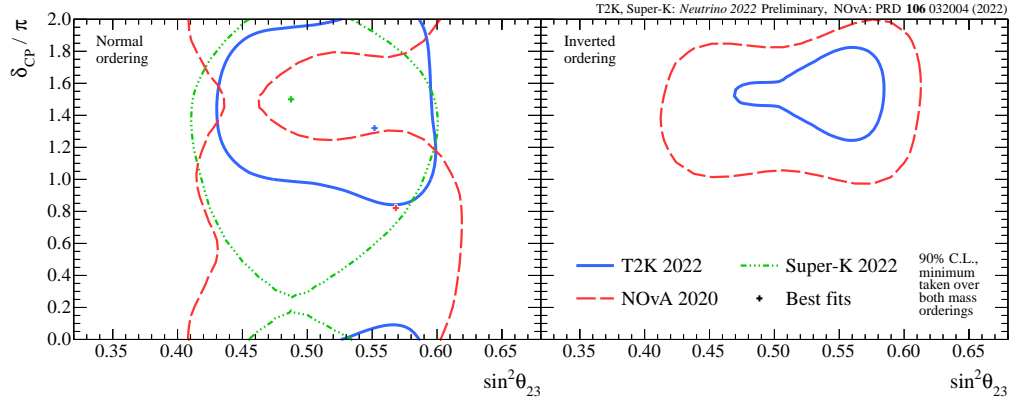


Figure 1.20: Latest constraints at 90% C.L. on  $\delta_{\text{CP}}$  and  $\sin^2 \theta_{23}$  in normal (left) and inverted (right) ordering from the T2K [61], Super-Kamiokande [63] and NOvA [62] experiments.

	T2K	NOvA
Baseline	295 km	810 km
Energy of Peak Flux	0.6 GeV	2.0 GeV
Detector Type	Water Čerenkov	Liquid scintillator
Detector Mass	22.5 ktons	14 ktons

Table 1.4: Comparison between the T2K and NOvA experiments.





## 2 T2K experiment

The Tōkai-to-Kamioka (T2K) experiment is a long-baseline neutrino oscillation experiment located in Japan. A high-intensity beam of  $\bar{\nu}_\mu$  is produced at the Japan Proton Accelerator Research Complex (J-PARC) site on the east coast of Japan and directed towards Super-Kamiokande on the west coast, with a traveling distance of  $\sim 295$  km. A set of near detectors is installed  $\sim 280$  m away from the neutrino source to monitor the beam and control systematic uncertainties, whereas at Super-Kamiokande, the appearance of  $\bar{\nu}_e$  and the disappearance of  $\bar{\nu}_\mu$  is measured to determine the oscillation probability and thus infer the neutrino oscillation parameters.

T2K started its first physics run in early 2010 with the initial goal of measuring the mixing angle  $\theta_{13}$  through electron neutrino appearance. One year later, it presented evidence for a non-zero  $\theta_{13}$  at a  $2.5\sigma$  C.L. [67] and reported in 2013 an excess of electron neutrino events of  $7.3\sigma$  with respect to the background as mentioned in Section 1.4.4. The Daya Bay experiment in the meantime started providing the most stringent constraints on  $\theta_{13}$  in 2012 through the disappearance of electron antineutrinos in reactors [75]. Since then, the physics program of T2K developed to also encompass the probe of CP-violation in the leptonic sector as the three mixing angles were measured to be non zero, in addition to the improvement of the atmospheric oscillation parameter measurements. Beside oscillation physics, T2K also conducts a rich program of neutrino cross-section measurements to better characterize their interactions with nuclei.

In this chapter, we describe the experimental setup of T2K in detail, from the production of the (anti)neutrino beam in Section 2.1, through the near detector complex in Section 2.2, to the far detector Super-Kamiokande in Section 2.3. We finish the chapter by highlighting the main physics outputs of the T2K experiment in Section 2.4.

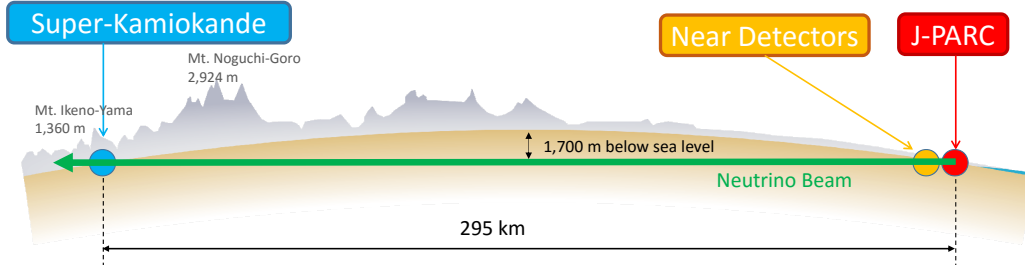


Figure 2.1: Overview of the T2K experiment.

### 2.1 Beamline

At J-PARC in Tōkai-mura, a proton beam is fired at a graphite target to produce leptons from hadron decays. The proton beam is obtained with  $H^-$  ions that are accelerated in a linear accelerator (LINAC) to an energy of 180 MeV and then converted to  $H^+$  ions (or bare protons) by removing the two electrons of  $H^-$  using charge-stripping foils at the injection point into the rapid cycling synchrotron (RCS). In the RCS, the protons are accelerated up to 3 GeV with 25 Hz cycle frequency, where each cycle contains two bunches. Four groups of two bunches are injected at a time into the main ring synchrotron (MR) and accelerated up to 30 GeV. Two extraction points are available in the MR: a slow extraction point for the hadron beamline where a ribbon is used to split the bunch while a kicker magnet directs a portion of each bunch to the hadron beamline over multiple turns, and a fast extraction point where all eight bunches are deflected into the neutrino beamline in a single turn with five kicker magnets. In this case, each bunch has a temporal width of 58 ns, and the separation between two bunches is of 581 ns. This precise timing information is sent to the near detector complex via direct fiber link and to the far detector via GPS to provide trigger signals for beam neutrino events. The spill, which consists of the eight bunches, has a duration of 5  $\mu$ s and contains  $\sim 3 \times 10^{14}$  protons.

As shown in Figure 2.2, the neutrino beamline is composed of two main sections: the primary beamline and the secondary beamline.

#### 2.1.1 Primary beamline

The primary beamline is where the protons are extracted and directed towards the target. The main goal here is to steer the beam towards the near and far detectors, and to focus it on the graphite target. In fact, as displayed in Figure 2.2, the arc section curves the beam direction by  $80.7^\circ$  towards the near detectors using superconducting steering magnets. It then reaches the final focusing station before impinging on the target where ten normal conducting magnets further bend the beam downwards by  $3.64^\circ$  towards Super-Kamiokande, taking into consideration the Earth curvature and the off-axis angle discussed in Section 2.1.3. At this stage, multiple systems are used to monitor the beam position and intensity to ensure its stability since these are essential for a well-understood neutrino beam [76, 77].

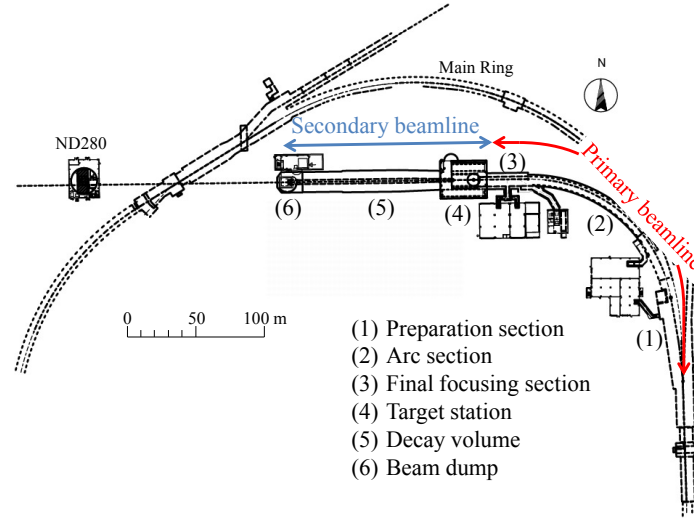


Figure 2.2: Overview of the T2K neutrino beamline.

### 2.1.2 Secondary beamline

The secondary beamline is where neutrinos are produced from the proton beam. As shown in Figure 2.2, it consists of the target station (TS), the decay volume and the beam dump. Figure 2.3 illustrates the composition of the TS: an optical radiation monitor (OTR) measures the beam profile followed by the 91.4 cm-long graphite target itself where hadrons, mainly charged pions and kaons, are produced from proton collisions and travel in a magnetic field generated by three magnetic horns.

These horns are pulsed with a current of<sup>1</sup> 250 kA, producing a toroidal magnetic field that collects, focuses and selects positively- or negatively-charged particles depending on the chosen polarity for the magnets. The *forward horn current* (FHC) mode selects the hadrons of positive charge which results in a neutrino-enhanced beam, whereas the *reverse horn current* (RHC) mode selects the ones with a negative charge which yields an antineutrino-enhanced beam. Despite the high efficiency of this charge-selection technique, wrong-sign charged particles are still present in both modes which inevitably leads to a contamination in the beam. This contamination is particularly greater in the RHC mode since the upstream collision always occurs with the positively-charged protons, favoring the production of positively-charged hadrons.

The selected hadrons are allowed to decay in the 96 m long tunnel. For instance, the main decay channels in the FHC mode are shown in Table 2.1. The length of the decay volume is filled with helium to reduce the hadron reinteractions with air. A beam dump composed of graphite, iron and copper is located at the downstream end of this tunnel. Neutrinos pass through it and travel to the near detectors, while all the hadrons and their decay remnants are

<sup>1</sup>This current is currently being increased to 320 kA for an improved separation between right- and wrong-sign hadrons.

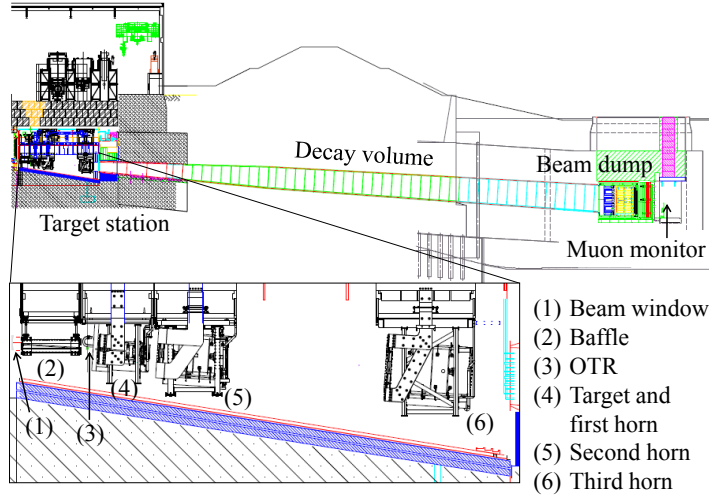


Figure 2.3: Side view of the secondary beamline. In this view, protons travel from the left to the right.

stopped except for muons of energy above 5 GeV. For instance, in the FHC mode, the goal is to obtain a beam of muon neutrino as pure as possible. As shown in Table 2.1, this is achieved mainly through the pion decay  $\pi^+ \rightarrow \mu^+ + \nu_\mu$ . The purpose of the beam dump is to prevent the produced antimuons from decaying into electron neutrinos and muon antineutrinos which contaminate the beam. Figure 2.4 shows the estimated contaminations in the (anti)neutrino flux. On the other hand, the high energy muons that can cross the beam dump are actually measured by the muon monitor (MUMON) which uses them to check the beam direction and intensity.

### 2.1.3 Off-axis angle

The T2K beam is tuned in order for the far detector Super-Kamiokande to be  $2.5^\circ$  off-axis from the primary direction of the beam. T2K is the first neutrino experiment to utilize this off-axis technique, originally proposed in Reference [79], in order to obtain a narrowly-peaked flux around the neutrino energy that gives maximal oscillations. As previously shown in the right panel of Figure 1.13, the ratio of the distance over the neutrino energy needs to be  $L/E \sim 0.5 \text{ km/MeV}$  to observe the first oscillation at which occurs a maximal disappearance of muon neutrinos. Given the fixed distance from J-PARC to Super-Kamiokande of 295 km, this means that the neutrino energy should be at  $\sim 600 \text{ MeV}$ .

Let us consider the pion disintegration  $\pi^+ \rightarrow \mu^+ + \nu_\mu$  along the decay tunnel, which is behind the majority of the neutrinos in the beam. The neutrino energy in the laboratory frame  $E_\nu$  can be obtained from its (fixed) value  $E_\nu^{\text{CM}}$  in the center-of-mass frame of the pion by a simple

Particle	Decay Products	Branching Ratio [%]
$\pi^+$	$\rightarrow \mu^+ \nu_\mu$	99.9877
	$\rightarrow e^+ \nu_e$	$1.23 \times 10^{-4}$
$K^+$	$\rightarrow \mu^+ \nu_\mu$	63.55
	$\rightarrow \pi^0 \mu^+ \nu_\mu$	3.353
	$\rightarrow \pi^0 e^+ \nu_e$	5.07
$K_L^0$	$\rightarrow \pi^- \mu^+ \nu_\mu$	27.04
	$\rightarrow \pi^- e^+ \nu_e$	40.55
$\mu^+$	$\rightarrow e^+ \bar{\nu}_\mu \nu_e$	100

Table 2.1: Decay modes that produce neutrinos in the FHC mode with the corresponding branching ratios [77].

boost given by Lorentz transformations as:

$$E_\nu^{\text{CM}} = \frac{M_\pi^2 - M_\mu^2}{2M_\pi} \approx 29.8 \text{ MeV} \quad \xrightarrow{\text{Lorentz boost}} \quad E_\nu = \frac{M_\pi^2 - M_\mu^2}{2(E_\pi - p_\pi \cos \theta_{\text{OA}})}$$

assuming a massless neutrino, where  $M_\pi$  and  $M_\mu$  are the pion and the muon masses,  $E_\pi$  and  $p_\pi$  the energy and momentum of the (parent) pion, and  $\theta_{\text{OA}}$  the angle between the pion and neutrino directions. As a spin zero particle, the pion emits muon neutrinos isotropically in its center-of-mass frame. But since it actually decays during its flight, as soon as the scattering angle is larger than  $0^\circ$ , there exists a maximal neutrino energy  $E_\nu^{\text{CM}} / \tan \theta_{\text{OA}}$  independently of the initial pion momentum as displayed in Figure 2.5. Therefore, all neutrinos produced in this decay are subject to this geometrical constraint and, as  $\theta_{\text{OA}}$  increases, their spectrum is narrower with a decreasing peak energy.

The cost of choosing an off-axis setup is a lower intensity beam in comparison with the on-axis configuration. Nevertheless, in addition to the narrow width at the desired neutrino energy, there are other benefits of this approach:

- As will be detailed in Chapter 3, neutrinos of energies around 600 MeV are more likely to interact quasielastically. This type of interaction is relatively well understood and allows for a better reconstruction of the neutrino energy.
- The choice of an off-axis configuration also reduces the background from other flavors of (anti)neutrinos in the beam. Indeed, this background mainly comes from the three-body decays of muons and kaons, and since the off-axis approach enhances the muon neutrino flux from the two-body decay, the amount of the produced electron neutrinos for instance is less affected. Consequently, their relative contribution to the beam decreases.

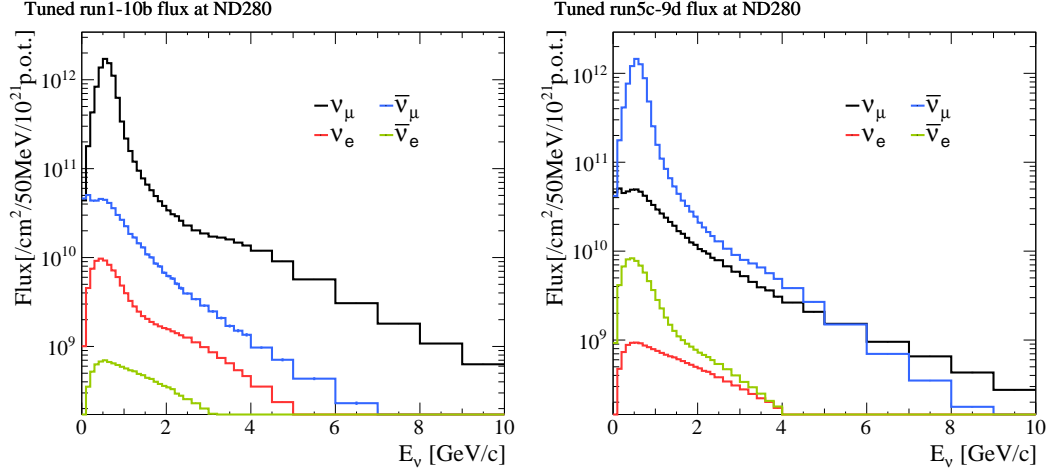


Figure 2.4: Breakdown of the neutrino flux at ND280 in the FHC (left) and RHC (right) modes. Figure from Reference [78].

### 2.1.4 Neutrino flux prediction

As shown in Figure 2.5, although the off-axis approach reduces the spread of the neutrino energy spectrum, it is still relatively large. Furthermore, the contaminations from other hadron decays, e.g. producing electron (anti)neutrinos which could mimic the appearance channel at the far detector, can cause biases in oscillation measurements. Therefore, a precise prediction of the T2K neutrino flux is an absolute necessity for robust results.

The prediction of the T2K neutrino spectrum is based on a chain of Monte Carlo simulations [77]. It begins by simulating the interactions of the  $\sim 30$  GeV protons on the graphite target with FLUKA [80]. Each simulated event of proton – carbon interaction with its outgoing particles is passed to the JNUBEAM simulation [77] which models the mechanics of the target, the helium vessel, the decay volume, the beam dump and the muon monitor using GEANT3 [81], whereas the hadronic interactions with their material are simulated with the GCALOR package [82].

Due to the lack of measurements of  $\sim 30$  GeV proton interactions with carbon, the NA61/SHINE experiment [83], based at the CERN SPS, measured hadron kinematics with graphite targets using a large-acceptance hadron spectrometer. Their data allows us to tune and constrain the uncertainties on the neutrino flux model obtained with JNUBEAM. They provided two sets of measurements:

1. *Thin target* hadron production measurements using a graphite target of 2 cm thickness [83, 84]. This has been used as the main source of external data to constrain the T2K flux model until 2019.
2. *T2K replica target* measurements use a similar target as the one in T2K [85]. They provide the yields from its surface for pions, protons and kaons. This data started to be included

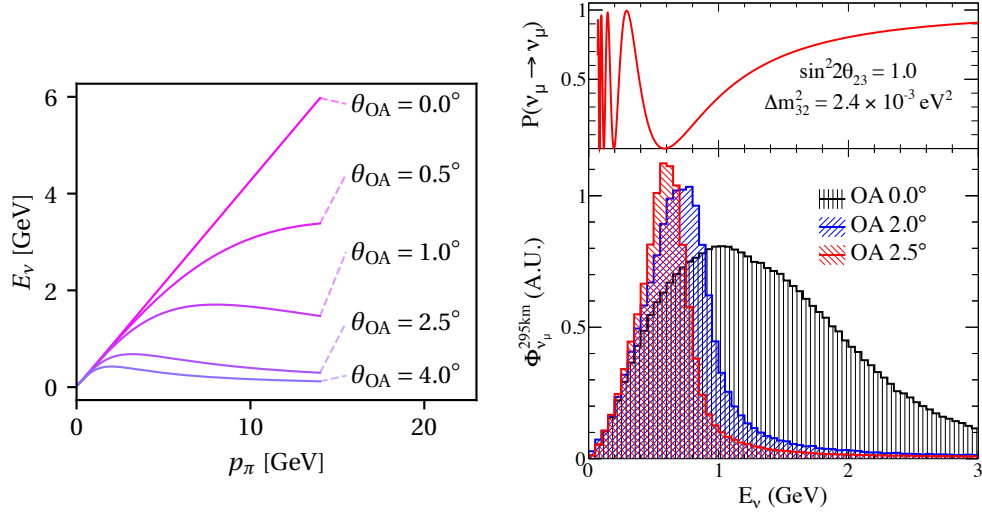


Figure 2.5: Left: neutrino energy from two-body pion decay as a function of the pion momentum for different values of the off-axis angle  $\theta_{OA}$ . Right: T2K neutrino flux for different off-axis angles (bottom) and the corresponding muon neutrino disappearance probability which is maximal at 600 MeV. Right panel from Reference [77].

to constrain the T2K flux model since 2020, and Figure 2.6 shows the dramatic reduction of the flux uncertainty between the thin target and the replica target constraints in the right-sign flux around the T2K peak at  $\sim 600$  MeV. This is mainly due to the significant improvement in the hadronic interaction modeling thanks to this new data.

## 2.2 Near detectors

The near detector complex illustrated in the left panel of Figure 2.7 is located 280 m away from the neutrino source and houses multiple detectors at different off-axis angles:

- an on-axis interactive grid detector called *INGRID* in the lower floor  $\sim 30$  m underground,
- a  $1.5^\circ$  off-axis detector named *WAGASCI/BabyMIND*,
- a  $2.5^\circ$  off-axis detector aligned with the far detector Super-Kamiokande known as *ND280*.

The main goal of these detectors is to sample the neutrino flux before oscillations. *INGRID* measures the position of its center and monitors its intensity, whereas *ND280* aims to precisely characterize the energy spectrum and flavor composition of the  $2.5^\circ$  off-axis beam as well as to constrain systematic uncertainties related to neutrino interaction modeling. All these detectors also measure neutrino cross sections at slightly different energy spectra due to the lower off-axis angle, and can provide complementary data to better understand neutrino interactions.



## Chapter 2. T2K experiment

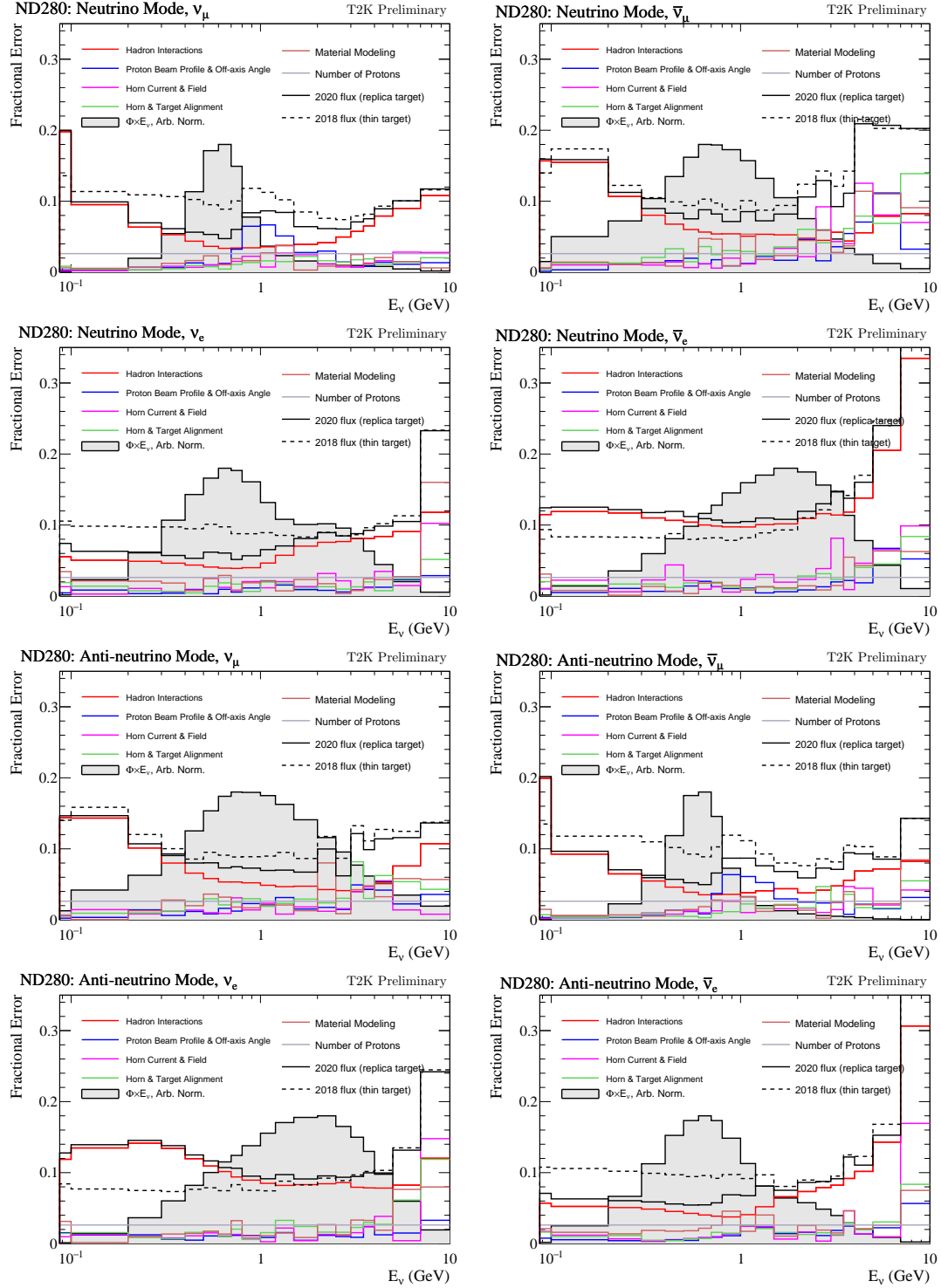


Figure 2.6: Breakdown of the neutrino flux at ND280 in the FHC (left) and RHC (right) modes. Figure from Reference [78].

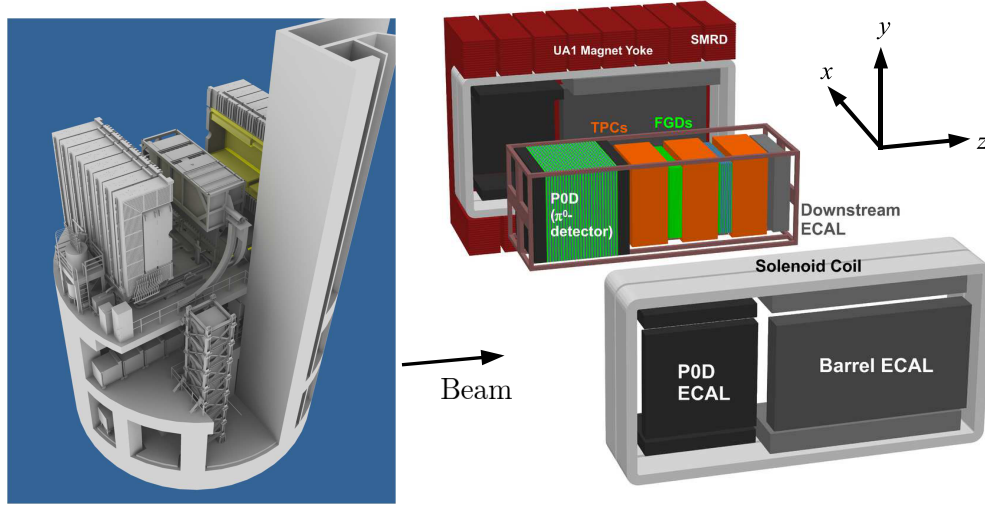


Figure 2.7: The T2K near detector complex (left) and an exploded view of the ND280 off-axis detector (right). Figure from Reference [86].

### 2.2.1 INGRID

INGRID is used to precisely monitor the neutrino beam by measuring its intensity and direction during a run. It is composed of 14 identical modules arranged horizontally and vertically in the form of a cross. Its center corresponds to the designed beam center as depicted in Figure 2.8. An INGRID module is displayed in Figure 2.9. It consists of alternating planes of 24 scintillator bars ( $10 \text{ mm}^3$  per bar) and iron plates. Each module is surrounded by scintillator planes that serve as a veto to reject tracks coming from outside the module.

INGRID samples the neutrino beam in a transverse section of  $10 \times 10 \text{ m}^2$ , and the neutrino spectrum it sees is broader due to its on-axis alignment (see Figure 2.5) in comparison to ND280 and Super-Kamiokande. The center of the cross is by design the center of the proton beam, and the event rates in both the horizontal and the vertical modules are fitted by a Gaussian distribution to accurately determine the beam center. This is important information that is used in the oscillation analysis to produce an appropriate neutrino flux prediction.

### 2.2.2 ND280

#### Overview

The goal of ND280 is to precisely characterize the unoscillated neutrino flux directed towards Super-Kamiokande. The right panel of Figure 2.7 shows the components of ND280, and an event display is depicted in Figure 2.10. All its subdetectors are embedded in a solenoid magnet, the *UA1 magnet*, that allows us to measure the charge of the lepton produced by a CC neutrino interaction and thus distinguish between neutrinos and antineutrinos. They are also surrounded by a *side muon range detector* (SMRD) [87] inserted in the gaps of the UA1 magnet

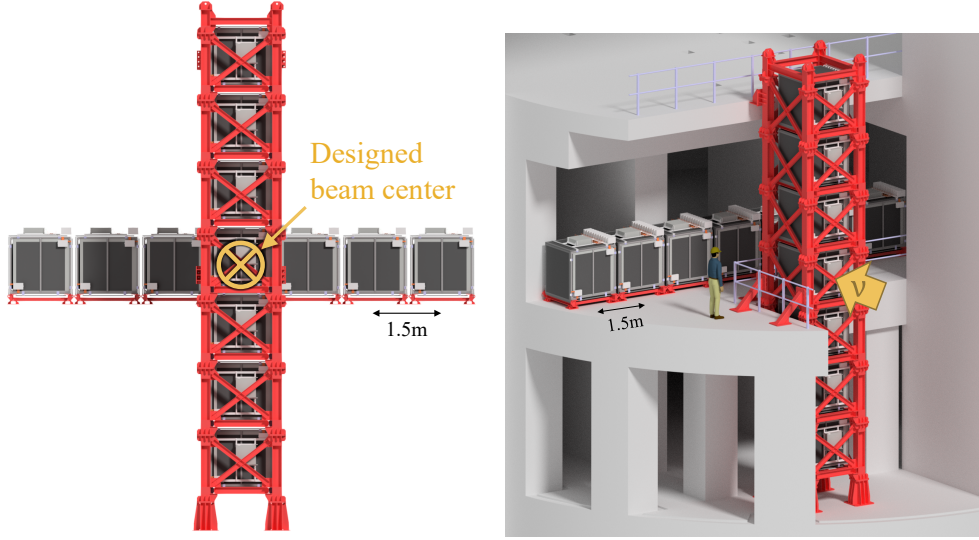


Figure 2.8: Illustrations of the INGRID setup.

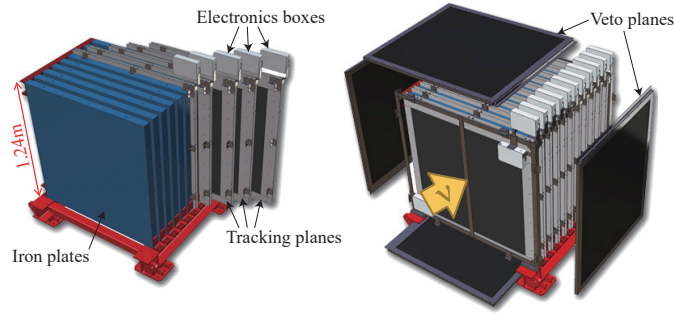


Figure 2.9: Left: tracking planes and iron plates of an INGRID module. Right: veto planes surrounding the INGRID module.

which detects muons that escape the detector at large angles and also provides a veto trigger for cosmic muons or muons from interactions in the magnet or the surrounding walls that enter ND280.

The incoming neutrino flux reaches the  $\pi^0$  detector (PØD) [88] which consists of layers of triangular scintillating plastic bars and had as a main purpose the measurement of the neutral pions produced in NC interactions. This is one of the dominant sources of background in the  $\nu_e$  appearance signal at Super-Kamiokande.

A tracker is located in the downstream part and is composed of three time projection chambers (TPCs) [89] alternated with two fine-grained detectors (FGDs) [90]. The FGDs, with a mass of  $\sim 2$  tons, act as neutrino targets and can provide the interaction vertex, i.e. the position of the neutrino interaction, whereas the TPCs track the particles produced in the interaction which exit the FGD and can perform particle identification (PID) and provide a precise measurement of their momenta.

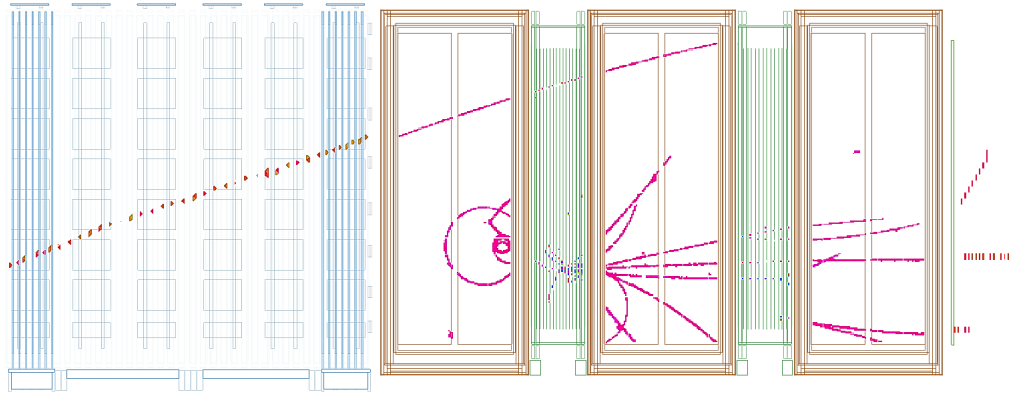


Figure 2.10: Example of an ND280 event display showing a highly inelastic neutrino interaction in FGD1 producing multiple tracks, and an unrelated muon track (likely a cosmic muon) going through the PØD and the tracker. The beam direction is from the left to the right.

These subdetectors (PØD, FGDs and TPCs) are surrounded by an electromagnetic calorimeter (ECal) [91] which is vital to the reconstruction of neutral particles and the identification of charged particle species.

### UA1 magnet

This magnet was refurbished from the UA1 experiment which contributed the initial discovery of the weak bosons (see Section 1.2.2). It provides a uniform magnetic field of 0.2 T orthogonal to the beam direction which bends charged particles and consequently identify their charges and measure their momenta. It is composed of four water-cooled aluminum coils operated at a 3 kA current which create the horizontal dipole field. A flux return yoke homogenizes this field. It is constituted by 16 C-shaped segments made of low-carbon steel plates and organized in two mirror-symmetric halves.

The magnetic field created by the UA1 magnet is mapped and has an excellent uniformity, with transverse components surpassing by 1% only in regions close to the coils. The trajectory of a charged particle that traverses ND280 is curved under the effect of this field. The direction of the curve allows us to determine the charge of the particle, whereas its momentum can be determined from the track curvature.

### Side muon range detector

The SMRD comprises 440 scintillator modules inserted in the gaps between the iron plates of the magnet yoke. Each module consists of a plastic scintillator plane composed of four to five plastic scintillator bars of  $875 \times 167 \times 7 \text{ mm}^3$ . Wavelength shifting (WLS) fibers cross the bars and are attached to silicon photomultipliers to read the scintillation light yield.

The role of the SMRD is to:

## Chapter 2. T2K experiment

---

- veto particles coming from outside the ND280 such as cosmic muons or *sand* muons, i.e. muons entering ND280 but produced from beam-related interactions outside the detector,
- detect and estimate the momenta of muons produced inside ND280 with a high angle with respect to the beam direction.

### Electromagnetic calorimeter

ECal refers to a number of sampling electromagnetic calorimeters that surround the inner subdetectors (PØD, FGDs and TPCs) that are made of layers of plastic scintillator bars with lead sheets in between. It is split into multiple sections: a PØD-ECal that surrounds the upstream part of ND280 where the PØD is located, a Barrel-ECal around the tracker part, and Ds-Ecal located in the downstream region.

Its main role is to complement the tracking capabilities of the detector. Its design encourages electromagnetic showering of electrons and photons, which allows us to further detect the signature of electron neutrinos and also identify the NC background (in the  $\nu_e$  appearance channel) characterized by the decay of neutral pions  $\pi^0 \rightarrow \gamma\gamma$ .

### $\pi^0$ detector

The PØD was designed to specifically measure  $\pi^0$  production cross section on water mainly from NC neutrino interactions from which no charged lepton is produced. It is composed of three modules: upstream and downstream electromagnetic calorimeters made of alternating plastic scintillator bars equipped with WLS fibers and lead sheets, and a water target region in the center consisting of layers of scintillator alternated with brass and high density polyethylene water bags.

The strategy to extract the cross section of the  $\text{NC}\pi^0$  interactions on water is the *water in – water out* technique: the event rate is measured when the water bags are filled, from which the measured event rate when they are empty is subtracted. This was performed in Reference [92]. Other cross-section measurements were also carried out with the PØD, such as the CC interaction of muon neutrinos [93] and antineutrinos [94] on water.

As of October 2022, and as part of the upgrade of ND280, the PØD was removed from the near detector complex to make place for a new set of subdetectors described in detail in Chapter 5.

### Fine-grained detectors

The two FGDs, FGD1 and FGD2, are the primary target of neutrino interactions. They consist of plastic scintillator bars arranged in planes with alternating orientation. FGD2 contains water layers which can be filled or drained, allowing the measurement of neutrino interactions

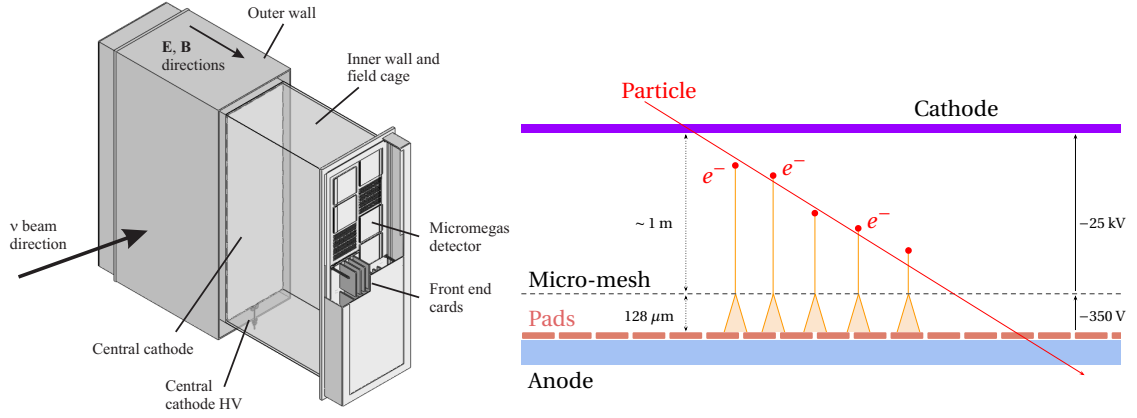


Figure 2.11: Left: schematic view of a TPC of ND280. Right: illustration of the principle of the standard bulk MicroMegas (not to scale). Left panel from Reference [86].

on water with the water in – water out approach.

Each FGD scintillator bar measures  $9.61 \times 9.61 \times 1864.3 \text{ mm}^3$  with a 1.5 mm diameter hole for a WLS fiber. The latter is connected to a multipixel photon counter (MPPC) which reads the scintillation light. The planes are arranged so that the bars in successive layers are perpendicular to each other. This allows for a three-dimensional reconstruction of tracks and an excellent determination of the vertex position. FGD1 consists of 5760 bars arranged in 30 layers of 192 bars each. Each pair of layers with alternating orientation is called *XY module*, referring to their orientation along the  $x$ - and  $y$ -axis while the  $z$ -axis denotes the neutrino beam direction (see the right panel of Figure 2.7). On the other hand, FGD2 is comprised of 7 XY modules alternated with 2.5 cm thick layers of (passive) water bags. Consequently, while FGD1 is a fully hydrocarbon target, FGD2 allows us to measure neutrino interactions on water as well, the same target as Super-Kamiokande.

The two FGDs provide a total mass of  $\sim 2$  tons, allowing for neutrinos to interact at a significant rate. However, the main limitation of this XY design is the poor reconstruction performance of particles produced at a high angle with respect to the beam direction. In fact, if the tracks are in the  $x - y$  plane, they would cross only one or a small number of bars, making them hard to identify.

### Time projection chambers

Three gaseous argon TPCs, alternated with FGD1 and FGD2 as depicted in Figure 2.7, are used in the tracker part of ND280 to provide precise information of the direction and the curvature of the tracks. In particular, the energy loss when crossing the TPCs along with the track curvature allows for particle identification and momentum measurements.

As shown in Figure 2.11, the TPC is designed as a double box, one inside the other. The inner

## Chapter 2. T2K experiment

---

box constitutes a field cage made of copper-clad G10 and holds the drift argon gas, while the outer aluminum box provides grounding and holds carbon dioxide as an electrical insulator. The inner box volume is divided in two halves by a central cathode, and an electric field parallel to the magnetic field is generated by a high-voltage potential difference between the central cathode and the field cage.

The inner drift box has a volume of 3000 L. A system was specifically design to purify the TPC gas, such that in a normal run, the drift volume is flushed five times per day and 90% of the gas is reused. The gas purity is controlled with two monitoring chambers within which the drift velocity, or the gain, is measured using radioactive sources.

A charged particle passing through the TPC ionizes the gas, and the ions drift from the cathode under the effect of the  $\sim 280$  V/cm electric field to the MicroMegas readout pads [95, 96] which collect the charge and the timing information. As displayed in Figure 2.11, the standard bulk MicroMegas used in the TPC readout consists of micro-mesh placed just before the anode and an additional voltage is applied between the mesh and the finely segmented anode pads to amplify the charge. The  $y$  and  $z$  coordinates of the track is obtained from the position of the triggered pad, whereas the  $x$  coordinate is given by the arrival time of the signal, which corresponds to the time difference between the entrance of the track in the chamber (given by an external trigger) and the readout of the charge (recorded by the MicroMegas).

### 2.2.3 WAGASCI/BabyMIND

WAGASCI/BabyMIND is one of the latest additions to the near detector complex, commissioned between 2018 and 2020 and positioned at a  $1.5^\circ$  off-axis angle to the beam. As displayed in Figure 2.12, it is composed of four subdetectors: the water grid and scintillator detector (WAGASCI module), the proton module (PM), the wall muon range detectors (Wall-MRDs), and the baby magnetized iron neutrino detector (BabyMIND).

WAGASCI aims to measure neutrino interactions on hydrocarbon and water in order to better understand the differences in the neutrino cross sections between ND280 (mainly composed of plastic) and Super-Kamiokande (water) with an improved acceptance for high angle particles with respect to the beam direction. Each WAGASCI module is a three-dimensional grid structure of plastic scintillator immersed in water, consisting of 1280 scintillator bars of  $3 \times 25 \times 1020$  mm<sup>3</sup> traversed by WLS fibers and read by silicon photomultipliers. The total water mass of one WAGASCI module is 0.6 tons and accounts for 80% of its fiducial volume.

The proton module, shown in the right panel of Figure 2.12, was initially designed as part of the INGRID detector and placed at its center. It is similar to the INGRID modules, but without any iron plates, making it a fully active detector with 36 layers of 32 bars of plastic scintillator alternating between horizontal and vertical orientations. It is placed between two WAGASCI modules and optimized to identify the muons, pions and protons from neutrino interactions.

Two Wall-MRDs surround the WAGASCI and PM modules as shown in Figure 2.12. These are

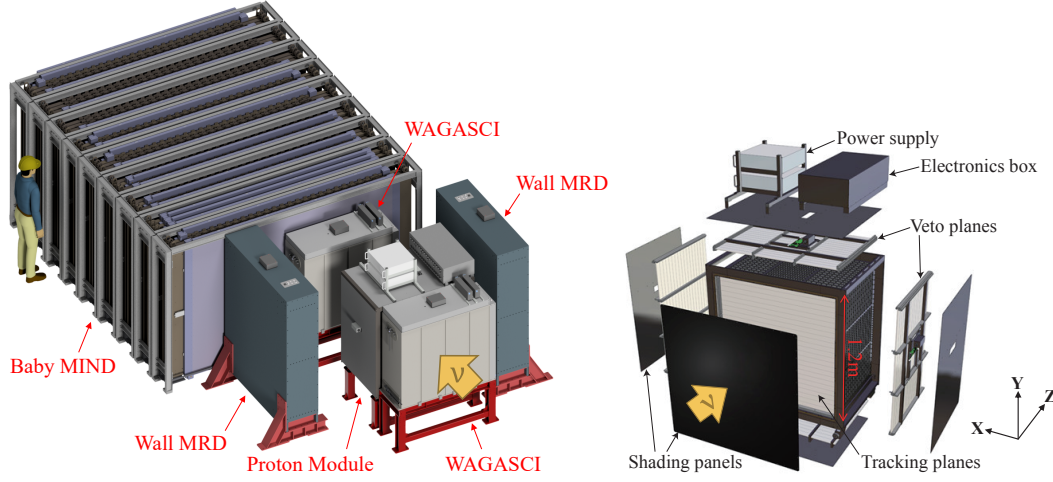


Figure 2.12: Left: setup of the WAGASCI-BabyMIND detector. Right: exploded view of the proton module.

steel scintillator sampling detectors placed at 20 – 65 cm from the central detectors, made of 11 iron plates of 3 cm thickness alternated with 10 scintillator planes. They particularly detect the high angle muons exiting WAGASCI or the PM, estimate their momenta and also allow us to measure their time of flight.

BabyMIND is located downstream of WAGASCI, the PM and the Wall-MRDs, a muon spectrometer used to accurately measure the charge and momentum of muons exiting the main WAGASCI modules with a 1.5 T magnetic field. It consists of 33 magnetized plates of iron with a 30 mm thickness, separated by 18 plastic scintillator planes optimized using simulation to measure the momenta of muons at the energies expected at a  $1.5^\circ$  off-axis angle.

### 2.2.4 ND280 upgrade

The fall of 2022 marked the beginning of the upgrade of ND280. While the ND280 has well performed to characterize the unoscillated T2K neutrino beam, some of its limitations will start to arise in the upcoming analyses with the expected increase in statistics over the new phase of data collection. This will be discussed in detail in Chapter 5.

## 2.3 Far detector: Super-Kamiokande

Super-Kamiokande, also known as *Super-K* or *SK* and depicted in Figure 2.13, is a versatile detector that detects neutrinos with energies between a few MeV and a few GeV from a broad range of terrestrial and astrophysical sources, located  $\sim 1000$  m underground in Kamioka, Japan. It started its activities in 1996, with the initial goal of observing the hypothetical nucleon decay, but proved effective in detecting neutrinos of energies spanning six orders of magnitude from the diffuse supernova background, galactic supernovae, the Sun, cosmic rays,



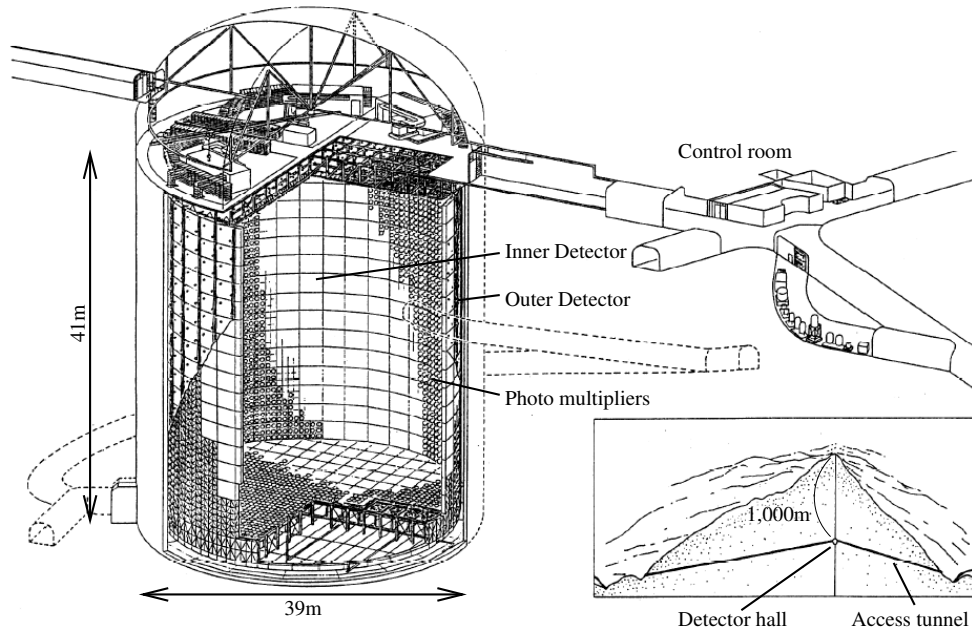


Figure 2.13: Schematic illustration of Super-Kamiokande. Figure from Reference [97].

and Earth-based sources.

It consists of a large tank filled with  $\sim 50,000$  tons of ultrapure water and  $\sim 13,000$  photomultiplier tubes (PMTs) installed on its walls. The PMTs measure the Čerenkov light emitted by the charged particles created in neutrino interactions when their velocity is above the speed of light in water.

Super-Kamiokande is a cylindrical stainless-steel tank with a 39 m diameter and 41 m height. It is divided into an inner detector (ID) and an outer detector (OD) by a 55 cm thick cylindrical structure that is covered on its outer surface by Tyvek, a light-proof material that ensures optical independence between the two regions. Its inner surface, which corresponds to the ID, is wrapped with opaque “black sheets”. This cylindrical structure supports the PMTs: 11,129 inward-facing 50-cm diameter PMTs for the ID, and 1885 outward-facing 20-cm PMTs attached to  $60\text{ cm}^2$  wavelength-shifting plates for the OD. In fact, even with the rock overburden of  $\sim 1000\text{ m}$  that attenuates the cosmic muon flux by a factor of  $10^{-5}$ , a significant fraction can still make it to the detector. The purpose of the OD is to act as a veto for these cosmic muons, as well as any beam-related neutrino interactions in the surrounding rocks. The upper floor above the detector houses a low-energy linear accelerator for detector calibration. It is also where the electronics that read the PMT signals are located.

Super-Kamiokande is able to distinguish between muons and electrons by the patterns of the rings due to Čerenkov light cones. The muons, which are of a relatively large mass, pass through water in the detector without rescattering and produce sharp rings. On the other hand, electrons, owing to their lower mass, scatter more often and produce electromagnetic showers,

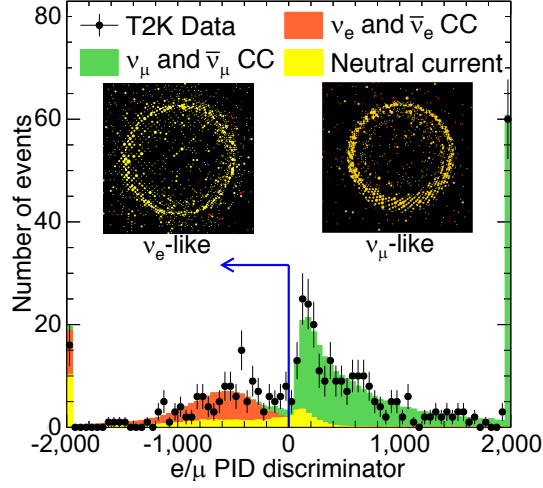


Figure 2.14: Distribution of the particle identification (PID) parameter used to discriminate between electron-like and muon-like Čerenkov rings. Figure from Reference [53].

yielding fuzzier rings. This is how the shape of the ring pattern allows for the identification of the particles as shown in Figure 2.14.

Contamination by radioactive species such as radon in the ultrapure water can be the source of important backgrounds. Additionally, impurities in the water may significantly impact the light detection with the PMTs. This is why purification systems are built in for water as well as for air at the surface level. The water filtration system is a closed loop that processes the 50,000 tons of water at a rate of 30 tons per hour.

Super-Kamiokande started doping its water with gadolinium since 2020 with the purpose of enhancing its ability to detect neutrons, often produced by antineutrino interactions. This idea was first proposed in Reference [98] and is especially important for low-energy neutrino physics. While neutrons can be detected through their capture on hydrogen protons in water when they thermalize, this capture produces a single photon of  $\sim 2.2$  MeV that is difficult to detect not only because the Compton-scattered electron would have an energy that is very close to the Čerenkov threshold, but also due to the Super-Kamiokande detection threshold that is around  $\sim 3 - 4$  MeV. This prompted the idea of enriching water with soluble gadolinium salt, because of the higher neutron cross section of gadolinium and the enhanced neutron capture signature that produces gamma rays of a total  $\sim 8$ -MeV energy, noticeably larger than that of the proton capture. The current concentration of gadolinium in water is 0.03 %, which provides neutron capture efficiency of 75%.

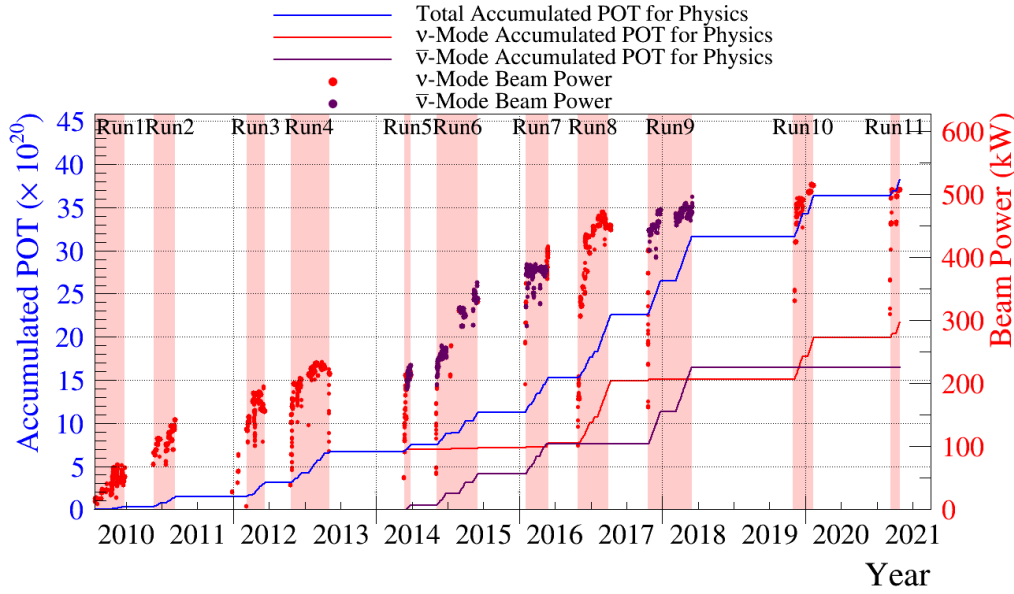


Figure 2.15: History of the delivered protons on target (POT) and the beam power since the start of the T2K experiment.

## 2.4 Physics results

### 2.4.1 Data

The T2K experiment began taking data in 2010. The beam exposure is expressed in the number of delivered protons on target (POT) as shown in Figure 2.15. In total, T2K gathered  $3.82 \times 10^{21}$  POT until now, of which  $2.17 \times 10^{21}$  POT is in neutrino mode (56.8%) and  $1.65 \times 10^{21}$  POT is in antineutrino mode (43.2%).

### 2.4.2 Oscillation measurements

The T2K collaboration regularly updates its measurements of the oscillation parameters with new data and/or new analysis techniques. The details of the latest oscillation analysis, presented in the Neutrino 2022 conference, will be shown in Chapter 7.

Studies beyond the standard PMNS paradigm of three-neutrino oscillations are also performed, such as possible Lorentz or CPT violations [99] and searches of light sterile neutrinos at Super-Kamiokande [100] and heavy neutrinos at ND280 [101].

### 2.4.3 Cross-section measurements

Along with the oscillation measurements, the T2K collaboration carries a rich program of neutrino cross-section measurements. This covers a wide range of targets at the near (hydro-

carbon, water, ...) and the far detectors (water) over different ranges of energies depending on the off-axis angle (INGRID, WAGASCI/BabyMIND, ND280 or Super-Kamiokande).

Table 2.2 summarizes all the cross-section measurements performed by T2K until now. This shows different types of measurements:

- CC *inclusive* measurements, when only the charged lepton coming out of the neutrino interaction is considered regardless of any other particles that were eventually produced,
- CC0 $\pi$  measurements, which correspond to a neutrino interaction producing a charged lepton and no pion in the final state,
- CC1 $\pi$  measurements, when both the charged lepton and the pion are observed from the interaction.

The measurement reports either the total cross section  $\sigma$ , or a differential cross section as a function of an observable, such as a single differential (1D) cross section in the muon momentum  $\frac{d\sigma}{dp_\mu}$  or a double differential (2D) cross section the muon momentum and direction  $\frac{d^2\sigma}{dp_\mu d\cos\theta_\mu}$ .

## Chapter 2. T2K experiment

Type	Measurement	Variables	Reference
$\bar{\nu}_\mu$ CC inclusive	$\nu_\mu$ on C	$\frac{d^2\sigma}{dp_\mu d\cos\theta_\mu}$	[102]
	$\nu_\mu$ on Fe and CH (on-axis)	$\sigma$	[103]
	$\nu_\mu$ to $\bar{\nu}_\mu$ ratio on the PØD	$\sigma$	[104]
	$\nu_\mu$ on C	$\frac{d^2\sigma}{dp_\mu d\cos\theta_\mu}$	[105]
	$\nu_\mu$ on H <sub>2</sub> O, CH, Fe	$\sigma$	[106]
$\bar{\nu}_e$ CC inclusive	$\nu_e$ on C	$\frac{d\sigma}{dp_e}, \frac{d\sigma}{d\cos\theta_e}, \frac{d\sigma}{dQ^2}$	[107]
	$\nu_e$ on H <sub>2</sub> O for $E_\nu > 1.5$ GeV	$\sigma$	[108]
	$\nu_e/\bar{\nu}_e$ on ND280	$\frac{d\sigma}{dp_e}, \frac{d\sigma}{d\cos\theta_e}$	[109]
$\bar{\nu}_\mu$ CC0 $\pi$	$\nu_\mu$ on C	$\frac{d^2\sigma}{dp_\mu d\cos\theta_\mu}$	[110]
	$\nu_\mu$ on C (on-axis)	$\sigma$	[111]
	$\nu_\mu$ on C <sub>8</sub> H <sub>8</sub>	$\frac{d^2\sigma}{dp_\mu d\cos\theta_\mu}$	[112]
	$\nu_\mu$ on H <sub>2</sub> O	$\frac{d^2\sigma}{dp_\mu d\cos\theta_\mu}$	[93]
	$\nu_\mu$ on CH	$\frac{d\sigma}{d\delta p_T}, \frac{d\sigma}{d\delta\alpha_T}, \frac{d\sigma}{d\delta\phi_T}$	[113]
	$\bar{\nu}_\mu$ on H <sub>2</sub> O	$\frac{d^2\sigma}{dp_\mu d\cos\theta_\mu}$	[94]
	$\nu_\mu/\bar{\nu}_\mu$ on CH	$\frac{d^2\sigma}{dp_\mu d\cos\theta_\mu}$	[114]
	$\nu_\mu$ on C, O	$\frac{d^2\sigma}{dp_\mu d\cos\theta_\mu}$	[115]
	$\nu_\mu/\bar{\nu}_\mu$ on CH, H <sub>2</sub> O (WAGASCI)	$\sigma$	[116]
$\bar{\nu}_\mu$ CC1 $\pi$	$\nu_\mu$ on C	$\sigma$	[117]
	$\nu_\mu$ on H <sub>2</sub> O	$\frac{d\sigma}{dp_\mu}, \frac{d\sigma}{dp_\pi}, \frac{d\sigma}{d\cos\theta_\mu}, \frac{d\sigma}{d\cos\theta_\pi}$	[118]
	$\nu_\mu$ on CH	$\frac{d^2\sigma}{dp_\mu d\cos\theta_\mu}$	[119]
	$\nu_\mu$ on CH	$\frac{d\sigma}{d\delta p_{TT}}$	[120]
Other	$\nu/\bar{\nu}$ NCQE on H <sub>2</sub> O at SK	$\sigma$	[121]
	$\nu_e$ NC1 $\pi^0$ on H <sub>2</sub> O	$\sigma$	[92]
	$\nu/\bar{\nu}$ NCQE on O	$\sigma$	[122]

Table 2.2: Summary of the T2K cross-section measurements. T2K reports either the total ( $\sigma$ ), single differential ( $\frac{d\sigma}{dX}$ ) or double differential ( $\frac{d^2\sigma}{dXdY}$ ) cross section in given observables. Unless mentioned otherwise in the table, the measurement is performed with the 2.5° off-axis neutrino beam.

# Neutrino scattering **Part II**



# 3 Modeling neutrino-nucleus interactions

Known for their elusiveness, neutrinos can only be detected through their interaction with the detector material by looking for their products, and particularly the associated charged lepton. Early neutrino experiments used bubble chambers or spark chambers where neutrinos mostly interacted with light nuclei such as hydrogen. However, as experimental neutrino physics advanced, the quest for more data using larger detectors motivated experiments to use heavier nuclear targets such as water, hydrocarbon or argon. This raised new challenges as to how nuclear effects in such complex nuclei can impact and bias the estimation of the neutrino energy from the products of its interaction. Indeed, many nuclear effects can dramatically impact this estimation, as will be shown in this chapter, and are therefore crucial to characterize for oscillation measurements.

In this chapter, we review how neutrinos interact with nuclei. First, Section 3.1 presents how the elementary neutrino-nucleon interaction can be described for various processes. In Section 3.2, we review the different nuclear effects that are due to interactions with nuclei instead of free nucleons. Section 3.3 describes how neutrino interactions are simulated. Finally, we highlight the importance of accurately modeling these effects to estimate the neutrino energy in Section 3.4.

## 3.1 Neutrino-nucleon scattering

At the energies of accelerator experiments, neutrinos interact with nucleons in the target nucleus. In this chapter, we focus on the charged-current (CC) interactions of the type  $\bar{\nu}_l + N \rightarrow l^\pm + \mathcal{X}$  where  $N$  is the nucleon and  $\mathcal{X}$  is the hadronic product of the interaction. In general, the cross section of such interaction can be expressed as:

$$d\sigma = \frac{1}{32\pi^2 M_N} \frac{|\vec{p}_l|}{E_\nu} |\mathcal{A}|^2 dE_l d\cos\theta_l \prod_{\mathcal{X}} \frac{d^3\vec{p}_{\mathcal{X}}}{(2\pi)^3 2E_{\mathcal{X}}} (2\pi)^4 \delta^{(4)}\left(\sum_{\mathcal{X}} p_{\mathcal{X}} - p_l - p_N - p_\nu\right) \quad (3.1)$$



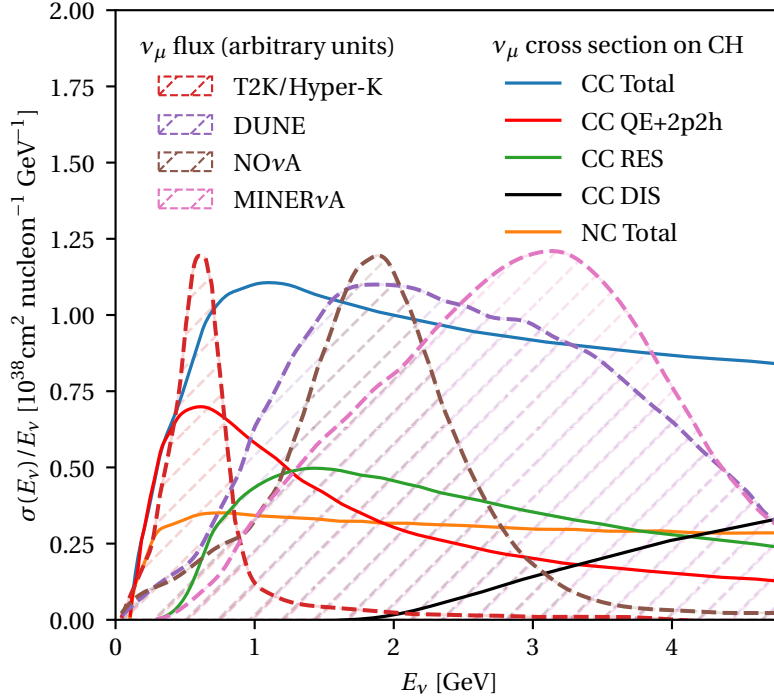


Figure 3.1: Muon neutrino cross section on hydrocarbon as a function of the neutrino energy, broken down by interaction mode and compared to the energy spectrum from neutrino experiments.

where  $p_\nu$ ,  $p_N$ ,  $p_l$  and  $p_{\mathfrak{X}}$  are the four-momenta of the incoming neutrino, the initial nucleon, the outgoing lepton and the hadronic products respectively,  $E_l$  the energy of the charged lepton,  $\theta_l$  its angle with respect to the incoming neutrino direction, and the amplitude  $\mathcal{A}$  is the invariant matrix element for the considered process.

Different channels of CC interactions are possible: quasielastic (QE) scattering off the nucleon, resonance production (RES), and deep inelastic scattering (DIS) for higher energy neutrinos. Therefore, the total CC cross section is the sum of the different channels:  $\sigma_{\text{CC}} = \sigma_{\text{CCQE}} + \sigma_{\text{CCRES}} + \sigma_{\text{CCDIS}}$ . In this section, we review these interaction modes and discuss the corresponding neutrino-nucleon interaction cross sections.

### 3.1.1 Quasielastic interactions

This is the most important contribution at intermediate energies (up to  $\sim 1$  GeV) as shown in Figure 3.1. When neutrinos have enough energy to produce the charged lepton's mass<sup>1</sup>,

<sup>1</sup>This is why only electron and muon neutrinos are observed in accelerator experiments such as T2K, since the tau mass is  $\sim 1.7 \text{ GeV}/c^2$  which typically requires a higher neutrino energy to be produced.

charged-current quasi-elastic (CCQE) interactions can occur:

$$\begin{aligned} \nu_l + n &\rightarrow l^- + p, \\ \bar{\nu}_l + p &\rightarrow l^+ + n. \end{aligned}$$

#### Interaction on a free quark

As a first step, let us consider the elementary interaction of the neutrino on a free quark, from which we can deduce the cross section on a nucleon:  $\nu_l(p) + d(k) \rightarrow l^-(p') + u(k')$ , where  $p$  and  $k$  are the four-momenta of the incoming neutrino and the down quark, and  $p'$  and  $k'$  the four-momenta of the outgoing charged lepton and the up quark respectively.

The CC Lagrangian derived in Equation (1.7) can be written as:

$$\mathcal{L}_{\text{CC}} = -\frac{g}{\sqrt{2}} \left( W_\mu^+ \bar{\nu}_{lL} \gamma^\mu l_L + W_\mu^- \bar{l}_L \gamma^\mu \nu_{lL} + W_\mu^+ \bar{u}_L \gamma^\mu d_L + W_\mu^- \bar{d}_L \gamma^\mu u_L \right).$$

where we also include the CC interaction terms for the up and down quarks. The amplitude  $\mathcal{A}_{\text{CCQE}}(\nu d \rightarrow l u)$  corresponding to this interaction for low energies such that the four-momentum squared transferred is smaller than the mass of the intermediate boson squared, i.e.  $q^2 \ll M_W^2$  where  $q = p - p' = k - k'$ , can be obtained from this Lagrangian and written as:

$$\mathcal{A}_{\text{CCQE}}(\nu d \rightarrow l u) = -\frac{G_F V_{ud}}{\sqrt{2}} \ell_\rho h^\rho \quad (3.2)$$

where:

- $V_{ud}$  is a coefficient of the quark mixing matrix, for which the weak states are not the same as the mass states similarly to the neutrinos.,
- $\ell_\rho = \bar{l}(p') \gamma_\rho (1 - \gamma^5) \nu_l(p)$  describes the leptonic part of the interaction, called *leptonic current*,
- $h_\rho = \bar{u}(k') \gamma_\rho (1 - \gamma^5) d(k)$  describes the hadronic part of the interaction, called *hadronic current*.

Since what appears in the expression of the cross section is the squared modulus of the amplitude (Equation (3.1)), it is also common to introduce the (second-rank) leptonic and hadronic tensors,  $L_{\alpha\beta}$  and  $H_{\alpha\beta}$  respectively, such that:

$$|\mathcal{A}_{\text{CCQE}}(\nu d \rightarrow l u)|^2 = \frac{G_F^2 |V_{ud}|^2}{2} L_{\alpha\beta} H^{\alpha\beta} \quad (3.3)$$

which can be directly deduced from  $\ell_\rho$  and  $h_\rho$ .

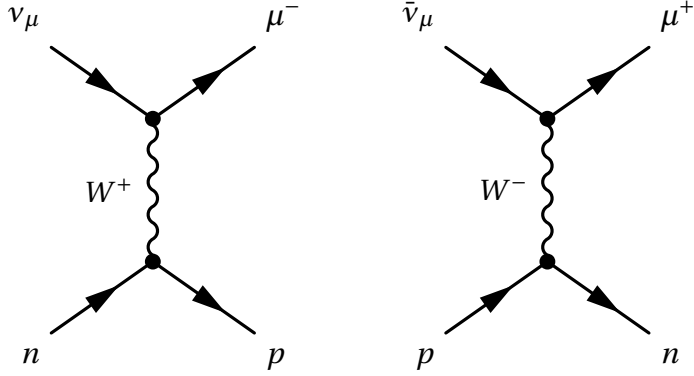


Figure 3.2: Example of Feynman diagrams for  $\nu_\mu$  and  $\bar{\nu}_\mu$  CCQE interactions.

#### Interaction on a nucleon

If we consider now the scattering off a free nucleon as shown in Figure 3.2, the leptonic part of the amplitude given in Equation (3.2) remains unchanged, whereas the hadronic part should be modified to describe the internal structure of the quarks within the nucleus. This is obtained in a phenomenological way that accounts for the chiral structure of the electroweak Lagrangian, also known as  $V - A$ . The hadronic part  $h_\rho$  of Equation (3.2) can be expressed as the difference between an axial term  $A_\rho$  which is proportional to  $\gamma_5$  and a vector term  $V_\rho$  that does not contain  $\gamma_5$ :

$$h_\rho = V_\rho - A_\rho$$

where  $V_\rho$  and  $A_\rho$  are expressed as [39]:

$$V_\rho = \bar{u}_p(k') \left[ \gamma_\rho F_1(Q^2) + \frac{i}{2M_N} \sigma_{\rho\eta} q^\eta F_2(Q^2) \right] u_n(k),$$

$$A_\rho = \bar{u}_p(k') \left[ \gamma_\rho F_A(Q^2) + \frac{q_\rho}{M_N} F_P(Q^2) \right] \gamma_5 u_n(k).$$

Here,  $u_N$  is the Dirac spinor of the nucleon,  $M_N$  its mass,  $Q^2 = -q^2$ , and  $\sigma_{\rho\eta} = \frac{i}{2} [\gamma_\rho, \gamma_\eta]$ . This expression introduces the *form factors*  $F(Q^2)$  which describe the internal structure of the quarks within the nucleon and can be determined experimentally.  $F_1$  and  $F_2$  are the vector form factors, whereas  $F_A$  and  $F_P$  are called the axial and the pseudoscalar form factors respectively. We can see that the case of interaction on a free quark corresponds to  $F_1(Q^2) = F_A(Q^2) = 1$  and  $F_2(Q^2) = F_P(Q^2) = 0$ .

The differential cross section of the quasielastic interaction of a neutrino with a nucleon as a function of the momentum transfer  $Q^2$  is often expressed with the Llewellyn – Smith

formula [123]:

$$\frac{d\sigma_{\text{CCQE}}^{\bar{\nu}}}{dQ^2} = \frac{G_F^2 M_N |V_{ud}|^2}{8\pi E_\nu^2} \left[ A(Q^2) \pm \frac{(s-u)}{M_N^2} B(Q^2) + \frac{(s-u)^2}{M_N^4} C(Q^2) \right] \quad (3.4)$$

where:

$$\begin{aligned} A(Q^2) &= \frac{(M_l^2 + Q^2)}{M_N^2} \left\{ (1+\eta)F_A^2 - (1-\eta)F_1^2 + \eta(1-\eta)F_2^2 + 4\eta F_1 F_2 \right. \\ &\quad \left. - \frac{M_l^2}{4M_N^2} [(F_1 + F_2)^2 + (F_A + 2F_P)^2 - 4(\eta+1)F_P^2] \right\}, \\ B(Q^2) &= \frac{Q^2}{M_N^2} F_A (F_1 + F_2), \\ C(Q^2) &= \frac{1}{4} (F_A^2 + F_1^2 + \eta F_2^2), \end{aligned}$$

with  $\eta = \frac{Q^2}{4M_N^2}$ , and the invariant Mandelstam variables:

$$\begin{aligned} s &= (p+k)^2 = (p'+k')^2, \\ t &= (p-p')^2 = (k-k')^2 = q^2, \\ u &= (p'-k)^2 = (k'-p)^2. \end{aligned}$$

The sign of the term proportional to  $B(Q^2)$  in Equation (3.4) is + for neutrinos and – for antineutrinos.  $B(Q^2)$  contains the interference between the axial and vector parts of the process, and implies a  $Q^2$ -dependent difference between the cross sections of neutrinos and antineutrinos on a nucleon.

### Form factors

The form factors describe the spatial charge distribution of the sea of quarks and gluons within the nucleon. This is conveniently probed in electron-nucleon scattering by measuring the angular distribution of the scattered electrons and comparing it to the known cross section of electrons interacting with a point-like charge. The form factor  $F(Q^2)$  appears by definition as:

$$\frac{d\sigma}{d\Omega} = \left( \frac{d\sigma}{d\Omega} \right)_{\text{point}} |F(Q^2)|^2.$$

When the charge distribution  $\rho$  is assumed to be of the form  $\rho(r) = \rho_0 \exp(-Mr)$ , the form factor can be described as a dipole, which is obtained by a Fourier transform of this distribution [124]:

$$F(Q^2) \propto \left( 1 - \frac{Q^2}{M^2} \right)^{-2}. \quad (3.5)$$

### Chapter 3. Modeling neutrino-nucleus interactions

---

The nucleon vector form factors  $F_1$  and  $F_2$  are derived from the electric and magnetic form factors. They are well known within the dipole approximation for momentum transfers  $Q^2 \lesssim$  few  $\text{GeV}^2$  thanks to the measurements of the interactions  $e^- + N \rightarrow e^- + N$  and the precise knowledge of the charge radial distributions. Electron scattering measurements for higher  $Q^2$  show deviations from the dipole approximation, and parametrized corrections can be applied to describe this data [125].

On the other hand, the axial form factor  $F_A$  is often expressed in the dipole approximation as:

$$F_A(Q^2) = \frac{F_A(0)}{\left(1 + Q^2/M_A^{\text{QE}2}\right)^2}, \quad (3.6)$$

where  $F_A(0)$  is the axial coupling constant which is extracted from polarized nucleon beta decay experiments and taken as  $F_A(0) = 1.2695 \pm 0.0029$  [126], leaving the axial mass  $M_A^{\text{QE}}$  as the least constrained parameter of the Llewellyn – Smith cross section.

The most direct probes of  $M_A^{\text{QE}}$  are neutrino scattering measurements on light targets such as hydrogen or deuterium. A number of experiments from the 1970s until 1990 used bubble chambers to measure these interactions [127–133], which access the value of  $M_A^{\text{QE}}$  by fitting the  $Q^2$  shape to the data. Additionally, pion electroproduction allows us to constrain this axial mass, and a recent combined fit shows that  $M_A^{\text{QE}} = 1.014 \pm 0.014 \text{ GeV}/c^2$  [134]. More recent neutrino scattering experiments use heavier targets which make the extraction of  $M_A^{\text{QE}}$  less straightforward due to the additional nuclear effects in neutrino-nucleus interactions (see Section 3.2). Nevertheless, the MINERvA experiment provided in 2023 the first statistically significant measurement of muon antineutrinos scattering on protons using the hydrogen of their plastic scintillator detector in Reference [135] and was able to extract the nucleon axial form factor.

Finally, the contribution from the pseudoscalar form factor  $F_P$  to the Llewellyn – Smith cross section appears in the term  $A(Q^2)$  proportional to  $(M_I/M_N)^2$ . For electrons and muons,  $(M_I/M_N)^2$  is of the order of  $\sim 10^{-7}$  and  $\sim 10^{-2}$  respectively, which means that the contribution from  $F_P$  is significantly suppressed for  $\bar{\nu}_e$  and  $\bar{\nu}_\mu$ . Nevertheless, this form factor can be determined in terms of  $F_A$  under the partially conserved axial current hypothesis as [136]:

$$F_P(Q^2) = \frac{2M_N^2}{Q^2 + M_\pi^2} F_A(Q^2).$$

#### 3.1.2 Single-pion production

As the energy transfer from the neutrino to the nucleon increases, the center-of-mass energy of a neutrino interaction exceeds the mass of a resonant excited state of the nucleon which promptly ( $\sim 10^{-24}$  s) decays and produces an additional meson. This is the dominant interaction mode for neutrino energies between 1 and 10 GeV as shown in Figure 3.1. The lightest

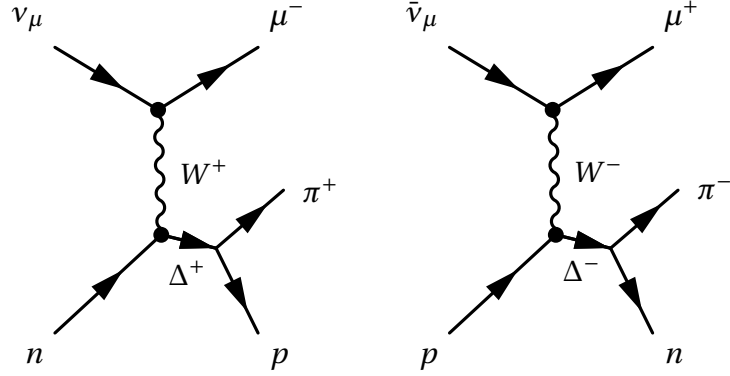


Figure 3.3: Example of Feynman diagrams for  $\nu_\mu$  and  $\bar{\nu}_\mu$  CC single-pion production via intermediate  $\Delta(1232)$  resonances.

and most prominent resonance is the delta  $\Delta(1232)$  of isospin  $3/2$ . Various neutrino resonant pion production interactions are possible. The CC resonant pion production (CCRES) ones are:

$$\begin{aligned}
 \nu_l + p &\rightarrow l^- + \Delta^{++} \\
 \Delta^{++} &\rightarrow p + \pi^+, \\
 \nu_l + n &\rightarrow l^- + \Delta^+ \\
 \Delta^+ &\rightarrow p + \pi^0 \text{ or } n + \pi^+, \\
 \bar{\nu}_l + p &\rightarrow l^+ + \Delta^0 \\
 \Delta^0 &\rightarrow p + \pi^- \text{ or } n + \pi^0, \\
 \bar{\nu}_l + n &\rightarrow l^+ + \Delta^- \\
 \Delta^- &\rightarrow n + \pi^-,
 \end{aligned}$$

and examples are displayed in Figure 3.3, whereas the NC resonant (NCRES) interactions are:

$$\begin{aligned}
 \bar{\nu}_l^{(-)} + p &\rightarrow \bar{\nu}_l^{(-)} + \Delta^+ \\
 \Delta^+ &\rightarrow p + \pi^0 \text{ or } n + \pi^+, \\
 \bar{\nu}_l^{(-)} + n &\rightarrow \bar{\nu}_l^{(-)} + \Delta^0 \\
 \Delta^0 &\rightarrow p + \pi^- \text{ or } n + \pi^0.
 \end{aligned}$$

Similarly to what was shown in Equation (3.2) for the CCQE interaction, the amplitude  $\mathcal{A}_{\text{CCRES}}$  of a CCRES interaction can be expressed as the product of a leptonic part which here again remains unchanged, and a hadronic part that can be decomposed into axial and vector contributions (see e.g. Reference [137]). The vector contribution depends on four vector form factors  $C_i^V(Q^2)$ ,  $i = 3, \dots, 6$ , which are well determined as well thanks to precise photoproduction and

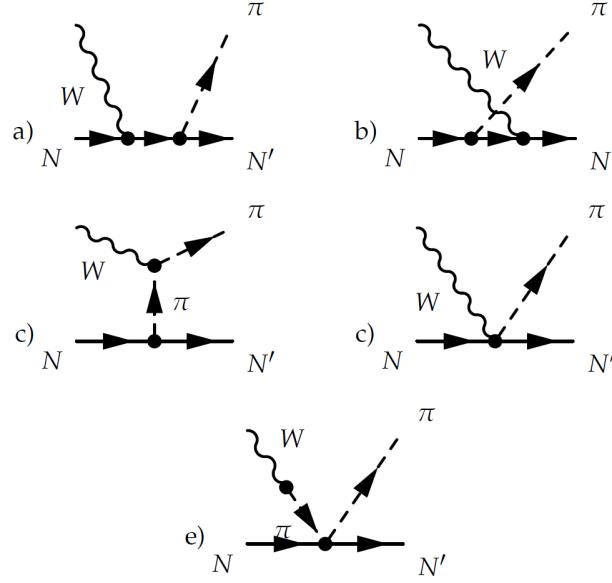


Figure 3.4: Non-resonant pion production Feynman diagrams. Figure from [151].

electroproduction data [138–141]. Similarly, the axial contribution is also function of four axial form factors  $C_i^A(Q^2)$ ,  $i = 3, \dots, 6$ , of which the most important is  $C_5^A$ . In fact, as early as 1965, it was observed to have the dominant contribution [142]. Additionally,  $C_6^A$  can be related to  $C_5^A$  using the same partially conserved axial current hypothesis [143] that relates  $F_P$  to  $F_A$  in the CCQE process. Furthermore, it is common to use the Adler model [144] where  $C_3^A(q^2) = 0$  and  $C_4^A(q^2) = -C_5^A(q^2)/4$ . As a first approximation, the form factor  $C_5^A$  can be expressed in the dipole form as:

$$C_5^A(Q^2) = \frac{C_5^A(0)}{(1 + Q^2/M_A^{\text{RES}2})^2}. \quad (3.7)$$

The axial mass  $M_A^{\text{RES}}$  and the constant  $C_5^A(0)$  are both poorly known. In fact, the only available measurements on a nucleon target were performed in the 1980s at ANL [145] and BNL [146]. They allow us to only weakly constrain these two parameters, and they do not give sensitivity to the other axial form factors.

The  $\Delta(1232)$  resonance is the lightest one, but there are 17 additional baryonic resonances that are considered in the Rein – Sehgal model [147], which is widely used in neutrino event generators. In particular, it features interferences between the intermediate resonant states. One of its shortcomings is its assumption of a massless lepton in its original calculations, and corrections that include mass effects were developed [148–150]. The Rein – Sehgal model also accounts for non-resonance contributions to the single pion production process as shown in Figure 3.4, although only for isospin-1/2 interaction channels, but does not include the interference between resonant and non-resonant effects.

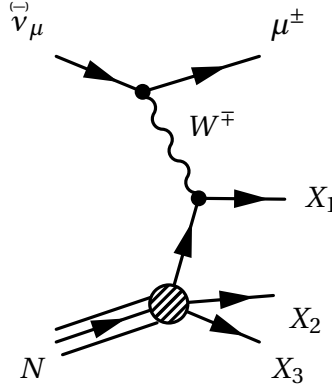


Figure 3.5: Feynman diagram of a CCDIS interaction with a nucleon.

### 3.1.3 Deep inelastic scattering

When the incoming neutrino has enough energy to resolve the individual quarks within the nucleon, deep inelastic scattering (DIS) becomes possible. The high energy neutrino is able to probe the structure of the nucleon and cause the quarks to become unbound and to undergo hadronization that typically produces multiple mesons and nucleons. The CCDIS interaction of a (anti)neutrino on a nucleon  $N$  can be typically written as  $\bar{\nu}_l + N \rightarrow l^\pm + \mathfrak{X}$  where  $\mathfrak{X}$  is the hadronic product as displayed in Figure 3.5.

The inclusive cross section of the DIS process can be expressed in terms of the inelasticity  $y = E_{\text{had}}/E_\nu$  where  $E_{\text{had}}$  is the energy of the hadrons, and the *Bjorken scaling variable*  $x = Q^2/2M_N E_\nu y$  as [152]:

$$\frac{d^2\sigma_{\text{CCDIS}}^{\bar{\nu}}}{dx dy} = \frac{G_F^2 M_N E_\nu}{\pi (1 + Q^2/M_W^2)^2} \left[ \frac{y^2}{2} 2x\tilde{F}_1(x, Q^2) + \left( 1 - y - \frac{M_N x y}{2E_\nu} \right) \tilde{F}_2(x, Q^2) \pm y \left( 1 - \frac{y}{2} \right) x\tilde{F}_3(x, Q^2) \right]$$

where  $\tilde{F}_i$  are the structure functions expressed within the quark-parton model in terms of the parton distribution functions  $q_i$ :

$$\begin{aligned} \tilde{F}_1(x, Q^2) &= \sum_j [q_j(x, Q^2) + \bar{q}_j(x, Q^2)], \\ \tilde{F}_3(x, Q^2) &= 2x \sum_j [q_j(x, Q^2) - \bar{q}_j(x, Q^2)], \\ \tilde{F}_2(x, Q^2) &= 2xF_1(x, Q^2). \end{aligned}$$

The parton distribution functions give the probability  $xq$  for a struck quark carrying a fraction  $x$  of the nucleon momentum to produce a quark with a given momentum fraction.



## 3.2 Neutrino-nucleus scattering

Neutrino-nucleon interaction mechanisms discussed in the previous section may be sufficient to describe observations of early neutrino scattering experiments that used light targets in bubble chambers. However, the discovery of neutrino oscillations brought a new era for neutrino physics, with modern experiments using more intense beams and heavier targets such as carbon, oxygen, argon and iron. The nuclear effects due to the fact that the nucleons with which neutrinos interact are bound within a heavy nucleus are important to take into account for an unbiased neutrino energy estimation. In this section, we will review the various processes that enter into play when considering neutrino-nucleus

In the quest for a thorough understanding of how neutrinos interact with nuclei, an important connection can be established with electron-nucleus scattering measurements. These provide precise data in well-controlled kinematics settings, where the energy of the electron beam is accurately adjusted. As such, they offer a detailed probe of the nuclear structure of the nucleus, which is all the more relevant for neutrino-nucleus interactions as their reaction mechanisms share multiple similarities, particularly related in the vector part of the leptonic tensor. We will also see in this section how this can be utilized to build neutrino-nucleus scattering models.

### 3.2.1 Impulse approximation

The impulse approximation (IA) is a crucial assumption in multiple neutrino-nucleus interaction models. It consists of assuming that the incident neutrino sees the target nucleus, of atomic number  $A$ , as a collection of individual nucleons. The incoming neutrino thus interacts with a single nucleon while the other  $(A - 1)$  nucleons are spectators forming a recoil system that evolves independently. This amounts to neglecting the statistical correlations between the bound nucleons that cause Pauli blocking as well as the final-state interactions. This assumption is well verified only for interactions with a large momentum transfer  $|\vec{q}|$ , and typically breaks down for  $|\vec{q}| < 300$  MeV [153].

### 3.2.2 Nuclear ground state

As seen in Equations (3.2) and (3.3), the cross section is generally expressed as the contraction of the leptonic and hadronic tensors  $d\sigma \propto L_{\mu\nu} H^{\mu\nu}$ . While the leptonic tensor remains unchanged, the hadronic tensor needs to contain all the information on the nuclear structure and reflect the fact that the target nucleon in a neutrino interaction is bound within the nucleus, thus subject for instance to Fermi motion.

The hadronic tensor  $H^{\mu\nu}$  in this case is often expressed as [154]:

$$H^{\mu\nu} = \sum_{\mathfrak{X}} \langle 0 | J^\mu | \mathfrak{X} \rangle \langle \mathfrak{X} | J^\nu | 0 \rangle \delta^{(4)}(p_0 + q - p_{\mathfrak{X}})$$

where  $J^\mu$  is called the nuclear electromagnetic current,  $|0\rangle$  and  $|\mathfrak{X}\rangle$  are the initial and final hadronic states, and the sum is over all the possible final states.

The impulse approximation consists of considering only the interactions on single nucleons, which means that the possible final states of the interaction are two independent systems: the product of the neutrino-nucleon interaction, and the recoil nucleus. This can be written as  $|\mathfrak{X}\rangle \rightarrow |\psi_p(\vec{p}_p)\rangle \otimes |\psi_i^{A-1}(-\vec{p}_p)\rangle$  where  $|\psi_p(\vec{p}_p)\rangle$  is the state of the elementary interaction product with a momentum  $\vec{p}_p$ , and  $|\psi_i^{A-1}(-\vec{p}_p)\rangle$  is the  $i$ -th intermediate state of the recoil system composed of  $(A-1)$  nucleons carrying a momentum  $-\vec{p}_p$  assuming that the initial nucleus is at rest.

Under the impulse approximation, the cross section of a neutrino-nucleus interaction  $\bar{\nu}_l + A \rightarrow l^\pm + \mathfrak{X}$  can be expressed as the incoherent sum of the cross sections on individual nucleons:

$$d\sigma_{\text{IA}}^{\bar{\nu}A} = \int d^3p_m dE_m P_h(\vec{p}_m, E_m) \left[ Z d\sigma^{\bar{\nu}p} + (A-Z) d\sigma^{\bar{\nu}n} \right] P_p(\vec{p} + \vec{q}, q^0 - E - E_{A-1})$$

where  $P_p$  and  $P_h$  are the particle and the hole spectral functions respectively,  $d\sigma^{\bar{\nu}N}$  is the elementary neutrino-nucleon interaction cross section, and  $E_{A-1}$  is the energy of the recoil system of  $(A-1)$  nucleons. This cross section is also called the *one particle – one hole* (1p1h) cross section. This expression assumes that the spectral functions are the same for both neutrons and protons.

#### Pauli blocking

The particle spectral function  $P_p(\vec{k}', T_{k'})$  describes the kinematics of the struck nucleon at its final state with a kinetic energy  $T_{k'}$  and momentum  $\vec{k}'$ , and particularly restricts it by *Pauli blocking*. Indeed, according to the Pauli principle, two fermions cannot be in the same quantum state. Therefore, a neutrino-nucleus interaction cannot occur if the struck nucleon is in a state that is already occupied by another nucleon within the nucleus.

The particle spectral function  $P_p(\vec{k}', T_{k'})$  encodes this, and the simplest method to write Pauli blocking is under the assumption that the nucleus can be modeled as a Fermi gas (FG), i.e. assuming that the nucleus is a gas of non-interacting nucleons within a potential. Within this picture, the average Fermi momentum  $\bar{p}_F$  obtained in the local density approximation (LDA) by:

$$\bar{p}_F = \int d^3r \rho(r) p_F(r)$$

where  $\rho(r)$  is the nuclear density and  $p_F(r) = (3\pi^2 A \rho(r)/2)^{1/3}$  is the Fermi momentum as a function of the distance  $r$  to the center of the nucleus. The Pauli blocking condition is expressed in the particle spectral function as:

$$P_p^{\text{FG}}(\vec{k}', T_{k'}) = \delta(E_{k'} - M_N - T_{k'}) \left[ 1 - \Theta(\bar{p}_F - |\vec{k}'|) \right] \quad (3.8)$$

### Chapter 3. Modeling neutrino-nucleus interactions

where  $\Theta$  is the Heaviside step function.

The LDA can also be used to write the Pauli blocking condition using the momentum distribution in the nuclear medium  $n$  which can be obtained from the hole spectral function (see next section) as [155]:

$$P_p^{\text{LDA}}(\vec{k}', T_{k'}) = \delta(E_{k'} - M_N - T_{k'}) \left[ 1 - \frac{4}{3} \pi p_F^3 n(\vec{k}') \right] \quad (3.9)$$

where the Heaviside function term in Equation (3.8) is replaced by the occupation probability of a nucleon in the nucleus.

#### Spectral functions

The hole spectral function  $P(\vec{p}_m, E_m)$ , which we will simply refer to as the (nuclear) spectral function and omit the subscript 'h', is the joint probability that when the nucleon of momentum  $\vec{p}_m$ , often called *missing* momentum, is removed from the nucleus, the residual nucleus, composed of the remaining  $(A - 1)$  nucleons, is left at an excited state with energy  $E^* = E_m - E_{\text{sep}}$ , where  $E_m$  is the *missing* (or *removal*) energy and  $E_{\text{sep}} = M_{A-1} + M_N - M_A$  the separation energy. In other words, it describes the distribution of nucleons in the  $(p_m, E_m)$  plane, and can be expressed as:

$$P(\vec{p}_m, E_m) = \sum_i |\langle 0 | \psi_p(\vec{p}_m); \psi_i^{A-1}(-\vec{p}_m) \rangle|^2 \delta(E_m - E_n^{A-1} + E_0^A)$$

where  $|\psi_i^{A-1}(-\vec{p}_p)\rangle$  is the  $i$ -th intermediate state of the recoil nucleus with energy  $E_n^{A-1}$ , and  $|0\rangle$  is the nuclear ground state of energy  $E_0^A$ .

The presently available many-body techniques allow us to compute analytically the spectral function starting from the nucleon-nucleon interaction for light nuclei with  $A \leq 4$  [156–159] as well as for infinite nuclear matter [160]. However, for medium-size nuclei like carbon and oxygen, they can only be obtained phenomenologically by combining theoretical calculations with experimental data mainly from electron scattering.

The simplest description of nucleons bound within the nucleus is given by the *relativistic* (or *global*) Fermi gas (RFG) model: the nucleons are considered as non-interacting fermions in a uniform binding potential. In order to minimize the total energy of the system, the nucleons fill all momentum states below the Fermi level given by  $\bar{p}_F$ , and the binding energy  $E_b$  is constant for all the nucleons. Quasielastic electron scattering data permitted the extraction of  $\bar{p}_F$  and  $E_b$  for a wide range of nuclei [161]. Using energy conservation, the spectral function in this case writes as:

$$P_{\text{RFG}}(\vec{p}_m, E_m) \propto \theta(\bar{p}_F - |\vec{p}_m|) \delta(M_A + E_m - m_N - \sqrt{M_{A-1}^2 + |\vec{p}_m|^2}) \quad (3.10)$$

Another approach, called the *local* Fermi gas (LFG) model, relies on the same assumptions as

RFG but employs the LDA to introduce a radial dependence in the Fermi momentum using the nuclear density measured from electron scattering experiments as  $p_F(r) = (3\pi^2 A\rho(r)/2)^{1/3}$ .

Alternatively, in the shell model, the nucleons are assumed to behave as independent particles moving in a mean field (MF). In this case, the spectral function can be written as:

$$P_{\text{MF}}^{\text{ind}}(\vec{p}_m, E_m) = \sum_i |\phi_i(\vec{p}_m)|^2 \delta(E_m - E_i)$$

with  $\phi_i(\vec{p}_m)$  the wave function corresponding to the  $i$ -th state of a single particle in the shell model, and  $E_i$  the associated energy. This equation shows that each energy level is at a well defined value  $E_i$ . However, while electron scattering measurements allow us to identify the peaks corresponding to such energy levels, they also show that the independent-particle picture is not sufficient to capture the involved nuclear dynamics, particularly related to nucleon-nucleon correlations. One of the consequences of these residual interactions is a quenching of the strength of single-particle states with a finite energy width. Therefore, the spectral function extracted from electron scattering data is often written as [154]:

$$P_{\text{MF}}(\vec{p}_m, E_m) = \sum_i Z_i |\phi_i(\vec{p}_m)|^2 F_i(E_m - E_i^{A-1}) \quad (3.11)$$

where the spectroscopic factor  $Z_i < 1$  and the functions  $F_i(E_m - E_i^{A-1})$  give a description of the energy width under these conditions.

Multiple electron scattering experiments measured the spectral functions of various nuclei, such as oxygen at NIKHEF-K [162] as well as carbon [163], and more recently argon [164] at Jefferson Lab.

As mentioned previously, nucleon-nucleon correlations have a significant impact on the nuclear dynamics. In addition to the effect encoded in Equation (3.11), the spectral function can also include contributions from *short-range correlations*. In fact, electron scattering experiments also show that  $\sim 20\%$  of the interactions occur on a pair of strongly repulsive nucleons, mainly proton-neutron pairs, whose individual momenta can be above the Fermi level, but their center-of-mass momentum is small [165]. The pair is ejected from the nucleus, leaving a residual system of  $(A - 2)$  nucleons. A correlation term can be added to the MF part of Equation (3.11), and can be estimated using the LDA as:

$$P_{\text{corr}}(\vec{p}_m, E_m) = \int d^3r \rho(\vec{r}) P_{\text{corr}}^{\text{NM}}(\vec{p}_m, E_m; \rho = \rho(\vec{r}))$$

where  $\rho(\vec{r})$  is the nuclear density distribution of the nucleus  $A$ , and  $P_{\text{corr}}^{\text{NM}}(\vec{p}_m, E_m; \rho)$  is the correlation part of the spectral function of the uniform nuclear matter of density  $\rho$  [166]. This yields the total spectral function:

$$P(\vec{p}_m, E_m) = P_{\text{MF}}(\vec{p}_m, E_m) + P_{\text{corr}}(\vec{p}_m, E_m) \quad (3.12)$$

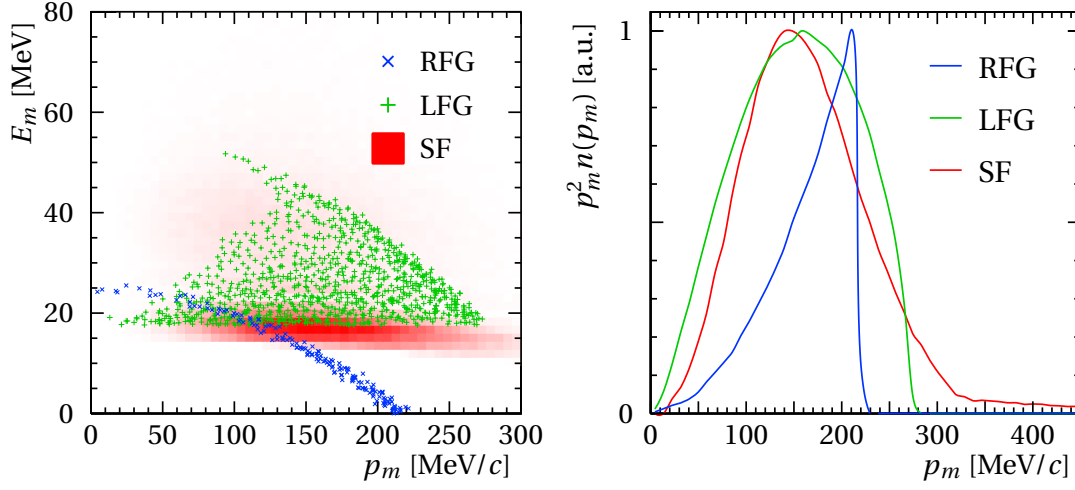


Figure 3.6: Left: comparison of the spectral-function distributions between the relativistic Fermi gas (RFG), the local Fermi gas (LFG) and the Benhar Spectral Function (SF) models for carbon using the NEUT event generator. The SF model captures the complex nuclear structure, featuring the sharp  $p$ -shell at  $E_m \sim 18$  MeV and the diffuse  $s$ -shell around  $E_m \sim 35$  MeV. Right: comparison of the missing-momentum distribution between the three models.

which we will refer to in this thesis as the *Benhar Spectral Function (SF) model*. The MF part typically vanishes when the missing momentum is beyond the Fermi level, i.e.  $p_m$  roughly larger than  $\sim 220$  MeV, and the correlation contribution becomes dominant.

The left panel of Figure 3.6 shows a comparison between the spectral function distributions for the RFG, LFG and SF models. The SF model clearly shows the nuclear shell structure, with the  $p$ - and the  $s$ -shells of carbon at  $E_m \sim 18$  MeV and  $E_m \sim 35$  MeV respectively. On the other hand, the simplistic RFG model fails at describing this complex shell structure of the nucleus, while the LFG model recovers only a part of the phase space in  $(p_m, E_m)$ .

The right panel of Figure 3.6 highlights the discrepancies in the prediction of the initial state nucleon momentum distribution  $n(p_m) = \int dE_m P(\vec{p}_m, E_m)$  between the models. The RFG model has a “cliff” feature at the Fermi level which disappears in the LFG model thanks to the LDA. On the other hand, the high  $p_m$  tail is only present in the SF model, which corresponds to the SRC contribution.

### 3.2.3 Beyond the impulse approximation

The IA relies on assuming that the interaction occurs on a single nucleon, independently of the rest of the nuclear matter. This is well satisfied for interactions with a high momentum transfer  $Q^2$ . However, there are number of effects that need to be considered beyond this approximation particularly because a significant proportion of the interactions in T2K occur for low  $Q^2$ . Among these effects are the final-state interactions and multinucleon processes.

### Final-state interactions

The hadrons produced in the primary interaction, whether it is pions from a CCRES interaction or nucleons from a CCQE one, can interact with the nuclear matter before exiting the nucleus. This is called final-state interactions (FSI).

An outgoing hadron can see its kinematics altered by elastic scattering against other nucleons, be absorbed in the medium, exchange its charge, or knock more hadrons out of the nucleus. An important consequence of this is how the final state from a neutrino interaction does not necessarily inform on the primary interaction. For instance, for a primary CCRES interaction, if the outgoing pion is absorbed in the nuclear medium, the interaction would appear as a CCQE one. Similarly, if the outgoing nucleon from a CCQE interaction interacts inelastically with the remnant nucleus and produces a pion, this would look like a CCRES interaction. Therefore, it is important to take into consideration this effect, and all the more so since neutrino energy estimation often relies on assumptions on the underlying primary interaction (see Section 3.4).

Hadronic FSI is usually modeled in neutrino interaction simulations by an intranuclear cascade. This consists of evolving the hadrons from the neutrino-nucleon interaction in a step-by-step scheme. Each hadron is propagated through the nuclear medium discretely with a step  $\lambda$  obtained from its mean free path  $\lambda = (\sigma\rho)^{-1}$ , which depends on the total cross section  $\sigma$  and the nuclear density. At each step, the probability is calculated for each interaction type, and the eventual subsequent hadrons are propagated similarly.

Another approach, first proposed in Reference [168] in the context of inclusive electron scattering data ( $e, e'$ ), relies on describing FSI with a complex optical nuclear potential. This uses a folding function  $f_q$  convoluted with the (inclusive) differential cross section with respect to the energy transfer  $\omega = q^0$  and the outgoing charged lepton solid angle  $\Omega_l$  such that:

$$\frac{d\sigma_{\text{FSI}}^{\vec{v}A}}{d\omega d\Omega_l} = \int d\omega' f_q(\omega - \omega') \frac{d\sigma_{\text{IA}}^{\vec{v}A}}{d\omega' d\Omega_l} \quad (3.13)$$

where  $f_q(\omega) = \sqrt{T_A}\delta(\omega) + (1 - \sqrt{T_A})F_q(\omega)$ .  $T_A$  is the nuclear transparency which can be extracted from ( $e, e'p$ ) experiments [169]. We can notice that the limit  $T_A \rightarrow 1$  corresponds to the case where there are no FSI effects, giving the IA cross section derived in Section 3.2.2. Furthermore,  $F_q(\omega)$  is a finite-width sharply peaked around  $\omega = 0$ , which encodes the impact of the optical potential. As described in Reference [168], the optical potential  $U$  can be expressed as  $U = U_V + iU_W$ , where the real part  $U_V$  modifies the spectrum of the final-state nucleon and shifts the energy transfer as  $\omega \rightarrow \omega - U_V$ , while the imaginary part  $U_W$  redistributes a fraction of the single-particle strength to more complex final states. This is expressed as [167]:

$$F_q(\omega) = \frac{1}{\pi} \frac{U_W}{U_W^2 + (\omega - U_V)^2}. \quad (3.14)$$

### Chapter 3. Modeling neutrino-nucleus interactions

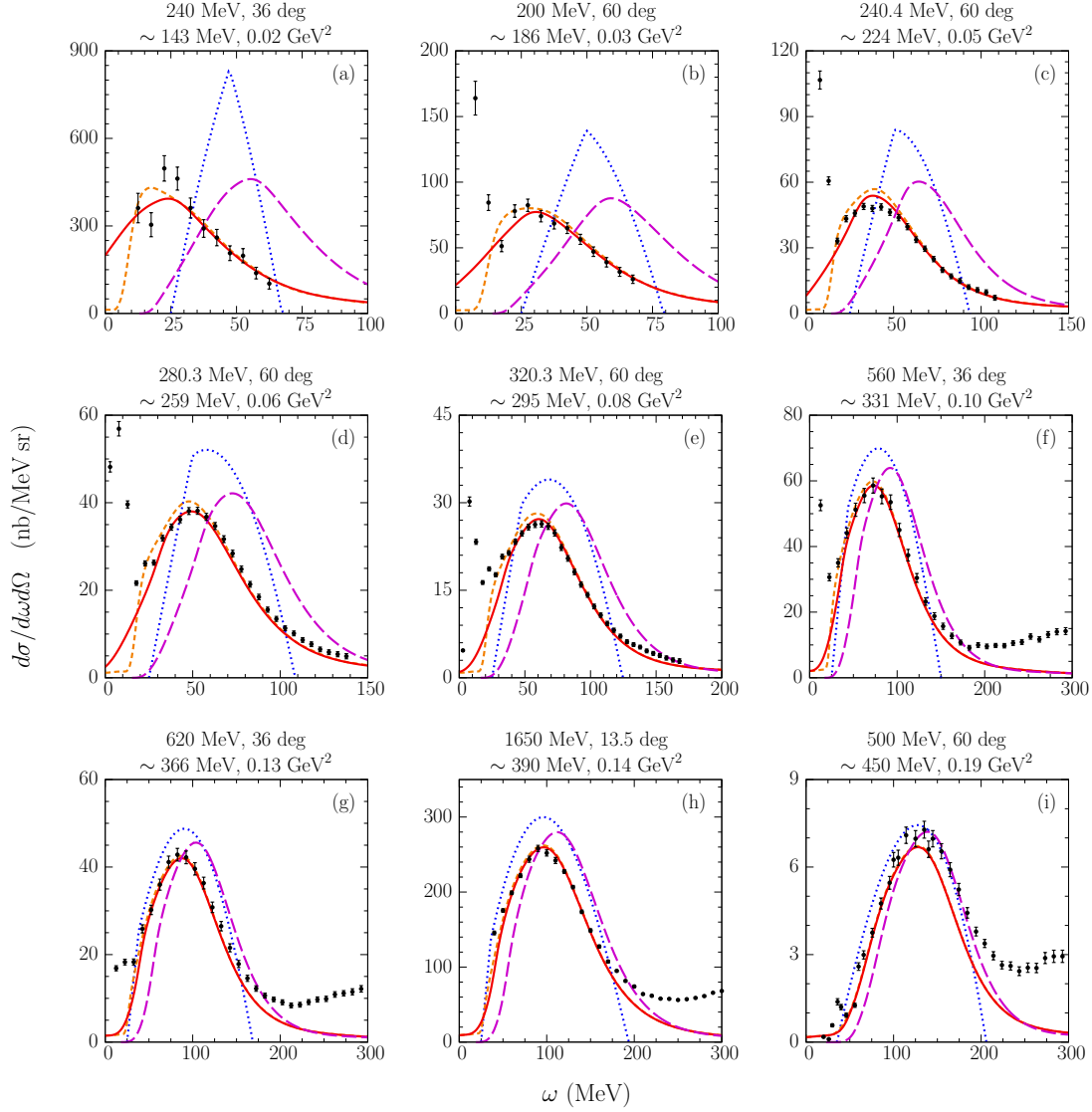


Figure 3.7: Double differential cross section of the quasielastic peak for electron scattering on carbon  $\frac{d\sigma}{d\omega d\Omega_e}$  from various experimental data. As a reference, the dotted blue lines and the purple long-dashed lines correspond to the RFG model and the SF model respectively in the IA formalism without any FSI corrections. The solid red and short-dashed orange lines show the result of the corrected SF-model cross section according to Equation (3.13), the former using the LDA-based Pauli blocking of Equation (3.9) while the latter uses the step-function Pauli blocking of Equation (3.8). The panels are labeled according to the beam energy, the scattering angle, and the values of  $|\vec{q}|$  and  $Q^2$  respectively. Figure from Reference [167]

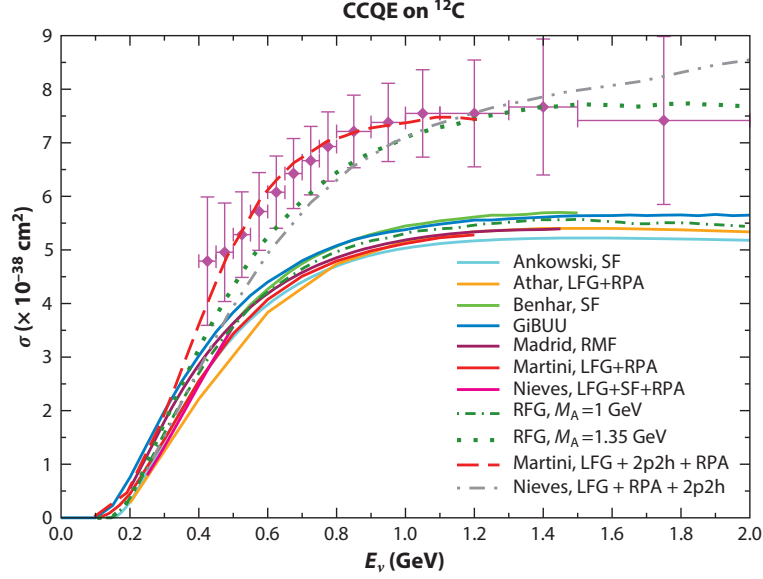


Figure 3.8: Comparison of various models with the MiniBooNE CCQE-like cross-section measurement on carbon of Reference [170]. A good agreement with the data is only achieved with a significantly high value of  $M_A$  at tension with bubble chamber data, or when taking into account 2p2h contributions. Figure from Reference [171].

A comprehensive study of electron scattering on carbon using the SF model for the single-nucleon cross section and this optical potential formalism for FSI was carried in Reference [167]. The results are shown in Figure 3.7. At high momentum transfer, all the models agree and well describe the data. However, as the momentum transfer decreases, the simplistic RFG model (dotted blue lines) significantly deviates from the data. The difference between the SF model with (solid red lines) and without FSI corrections (long-dashed purple lines) also starts to appear for low  $Q^2$  values. The real part of the optical potential  $U_V$  allows for a shift of the bare SF model under the IA towards the quasielastic peak of the data, while the imaginary part  $U_W$  slightly quenches it. The FSI correction gives a remarkable agreement with the data in the various considered kinematic settings, regardless of the chosen Pauli blocking model (red vs. orange).

### Multinucleon effects

Another correction to the IA approach is the effect due to nucleon-nucleon correlations within the nucleus. The SF model shown in Equation (3.12) includes SRC, which correspond to a fraction of the two-particle two-hole (2p2h) contributions due to initial-state correlations between nucleons. This particularly allows us to describe the high- $\omega$  tail at low momentum transfer in the top panels of Figure 3.7. At higher momentum transfer ((d) to (i) in Figure 3.7), other 2p2h mechanisms are necessary to describe the tail of the data.

In this context, the *MiniBooNE CCQE puzzle* [170] represents a historical example of the



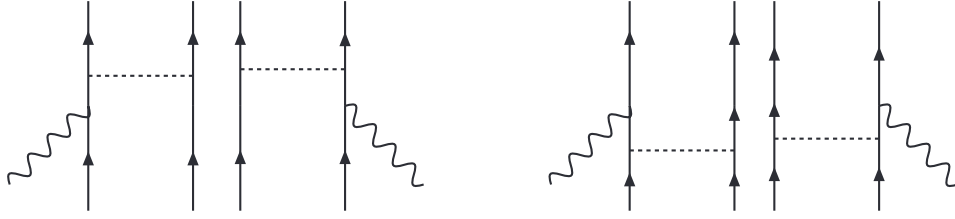


Figure 3.9: Diagrams of coupling to a pair of correlated nucleons, also called the nucleon-nucleon correlations in the 2p2h processes. The SF model takes this contribution into account in its SRC prediction.

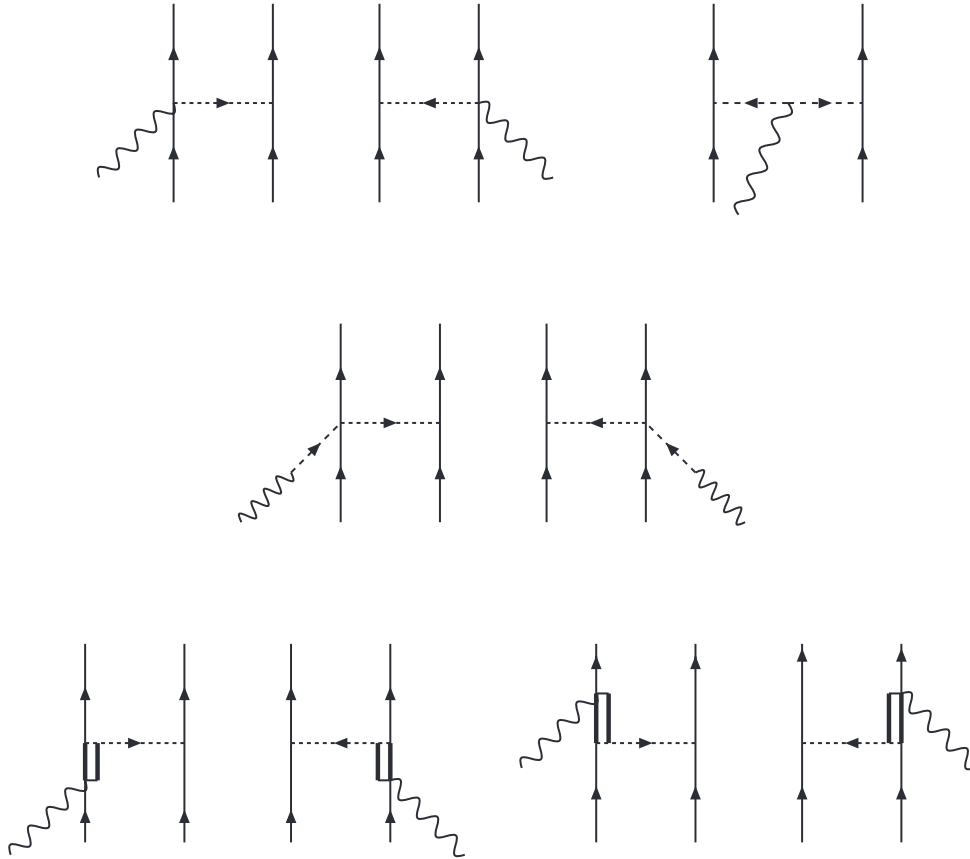


Figure 3.10: Diagrams of the meson exchange currents of 2p2h processes. Solid (dashed) lines denote nucleons (pions), whereas double lines represent  $\Delta(1232)$ . The top row corresponds to the so-called contact term and the pion-in-flight diagrams, the middle row to the pion-pole diagrams, and the bottom row to the coupling to a delta resonance. Adapted from Reference [172].

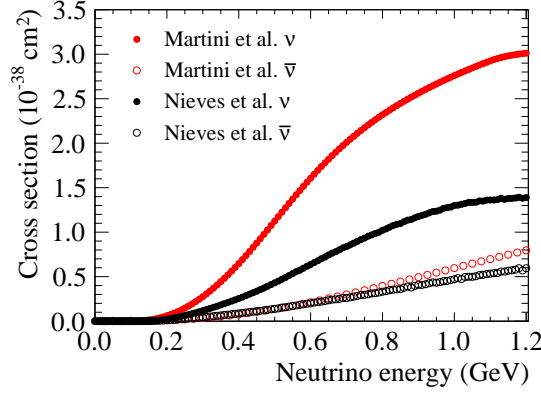


Figure 3.11: Cross section of 2p2h on carbon as a function of the neutrino energy from the Nieves et al. (black) and the Martini et al. (red) models for neutrinos (filled circles) and antineutrinos (empty circles). Figure from Reference [175].

importance of taking into accounts such effects. As mentioned in Section 3.1.1, the most direct probes of the axial mass  $M_A^{\text{QE}}$  are the measurements of neutrino interactions on light targets as in bubble chamber experiments. A combined fit to this data gives a value of  $M_A^{\text{QE}} = 1.026 \pm 0.021 \text{ GeV}/c^2$  [173]. The MiniBooNE collaboration reported a CCQE-like cross-section measurement significantly low than the theoretical CCQE expectation. The agreement of the model with the data could be restored when assuming  $M_A^{\text{QE}} = 1.35 \pm 0.17 \text{ GeV}/c^2$  [170] which is significantly higher. Reference [174] pointed out the significance of the 2p2h processes for the more complex nuclear targets, and showed that the high  $M_A^{\text{QE}}$  obtained by MiniBooNE can be attributed to the contribution of the 2p2h processes that were also selected as signal events in the MiniBooNE analysis, but were not taken into account at the level of the neutrino interaction model, thus being at the origin of the discrepancy. When accounting for 2p2h, the value of  $M_A^{\text{QE}}$  is found to be more consistent with bubble chamber data [174]. This is displayed in Figure 3.8.

Figures 3.9 and 3.10 show different diagrams that contribute to the two-body currents. While the inclusion of such multinucleon processes is widely accepted to explain various cross-section measurements, there are several theoretical approaches to their calculations. Figure 3.9 corresponds to nucleon-nucleon correlations that are already considered in sophisticated 1p1h models like the SF model. On the other hand, Figure 3.10 shows different diagrams that contribute to the *meson exchange current* part of 2p2h processes. The most common theoretical calculations in the neutrino community are the Nieves et al. [176–180], Martini et al. [174, 181–188], and Amaro et al. [189–198] models. The calculations of Amaro et al. start from the full relativistic model of Reference [199] developed for the electromagnetic response and extend it to the weak sector [196], while the Martini et al. and Nieves et al. models are more similar since they are obtained from microscopic calculations to take into account nuclear collective effects with the random phase approximation starting from the LFG model of the nucleus. They differ however in the predicted 2p2h cross section, which is twice (30%) larger

in the Martini et al. model for neutrinos (antineutrinos) as shown in Figure 3.11. The relative proportion of nucleon-nucleon correlations, meson exchange currents and their interference are also different in the calculations of the two models.

### 3.3 Neutrino event generators

Neutrino scattering and long baseline experiments rely on Monte Carlo (MC) simulations, called *neutrino event generators*, to obtain the predictions from various neutrino interaction models. As seen previously, an accurate prediction of the outgoing particles from each interaction mode and their kinematics is crucial for the estimation of the neutrino energy.

The typical steps to simulate an interaction event are the following:

1. The energy of the incoming neutrino is drawn from the spectrum of the neutrino beam, and the target nucleus is chosen according to the total cross section of each material.
2. The kinematics (or four-momentum) of the target nucleon within the nucleus are drawn from the spectral function distribution according to the chosen model (e.g. RFG, LFG, SE..).
3. The interaction type is selected according to the probability given by the cross section for each interaction type for the energy of the neutrino as shown in Figure 3.1.
4. The interaction is simulated and the four-momenta of the outgoing particles from the neutrino-nucleon scattering are determined using the differential cross section of the interaction.
5. The outgoing hadrons are propagated through the nucleus and undergo FSI using an intranuclear cascade which can alter their kinematics, absorb them, or produce additional hadrons.

The output of a neutrino event generator gives the details of all events and the corresponding particles, from their initial state to their final state and the undergone interaction types. Comparison with data often requires an additional step that simulates the detector geometry and response, which is usually achieved with other tools.

NEUT [200], GENIE [201], NuWro [202] and GiBUU [203] are four of the main generators that are currently used in experiments, which include a variety of theoretical and empirical models and approximations. They are tuned and extensively validated against a wide range of electron, pion, photon and neutrino scattering measurements which ensures their reproducibility.

In this thesis, NEUT is the main event generator that we will employ. Below is a break down of the different models used in the simulations used in this thesis:

- **CCQE:** The ground state is described by the SF model. For the neutrino-nucleon interaction, the parametrization of the dipole vector form factors of Reference [204] and the dipole axial form factor as given by Equation (3.6) are used with  $M_A^{\text{QE}} = 1.03$  GeV. Pauli blocking is applied using the simple RFG-like prescription given in Equation (3.8).
- **2p2h:** It uses the Nieves et al. model.
- **CCRES:** It uses the Rein – Sehgal model with an improved description of the axial form factors [205, 206] and including effects of final-state lepton mass [148–150], with  $M_A^{\text{RES}} = 0.95$  GeV/ $c^2$ . The kinematics of the initial state nucleon are given by the RFG model with no binding energy.
- **DIS:** The parton distribution functions are given by Reference [207] with the so-called Bodek – Yang modifications for low  $Q^2$  [208, 209]. The kinematics of the initial state nucleon are simply given by the RFG model.
- **Hadronization:** Non-resonant hadron production uses the Koba – Nielsen – Olesen scaling [210] for the low invariant mass region, whereas the high invariant mass region relies on PYTHIA 5.72 [211].
- **FSI:** A semiclassical intranuclear cascade based on the Salcedo – Oset model [212, 213] tuned to external data [214] is implemented.

## 3.4 Neutrino energy reconstruction

Long-baseline neutrino experiments like T2K and NOvA measure oscillations by comparing the event rate of neutrino interactions at a given neutrino energy between the near and far detectors. As a result, the neutrino energy must be reconstructed for each event from the products of the interaction. This is accomplished through two methods: the kinematic method and the calorimetric method.

### 3.4.1 Kinematic method

Assuming a CCQE interaction of a neutrino on a nucleon at rest, the incoming neutrino energy is completely determined from the kinematics of the outgoing charged lepton. This is given by the expression:

$$E_\nu^{\text{QE}} = \frac{2E_l \tilde{M}_N - (M_l^2 + \tilde{M}_N^2 - M_N^2)}{2(\tilde{M}_N - E_l + p_l \cos \theta_l)} \quad (3.15)$$

where  $E_l$ ,  $p_l$  and  $\theta_l$  are the energy, momentum and angle of the outgoing charged lepton respectively, and  $\tilde{M}_N = M_N - E_b$  with  $E_b$  being the nucleon removal energy.

The T2K experiment, with neutrino energies typically below 1 GeV, uses this method to estimate the energy since the dominant interaction mode is indeed the CCQE channel. Figure 3.12

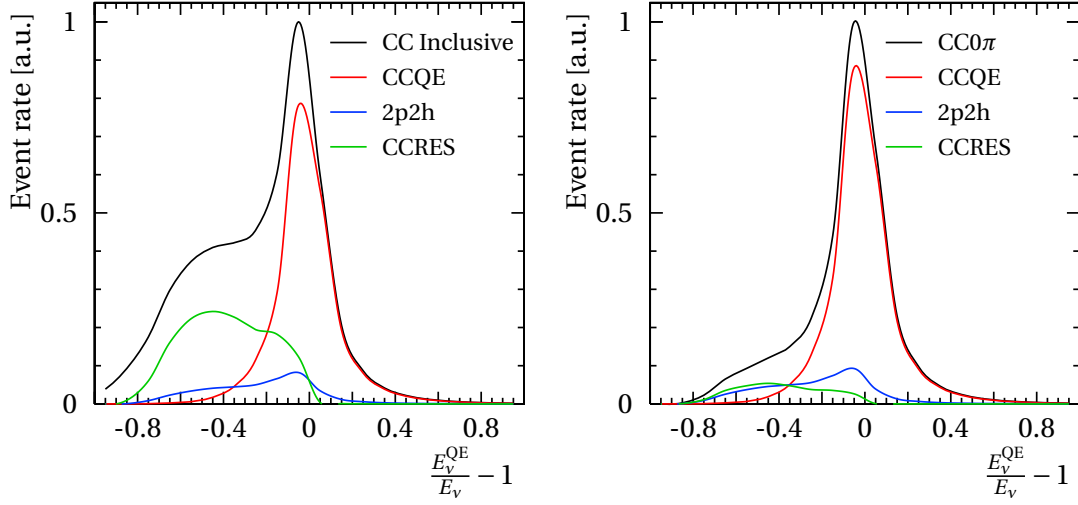


Figure 3.12: Resolution and bias of the neutrino energy estimator  $E_v^{\text{QE}}$  for all CC events (left) and for CC0 $\pi$  events (right) with the contributions from the different interaction modes using the T2K neutrino flux with the NEUT event generator.

exhibits the bias of the neutrino energy estimation given by  $E_v^{\text{QE}}$  broken down by the interaction type for all CC events (left panel) and the CC0 $\pi$ , or CCQE-like, events (right panel). It shows that the assumption of a CCQE interaction significantly biases the estimation for 2p2h and particularly CCRES events. Consequently, characterizing the final state of the interaction and excluding events with pions in the final state reduces this discrepancy. There remains however a fraction of CCRES events for which the outgoing pion is absorbed in the nucleus through FSI and thus not observed. On the other hand, the symmetric spread of  $E_v^{\text{QE}}$  around the true neutrino energy for CCQE events is mainly due to the isotropic Fermi motion of the nucleons in their initial state. In particular, the left panel of Figure 3.13 shows the impact of the ground state model on this bias, highlighting that the more realistic LFG and SF models can give a better estimation of the neutrino energy.

### 3.4.2 Calorimetric method

Multi-GeV oscillation experiments such as NOvA usually rely on a calorimetric method to estimate the neutrino energy. As shown in Figure 3.1, the dominant interaction mode is not the CCQE channel, but rather CCRES and CCDIS which produce more complex hadronic final states. The calorimetric estimator of the energy writes as:

$$E_v^{\text{cal}} = E_l + E_{\text{had}}$$

which is the sum of the charged lepton energy and the visible hadronic energy obtained from the sum of all energy deposits  $E_{\text{had}} \approx \sum_{\text{protons}} T_p + \sum_{\text{pions}} T_\pi + \sum_{\text{photons}} E_\gamma$  where  $T_X$  is the kinetic energy and  $E_\gamma$  is the energy of a produced photon. Neutrons are often not observed

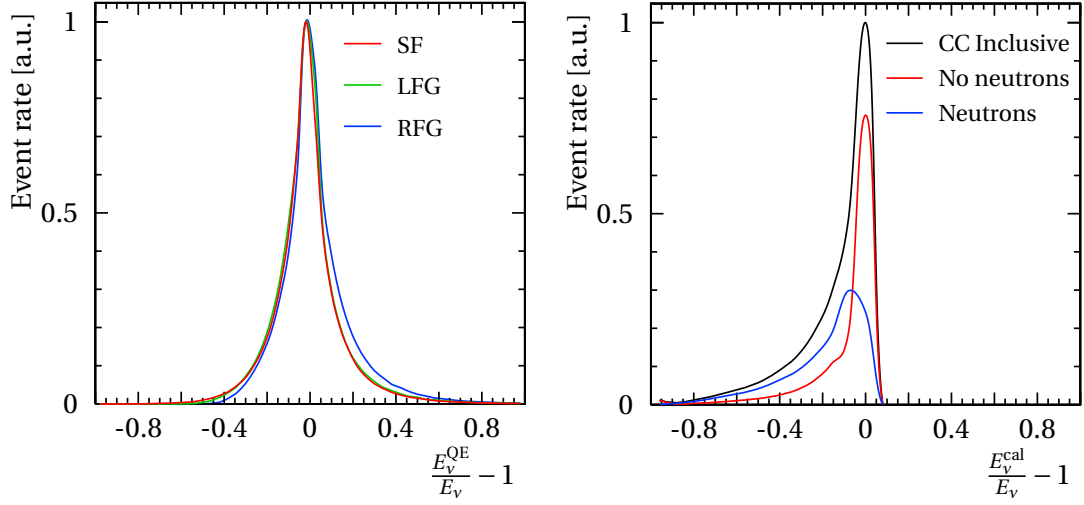


Figure 3.13: Left: resolution and bias of the neutrino energy estimator  $E_v^{\text{QE}}$  for CCQE events when using RFG, LFG and SF models. Right: resolution and bias of  $E_v^{\text{cal}}$  for all CC events with the contributions from events with (blue) and without (red) neutrons in the final state using the MINERvA flux (shown in Figure 3.1) with the NEUT event generator.

and do not have an associated energy deposit.

While the calorimetric method does not assume the interaction type like the kinematic method, it comes with its own challenges. The Fermi motion still impacts the kinematics of the interaction, although to a lesser extent for high energy neutrinos. More importantly, the inability to detect neutrons and the corresponding energy deposit has a significant impact on smearing and biasing the estimator  $E_v^{\text{cal}}$  as illustrated in the right panel of Figure 3.13. This introduces a model dependence in the estimation of the neutrino energy since it relies on the prediction of neutron multiplicity which itself depends on for instance the chosen models of 2p2h and FSI effects.

### 3.4.3 Impact on oscillation measurements

Neutrino interaction simulations described in the next section take into account the known nuclear effects that can bias the neutrino energy estimation. However, different models can yield different neutrino energy reconstructions. For instance, the Nieves et al. and the Martini et al. models for 2p2h, which can bias the  $E_v^{\text{QE}}$  estimator as shown in Figure 3.12, have contrasting predictions of the total cross section impacting differently neutrinos and antineutrinos (see Figure 3.11). This discrepancy would impact the sensitivity to oscillation parameters, and particularly  $\delta_{\text{CP}}$ , even with limited statistics [175].

To remedy the possibly large impact of mismodeling neutrino interactions, oscillation experiments define a wide set of uncertainties to cover plausible model variations. This consists of

### Chapter 3. Modeling neutrino-nucleus interactions

---

including nuisance parameters that can vary, such as the axial mass  $M_A^{\text{QE}}$  and the coupling  $C_5^A(0)$  within the range given by bubble chamber constraints, normalizations of the different interaction modes, and shape variations in given variables. The neutrino interaction data at the near detector allow us to constrain these nuisance parameters which can then be used to extract the oscillation parameters with the far detector data.

In certain cases, these nuisance parameters cannot account for the uncertainty between models with extreme variations. For each round of oscillation results, T2K tests its nominal interaction model against multiple alternative models to estimate the potential bias in the measurement. This can yield in an inflated uncertainty on the measured oscillation parameter to account for these mismodeling effects, which will be further detailed in Section 7.5.3.

## 4 Uncertainties in the charged-current quasielastic interactions

Chapter 3 described in detail how neutrino-nucleus interactions can be modeled and their importance for oscillation measurements in long-baseline experiments. In particular, it is expected that the upcoming experiments SBN [215], DUNE [74] and Hyper-Kamiokande [73] will collect such a large amount of data that systematic uncertainties related to the complex nuclear physics of neutrino interactions will become the limiting factor in the oscillation analyses. As shown in Figure 3.1, the CCQE interaction mode is the dominant channel for T2K and Hyper-Kamiokande, but also constitutes an important fraction of interaction events in other experiments. Therefore, a good understanding of this process is key to a robust measurement of neutrino oscillations.

Measurements of neutrino scattering on various nuclear targets allow us to probe such physics and test the different theoretical models. The neutrino community dedicates a special effort to provide these measurements, and multiple experiments (e.g. T2K, NOvA, MiniBooNE, MicroBooNE, MINERvA, ...) continuously publish new data to test the models in novel ways. While the models implemented in MC neutrino event generators are able to describe some of the available measurements, and particularly the inclusive ones, they most of the time fail at giving a proper description of the semi-exclusive data<sup>1</sup>. A careful attention to the assumptions and approximations in the models allow us to identify systematic uncertainties that could explain these discrepancies.

In this chapter, we present a parametrization of NEUT, based on the SF model for CCQE interactions, that improves the description of various cross-section measurements after tuning to the data. In Section 4.1, we present an overview of relevant cross-section measurements and how they are obtained. Section 4.2 introduces a new parametrization of systematic uncertainties in the SF model. Finally, we show a new method that mitigates Peelle's pertinent puzzle when fitting strongly-correlated data, and discuss how the agreement of the model with a number of available cross-section measurements can be improved in Section 4.3.

---

<sup>1</sup>As briefly mentioned in Section 2.4.3, inclusive measurements refer to the ones where the kinematics of only the charged lepton are measured, while semi-exclusive measurements correspond to the ones where the kinematics of the leading hadron (often proton) is also measured in addition to the charged lepton.



## Chapter 4. Uncertainties in the charged-current quasielastic interactions

---

The parametrization developed in this chapter is also employed in the latest T2K oscillation measurements as we will discuss in Chapter 7. Indeed, T2K recently started using the SF model as a relatively sophisticated description of the CCQE ground state, and with this comes the need for an appropriate suite of parametrized systematic uncertainties.

### 4.1 Cross-section measurements

#### 4.1.1 Extracting a cross section

The differential cross section is extracted as a function of a set of variables in a given interaction topology. The variables and the topology are chosen to limit the model dependence of the measurement. The topology is usually defined based on the final-state particles that exit the nucleus after FSI and that can be observed in the detector. Below is a list of the most common ones:

- CC inclusive: this topology refers to events for which a track of the charged lepton is identified, regardless of the other particles that are eventually observed in the detector.
- CC0 $\pi$ : this corresponds to the CCQE-like topology, i.e. interaction events for which a clear muon track is identified (CC) and no mesons are observed. This can further be divided for instance into CC0 $\pi$ 0 $p$  and CC0 $\pi$  $Np$  topologies depending on the proton multiplicity in the interaction.
- CC1 $\pi$ : this corresponds to interactions where both a muon track and a pion track of opposite charge are observed. This topology is dominated by the CCRES channel.

Similarly, the chosen observables are often related to the kinematics of the final-state particles that are well reconstructed in the detectors.

If we take as an example a single differential cross-section measurement with respect to a variable  $x$  in the CC0 $\pi$  topology, it can be expressed as:

$$\frac{d\sigma}{dx_i} = \frac{1}{\Delta x_i} \times \frac{N_{\text{true},i}^{\text{CC0}\pi}}{\Phi N_{\text{nucleons}}^{\text{FV}}} \quad (4.1)$$

where  $\Delta x_i$  is the chosen width of the  $i$ -th bin in  $x$ ,  $N_{\text{nucleons}}$  the total number of nucleons in the fiducial volume,  $\Phi$  the neutrino flux, and  $N_{\text{true},i}^{\text{CC0}\pi}$  the number of (true) CC0 $\pi$  interactions in the  $i$ -th bin  $\Delta x_i$ . Extracting the cross section in the truth space is naturally challenging since the only measured quantity is the event rate observed in the detector with only an estimation  $x^{\text{reco}}$  of the true variable  $x$ .

To extract  $N_{\text{true},i}^{\text{CC0}\pi}$ , the experiment performs a selection of events that provides a sample enriched in the CC0 $\pi$  signal. Then, the challenges in obtaining the cross section of Equation (4.1) are the following:

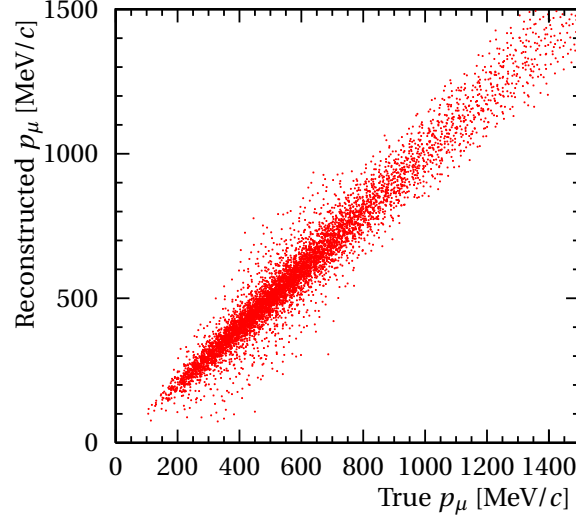


Figure 4.1: Distribution of the true and reconstructed muon momentum in ND280.

1. The efficiency of the selection needs to be estimated. This is usually extracted using a MC simulation of the detector response, which allows us to define the efficiency  $\epsilon_i^{\text{MC}}$  in the bin  $\Delta x_i$  such that the number of events in the selection relates to  $N_{\text{true},i}^{\text{CC0}\pi}$  by:  $n_{\text{true},i}^{\text{CC0}\pi} = \epsilon_i^{\text{MC}} N_{\text{true},i}^{\text{CC0}\pi}$ .
2. The selected sample includes a non-CC0 $\pi$  background which needs to be subtracted.
3. The measured interactions are obtained in the reconstructed variable  $x^{\text{reco}}$ . Since the cross section is needs to be extracted as a function of the true  $x$ , it is necessary to “undo” the detector effects. In other terms, if  $X^{\text{reco}} = (x_i^{\text{reco}})$  is the vector of bins in the variable of interest in the reconstructed space, then it can be related to the vector of bins in the true space  $X = (x_i)$  by a function  $f_{\text{det}}$  that encodes the detector smearing as:

$$X^{\text{reco}} = f_{\text{det}}(X).$$

The function  $f_{\text{det}}$  is called the *folding* function. Figure 4.1 shows for instance this mapping  $f_{\text{det}}$  between the true and reconstructed muon momentum in ND280 as estimated by the T2K simulation.

Various unfolding techniques allow us to overcome the challenges of subtracting the background and removing the detector effects, such as the Bayesian procedure originally proposed in Reference [216], and binned likelihood fits done for instance in References [114, 115]. In any case, as one can expect, the unfolding is equivalent to an inversion of the detector response matrix which leads to strong correlations between neighboring bins in the true variable  $x$  if the binning widths  $\Delta x_i$  are comparable to the detector resolution. Therefore, the reported cross section by collaborations not only provide the bin-by-bin event rates, but also the full covariance matrix that encodes the bin-to-bin correlations as well as all the estimated errors

## Chapter 4. Uncertainties in the charged-current quasielastic interactions

---

coming from the statistical and systematic uncertainties in the measurement (usually related to the flux, the detector and the neutrino interaction models).

Table 2.2 shows a summary of all the cross-section measurements performed to date by T2K. Other experiments also measure neutrino scattering on various targets such as Mini-BooNE [217], MicroBooNE [218], MINERvA [219], NOvA [69], and SBN in the near future [215].

### 4.1.2 CC0 $\pi$ measurements on carbon and oxygen

The purpose of the study described in this chapter is to understand the systematic uncertainties related to the SF model CCQE interactions in the T2K experiment. Naturally, the most suitable topology to consider is CC0 $\pi$  which provides an enriched sample of CCQE events, and the nuclear targets of interests are oxygen and carbon.

Consequently, we consider three sets of  $\nu_\mu$  CC0 $\pi$  cross-section data:

1. the T2K simultaneous measurement in muon kinematics on carbon and oxygen [115]: it provides the inclusive double differential cross section of  $\nu_\mu$  interactions on the two nuclei as a function of the outgoing muon momentum  $p_\mu$  and the cosine of its angle with respect to the neutrino direction  $\cos\theta_\mu$ .
2. the T2K semi-exclusive measurement on carbon in CC0 $\pi$ 0 $p$  and CC0 $\pi$  $Np$  topologies [113]: in the 0 $p$  topology, the double differential cross section is reported as a function of the muon kinematics  $(p_\mu, \cos\theta_\mu)$ , whereas in the  $Np$  case it is given as a single differential cross section as a function of the single-transverse variables (see below).
3. the MINERvA measurement on carbon in CC0 $\pi$  $Np$  [220]: it provides a single differential cross section as a function of the single-transverse variables as well. It is important to note that the neutrino flux in MINERvA is at a higher energy in comparison with T2K, spread around  $\sim 3$  GeV as shown in Figure 3.1.

### Cross-section measurements in the muon kinematics

The two T2K cross-section measurements in the muon kinematics find a preference for the LFG model with additional corrections related to long-range correlations described by the random-phase approximation (RPA) [174, 221–223]. This approach consists of approximating the collective excitations a superposition of 1p1h excitations in the Fermi-gas based models.

In contrast, the nominal SF model prediction in NEUT is found to poorly describe the data due to its overestimation of the cross section in the forward region of the muon kinematics. This angular region corresponds to interactions with a low energy-momentum transfer  $Q^2$ . As detailed in Section 3.2.3, the SF model is based on the impulse approximation which breaks



decelerating ( $\delta\alpha_T > 90^\circ$ ) the final-state hadron. It is undefined in the case of transverse balance. When no FSI effects are considered, it is expected to have a flat distribution to first approximation as the Fermi motion within the nucleus is isotropic [224].

The T2K measurement of  $\delta p_T$  find that the Fermi gas models are largely disfavored and prefer the SF model, unlike the inclusive measurements. In fact, the detectors are unable to track protons below a certain threshold (e.g.  $\sim 450$  MeV/ $c$  in ND280). Therefore, in order to measure the STV, the momentum transfer needs to be large enough for the proton to be detected. In this regime, the impulse approximation is well satisfied, and the SF model gives the best description since it accurately captures the initial-state kinematics thanks to the precise constraints from electron scattering data. However, while the T2K measurement of  $\delta p_T$  shows that the SF model, MINERvA data suggests that it is still not completely satisfactory for its  $\delta p_T$  data.

## 4.2 Systematic uncertainties

In the previous section, we discussed how the SF model, while being describing more accurately the nuclear ground state than its RFG and LFG counterparts, seems disfavored by inclusive measurements. Besides, while the semi-exclusive measurements do prefer it, they also suggest that it is still incomplete. Therefore, a detailed study of the systematic uncertainties in this model is important to understand the sources of these disagreements. This section presents a novel set of parametrized systematic uncertainties adapted for the SF model. Several inputs are used to identify the most uncertain aspects of this model, spanning measurements from electron scattering experiments which for instance constrain the missing energy and momentum distributions, observed differences in the implementation with other neutrino event generators, and also the known overly simplistic descriptions of some effects in NEUT (e.g. Pauli blocking and final-state interactions).

### 4.2.1 Event reweighting

Neutrino event generators provide predictions from neutrino interaction models for oscillation measurements. The MC events are generated according to the distribution dictated by the chosen theoretical model usually using rejection sampling or other MC techniques. The models often come with a set of tuning parameters that need to be adjusted, and regenerating events with the full simulation for each parameter variation is computationally expensive. In other cases, calculations performed by theory groups cannot be implemented in the event generators in a straightforward way.

Therefore, neutrino event generators rely on *reweighting* which allows us to vary the total distribution of the events by changing the weight of each individual event. For instance, let us suppose that the simulation generates events according to a model, which we call the *nominal* model, and gives a distribution  $a_{\text{nom}}(x)$  in a variable of interest  $x$ , and that an alternative

model provides a different distribution  $a_{\text{alt}}(x)$  in the same variable  $x$ . In this case, reweighting would consist of taking each event from the nominal distribution and multiplying its weight by  $a_{\text{alt}}(x)/a_{\text{nom}}(x)$ . This procedure requires no MC techniques which makes it an extremely efficient and important tool for neutrino interaction simulations.

There are however limitations to the use of this reweighting method. One obvious case is when there is a mismatch in the covered phase space between the nominal and the alternative models, particularly if  $a_{\text{nom}}(x) = 0$  in a significant region of interest in  $x$  where  $a_{\text{alt}}(x) \neq 0$ . Another challenge in this procedure is the choice of the variable(s) in which the reweighting is applied. In some cases, reweighting in a given variable  $x$  may impact the event distribution of another relevant variable  $y$  in the analysis in an undesirable way. When possible, multidimensional reweighting, i.e. expressing the nominal and alternative models as functions of all the variables of interest  $(x, y, \dots)$ , can provide a way to mitigate this issue. However, additional dimensions exponentially increase the complexity of the reweighting.

The following sections describe a set of parameters that allow us to perform model variations by reweighting events from MC event generators. This corresponds to multiplying the event weights by  $a_{\text{alt}}(x, \vec{\lambda})/a_{\text{nom}}(x)$  where  $a_{\text{alt}}(x, \vec{\lambda})$  is the alternative model distribution that depends on a vector of parameters  $\vec{\lambda}$ . The NUISANCE framework [225] is used to implement these parameters as well as to compare and fit available neutrino interaction measurements.

### 4.2.2 Novel shell-model uncertainties

Since the SF model is mainly built from  $(e, e'p)$  data, inputs from such experiments are used to prescribe several model uncertainties affecting the SF predictions at both the initial and the final state of the CCQE interaction.

#### Shell occupancy

As discussed in Section 3.2.2 and shown in Figure 4.3, the missing energy distributions predicted by the SF model exhibit multiple peaks which correspond to the nucleon energy levels in the shell model. Electron scattering  $(e, e'p)$  measurements of the SF model such as Reference [226] indicate that the distribution of the missing energy  $E_m$  may<sup>2</sup> depend on the energy-momentum transfer of the interaction  $Q^2$ . In order to take into account this variation, a parameter able to modify the shell occupancy is introduced as a normalization uncertainty for each shell in the MF region of the SF model (see Equation (3.12) and fig. 4.3). To do so, a reweighting function is applied to CCQE events as a function of  $E_m$  in this region which is

<sup>2</sup>This effect could also be due to the variation of the detector acceptance in the different kinematic settings.

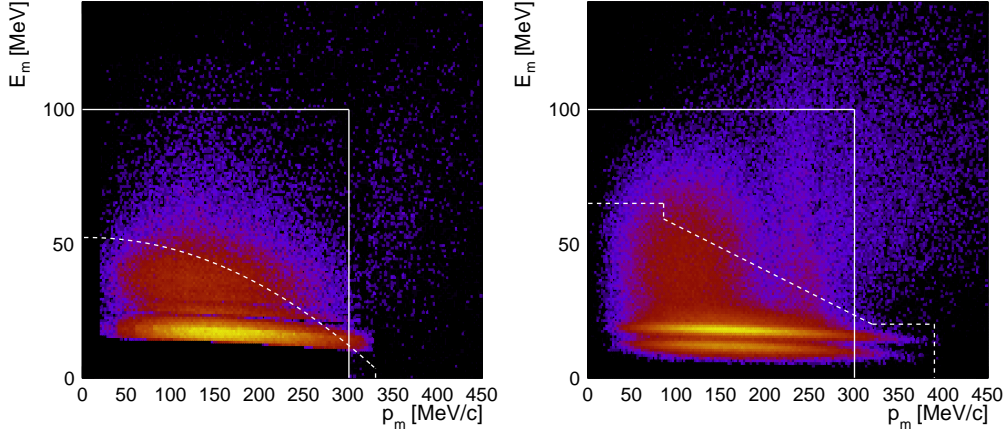


Figure 4.3: NEUT prediction of the two-dimensional distribution of the missing energy and the missing momentum for carbon (left) and oxygen (right). The brightness of the color represents the probability of finding an initial-state nucleon with a particular removal energy and momentum state. The white lines indicate the cuts used to separate the MF region (low  $E_m, p_m$ ) from the SRC region (high  $E_m, p_m$ ) in NuWro (dashed) and NEUT (full).

defined as:

$$\begin{aligned} f_{\text{shell}}(E_m) &= 1 + N_{\text{shell}} \times \exp\left(-\frac{(E_m - E_{\text{shell}})^2}{2\sigma_{\text{shell}}^2}\right) \\ &= 1 + N_{\text{shell}} \times g_{\text{shell}}(E_m) \end{aligned}$$

where  $N_{\text{shell}}$  is the normalization parameter of a given shell, and  $E_{\text{shell}}$  and  $\sigma_{\text{shell}}$  correspond to the center and the width of the Gaussian function,  $g_{\text{shell}}(E)$ , which are fixed for each shell. In total, this gives two shell normalization parameters for carbon interaction events and three for oxygen ones. The fixed values of  $E_{\text{shell}}$  and  $\sigma_{\text{shell}}$ , derived from an analysis of the missing energy distributions in NEUT, are shown for each shell in Table 4.1.

Target	Shell	$E_{\text{shell}}$ [MeV]	$\sigma_{\text{shell}}$ [MeV]	$N_{\text{shell}}$ prior error
Carbon	$p$	18	15	0.2
	$s$	36	25	0.4
Oxygen	$p_{1/2}$	12	8	0.25
	$p_{3/2}$	19	8	0.45
	$s$	42	25	0.75

Table 4.1: Energy levels with their widths for the different shells as in NEUT. Last column represents the relative prior uncertainty set on the corresponding shell normalization parameter, which all have central value set to 0.

One important effect of these shell occupancy parameters is how they can also alter the total

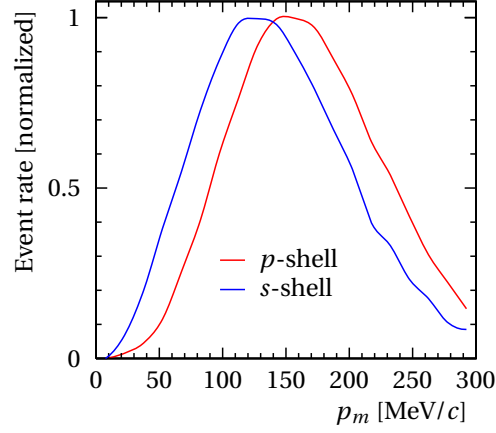


Figure 4.4: Distribution of the missing momentum within each shell for carbon.

$p_m$  distribution, since the initial-nucleon momentum distribution differs between the shells as shown in Figure 4.4. Therefore, a change in the relative strength of a shell impacts the shape of the overall distribution of the missing momentum, and consequently the distribution of  $\delta p_T$ . This is illustrated in Figure 4.4 where the shape impact on the  $E_m$  and  $\delta p_T$  distributions is shown. Therefore, such parameters allow for the variation of the exclusive cross section and particularly the nucleon kinematics in a way that is properly propagated through the model.

The prior errors on the  $N_{\text{shell}}$  parameters, reported in Table 4.1, are conservatively chosen to cover shape differences beyond the measured  $E_m$  distributions in  $(e, e'p)$  data of Reference [226]. Figure 4.5 shows the impact of varying individually each shell normalization parameter  $N_{\text{shell}}$  on the total CCQE cross section. We choose the  $1\sigma$  variation of each shell occupancy parameter to correspond to a 10% variation of this cross section. Since they affect the overall CCQE normalization, these parameters are expected to impact several standard observables in neutrino experiments. This choice of relatively loose prior uncertainties is motivated not only by offering effective degrees of freedom to account for physics beyond the impulse approximation, but also by the sensitivity to the shape of the  $\delta p_T$  distribution as shown in Figure 4.5 which can be well constrained by the measurements.

### Missing momentum shape

Electron scattering data from Reference [226] provides measurements of the missing momentum distributions  $p_m$  for carbon. By comparing the predicted NEUT distributions of  $p_m$  in each shell with this data, we can notice shape differences as illustrated in Figure 4.7. This shows two “extreme” distributions of the measured missing momentum (blue and red) which correspond to  $(e, e'p)$  kinematics with the most different  $Q^2$ , compared to the NEUT prediction. This allows us to prescribe a missing momentum shape uncertainty for each shell, which varies the shape of the  $p_m$  distribution within these extreme variations. Each shell parameter is defined between -1 and 1, corresponding to the two extreme  $p_m$  distributions and a linear



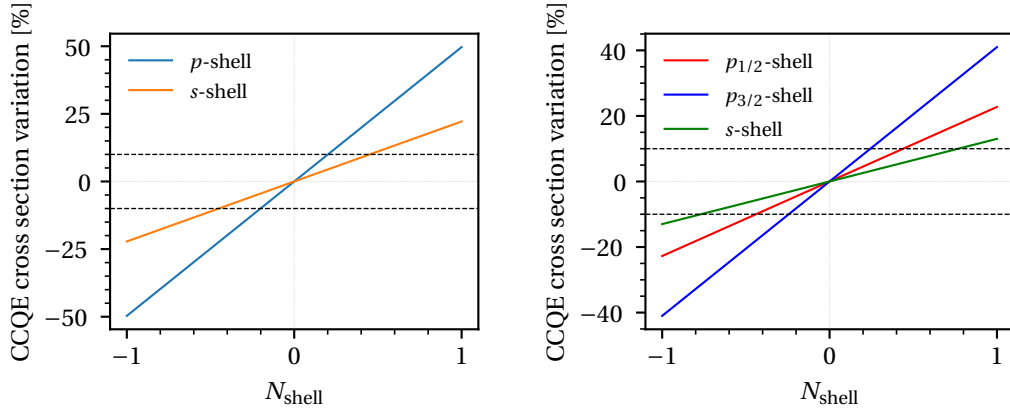


Figure 4.5: Impact of the shell normalization parameter  $N_{\text{shell}}$  on the total CCQE cross section for each shell in carbon (left) and oxygen (right). The dashed horizontal lines indicate the  $\pm 10\%$  variations, chosen to correspond to the  $1\sigma$  error for these parameters.

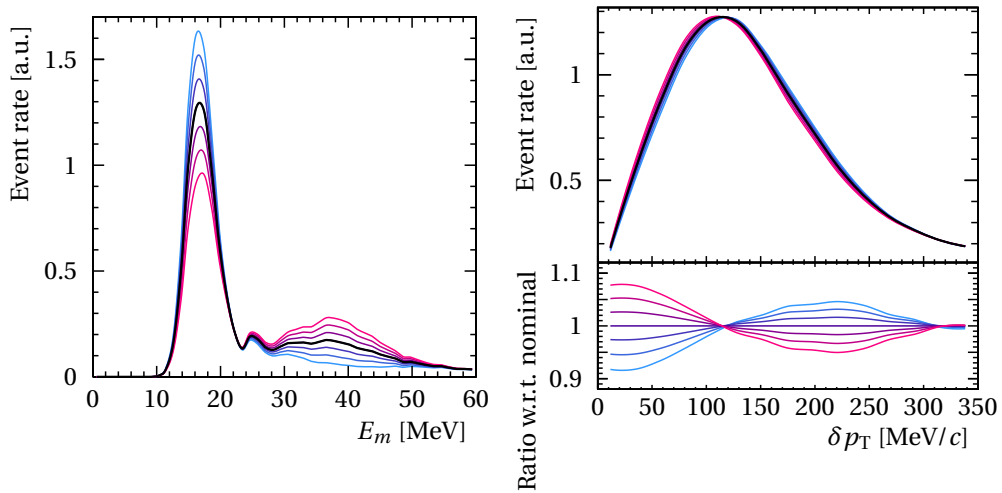


Figure 4.6: Variations of the shell normalizations from  $-1.5\sigma$  to  $+1.5\sigma$  in  $E_m$  (left) and the impact on  $\delta p_T$  (right) compared to the nominal distributions (black).

extrapolation is implemented beyond the interval  $[-1, 1]$ .

These  $p_m$  shape parameters are expected to mainly affect observables sensitive to the initial nuclear momentum. Figure 4.8 shows the impact of the  $p$ -shell shape parameter on the distributions of the muon angle and the transverse momentum imbalance. The lepton kinematics have no discernible sensitivity to these variations, whereas the bulk of  $\delta p_T$  is indeed affected by this uncertainty since it corresponds to the transverse projection of Fermi motion.

### Short-range correlations

As mentioned in Section 3.2.2, the SRC contribution corresponds to CCQE events yielding two outgoing nucleons at the primary interaction. The calculated input tables in  $(p_m, E_m)$  provided by Benhar et al. [166] for neutrino event generators give only the total SF distribution containing both the MF and SRC components. Therefore, it is necessary to define a scheme that separates the two contributions. NEUT uses hard cuts on  $E_m$  and  $p_m$  to distinguish between them as shown in Figure 4.3 (full lines): a SRC two-nucleon knock-out only occurs if the neutrino interacts with a nucleon for which  $E_m > 100$  MeV and  $p_m > 300$  MeV/c. The spectator nucleon of the pair is taken to have opposite isospin and momentum compared to the “active” nucleon. Using this implementation, NEUT predicts that SRC events represent  $\sim 5\%$  of the total CCQE interactions both for carbon and oxygen. Alternatively, the SF implementation in NuWro takes a different approach by making non-rectangular cuts in the  $(p_m, E_m)$  phase space adapted to each target in a more phenomenological manner as shown in Figure 4.3 (dashed lines). Furthermore, while the hard cuts in NEUT fully determine the MF-SRC separation, NuWro applies an additional condition to allow for the knock-out of the SRC pair. It requires the energy of the pair to be higher than 14 MeV, i.e. approximately twice the average nucleon removal energy. As a consequence, the SF model implementation in NuWro predicts a larger SRC contribution, amounting to  $\sim 15\%$  of the total CCQE interactions.

The impact of these different implementation choices in NEUT and NuWro on the missing momentum distribution is displayed in Figure 4.9. While the high  $p_m$  tail in NEUT is exclusively due to SRC, it is not necessarily the case in NuWro because of the additional condition on the energy of the SRC pair. These clear differences motivate the need for a large uncertainty on the SRC contribution. This is applied as a normalization parameter of SRC events. We loosely set its prior error of to a value of 100%. Although this uncertainty does not allow us to cover the  $p_m$  shape differences that can be seen in Figure 4.9, the additional nucleon momentum shape freedom it offers, in conjunction with the aforementioned shell normalization and shape uncertainties, provides enough flexibility to account for differences between the two implementations of the SF model.

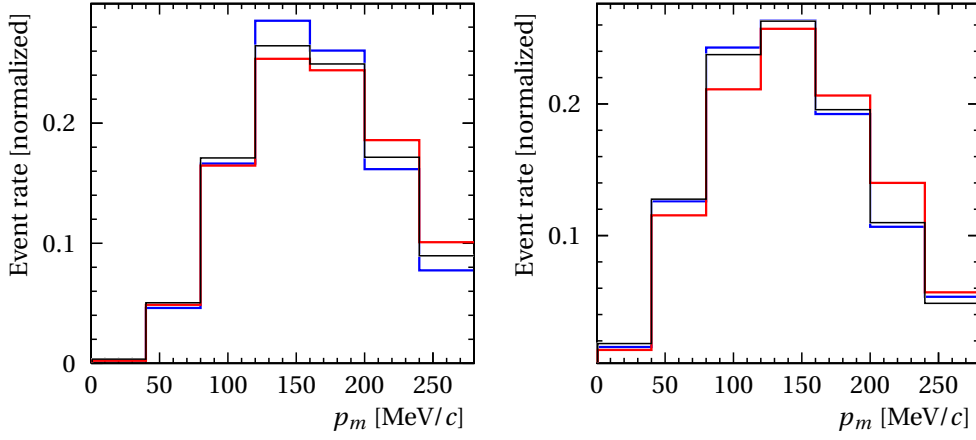


Figure 4.7: Distributions of the missing momentum from the NEUT SF inputs (black) compared to electron scattering measurements (blue and red) made for different nucleon and lepton kinematics for carbon in the  $p$ -shell (left) and the  $s$ -shell (right). The data is from Reference [226]

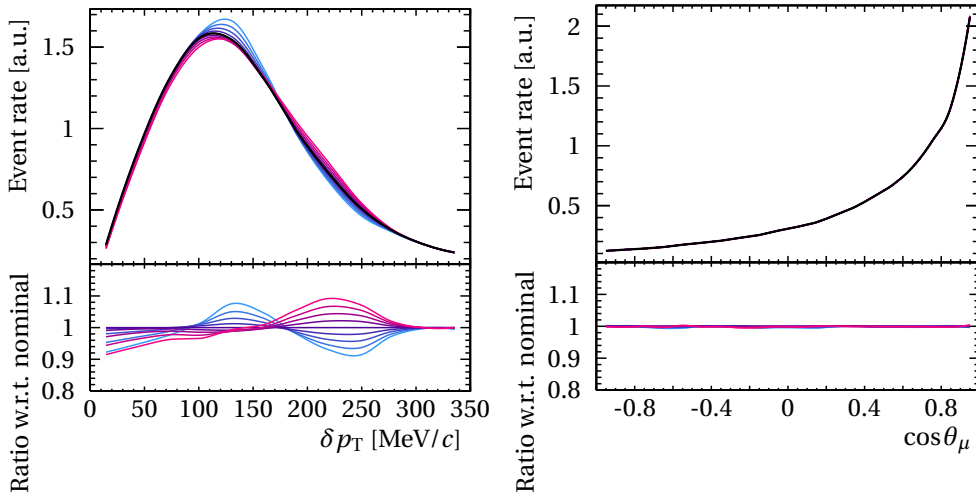


Figure 4.8: Impact of varying the  $p$ -shell shape uncertainty from  $-2\sigma$  (pink) to  $2\sigma$  (cyan) on  $\cos \theta_\mu$  (left) and on  $\delta p_T$  (right) compared to nominal distributions (black) for carbon.

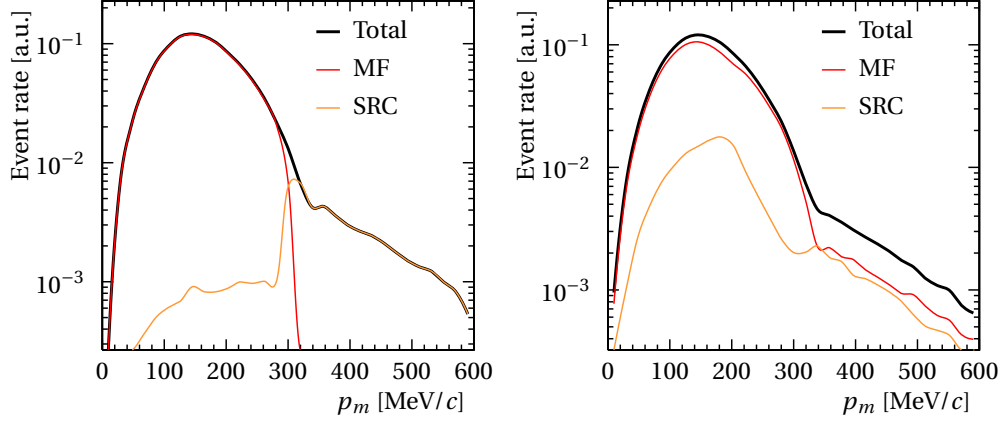


Figure 4.9: Distribution of the missing momentum in the SF model in NEUT (left) and in NuWro (right) for carbon with the MF and SRC contributions.

### Pauli blocking

As discussed in Section 3.3, the SF model in NEUT features a simple description of PB inspired by the RFG model of the nuclear ground state [200]. With this approach, the cross section for the portion of the phase space in which the pre-FSI outgoing primary nucleon has a lower momentum than Fermi level  $p_F$  is set to 0. It both reduces the cross section predicted by the SF model and causes significant shape changes at low momentum transfer, which generally corresponds to low momentum outgoing nucleons. Due to the fairly wide plausible range of  $p_F$  values in the literature from both theoretical estimations and  $(e, e'p)$  measurements [154, 161, 167, 227] vary between  $\sim 210 - 230$  MeV/ $c$ , and the simplistic model of PB used in NEUT, it is important to add some freedom to this value of the Fermi momentum. Consequently, a parameter varying this threshold  $p_F$  around its central value 209 MeV/ $c$  is prescribed separately for each type of target with a conservative prior error of  $\pm 30$  MeV/ $c$ .

Nominally, NEUT provides its prediction with a default PB threshold. Increasing this threshold is straightforward since it simply corresponds to suppressing events for which the pre-FSI momentum of the struck nucleon is below it. However, decreasing it is not as easy since the nominal NEUT does not generate events below the default PB threshold. Therefore, in the study presented in this chapter, we generate neutrino interaction events by turning off the effect of PB in NEUT and apply it *a posteriori* by setting to zero the cross section of the events with a pre-FSI nucleon momentum below a custom PB threshold, which corresponds to our PB parameter as shown in the top panel of Figure 4.10.

Figure 4.10 shows the impact of varying the PB threshold parameter on the pre-FSI nucleon momentum (top) as well as on the muon angle (bottom left) and momentum in the forward region (bottom right). As expected, since PB only affects low momentum transfer interactions, its impact is most noticeable in for forward leptons. By contrast, since this also corresponds to events where the struck nucleon carries a low momentum, the impact of varying PB in would

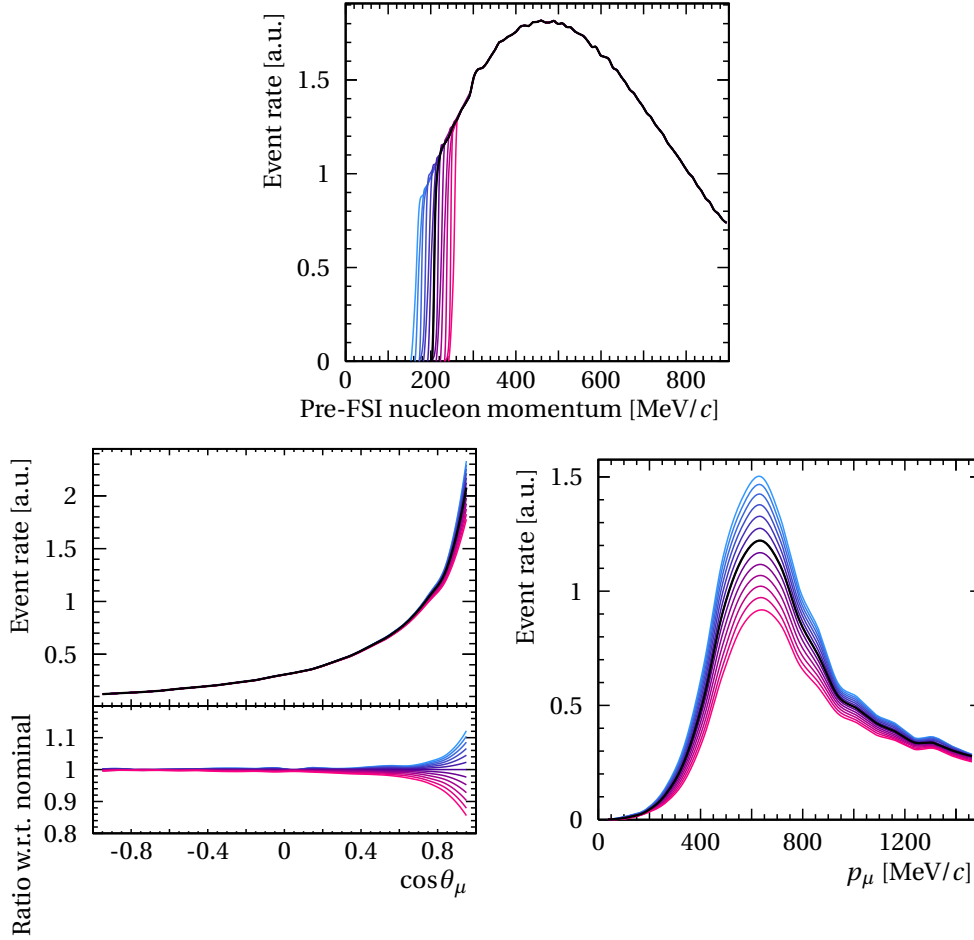


Figure 4.10: Impact of varying the PB threshold from  $-1.5\sigma$  (cyan) to  $+1.5\sigma$  (pink) on the pre-FSI nucleon momentum (top),  $\cos\theta_\mu$  (bottom left) and on the muon momentum in the forward region for  $\cos\theta_\mu > 0.9$  (bottom right) compared to the NEUT nominal distributions (black).

not be significant in semi-exclusive measurements (e.g.  $\delta p_T$  data) because such nucleons are almost always under the detection threshold.

### Optical potential

The SF model is based on the impulse approximation and the impact of FSI is not included in the cross-section predictions of NEUT except for PB and the intranuclear cascade. The latter distorts the outgoing nucleon momentum distribution and accounts for additional hadron ejection but does not allow the inclusive CCQE cross section to vary as would a full treatment of the distortion of the outgoing nucleon wave-function. One way to account for this missing alteration is based on introducing a nuclear optical potential that shifts and quenches the energy transfer as shown in Equations (3.13) and (3.14) which can be calculated as an *ad hoc*

correction to the SF model prediction of the lepton kinematics. The formalism was introduced in Reference [167] and discussed in Section 3.2.3.

Contrary to NEUT, the NuWro (version 19.02.01) has an option to include this correction. Its effect is shown in Figure 4.11, where it is clear that it strongly suppresses the cross section at low energy-momentum transfer, where the effects beyond the impulse approximation are the most prominent. The ratio histogram (bottom) can be used as a “template” to reweight in the  $(q_0, |\vec{q}|)$  space the nominal NEUT distribution to the corrected spectrum. We define an OP uncertainty as the strength by which this correction is applied. This parameter corresponds to the slope of the bin-by-bin linear interpolation between the two distributions and varies from 0% (no correction) to 100% (full correction). A calculation for this effect is only available for carbon but it is not expected to be dramatically different for oxygen. Therefore, this uncertainty is applied for each target independently. In order to avoid convergence issues at the boundaries [0, 100%] of this parameter in the fits shown later, the prior is set at 50% with a  $\pm 50\%$  uncertainty.

Effects beyond the impulse approximation appear at low  $Q^2$ , where the bound nucleons can no longer be treated as independent entities. Similarly to PB, Figure 4.12 illustrates the impact of applying the OP correction on the lepton angle (left) and momentum in the forward region (right). The largest impact is indeed for forward-going leptons since the transferred momentum in such interactions is the smallest.

As mentioned in Section 4.2.1, it should be noted that, since the impact of this correction is calculated only for the outgoing lepton kinematics, the proposed method of applying a correction on the NEUT distribution of  $(q_0, |\vec{q}|)$  from the NuWro one may lead to undesirable variations in the kinematics of the outgoing nucleon. Nevertheless, as will be shown in the next section, an additional uncertainty for the nucleon kinematics via the FSI cascade is applied, which allows for more freedom to mitigate this caveat.

### 4.2.3 Additional CC0 $\pi$ uncertainties

As mentioned in Section 4.1.2, the topology of interest corresponds to CC0 $\pi$  as it provides an enriched sample of CCQE events which is relevant for the SF model uncertainties. In addition to these parameters, there are additional uncertainties that need to be considered, particularly related to 2p2h and CCRES events that can form a non-negligible fraction of CC0 $\pi$  interactions.

#### CCQE axial form factor

Since it can significantly impact the CCQE cross section, we also consider the systematic uncertainty related to the axial form factor. The value of the nucleon axial mass  $M_A^{\text{QE}}$  in the dipole form is set at 1.03 GeV/ $c$  with a prior uncertainty of  $\pm 0.06$  GeV/ $c$ , estimated from bubble chamber data [127–132, 228] and other global fits [229].

## Chapter 4. Uncertainties in the charged-current quasielastic interactions

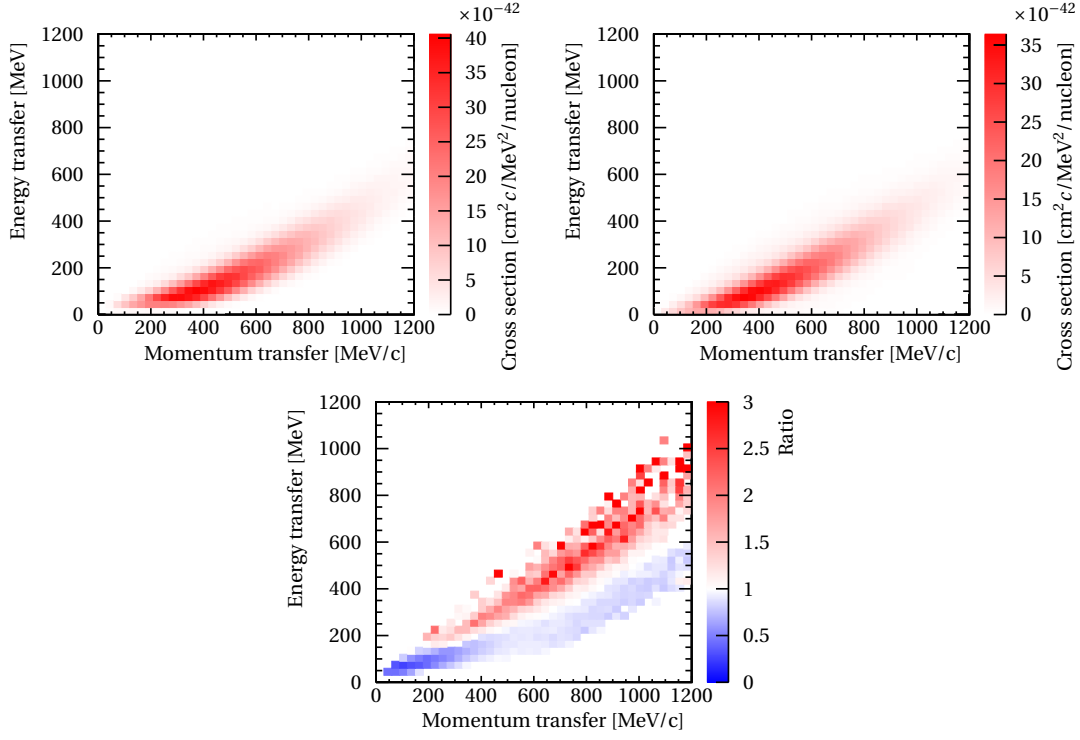


Figure 4.11: Comparison of the two-dimensional distributions predicted by NuWro of  $(q_0, |\vec{q}|)$  with (top right) and without (top left) applying the OP-based FSI correction, as well as their ratio (bottom).

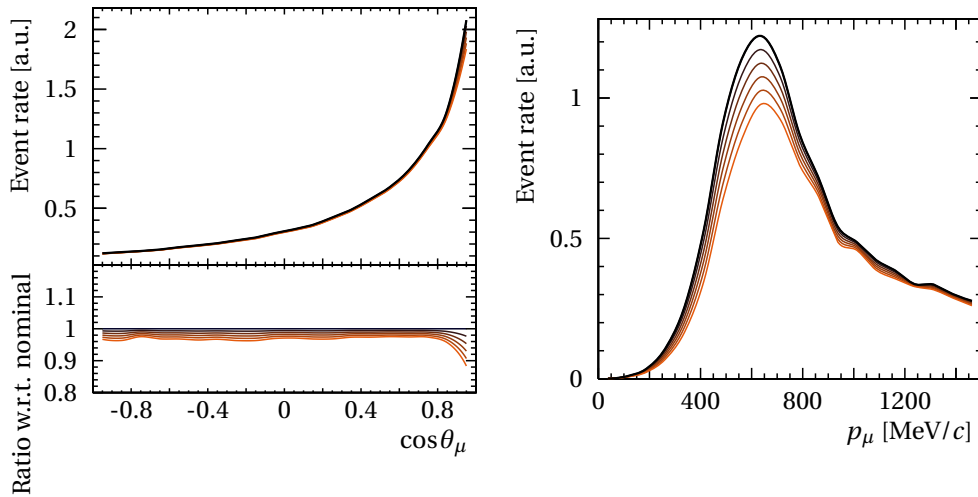


Figure 4.12: Impact of applying OP correction from 0%, i.e. nominal, (black) to 100% (orange) on  $\cos\theta_\mu$  (left) and on the muon momentum in the forward region for  $\cos\theta_\mu > 0.9$  (right).

On the other hand, it is known that the dipole approximation of the form factor given in Equation (3.6) may not be accurate. Therefore, three high  $Q^2$  parameters are applied to allow for additional freedom beyond the dipole form factor. The corresponding uncertainties are derived from comparisons between the high  $Q^2$  shape of the dipole form and the so-called *z-expansion* models [230].

### Nucleon final-state interactions

As already mentioned, FSI play a crucial role in altering the outgoing nucleon kinematics and distorting interaction topologies in the intranuclear cascade model. This is especially relevant when the cross-section measurements are performed in variables that use both the lepton and the hadron information. To simply account for nucleon FSI uncertainty, CC0 $\pi$  events are divided into two classes:

- “With FSI”: when the outgoing nucleon kinematics are modified due to FSI,
- “Without FSI”: in the opposite case, when the nucleon exits the nucleus without being impacted by the intranuclear cascade.

A normalization parameter for each class is applied with a broad 30% prior uncertainty. The two parameters are fully anticorrelated to ensure that the total cross section remains constant for each interaction mode. This means that, if the amount of “Without FSI” events in a certain interaction mode is reduced, these are compensated for by increasing the amount of “With FSI” events in that same interaction mode, yielding a shape-only variation of the cross section. This implementation has a similar impact as changing the mean free path of the nucleon within the nucleus.

### Resonant production component

A non-negligible fraction of resonant production (CCRES) contributes to the CC0 $\pi$  topology, which occurs when the produced pion is absorbed within the nucleus. This is particularly important for multi-GeV neutrinos like in the MINERvA flux ( $E_\nu \sim 3$  GeV). Therefore, a normalization parameters that varies the amount of CCRES events with an absorbed pion in this specific topology is applied. On top of that, we use the three parameters that modify the Rein –Sehgal model (see Sections 3.1.2 and 3.3) implemented in NEUT: the axial mass  $M_A^{\text{RES}}$ , the value of the axial form factor when  $Q^2 = 0$  denoted by  $C_5^A$ , and the normalization of the isospin-1/2 non-resonant background  $I_{1/2}$ . The prefit values and uncertainties of these three parameters, reported in Table 4.2, are fixed from fits using NUISANCE to deuterium bubble chamber data from ANL [145] and BNL [146], which also yield the correlation matrix of Figure 4.13 that we use as an input.



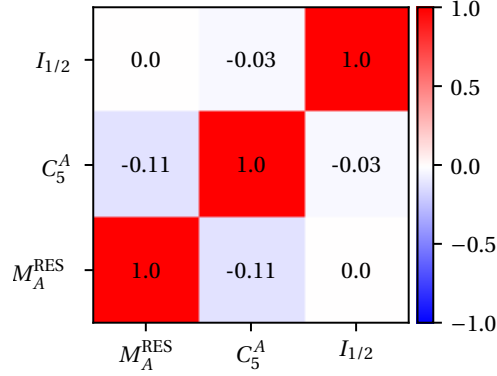


Figure 4.13: Correlations between the three parameters of the Rein – Sehgal model obtained from fits to ANL [145] and BNL [146] data.

### 2p2h interactions

2p2h interactions can also end up in the  $\text{CC}0\pi$  topology since there are usually no pions in its final state. NEUT relies on the Nieves et al. model which features two distinct peaks in the energy transfer  $q_0$  and momentum transfer  $|\vec{q}|$  space which correspond to  $\Delta$  and non- $\Delta$  excitations as illustrated in the left panel of Figure 4.14. The  $\Delta$ -like component corresponds to the diagrams in the bottom row of Figure 3.10, while the non- $\Delta$  contribution corresponds to the rest of the 2p2h diagrams. The right panel shows that these contributions induce different biases to the estimator  $E_V^{\text{QE}}$ .

An uncertainty on the amount of 2p2h events is considered as a simple normalization parameter able to adjust the number of 2p2h interactions for each target, with a 30% prior error. Besides, similarly to the approach used in Reference [53, 231], a 2p2h shape uncertainty is prescribed as a parameter that allows us to vary the relative strength between the  $\Delta$  and non- $\Delta$  peaks in the  $(q_0, |\vec{q}|)$  space.

Table 4.2 summarizes all the parametrized systematic uncertainties discussed in this section, along with their central values and prior errors.

## 4.3 Fits to cross-section measurements

Now that we have defined a set of parametrized uncertainties in the NEUT model, we will present fits to the cross-section measurement discussed in Section 4.1.2. This step is fundamental not only to validate the ability of the proposed parametrization in tuning the SF model in NEUT, but also to confirm the sensitivity of the data in constraining a certain category of systematic uncertainties depending on the used observables.

### 4.3 Fits to cross-section measurements

Parameter	Central value	Prior error [ $1\sigma$ ]	Notes
$p$ -shell norm. C	0	20%	
$p$ -shell shape C	0	100%	From $(e, e'p)$ data
$s$ -shell norm. C	0	40%	
$s$ -shell shape C	0	100%	From $(e, e'p)$ data
SRC norm. C	1	100%	
Pauli Blocking C	209 MeV/ $c$	30 MeV/ $c$	Used only with $(p_\mu, \cos\theta_\mu)$ fits
Optical Potential C	50%	50%	Used only with $(p_\mu, \cos\theta_\mu)$ fits
2p2h norm. C	1	30%	
2p2h shape C	0	300%	
Pion abs. norm. C	1	30%	
$p_{1/2}$ -shell norm. O	0	45%	
$p_{3/2}$ -shell norm. O	0	25%	
$s$ -shell norm. O	0	75%	
SRC norm. O	1	100%	
Pauli Blocking O	209 MeV/ $c$	30 MeV/ $c$	Used only with $(p_\mu, \cos\theta_\mu)$ fits
Optical Potential O	50%	50%	Used only with $(p_\mu, \cos\theta_\mu)$ fits
2p2h norm. O	1	30%	
2p2h shape O	0	300%	
Pion abs. norm. O	1	30%	
$M_A^{\text{QE}}$	1.03 GeV/ $c^2$	0.06 GeV/ $c^2$	
High $Q^2$ norm. 1	1	11%	$Q^2 \in [0.25, 0.50 \text{ GeV}^2[$
High $Q^2$ norm. 2	1	18%	$Q^2 \in [0.50, 1.00 \text{ GeV}^2[$
High $Q^2$ norm. 3	1	40%	$Q^2 \in [1.00 \text{ GeV}^2, +\infty[$
With FSI	1	30%	Fully correlated
Without FSI	1	30%	Used only in semi-inclusive fits
$M_A^{\text{RES}}$	0.91 GeV/ $c^2$	0.1 GeV/ $c^2$	
$C_5^A$	1.06	0.1	Correlated, see Figure 4.13
$I_{1/2}$ non-res. bkg.	1.21	0.27	

Table 4.2: Summary of the parameters described in Section 4.2 and their prior uncertainties.

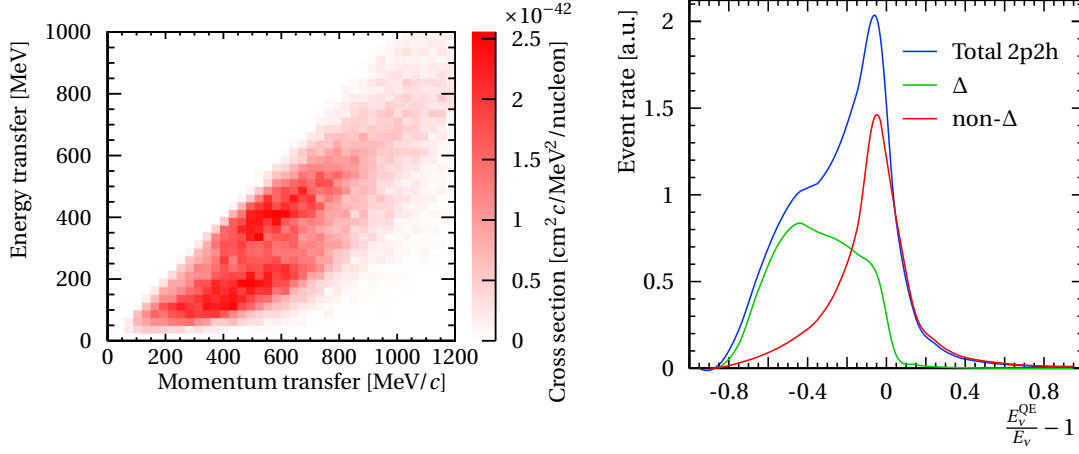


Figure 4.14: Two-dimensional distribution of energy and momentum transfer (left) and the neutrino energy bias broken down by  $\Delta$ -like and non- $\Delta$ -like contributions (right) as predicted by the 2p2h Nieves et al. model implemented in NEUT.

#### 4.3.1 Fit method

NUISANCE allows us not only to implement reweighting parameters, but also to compare and fit a large number of available cross-section measurements. As mentioned in Section 4.1.1, experiments publish their measurements in true observables where the detector response is unfolded. The data release of such measurements usually consists of a histogram in the cross-section variable along with a covariance matrix. This covariance encodes the overall estimation of errors from all the sources, including the detector response as well as the neutrino flux in the experiment (shape and normalization uncertainties) in addition to the statistical errors. This usually produces bin-to-bin correlations particularly due to normalization uncertainties.

The common way to evaluate the agreement of a model with the data is to use a chi-square test-statistic which is expressed as:

$$\chi^2(\vec{\lambda}) = \sum_{i,j} \left( B_i^{\text{data}} - B_i^{\text{MC}}(\vec{\lambda}) \right) (M^{-1})_{i,j} \left( B_j^{\text{data}} - B_j^{\text{MC}}(\vec{\lambda}) \right) \quad (4.3)$$

where  $B^{\text{data}} = (B_1^{\text{data}}, \dots, B_n^{\text{data}})$  and  $M = \text{Cov}[\{B_i\}]$  are respectively the bins of the histogram and the covariance published by the experiment, whereas  $B^{\text{MC}} = (B_1^{\text{MC}}(\vec{\lambda}), \dots, B_n^{\text{MC}}(\vec{\lambda}))$  corresponds the histogram of model predictions which depend on a set of parameters  $\vec{\lambda}$ .

In the previous section, we introduced a set of parameters that can vary the model. To evaluate its ability to describe the data, we perform fits to the three cross-section measurements presented in Section 4.1.1. This consists of finding the optimal set of parameters  $\vec{\lambda}_0$  that minimizes the chi-square given by Equation (4.3) such that:

$$\chi_{\text{tot}}^2(\vec{\lambda}_0) = \min_{\vec{\lambda} \in I} \left( \chi^2(\vec{\lambda}) + \chi_{\text{syst}}^2(\vec{\lambda}) \right)$$

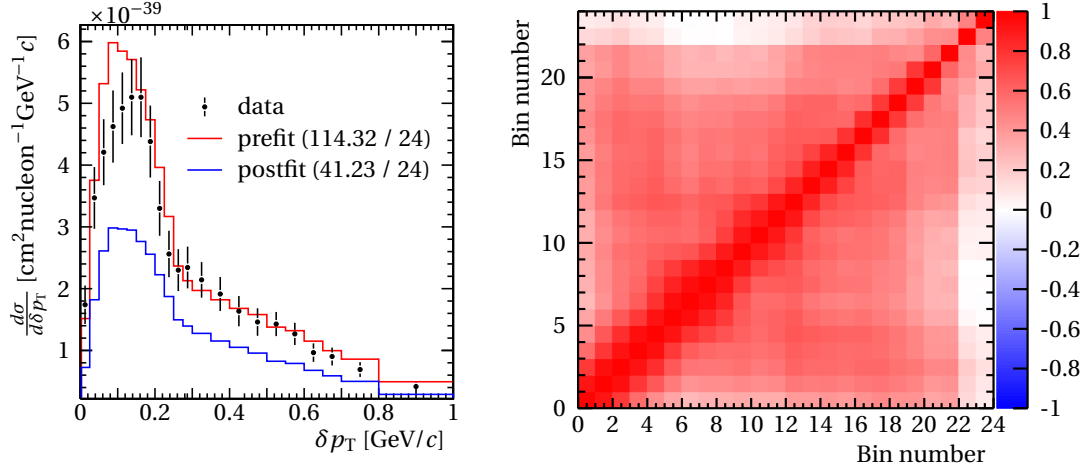


Figure 4.15: Left: manifestation of Peelle’s pertinent puzzle when fitting the MINERvA  $\delta p_T$  data by minimizing the chi-square given by Equation (4.3). Right: the bin-to-bin correlation matrix in the  $\delta p_T$  measurement of MINERvA.

where  $\chi_{\text{syst}}^2(\vec{\lambda})$  is the penalty term that encodes the Gaussian prior uncertainties as provided in Table 4.2.

This multidimensional minimization is done with the Minuit2 package [232], particularly with its gradient descent algorithm. All this is performed within the NUISANCE framework.

### Peelle’s pertinent puzzle

Our first attempt to fit the MINERvA  $\delta p_T$  data yielded a postfit (or bestfit) result with an unphysically low normalization as shown in the left panel of Figure 4.15. This is commonly known as *Peelle’s pertinent puzzle* [233, 234], which often occurs when the covariance matrix  $M$  is highly correlated, as is the case for this measurement (right panel of Figure 4.15). This happens due to the inadequate assumption of Gaussianity in the chi-square given by Equation (4.3). In fact, it assumes that the absolute uncertainty on the measurement is independent of its normalization. This implies that the relative uncertainty is larger when fitting to models that predict lower normalizations, thus ending in favoring artificially low normalizations if the Gaussian assumption of measurement uncertainties is not well satisfied.

### “Norm-shape” chi-square

Various workarounds have been employed to address this issue caused by PPP, such as using a shape-only chi-square [234], or neglecting the bin-to-bin correlations [235]. None of these methods are satisfactory since the former ignores the valuable information on the total cross section from the measurement, while the latter disregards the correlations that can play a crucial role in interpreting the results. We propose a way to mitigate PPP which consists in

## Chapter 4. Uncertainties in the charged-current quasielastic interactions

separating the normalization and shape contributions of the covariance matrix, that corresponds to constructing a new covariance matrix where we isolate the relative uncertainty from the cross-section normalization, thus making the absolute uncertainty larger for models predicting lower normalizations. This results in a relative uncertainty that remains constant as a function of the normalization, as motivated by the arguments of Reference [236].

Concretely, this can be obtained by applying a transformation to both the data and MC histograms as well as to the covariance matrix, in order to separate them into a "shape" and a "norm" parts. The new histograms  $C = (C_1, \dots, C_n)$  are defined as:

$$C_i = f(B_i) = \begin{cases} \alpha \frac{B_i}{\sum_k B_k}, & 1 \leq i \leq n-1 \\ B_T = \sum_k B_k, & i = n \end{cases} \quad (4.4)$$

where  $\alpha$  is a scale parameter. The function  $f : B \mapsto C$  is bijective, meaning that no information is lost by moving from  $B$  to  $C$ .

In this new basis, the covariance matrix  $N = \text{Cov}[\{C_i\}]$  is obtained via a non-linear transformation of the original covariance matrix  $M$ , using the following formula in the linear approximation:

$$N \approx J(f) \cdot M \cdot J(f)^T \quad (4.5)$$

where  $J(f)$  is the Jacobian of the non-linear transformation  $f$ . The new covariance matrix is expressed as follows:

$$N = \left( \begin{array}{c|c} (N_S)_{i,j} = \frac{\alpha^2}{B_T^2} \left( M_{i,j} - \frac{B_i}{B_T} \sum_l M_{i,l} - \frac{B_j}{B_T} \sum_k M_{k,j} - \frac{B_i B_j}{B_T^2} \sum_{kl} M_{kl} \right) & \begin{matrix} \frac{\alpha}{B_T} \left( \sum_l M_{1,l} - \frac{B_1}{B_T} \sum_{kl} M_{kl} \right) \\ \vdots \\ \frac{\alpha}{B_T} \left( \sum_l M_{n-1,l} - \frac{B_{n-1}}{B_T} \sum_{kl} M_{kl} \right) \end{matrix} \\ \hline \begin{matrix} \frac{\alpha}{B_T} \left( \sum_k M_{k,1} - \frac{B_1}{B_T} \sum_{kl} M_{kl} \right) & \dots & \frac{\alpha}{B_T} \left( \sum_k M_{k,n-1} - \frac{B_{n-1}}{B_T} \sum_{kl} M_{kl} \right) \end{matrix} & \sum_{kl} M_{kl} \end{array} \right)$$

The matrix  $N$  has the same dimension and the same positive-definiteness properties as  $M$  since the mapping  $B \mapsto C$  is a bijection.  $N$  is composed of two diagonal blocks: the  $N_S$  block which corresponds to the shape-only covariance, and the  $\sum_{kl} M_{kl}$  element which corresponds to the variance of the data normalization. The off-diagonal blocks represent the correlations between the norm and the shape components.

Finally, by transforming the MC histogram using this same function  $f$ , the "norm-shape" (NS) chi-square can be computed in this basis:

$$\chi_{\text{NS}}^2 = \sum_{1 \leq i, j \leq n} (C_i - C_i^{\text{MC}}) (N^{-1})_{i,j} (C_j - C_j^{\text{MC}}) \quad (4.6)$$

This new computation of the covariance matrix and the chi-square were implemented in

NUISANCE and the correctness of the implementation was validated by comparisons with covariance matrices computed from random throws according to the initial matrix  $M$ . The use of the  $\chi_{\text{NS}}^2$  allows us to mitigate Peele's pertinent puzzle observed Figure 4.15 when using the standard  $\chi^2$  of Equation (4.3) in the fit. We first briefly discussed this new method in Reference [237], which was later used by other collaborations [238, 239].

#### 4.3.2 Fit results

In this section, the results of the fits to T2K and MINERvA data will be presented and discussed. The systematic uncertainties are implemented in NUISANCE, which allows us to compare and fit available cross-section measurements. Each fit is based on the minimization of  $\chi_{\text{NS}}^2$  defined in the previous section using Minuit2, and the fit parameters are summarized in Table 4.2.

The different fits use different sets of parameters depending on their sensitivities. For instance, the missing-momentum shape parameters are fixed when fitting the muon kinematics data as it is expected to be insensitive to its variations (see Figure 4.8). On the other hand, the PB and OP uncertainties are not expected to impact measurements that require the detection of a proton. In fact, the experimental threshold to observe them is at  $\sim 500 \text{ MeV}/c$ , which means that the energy momentum transfer is relatively high, beyond the region where the impulse approximation corrections are needed. The last column of Table 4.2 indicates when the parameters are not used in all the fits.

#### Fit to T2K CC0 $\pi$ cross-section data on oxygen and carbon in muon kinematics

Figure 4.16 shows the results of the fit to T2K oxygen and carbon data [115]. The prefit, i.e. the nominal spectra predicted by NEUT, and the postfit distributions are displayed and compared with the data. The value of the corresponding  $\chi_{\text{NS}}^2$  as well as the usual  $\chi^2$  are reported in Table 4.3.

First, we can immediately notice that the agreement of the model with the data is dramatically improved after the fit adjustment of the systematic parameters, which is also reflected in the important decrease of the chi-square below the number of the measurement bins. It should be noted that, as discussed in Section 4.1.2 and detailed in Reference [115], the disagreement between the prefit model and the data comes mainly from the bins that correspond to the forward lepton kinematics (last bin in  $\cos\theta_\mu$ ). This is the region of low momentum transfer which, as previously mentioned, is known to be more complicated to model due to the effects beyond the impulse approximation, where for instance RFG and LFG models are often corrected using RPA. Consequently, it is expected to see, as shown in Figure 4.17, that the postfit agreement is driven by large variations in the PB and OP parameters. Indeed, these precisely target this poorly-modeled low momentum transfer region as shown in Figures 4.10 and 4.12. This is particularly true for the oxygen part of the measurement where the prefit disagreement is more important. Figure 4.17 also shows a fair sensitivity to the shell normalization parameters which

## Chapter 4. Uncertainties in the charged-current quasielastic interactions

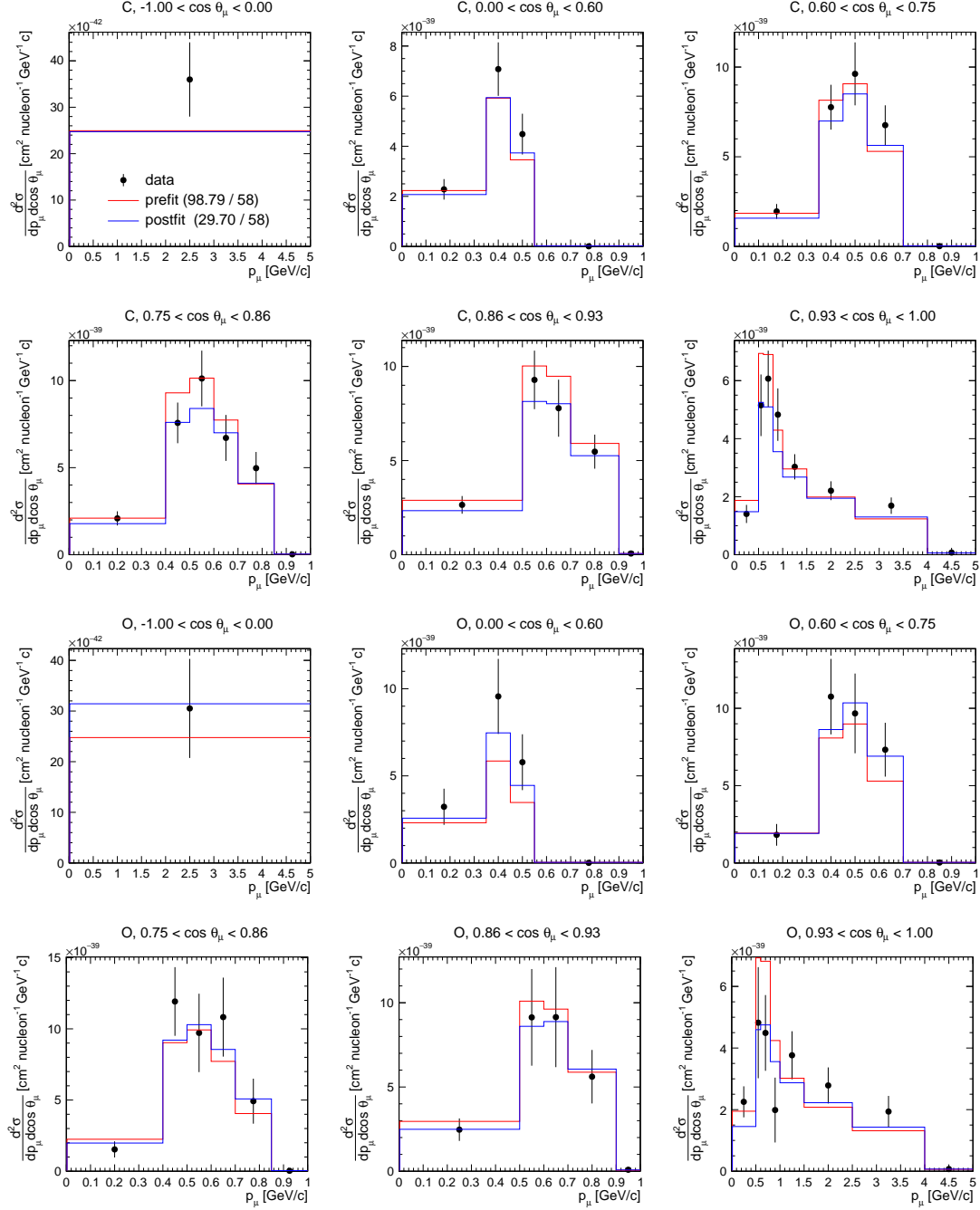


Figure 4.16: Prefit (red) and postfit (blue) distributions of  $p_\mu$  in bins of  $\cos \theta_\mu$  from the fit to T2K CC0 $\pi$  joint measurement of lepton kinematics on carbon and oxygen. The usual chi-squares as well as the number of bins are quoted in the legend. The NS chi-square  $\chi^2_{\text{NS}}$  used in the minimization is reported in Table 4.3.

### 4.3 Fits to cross-section measurements

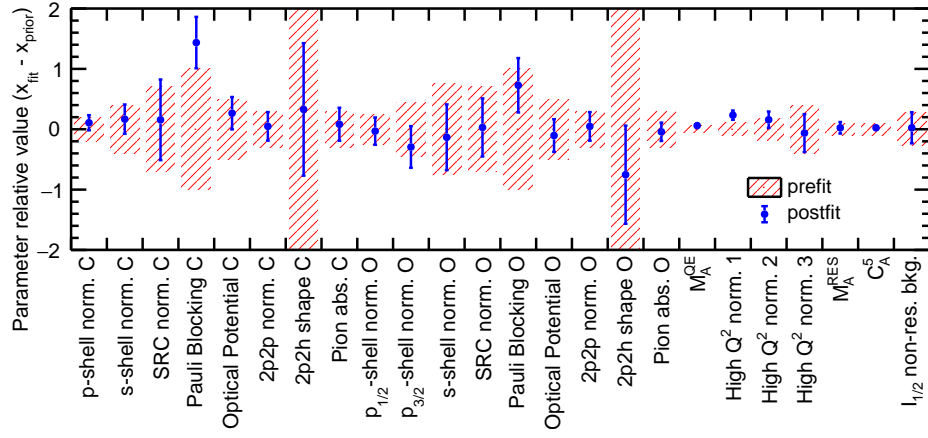


Figure 4.17: Prefit (red) and postfit (blue) values and constraints on the uncertainties from the fit to T2K CC0 $\pi$  joint measurement of lepton kinematics on carbon and oxygen.

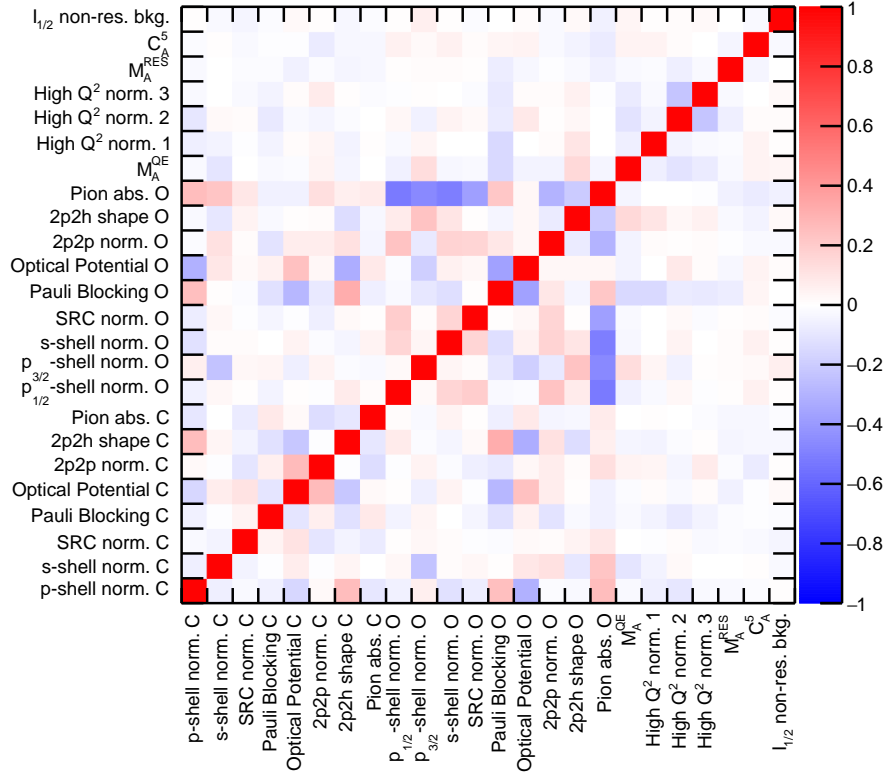


Figure 4.18: Postfit correlation matrix from the fit to T2K CC0 $\pi$  joint measurement of lepton kinematics on carbon and oxygen.



## Chapter 4. Uncertainties in the charged-current quasielastic interactions

---

assist in compensating the effects of the PB and OP parameters. This is particularly visible for the carbon part, where the data presents larger statistics<sup>3</sup>. The overall CCQE normalization is also adjusted by a slight variation of the  $M_A^{\text{QE}}$  parameter.

The postfit covariance matrix is shown in Figure 4.18. Some anticorrelations are present between the shell normalization parameters for oxygen considering that they significantly impact the total CCQE cross-section normalization, albeit with different shapes. There are also anticorrelations between the PB and OP uncertainties for carbon and more prominently for oxygen.

It may be noteworthy to highlight that the parametrization developed in this work treats the oxygen and carbon uncertainties as two independent groups (except for the nucleon-level parameters such as  $M_A^{\text{QE}}$ ,  $M_A^{\text{RES}}$ , etc., which are not specific to the nuclear target), but the postfit correlation matrix shown in Figure 4.18 exhibits correlations between these two sets of parameters. In fact, since the measurement corresponds to a *joint* cross section on the two targets, the data covariance includes correlations between carbon and oxygen bins, which is then reflected on the parameters. Such simultaneous measurements are increasingly important for oscillation measurements to better understand the extrapolation of model constraints between targets, as we will highlight in Chapter 9.

### Fit to T2K cross-section data in $\text{CC}0\pi0p$ and $\text{CC}0\pi Np$ topologies on carbon

In this section, we fit T2K cross-section measurements on carbon in the transverse-momentum imbalance  $\delta p_T$  and lepton kinematics for the  $\text{CC}0\pi$  with and without protons in the final state respectively [93]. Three different fits are performed:

- (a) fitting data in lepton kinematics for  $\text{CC}0\pi0p$ ,
- (b) fitting data in  $\delta p_T$  for  $\text{CC}0\pi Np$ ,
- (c) simultaneously fitting data in lepton kinematics for  $\text{CC}0\pi0p$  and  $\delta p_T$  for  $\text{CC}0\pi Np$ .

One of the interests of performing this last simultaneous fit is to evaluate the ability of the model to describe neutrino interactions at different energy spectra. Indeed, the  $\text{CC}0\pi0p$  and the  $\text{CC}0\pi Np$  topologies correspond to distinct distributions of  $E_\nu$  as illustrated in Figure 4.19. Another goal is to also test the relevance of simultaneously exploiting data provided in different set of variables, an approach we will employ in the studies presented in Chapter 9.

The highest momentum bin in each angular slice of the lepton kinematics measurement in  $\text{CC}0\pi0p$ , which goes up to 30 GeV/ $c$ , is removed from the fit. They constitute a negligible fraction of the interaction events of interest, and the reconstruction is not necessarily reliable for this momentum range. Actually, while these bins are present within the data release, they were not shown in Reference [93].

---

<sup>3</sup>In this measurement, the amount of carbon data is roughly three times more than the oxygen ones

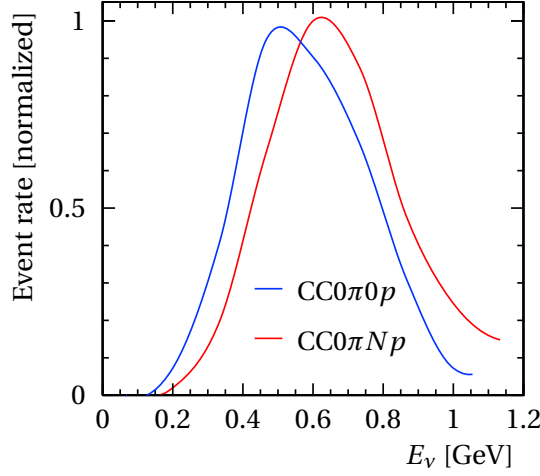


Figure 4.19: Neutrino energy distribution from the T2K beam for the  $CC0\pi0p$  (blue) and  $CC0\pi Np$  (red) topologies.

Figures 4.20 and 4.21 show the prefit and postfit distributions from fits (a) and (b) respectively, whereas Figures 4.22 and 4.23 display respectively the prefit vs. postfit parameters and correlations from the three fits. Let us first note that these fits do not use the same set of parameters. In fact, PB and OP uncertainties are not used when fitting only  $\delta p_T$  since they only affect the low  $Q^2$  events which typically produce low momentum protons that are well below the tracking threshold of the detectors (e.g.  $\sim 450$  MeV/ $c$  at ND280). On the other hand,  $p_m$  shape parameters are fixed in the  $(p_\mu, \cos\theta_\mu)$ -only fit since the outgoing proton kinematics are not measured.

The binning of  $\delta p_T$ , as shown in Figure 4.20, is rather coarse, and the prefit chi-squares reported in Table 4.3 are already relatively low. Nevertheless, the systematic parametrization presented in this work yields an even improved postfit agreement as demonstrated in the chi-squares. This is achieved mainly thanks to the SF model shell parameters as indicated in Figure 4.22 (black). This fit also shows sensitivity to SRC, nucleon FSI and 2p2h shape uncertainties which appears in the reduction of their postfit errors. Indeed, these are effects that are probed by  $\delta p_T$  and particularly at the tail of its distribution. The correlations between them that appear in the postfit correlation matrix (top left of Figure 4.23) indicate that these effects cannot be disentangle solely with  $\delta p_T$ . On the other hand, even with the coarse binning, its bulk allows for noticeable constraints on the shell normalization and shape parameters.

Similarly to the fit of T2K data on oxygen and carbon, the improved agreement of the model with the data in the  $CC0\pi0p$ -only is mainly driven by the increase in the PB parameter, as shown in Figure 4.22 (blue), which affects the forward angular region where the discrepancies are the largest. The binning of this measurement is about twice finer than the oxygen and carbon one, and the postfit chi-squares, while they do improve, show that the model still has limitations to fully describe the data. The FSI parameters, also impact the event rate in the

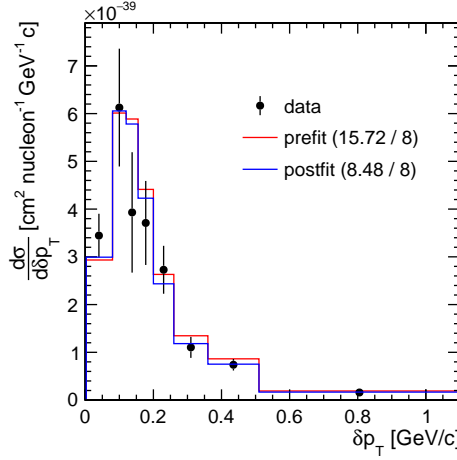


Figure 4.20: Prefit (red) and postfit (blue) distributions of  $\delta p_T$  from fitting the T2K CC0 $\pi Np$  data only. The usual chi-squares as well as the number of bins are quoted in the legend. The NS chi-square  $\chi^2_{\text{NS}}$  used in the minimization is reported in Table 4.3.

CC0 $\pi$ 0 $p$  sample since more FSI means that it is more likely for the proton to be absorbed within the nucleus, which can be translated into more CC0 $\pi$ 0 $p$  events. Consequently, the fit varies these parameters as well. The top right panel of Figure 4.23 shows anticorrelations between OP and PB uncertainties, as well as 2p2h and PB parameters as. FSI parameters are also (anti)correlated with PB and OP since they all have an important impact on the total event rate in this topology. The high  $Q^2$  parameter that affects the region  $0.25 \leq Q^2 < 0.50 \text{ GeV}^2$  converges to approximately the same value as in the fit of the carbon+oxygen data (see Figure 4.17), which is also an indication of missing freedom for high  $Q^2$  interactions.

For the simultaneous fit of CC0 $\pi$ 0 $p$  and CC0 $\pi Np$ , the correlations between the two datasets are not provided in the release, and can actually be neglected since they correspond to different regions of the proton kinematics. Therefore, the fit simply minimizes the sum of the individual  $\chi^2_{\text{NS}}$  of each dataset. The postfit values of the parameters from this fit are also displayed in Figure 4.22 (purple). Most of the parameters converge to similar values as in the CC0 $\pi$ 0 $p$ -only fit since the corresponding data statistically dominates the chi-square and drives the fit. It can be noticed that the FSI parameters are less pulled from their prior due to the constraint by the added  $\delta p_T$  sample. The bottom panel of Figure 4.23 shows strong (anti)correlations between parameters related to PB, OP, FSI and multinucleon effects. This explains the slightly different postfit values of these parameters between the CC0 $\pi$ 0 $p$ -only and the simultaneous fit. With a more statistically significant  $\delta p_T$  measurement, we could expect a better disentanglement between the struck nucleon-related uncertainty (FSI, SRC, 2p2h) probed by  $\delta p_T$  and the low  $Q^2$  effects sensitive to the forward angular region.

### 4.3 Fits to cross-section measurements

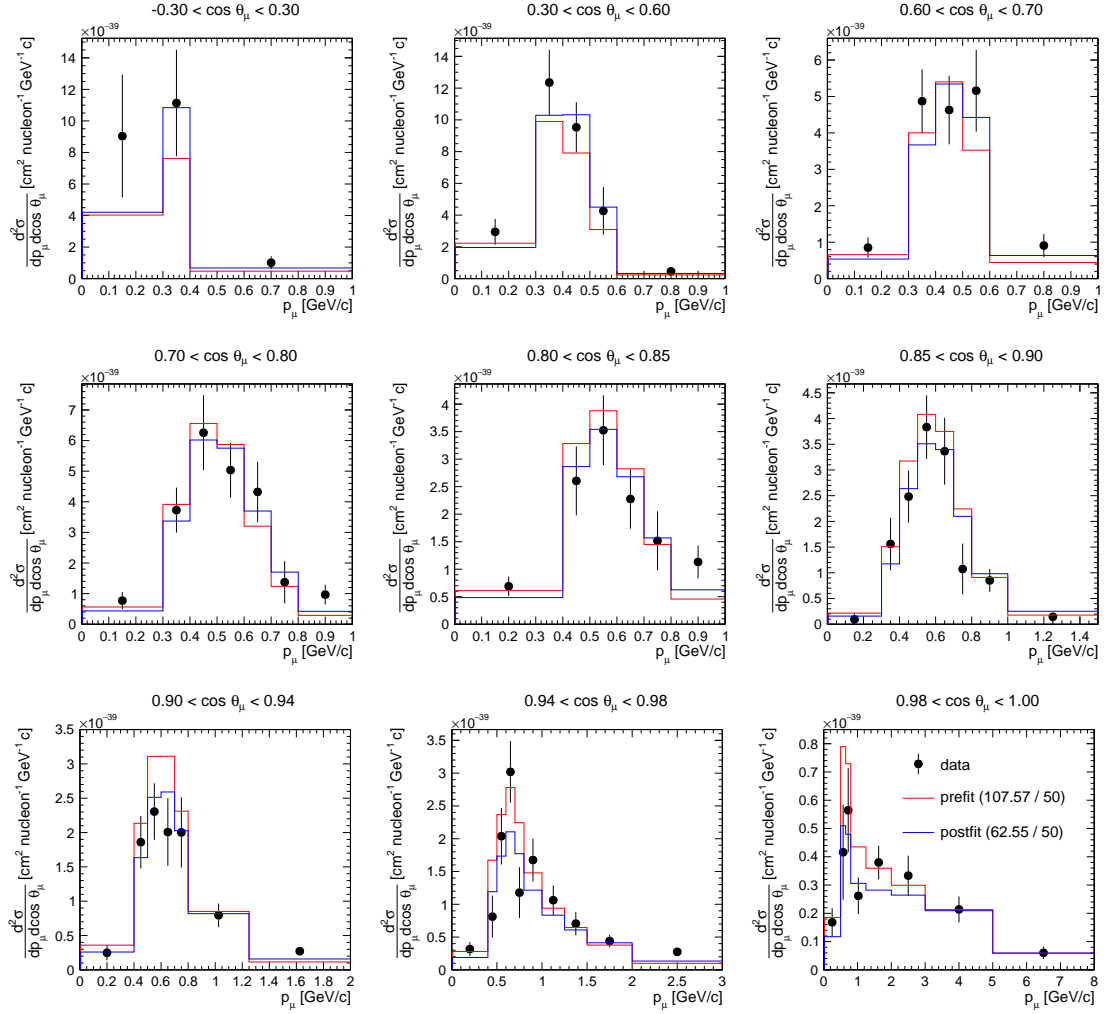


Figure 4.21: Prefit (red) and postfit (blue) distributions of  $p_\mu$  in bins of  $\cos\theta_\mu$  from fitting T2K CC0 $\pi$ 0 $p$  data only. The usual chi-squares as well as the number of bins are quoted in the legend. The NS chi-square  $\chi^2_{\text{NS}}$  used in the minimization is reported in Table 4.3.

## Chapter 4. Uncertainties in the charged-current quasielastic interactions

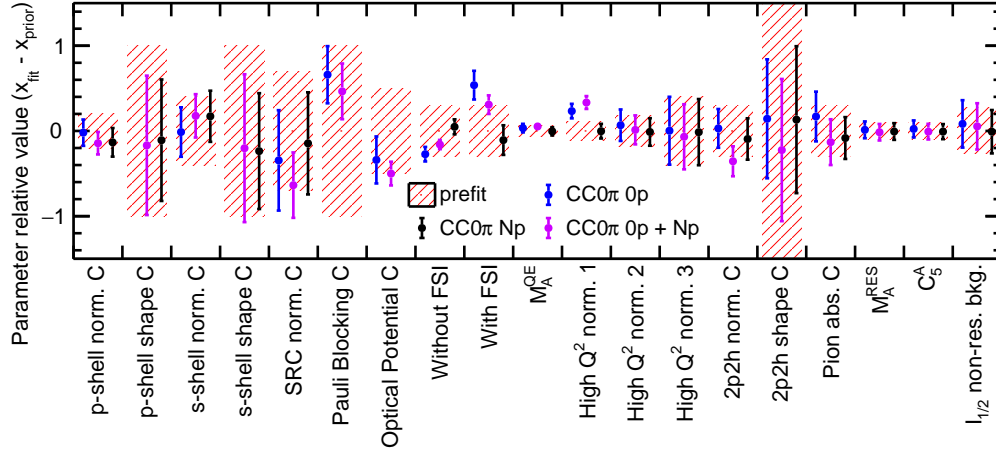


Figure 4.22: Prefit (red) and postfit (blue) values and constraints on the uncertainties from the fit to T2K  $\text{CC}0\pi 0p$  measurement of lepton kinematics and  $\text{CC}0\pi Np$  measurement of  $\delta p_T$  on carbon.

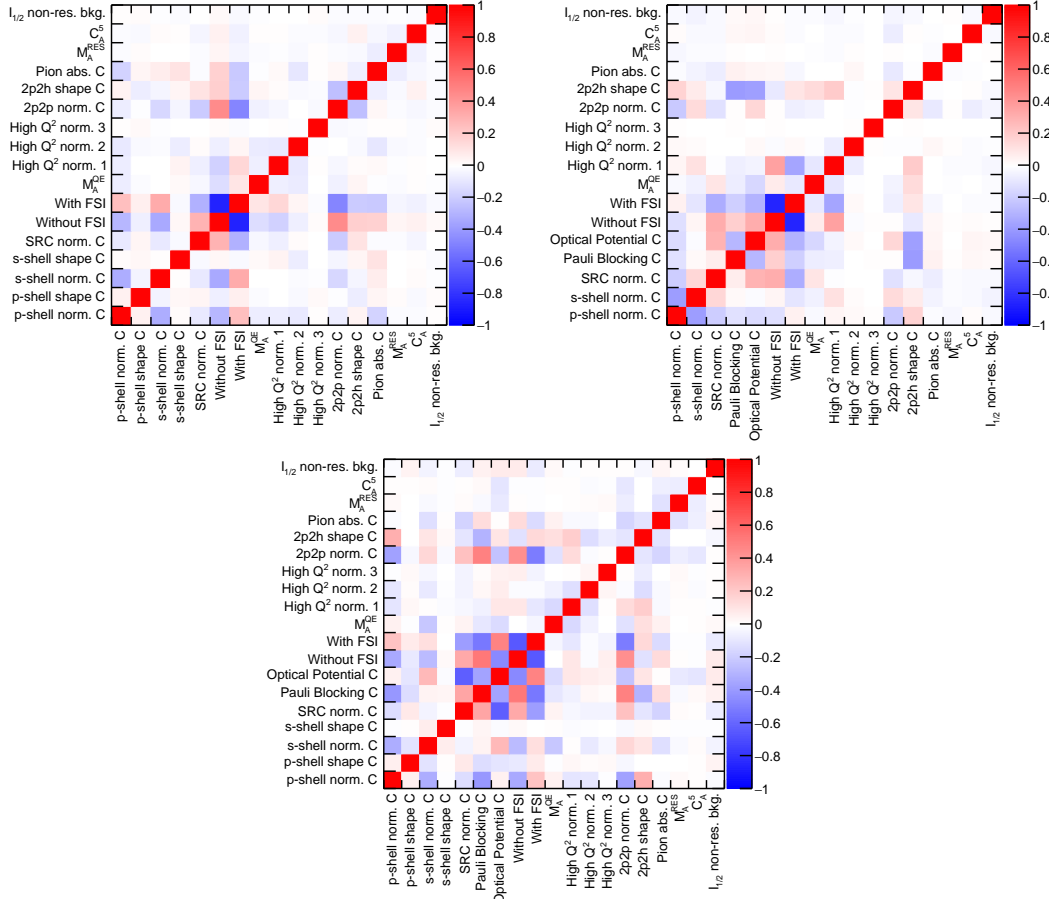


Figure 4.23: Postfit correlation matrices from the fit to T2K  $\text{CC}0\pi 0p$  measurement of lepton kinematics (top left) and  $\text{CC}0\pi Np$  measurement of  $\delta p_T$  (top right), as well as the simultaneous fit (bottom).

### Fit to MINERvA cross-section data in $CC0\pi Np$ topology on carbon

Result from the fit to MINERvA data is shown in the left panel of Figure 4.24. As suggested by the chi-square values quoted in Table 4.3, the prefit agreement between the model and the measurement is quite poor, and is only slightly improved in the postfit. Nevertheless, Figure 4.25 exhibits a clear sensitivity to most of the considered parameters, including the missing-momentum shape uncertainties. This is partially due to the significantly finer binning in the MINERvA data in comparison with the T2K measurement. This provides more precise probe of the nuclear effects that impact the  $\delta p_T$  distribution. In fact, as discussed in Section 4.1.2, the bulk is sensitive to Fermi motion which is mainly affected by the shell normalization and shape parameters (see Figures 4.6 and 4.8). On the other hand, its tail can be altered by SRC, 2p2h, CCRES and FSI uncertainties.

However, it is clear from the relatively high value of the postfit  $\chi^2_{\text{NS}}$  that the present parametrization of the SF model does not provide enough freedom to entirely cover discrepancies with the data. This can be attributed to the fact that, due to the higher energy of the MINERvA flux (see Figure 3.1), there is a significant contribution from the other interaction channels (like CCRES) through pion absorption which would need a more suitable parametrization. For instance, the predicted fraction of CCRES events by NEUT corresponds to almost  $\sim 20\%$  of the  $CC0\pi$  topology, which is below 10% in the case of T2K. This larger CCRES component is behind the tighter constraints on the Rein-Sehgal model parameters in comparison with the previous fits. The relatively poor agreement can also mean that the current parametrization of the CCQE model may need further improvements, especially for FSI effects.

The postfit correlation matrix for this fit is reported in the right panel of Figure 4.24. In comparison with the T2K  $\delta p_T$  fit, we can notice that the anticorrelation between the  $p$ - and the  $s$ -shell normalization parameters is less prominent thanks to the finer binning which alleviates their degeneracy with a more precise probe of the shape of the  $\delta p_T$  distribution. Besides, the SRC, 2p2h, FSI and CCRES uncertainties are correlated as expected since they affect the same high- $\delta p_T$  region.

## 4.4 Implications for oscillation analyses

In order to qualitatively estimate the impact of this new parametrization of the SF model for neutrino oscillation analyses, we can evaluate the constraints on the true neutrino energy as well as the  $E_\nu^{\text{QE}}$  bias. Figure 4.26 shows the prefit and postfit spectra and constraints for the distribution of true neutrino energy and the  $E_\nu^{\text{QE}}$  bias. This split is informative as it allows for a separation of the overall constraint placed on the total normalization of the cross section, which should be relatively independent of the uncertainty parametrization used, from the constraint placed on the shape of the distributions. These postfit (prefit) distributions are obtained using 500 distributions sampled from the posfit (prefit) values and covariance from the fit to the joint cross-section data on carbon and oxygen.

## Chapter 4. Uncertainties in the charged-current quasielastic interactions

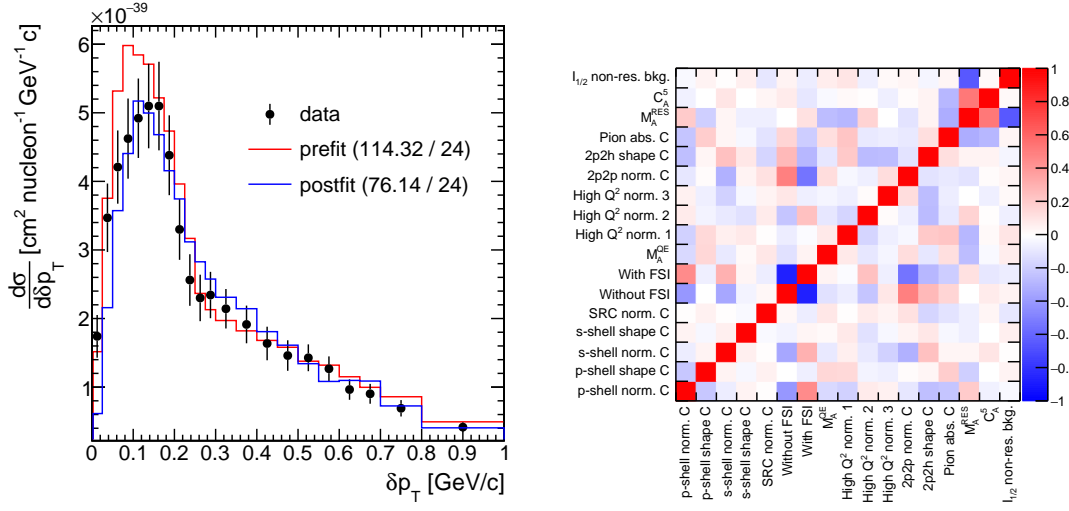


Figure 4.24: Left: prefit (red) and postfit (blue) distributions from the fit to MINERvA CC0 $\pi$ N $p$  measurement of  $\delta p_T$  on carbon. The usual chi-squares as well as the number of bins are quoted in the legend. The NS chi-square  $\chi_{\text{NS}}^2$  used in the minimization is reported in Table 4.3. Right: postfit correlation matrix between the parameters for the same fit.

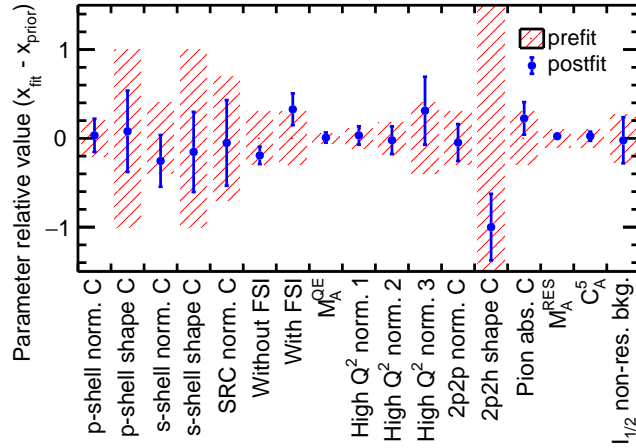


Figure 4.25: Prefit (red) and postfit (blue) values and constraints on the uncertainties from the fit to MINERvA CC0 $\pi$ N $p$  measurement of  $\delta p_T$  on carbon.

#### 4.4 Implications for oscillation analyses

Measurement	Prefit $\chi^2_{\text{NS}}$	Postfit $\chi^2_{\text{NS}}$	Number of bins
T2K oxygen + carbon	110.88	35.895	58
T2K CC0 $\pi$ Np $\delta p_T$ only	12.59	7.37	8
T2K CC0 $\pi$ 0p ( $p_\mu, \cos\theta_\mu$ ) only	144.35	87.165	50
T2K CC0 $\pi$ 0p + CC0 $\pi$ Np	144.35 + 14.56	86.80 + 10.01	50 + 8
MINERvA $\delta p_T$	109.10	79.51	24

Measurement	Prefit $\chi^2$	Postfit $\chi^2$	Number of bins
T2K oxygen + carbon	98.79	29.70	58
T2K CC0 $\pi$ Np $\delta p_T$ only	15.72	8.48	8
T2K CC0 $\pi$ 0p ( $p_\mu, \cos\theta_\mu$ ) only	107.57	69.41	50
T2K CC0 $\pi$ 0p + CC0 $\pi$ Np	107.57 + 16.76	64.19 + 11.83	50 + 8
MINERvA $\delta p_T$	114.32	76.14	24

Table 4.3: Summary of the prefit and postfit NS chi-square  $\chi^2_{\text{NS}}$  used in the minimization (top) as well as the usual  $\chi^2$  given by Equation (4.3) (bottom) for the different fits along with the corresponding number of bins.

The postfit constraints on  $E_\nu$  are significantly reduced in comparison with the prefit ones as shown in the top left panel of Figure 4.26. This is more visible in the bottom left panel for the bias of  $E_\nu^{\text{QE}}$  particularly around the true  $E_\nu$  (i.e. around 0 in this plot), which is the region that is most affected by CCQE events and the SF model. The negative tail, more affected by multinucleon effects and CCRES interactions, is only slightly impacted since the data used in the fit has only a small component of these interactions. It is also clear from the bottom-right plot of Figure 4.26 that the uncertainty model we introduced in this chapter offers significant freedom in the shape of the neutrino energy bias and that this is well constrained from the fit to the T2K cross-section measurement. On the other hand, the top-right plot shows that the freedom in the shape of the neutrino energy dependence of the cross section is fairly limited and is not strongly constrained by the fit.

The postfit (anti)correlations from the various fits indicate that the available data is not sufficient to disentangle the different effects. For instance, the fits previously shown to T2K  $\delta p_T$  data suggest that more statistics in  $\delta p_T$  measurements could provide more stringent constraints on effects that are distinct from those probed by the lepton kinematics.

Such measurements will be possible thanks to the new detectors like the Super-FGD in the upgrade of the T2K near detector, which we will extensively discuss in the next chapters of this thesis. Its fine-grained design will allow us to precisely measure the kinematics of the hadronic products from neutrino interactions, enabling for instance the reconstruction of protons with momenta down to 300 MeV/c. Reference [240] used a simplified version of the SF



## Chapter 4. Uncertainties in the charged-current quasielastic interactions

---

model uncertainties to estimate the performances of the upgrade. In Chapter 9, we will further show quantitatively the expected improvements of the constraints on the nuclear effects with the parametrization introduced in this chapter in the context of the T2K oscillation analysis. We will demonstrate how larger statistics in both the  $CC0\pi0p$  and the  $CC0\pi Np$  samples probe at an unprecedented level of precision these uncertainties (and beyond) thanks to not only measurements of the single-transverse variables, but also an improved estimator of neutrino energy based on the sum of muon energy and nucleon kinetic energy. We will also show the potential impact on the sensitivity to the oscillation parameters.

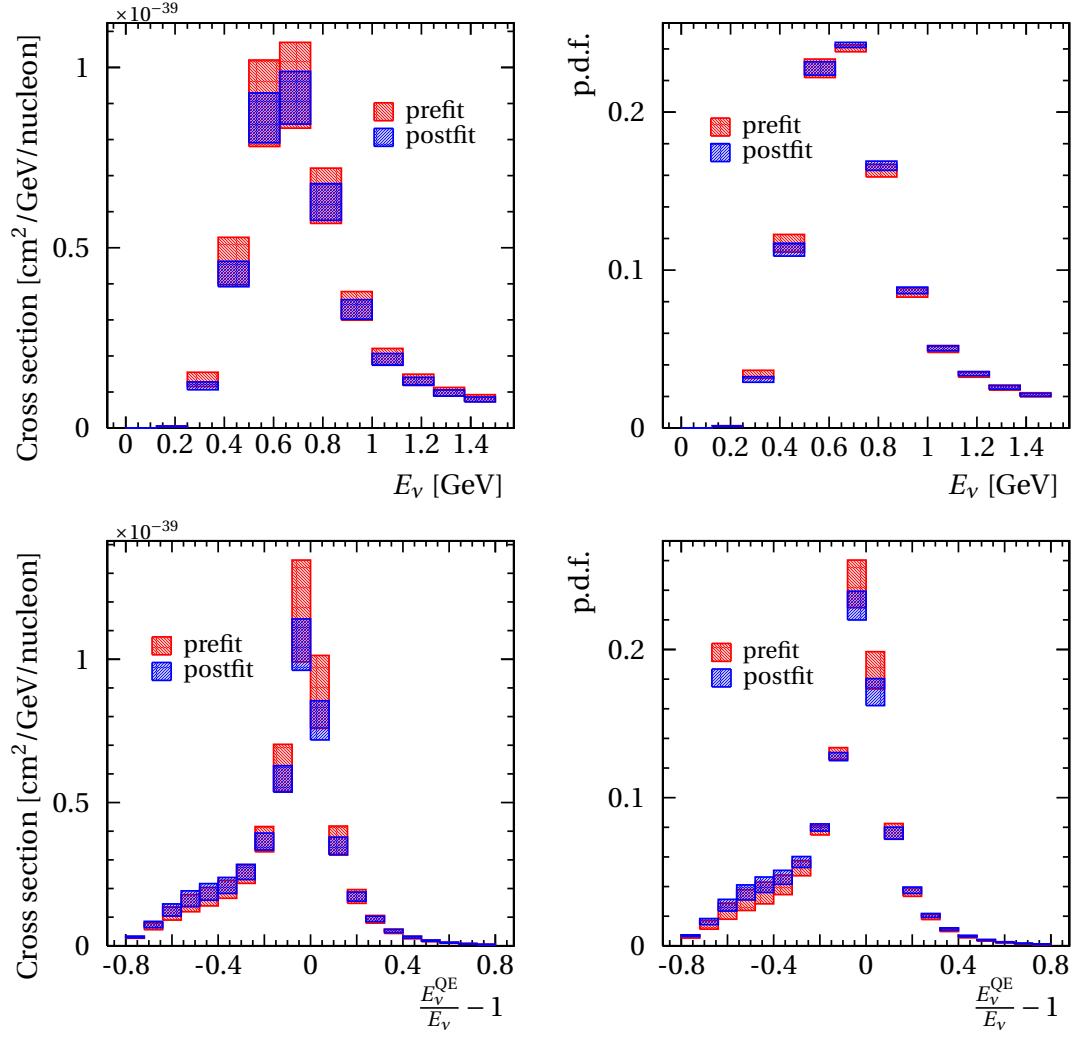


Figure 4.26: Prefit (red) and postfit (blue) constraints on the true neutrino energy (top) and the bias of  $E_\nu^{\text{QE}}$  (bottom) for carbon from the fit to the T2K CC0 $\pi$  joint measurement of lepton kinematics on carbon and oxygen. The plots on the left show the overall constraint on the cross section, while the plots on the right indicate the constraint on the shape of the distribution.



## **Upgraded near detectors**

### **Part III**



## 5 T2K near detector upgrade

With its initial setup, the T2K experiment provided a wealth of world-leading measurements of neutrino oscillations and cross sections and reached multiple milestones. To name a few, it was the first experiment to show evidence of electron neutrino appearance in its muon neutrino beam, thus excluding the  $\theta_{13} = 0$  hypothesis and opening the door to probe  $\delta_{\text{CP}}$ . More recently, it showed the first hints of CP violation in the lepton sector. And now, T2K has started a new phase of data taking with an increased beam power until the beginning of Hyper-Kamiokande in 2027. Hyper-Kamiokande will provide a generational leap in oscillation physics thanks to the large statistics it is expected to collect. This will require a better control over the systematic uncertainties, particularly those related to neutrino interactions. Therefore, an upgrade of the near detector is currently ongoing to make the most of this data taking phase until 2027.

This upgrade targets the limitations of the existing ND280 and will allow us to further probe nuclear effects relevant to the oscillation analysis thanks to its capabilities of full polar angle acceptance, lower proton tracking threshold as well as reconstruction of neutron kinematics. In this chapter, we review the T2K near detector upgrade. First, Section 5.1 describes the limitations of the current ND280 and the motivations for an upgrade. Then, Section 5.2 introduces the new detectors of this upgrade. Finally, Section 5.3 summarizes the main tests of prototypes that confirmed this new hardware design and Section 5.4 gives an overview of the expected physics performance of this upgrade.

### 5.1 Limitations of the current ND280

The current ND280 detector, presented in Section 2.2, is well suited for the measurement of charged particle tracks in the same direction as the incoming neutrinos ( $z$  axis in Figure 2.7). This is achieved thanks to the three vertical TPCs and the XY layers in the FGDs. However, the efficiency decreases rapidly for higher angles as shown in the left panel of Figure 5.1. Particles produced in the FGDs at around  $\sim 90^\circ$  from the beam direction cross only a limited number of scintillator bars and might not even cross the TPCs, making their reconstruction complicated. Besides, the backward-going muons naturally tend to be of low momentum, which means

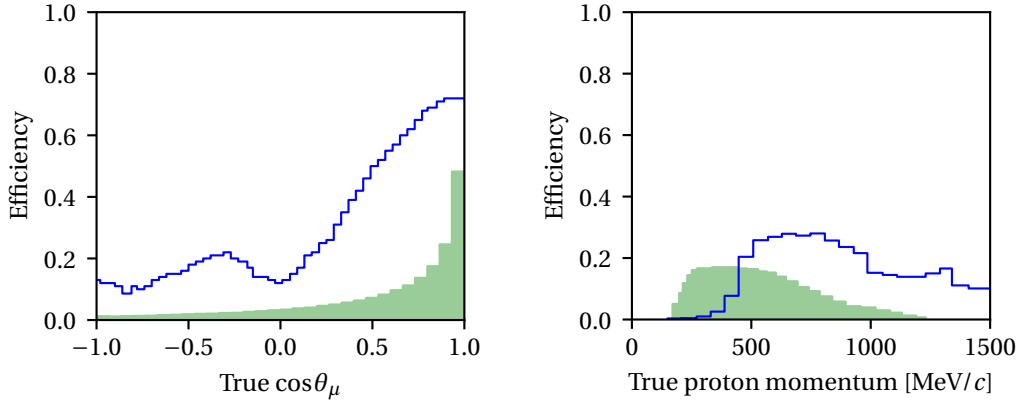


Figure 5.1: Reconstruction efficiency of the muon as a function of the cosine of its angle with respect to the neutrino direction in the  $CC0\pi$  selection (left) and of the proton as a function of its momentum in the  $CC0\pi Np$  selection (right) in the current ND280 (blue) compared to the NEUT-predicted distributions (green).

that their tracks are relatively short and thus difficult to reconstruct.

The far detector Super-Kamiokande on the other hand has a more isotropic efficiency. This is displayed in Figure 5.2 where we clearly see that Super-Kamiokande (right) observes a higher fraction of events at large angles in comparison with ND280 (left). This compromises to some extent the power of ND280 to constrain neutrino interaction uncertainties since it is only able to cover a fraction of the phase space of the measured neutrinos at the far detector. It is important to mention that, regardless of the acceptance of the detectors, most of the charged-lepton tracks are forward at ND280 due to the closeness to the beam production source (see left panel of Figure 5.1), whereas at Super-Kamiokande the beam is far more angularly extended and as such the direction of the produced charged leptons is relatively spread across all directions (see e.g. data points in Figure 7.4).

Furthermore, most of the interaction events at ND280 have only one visible track corresponding to the muon, while the hadronic part is often undetected. The threshold for proton detection is relatively high, at  $\sim 450$  MeV/ $c$  as shown in the right panel of Figure 5.1, and the corresponding efficiency is  $\sim 30\%$  at best. This allows us to only detect a small fraction of the events that produce protons. While this allows for interesting (but limited) cross-section measurements as the ones studied in Chapter 4, the samples used in the oscillation analysis are defined using the muon kinematics only as we will discuss in Chapter 7 due to these limitations.

The upgrade project aims at overcoming these limitations. It consists of three subdetectors that we will present in the next section, placed where the PØD was located (see Figure 2.7). It was estimated that removing the PØD and replacing it with these new subdetectors will significantly improve the overall performance of the T2K near detector. As mentioned in Sec-

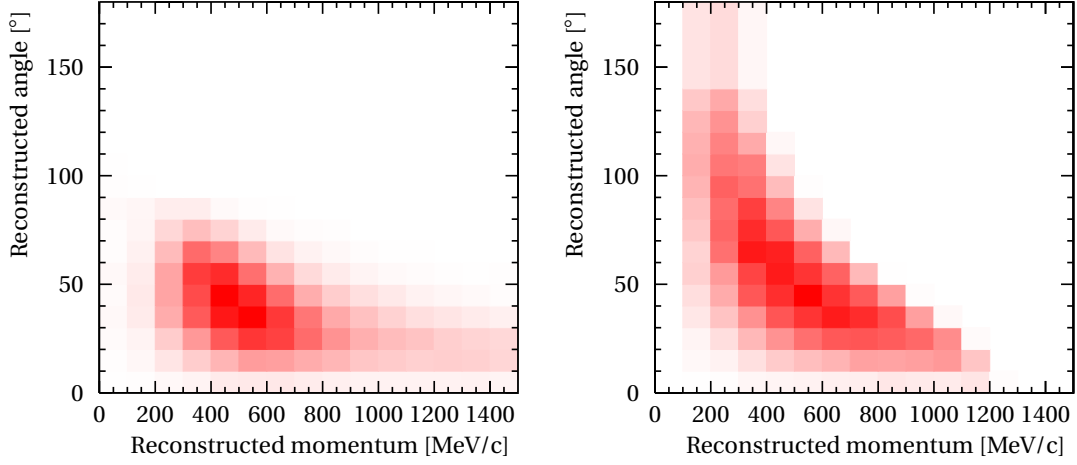


Figure 5.2: Two-dimensional distributions of the reconstructed momentum and angle of the charged lepton from  $\nu_\mu$  interactions at ND280 (left) and  $\nu_e$  interactions at Super-Kamiokande (right).

tion 2.2, the initial goal of the PØD was to estimate the  $\pi^0$  production in neutrino interactions to constrain the corresponding background in the  $\bar{\nu}_e$  samples at Super-Kamiokande. However, the data collected with this detector in the past  $\sim 10$  years is limited by systematic uncertainties, and more data would not necessarily improve the results. Furthermore, the analysis developments have allowed for a relatively good control over this background and reduced its significance for the oscillation analysis. Besides, the capabilities of the PØD are limited to measure the charged particles from CC interactions that are crucial for the oscillation analysis as the lead used to tag neutral pions in the PØD make its tracking ability quite poor due to its high radiation length. Consequently, this detector was removed in October 2022, freeing up the space for the installation of new subdetectors within the UA1 magnet.

## 5.2 Subdetectors

In this section, we review the three subdetectors that form the upgrade. These are the Super-FGD, the high-angle TPCs (HA-TPCs), and the time-of-flight (ToF) detector. These are displayed in Figure 5.3. The Super-FGD is located between the two HA-TPCs placed above and below it, and the whole system is surrounded by 6 planes of the ToF.

### 5.2.1 Super-FGD

#### Overview

The Super-FGD was designed with the main goal of lowering the momentum threshold for hadron tracking in a fully active target and offering an improved spatial resolution to identify



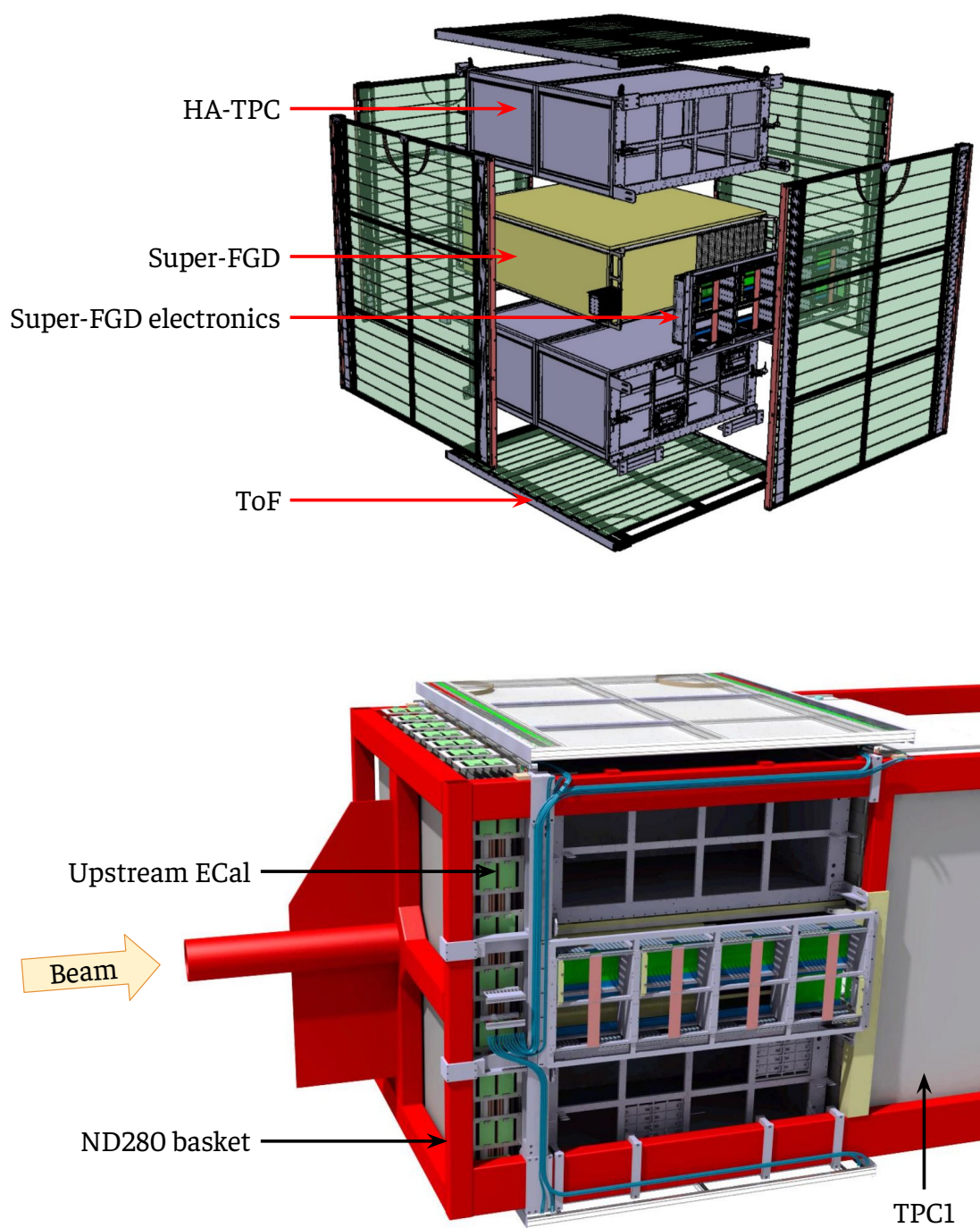


Figure 5.3: Illustrations of the near detector upgrade in an exploded view (top) and within the ND280 basket where one of the ToF panels is not shown to display the inner components of the detector (bottom). The neutrino beam comes from the left to the right.

the particles with short tracks near the neutrino interaction vertex in all the directions. It was proposed as an evolution of the technique used in the existing FGDs of ND280 which rely on bars with alternating XY orientations. This novel concept consists of replacing the bars read by a single WLS fiber with an ensemble of finer plastic scintillator cubes, each read in three orthogonal directions by WLS fibers as illustrated in Figure 5.4.

The final design of the Super-FGD is shown in Figure 5.5 and consists of  $182 \times 192 \times 56$  cubes, each of 1 cm per side. This amounts to around two million cubes, which corresponds to a total active mass of  $\sim 2$  tons comparable to the mass of the two FGDs combined. The cubes are covered with a reflective coating, and are read by 55,888 WLS fibers with silicon photomultipliers positioned at one end of each fiber to collect the light they carry. This allows us to obtain three two-dimensional “images” of the tracks, which can be used to reconstruct them in three dimensions as shown in Figure 5.6 and done for instance in Reference [241]. This is often called a *quasi*-3D readout because of the geometrical ambiguities that can remain when reconstructing the full three-dimensional track from the two-dimensional projections. An LED-based light injection system is located at the other end of each fiber, which is used to calibrate the electronics as we will discuss below.

### Cube production and assembly

The production of the two million cubes was performed by Uniplast in Russia using injection molding. Each cube is then covered with a reflective layer by etching its surface with a chemical agent that results in the formation of a white polystyrene micropore deposit. After that, three orthogonal through-going holes are drilled in the cube with a diameter of 1.5 mm, which is 0.5 mm larger than the nominal WLS fiber diameter.

The size of the cubes need careful monitoring as any small excess can quickly add up and significantly impact the final dimensions due to the large number of stacked cubes. Prior to the full production, around 10,000 cubes were manufactured for testing and prototyping purposes (see Section 5.3.1). Metrology studies were carried using a digital micrometer and showed that the cube side length is  $10.29 \pm 0.023$  mm [243]. The position of the drilled holes was also monitored and the variations were found to be around  $\sim 0.1$  mm, which is not concerning due to the free gap between the 1.5 mm hole and the 1 mm fiber. This confirmed the production technique of the cubes and gave the green light for the full-scale production. It was at a rate of 100,000 cubes per month, and took over a year with the last batch delivered in the end of 2020.

The main challenge in the assembly is the possible offsets in the hole position between adjacent cubes due to the stacked variations of the cube side lengths. If this offset is larger than 0.2 mm, then the fiber can be jammed and break during the insertion. Consequently, the preassembly of the cubes used fishing lines, i.e. plastic threads of 1.3 mm diameter, to join them in 56 layers of  $182 \times 192$  cubes as shown in Figure 5.7. Afterwards, the layers would be inserted in the Super-FGD mechanical box and the fishing lines replaced with the WLS fibers for the final assembly. The larger diameter of the fishing lines is chosen to allow for a smooth

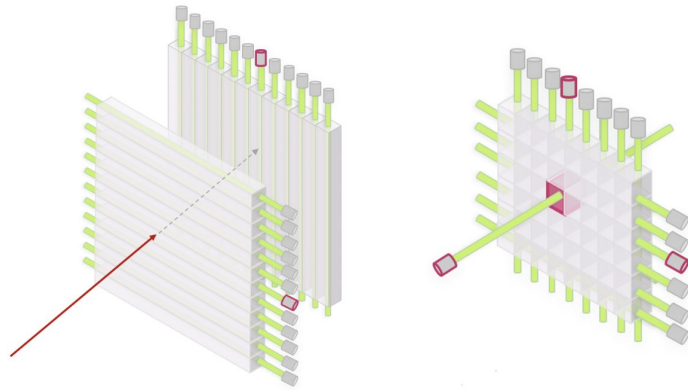


Figure 5.4: Comparison of the XY bars used the FGDs (left) and the novel concept of cubes in the Super-FGD (right). Figure from Reference [242].

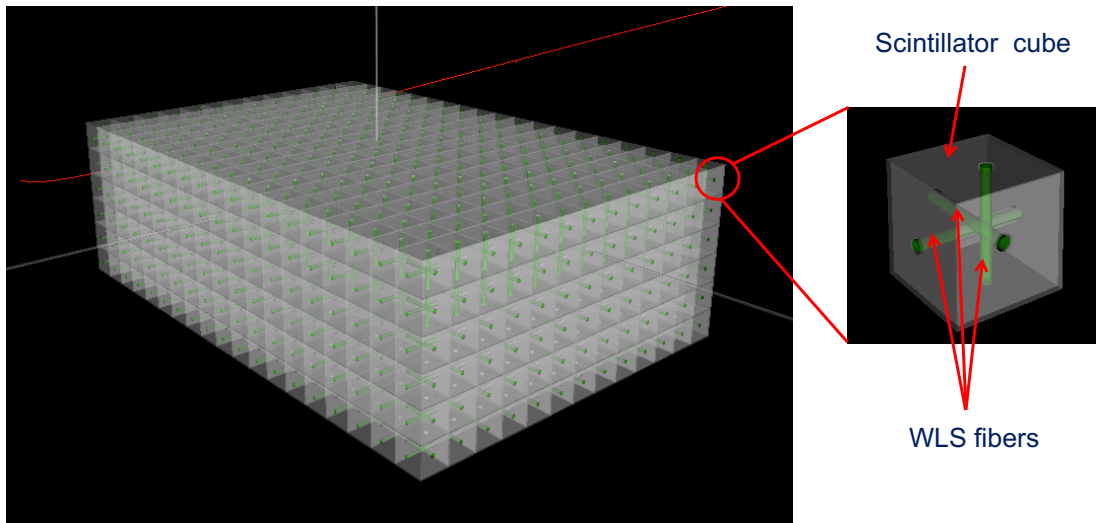


Figure 5.5: Schematic representation of the Super-FGD. Figure from Reference [243].

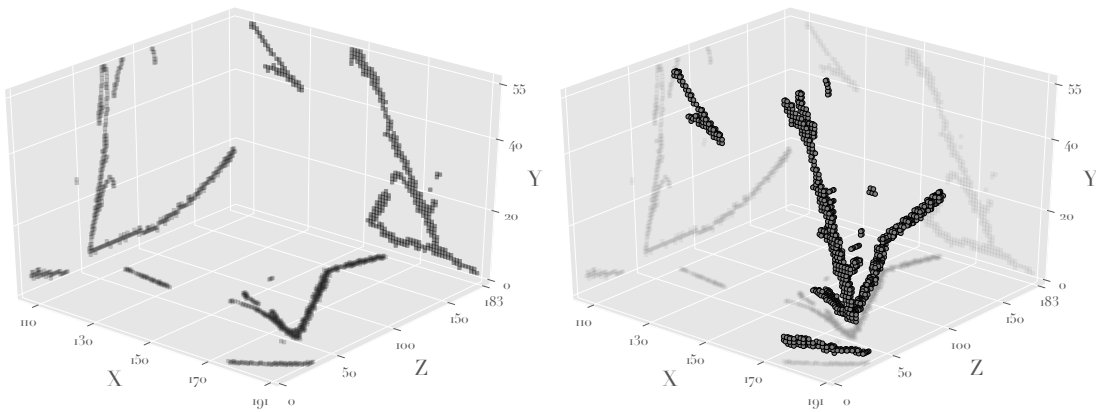


Figure 5.6: Left: the three two-dimensional views of a neutrino interaction the Super-FGD. Right: the reconstructed tracks in three dimensions. Figure from Reference [241]

replacement by the WLS fibers. The preassembly in layers with fishing lines was completed in early 2021, and the layers were placed in a wooden box for shipment to J-PARC.

### **Super-FGD box**

The cubes of the Super-FGD are arranged in a box that is strong enough to hold the 2 ton detector, and small enough to minimize the dead volume and leave enough space for the HA-TPCs (see Figure 5.3). The panels of this mechanical box are designed using carbon fiber with drilled holes for the WLS fibers and the silicon photomultipliers. As will be shown in Figure 6.1, these photosensors are arranged as groups of 64 in printed circuit boards, which will be screwed on this box once it is closed.

The cube layers are positioned one by one into the mechanical box as displayed in Figure 5.8. For each layer, the fishing lines are inserted through the corresponding hole in the box which ensures the horizontal alignment. The vertical alignment of the holes is guaranteed with metallic rods which are passed vertically through a portion of the holes for each added layer. The layers were all inserted and the box was closed (once and for all) by the end of 2022. The following step is to simply replace the fishing lines with the WLS fibers. This proceeded rather smoothly thanks to the accurate alignment between the holes and the larger diameter of the fishing lines.

To check the quality of the light yield from each fiber, a source injects LED light in one end of the fibers and a dedicated photosensor system measures it at the other end. Only few fibers needed replacement due to damages during the insertion. After confirming that all the fibers are correctly inserted, the silicon photomultiplier boards (Figure 6.1) were screwed and the calibration system was installed.

### **Calibration system**

As we will detail in Chapter 6, a channel-by-channel gain calibration of the electronics is necessary for robust measurements of the energy deposition. In the Super-FGD, the silicon photomultiplier is located at one end of the WLS fiber, while at the other end a light source for the calibration is placed. Given the space constraints, this system needs be of a few-centimeter thickness only.

The idea of the light guide plate (LGP) pursued for this system followed the LED calibration system of the hadron calorimeter of CALICE [244]. As illustrated in Figure 5.9, it consists of an array of LEDs mounted on one end of the a transparent plate with “notches” on its bottom surface and a diffuser for a more uniform light distribution on the WLS fibers. In Section 6.2.2, we will discuss in detail the calibration procedure of the channel gains that will be performed in the Super-FGD.

The installation of the LGP modules and the photosensor boards around the Super-FGD box



Figure 5.7: Preassembly of the Super-FGD layers with fishing lines. Credits: M. Khabibullin.

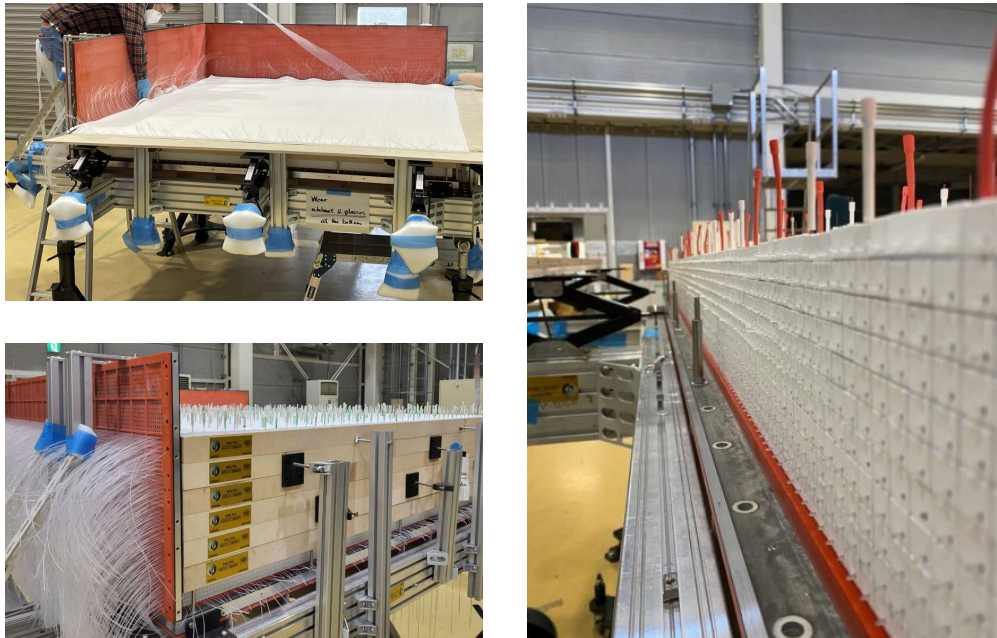


Figure 5.8: Assembly operation of the Super-FGD cubes into the mechanical box.

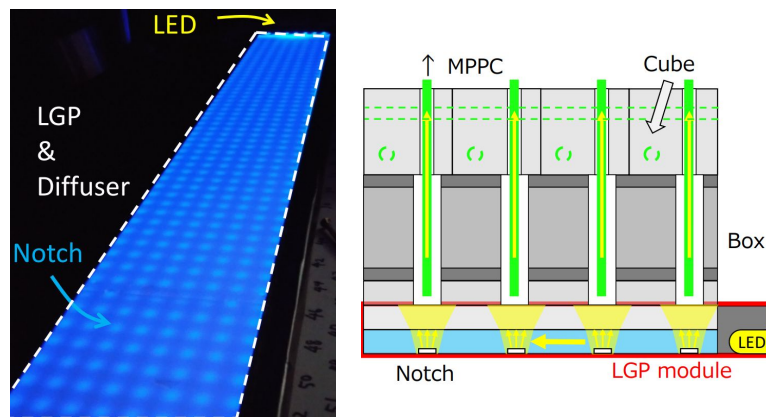


Figure 5.9: Light guide plate for the gain calibration of the Super-FGD electronics.



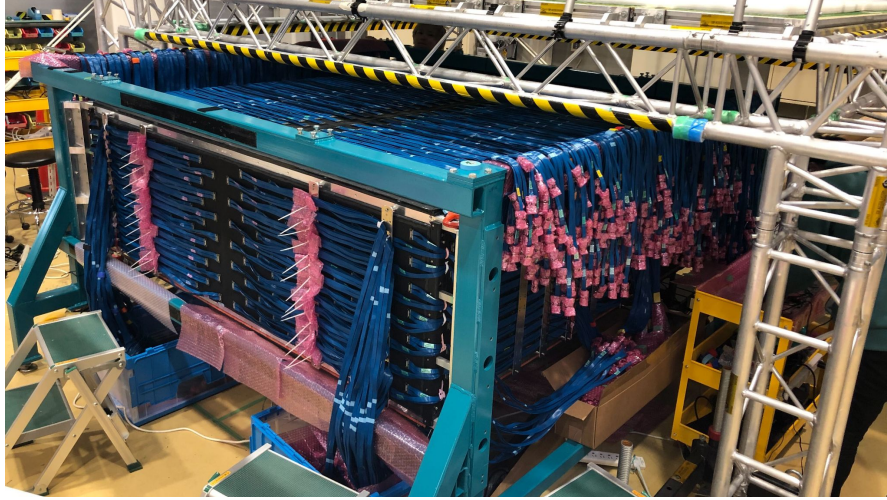


Figure 5.10: Super-FGD with its cabled photosensor boards.

was achieved early March 2023, and the cabling of the photosensors was performed through April 2023. Figure 5.10 shows a picture of the cabled Super-FGD. The following step is naturally the installation of the electronics in the crates that can be seen in Figure 5.3. This is planned by the summer of the same year, and the architecture of the Super-FGD electronics will be discussed in great details in Chapter 6.

### 5.2.2 High-angle time projection chambers

#### Overview

The upgrade also comprises two horizontal TPCs as displayed in Figure 5.3, which surround the Super-FGD from its bottom and top. The available space is significantly limited in comparison with the three vertical TPCs of ND280, making their design more challenging. In fact, the requirements for these TPCs is a similar performance of the existing ones, as they have provided completely satisfactory capabilities, but within the smaller space. These requirements are:

- a momentum resolution below 10% for 1 GeV/ $c$  charged particles, which corresponds to a spatial resolution of  $\sim 800\text{ }\mu\text{m}$  in the 0.2 T magnetic field,
- a resolution on the energy loss below 10% to allow for a clear separation between muons and electrons.

The design of these new HA-TPCs is similar to that of the current TPCs, with particularly two improvements. The first improvement is the optimized field cage with a design that minimizes the dead space and maximizes the tracking volume. The second improvement is the use of resistive Micromegas instead of the standard bulk Micromegas.

### Design

The two HA-TPCs are identical, and their design is displayed in Figure 5.11. Each HA-TPC comprises a drift volume enclosed within a field cage, separated at the center by a cathode. The two ends opposite to the cathode correspond to the anodes where 8 encapsulated resistive anode Micromegas (ERAM) modules per side are mounted on the frame displayed in Figure 5.11. Copper strips on the inner surface of the box, joined by precision resistors to form a voltage divider, ensure the uniformity of the electric field and the accuracy of the field gradient.

### ERAM modules

The standard bulk Micromegas technology, sketched in Figure 2.11, was designed as early as 2004 and used in the existing vertical TPCs. In this design, the charge is often deposited on a single pad, which means that the width of the pad is the limiting factor in the spatial resolution. One way to mitigate this limitation is proposed with the resistive Micromegas in the ERAM modules as displayed in Figure 5.12. This consists of covering the segmented pads using a foil of insulating material with a resistive layer on its top. When the electrons drift to the mesh and create an avalanche within the amplification gap, this avalanche is quenched due to the local drop of the potential difference in the presence of a high charge density. The resistive layer forms a two-dimensional resistor-capacitor (RC) network with respect to the anode plane, causing an induced signal on the adjacent pads. This charge spread over multiple pads is the major benefit of the ERAMs as it significantly improves their spatial resolution.

Furthermore, with the ERAMs, it is possible to match the performances of the bulk Micromegas with a reduced pad density and consequently a lower number of readout channels. The ERAMs consist of 1152 pads per module, which is 2/3 of the number of pads in the Micromegas of the existing TPCs. On the other hand, the resistive layer significantly reduces the Micromegas discharges, or sparks, which allows us to eliminate the antispark protection circuitry necessary for the front-end electronics with the standard bulk Micromegas. Removing this circuitry also reduces the amount of dead space on the readout plane.

Following the extensive tests at CERN and DESY starting from 2018 to optimize the design (see Section 5.3.2), the pre-series and series production of the ERAMs began in 2021. In September 2022, a first half of a HA-TPC was completed and tested at CERN. The bottom HA-TPC, fully populated with the ERAMs and the readout electronics, is expected to be ready in July 2023 and installed in the ND280 basket. The Super-FGD installation can be carried out afterwards, while the top HA-TPC is expected to be delivered to J-PARC later in September 2023.

### Readout electronics

As shown in Figure 5.11, each side of an HA-TPC consists of 8 ERAM modules. Figure 5.13 displays an exploded view of an ERAM module with its front-end electronics. The Micromegas

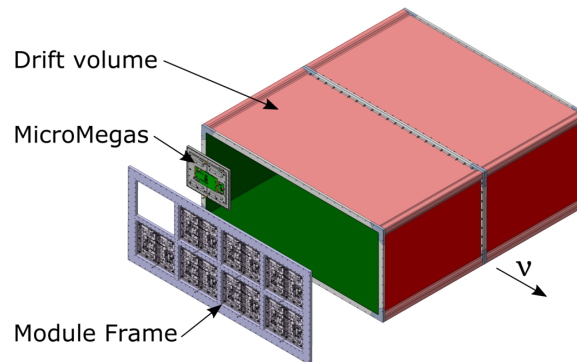


Figure 5.11: Illustration of the HA-TPC design. Figure from Reference [243].

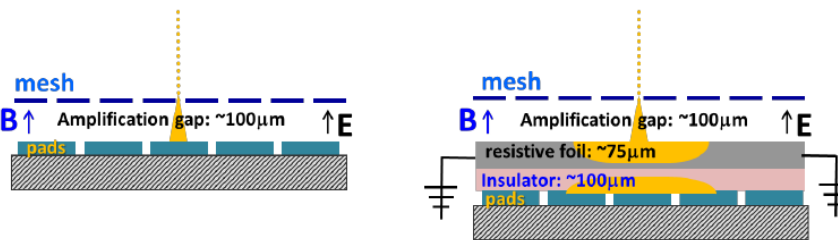


Figure 5.12: Left: standard bulk Micromegas used in the existing TPCs. Right: resistive Micromegas with the additional insulating layer. Figure from Reference [243].

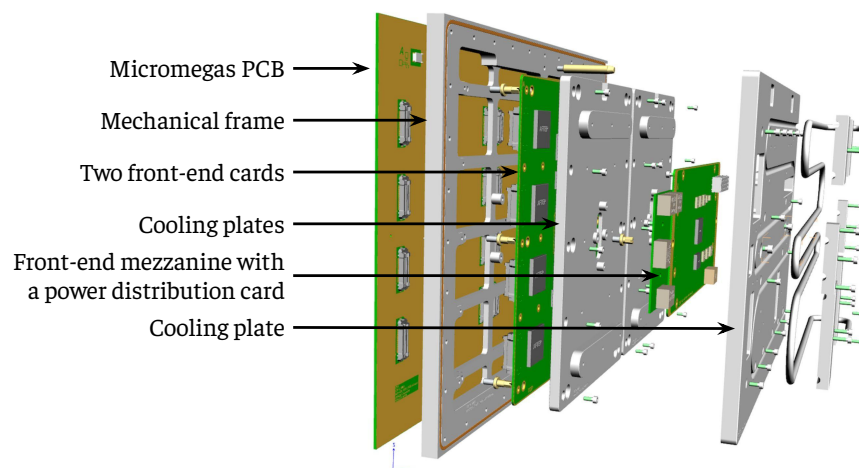


Figure 5.13: Exploded view of an ERAM module with its mechanical structure and readout electronics. Adapted from Reference [243].



are printed on a circuit board, which is glued to an aluminum mechanical frame to stiffen it and ensure a high level of planarity. Then two front-end cards, with 576 channels each, read the analog signal from the 1152 pads of the module and convert it using an analog-to-digital converter. The two cards are piloted by the front-end mezzanine that also performs initial data processing and stores data temporarily. A power distribution card converts the input voltage of 24 V to the 4 – 5 V used by the boards of the system. Aluminum plates are used for shielding and mechanical protection, but also as cooling plates to conduct the dissipated heat to the water pipe serpentine displayed in the right end of Figure 5.13.

In comparison with the existing TPCs, this setup is highly compact thanks to the simplifications introduced by the resistive Micromegas. In fact, the reduction of the number of channels and the suppression of the antispark protection circuitry allows us to mount the electronics in parallel to the detector plane, instead of the perpendicular configuration with the bulk Micromegas in the vertical TPCs due to the larger space required by its electronics.

The digitized output of each of the 16 modules in a single HA-TPC is transferred to a trigger and data concentrator module which collects the data and distributes the global trigger signals to the front-end electronics.

### 5.2.3 Time-of-flight detector

#### Overview

An important source of background in ND280 analyses is the tracks of charged particles produced outside of the detector fiducial volume. This particularly occurs because, when no timing information is available, the tracks are assumed to be forward. Furthermore, in many cases, even if this timing information is recorded, it does not allow for an unambiguous determination of the sense of motion due to the limited timing resolution of the subdetectors in ND280.

To avoid these limitations with this upgrade, a ToF detector is installed around the Super-FGD and the two HA-TPCs, forming a cage as illustrated in Figure 5.3. An unambiguous determination of the flight direction for charged particles requires a timing resolution below 500 ps. Besides, if this resolution can be further improved to 100 – 200 ps, it can also be used to improve the identification of particles, particularly in the discrimination between electrons and muon of energies 0.1 – 0.3 GeV as well as protons and positrons at 1 – 2 GeV which is not possible using only the ionization energy loss.

#### Design

Each panel of the ToF consists of 20 cast plastic scintillator bars (EJ-200) of  $12 \times 1 \times 230 \text{ cm}^3$  size. A total of 16 silicon photomultipliers read the scintillation light at both ends of each bar. The choice of the EJ-200 cast plastic scintillator was motivated by its high light yield, low

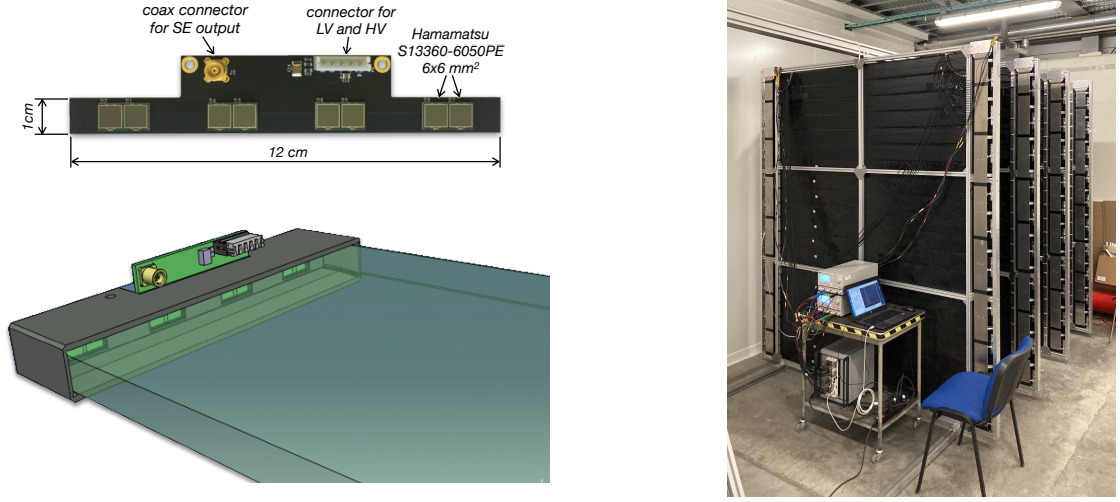


Figure 5.14: Left: printed circuit board with the 8 photosensors (top) and its setup on one end of the scintillator bar (bottom). Right: picture of the assembled ToF panels. Figure from Reference [247].

attenuation length, fast timing, and also its light spectrum more centered around the green in comparison with other options which corresponds to a higher photon detection efficiency of the photosensors. The 20 bars are arranged in a plane that covers an area of 5.4 m<sup>2</sup>. A picture of the assembled planes is shown in the right panel of Figure 5.14.

The selected photomultipliers are the Hamamatsu S13360-6050PE [245], which are soldered in groups of four pairs on a printed circuit board and positioned at one end of the bar as shown in the left panel of Figure 5.14. The main criteria for the acquisition system is its internal time resolution, which needs to be significantly better than the scintillator resolution. The readout of the photosensor signal employs a waveform and time digital converter chip called SAMPIC [246]. It is a 16-channel chip that uses a novel type of digitization electronics that not only functions as a time digital converter, but also as a waveform sampler which allows for a precise timing measurement.

As will be discussed in Section 5.3.3, tests with a single bar of the ToF show that the achieved resolution is about  $\sim 130$  ps.

### 5.3 Tests and prototypes

The conception and design phase of the upgrade subdetectors consisted of a series of testing and prototyping to validate the concepts and tune the design parameters. In this section, we present a summary of the tests for each subdetector.

### 5.3.1 Super-FGD prototypes

After a small  $5 \times 5 \times 5$  prototype presented in Reference [248], a larger detector comprising 9216 cubes was developed in a  $24 \times 8 \times 48$  array as displayed in the left panel of Figure 5.15. It was built with the fishing line technique, and contained a reflective Tyvek sheet between the eight layers. Furthermore, it was equipped with three types of Hamamatsu silicon photomultipliers to study their performance, while the readout electronics used BabyMIND front-end boards. A custom LED system was used to calibrate the photosensors and the electronics as described in Section 6.2.2, which motivated the use of the LGP in the final Super-FGD design.

This prototype was placed during the summer of 2018 in the T9 beamline at CERN, within the MNP17 magnet<sup>1</sup> to provide a 0.2 T field as in ND280. The goal of these tests was to qualify the detector response and study its capabilities for various particles.

With the large number of recorded events, the response of the detector was studied in detail in Reference [249]. This particularly allowed us to quantify the optical cross talk between adjacent cube, estimated at  $\sim 3\%$  per side from the scintillating cube to its neighbors. In fact, their surface is not completely opaque even with the reflective layer. Another measured characteristic is the light attenuation in the WLS fibers by using the collected data and comparing the light yield along the 8-cm and the 24-cm long fibers. The timing resolution was also studied in Reference [250] using the 2 GeV/ $c$  muon tracks, and was found to be of 0.97 ns for one readout channel after a proper calibration, while averaging the timing information from  $N$  channels yields a  $\sim 1/\sqrt{N}$  improvement.

The other purpose of these tests is to study the ability of the detector to identify the different particles. In particular, one of the features of Super-FGD is to clearly identify the stopping protons thanks to their Bragg peak. The top panels of Figure 5.16 show an event display for an 800 MeV/ $c$  proton, where we can see clearly the large energy deposition at the stopping point. The detector can resolve this type of tracks, which is further demonstrated in the bottom panels Figure 5.16 that show a photon separation into an electron and a positron. The left panel of Figure 5.17 shows the average energy loss of the different particles along the beam direction. The pions and the muons, for which the ionization is closer to a minimum ionizing particle, show a more constant energy loss along their range, while the proton displays a larger loss as it gets closer to its stopping point. The right panel of Figure 5.17 also illustrates the difference in the response to the different particles when measuring the average light yield along the track.

Another, slightly smaller prototype, called the *US-Japan prototype* and displayed in the right panel of Figure 5.15, was also tested. It consists of an  $8 \times 8 \times 32$  array of cubes, read with the same type of photosensors as the final Super-FGD design. Along with the  $24 \times 8 \times 48$  prototype, they were exposed to a neutron beam with kinetic energies up to 800 MeV at the Los Alamos National Laboratory in 2019 and 2020.

---

<sup>1</sup>This is the same magnet used in the tests of the Super-FGD front-end board described in Section 6.3



Figure 5.15: Pictures of the  $24 \times 8 \times 48$  prototype (left) and the US-Japan prototype (right).

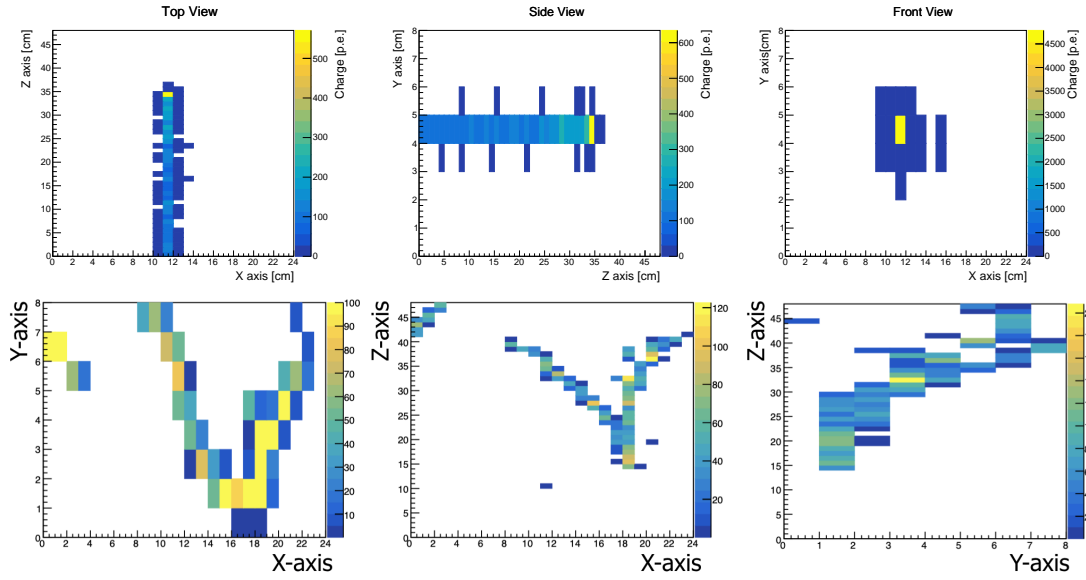


Figure 5.16: Event display from the three readout planes of a stopping proton (top) and a photon interaction (bottom). Figure from Reference [249].

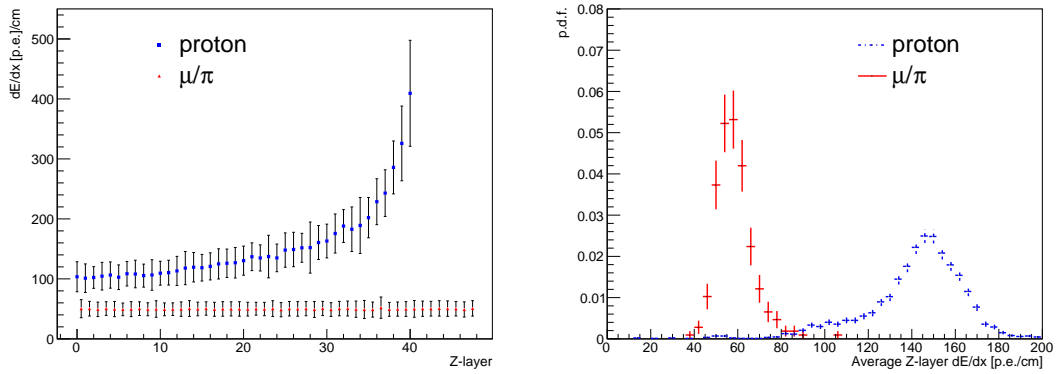


Figure 5.17: Energy loss along the beam direction (left) and the average energy deposit (right) for protons, pions and muons at 800 MeV/c. Figure from Reference [249].

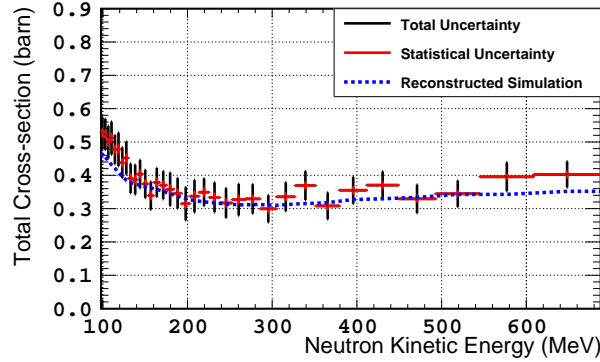


Figure 5.18: The total neutron-CH cross section as a function of the neutron kinetic energy, where the black (red) vertical bars represent the total (statistical) uncertainty. Figure from Reference [251].

Unlike charged particles, neutrons do not deposit energy when they cross the scintillator. However, they do interact with the detector nuclei which can produce charged particles that can be tracked. In this beam test, it was possible to evaluate the total neutron cross section on hydrocarbon with this type of detector [251]. This relied on the so-called *extinction method*, which corresponds to the fact that the neutron flux decreases as a function of the traveled distance within the detector. This attenuation allows us to express the event rate  $N$  as a function of the depth  $z$  in the detector as:

$$N(z) = N_0 e^{-T\sigma_{\text{tot}}z}$$

where  $N_0$  is the event rate at the first layer,  $T$  is the nuclear density and  $\sigma_{\text{tot}}$  is the neutron total cross section. This total cross section can be extracted simply by fitting the distribution of the event rate along the  $z$  axis with an exponential. By doing this for each bin of the neutron kinetic energy, we can obtain the total neutron-CH cross section as a function of neutron kinetic energy as displayed in Figure 5.18. The leading systematic uncertainty in this measurement was found to be related to the cube misalignment.

### 5.3.2 Beam tests of the high-angle time projection chambers

Multiple tests of the new concept of the resistive Micromegas which equip the HA-TPCs were carried at CERN and DESY between 2018 and 2021 [252–254]. Their goal is to characterize the performance of this design with various charged particles and fine-tune the detector parameters.

The first ERAM module prototype was tested at CERN with charged particles in 2018 [252]. It was located in the T9 beamline and measured protons, pions and electrons at 800 MeV/ $c$  with three different drift distances: 10, 30, and 80 cm. Figure 5.19 shows the achieved spatial (left) and energy loss (right) resolution for the tested particles. In the final HA-TPC design, the

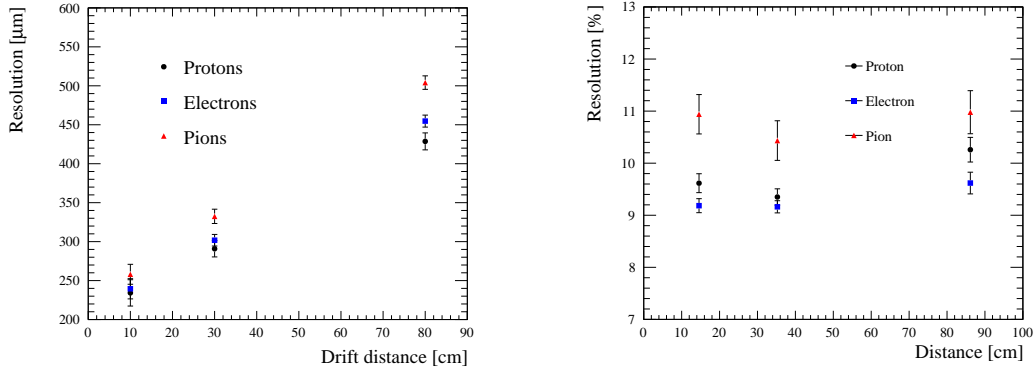


Figure 5.19: Spatial resolution (left) and energy loss resolution (right) as a function of the drift distance for the tested particles. Figure from Reference [252].

drift will be of 90 cm, and the spatial resolution is found well below the 800  $\mu\text{m}$  requirement. The resolution on the energy loss on the other hand is obtained at  $\sim 10\%$ . An excellent gain uniformity was also measured in the tests, and the data was used to characterize the charge spreading properties in this new Micromegas design. These performances fully satisfy the upgrade requirements.

The second ERAM module, tested at DESY in 2019, used the final layout for the HA-TPC, exposed to an electron beam of 4 GeV/c with and without the ND280 nominal 0.2 T magnetic field in a short chamber with 15-cm drift distance [253]. The goal was to validate the final design of the detector and precisely measure the resistivity of the ERAM module as a function of the pad position. The spatial and energy loss resolutions were also studied this time as a function of the track angle with respect to the ERAM plane. A dedicated clustering algorithm was developed for the non-horizontal tracks, and the attained spatial resolution is better than 600  $\mu\text{m}$  for all the angles. Similarly, an energy loss resolution below 9% was obtained, which is within the upgrade requirements. This allowed us to finalize the design and launch the production of the preseries of the ERAM modules after a final optimization of the RC constant of the detector, i.e. the amount of the insulator and the resistive foil shown in Figure 5.13.

In 2021, another test took place at DESY, but this time with the full length of one HA-TPC using the final ERAM module with the optimized charged spreading [254]. The preliminary results show that the requirements are fully satisfied for the upgrade, where the resolution on the energy loss is still below 10% and the spatial resolution is better than 800  $\mu\text{m}$  both for horizontal and inclined tracks.

### 5.3.3 Performance of the time-of-flight detector

The setup displayed in the left panel of Figure 5.20 is used to estimate the resolution on the crossing time of a charged particle with a single scintillator bar. Cosmic muons are used

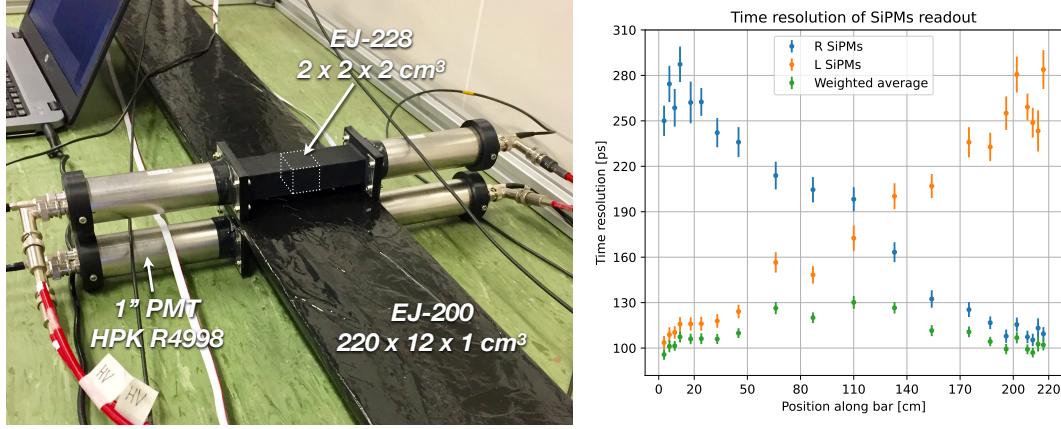


Figure 5.20: Left: setup to test the timing resolution from a single ToF bar. Right: timing resolution obtained from the photosensors at each end of the bar separately (blue and orange) and their weighted average (green).

for this test, where the trigger is formed by the coincidence of signals from two scintillator counters installed above and below the bar on a moving structure. The average of the timing recorded by the two counters is used as the reference for the measurements described below.

The measurement was performed on 21 positions along the 2 m bar, with about a day of exposure time at each position which results in  $\sim 600$  events per exposure. The signal recorded by the photosensors at each side of the bar is used to estimate the arrival time. The time corresponding to 10% of the signal amplitude was taken in the analysis. The right panel of Figure 5.20 shows the obtained time resolution. With a one-side measurement (orange and blue), the resolution varies from  $\sim 280$  ps from the furthest end of the bar to  $\sim 100$  ps at the closest position to the photosensors. By averaging the measurements from the two sides, the obtained overall timing resolution is below  $\sim 130$  ps. This not only satisfies the upgrade requirement, but also opens the door to using the ToF timing information to complement the particle identification capabilities of the detectors.

## 5.4 Expected physics performance

### 5.4.1 Muons

The goal of the upgrade is to measure neutrino interactions at a significantly improved precision in regions of the phase space kinematics that were not probed before at the near detector. First, as shown in the top left of Figure 5.21 for muons, the upgraded ND280 covers the full polar angle with a significantly improved acceptance (black) in comparison with the current ND280 (blue). This is particularly enabled thanks to the fine granularity along the non-horizontal direction, unlike the XY layers of the FGDs. The horizontal HA-TPCs also play a crucial role in tracking the charged particles that escape the Super-FGD at a large angle. The

expected event distributions from  $\nu_\mu$  interactions are also displayed in the bottom panels of Figure 5.21, and the phase space coverage with the upgrade (right) is clearly more important at high angles in comparison with the performance of the current ND280 (left). This better matches the acceptance at Super-Kamiokande as shown in the right panel of Figure 5.2.

Besides, the top panels of Figure 5.22 compare the resolution on the muon momentum in the current ND280 (Figure 5.22a) and in the upgrade (Figure 5.22b). Within the upgrade, this resolution varies from  $\sim 2\%$  for 200 MeV/ $c$  muons, which correspond to fully contained tracks within the Super-FGD, to  $\sim 8\%$  for 1 GeV/ $c$  where the resolution worsens since these muons escape the Super-FGD and the curvature of their track in the TPCs is small. This is significantly better than the  $\sim 11\%$  average resolution with the current ND280.

### 5.4.2 Protons

Another crucial improvement brought by this upgrade is the more precise tracking of the hadronic product of the neutrino interaction. In particular, as shown with the Super-FGD prototypes in Section 5.3.1, a contained proton has a clear signature with its Bragg peak where it deposits most of its energy at the stopping point. The fine granularity of the Super-FGD enables a lower threshold for detecting protons as displayed in the top right panel of Figure 5.21 (black) which is at  $\sim 300$  MeV/ $c$ . It also allows us to capture a more important fraction of the expected outgoing protons with a higher acceptance in comparison with the  $\sim 450$  MeV/ $c$  threshold with the current FGDs. This acceptance reaches its maximum at 80% for mid-range momenta and decreases for higher momentum protons due to the secondary interactions with the detector material that make the tracks ambiguous.

The bottom left panel of Figure 5.22 illustrates the excellent resolution on the proton momentum. It is around 5% at the detection threshold due to the shorter size of the tracks, while the best resolution is achieved for the range 500 – 1000 MeV/ $c$  at 2%, where the proton tracks can be clearly identified. For reference, the current ND280 has an average resolution of 9% on the proton momentum.

### 5.4.3 Neutrons

The granularity of the Super-FGD also offers the possibility to not only tag neutrons, but also estimate their kinematics as discussed in Reference [255]. Antineutrino interactions with nuclei often produce neutrons that are undetected in most of the oscillation experiments. Neutrino interactions can also occasionally produce neutrons, particularly due to CCRES and CCDIS interactions, although with a smaller rate in comparison with the antineutrino scattering. In the Super-FGD, this ejected neutron can be observed when it scatters on the hydrogen proton or the carbon nucleus. The tracks of the charged products from this scattering are directly observed, and their energy deposit is measured. Consequently, the kinematics of the neutron can be determined using its time-of-flight as illustrated in Figure 5.23: the primary



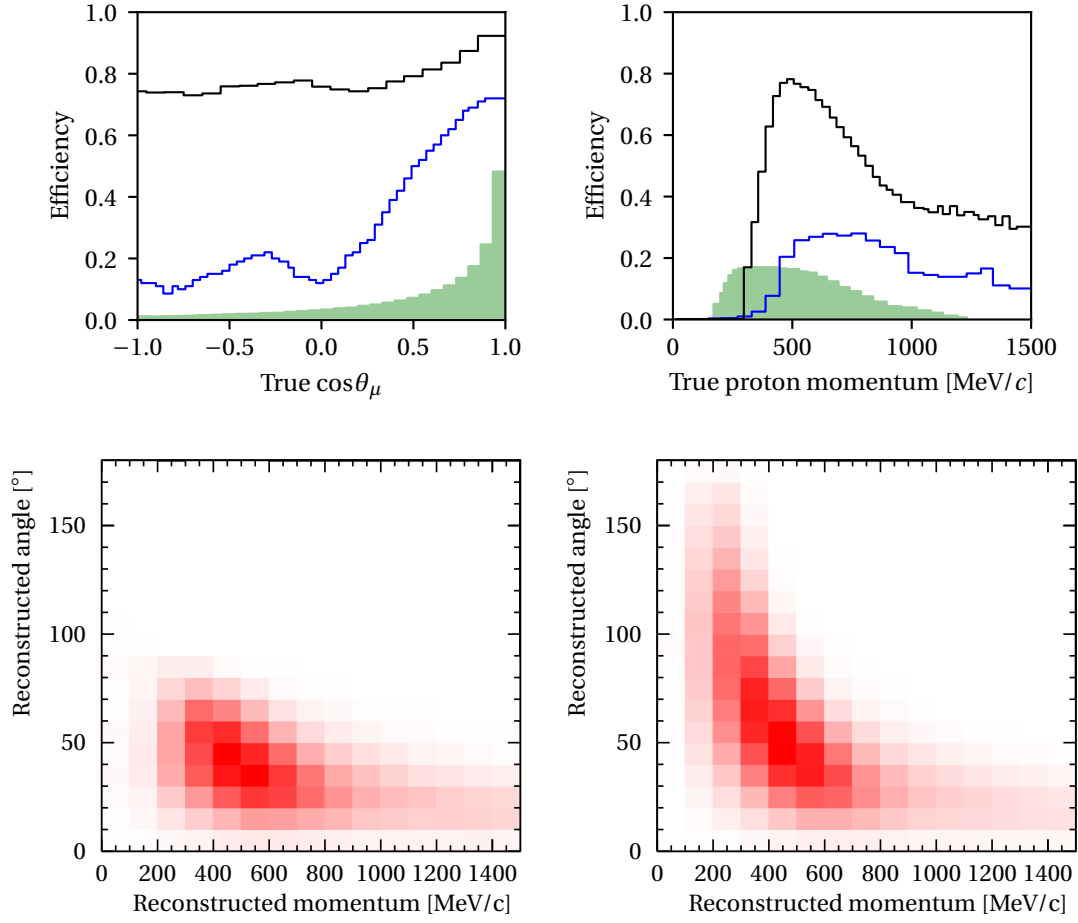


Figure 5.21: Top: reconstruction efficiency of the muon as a function of the cosine of its angle with respect to the neutrino direction (left) and of the proton as a function of its momentum (right) for the current (blue) and the upgraded (black) ND280, compared to the NEUT-predicted distributions (green). Bottom: two-dimensional distributions of the reconstructed momentum and angle of the charged lepton from  $\nu_\mu$  interactions at the current (left) and upgraded (right) ND280.

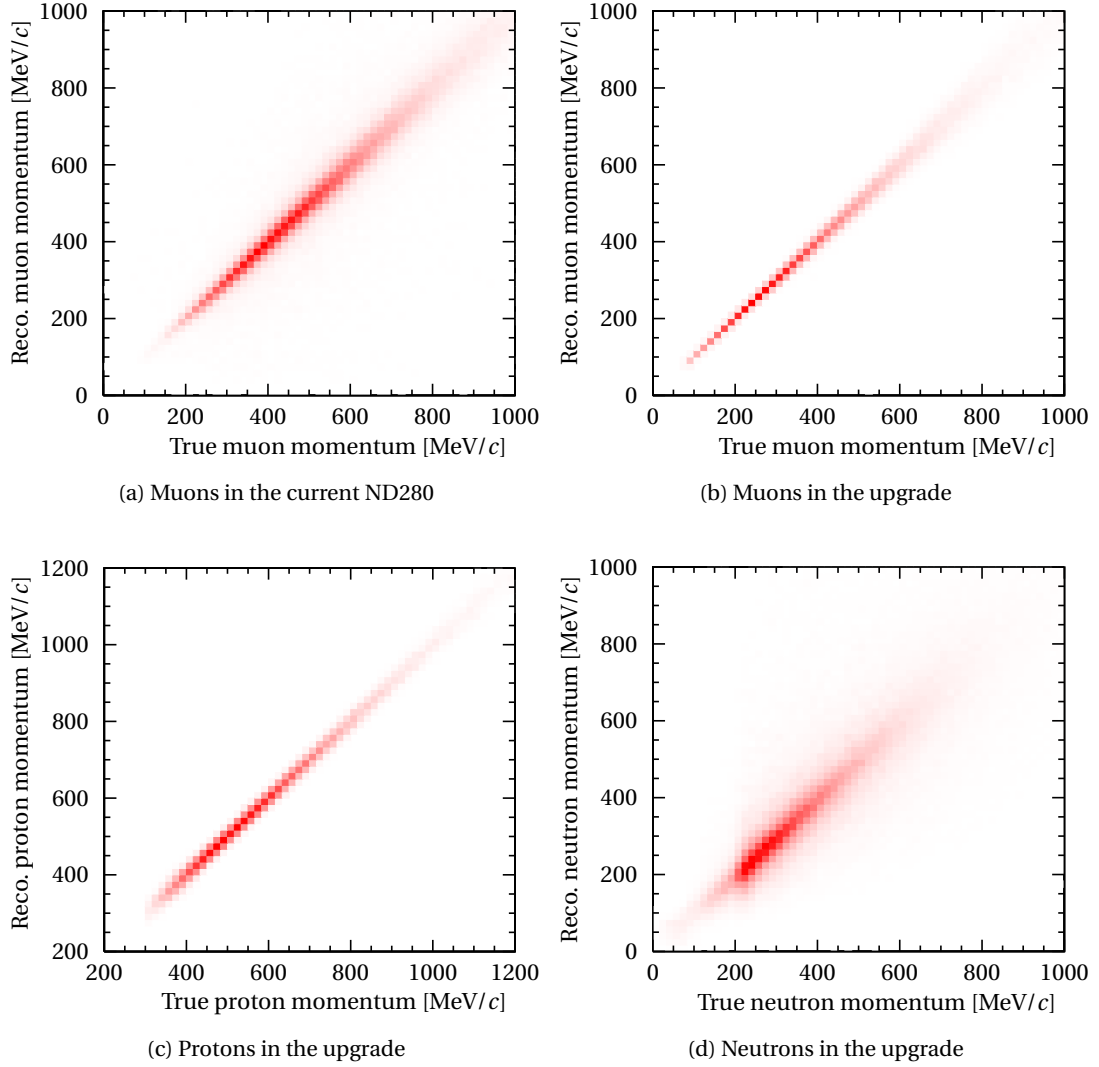


Figure 5.22: Two-dimensional distributions of the true vs. reconstructed momentum for various particles in ND280 and as expected in the upgrade.

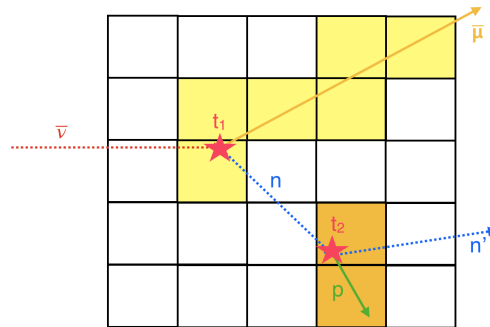


Figure 5.23: Schematic illustration of the measurement of the neutron kinematics using their time-of-flight. Figure from Reference [255].

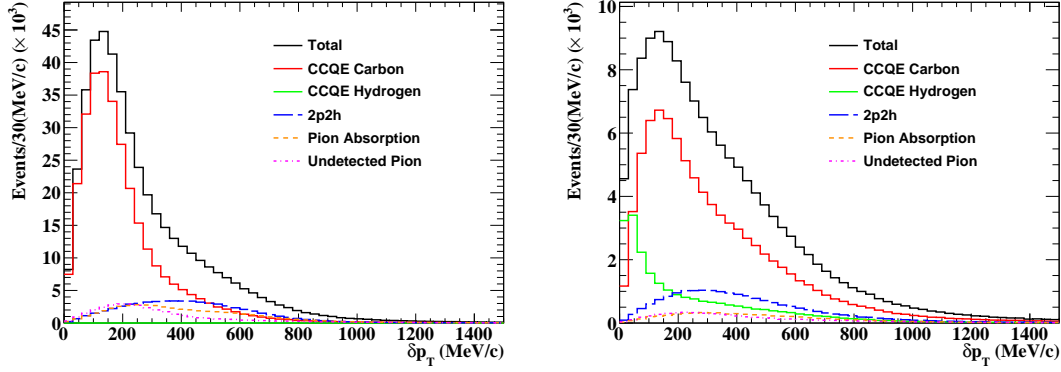


Figure 5.24: Distribution of  $\delta p_T$  for neutrinos (left) and antineutrinos (right) in the  $CC0\pi Np$  topology, broken down by the type of contribution. Figure from Reference [240].

interaction vertex is accurately determined since it corresponds to the starting point of the long muon track at the instant  $t_1$ , while the start of the secondary recoil particle indicates the reinteraction point at the instant  $t_2$ . The difference between the two instants  $t_1$  and  $t_2$  can be used to infer the neutron energy, and the position of the corresponding cubes indicate its direction. Such measurement can only be possible with a highly precise timing resolution from the detector, which motivates its careful study in Reference [250] and the exhaustive electronics tests in Section 6.2.5.

As displayed in the bottom right panel of Figure 5.22 and detailed in Reference [255], the resolution varies between 15 – 30% on the neutron momentum. This was estimated from a GEANT4 simulation of the detector response where all the relevant effects were included such as the light quenching in the plastic, the light capture efficiency and light attenuation in the fiber and the photodetection efficiencies of the silicon photomultipliers. Any improvement on the timing resolution can greatly impact this neutron momentum resolution. As will be mentioned in Chapter 6, the sampling rate in the Super-FGD front-end boards is currently at 400 MHz which provides the time information in 2.5 ns steps. While it might be challenging, it is planned to double this sampling rate to reach an 800 MHz sampling rate.

#### 5.4.4 New observables

The improved measurement of the hadronic part of the neutrino interaction products will enable an unprecedented level of precision in probing nuclear effects that impact the oscillation analysis. This can be achieved thanks to new observables that can be defined from the kinematics of the outgoing particles such as those related to the transverse-kinematic imbalance discussed in Chapter 4.

As seen in Chapter 4, the transverse momentum imbalance  $\delta p_T$  gives a great sensitivity to the initial Fermi motion of the nucleons and the nuclear effects experienced by the struck nucleons as they exit the nucleus. Figure 5.24 shows its distribution for neutrino (left) and

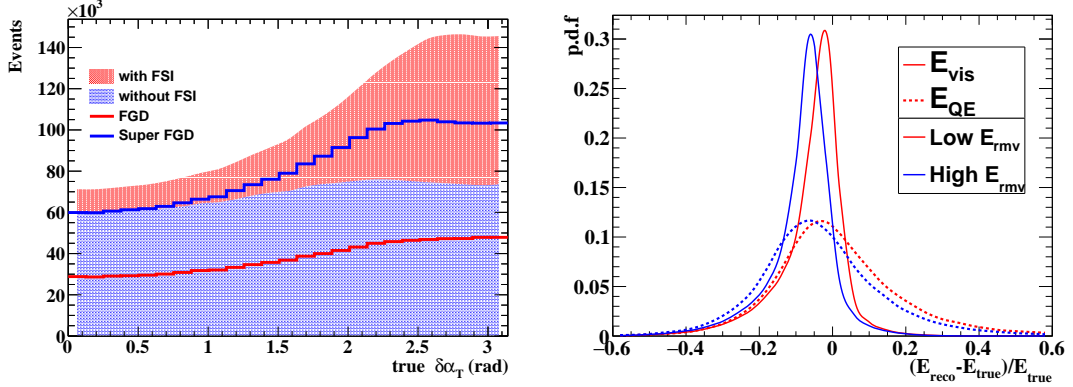


Figure 5.25: Left: distribution of  $\delta\alpha_T$  for the  $CC0\pi Np$  neutrino interactions at the truth level (shaded) where the contribution from events with (red shade) and without FSI (blue shade) is highlighted, compared to the current ND280 (red line) and the Super-FGD (blue line). Right:  $E_{\text{vis}}$  (full) and  $E_{\text{QE}}$  (dashed) bias to estimate the true neutrino energy  $E_{\nu}$ , with the impact of a global  $\pm 10$  MeV shift to the removal energy. Figure from Reference [240].

antineutrino (right) interactions in the  $CC0\pi Np$  topology. Its bulk is dominated by the pure CCQE interactions on carbon, while the high- $\delta p_T$  tail separates the non-CCQE modes including 2p2h and CCRES events. The antineutrino distribution (right) shows that the low- $\delta p_T$  region is enriched with  $\bar{\nu}_{\mu}$  interactions on hydrogen protons. Indeed, the free hydrogen protons in the plastic of the scintillator do not experience any nuclear effects and therefore the corresponding transverse momentum imbalance is almost zero. This enriched sample will have an important impact on constraining the flux uncertainties independently from the cross-section systematic errors, as will be discussed in Chapter 9.

Furthermore, the transverse boosting angle  $\delta\alpha_T$  (see Equation (4.2) and Figure 4.2) allows us to probe FSI effects independently from the multinucleon processes as shown in the left panel of Figure 5.25. In fact, if there were no FSI, its distribution would be flat due to the isotropic Fermi motion. On the other hand, when the struck nucleon undergoes the intranuclear cascade, it mostly decelerates which shifts the  $\delta\alpha_T$  distribution towards  $\pi$  as shown in Figure 5.25. With the high threshold in the existing FGDs in ND280 for protons, this effect on  $\delta\alpha_T$  cannot be clearly observed. Indeed, due to the low statistics and to the high momentum threshold, the cross-section measurement of the STV in Reference [113] showed no significant sensitivity to this effect. On the other hand, thanks to the low tracking threshold of the Super-FGD, it would be possible to disentangle this effect as displayed in the left panel of Figure 5.25.

Finally, the neutrino energy can be better estimated if more final-state particles are observed in the detector. Similarly to the calorimetric method discussed in Section 3.4.2, we can define the visible energy as the sum of the muon energy  $E_{\mu}$  and the nucleon kinetic energy  $T_N$  as:

$$E_{\text{vis}} = E_{\mu} + T_N. \quad (5.1)$$

This yields an improved estimation of the neutrino energy in comparison with the  $E_{\text{QE}}$  estima-

tor introduced in Equation (3.15) which relies only on the kinematics of the charged lepton. The distributions of the bias from both estimators are shown in the right panel of Figure 5.25. In particular, this improved estimator  $E_{\text{vis}}$  is also more sensitive to the details of the nuclear ground state and can for instance capture global shifts in the distribution of the removal (or missing) energy in the SF model.

Chapter 9 will present in detail how these new observables in the  $CC0\pi Np$  sample can impact the oscillation analysis when combining it with the collected data from the existing ND280 detectors. We will also discuss its potential impact on the constraints of the oscillation parameters in the upcoming phase of data taking for T2K.

## 6 Electronics of the Super-FGD

With its two-million plastic scintillator cubes, the Super-FGD includes a complex architecture of digitization electronics to read the incoming signals from  $\sim 56,000$  optical fibers. This needs to satisfy multiple requirements such as a large dynamic range for signals up to  $\sim 1500$  p.e., a fine resolution of  $\sim 2$  p.e. for minimum ionizing particle, a low detection threshold of  $\sim 0.5$  p.e., a hit time resolution of  $\sim 1$  ns, and the ability to operate in the ND280 magnetic field of 0.2 T [243]. The relatively short period of time allocated for the development of the electronics constrained the collaboration to adapt the design of well-known existing systems. Consequently, the structure of the electronics is centered on the use of the so-called *Čerenkov Imaging Telescope Integrated Read Out Chip* (CITIROC) developed by the Omega laboratory at École polytechnique [256], on which is based the BabyMIND readout electronics [257].

In this chapter, we present an overview of the design of the electronics for the Super-FGD in Section 6.1. We then focus in Section 6.2 on a series of tests specific to the front-end boards to qualify their performances for the physics of interest, and evaluate the impact of a magnetic field on their operations in Section 6.3. We finish this chapter by discussing in Section 6.4 ongoing tests of the front-end boards and more generally the full electronics chain.

### 6.1 Architecture of the electronics in the Super-FGD

#### 6.1.1 From the neutrino interaction to the front-end boards

In the Super-FGD, the target material for neutrino interactions is the plastic scintillator itself. When such interaction occurs, it often produces charged particles that travel through the rest of the Super-FGD and deposit energy in the material which is absorbed by the organic scintillator molecules (paratherphenyl and POPOP). These molecules in turn emit scintillation light within the cube, which is carried by the wavelength-shifting (WLS) fibers that adapt its wavelength for the silicon photomultiplier (SiPM), also known as multi-pixel photon counter (MPPC), positioned at one of its ends.

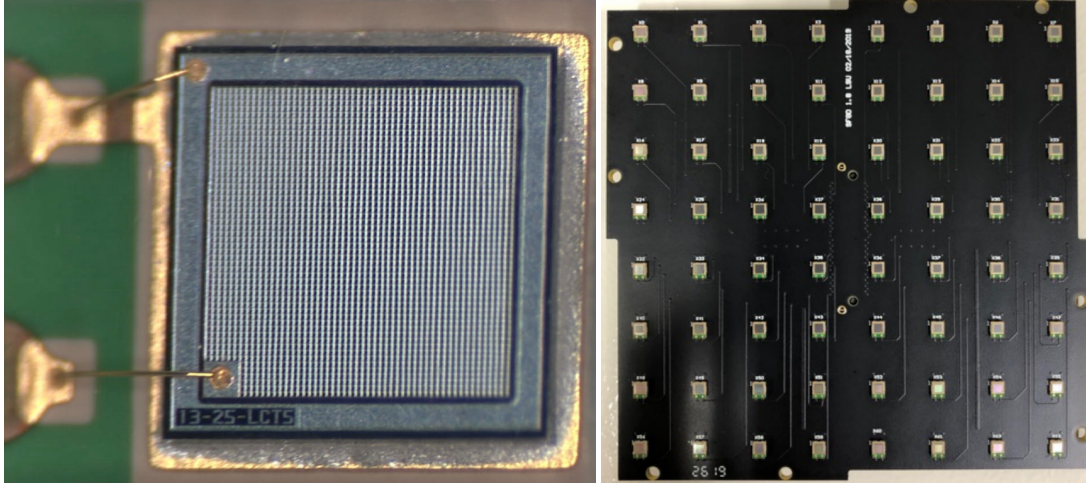


Figure 6.1: Left: zoomed-in picture of the Hamamatsu MPPC S13360-1325CS used in the Super-FGD. The pixelized area is of size  $1.3 \times 1.3 \text{ mm}^2$ . Right: picture of the MPPC64 board ( $83.8 \times 83.8 \text{ mm}^2$ ) designed for the Super-FGD which contains 64 of the MPPCs displayed in the left panel. Credits: T. Kutter.

MPPCs are solid-state photomultipliers comprised of a high-density array of avalanche photodiodes (APDs) operated in the Geiger mode: a reverse bias voltage, also called high voltage (HV), is applied to the APD with a value slightly above its breakdown voltage which allows it to produce a fast electrical pulse when it detects even a single photon. The Hamamatsu MPPC S13360-1325CS [245], pictured in the left panel of Figure 6.1 and used in the Super-FGD, is of size  $1.3 \times 1.3 \text{ mm}^2$  and features 2668 pixels of  $25 \mu\text{m}$  pitch. Each pixel corresponds to a single APD circuit, which outputs a pulse at the same amplitude when it detects a photon. The MPPC output signal is the superposition of the pulses from all the pixels. It is important to note that a single APD is a binary device, which means that the pulse it generates does not vary with the number of incident photons. For a low number of photons in comparison with the number of pixels of the MPPC, it is unlikely that multiple photons reach the same pixel. However, the linearity of the MPPC response worsens for larger photon numbers. To the first order, the number of observed photons  $N_{\text{obs}}$  from the output of the MPPC can be related to the number of incident photons  $N_{\text{in}}$  and the number of pixels in the MPPC  $N_{\text{pix}}$  by [258]:

$$N_{\text{obs}} \approx N_{\text{pix}} \left[ 1 - e^{-\epsilon N_{\text{in}} / N_{\text{pix}}} \right]$$

where  $\epsilon$  is the photon detection efficiency (PDE) of a single APD which depends on the applied bias voltage and the photon wavelength. This explains the choice of these 2668-pixel MPPCs for the Super-FGD since the largest signal of interest is at  $\sim 1500$  p.e.

The MPPCs are arranged for the Super-FGD in groups of 64 and form the *MPPC64* boards, as displayed in the right panel of Figure 6.1. They are designed so that each MPPC faces a fiber when installed around the Super-FGD, which means that the MPPC-to-MPPC distance is of  $\sim 1 \text{ cm}$ . A connector is designed in the back of the board, allowing us to link it to the front-end

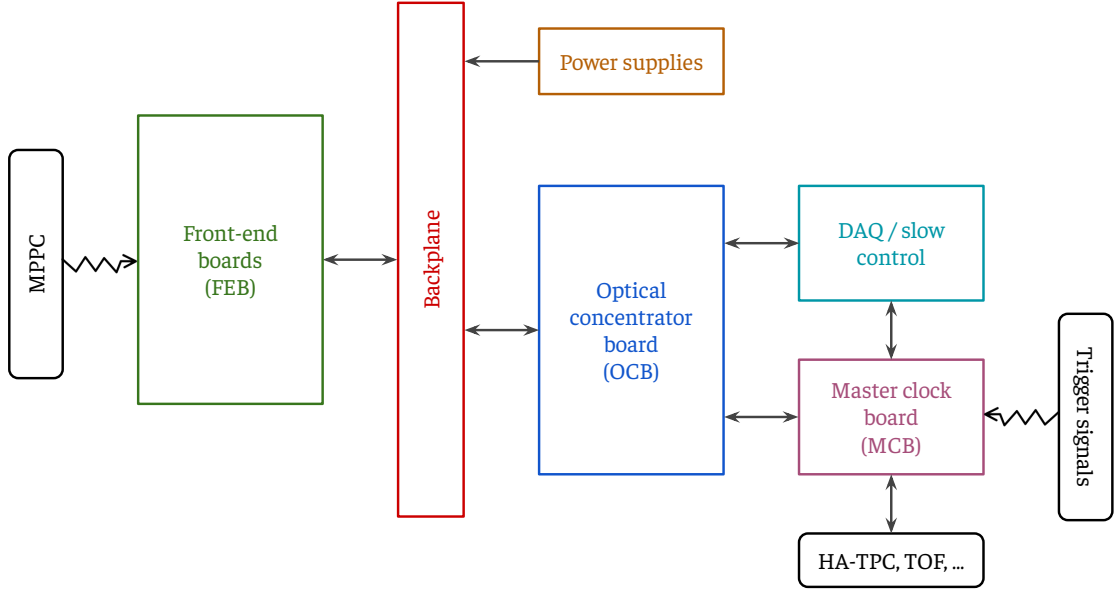


Figure 6.2: Schematic illustration of the Super-FGD electronics.

boards that perform the signal readout.

### 6.1.2 From the front-end boards to the data

Figure 6.2 summarizes the architecture of the Super-FGD readout electronics. The front-end boards (FEBs) are the first to receive the MPPC signal. The amount of fibers (or channels) to read is more than 56,000. Consequently, around 220 FEBs are designed, each with the ability to read up to 256 channels. The top panel of Figure 6.3 shows a picture of this board.

As can be seen in the left part of the top panel in Figure 6.3, the baseline design of the FEB is structured around 8 CITIROC chips. CITIROC is a 32-channel front-end application-specific integrated circuit (ASIC) designed for the readout of large numbers of MPPCs. The bottom panel of Figure 6.3 shows a schematic representation of the path a signal takes from a single MPPC in the CITIROC. In each CITIROC channel, the signal is divided into a high gain (HG) path and a low gain (LG) path corresponding to two preamplifiers (with a 1:10 ratio) with tunable gains and two slow shapers with adjustable shaping time constants. The slow shaper integrates the charge over a time window. Besides, a timing path comprised of a fast shaper together with a discriminator with an adjustable threshold provides trigger outputs at the rising and falling edges of the signal. The Altera Arria 10 field programmable gate array (FPGA) samples these triggers at a 400 MHz rate<sup>1</sup>, which provides a timestamp on these triggers and

<sup>1</sup>The sampling rate may be increased up to 800 MHz in the FPGA firmware in the future for an improved timing resolution.



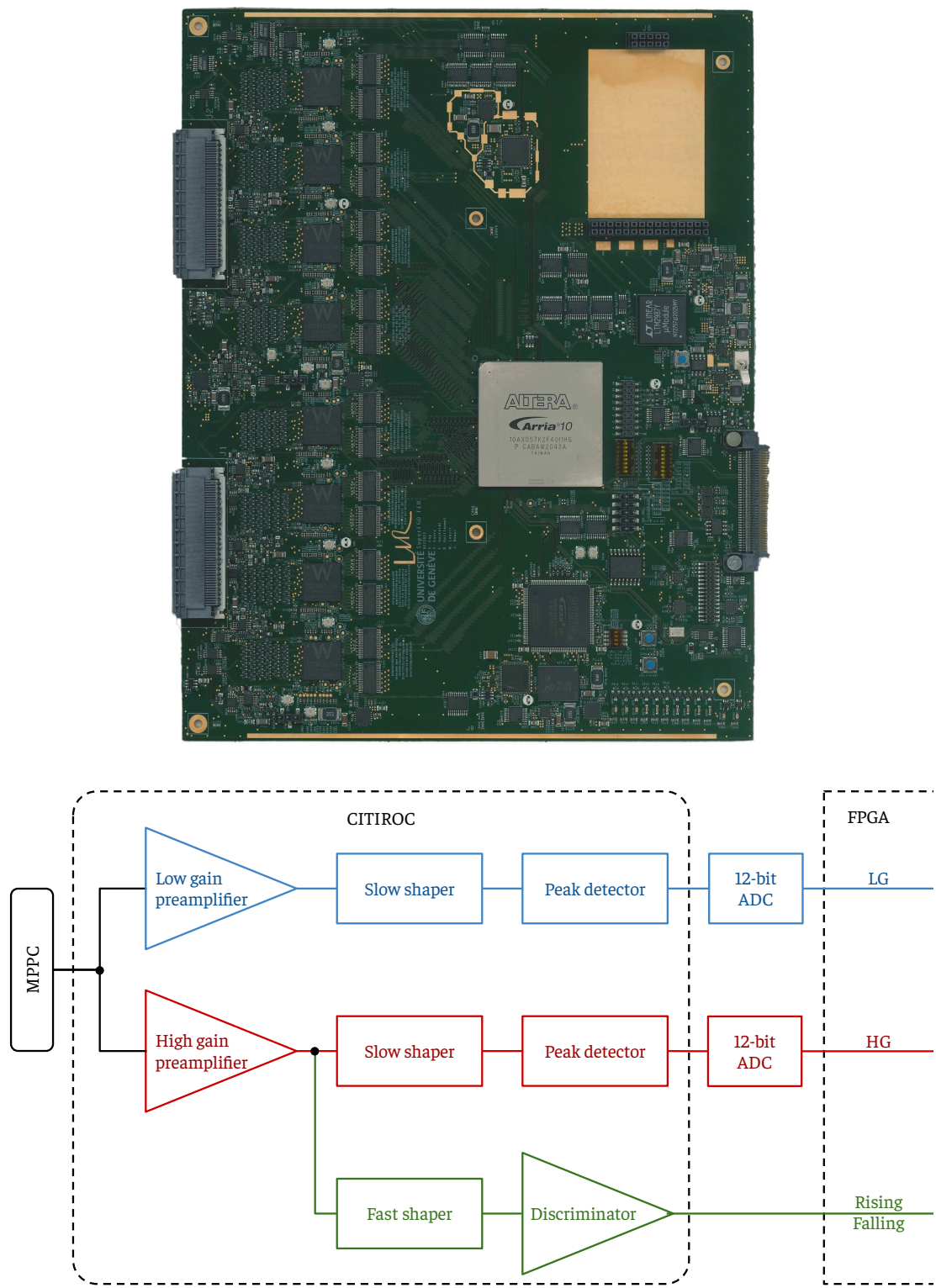


Figure 6.3: Top: picture of the top side of the FEB. Bottom: simplified diagram of a CITIROC channel.

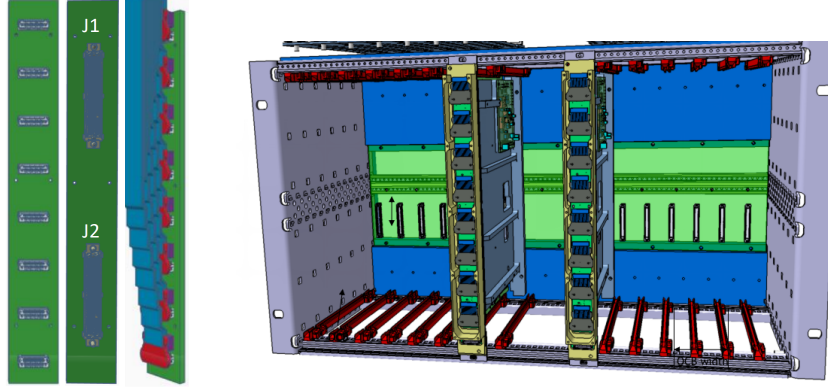


Figure 6.4: Schematic illustrations of the MIB (left) and a crate with two FEBs (right).

allows us to obtain the timing of the rising and falling edges of each hit signal in 2.5-ns steps. The time-over-threshold, calculated from the timing difference of the two edges, can give a rough measure of the signal amplitude. It can be used in conjunction with the charge, but more importantly, it is particularly useful when more than one signal comes from the MPPC within the  $\sim 9 \mu\text{s}$  dead time of the CITIROC due to the charge readout. The FPGA also manages the digitization of the HG and LG outputs via 12-bit analog-to-digital converters (ADCs).

The power in the FEB is distributed by a dedicated board that provides the required voltages for the active components (CITIROC, FPGA, etc.) called the *power mezzanine*. It is inserted on top of the ground area in the top right of the FEB picture shown in Figure 6.3. The power mezzanine is specifically designed to withstand the 0.2 T magnetic field in the Super-FGD setup.

Besides, an intermediate board, called the MPPC64 injection board (MIB), acts as an interface between the 4 MPPC64 boards that can populate the 256 channels and the FEB through SAMTEC cables [259]. This displayed in the left panel of Figure 6.4. The MPPC side of the MIB is composed of 8 connectors, while its FEB side comprises two large 400-pin connectors.

The 220 FEBs are arranged in 16 groups of 14 FEBs within crates as depicted in the right panel of Figure 6.4. Moreover, each crate hosts two additional boards: the *optical concentrator board* (OCB) which fits in a slot similarly to the FEBs, and the *backplane* inserted in the back side of the crate. As shown in Figure 6.2, the role of the OCB is to manage the slow control, i.e. setting the adjustable FEB parameters (e.g. CITIROC thresholds and gains, FPGA options, etc.), as well as to concentrate the readout of all the FEBs in the crate. It also distributes the trigger signals of the beam, which tell the FEBs when to record potential beam-related events. The *master clock board* (MCB), on the other hand, is responsible for receiving the trigger and distributing it to all the 16 OCBs, in addition to the other detectors of the upgrade. The backplane of each crate is responsible of delivering the required power (also called *low* voltage) to the FEBs and the OCB, as well as the *high* voltage that is distributed by the FEBs to the MPPCs so that the APDs function in the Geiger mode as photoelectron counters.

When a beam trigger is received and distributed by the OCB to the FEBs, each FEB starts recording data that are sent to the OCB. The OCB organizes the data into event fragments, with the corresponding trigger timing, analog charge and rising/falling edge timing for each channel. These are then sent to the data acquisition (DAQ) system which is in charge of storing them, along with the data coming from the other subdetectors.

## 6.2 Performance tests of the FEB

### 6.2.1 Overview

The goal of the tests presented in this section is to validate the performances of the FEB and the MIB. The responsibility of their delivery to the experiment is shared between LLR and the University of Geneva (UniGe), and these tests were performed in close collaboration between the two institutes.

As shown in the bottom panel of Figure 6.3, the FEB provides a measurement of the charge, referred to as *analog* data, as well as the timing. The analog data is what allows for the estimation of the light yield, which can then be related to the energy deposition for instance with the semiempirical Birks model [260]. To do so, a proper calibration is always needed for each channel in order to convert the ADC count returned by the FEB where a hit is recorded to a number of photoelectrons.

Furthermore, the linearity of the FEB response is another important effect to characterize. This consists of evaluating how the FEB output varies as a function of the amplitude of a well-known input signal. Multiple electronic components can significantly affect the linearity of this response, including the CITIROC itself as well as the ADCs.

Additionally, the compactness requirements of the electronics constrained the possible size of the FEB and the MIB, making them significantly denser than in the BabyMIND designs. In particular, the printed circuit board (PCB) of the FEB and the MIB feature respectively 14 and 16 layers, which raises the question of possible electronic cross talk within the boards.

Finally, the timing measurement that the FEB provides is of great interest particularly for the estimation of the neutron kinematics in the Super-FGD, which relies on a precise assessment of their time-of-flight.

Consequently, we devised a list of four performance tests to conduct as summarized below:

- analog data calibration using a signal of the MPPC64 board,
- evaluation of the linearity of the FEB response,
- estimation of the electronic cross talk,
- validation of the timing information.

A schematic illustration of the setups used in these tests is shown in Figure 6.5. Most of them require a signal injection in a single channel out of the 256 ones of the FEB, which is done by the intermediate of an injection board (not shown here). Tests that include the use of an MPPC (top panel) require a light injection system, which can simply be obtained with an LED pulsed by a waveform generator and placed with the MPPC in a light-tight box. In this case, the setup also requires a high voltage which is distributed by the FEB and the MIB to the MPPC.

On the other hand, tests that require a precise knowledge of the input signal, such as the linearity and the timing tests, use directly pulses from the waveform generator, filtered with a high-pass circuit as displayed in the bottom panel of Figure 6.5. This filtering is strongly recommended by the CITIROC manufacturer because the shapers located after the preamplifiers (see Figure 6.3) are adapted only for signals with shapes similar to an MPPC pulse. The recommended filter is a resistor-capacitor (RC) circuit of the characteristics  $R = 50 \, \Omega$  and  $C = 100 \, \text{pF}$  as depicted in the left panel of Figure 6.6. The leading edge of a pulse of  $2 \, \mu\text{s}$  duration produced with the waveform generator has the form of a ramp with a characteristic time of  $t_c = 10 \, \text{ns}$  to reach the target amplitude  $V$ . With this input, the output of the RC circuit can be analytically obtained using Kirchhoff's current law, which results in a differential equation that gives the output voltage  $V_{\text{out}}(t)$  around the leading edge as:

$$V_{\text{out}}(t) = \begin{cases} \frac{RC}{t_c} V (1 - e^{-t/RC}) & \text{if } t \in [0, t_c], \\ \frac{RC}{t_c} V (1 - e^{-t_c/RC}) e^{-(t-t_c)/RC} & \text{if } t > t_c. \end{cases} \quad (6.1)$$

This is illustrated in the right panel of Figure 6.6 where we can notice that the shape of  $V_{\text{out}}(t)$  (red) is more similar to that of an MPPC signal, and that its amplitude is reduced by 30 – 40% in comparison with the input voltage (blue), which was also checked with an oscilloscope.

At the time when these tests were conducted, the FEB was the only board of the SFGD electronics chain (see Figure 6.2) to be available. Consequently, a custom bench test was required for the purpose of these tests. This was possible thanks to the general-purpose input/output (GPIO) board designed by UniGe, which offers an interface with the board through a PC as illustrated in Figure 6.5. It particularly allows us to configure all of the FEB parameters and read its data.

Another important goal of these performance tests is to validate the impact of the FEB parameters. In fact, the CITIROCs come with a large array of adjustable parameters that are necessary to set in a real detector setup corresponding to the experimental needs. Some of these parameters can be tuned on an ASIC-by-ASIC basis like the reference signal baseline, the coarse-tuning of the analog and timing thresholds and the MPPC high voltage, or on a channel-by-channel basis such as the gains of the LG and the HG paths (encoded in 6 bits from 0 to 63) and the fine-tuning of the thresholds and the bias voltage. Therefore, these tests will also explore how varying these parameters impact the FEB output.

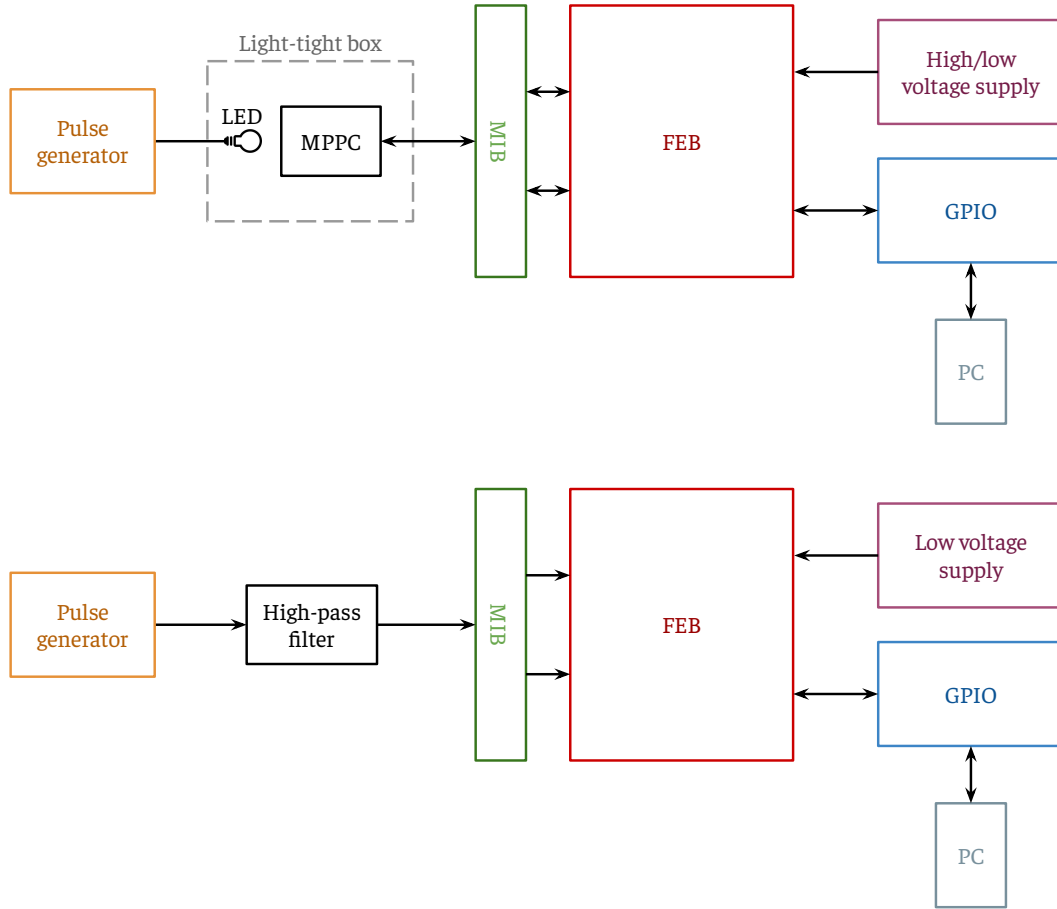


Figure 6.5: Setup for single-channel injection tests with a pulsed LED and an MPPC (top) or with a filtered pulse from a waveform generator (bottom).

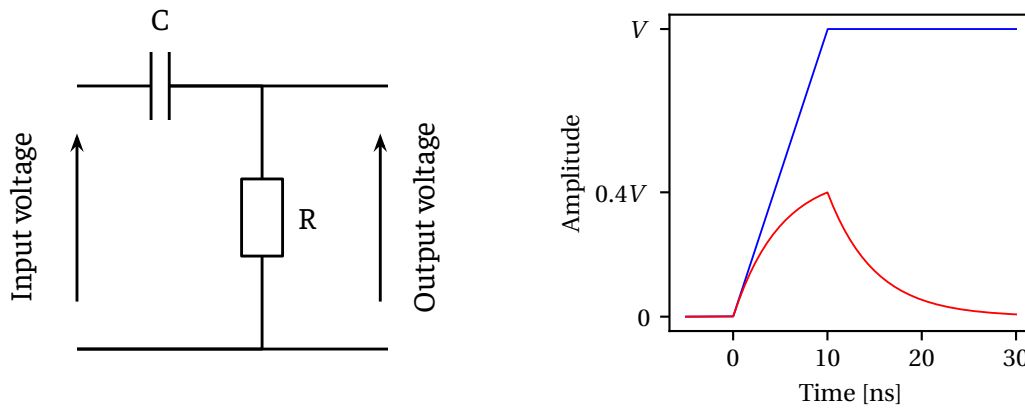


Figure 6.6: Left: high-pass RC circuit used with the pulse generator such that  $R = 50\ \Omega$  and  $C = 100\text{ pF}$ . Right: the leading edge of the waveform generator with a characteristic time of  $10\text{ ns}$  (blue) and the corresponding RC circuit output (red).

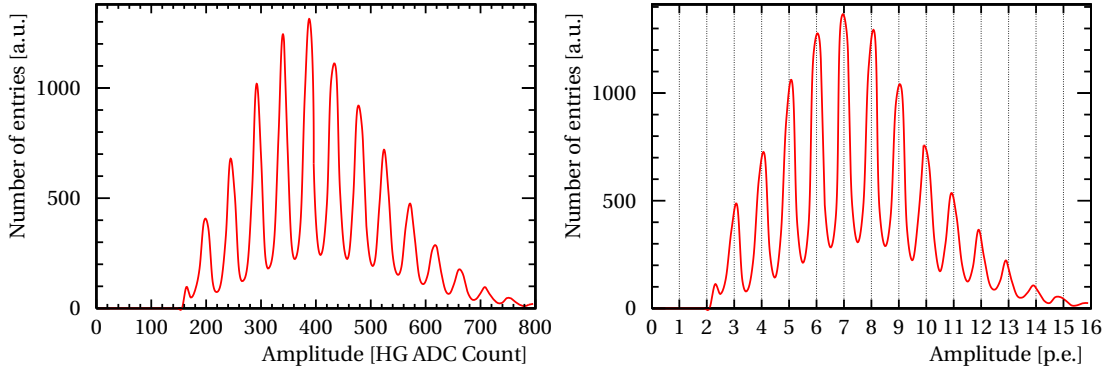


Figure 6.7: Example of the distribution of the amplitude recorded in a single channel receiving a signal from an MPPC with LED light injection in the raw HG ADC counts (left) and in p.e. units after calibration (right). An excellent peak-to-valley ratio is achieved thanks to the low noise obtained with the FEB design.

### 6.2.2 Analog calibration

The goal of this first test is to check and validate the response from each of the 256 channels to an MPPC signal by performing basic calibration steps for the analog data.

#### Overview of analog calibration steps

For each recorded hit, the FEB returns a LG and a HG amplitude given in ADC counts on 12 bits (0 to 4095) for the corresponding channel. A proper calibration would allow us to relate the ADC counts to a light yield expressed in p.e. units. The calibration system designed for the Super-FGD includes the LGP modules (see Section 5.2.1) which inject a small amount of light from pulsed LEDs. The distribution of the HG ADC counts from this signal, often called *finger plot*, features evenly-spaced peaks that correspond to individual photoelectrons, as we observe in the left panel of Figure 6.7. The gain is given by the distance between two neighboring photoelectron peaks:

$$\text{gain} = p_{i+1} - p_i$$

where  $p_i$  is the center of the  $i$ -th photoelectron peak. It is also referred to as the HG ADC count to p.e. ratio. The gain is in principle constant across the HG dynamic range if we assume that the response of the electronics is linear, and gives a scale of conversion between HG ADC counts and p.e. units. In fact, if the first peak of this distribution, corresponds to  $n$  p.e., then the  $(m + 1)$ -th peak corresponds to  $n + m$  p.e. The gain is a user-adjustable parameter for each channel, but it highly depends on the MPPC temperature and the value of the high voltage.

In general, with just one finger plot, the absolute scale of the photoelectron number cannot be determined because the electronics baseline is not recorded as the CITIROC applies a signal

threshold whose value is larger than 0.5 p.e. and is unknown *a priori*. The value in HG ADC counts of the “0 p.e.” peak, also referred to as the *pedestal*, can be determined by varying the gain, which is achieved either by adjusting the corresponding CITIROC parameter or by changing the applied voltage. While the positions of the photoelectron peaks are expected to change for each gain setting, the pedestal is expected to always be at the same HG ADC count value. Consequently, a simple linear extrapolation to small HG ADC counts allows us to determine its position. Finally, the conversion between the raw HG ADC counts and the corresponding light yield in p.e. units is simply given by:

$$\text{amplitude [HG ADC Count]} = \text{pedestal} + \text{gain} \times (\text{amplitude [p.e.]}) .$$

The right panel of Figure 6.7 shows the finger plot with the calibrated amplitude values, where each peak is well centered around the p.e. value to which it corresponds. It can also be observed that the threshold used here is around  $\sim 2$  p.e.

In the actual Super-FGD setup, the easiest way to vary the gain is by changing the high voltage value directly from the power supply. In the present tests, we opt for changing the gain on the CITIROC parameter because the GPIO provides an easy and efficient interface to automate these procedures. Conversely, reprogramming the FEBs by changing the gain parameter for more than the 56,000 channels multiple times might be too time consuming on the slow control side.

Once the HG path is calibrated, it is straightforward to proceed with the LG calibration. This simply consists of obtaining the ratio of the HG and LG ADC counts by drawing their two-dimensional distribution spanning the HG dynamic range for relatively high yield signals ( $\lesssim 100$  p.e.). This ratio can then be used for a linear extrapolation that can relate the LG ADC counts to the values in p.e. In the following tests, we simply increase the intensity of the LED to obtain this LG/HG ratio. However, the calibration system in the Super-FGD can only provide signals of few photoelectrons. Therefore, its LG calibration will rather rely on cosmic muons or beam-related tracks for a higher light yield to compute the LG/HG ratio.

In the following calibration tests, the signal applied on the LED by the waveform generator is a pulse of 20 ns width and a frequency of 200 kHz. The setup is illustrated in the top panel of Figure 6.5.

### **Pedestal finding**

To determine the pedestal, we inject a small amount of light by adjusting the amplitude of the signal applied on the LED and take data in each of the 256 channels for different gain settings of the CITIROC. Figure 6.8 shows the distribution of the HG amplitude for different values of the gains for a single channel.

As previously discussed, since the threshold used in these tests is larger than 1 p.e., the

electronics baseline is not recorded and the pedestal needs to be determined by performing a linear fit on the position of the peaks for each value of the HG gain as displayed in Figure 6.9. The pedestal can be taken as the intersection of these fitted lines. Furthermore, the slope of each line gives the gain for each HG gain setting.

This test is performed on all the 256 channels of the FEB. Figure 6.10 summarizes the distribution of the pedestal position across all the channels.

It can be observed that the pedestal positions are relatively similar among the channels within the same CITIROC, but their variation across all channels is relatively large, at  $\sim 100$  ADC counts. Establishing the pedestal values on a channel-by-channel basis will therefore be a significant part of the Super-FGD calibration process. The FEB also has a “baseline” parameter that can be adjusted for each ASIC, in case a more homogeneous distribution of the pedestals between the CITIROCs is needed.

### **HG ADC Count to photoelectron ratio**

The determination of the ratio of the HG ADC counts to p.e. (gain) is also an important step of the calibration as this allows us to convert the observed ADC counts to an energy deposition quantity for a given HG gain setting as previously mentioned. It can be computed from the slope of the linear fit to the position of the photoelectron peaks as shown Figure 6.9. Figure 6.11 displays the distribution of this ratio across all the 256 channels of the FEB for the different HG gain settings. It can be noticed that it varies between the channels but, unlike the pedestal, it does not seem to change significantly from ASIC to ASIC. This hints at the fact that the large pedestal variations may not come from the CITIROC itself, but rather from a slightly different baseline applied at the level of each ASIC.

### **LG vs. HG ratio and HG saturation**

As shown in the bottom panel of Figure 6.3, the CITIROC separates the incoming signal from the MPPC into HG and LG paths with different preamplifier settings. In this test, the relationship between the HG and LG amplitudes can be obtained by varying the amplitude of the signal applied on the LED from lower to higher values. Figure 6.12 shows the HG versus LG ADC Count for all the channels. There is a linear relationship between the LG and HG amplitudes until the HG path is saturated when the light intensity level is too high. The LG to HG ratio can be determined on a channel-by-channel basis as well by a linear fit on the HG amplitude range below saturation.

This is also an important calibration element as this information would allow us, along with the HG ADC Count to photoelectron ratio, to obtain the corresponding energy deposition from a signal that saturates the HG path<sup>2</sup>, as would be the case from the Bragg peak of a stopping

---

<sup>2</sup>The linearity between the HG and LG amplitudes is different from the linearity between the amplitudes and the injected signal. The latter is studied in Section 6.2.3.



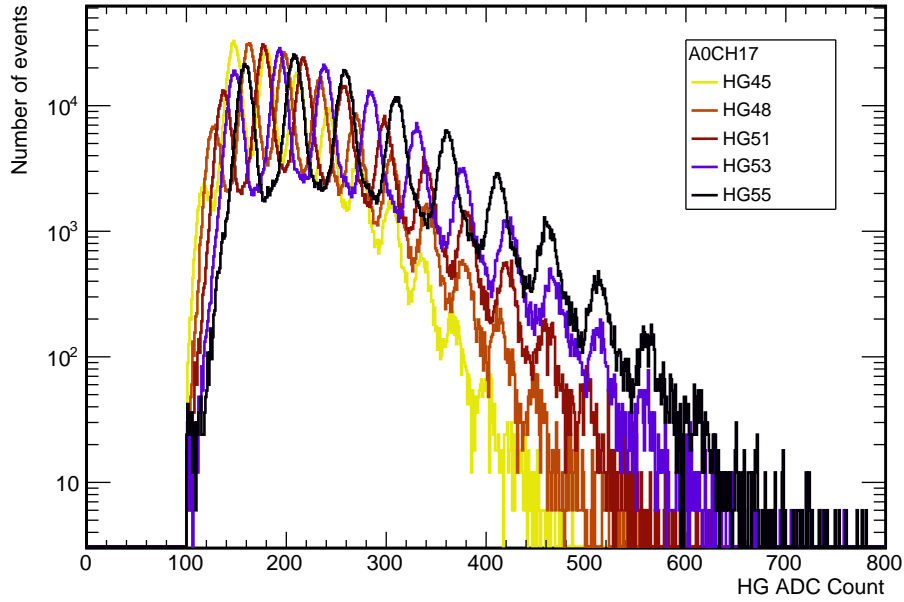


Figure 6.8: Example of the HG amplitude distribution for different values of the HG gain in one channel.

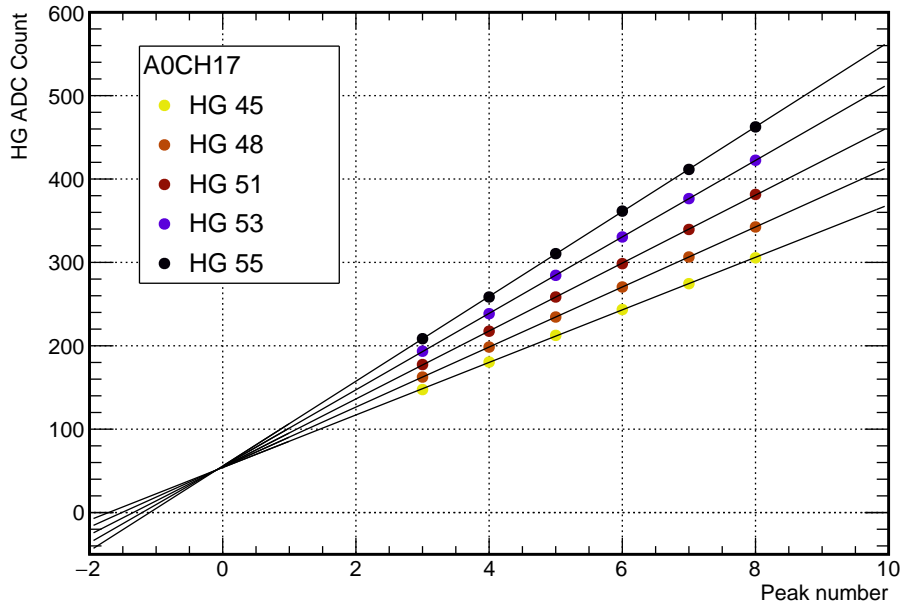


Figure 6.9: Example of linear fits to the photoelectron peak positions for different values of the HG gain in one channel. The pedestal is obtained at the intersection of the lines, which corresponds to the amplitude of the 0 photoelectron position.

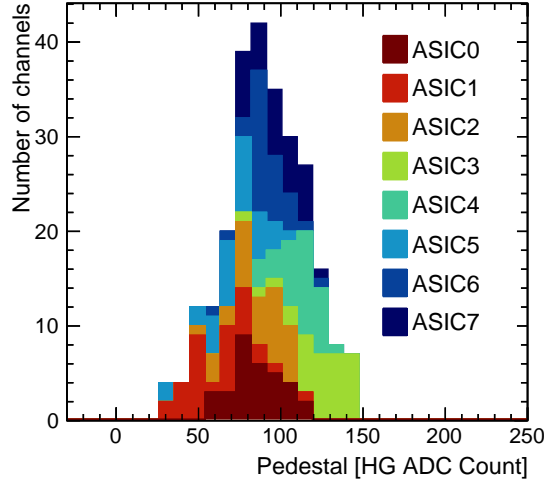


Figure 6.10: Stacked histogram of the pedestal position for all the 256 channels.

proton for instance.

As shown in Figure 6.13, the LG/HG ratio for the preamplifier settings in this test is around  $\sim 0.25$ . This can be further decreased by lowering the LG gain setting, in order to maximize the dynamic range. Figure 6.13 also shows that this ratio depends on the CITIROC and can vary between the channels for up to 10%.

On the other hand, it can be distinguished from Figure 6.12 that the HG saturation also varies between 3800 and 4095 HG ADC Counts. Figure 6.13 shows this variation across all the channels, and here as well, it can be seen that it varies from CITIROC to CITIROC. This information, along with the loss of linearity point introduced in Section 6.2.3, can be useful inputs to choose the proper gain settings for the physics run of the Super-FGD.

### Impact of varying the threshold

In addition to the preamplifier settings, each CITIROC has an adjustable threshold parameter in a charge discriminator. As an example, we can measure the so-called *dark noise* of the MPPC that is seen by the FEB as a function of this threshold. The dark noise is a characteristic of MPPCs which is mainly due to thermal electron-hole pair production which causes avalanches in a single APD and can mimic low light signals even with no injected light. The selected MPPCs for the Super-FGD are characterized by a dark rate of around  $\sim 50$  kHz above 0.5 p.e. which is low in comparison with INGRID or BabyMIND MPPCs [245].

To check this dark rate, we connect an MPPC to the FEB but without any light injection. Figure 6.14 shows the impact of varying the CITIROC threshold on the data rate from the FEB. As we can expect, increasing the threshold decreases the dark noise rate. When the threshold varies in the valley between two photoelectron peaks, which corresponds to  $\sim 1/2$  p.e., the

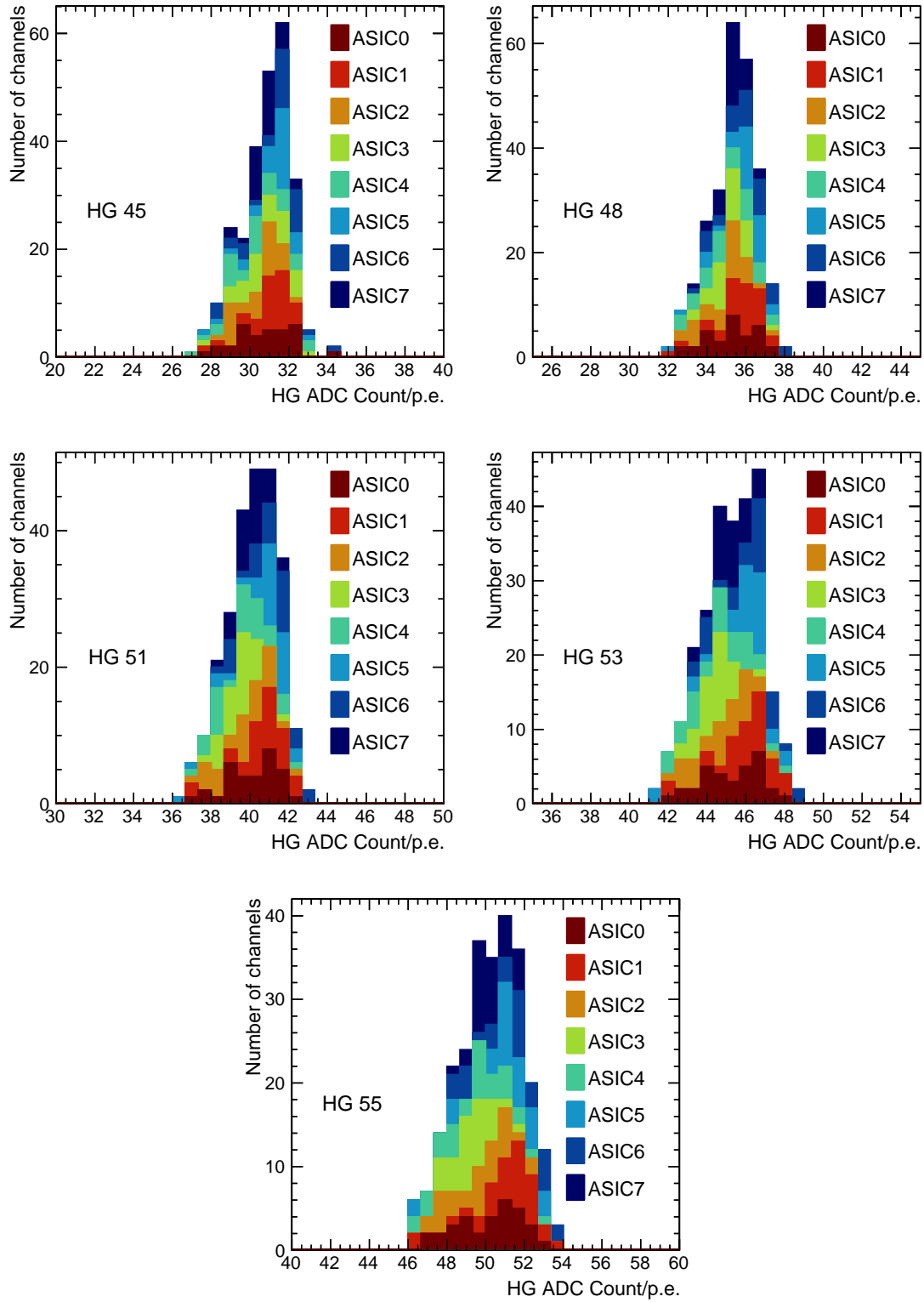


Figure 6.11: Stacked histogram of the HG ADC Count to photoelectron ratio for all the 256 channels with different values of the HG gain.

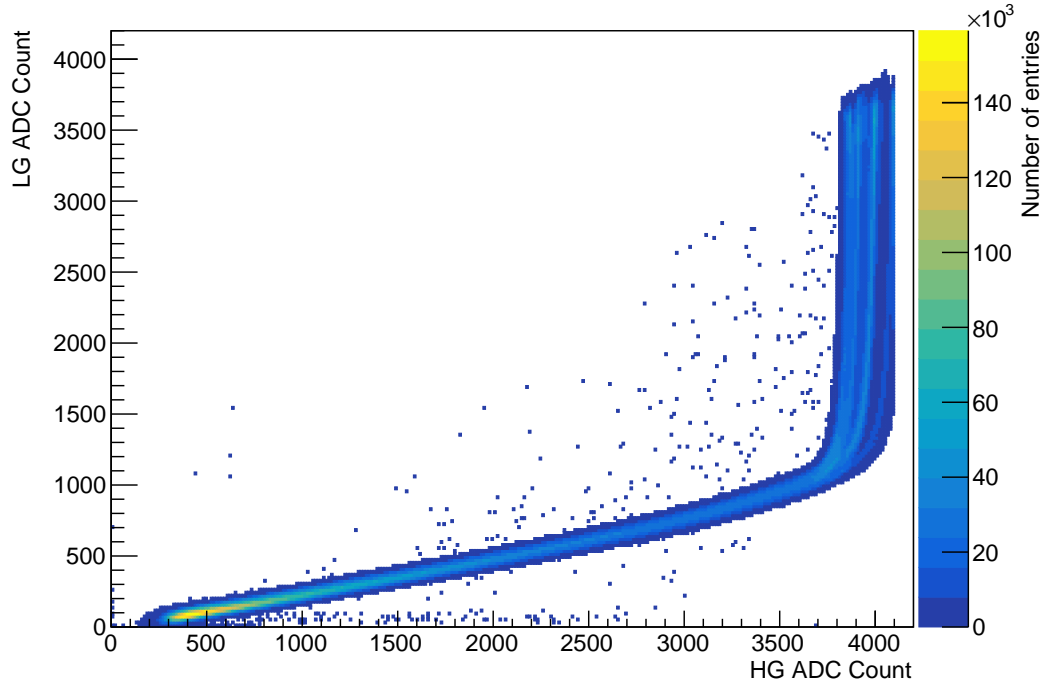


Figure 6.12: HG versus LG amplitudes for all the 256 channels.

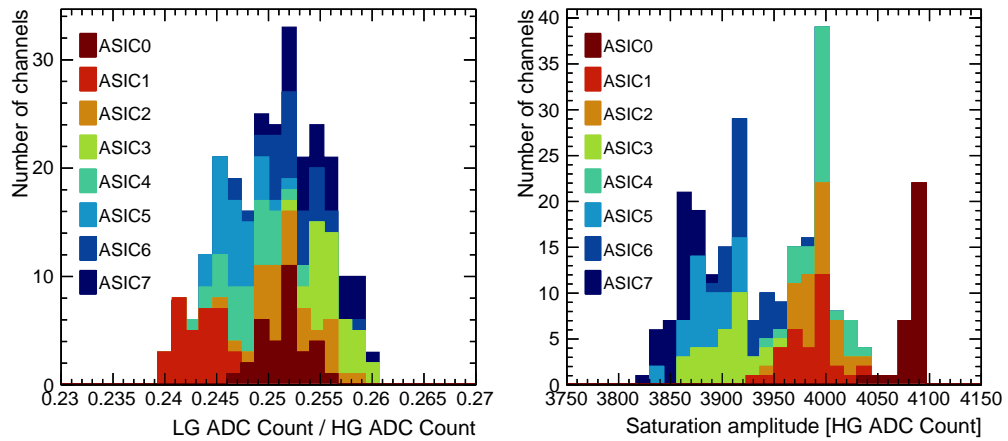


Figure 6.13: Left: stacked histogram of the LG to HG ratio for all the 256 channels (preamplifier settings: HG 55 and LG 61). Right: stacked histogram of the amplitude of the HG saturation across all the 256 channels. The saturation can also be distinguished for the CITIROCs separately in Figure 6.12.

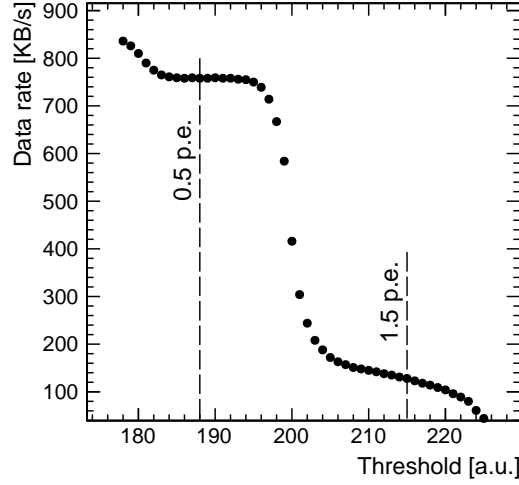


Figure 6.14: Data rate of the FEB as a function of the threshold set on the ASIC for channel 0 with the MPPC dark noise.

data rate does not change significantly, while the sharp drop in the data rate corresponds to a threshold coinciding with a photoelectron peak.

In this particular setup, the data rate can be directly related to the MPPC dark rate. Knowing that the FEB pushes four 32-bit words for each hit, we can find that the rate  $\sim 750$  KB/s at 0.5 p.e. corresponds to a hit frequency of  $\sim 50$  kHz, consistent with the value specified in the MPPC data sheet [245].

### Summary

The goal of the tests reported in this section is to check the analog response of all the 256 channels of the FEB. This is conducted by performing on a test bench the basic calibration steps that will be followed in the actual Super-FGD setup. The results of these tests show that the FEB behaves as expected and that its performance is satisfactory.

### 6.2.3 Linearity

#### Setup

This test consists in evaluating the linearity of the response of the FEB when varying the amplitude of the input signal. Since such a test requires a precise knowledge of the input signal, we use the setup displayed in the bottom panel of Figure 6.5. The goal is to find the mapping between the ADC counts in the HG and the LG for different gain settings and evaluate its linearity. As discussed in Section 6.1.2, the gains can be set separately for the LG and the HG preamplifiers with a 6-bit parameter spanning the range 0 to 63.

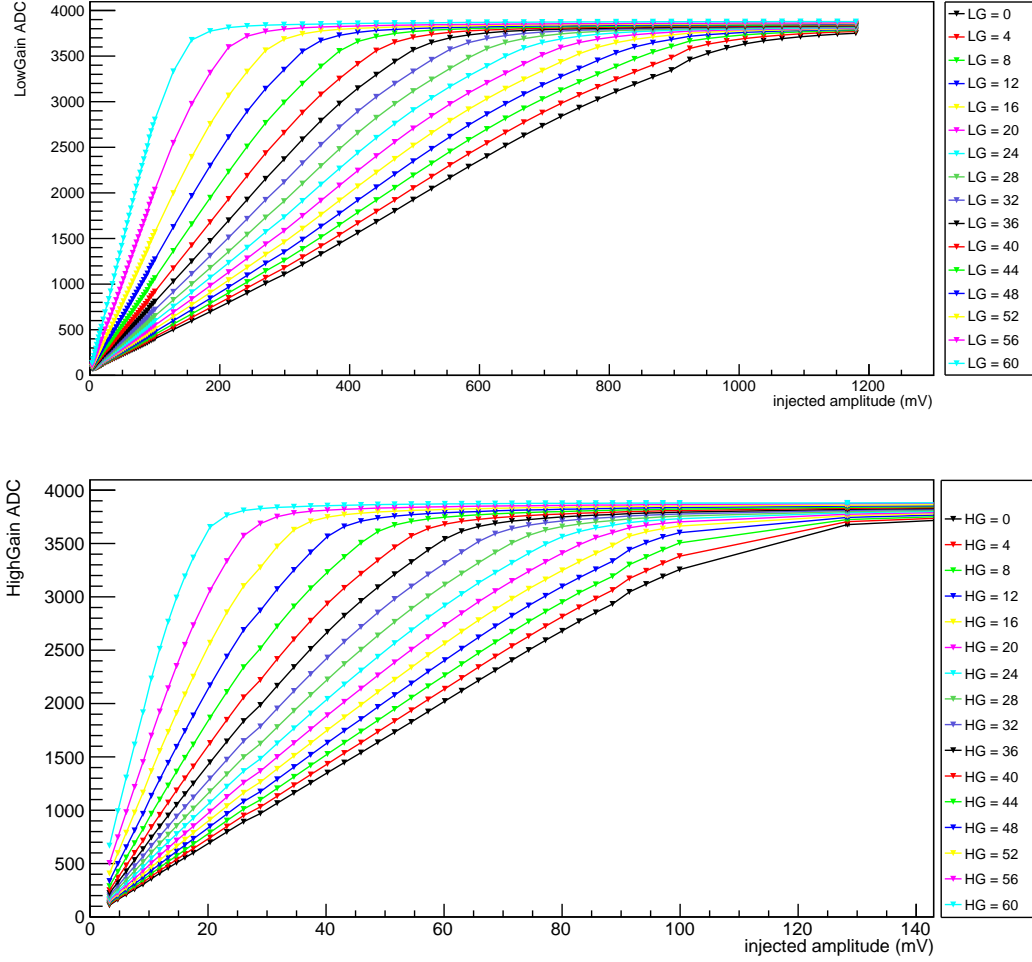


Figure 6.15: Example of the measured mapping between the injected amplitude and the measured ADC count in the HG (top) and the LG (bottom) in a single channel for different preamplifier gain values. Credits: L. Giannessi.

This test requires a large number of elementary measurements where each time a single variable is changed. These variables are: the channel, the gains on the HG and the LG, and the amplitude of the input signal. The total number of required operations is therefore  $256 \times N_g \times N_{in}$  where  $N_g$  and  $N_{in}$  are respectively the number of the gains and the input amplitudes to be tested. Consequently, these tests involve a large number of operations which requires automation. A setup develop in UniGe allows us to control at the same time the FEB parameters and the input pulse from the waveform generator. The human intervention in this test simply corresponds to changing the cable position to switch the injection channel.

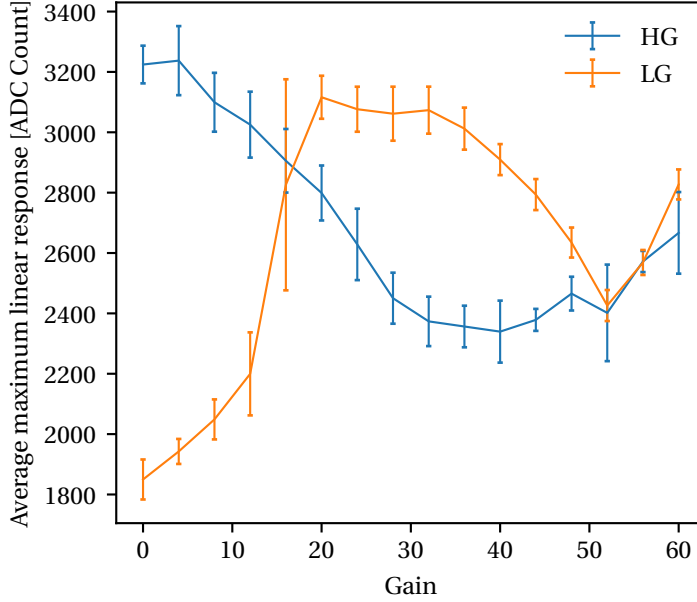


Figure 6.16: The maximum linear response point in ADC counts for different gain settings in the HG (blue) and the LG (orange), averaged over the 256 channels of the FEB.

### Results

Figure 6.15 shows an example of the test result for a single channel. When a pulse is injected into the FEB, it corresponds to a precise value of the ADC count that depends on its amplitude. The top (bottom) panel shows the obtained mapping between the ADC count and the injected amplitude on the HG (LG) path for a range of gain settings spanning the interval  $[0, 63]$ .

Quantifying the linearity relies on computing the residuals with respect to a linear fit to the lowest injection amplitudes for which the response is expected to be broadly linear. Concretely, this is performed by fitting a line to the first  $N$  points, then evaluating the residual at each amplitude value, i.e. the difference between the corresponding ADC count and the linear fit expectation. The linearity threshold is chosen to be at 1% of the whole ADC count range which corresponds to 4096 (12 bits). The linearity is considered to be lost at the first ADC count that exceeds this threshold. To ensure that this metric is not biased by non-linear effects in the very low amplitudes, this procedure is repeated varying the number of points  $N$  in the linear fit, and the *maximum linear response* point is determined as the maximum ADC count value that exceeds the threshold among all the different fits.

The point of maximum linear response is obtained for each channel and for each gain setting. Figure 6.16 shows the averaged maximum linear response over all the 256 channels as a function of the preamplifier gain setting for the LG (orange) and the HG (blue). The error bars reflect the spread of its value across the channels. Overall, it is found to be rather uniform

across the different channels for each gain value. Furthermore, the linearity in the LG path gives an optimal gain range between 20 and 40, whereas the HG linearity appears to decrease as the gain increases.

This study is particularly important for the tuning and the calibration of the Super-FGD since it can help with the choice of the FEB parameters. As a reference, the gain of the HG path needs to be chosen so that the individual photoelectron peaks can be resolved, while providing a dynamic range of  $\sim 100$  p.e. so that a minimum ionizing particle (expected at  $\sim 50$  p.e.) can be detected in the mid-ADC range. With the initial tests of Section 6.2.2, this could be satisfied for HG preamplifier values around  $\sim 45$ , while any value below 40 would make complicated identification of these peaks. Figure 6.16 shows that this does not necessarily lie in the most optimal linearity region of the HG. On the other hand, the LG preamplifier gain needs to be chosen to allow us to detect the maximum energy deposition expected in the Super-FGD, which can go up to  $\sim 1500$  p.e. from the Bragg peak of a stopping proton for instance. This could be achieved with a gain of  $\sim 30 - 40$ , which in contrast lies in the region where we would expect the best linearity at the LG.

### 6.2.4 Channel-to-channel cross talk

#### Setup

The goal of this test is to study the electronic cross talk between the channels. To do so, we use the setup shown in the top panel of Figure 6.5. In this case, a high charge of  $\sim 1200$  p.e. is injected in *one* MPPC that is connected to a *single* given channel, whereas no signal is injected on the other channels. All the channels are read at the same time<sup>3</sup> as soon as one channel is triggered with a hit.

This test is performed with two versions of the MIB. In its first version (MIBv1), the mappings from its front connectors (see Figure 6.4) to the CITIROC channels change from ASIC to ASIC. This caused an additional (unnecessary) layer of complication and was addressed in the second version (MIBv2) for more consistency where the mapping is the same for all the connectors.

#### Results

When injecting the large charge on a given channel, a signal can be observed on some of the other channels of the FEB. An example of this is displayed in Figure 6.17, where the 1200 p.e. charge on the channel 0 of the FEB induces a signal that can be observed in the channel 1. The variation of the signal with (red) and without (blue) the light injection is what we use to

<sup>3</sup>This uses the *external trigger* option of the CITIROC, where the trigger is sent by the FPGA to all the other CITIROCs once it receives a signal from one channel (here the injection channel). The delay this introduces is estimated at  $\sim 10$  ns, which does not have a significant impact on this test. An FPGA firmware with this feature was developed specifically for this test.



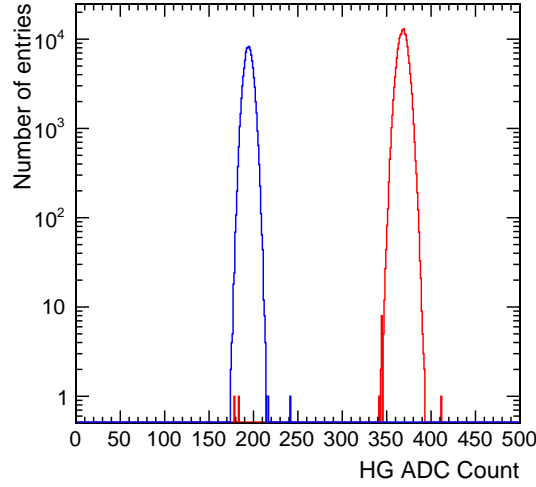


Figure 6.17: Amplitude observed in channel 1 when  $\sim 1200$  p.e. charge is injected in channel 0 (red) compared to when no light is injected, i.e. pedestal (blue).

quantify the cross talk. This is reported for both MIBv1 and MIBv2 in the form of a matrix as shown in Figure 6.18 in percentage of the injected charge, using the calibration data of Section 6.2.2 to convert the variation from HG ADC counts to p.e. units.

The first observation is that the two matrices are broadly symmetric which confirms that what we measure is actual cross talk due to the mutual electric influence between the channels: if the charge is injected in a channel  $n$  and a signal is observed in channel  $m$ , then injecting in channel  $m$  would yield similar impact on channel  $n$ . Furthermore, we notice that they are diagonal with blocks of  $32 \times 32$ , which means that the cross talk occurs only between the channels of the same CITIROC.

With the MIBv1 (top panel in Figure 6.18), the pattern of the cross talk in each  $32 \times 32$  ASIC block is different. On the other hand, the MIBv2 (bottom panel) gives the same pattern among the different ASICs. This hints at the fact that the MIB is the main source of the cross talk, since the mapping MIB connector to ASIC was changed to be the same for MIBv2 in comparison with MIBv1.

Indeed, the MIB is a dense 16-layer board where all the traces are bound to be close especially around the connectors. This is observed in the layout of the MIB as shown in Figure 6.19. The top panel highlights two lines on two successive layers with no separating ground plane. The bottom panel shows an example where the traces are very close to each other. By following each of these lines until the CITIROC, we do find that they correspond to channels for which a significant cross talk is observed in the corresponding matrix of Figure 6.18.

One way to mitigate this is to add more layers in the MIB design. This comes at a significant increase of their cost, while the  $\sim 0.4\%$  maximum amplitude of this cross talk is not necessarily

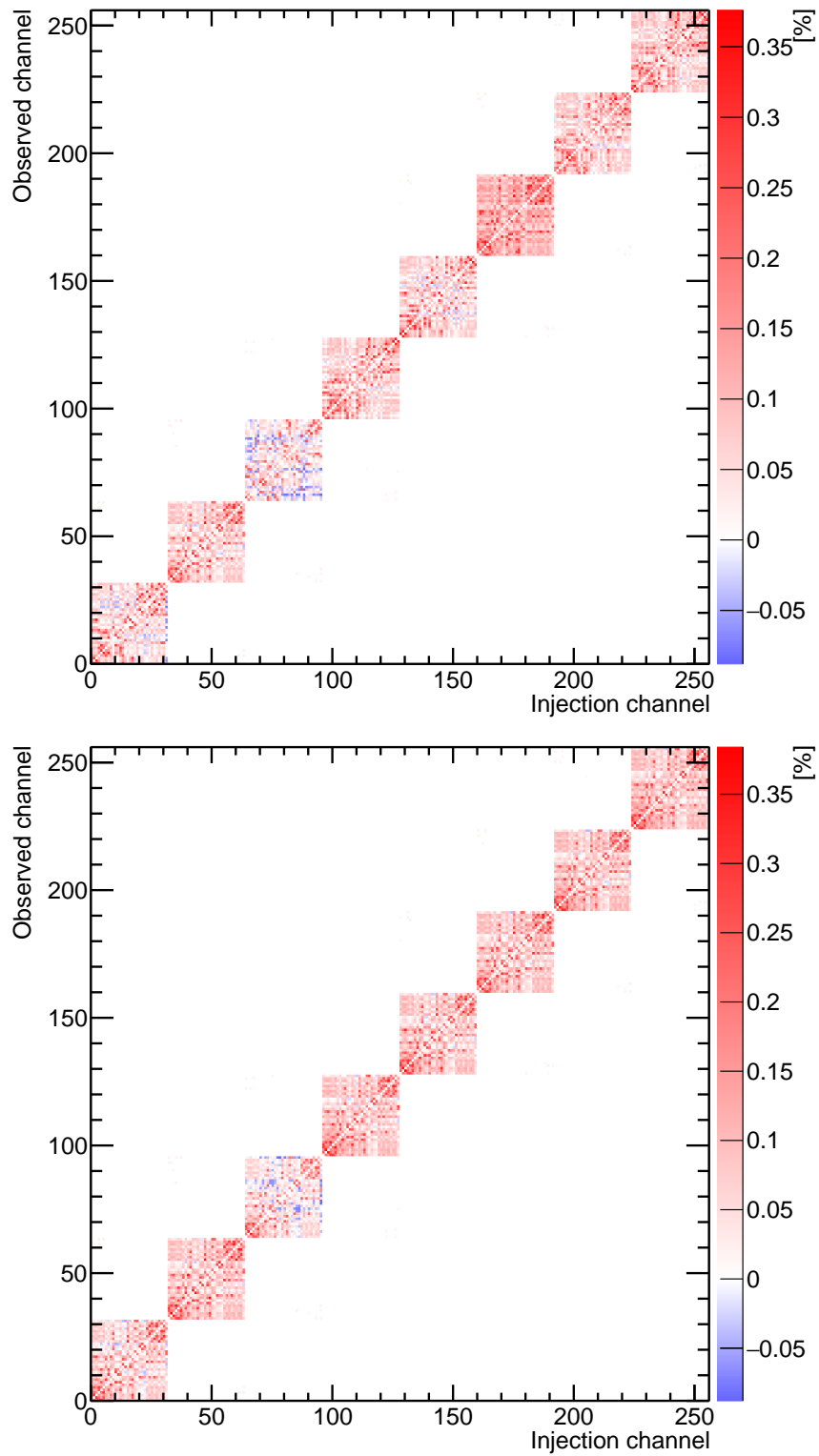


Figure 6.18: Channel-to-channel cross talk matrix for MIBv1 (top) and MIBv2 (bottom). A charge of  $\sim 1200$  p.e. is injected in the injection channel.

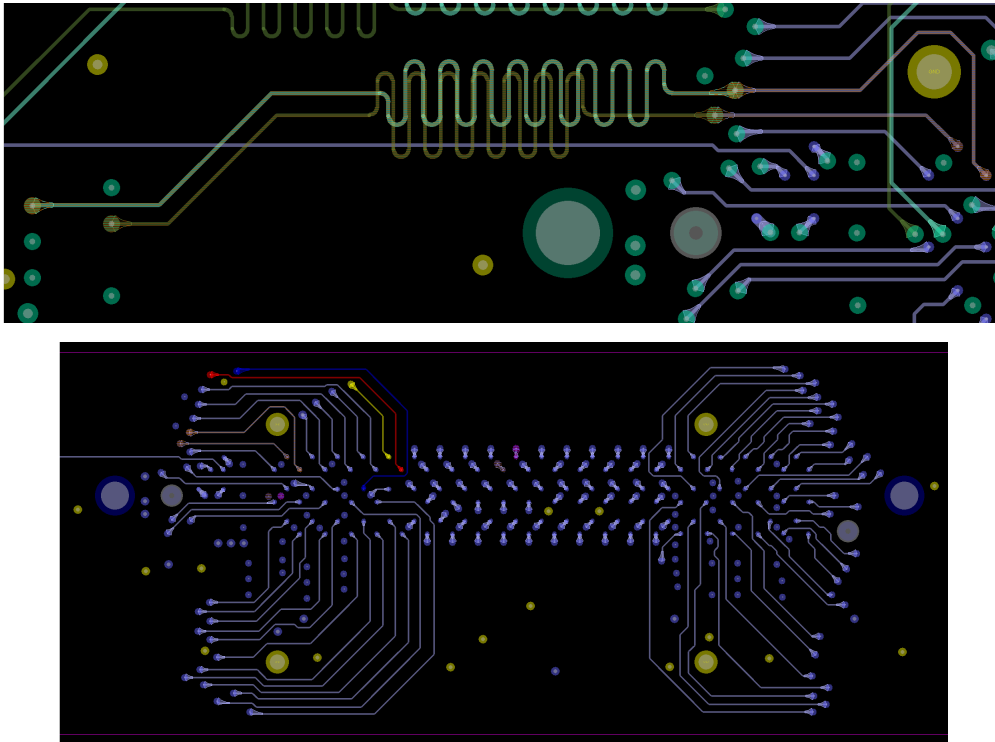


Figure 6.19: Layout of parts of the MIB that might be responsible for the cross talk (MIBv1). Top: two traces on adjacent layers with no separation layer. Bottom: traces on the same layer around the 400-pin MIB-to-FEB connector.

concerning and does not warrant further action.

This test also highlighted a “negative cross talk” as shown in Figure 6.18 (blue shades). This is actually a characteristic of the CITIROC: when a large signal is injected in one or a few channels of the ASIC, it tends to drain current from the other channels which leads to a negative shift of their baseline. A discussion with the manufacturer allowed us to identify an additional decoupling capacitor for each CITIROC in the final FEB design which can reduce to some extent this effect, to ensure that it is negligible in our case.

### Summary

In conclusion, when injecting a signal of  $\sim 1200$  p.e., the maximum cross talk that we observe is less than  $\sim 0.4\%$ . This cross talk occurs between the channels of the same ASIC and is mostly due to the MIB. The MIB is a dense board with 16 layers, where the traces get close especially at the level of the connectors. Its design could likely be improved by adding layers to further separate the traces, but this is estimated to come at a significantly higher cost and a longer lead time for an improvement that is virtually negligible.

### 6.2.5 Timing

All the previous tests used only the analog capability of the FEB. In this section, the focus is on the timing part. As mentioned in Section 6.1.2, the timing information is recorded with a fast shaper and a discriminator (with an adjustable threshold) applied on the HG path<sup>4</sup>. With a sampling rate of 400 MHz, the FPGA is responsible for time stamping the output of the discriminator, giving the timing information of the rising and the falling edges for each hit.

In the Super-FGD setup, the MCB sends a global time stamp (GTS) to the FEBs every 10  $\mu$ s to timestamp data. In these tests, since the other boards of the full chain of the Super-FGD electronics are not available, we use an internal counter in the FPGA to emulate the GTS signal.

Two distinct tests are performed to evaluate the response of the FEB. The goal of the first test is a simple check of its output when injecting a periodic signal, while the second aims at evaluating the timing difference between the channels.

#### Response to a periodic signal

The setup of this test is the one displayed in the bottom panel of Figure 6.5. A signal produced by the pulse generator and filtered with the RC circuit is injected on a *single* channel. Testing the timing acquisition requires a precise knowledge of the input signal, which is why we opt for adjustable pulses produced by the waveform generator.

The preliminary FPGA firmware used in this test provides only the two least significant bits of the GTS signal, which limits the range of the frequencies that can be tested since a low frequency signal with a period significantly larger than the GTS period would be incorrectly decoded. Consequently, we test the response with multiple signals of frequencies ranging from 100 to 400 kHz.

In this test, we measure the period of the signal with the FEB by computing the difference between the timing of the rising edge it records for two successive hits. We choose the rising edge instead of the falling edge for these measurements because the shape of the signal (shown in Figure 6.6) has a sharp rise which is more precisely timestamped from the discriminator output than the longer tail of the falling edge. Since the FPGA sampling rate is 400 MHz, the FEB output is in steps of 2.5 ns. Figure 6.20 shows the distributions of the timing difference between two successive rising edges read by the FEB for different periods  $\Delta T_{\text{gen}}$  of the pulse signals set in the waveform generator. All of the distributions are within two bins of 2.5 ns as we can expect, and their mean can provide an “FEB-measured” period of the signal  $\Delta T_{\text{mes}}$ .

In each panel of Figure 6.20, the period of the signal that is set on the pulse generator  $\Delta T_{\text{gen}}$  is shown, along with the measured period  $\Delta T_{\text{mes}}$  which is obtained from the mean of the displayed distribution. For all the frequencies that were tested, the timing difference

<sup>4</sup>A CITIROC parameter actually allows us to select whether the timing information should be obtained from the HG or the LG path. The default usage is the HG.

## Chapter 6. Electronics of the Super-FGD

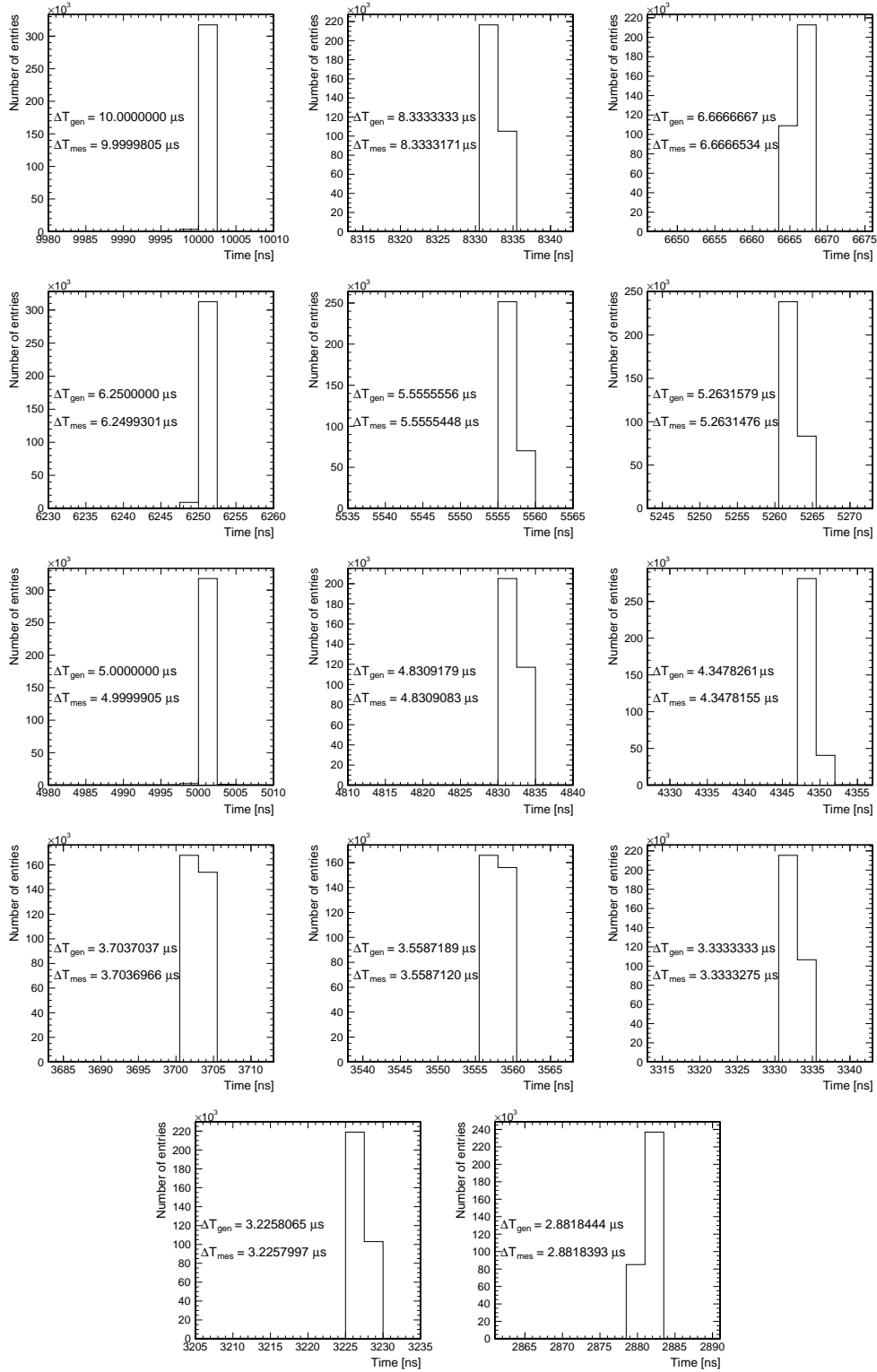


Figure 6.20: Distributions of the timing difference between two successive rising edges in one channel of the FEB, with the period of the signal  $\Delta T_{\text{gen}}$  as set on the pulse generator, and the mean of the distribution  $\Delta T_{\text{mes}}$  as the measured timing difference.

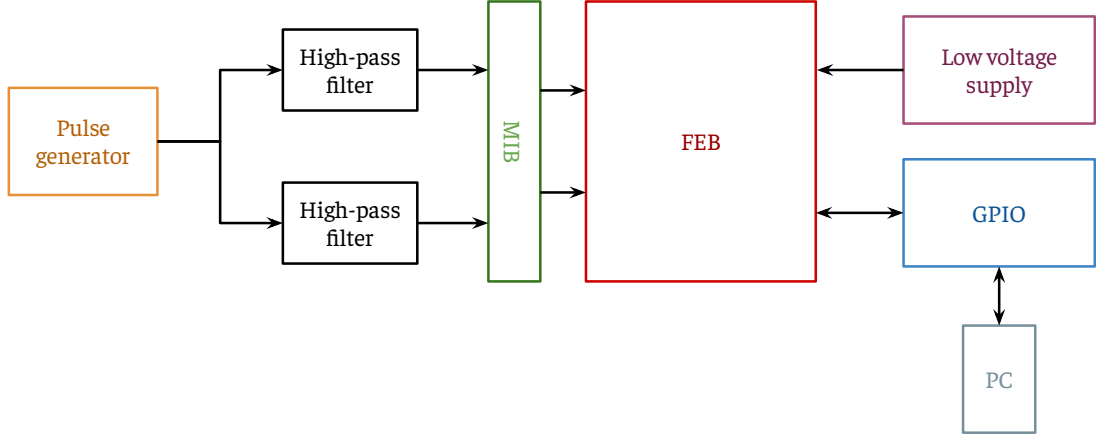


Figure 6.21: Sketch of the setup used to measure the timing difference between the channels.

between the successive rising edges gives an accurate measurement of the period of the input signal. The statistical uncertainty on  $\Delta T_{\text{mes}}$  can be estimated to be in the order of  $\sim 2.5 \text{ ns} / \sqrt{N_{\text{entries}}} \sim 5 \times 10^{-6} \mu\text{s}$  with a sample of  $N_{\text{entries}} \approx 320,000$  hits. In addition to the statistical error, uncertainties on this measurement also come from the jitter of the pulse generator, which is below 1 ps, as well as the potential drift due to the phase difference between the clocks of the FPGA and the pulse generator. This test was carried on all the channels of the FEB, and they were all found to perform in the same way.

### Channel-to-channel timing difference

The goal of this test is to evaluate the timing difference between the channels of the FEB. Unlike the setup used in the previous sections, this requires a simultaneous injection of the same pulse in two different channels. This is achieved by dividing the output of the pulse generator with a simple “T” connector. The two signals are then injected into two channels of the FEB through the same high-pass filter as displayed in Figure 6.21. The cables that link the output of the generator to each FEB channel are carefully chosen to have matching lengths. The amplitude of the generator is increased, and we use a relatively higher timing threshold in the discriminator to avoid triggering on reflected signals due to the T connector. The two injection channels are activated on the FEB, and the goal is to compare the timing information they record. In all of this section, we use the channel 0 as a reference, i.e. the timing delay of channel  $n$ ,  $1 \leq n \leq 255$  is computed with respect to channel 0.

With the same idea of the previous single-channel test, this is achieved by computing the timing difference of the rising edge of the signals arriving in the two channels. The distribution of this timing difference is usually in two bins as observed in Figure 6.20, and the mean of this distribution is our measurement of the timing difference.

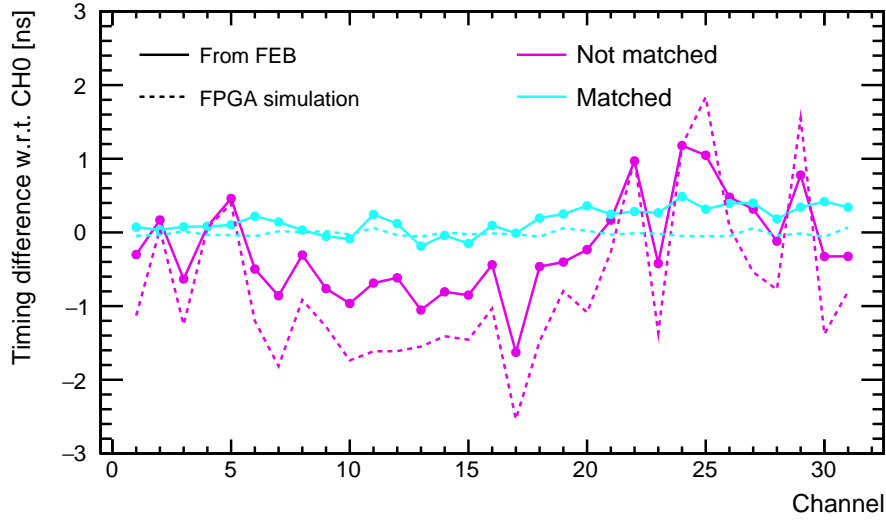


Figure 6.22: Timing difference between the channel 0 and the other 31 channels of the ASIC 0 as simulated by the FPGA programming software (dashed) and measured from the FEB data (full) for the version of the FPGA firmware where the timing trigger lines are not matched (pink) and when matched within  $\pm 150$  ps (cyan).

As a very first step, the timing delays were evaluated within one ASIC as shown in Figure 6.22 (full magenta line). The FPGA firmware used in this first test did not have any internal constraints on the timing trigger lines. This means that when multiple signals arrive around the same time to the FPGA, the firmware can take a long time to timestamp due to the high data load which causes channel-to-channel delays.

Intel provides a functionality in its FPGA programming software that performs timing simulations of the delays within the FPGA chip in the worst case scenario of its performance (temperature, data load, etc.). The result of this simulation is compared to the measured delay from the FEB data in Figure 6.22 for the channels of the same ASIC (dashed magenta). There is a clear correlation between the two results, which means that in this case the measured time delay in the FEB, of maximum  $\sim 3$  ns within ASIC 0, is dominated by the delays due to the FPGA firmware. In most channels, the delay as measured in the FEB is less than predicted by the FPGA simulation. This is not the case of all channels, which hints at the existence of other sources of delay other than the FPGA since this test bench is located in a room with a controlled temperature and the data load is not unreasonably high.

Following this initial test, the FPGA firmware was updated with constraints on the timing trigger lines to be matched within  $\pm 150$  ps. In Figure 6.22, we also compare the results with this new firmware of the measurement with the FEB (full cyan) against the FPGA simulation (dashed cyan). The timing difference is now significantly smaller (cyan) than when the trigger lines were not matched (pink). However, it can be noticed that there is a residual delay in the FEB data that is noticeably larger than what is predicted by the FPGA simulation.

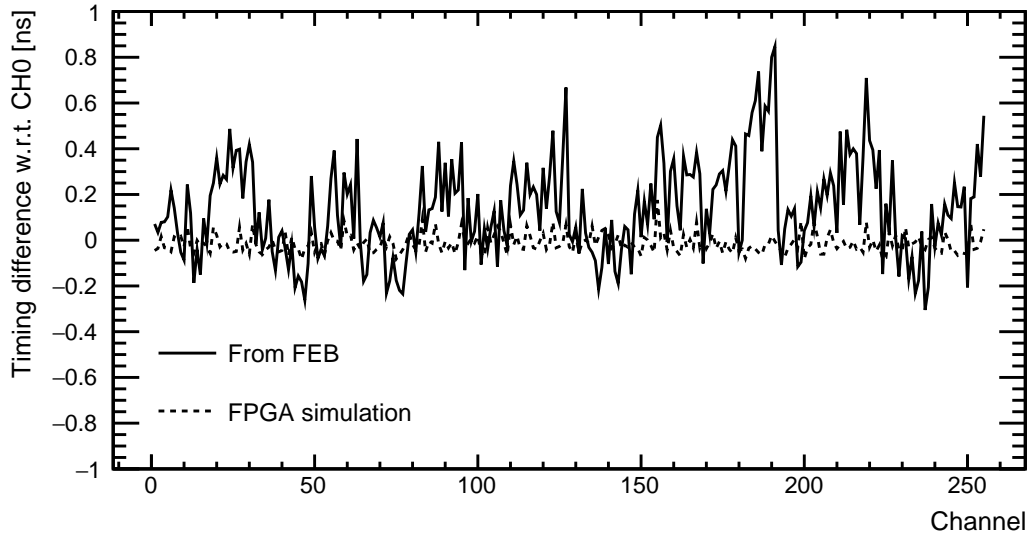


Figure 6.23: Timing difference between the channel 0 and the other 255 channels of the FEB as measured from the data (full) and simulated by the FPGA programming software (dashed) with the firmware where timing trigger lines are matched within  $\pm 150$  ps.

Furthermore, with this updated FPGA firmware, we measure the timing difference between all the channels of the FEB. Figure 6.23 shows the results compared to the FPGA simulation. The maximum timing delay that is observed is of  $\sim 1$  ns, which is significantly larger than the  $\pm 150$  ps matching of trigger lines in the FPGA. An additional check of the line lengths in the PCB layout of the MIB+FEB chain shows that they are matched within  $\pm 20$  ps. Consequently, neither the FPGA firmware nor the trace lengths could explain this large mismatch.

A trend can somewhat be observed where, on average, the first 16 channels of each ASIC are less delayed in comparison to its last 16 channels. This indicates that the delay might be due to the ASIC itself, or the level shifters at its output. In fact, at the output of each ASIC (immediately to the right of each CITIROC in the top panel of Figure 6.3), there are two level shifters that switch the voltage level at the CITIROC output of 16 channels from 3.3 V to 1.8 V so that it is adapted for the FPGA. The data sheet of this component indicates an overall propagation delay through the switch of 225 ps, and an estimated channel-to-channel matching below 22.5 ps [261]. This is still at a level that is notably below the observed  $\sim 1$  ns.

To better understand the source of these delays, we directly probed with an oscilloscope the signals along their path from the pulse generator to the FPGA on the FEB. Since the FEB and the MIB have 14 and 16 PCB layers respectively, it is a challenging task because we can only probe components on the top of the FEB with accessible pins while most of the lines are in the inner layers. For instance, it was not possible to probe at the level of the MIB, as none of the traces of the channels are accessible.

The first check consisted in verifying the signal matching upstream to the MIB. They were



found to be perfectly synchronous within a few picoseconds thanks to the choice of cables with matching lengths. Downstream of the MIB, we identified probe points where this procedure can be performed at the level of components on the top layer of the FEB shown in Figure 6.24. The P1 and P2 points allow us to probe the signals after the MIB and before they reach the CITIROC. These components serve as a protection circuit to the ASIC channels. At the output of the CITIROC, the signal goes to the two level translating switches which have accessible pins. We use these to probe the signals at their input (P3 and P4) as well as their output (P5 and P6).

We choose as an example the channels 169 and 185 to probe their relative delay. These have one of the largest timing differences according to Figure 6.23. The corresponding signals at P1 and P2 were found to be synchronous within  $\sim 10$  ps as shown in the top panel of Figure 6.25, which is within the expected delay margin due the line lengths in the MIB. This confirms that the signals do reach the ASIC almost at the same time, and that the lengths of the traces are correctly matched from the pulse generator through the MIB until the input of the CITIROC.

On the other hand, the bottom panel of Figure 6.25 shows that the measured signals at the ASIC output (or level shifter input) at P3 and P4 are noticeably delayed, with a timing difference of  $\sim 1$  ns consistent with the estimated delay with the FEB data as shown in Figure 6.23. This measurement was performed on several pairs of channels, yielding results in agreement with Figure 6.23. This corroborates the hypothesis that the source of the delay is the ASIC itself. We further confirmed this by measuring the timing delay at the output of the level shifters at the P5 and P6 points (see Figure 6.24) which showed no significant additional delay in comparison with the measurement at its input.

To conclude, we evaluated the channel-to-channel delays in the FEB, and a maximum delay of around  $\sim 1$  ns is observed (Figure 6.23). Investigating this shows that the main source of this delay is the CITIROC chip itself. This channel-to-channel time matching within the chip was not evaluated by the manufacturers. Great care was taken to match the lengths of all the lines on the PCB, but this timing difference cannot be compensated for neither on the hardware nor on the firmware of the FPGA. Indeed, this delay varies from chip to chip, and testing the timing difference on a second FEB yields delays distributed differently from what is obtained in Figure 6.23.

As part of the Super-FGD calibration, it is already planned to record the timing delay information on a channel-by-channel basis with cosmic muons for instance. These tests further confirm the importance of such calibration in order to achieve precise timing measurements in the Super-FGD, which are particularly relevant for the estimation of the neutron kinematics.

### 6.3 Tests in a magnetic field

A crucial test of the FEB design is the evaluation of its performance within a magnetic field in similar conditions to the actual Super-FGD setup. The power mezzanine is the part that

### 6.3 Tests in a magnetic field

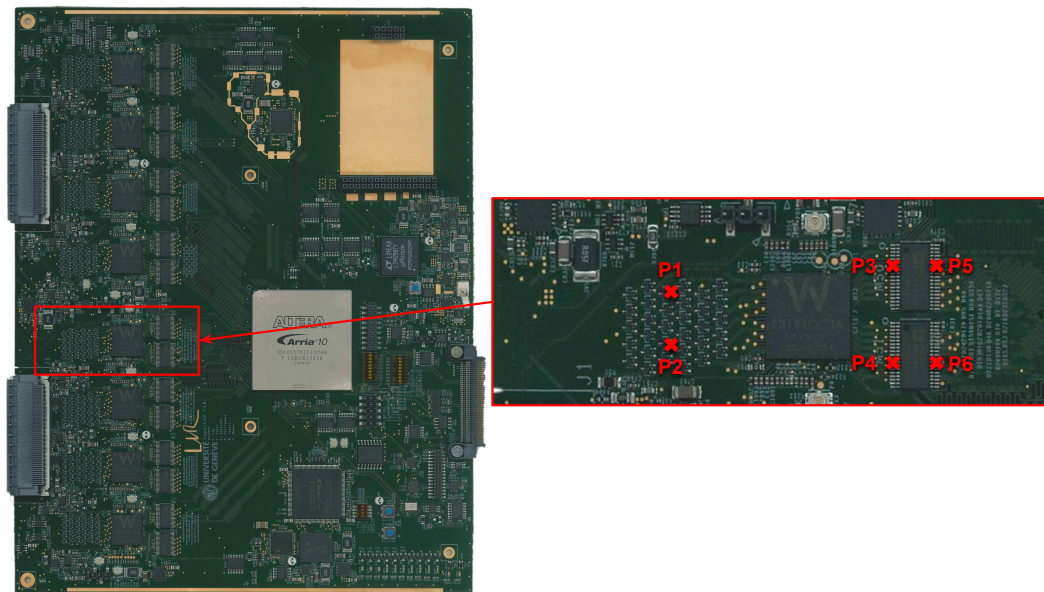


Figure 6.24: Points of probe with the oscilloscope on the FEB. P1 and P2 correspond to a probe at the input of the CITIROC, P3 and P4 to its output, which is also the input to the level shifters, and P5 and P6 to their output. The signals flow from the left (where the MIB is connected) to the right.

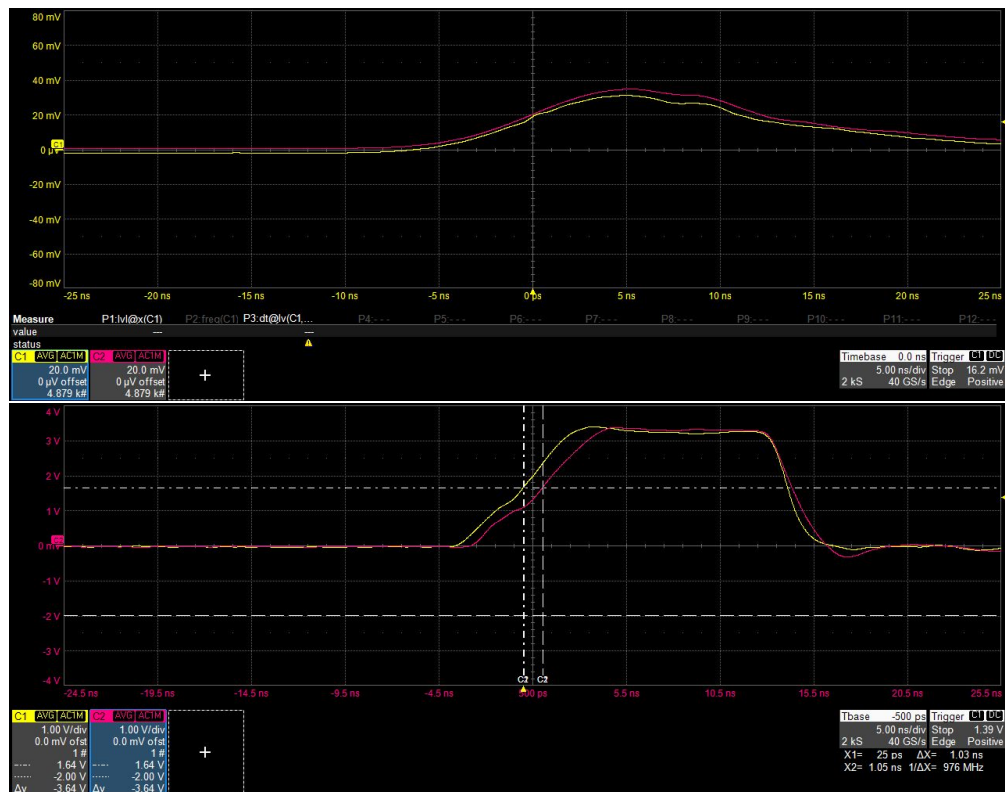


Figure 6.25: The signals probed with the oscilloscope both at P1 and P2 (top), as well as P3 and P4 (bottom) for channels 169 and 185.

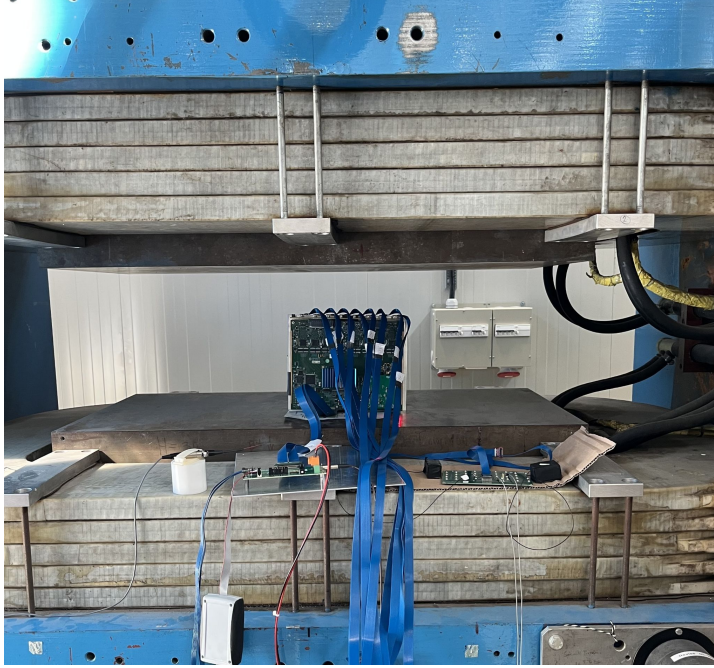


Figure 6.26: Picture of the FEB setup in the MNP17 magnet at CERN.

requires careful attention since it manages the distribution of the voltage levels to the active components of the FEB and can particularly react to the presence of a magnetic field.

This test was performed in the MNP17 magnet at CERN displayed in Figure 6.26. It is a 20-ton dipole magnet that can provide a homogeneous field of up to  $\sim 1$  T that can be adjusted by varying the current. Due to the high demand on the magnet and the tight schedule of the Super-FGD, only a few days were allocated for testing the FEB in MNP17. Consequently, an expedited version of the performance tests presented in the previous section was devised.

These tests were performed with three values of the magnetic field: first, as a reference, no B field, then a 0.2 T field which corresponds to the nominal Super-FGD setup, and finally a 0.4 T field to test the electronics in a more extreme condition. These values were monitored at all times using a Gauss/Tesla-meter (F.W. Bell 4048). Furthermore, different orientations of the FEB with respect to the magnetic field were considered as sketched in Figure 6.27. When installed in the near detector complex, the electronics will be located on both sides of the Super-FGD in crates. If  $z$  corresponds to the beam direction, the electronics will see a field along the  $x$  axis which corresponds to Figures 6.27a and 6.27b. Although the configurations in Figures 6.27c and 6.27d are not relevant for the Super-FGD, they were tested as well for completeness.

Due to the time constraints, we selected four of the most important items to test for the different configurations at the three field intensities:

### 6.3 Tests in a magnetic field

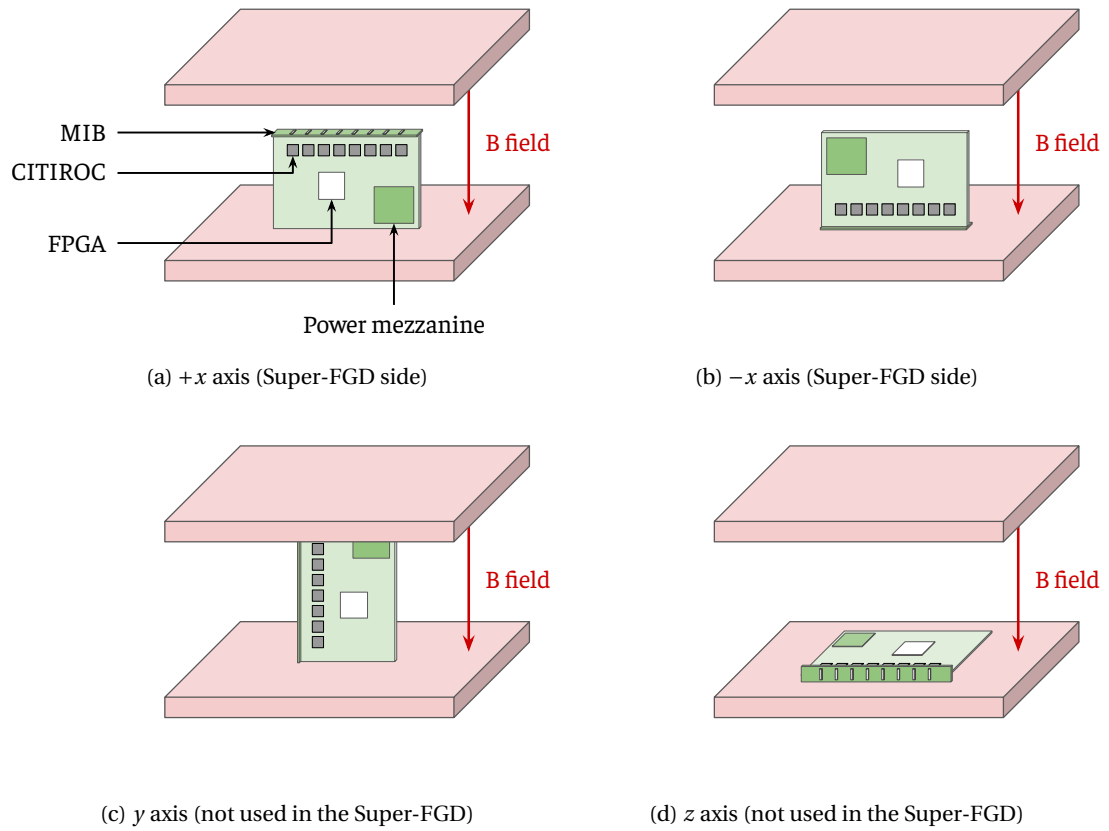


Figure 6.27: Different FEB configurations tested in the MNP17 magnet (pink). The top row corresponds to the magnetic field that will be experienced by the FEBs in the Super-FGD setup within the UA1 magnet, while the bottom two configurations are tested as well although they do not reflect any considered Super-FGD setting.

Magnetic field	+ $x$ axis	- $x$ axis	$y$ axis	$z$ axis
0.2 T	1.9	1.8	2.1	3.3
0.4 T	6.0	5.5	6.0	16.1

Table 6.1: Variation in percentage at 0.2 and 0.4 T fields of the average consumed current on the low-voltage (12 V) power supply as recorded by a sensing chip on the FEB with respect to the reference 0 T field (1.79 A) case for the different configurations shown in Figure 6.27.

1. the power consumption,
2. the quality of the finger plots,
3. the linearity,
4. the timing.

The low-voltage supply powers the active components of the FEB through the power mezzanine with 12 V at its input. The average overall current consumption at the reference when no B-field is applied corresponds to  $\sim 1.79$  A. Table 6.1 shows the relative variation of this current in the different tested conditions in the magnet. While this variation at the nominal ND280 magnetic field of 0.2 T is below 2% in the configurations relevant to the Super-FGD ( $\pm x$  axis), the worst case scenario corresponds to the  $z$ -axis setting at 0.4 T which goes up to 16%.

The impact on the high-voltage lines that go to the MPPCs was also evaluated and no significant discrepancies were observed. Consequently, only the low-voltage overconsumption needs to be taken into account in the Super-FGD electronics for its overall cooling and power supply requirements.

The second test concerned the impact of the B-field on the HG amplitude distributions from an MPPC signal. The finger plots were obtained by fully populating all the channels of the FEB with four MPPC64 boards, inserted in a light-tight box with a pulsed LED injection similarly to the top panel of Figure 6.5. The distributions at the nominal 0.2 T field in the  $\pm x$ -axis configurations are indistinguishable from the reference case as illustrated in Figure 6.28. The peak-to-valley ratio remains the same, indicating that no significant additional noise is induced by the presence of the magnetic field. The bottom panels show the most extreme impact that was observed which corresponds to the  $z$  axis configuration at 0.4 T, where we can see shifts of a few ADC counts in the peak positions. This can be interpreted as a gain variation. Since the previous tests showed that the high-voltage lines were almost unaffected by the magnetic field, this gain drift can be related to the overall over-consumption of the FEB which increases its temperatures and may cause the gain to decrease.

The third set of tests consisted of reproducing the linearity study of Section 6.2.3. Due to the short allocated time, only two channels per CITIROC were tested for the different considered settings. Figure 6.29 shows the linearity of the HG (left) and LG (right) ADC counts as a function

### 6.3 Tests in a magnetic field

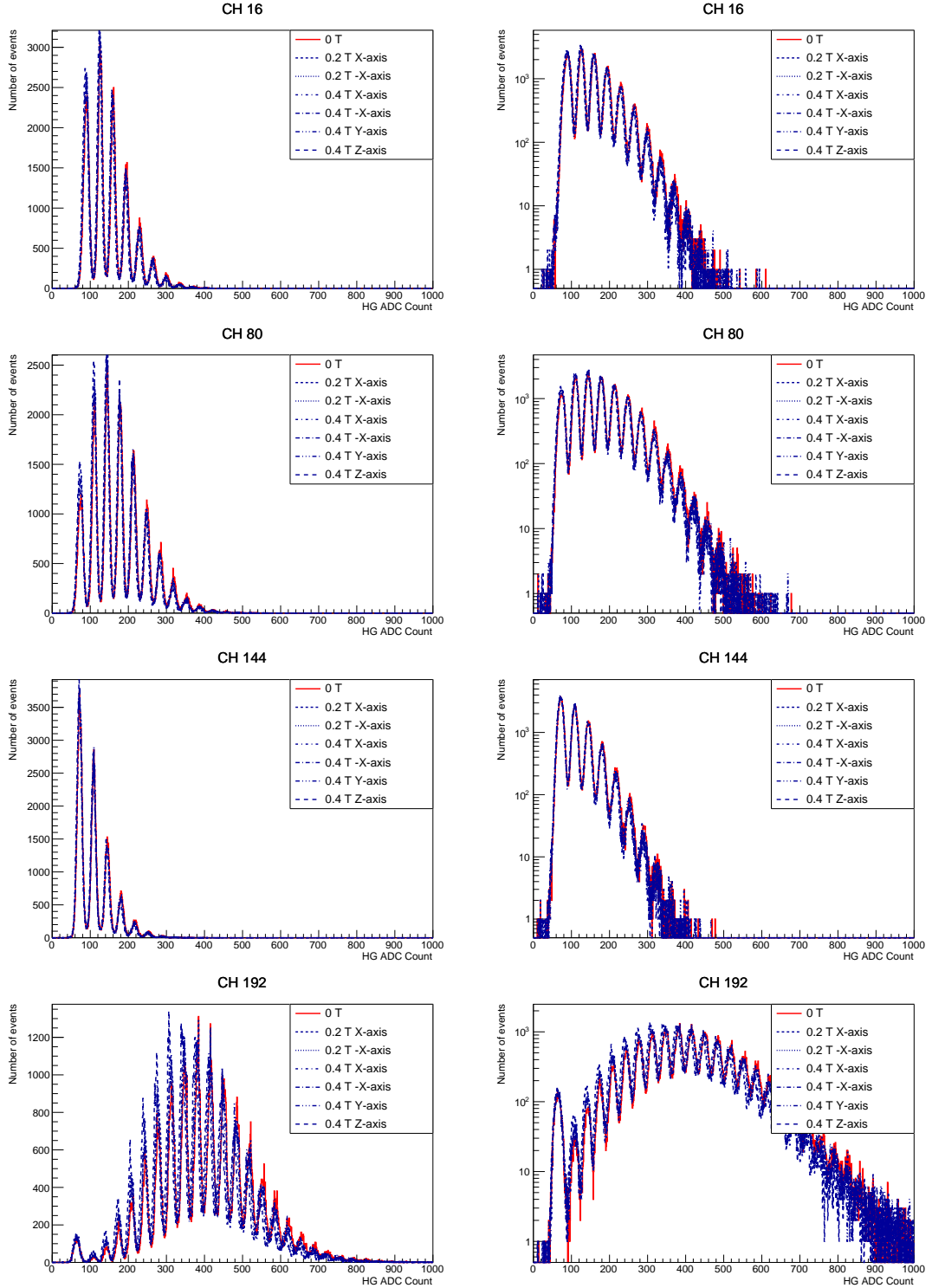


Figure 6.28: Examples of HG amplitude distributions for a few channels in linear (left) and logarithmic (right) scales compared between the reference 0 T field (red) and the other tested configurations (blue) shown in Figure 6.27. Note that the light source used in this test does not provide a uniform light distribution on all the four MPPC64 channels.

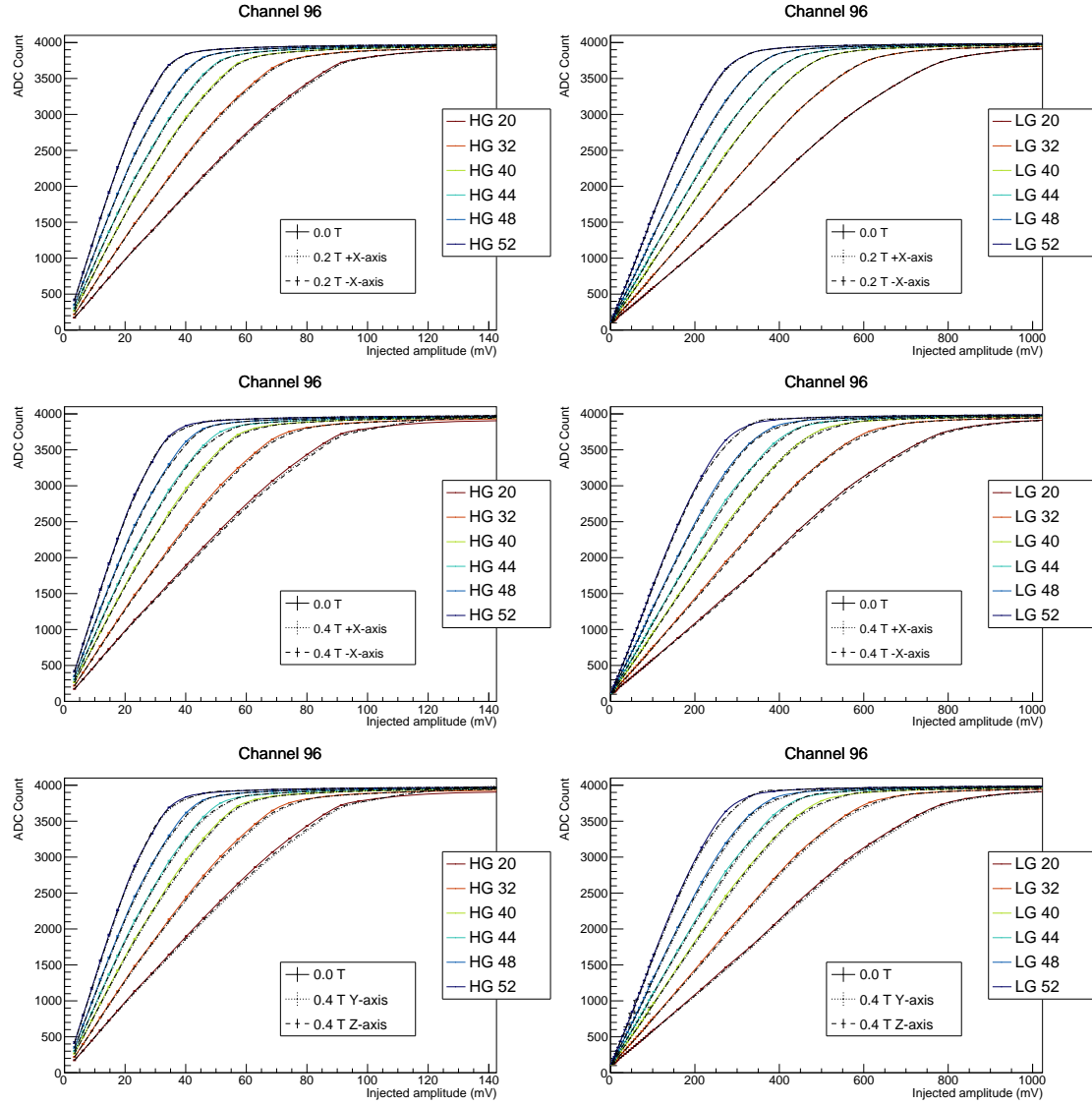


Figure 6.29: Linearity of the FEB channel 96 in the HG (left) and the LG (right) amplitudes for the ND280 nominal 0.2 T (top row) as well as 0.4 T field (middle row) in the  $\pm x$ -axis configuration, and the y- and z-axis settings at 0.4 T (bottom row) for different gain settings of the CITIROC HG and LG preamplifiers.

of the input signal amplitude. The different colors correspond to different gain settings of the corresponding CITIROC preamplifiers. The lines are almost indistinguishable for the nominal 0.2 T B-field in the  $\pm x$ -axis configuration (top panels). The 0.4 T field appears to cause a small but noticeable deviation at high input amplitudes with respect to the reference no B-field case, which indicates a similar gain drift as the one observed in the finger plots.

The last test consisted in measuring the timing information in the different configurations. The obtained timing data was always consistent within few tens of picoseconds, which correspond to the measurement uncertainty. Therefore, no significant impact of the magnetic field was found on the timing path.

In conclusion, the tests performed with the FEB at the nominal ND280 B-field in the Super-FGD configuration did not show any significant impact that needs to be addressed. We observed nevertheless a noticeable impact at twice the nominal B-field on the power consumption and the gain in some of the configurations displayed in Figure 6.27 that are not relevant for the Super-FGD.

## 6.4 Other ongoing tests

### 6.4.1 Integration tests

The different boards of the Super-FGD electronics chain (see Figure 6.2) were designed at different institutes. While the FEB, the MIB and the mechanical crate are prepared in LLR and UniGe, the OCB and the backplane were conceived at the University of Pennsylvania, whereas the power mezzanine and the MCB were designed at Louisiana State University. Consequently, even if all these components work well individually, one of the most crucial tests is how they behave when put together.

As these boards started to be ready, we began planning a *vertical-slice test* (VST) with the purpose of building little by little the full chain shown in Figure 6.2. As previously discussed, the role of the OCB is to communicate with the 14 FEBs of the crate by setting their parameters, sending the triggers and receiving their data, while the backplane distributes the low and high voltage and ensures the communication between the boards of the crate.

The tests of Section 6.2 used instead the custom GPIO to temporarily fulfill the role of the OCB. The very first milestone of the VST consisted in a setup with one backplane, one FEB and one OCB where we successfully took FEB data without the mediation of the GPIO. The boards were inserted in a crate which allowed us to discover a mechanical mismatch due to a centimeter-inch conversion, hence the importance of such tests!

As more boards were ready and tested, the VST became more complete and at the same time more complex. A large effort to develop the DAQ framework used this setup to experiment the possible solutions. And in late January 2023, the first fully functional crate with all the



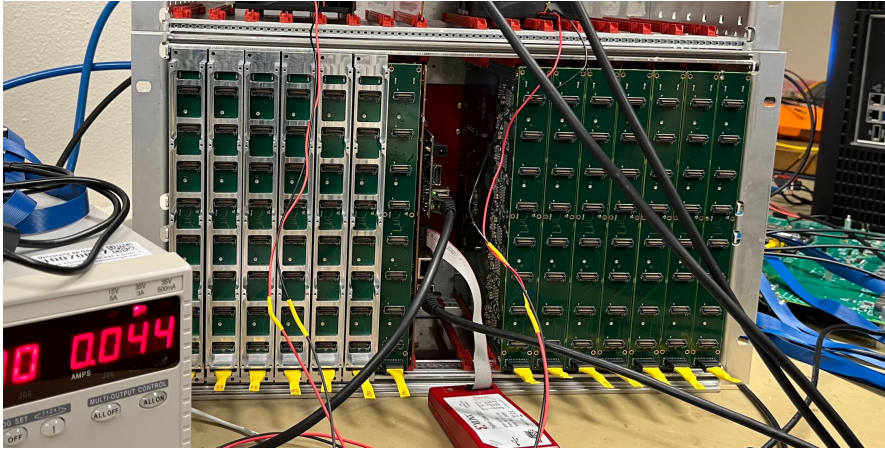


Figure 6.30: Picture of the first fully populated crate with all the electronic boards in the VST.

boards displayed in Figure 6.30 was tested and its basic board-to-board communications were validated.

The most urgent efforts surrounding the VST are now the finalization of the firmwares of the OCB and FEB, as well as the development of the DAQ. This crate, which can read up to  $14 \times 256 = 3584$  channels, could potentially be used for further beam tests with the Super-FGD prototypes mentioned in Section 5.3.1.

### 6.4.2 FEB functional tests

While the tests shown in Section 6.2 were all performed using a single FEB prototype, the mass production of the 240 FEBs (220 to be installed and 20 spares) requires a dedicated test bench that can allow for a fast and comprehensive evaluation of the functionalities of the FEB. These include checks of noisy or dead channels, the slow control lines, and the monitoring sensors.

One challenging part is injecting in all the 256 channels a well-known input signal to identify any problems. A dedicated board developed at SOKENDAI takes as an input a pulse from a waveform generator, and injects the signal to the desired channel(s). The channel switching is piloted using a Raspberry Pi, which allows for the full automation of the functional test: the FEB can be simply inserted in the test bench, and a programmed script tests the response of all the channels to detect any faulty ones. This setup is established at UniGe where the mass production FEBs are delivered.

## **Oscillation measurements** **Part IV**



## 7 T2K oscillation analysis

The measurement of the PMNS parameters of neutrino oscillations is one of the main physics output of the T2K experiment. T2K is particularly sensitive to  $\Delta m_{32}^2$ ,  $\theta_{23}$ ,  $\delta_{\text{CP}}$  as well as to some extent to  $\theta_{13}$  and the neutrino mass ordering. In simple terms, the rate of neutrino interactions at Super-Kamiokande is compared to the event rate at ND280, where the traveled distance is too small for any significant oscillations, to infer the oscillation parameters. By observing the disappearance of  $\bar{\nu}_\mu$ , we can constrain the atmospheric parameters  $\Delta m_{32}^2$  and  $\theta_{23}$ , while the appearance of  $\bar{\nu}_e$  gives sensitivity to the CP-violating phase  $\delta_{\text{CP}}$ .

The actual oscillation analysis is complex and involves multiple steps particularly due to the many systematic uncertainty sources that can affect the results. In Chapter 4, we presented only a fraction of these parametrized uncertainties in neutrino interaction modeling, whereas the other major sources of systematic errors are the modeling of the flux and the detector response. The analysis is consequently designed to best utilize the near-detector data in order to constrain most of these uncertainties for the inference of the oscillation parameters.

This chapter describes the various steps in the T2K oscillation analysis. First, in Section 7.1, we present an overview of the analysis pipeline, then discuss the near- and far-detector data and their selection in Section 7.2. Section 7.3 summarizes the parametrized uncertainty model of the flux, the detector response and the neutrino-nucleus interactions, while Section 7.4 shows how the data are fitted and the oscillation parameter inferred. Finally, Section 7.5 presents the results of the 2022 oscillation analysis and Section 7.6 gives a broad summary.

### 7.1 Overview

As discussed in Section 1.3, the neutrino oscillation probability is a function of the neutrino energy. Figure 7.1 shows how the sensitivity to the CP-violating phase  $\delta_{\text{CP}}$  is attained from the event rates of the appearance channels for  $\nu_e$  and  $\bar{\nu}_e$ . It indicates for instance that a maximal CP-violation with  $\delta_{\text{CP}} = -\pi/2$  corresponds to higher event rate in  $\nu_e$  and a lower event rate in  $\bar{\nu}_e$  assuming normal ordering.

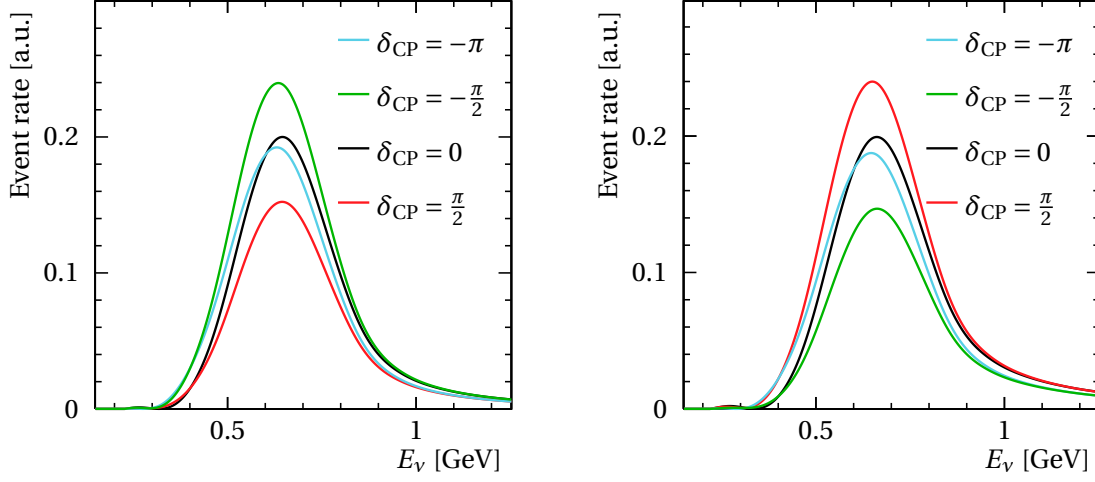


Figure 7.1: Impact of varying  $\delta_{\text{CP}}$  on the observed  $\nu_e$  (left) and  $\bar{\nu}_e$  (right) event rate at Super-Kamiokande as a function of the true neutrino energy  $E_\nu$  assuming normal ordering.

Besides, the frequency of the  $\bar{\nu}_\mu$  disappearance probability displayed in Figure 1.17 is governed by the value of  $\Delta m_{32}^2$ . The impact of  $\Delta m_{32}^2$  on the observed  $\bar{\nu}_\mu$  rate is displayed in the left panel of Figure 7.2 where its value is varied from the T2K best-fit value (black) to the corresponding 90% C.L. limits (red and cyan). This shows how it can shift the position of the disappearance “dip” around  $\sim 600$  MeV. Furthermore, as shown in the right panel of Figure 7.2,  $\theta_{23}$  has a different effect and alters the neutrino energy distribution by particularly modifying the “depth” of the oscillation dip. All this means that a good estimation of the oscillation parameters needs the measurement to capture the shape dependence on  $E_\nu$  of the event rate in order to disentangle all these effects, and not to simply count the total number of interaction events.

In practice, the observed event rate at the near and far detectors is a function of the reconstructed neutrino energy  $E_\nu^{\text{reco}}$  and can be expressed as [262]:

$$\begin{aligned} N_\alpha^{\text{ND}}(E_\nu^{\text{reco}}) &= \sum_i R_i^{\text{ND}}(E_\nu, E_\nu^{\text{reco}}) \times \epsilon_\alpha^{\text{ND}}(E_\nu) \times \sigma_\alpha^i(E_\nu) \times \phi_\alpha^{\text{ND}}(E_\nu), \\ N_{\alpha \rightarrow \beta}^{\text{FD}}(E_\nu^{\text{reco}}) &= \sum_i R_i^{\text{FD}}(E_\nu, E_\nu^{\text{reco}}) \times \epsilon_\beta^{\text{FD}}(E_\nu) \times \sigma_\beta^i(E_\nu) \times \phi_\alpha^{\text{FD}}(E_\nu) \times P(\nu_\alpha \rightarrow \nu_\beta, E_\nu), \end{aligned} \quad (7.1)$$

where:

- $N_\alpha^{\text{ND}}$  is the event rate of  $\nu_\alpha$  interactions observed at the near detector, whereas  $N_{\alpha \rightarrow \beta}^{\text{FD}}$  is the far detector event rate of  $\nu_\beta$  interactions from the  $\nu_\alpha \rightarrow \nu_\beta$  oscillation,
- $\sigma_\alpha^i(E_\nu)$  is the cross section of the interaction  $i$  (e.g. CCQE, CCRES, ...) for the neutrino flavor  $\alpha$ ,
- $\phi_\alpha^{\text{ND}}(E_\nu)$  and  $\phi_\alpha^{\text{FD}}(E_\nu)$  correspond to the neutrino flux of the flavor  $\alpha$  as a function of the true neutrino energy  $E_\nu$  at the near and far detector respectively, which can be slightly

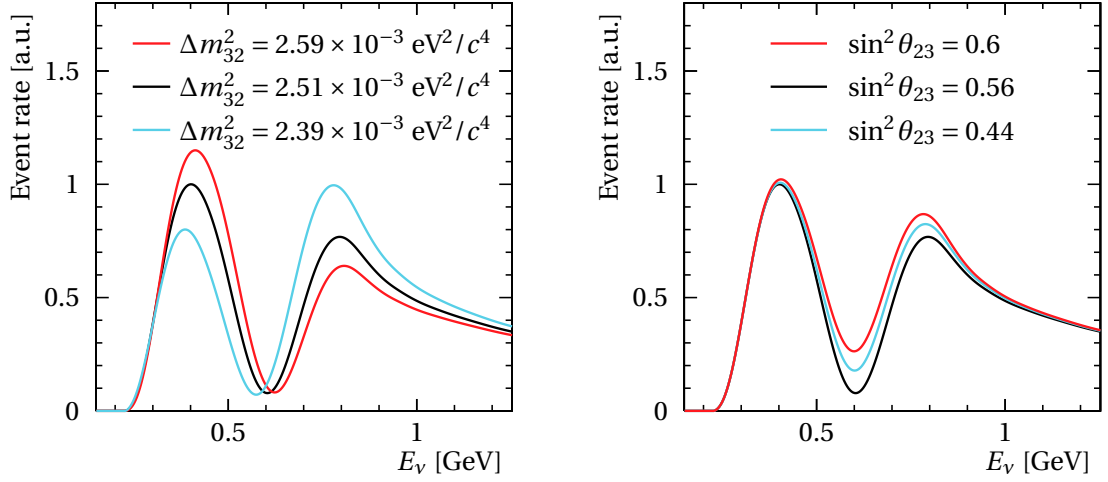


Figure 7.2: Impact of varying  $\Delta m_{32}^2$  (left) and  $\theta_{23}$  (right) from the T2K best fit values (black) to the corresponding 90% C.L. limits values (red and cyan) on the observed  $\nu_\mu$  event rate at Super-Kamiokande as a function of the true neutrino energy.

different because the two detectors do not sit exactly at the same angle with respect to the beam,

- $R_i(E_\nu, E_\nu^{\text{reco}})$  encodes the probability for the true neutrino energy  $E_\nu$  to be reconstructed as  $E_\nu^{\text{reco}}$  due not only to the impact of the detector response but also to the nuclear effects corresponding to the interaction  $i$  as discussed in Section 3.4 and shown in Figures 3.12 and 3.13,
- $\epsilon_\alpha(E_\nu)$  is the detector efficiency for  $\nu_\alpha$  interactions.

The difference between the two expressions is that the far detector event rate has an additional factor corresponding to the probability  $P(\nu_\alpha \rightarrow \nu_\beta, E_\nu)$  which depends on the PMNS oscillation parameters defined in Section 1.3, i.e. the *parameters of interest* in the oscillation analysis.

Equation (7.1) shows that the event rates can be affected by three sources of systematic uncertainties which, if not well taken into account, can mimic the effect of oscillations. These correspond to the neutrino flux, the neutrino cross section and the detector response. The T2K oscillation analysis strategy relies on using the near-detector data to constrain as tightly as possible these systematic uncertainties. As we discussed in Section 2.1.4 and will further detail in Section 7.3.1, the flux uncertainties are defined from simulating the interaction of the 30-GeV protons with the target and the decays of the produced hadrons. The cross-section uncertainties are generally motivated by discrepancies in the used interaction model with external measurements as we saw in Chapter 4. The uncertainty from the detector response is simply related to how the measured observables are affected by the (well-characterized) detector performances, i.e. its acceptance and resolution. To perform a fit to data, all these uncertainties are encoded in a set of parameters, called the *nuisance parameters*.

Run	ND280		Super-Kamiokande	
	FHC	RHC	FHC	RHC
1	–	–	3.26	–
2	7.93	–	11.22	–
3	15.81	–	15.99	–
4	34.26	–	35.97	–
5	–	4.34	2.44	5.12
6	–	34.09	1.92	35.46
7	–	24.38	4.84	34.98
8	57.31	–	71.69	–
9	–	20.54	2.04	87.88
10	–	–	47.26	–
Total	115.31	83.35	196.63	163.44
Combined Total	198.66		360.07	

Table 7.1: Summary of the collected data used in the 2022 oscillation analysis in units of  $10^{19}$  POT at both ND280 and Super-Kamiokande, separated by the beam mode.

Using the near-detector data allows us to significantly reduce the uncertainty on these nuisance parameters, but it is important to note that there are uncertainties that can remain unconstrained with this data. The most obvious unconstrained systematic uncertainties are the ones related to the detector response since the near and the far detectors are based on completely different technologies (Čerenkov vs. scintillation & TPC). Additionally, the near detector mostly sees  $\bar{\nu}_\mu$  interactions on carbon, while Super-Kamiokande measures the scattering of  $\bar{\nu}_\mu$  and  $\bar{\nu}_e$  on a different target and with a different energy spectrum (mostly due to oscillations). As shown in Figure 5.2, due to the ND280 design, its efficiency is limited for high-angle particles and consequently only measures a fraction of the covered phase space by Super-Kamiokande. This particular limitation is expected to be addressed with the upgraded ND280<sup>1</sup>.

## 7.2 Data selection

Figure 2.15 showed the collected data by T2K since the start of the experiment with the corresponding run period number. The 2022 oscillation analysis used the data from run 1 to run 10, and the breakdown of the collected POT is summarized in Table 7.1. This corresponds to the same data used in the previous oscillation analysis [263].

In this section, we briefly review the procedure of generating the MC simulation and selecting

<sup>1</sup>The NOvA experiment uses a somewhat different strategy as its near and far detectors rely on the same technology. It can thus exploit the cancellation of many of their systematic uncertainties using the correlations between the near- and far-detector systematic effects. This strategy is not perfect either as there are naturally other uncertainties that cannot be canceled, such as those related to the different energy spectrum in neutrino interactions due to the geometry and the oscillations.

the near- and the far-detector data for the oscillation analysis.

### 7.2.1 Monte-Carlo simulations

T2K employs the NEUT event generator to simulate neutrino interactions at both the near and the far detector using the simulated neutrino flux as well as the detector geometry and its material composition. The underlying models for the different interaction channels are described in Section 3.3. The generated events are then propagated through the detector simulations.

The ND280 software is based on the GEANT4 package [264] that simulates the energy deposits from the final-state particles generated by NEUT in the active material of the detector. The response of the scintillator, the light attenuation in the fibers as well as the response of the photosensors and the electronics are taken into account in this software. The responses of the TPCs and the ECals are also implemented in this same framework. A significant amount of work is currently ongoing to include the additional subdetectors of the upgrade.

On the Super-Kamiokande side, the detector simulation relies on a dedicated software called SKDETSIM [265] which is based on the GEANT3 package. The wavelength-dependent quantum efficiency of the photomultiplier tubes, the reflection effects on their surface as well as the electromagnetic processes related to the propagation of the Čerenkov radiation in water are all implemented. As discussed in Section 2.3, Super-Kamiokande is starting a new phase with its water doped with gadolinium to enhance its ability to detect neutrons. Consequently, it is important to update this simulation software with more adapted physics that are not necessarily present in GEANT3. A GEANT4-based package, called SKG4, was specifically developed by the Super-Kamiokande collaboration to use the most up-to-date physics models relevant for the gamma-ray emission from the neutron capture on gadolinium [266]. This will be employed for upcoming T2K oscillation analyses since starting from run 11, the T2K data is taken with the gadolinium-doped Super-Kamiokande.

### 7.2.2 Near-detector selection

In the 2022 oscillation analysis, the events are categorized into 22 samples depending on the beam mode (FHC vs. RHC<sup>2</sup>), the position of the interaction vertex (FGD1 vs. FGD2) and the multiplicity of the outgoing particles (pions, protons and photons). As discussed in Section 2.1, the accelerated protons impinge on the graphite target in 8 bunches of 15 ns width. This allows us to select only events associated with a beam trigger and compatible with one of the 8 bunches.

All the samples target CC interactions and consequently require a reconstructed muon track. As a magnetized detector, ND280 has the ability to identify the sign of the muon charge.

<sup>2</sup>As introduced in Section 2.1, FHC and RHC designate the chosen magnetic horn polarity, and correspond respectively to the neutrino-mode and the antineutrino-mode of the beam.



Consequently, this allows us to define control samples that characterize the event rate of the  $\nu_\mu$  background in the  $\bar{\nu}_\mu$  samples of the RHC beam mode<sup>3</sup>.

Once the muon track is identified in the event with a corresponding interaction vertex at one of the two FGDs, we look at the potential secondary tracks. The first cut that is applied is related to photon tracks for the FHC samples. This allows us to separate the CC selection into two classes: CC with no photons (CC0 $\gamma$ ), and CC with photons (CC $\gamma$ ). This cut particularly targets events with a neutral pion in the final state through its decay  $\pi^0 \rightarrow 2\gamma$ , where the photons are observed through their electromagnetic showering in the surrounding ECals. CC DIS interactions are behind  $\sim 70\%$  of the events with a neutral pion in the final state, while the rest is mostly due to the CCRES channel.

Then, the FHC CC0 $\gamma$  and the RHC CC selections are divided into three subcategories depending on the pion multiplicity:

- 0 $\pi$ : no pion tracks are identified,
- 1 $\pi$ : one pion of opposite charge with respect to the detected muon is identified,
- Other: events that do not fall in the previous two categories.

The 0 $\pi$  (1 $\pi$ ) cut allows us to provide a sample enriched in CCQE (CCRES) events. The pion track is required to start at the same vertex as the muon track within the same bunch, and its particle identification is performed using three methods. If its momentum is high enough (typically  $\gtrsim 400$  MeV/ $c$ ), its energy deposit can be observed in a TPC and the energy loss is used to identify it. If the momentum is small, then its track does not escape the FGD where the neutrino interaction occurred. In this case, the pion track is identified either using the corresponding energy loss in the FGD, or by looking for the associated *Michel electron*. A Michel electron is produced from the decay of the pion into a muon which decays itself and generates an electron. The time difference between the pion and the electron is dominated by the 2.2- $\mu$ s lifetime of the intermediate muon, and consequently these Michel electrons would eventually appear outside of the beam time window.

The FHC CC0 $\pi$ 0 $\gamma$  selections are further divided into two categories by tagging the outgoing protons, namely the 0 $p$  and the  $Np$  samples. The tracks originating from the same interaction vertex as the muon that have not been selected in the pion cuts are considered as proton candidates. A likelihood-based cut is applied on each track using the corresponding energy loss to decide if it is a proton or not. This separation of the CC0 $\pi$  sample by tagging the proton allows us to further disentangle the CCQE interactions from the multinucleon effects since the latter are more likely to fall in the  $Np$  category. This is also a very first step in introducing the information related to the protons in the oscillation analysis, which is expected to be more

---

<sup>3</sup>The  $\bar{\nu}_\mu$  background in the  $\nu_\mu$  samples of the FHC mode is very small and therefore no dedicated sample is considered.

developed with the near-detector upgrade thanks to its significantly lower tracking threshold and higher detection efficiency. This will be explored in Chapter 9.

With these separations, 22 near detector samples are defined and summarized in Table 7.2. They are all binned in two dimensions using the momentum of the muon and the cosine of its angle. Two examples of these distributions projected in the muon momentum are shown in Figure 7.3. It can be noted that the photon tagging for RHC samples is under developments, while a proton tagging in addition to that is not necessarily the most suitable cut as antineutrinos are more likely to produce (undetected) neutrons. Besides, there are currently no neutral current or  $\bar{\nu}_e$  selections in the oscillation analysis at the near detector.

### 7.2.3 Far-detector selection

In Super-Kamiokande, the particles are reconstructed using their Čerenkov radiation rings. The photomultiplier tubes allow us to record both the charge and the timing information for each hit. As shown in Figure 2.14, the profile of the ring is used to distinguish between muons and electrons. Single-ring events, i.e. observing one electron-like (1Re) or muon-like (1R $\mu$ ) Čerenkov ring with eventually a certain number delayed signals from Michel (or *decay*) electrons (de), have been the cornerstone samples of the T2K oscillation analysis. Since 2022, a new multi-ring sample has been introduced in the far-detector selection which targets the CC1 $\pi$  topology in  $\nu_\mu$  interactions.

Four samples in the neutrino mode are selected, two for electron-like events and two for muon-like events defined as follows:

- FHC 1Re0de (or  $\nu_e$ 1R): this is the equivalent of a  $\nu_e$  CC0 $\pi$  sample, enriched with CCQE events, which requires that the Čerenkov ring is electron-like and that no delayed muon decay electrons are observed,
- FHC 1Re1de (or  $\nu_e$ 1RD): this corresponds to a  $\nu_e$  CC1 $\pi$  sample, enriched with CCRES events where the Čerenkov ring is identified as electron-like and one delayed Michel electron is observed, indicating the production of a pion from the neutrino interaction,
- FHC 1R $\mu$  (or  $\nu_\mu$ 1R): this represents the  $\nu_\mu$  CC0 $\pi$  sample with a muon-like ring and no or one decay electron compatible with the decay of this muon,
- FHC multi-R $\mu$  (or  $\nu_\mu$ CC1 $\pi^+$ ): this is the newly-introduced multi-ring sample for muon-like events, targeting  $\nu_\mu$  CCRES events, which attempts to identify multiple rings compatible with the muon ring, and decay electron(s) from the muon and/or the pion.

On the other hand, two samples are similarly defined in the antineutrino mode:

- RHC 1Re0de (or  $\bar{\nu}_e$ 1R) with one electron-like ring and no delayed Michel electron,

## Chapter 7. T2K oscillation analysis

Sample	Data	Prefit MC	Data/MC
FHC FGD1 $\nu_\mu$ CC0 $\pi$ 0 $p$ 0 $\gamma$	21329	18523.7	1.15
FHC FGD1 $\nu_\mu$ CC0 $\pi$ N $p$ 0 $\gamma$	9257	9054.78	1.02
FHC FGD1 $\nu_\mu$ CC1 $\pi$ 0 $\gamma$	6224	6493.39	0.96
FHC FGD1 $\nu_\mu$ CCOther 0 $\gamma$	1737	1621.28	1.07
FHC FGD1 $\nu_\mu$ CC $\gamma$	11156	10529.5	1.06
FHC FGD2 $\nu_\mu$ CC0 $\pi$ 0 $p$ 0 $\gamma$	22935	19596.8	1.17
FHC FGD2 $\nu_\mu$ CC0 $\pi$ N $p$ 0 $\gamma$	7373	7409.64	0.99
FHC FGD2 $\nu_\mu$ CC1 $\pi$ 0 $\gamma$	5099	5312.36	0.96
FHC FGD2 $\nu_\mu$ CCOther 0 $\gamma$	1620	1560.56	1.04
FHC FGD2 $\nu_\mu$ CC $\gamma$	10460	9543.03	1.10
RHC FGD1 $\bar{\nu}_\mu$ CC0 $\pi$	8676	8283.17	1.05
RHC FGD1 $\bar{\nu}_\mu$ CC1 $\pi$	719	699.859	1.03
RHC FGD1 $\bar{\nu}_\mu$ CCOther	1533	1372.25	1.12
RHC FGD2 $\bar{\nu}_\mu$ CC0 $\pi$	8608	7910.16	1.09
RHC FGD2 $\bar{\nu}_\mu$ CC1 $\pi$	660	654.384	1.01
RHC FGD2 $\bar{\nu}_\mu$ CCOther	1396	1231.45	1.13
RHC FGD1 $\nu_\mu$ (bkg.) CC0 $\pi$	3714	3460.1	1.07
RHC FGD1 $\nu_\mu$ (bkg.) CC1 $\pi$	1147	1212.69	0.95
RHC FGD1 $\nu_\mu$ (bkg.) CCOther	1425	1164.39	1.22
RHC FGD2 $\nu_\mu$ (bkg.) CC0 $\pi$	3537	3373.8	1.05
RHC FGD2 $\nu_\mu$ (bkg.) CC1 $\pi$	955	974.874	0.98
RHC FGD2 $\nu_\mu$ (bkg.) CCOther	1334	1101.85	1.21
Total	130894	121084.017	1.08

Table 7.2: Summary of the 22 samples of the 2022 oscillation analysis with the data and prefit MC event rates as well as their ratio.

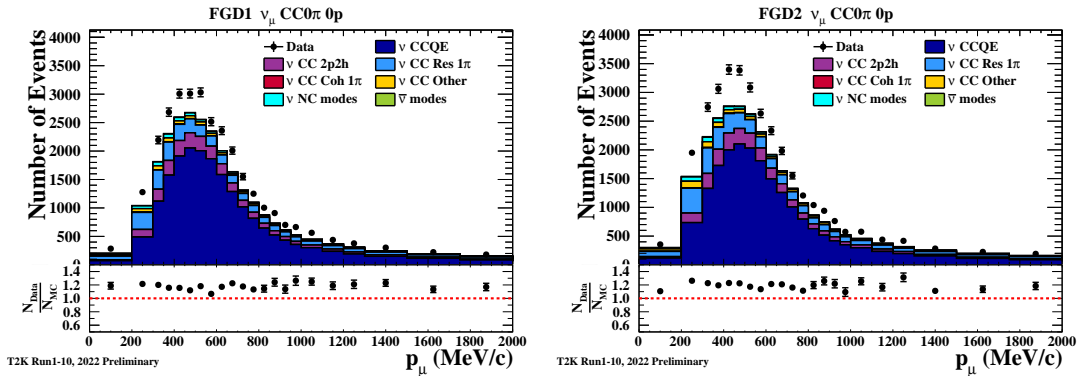


Figure 7.3: One-dimensional projection on the prefit muon momentum distribution in the FHC FGD1  $\nu_\mu$  CC0 $\pi$ 0 $p$ 0 $\gamma$  (left) and the FHC FGD2  $\nu_\mu$  CC0 $\pi$ 0 $p$ 0 $\gamma$  (right) samples.

- RHC  $1R\mu$  (or  $\bar{\nu}_\mu 1R$ ) with a muon-like ring and no or one decay electron compatible with the decay of this muon.

It is important to mention that, unlike ND280, Super-Kamiokande is not magnetized and thus unable to determine the charge of the particles. It only relies on the triggers related to the start of the spill at J-PARC to identify beam-related interactions. The reconstruction is performed with the FiTQun algorithm [267] based on a maximum likelihood estimation. All the events are required to be fully contained within the inner detector by vetoing any track with an associated activity on the outer detector. A cut related to the fiducial volume is also applied: for electron-like (muon-like) events, the distance from the interaction vertex to the closest wall is required to be larger than 80 cm (50 cm) and the distance to the wall along the track direction needs to be larger than 170 cm (250 cm). This ensures a good quality of the selected events.

The samples are binned using the reconstructed kinematics of the charged lepton by combining either its reconstructed momentum  $p_l$  or the reconstructed neutrino energy  $E_\nu^{\text{reco}}$  with the charged lepton angle  $\theta_l$ . This reconstructed neutrino energy is calculated for the  $\bar{\nu}_e 1R$  and  $\bar{\nu}_\mu 1R$  samples (i.e. CCQE-enriched selections) using the  $E_\nu^{\text{QE}}$  formula given in Equation (3.15) which relies on the assumption of a CCQE interaction on a static nucleon. On the other hand, it is reconstructed for the  $CC1\pi$ -like events under the assumption of a single-pion production from a  $\Delta^{++}$  decay with the following expression:

$$E_\nu^{\Delta^{++}} = \frac{2M_p \sqrt{p_l^2 + M_\pi^2} + M_{\Delta^{++}}^2 - M_p^2 - M_\pi^2}{2 \left( M_p - \sqrt{p_l^2 + M_\pi^2} + p_l \cos \theta_l \right)}, \quad (7.2)$$

where  $M_\pi$  and  $M_{\Delta^{++}}$  are respectively the masses of the pion and the  $\Delta^{++}$  resonance.

The number of events in each sample as predicted by the simulation when varying the  $\delta_{\text{CP}}$  phase is compared to the observed data later in Table 7.12. Additionally, Figure 7.4 shows the two-dimensional distributions of the best-fit MC and the data for the  $1R\mu$  (left) and the  $1Re$  (right) samples in the FHC mode.

## 7.3 Systematic uncertainties

This section summarizes the parameters that describe the three sources of systematic uncertainties discussed in Section 7.1, i.e. the neutrino flux, the response of the detectors, and the neutrino-nucleus interactions.

### 7.3.1 Flux

As discussed in Section 2.1.4, T2K predicts its (anti)neutrino beam by relying on an MC simulation pipeline tuned to external data from the NA61/SHINE experiment. Before the 2020

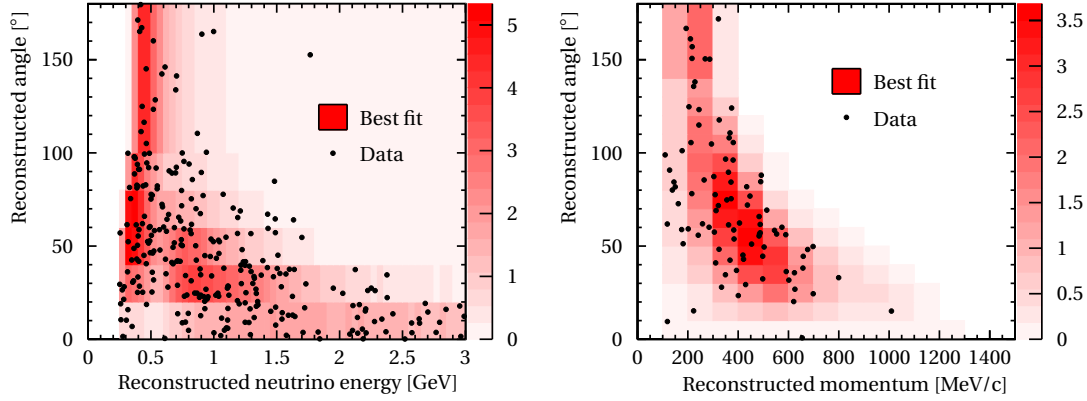


Figure 7.4: Left: two-dimensional distribution of the events in the FHC  $1R\mu$  sample in the reconstructed neutrino energy  $E_{\nu}^{\text{reco}}$  based on the CCQE assumption given by Equation (3.15) and the reconstructed charged lepton angle. Right: two-dimensional distribution of the events in the FHC  $1Re$  sample in the reconstructed charged lepton momentum and its angle.

oscillation analysis, the only external data that was used was measured on a thin target. Since 2020, the results from measuring the hadron production in the T2K replica target began to be included in the analysis, yielding improved constraints on the flux prediction particularly related to the produced pions and kaons from the interaction with the target material.

The uncertainty model on the flux is defined by a set of normalization parameters binned in the true neutrino energy, separated for each beam mode and neutrino type, and also split between ND280 and Super-Kamiokande. This binning is summarized in Table 7.3, and it is finer for the neutrino types that are expected to constitute a larger fraction of the flux. This binning is the same for both the near and the far detector, yielding a total of 100 flux parameters. The uncertainty on each of these normalization parameters is set from the tuning of the flux model to the NA61/SHINE data. On the other hand, the correlation matrix for these parameters is shown in Figure 7.5, where we can see that the ND280 and Super-Kamiokande parameters are highly correlated. They are not fully correlated because as mentioned previously the flux is expected to be slightly different geometrically.

The total flux uncertainty at the 600-MeV peak energy is estimated at  $\sim 5\%$  for the main component of the neutrino beam (i.e.  $\nu_{\mu}$  in FHC and  $\bar{\nu}_{\mu}$  in RHC). As shown in Figure 2.6, the leading source of uncertainty is related to the interaction of the protons on the target and the corresponding hadron production. A significant contribution to the uncertainty just above the peak energy also comes from the impact of the off-axis angle on the position of the peak.

### 7.3.2 Detector response

Parameterized uncertainties are also used in the analysis to account for the detector response of ND280 and Super-Kamiokande. The two detectors employ completely different technologies,

Beam mode	Neutrino type	True $E_\nu$ bins [GeV]
FHC	$\nu_\mu$	0.0, 0.4, 0.5, 0.6, 0.7, 1.0, 1.5, 2.5, 3.5, 5.0, 7.0, 30.0
	$\bar{\nu}_\mu$	0.0, 0.7, 1.0, 2.5, 30.0
	$\nu_e$	0.0, 0.5, 0.7, 0.8, 1.5, 2.5, 4.0, 30.0
	$\bar{\nu}_e$	0.0, 2.5, 30.0
RHC	$\nu_\mu$	0.0, 0.7, 1.0, 2.5, 30.0
	$\bar{\nu}_\mu$	0.0, 0.4, 0.5, 0.6, 0.7, 1.0, 1.5, 2.5, 3.5, 5.0, 7.0, 30.0
	$\nu_e$	0.0, 2.5, 30.0
	$\bar{\nu}_e$	0.0, 0.5, 0.7, 0.8, 1.5, 2.5, 4.0, 30.0

Table 7.3: Binning used to define the flux uncertainty parameters as a function of the beam mode and the neutrino type.

and consequently the way these parameters are defined is different.

### ND280 response

The response of ND280 depends on multiple sources of systematic uncertainties, summarized in Table 7.4, which can be broken down into three categories:

- *Observable-variation* uncertainties: These are uncertainties that directly affect the high-level observables used in the analysis, such as the identity of the particles and the muon momentum and angle. A variation due to such uncertainties may lead a given event to migrate to a different analysis bin, or even to another sample. For instance, variations due to the strength and the non-uniformity of the magnetic field within ND280 cause an uncertainty on the TPC momentum scale. On the other hand, the particle identification (PID) relies on the energy loss both in the FGD and the TPC and may yield sample-to-sample migrations since the selections rely on identifying the outgoing particles. The TPC PID is the leading uncertainty in this category, and it is estimated using a pure control sample of sand muons, i.e. issued from beam-related neutrino interactions with the matter surrounding the detector. The observed differences between this control sample and the simulation is used as an uncertainty in the analysis.
- *Efficiency-like* uncertainties: These affect the efficiency of the selection, which is defined as the ratio of the selected true events divided by the total number of true events in a given selection. Well-known control samples are typically compared to the MC predictions, and the efficiency differences between these predictions and the control samples are considered to be the same for the selections in the analysis. Unlike the previous category, these do not affect the observables of a given event, but rather its relative weight which can change the overall distributions within the samples in the

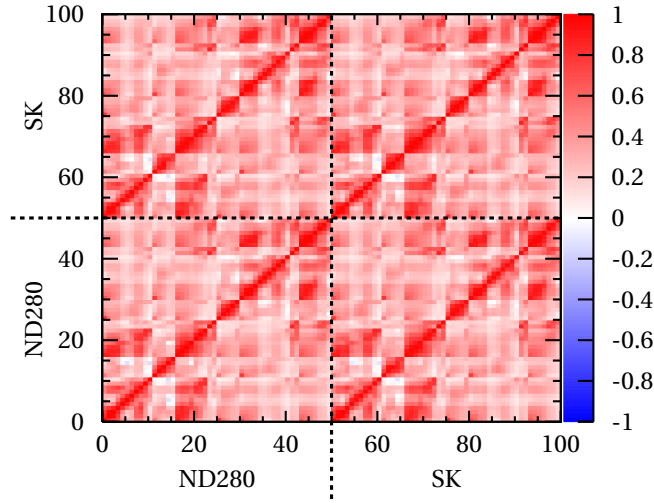


Figure 7.5: Prefit correlation matrix of the 100 flux parameters. Each parameter corresponds to a normalization in a bin of the true neutrino as given by Table 7.3.

considered observables.

- *Normalization uncertainties*: These correspond to overall normalization alterations for a given class of events. The pion and the proton secondary interactions are among the leading uncertainties in this category. These correspond to the interactions of the proton and the pion within the detector material after they escaped the nucleus from the primary neutrino interaction. As discussed in Section 7.2.2, GEANT4 is used to model this propagation, and the uncertainty is estimated from comparisons between its predictions and external pion and proton scattering measurements. Other uncertainties in this category are for instance related to the mass of the target FGDs and the backgrounds due to interactions out of the fiducial volume (OOFV) or to sand muons.

Currently, the parameters that define the detector-related uncertainties are not directly used in the analysis. This is partly due to the non-multiplicative nature of their effect (e.g. observable-like uncertainties), as well as their non-Gaussian behavior. Instead, their impact is included in an effective way: a large number of variations in these parameters are sampled from their prior knowledge, and their propagated impact on the distributions of the analysis observables (i.e. the muon momentum and direction) is used to define a normalization parameter in each analysis bin with a given central value. This procedure also provides a covariance matrix between all these parameters which determines the size of the uncertainty and the correlations between these bin-normalization parameters. Given the large number of analysis bins ( $\sim 5000$ ), this would mean as many additional parameters in the fits which is computationally expensive. To reduce their number, the adjacent bins that have an overall uncertainty within 5% of each other are merged, yielding a total number of 552 parameters, referred to as *observable-normalization*, or “ObsNorm”, parameters. The corresponding covariance matrix is displayed in Figure 7.6.

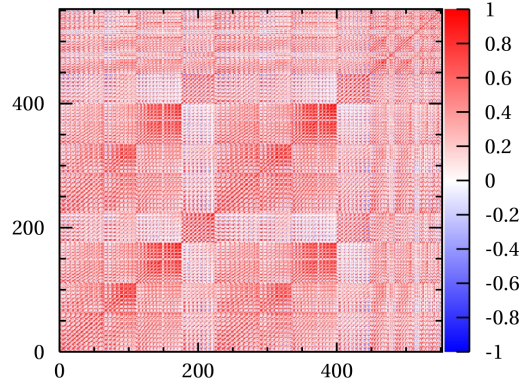


Figure 7.6: Correlation matrix between the 552 “ObsNorm” parameters of the uncertainty on the ND280 response.

### Super-Kamiokande response

The main sources of systematic uncertainties related to the response of Super-Kamiokande are the water transparency, the timing resolution and the gain of the photomultiplier tubes. Similarly to ND280, the estimation of their effect relies on comparisons of the simulation with well-known control samples from stopping cosmic muons, atmospheric neutrinos, and neutral pions.

The neutral pion samples are actually hybrid samples that are used to estimate the uncertainty to reject events containing a  $\pi^0$ , and particularly those related to NC production of  $\pi^0$  that constitute an important background in the  $e$ -like samples (see e.g. Figure 2.14). Data hybrid samples are constructed by taking real data of  $e$ -like events and superimposing on them a simulated photon ring generated with kinematics as expected from the T2K flux. MC hybrid samples are also constructed in the same way, where the  $e$ -like data is replaced with the MC predictions. The uncertainty is consequently estimated from the difference in the event selection efficiency between the real data and the MC hybrid samples.

Most of the parameters are defined as normalizations of the analysis bins as done for ND280. An exception to this is the energy-scale uncertainty, which describes the difference in the scale between the true and the reconstructed energy in Super-Kamiokande. It is related to the detector calibration and is estimated using control samples from cosmic muons as well as from the LINAC electrons.

Other contributions are also taken into account, such as pion secondary interactions and photonuclear effects. The former are considered in the same way as in ND280 by comparing the predictions with pion scattering measurements, while the latter correspond to photon absorption by the surrounding nuclei and are assigned a 100% uncertainty due to the lack of data measuring this effect.



Systematic error source		Total error in [%]									
		CC0 $\pi$ 0p		CC0 $\pi$ Np		CC1 $\pi^+$		CC $\gamma$		CCOther	
		FGD1	FGD2	FGD1	FGD2	FGD1	FGD2	FGD1	FGD2	FGD1	FGD2
Observable-like:	Magnetic field distortions	0.003	0.007	0.003	0.009	0.004	0.02	0.007	0.03	0.02	0.02
	Momentum resolution	0.005	0.004	0.008	0.008	0.01	0.01	0.03	0.04	0.04	0.07
	Momentum scale	0.01	0.02	0.01	0.02	0.02	0.02	0.02	0.04	0.04	0.04
	TPC PID	0.31	0.45	0.62	0.79	0.88	1.18	0.48	0.43	1.27	1.40
	FGD PID	0.09	0.04	0.18	0.10	0.03	0.04	–	–	0.03	0.03
Efficiency-like:	Charge ID efficiency	0.08	0.20	0.24	0.37	0.11	0.32	0.03	0.17	0.07	0.16
	TPC cluster efficiency	0.01	0.01	0.02	0.02	0.02	0.02	0.03	0.03	0.03	0.03
	TPC tracking efficiency	0.30	0.74	0.75	1.38	0.67	1.40	0.49	0.89	0.66	1.62
	TPC-FGD matching efficiency	0.08	0.16	0.19	0.33	0.15	0.23	0.09	0.14	0.14	0.18
	FGD tracking efficiency	0.26	0.05	0.82	0.16	0.27	0.03	0.27	0.05	0.30	0.07
	Michel electron	0.05	0.08	0.08	0.17	0.28	0.52	0.06	0.06	0.10	0.15
	ECal tracking efficiency	0.34	0.38	0.52	0.69	1.07	1.51	1.00	0.89	2.64	4.35
	TPC-ECal matching efficiency	0.61	0.32	1.01	1.03	0.74	0.67	0.99	1.04	1.27	1.25
	ECal PID	0.08	0.06	0.06	0.06	0.10	0.07	0.42	0.33	0.09	0.09
	ECal photon pile-up	0.07	0.05	0.04	0.04	0.08	0.04	1.17	1.11	0.05	0.04
Normalization:	OOFV background	0.54	0.72	0.14	0.20	0.80	0.67	0.70	0.76	0.17	0.17
	Pile-up	0.18	0.17	0.18	0.17	0.18	0.17	0.19	0.18	0.18	0.18
	FGD mass	0.57	0.39	0.58	0.40	0.56	0.38	0.54	0.37	0.58	0.40
	Pion secondary interactions	0.36	0.38	1.38	1.33	1.31	1.47	1.62	1.21	3.48	3.18
	Proton secondary interactions	1.06	1.26	2.61	3.08	0.59	0.75	0.64	0.73	0.84	1.04
	Sand muon background	0.06	0.03	0.01	0.01	0.07	0.02	0.02	0.01	0.02	0.006
Total systematic uncertainty		1.68	1.97	3.66	4.25	2.56	3.06	2.75	2.82	4.72	5.69

Table 7.4: Summary of the systematic uncertainty sources related to the response of ND280 for FHC samples and the corresponding integrated relative errors in % for each source. Table adapted from Reference [268].

### 7.3.3 Neutrino interactions

As described in Section 3.3, neutrino interactions are simulated using NEUT both at ND280 and Super-Kamiokande, and a suite of parametrized systematic uncertainties are considered as detailed in this section. Tables 7.6 and 7.7 summarize the full set of cross-section uncertainties at the end of this section.

#### CCQE

The CCQE interactions rely on the SF model, and the set of systematic uncertainties employed in the oscillation analysis is mostly described in Section 4.2. These include the nuclear shell occupancies, short-range correlations, Pauli blocking, optical potential corrections, nucleon FSI,  $M_A^{QE}$  and the three high- $Q^2$  normalization parameters. On the other hand, the missing momentum shape parameters are fixed in the analysis since we showed that using only the muon kinematics, as is the case in this oscillation analysis, does not give any sensitivity to their effects. Also, the Pauli blocking uncertainties are 80% correlated between neutrinos and antineutrinos, but no correlations are considered between oxygen and carbon.

One difference in the implementation with respect to the study described in Chapter 4 is related to Pauli blocking. In that study, the Pauli blocking effect was turned off in NEUT and applied *a posteriori* within the NUISANCE framework, while in this analysis, the MC production relies on the nominal NEUT which includes Pauli blocking at  $p_F = 209 \text{ MeV}/c$ . Consequently, if increasing the Pauli blocking threshold is easily obtained by setting to zero the weight of the corresponding events based on their pre-FSI momentum, it is not feasible to decrease this threshold below the nominal  $209 \text{ MeV}/c$ . In this case, we define two-dimensional histograms in  $(q_0, |\vec{q}|)$  where the effect of decreasing the Pauli blocking threshold is captured, and use them to reweight the nominal NEUT prediction. This has broadly the same impact on the lepton kinematics, but may alter the nucleon kinematics in an undesirable way. Nevertheless, this is not an issue since this analysis uses only the muon momentum and direction as observables. For future analyses, producing a NEUT MC without any Pauli blocking effect (which would be applied *a posteriori* as done in Chapter 4) is under consideration. This would increase the overall number of events to be processed by the reconstruction pipeline by only  $\sim 5\%$  and would open the door to use other Pauli blocking models such as the LDA-based one expressed in Equation (3.9).

Another implementation difference concerns the nucleon FSI uncertainty. In Chapter 4, we used two fully correlated normalization parameters for “With FSI” and “Without FSI” event classes to ensure that the cross section remains constant. In the oscillation analysis, we opt for one parameter named “Nucleon FSI” that simultaneously alters the relative fraction of events in each of the two classes while maintaining the cross section constant. This has thus a shape-only effect, equivalent to a change in the mean free path of the nucleon.

In addition to these uncertainties, four global-shift parameters on the removal energy, referred

to as  $E_b$  parameters, are prescribed separately for neutrinos and antineutrinos, as well as for carbon and oxygen targets. This is motivated by the fact that the resolution on the missing-energy peaks in Reference [163] ranges between 2 and 6 MeV. Furthermore, as demonstrated in Reference [269], the electron scattering ( $e, e' p$ ) data used to build the SF model covers only initial-state protons (the target for  $\bar{\nu}$  interactions), which can be different in the case of neutrons (the target for  $\nu$  interactions). This difference is extracted from shell-model calculations which show that the ground states vary between 1 and 4 MeV for protons and neutrons depending on the target. This is accounted for by shifting the central value of  $E_b$  for neutrinos by 2 and 4 MeV for carbon and oxygen respectively. A covariance matrix encodes the correlations between these four parameters: the difference between neutrinos and antineutrinos is taken with a  $\pm 2$  MeV uncertainty, and between oxygen and carbon with a  $\pm 1.5$  MeV uncertainty.

Furthermore, Reference [269] also suggests that to describe electron scattering data, a dependence on the momentum transfer  $|\vec{q}|$  needs to be taken into account as part of effects beyond the impulse approximation. This is studied in Reference [270], where NEUT is adapted to simulate electron scattering, and its prediction is compared to ( $e, e'$ ) data for various kinematic settings corresponding to different momentum transfers. To match this data, it is necessary to shift the removal energy at each momentum-transfer value. The value of this shift as a function of the momentum transfer can be used to derive a  $|\vec{q}|$ -dependent linear correction to be applied to the removal energy of NEUT. In summary, the NEUT removal energy is corrected in the oscillation analysis according to the following expression:

$$\Delta E_{\text{rmv}}^{\nu, A} = \delta^{\nu, A} + \alpha (m |\vec{q}| + c) \quad (7.3)$$

where  $\delta^{\nu, A}$  is the global  $E_b$  shift parameter separated by the neutrino type ( $\nu$  vs.  $\bar{\nu}$ ) and the target (oxygen vs. carbon),  $m |\vec{q}| + c$  is the derived linear correction from ( $e, e'$ ) data, and  $\alpha$  is the strength of this correction.

### 2p2h

As with Chapter 4, 2p2h normalization uncertainties are considered, but here separately for neutrinos and antineutrinos and without any prior uncertainty. An additional parameter with a 20% uncertainty scales the relative 2p2h contribution between oxygen and carbon, which allows us to use to some extent the carbon constraints at the near detector for the interactions on oxygen at Super-Kamiokande.

Furthermore, as done in Chapter 4 and shown in Figure 4.14, a shape uncertainty is considered to vary the  $\Delta$  and non- $\Delta$  relative contributions for 2p2h interactions. In this analysis, this variation is separated for nucleon pairs of the same isospin ( $NN$ ) and for pairs of opposite isospin ( $np$ ).

Another parameter is also considered here, called *PNNN shape*. 2p2h interactions can occur on

$np$  pairs for both  $\nu$  and  $\bar{\nu}$ , while interactions on  $pp$  pairs are only possible for  $\bar{\nu}$  and  $nn$  pairs for  $\nu$ . This parameter changes the ratio of the  $np$  and  $NN$  pairs produced in this interaction channel. This is mainly motivated by the differences in this ratio across the different 2p2h models.

To further account for the  $E_\nu$ -dependent difference between the 2p2h models, four parameters referred to as  $E_{\text{dep}}$  uncertainties allow us to scale the cross section from the Nieves et al. model used in NEUT to that of the Martini et al. model below and above the 600-MeV neutrino energy, separately for neutrinos and antineutrinos. This provides an additional energy-dependent variation of the cross section to cover the possible model variations.

#### Single-pion production

The same uncertainties introduced in Section 4.2.3 are applied in this analysis, namely the three Rein-Sehgal model parameters of CCRES interactions: the axial mass  $M_A^{\text{RES}}$ , the value of the axial form factor when  $Q^2 = 0$  denoted by  $C_5^A$ , and the normalization of the isospin-1/2 non-resonant background  $I_{1/2}$ , with their prior values and covariance obtained from bubble chamber data. Besides, an additional non-resonant  $I_{1/2}$  background parameter is included specifically for antineutrino interactions producing a low-momentum  $\pi^-$  since such event is likely to be reconstructed as a  $0\pi$  event at Super-Kamiokande.

Similarly to the global-shift uncertainty for the removal energy in CCQE, four resonant binding energy shift parameters are also considered. In fact, the CCRES interactions rely on the RFG model for which the constant binding energy is a natural degree of freedom that can be varied in the fits.

Additionally, the  $\Delta$ -resonance decay in the Rein-Sehgal model can be modeled in two different ways: either by isotropically ejecting the nucleon and the pion back-to-back in the  $\Delta$  rest frame, or computing the matrix elements for the nucleon-to- $\Delta$  transition and contracting them with spherical harmonics. Consequently, a parameter that encodes the different predictions from the two methods is prescribed.

Furthermore, two normalization parameters for neutral-pion production are applied separately for  $\nu_\mu$  and  $\bar{\nu}_\mu$  interactions. Also, for low momentum transfers, the neutrino may interact coherently with the nucleus and produce a pion. The strength of this CC coherent (CCCOH) interaction is controlled using two fully correlated normalization parameters for oxygen and carbon, with a 30% prior uncertainty.

#### DIS

As mentioned in Section 3.3, NEUT uses for the DIS channel the parton distribution functions given by Reference [207] with the Bodek – Yang (BY) modifications for low  $Q^2$  [208, 209]. The first parametrized uncertainty in the NEUT model, named *CCDIS BY*, covers the difference

Target	$l^-$	$l^+$
Carbon	-3.6 MeV	+2.6 MeV
Oxygen	-4.3 MeV	+3.3 MeV

Table 7.5: Shifts applied to the charged-lepton momentum to correct for the Coulomb effect.

between applying and not applying the BY correction. An updated correction, especially at low energy transfer, was also provided in Reference [271] and two shape uncertainties are included to provide freedom in the model to cover the predictions of this correction: the *BY Vector* and the *BY Axial* parameters.

Furthermore, in NEUT, the hadronization for the DIS interaction products is described differently for the low and the high invariant mass regions. In particular, the low region relies on a custom multi-pion model. First, a total cross-section normalization parameter is applied to account for differences between the pion multiplicities in different neutrino event generators. Another shape parameter is considered to cover shape differences between the NEUT model and the predictions of Reference [272]. On the other hand, two normalization parameters are included to alter the total number of multi-pion events for neutrino and antineutrino interactions.

Other DIS interactions such as those that produce  $\eta$  or  $K$  particles are covered by a single normalization parameter called *CC miscellaneous* (CC misc.) with a 100% uncertainty.

### Neutral currents

NC interactions can constitute an important background at the far detector since a  $\gamma$  or a  $\pi^0$  ring can be misidentified as an  $e$ -like event. Four normalization parameters address this type of interactions: one related to the coherent interaction on the nucleus (NCCOH), one for the interactions that produce a photon (NC1 $\gamma$ ), and two uncorrelated NCOther parameters for the other NC interactions separated for the near and the far detector.

### Coulomb correction

When the neutrino interacts with the nucleon and produces a charged lepton, the charge of the recoil nucleus may impact the moment of the outgoing charged lepton. This is known as *Coulomb effect*, and its impact can be estimated from electron and positron scattering measurements [273]. This effect is not directly implemented in NEUT, and is applied *a posteriori* as a one-time shift to the momentum of the charged lepton with the values given in Table 7.5, which are obtained using the parametrized Coulomb potential as a function of the nucleus radius obtained in Reference [273].

In addition to these momentum shifts, Reference [273] shows that the Coulomb corrections

can also lead to extracted cross sections with up to 3% difference. These effects were also studied in Reference [274] where the Coulomb distortion was calculated and found to affect the interaction cross section depending on the neutrino energy: at 500 MeV, the cross section increases by 2% for neutrinos and decreases 1% for antineutrinos. Consequently, two normalization parameters for all CC events with neutrino energies between 400 and 600 MeV are considered separately for neutrinos and antineutrinos, with a prior uncertainty of 2% and 1% respectively.

#### Final-state interactions

A custom intranuclear cascade is implemented in NEUT to model the scattering with the remnant nucleus of hadrons produced in a neutrino interaction. In particular, an outgoing pion is propagated through the nucleus and can undergo different processes: quasielastic scattering, charge exchange, absorption or hadron production. These processes are modeled according to the Salcedo – Oset model [212, 213] and their probabilities are tuned to external data [214]. A total number of six parameters are used to vary these probabilities:

- an absorption (FEFABS) parameter: the pion is absorbed in the cascade,
- quasielastic scattering parameters: one pion is present at the final state with the same charge as the one produced at the primary interaction, separated for pions below (FEFQE) and above (FEFQEH) 500 MeV/c,
- charge exchange parameters: one neutral pion is present at the final state, separated for pions below (FEFCX) and above (FEFCXH) 500 MeV/c,
- an inelastic scattering parameter (FEFINEL): additional hadrons are produced in the cascade.

The prior uncertainties and correlations between these parameters are obtained by fitting a wide range of  $\pi^\pm$  scattering data as shown in Reference [214]. The corresponding correlation matrix is displayed in Figure 7.7.

On the other hand, one nucleon FSI parameter is used, which changes the probability for a nucleon to reinteract with the nucleus. A more detailed description similar to the pion FSI parameters is under development and will be used starting from the next oscillation analysis.

#### Differences between $\bar{\nu}_e$ and $\bar{\nu}_\mu$

The majority of neutrino interactions measured at ND280 are  $\bar{\nu}_\mu$  interactions, and the samples used for the near-detector analysis are exclusively  $\bar{\nu}_\mu$  samples. However, the far detector measures both  $\bar{\nu}_e$  and  $\bar{\nu}_\mu$  to measure the oscillation parameters. To be able to propagate the cross-section model constraints from the  $\bar{\nu}_\mu$  interactions, it is necessary to take into account

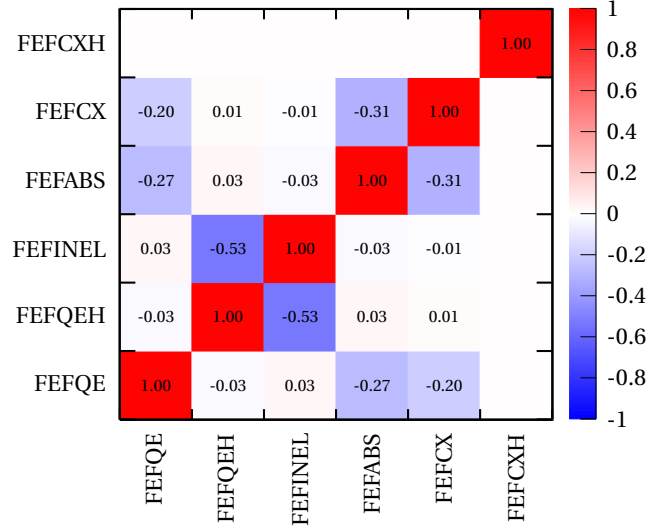


Figure 7.7: Prefit correlation matrix of the pion FSI parameters.

plausible correlations between the cross sections of the two neutrino flavors. These differences are mainly due to two effects: first, the mass difference between the electron and the muon means that the kinematic phase space is not the same, and second, radiative corrections (real-photon emission, exchange of virtual photons, photon loops, etc.) which are not included in the NEUT model and are expected to be larger for electrons. Consequently, two uncertainties are applied to account for the difference between  $\nu_e/\nu_\mu$  and  $\bar{\nu}_e/\bar{\nu}_\mu$  interactions including a 2% contribution uncorrelated between neutrinos and antineutrinos and an additional fully anticorrelated contribution of 2%.

## 7.4 Fitting frameworks

We presented in Section 7.2 how the model simulation is generated and the data is selected, and in Section 7.3 the systematic uncertainty parameters from various sources. In order to find the best model parameters that describe the data (both at the near and the far detector), we rely on the maximization of a likelihood function  $\mathcal{L}$ , or equivalently the minimization of the negative log-likelihood function  $-2\log\mathcal{L}$ . This function described the goodness-of-fit of the prediction from the model at a given set of parameters to an observed sample of data. Section 7.4.1 summarizes the definition of the likelihood functions used in the oscillation analysis, and Section 7.4.2 describes the tools and the frameworks employed to optimize these functions.

## 7.4 Fitting frameworks

Parameter	Central value	Prior error [ $1\sigma$ ]	ND/FD
$p$ -shell norm. C	0	0.2	ND
$s$ -shell norm. C	0	0.45	ND
SRC norm. C	1	2	ND
$p$ -shell $p_m$ shape C	0	1	–
$s$ -shell $p_m$ shape C	0	1	–
$p_{1/2}$ -shell norm. O	0	0.2	ND, FD
$p_{3/2}$ -shell norm. O	0	0.45	ND, FD
$s$ -shell norm. O	0	0.75	ND, FD
SRC norm. O	1	2	ND, FD
$p_{1/2}$ -shell $p_m$ shape O	0	1	–
$p_{3/2}$ -shell $p_m$ shape O	0	1	–
$s$ -shell $p_m$ shape O	0	1	–
Pauli Blocking C $\nu$	0	30 MeV/ $c$	ND
Pauli Blocking C $\bar{\nu}$	0	30 MeV/ $c$	ND
Pauli Blocking O $\nu$	0	30 MeV/ $c$	ND, FD
Pauli Blocking O $\bar{\nu}$	0	30 MeV/ $c$	ND, FD
Optical Potential C	0	1	ND
Optical Potential O	0	1	ND, FD
$Q^2$ norm. 1	1	0.11	ND, FD
$Q^2$ norm. 2	1	0.18	ND, FD
$Q^2$ norm. 3	1	0.40	ND, FD
$M_A^{\text{QE}}$	1.03 GeV/ $c^2$	0.06 GeV/ $c^2$	ND, FD
$E_b$ C $\nu$	2 MeV	6 MeV	ND
$E_b$ C $\bar{\nu}$	0	6 MeV	ND
$E_b$ O $\nu$	4 MeV	6 MeV	ND, FD
$E_b$ O $\bar{\nu}$	0	6 MeV	ND, FD
$E_b$ $\alpha$	0	1	ND, FD
2p2h norm. $\nu$	1	–	ND, FD
2p2h norm. $\bar{\nu}$	1	–	ND, FD
2p2h norm. C to O	1	0.2	ND
2p2h $E_{\text{dep}}$ low $E_\nu$	1	1	FD
2p2h $E_{\text{dep}}$ high $E_\nu$	1	1	FD
2p2h $E_{\text{dep}}$ low $E_{\bar{\nu}}$	1	1	FD
2p2h $E_{\text{dep}}$ high $E_{\bar{\nu}}$	1	1	FD
PNNN shape	0	0.33	ND, FD
2p2h shape C $np$	0	3	ND
2p2h shape C $NN$	0	3	ND
2p2h shape O $np$	0	3	ND, FD
2p2h shape O $NN$	0	3	ND, FD

Table 7.6: Summary of the CCQE and 2p2h uncertainties and their related priors.



## Chapter 7. T2K oscillation analysis

Parameter	Central value	Prior error [ $1\sigma$ ]	ND/FD
FEFQE	1.069	0.313	ND, FD
FEFQEH	1.824	0.859	ND, FD
FEFINEL	1.002	1.101	ND, FD
FEFABS	1.404	0.432	ND, FD
FEFCX	0.697	0.305	ND, FD
FEFCXH	1.8	0.288	ND, FD
Nucleon FSI	0	0.3	ND, FD
$C_5^A$	1.06	0.1	ND, FD
$M_A^{\text{RES}}$	0.91 GeV/ $c^2$	0.1 GeV/ $c^2$	ND, FD
Non-res. $I_{1/2}$ bkg.	1.21	0.27	ND, FD
Non-res. $I_{1/2}$ bkg. low $p_\pi$	1.3	1.3	FD
CCRES $E_b$ C $\nu_\mu$	25 MeV	25 MeV	ND
CCRES $E_b$ C $\bar{\nu}_\mu$	25 MeV	25 MeV	ND
CCRES $E_b$ O $\nu_\mu$	25 MeV	25 MeV	ND, FD
CCRES $E_b$ O $\bar{\nu}_\mu$	25 MeV	25 MeV	ND, FD
Rein-Sehgal $\Delta$ decay	1	1	ND, FD
CCRES $\pi^0$ norm. $\nu_\mu$	1	0.3	ND, FD
CCRES $\pi^0$ norm. $\bar{\nu}_\mu$	1	0.3	ND, FD
CCCOH C	1	0.3	ND
CCCOH O	1	0.3	ND, FD
CC multi- $\pi$ TotXSec	0	1	ND, FD
CC multi- $\pi$ BY Vector	0	1	ND, FD
CC multi- $\pi$ BY Axial	0	1	ND, FD
CC multi- $\pi$ shape	0	1	ND, FD
CCDIS BY	0	1	ND, FD
CC multi- $\pi$ norm. $\nu$	1	0.035	ND, FD
CC multi- $\pi$ norm. $\bar{\nu}$	1	0.065	ND, FD
CC Misc	1	1	ND, FD
NCCOH	1	0.3	ND, FD
NC1 $\gamma$	1	1	FD
NCOther ND	1	0.3	ND
NCOther FD	1	0.3	FD
Coulomb correction norm. $\nu$	1	0.02	ND, FD
Coulomb correction norm. $\bar{\nu}$	1	0.01	ND, FD
$\nu_e/\nu_\mu$	1	0.02	ND, FD
$\bar{\nu}_e/\bar{\nu}_\mu$	1	0.02	ND, FD

Table 7.7: Summary of the non-QE uncertainties and their related priors.

### 7.4.1 Likelihoods

#### Poisson likelihood

As in many counting experiments in particle physics, the number of events is a discrete random variable where two successive events are independent. This is commonly described by a Poisson distribution, which gives the probability of observing  $N^{\text{data}}$  events assuming a prediction of  $N^{\text{MC}}(\vec{\lambda})$  events as:

$$\mathbb{P} \left[ N^{\text{data}} \middle| N^{\text{MC}}(\vec{\lambda}) \right] = \frac{\left[ N^{\text{MC}}(\vec{\lambda}) \right]^{N^{\text{data}}}}{N^{\text{data}}!} e^{-N^{\text{MC}}(\vec{\lambda})}$$

where  $N^{\text{MC}}(\vec{\lambda})$  is the number of events predicted by the model at a set of parameters  $\vec{\lambda}$ . In practice, as with the oscillation analysis, the events are counted in bins according to some observables, and consequently the overall (statistical) likelihood is simply given by the product of the Poisson distributions corresponding to each measurement bin:

$$\mathcal{L} = \prod_i^{\text{bins}} \frac{\left[ N_i^{\text{MC}}(\vec{\lambda}) \right]^{N_i^{\text{data}}}}{N_i^{\text{data}}!} e^{-N_i^{\text{MC}}(\vec{\lambda})}. \quad (7.4)$$

The quantity that is commonly optimized in the analyses is the negative log-likelihood ratio given by Equation (7.4) over the likelihood of the most likely outcome of the nominal model, i.e. for which  $N_i^{\text{data}} = N_i^{\text{MC}}$ . This allows for the cancellation the normalization terms as:

$$-2 \log \left( \frac{\prod_i^{\text{bins}} \frac{\left[ N_i^{\text{MC}} \right]^{N_i^{\text{data}}}}{N_i^{\text{data}}!} e^{-N_i^{\text{MC}}}}{\prod_i^{\text{bins}} \frac{\left[ N_i^{\text{data}} \right]^{N_i^{\text{data}}}}{N_i^{\text{data}}!} e^{-N_i^{\text{data}}}} \right) = 2 \sum_i^{\text{bins}} \left[ N_i^{\text{MC}}(\vec{\lambda}) - N_i^{\text{data}} + N_i^{\text{data}} \log \frac{N_i^{\text{data}}}{N_i^{\text{MC}}(\vec{\lambda})} \right]. \quad (7.5)$$

In the following, we will simply refer to this quantity as the (statistical) negative log-likelihood  $-2 \log \mathcal{L}_{\text{stat}}(\vec{\lambda})$ , which depends on the parameters of the model  $\vec{\lambda}$ . On occasion, we will also refer to it as a chi-square difference  $\Delta\chi^2$ .

#### Barlow – Beeston likelihood

The quantities  $N_i^{\text{MC}}(\vec{\lambda})$  are obtained from MC simulations that involve a finite number of generated events and, consequently, care must be taken regarding the possible fluctuations of the MC predictions. If the statistics of the observed samples are orders of magnitude smaller than the number of simulated events, which is the case for instance when fitting Super-Kamiokande data, then MC fluctuations are much smaller than the statistical fluctuations of the data and can be neglected. On the other hand, if the number of generated MC events is comparable with the statistics of the data, then the fluctuations of the MC predictions can start to have a large impact on the results. As a reference, the number of simulated events in

the near-detector analysis is  $\sim 10 - 20$  times higher than the observed data, yet the effects of MC fluctuations can already have a noticeable impact. Reference [275] proposed a technique to take this into account which modifies the statistical negative log-likelihood of Equation (7.5) to include a smearing effect on the MC predictions. This is known as the *Barlow – Beeston likelihood*, where a scaling parameter  $\beta_i$  is introduced for each bin  $i$  such that the number of predicted events is modified as  $N_i^{\text{MC}} \rightarrow \beta_i N_i^{\text{MC}}$ , and  $\beta_i$  is constrained by the number of generated events in the simulation.

The main drawback of this approach is that it can introduce a large number of additional parameters (same as the number of bins, e.g.  $\sim 5000$  in the near-detector analysis). To mitigate this issue, Reference [276] showed that when assuming that the MC fluctuations are Gaussian with a central value given by  $N_i^{\text{MC}}$  and a standard deviation of  $\sigma_{\beta_i} = \sqrt{\sum_j w_j^2 / N_i^{\text{MC}}}$  where  $\sum_j w_j^2$  is the sum of the weights over all the MC-generated events in the  $i$ -th bin, the parameters  $\beta_i$  can be analytically determined as the solution of<sup>4</sup>:

$$\beta_i^2 + \left( N_i^{\text{MC}} \sigma_{\beta_i}^2 - 1 \right) \beta_i - N_i^{\text{data}} \sigma_{\beta_i}^2 = 0$$

and the modified likelihood can be expressed as:

$$-2 \log \mathcal{L}_{\text{stat}} = 2 \sum_i^{\text{bins}} \left[ \left( \beta_i N_i^{\text{MC}}(\vec{\lambda}) - N_i^{\text{data}} + N_i^{\text{data}} \log \frac{N_i^{\text{data}}}{\beta_i N_i^{\text{MC}}(\vec{\lambda})} \right) + \frac{(\beta_i - 1)^2}{2 \sigma_{\beta_i}^2} \right]. \quad (7.6)$$

This is the likelihood used for the near-detector analysis. Nevertheless, other alternatives were also tested, such as the likelihoods introduced in Reference [277]. These were found to give similar results, except in the case of very few MC events for which the Gaussian assumption of Equation (7.6) no longer holds. When the results from the likelihoods that account for the MC statistical fluctuations are compared to the simple Poisson likelihood of Equation (7.5), the former are found to provide more conservative estimates as we can expect.

In principle,  $\beta_i$  and  $\sigma_{\beta_i}$  depend on the values of the model parameters  $\vec{\lambda}$  and need to be recalculated for each parameter variation (i.e. at every step of the minimization). It was chosen for the 2022 analysis to only compute their values at the nominal MC predictions and keep their values fixed throughout the minimization process for simplification and fit stability reasons.

### Penalty term

The prior knowledge on the model parameters  $\vec{\lambda}$  is given by their central values  $\vec{\lambda}_{\text{nom}}$  shown for instance in Tables 7.6 and 7.7 for neutrino interaction uncertainties, and their prior uncertainties are encoded in a covariance matrix  $V = \text{Cov}[\vec{\lambda}]$  along with their eventual correlations as is the case for e.g. the flux (see Figure 7.5) and the pion FSI (see Figure 7.7) parameters.

<sup>4</sup>This is obtained by minimizing the modified  $-2 \log \mathcal{L}_{\text{stat}}$  with respect to  $\beta_i$  under the Gaussian assumption.

Assuming a Gaussian prior, the likelihood of the model parameters can be written as:

$$\mathcal{L}_{\text{syst}} = \frac{1}{\sqrt{(2\pi)^{N_{\text{syst}}} \det(V)}} \exp\left(-\frac{1}{2}(\vec{\lambda} - \vec{\lambda}_{\text{nom}})^T V^{-1}(\vec{\lambda} - \vec{\lambda}_{\text{nom}})\right),$$

where  $N_{\text{syst}}$  is the number of the model parameters and  $\det(V)$  the determinant of their covariance. This yields the following negative log-likelihood after taking the ratio with respect to the nominal likelihood:

$$-2\log \mathcal{L}_{\text{syst}} = (\vec{\lambda} - \vec{\lambda}_{\text{nom}})^T V^{-1}(\vec{\lambda} - \vec{\lambda}_{\text{nom}}). \quad (7.7)$$

### Total likelihood

The total negative log-likelihood is simply obtained as the sum of the statistical and the penalty contributions:  $-2\log \mathcal{L} = -2\log \mathcal{L}_{\text{stat}} - 2\log \mathcal{L}_{\text{syst}}$ . The penalty likelihood is given in Equation (7.7), while depending on the analysis, we either use the Barlow – Beeston likelihood of Equation (7.6) which takes into account the fluctuations of the simulated events (typically for ND280 analyses), or simply the Poisson likelihood given by Equation (7.5) when these fluctuation effects are not relevant (typically for the far-detector studies).

### Profiling and marginalization

As mentioned in Section 7.1, the likelihood  $\mathcal{L}(\vec{\lambda})$  in the oscillation analysis with the far-detector data consists of nuisance parameters  $\vec{\lambda}_{\text{nuis}}$  (i.e. the flux, detector response, and cross-section uncertainty model) and parameters of interest  $\vec{\lambda}_{\text{int}}$  (oscillation parameters). Maximizing the likelihood consists of finding the values for both classes of parameters that best describe the data. This approach is often called *profiling*, where the nuisance parameters and the parameters of interest are treated on an equal footing. However, while the nuisance parameters are included to make sure that the model has the appropriate degrees of freedom, their exact values are not as interesting as the oscillation parameters. An alternative approach consists of *marginalizing* over the nuisance parameters  $\vec{\lambda}_{\text{nuis}}$  as:

$$\mathcal{L}_{\text{marg}}(\vec{\lambda}_{\text{int}}) = \int d\vec{\lambda}_{\text{nuis}} \mathcal{L}(\vec{\lambda}_{\text{int}}, \vec{\lambda}_{\text{nuis}}).$$

In practice, this integration is performed numerically by generating a large sample of values for the nuisance parameters  $\{\vec{\lambda}_{\text{nuis}}^k\}_{1 \leq k \leq N_{\text{marg}}}$  from their prior Gaussian distribution and averaging the likelihood as:

$$\mathcal{L}_{\text{marg}}(\vec{\lambda}_{\text{int}}) = \int d\vec{\lambda}_{\text{nuis}} \mathcal{L}(\vec{\lambda}_{\text{int}}, \vec{\lambda}_{\text{nuis}}) \approx \frac{1}{N_{\text{marg}}} \sum_{k=1}^{N_{\text{marg}}} \mathcal{L}(\vec{\lambda}_{\text{int}}, \vec{\lambda}_{\text{nuis}}^k). \quad (7.8)$$

### 7.4.2 Fitting tools

Various algorithms allow us to not only estimate the optimal set of parameters in the model that best describes the data by minimizing the negative log-likelihood, but also evaluate its shape around this optimum in order to derive uncertainties and confidence intervals. There are four fitting framework used in the T2K experiment for oscillation analyses<sup>5</sup>, each employs different methods and approximations: BANFF, MaCh3, P-Theta and VaLOR. Chapter 8 introduces GUNDAM, a new framework that will replace BANFF following its validation.

#### Fitting methods

In order to minimize the negative log-likelihood  $-2\log\mathcal{L}$ , the three commonly-used methods are:

- **Grid search:** This method consists of evaluating the likelihood across the allowed range of the parameters at regular intervals (i.e. over a predefined *grid*) to find the optimal set of parameters. It is clear that the complexity of this methods exponentially increases with the dimension of the likelihood which makes it impractical for high-dimensional problems. Nevertheless, for a small number of parameters, this method is of great interest as it not only finds the optimum, but also gives an accurate description of the shape of the likelihood over the considered range.
- **Gradient descent:** This technique relies on evaluating the gradient of the negative log-likelihood iteratively to move in the direction of the steepest descent given by the negative of the gradient. It is a simple and efficient method for high-dimensional likelihoods, but requires them to be differentiable and may converge to local minima (as we will briefly see in Section 8.3) if they do not satisfy convexity criteria.
- **Markov chain Monte Carlo (MCMC):** This method samples the likelihood over the parameter space by randomly varying the parameters according to the probability dictated by the likelihood. The Metropolis-Hastings algorithm [278, 279] can be used to generate a sequence of correlated draws from a probability distribution function for which direct sampling is difficult, particularly for high-dimensional distributions. This typically requires a large number of iterations, called *burn-in*, to find the region of the likelihood that will be most sampled, which are removed from the chain in the analysis.

#### T2K fitters

The oscillation analysis consists of near-detector and far-detector data, which motivates the two analysis streams followed in T2K. The first approach relies on two sequential analyses

---

<sup>5</sup>Various other frameworks exist within the different T2K working groups, such as for cross-section analyses or studies beyond the standard three-flavor oscillations.

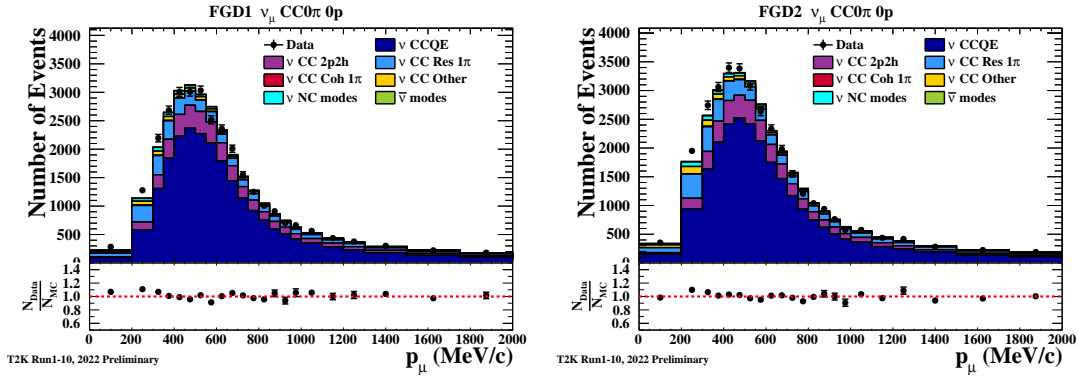
starting from a fit to the near-detector data, and then a far-detector data fit using the near-detector results. In this case, the near detector is used to tune and constrain the uncertainties in the model using BANFF (which will be replaced by GUNDAM in the future analyses). Both BANFF and GUNDAM use the gradient-descent algorithm of Minuit2, which also features the HESSE routine that estimates the postfit covariance of the parameters. The relevant parts of the constrained model, i.e. the Super-Kamiokande components of the postfit flux matrix (see Figure 7.5), and the cross-section parameters indicated in the last column of Tables 7.6 and 7.7, are then used to fit the far-detector data. This is done with P-Theta and VaLOR fitters, which use the output of the near-detector analysis to extract the oscillation parameters. This sequential procedure not only allows us to reduce the dimensionality of the minimization problem, but also permits to test and validate the model against the large neutrino-interaction samples of the near detector. P-Theta and VaLOR marginalize over all the parameters except the oscillation parameters of interest as described in Equation (7.8), then evaluate the negative log-likelihood and find the minimum using a grid search. In this thesis, we will focus on this sequential analysis stream using BANFF (replaced by GUNDAM in Chapters 8 and 9) and P-Theta. The results of this analysis are expressed as Frequentist confidence limits on the oscillation parameters. P-Theta and VaLOR can also provide Bayesian credible intervals and determine the global best-fit point using the gradient-descent algorithm of Minuit2.

The second T2K analysis stream employs the MaCh3 fitting framework which uses an MCMC technique to sample the likelihood and provide a posterior probability density function. The particularity of this framework is that it can simultaneously fit the measurements of both the near and the far detector. The results of this analysis are expressed as Bayesian credible intervals. It can also perform a near-detector-only fit, which not only allows us to cross-check with the BANFF/GUNDAM results, but also assess the effect of the Gaussian approximation implied when using the post-near-detector-fit covariance in the first T2K analysis stream. In fact, a routine test in each oscillation analysis consists of testing with P-Theta the impact of drawing the marginalization samples of the nuisance parameters directly from the MaCh3 posterior distribution function instead of using a Gaussian sampling from the BANFF (or GUNDAM) postfit covariance. This comparison often shows that the two approaches give almost the same results which indicate that the Gaussian assumption is enough for the current statistics. While MaCh3 has the advantage of capturing the non-Gaussian behavior of the parameters, it typically requires  $\sim 5,000,000$  iterations (including the burn-in) to find the minimum, while BANFF/GUNDAM reach it in  $\sim 100,000$  iterations which motivates their use for more computationally intensive studies that require running a large number of fits such as the  $p$ -value calculation described in the next section.

The T2K fitters are summarized in Table 7.8. The main purpose of having different analysis streams with multiple fitters is to be able to validate the results when using different and (some-what) independent approaches. They allow us to ensure the coherence of the analysis and the robustness of the results when employing different approximations and techniques. The cross-fitter validation steps, which will be detailed for the new GUNDAM framework in Chapter 8, are the most crucial (and time-consuming) procedure during the oscillation analysis.

Fitter	Analysis data	Statistical approach	Fit algorithm
BANFF/ GUNDAM	ND	Frequentist	Gradient descent
MaCh3	ND – FD	Bayesian	MCMC
P-Theta	ND	Frequentist/Bayesian	Grid search/Gradient descent
VaLOR	ND	Frequentist/Bayesian	Grid search/Gradient descent

Table 7.8: Comparison between the fitters used in the two T2K analysis streams.


 Figure 7.8: One-dimensional projection on the postfit muon momentum distribution in the FHC FGD1  $\nu_\mu$  CC0 $\pi$ 0 $p$ 0 $\gamma$  (left) and the FHC FGD2  $\nu_\mu$  CC0 $\pi$ 0 $p$ 0 $\gamma$  (right) samples.

## 7.5 Results of the 2022 oscillation analysis

This section shows the latest results presented in the Neutrino 2022 conference [61] for the first analysis stream which consists of the two sequential fits to the near-detector data with BANFF and to the Super-Kamiokande data with P-Theta. These results, as well as those of the previous iteration of the oscillation analysis performed by the collaboration in 2020 [263], were also reproduced within the new GUNDAM framework to validate it as will be described in Chapter 8.

### 7.5.1 Near-detector analysis

As mentioned previously, a set of validation steps are necessary before proceeding with a reliable data fit. Since a similar validation has been also carried out for GUNDAM and described in detail in Section 8.2, we will directly focus here on the data results.

#### Data fit

Figure 7.8 shows the postfit muon momentum distribution in the FHC FGD1  $\nu_\mu$  CC0 $\pi$ 0 $p$ 0 $\gamma$  (left) and the FHC FGD2  $\nu_\mu$  CC0 $\pi$ 0 $p$ 0 $\gamma$  (right) samples. It displays a significantly improved agreement with the data in comparison with Figure 7.3. This improvement is due to adjustments in various parameters illustrated in Figure 7.9.

## 7.5 Results of the 2022 oscillation analysis

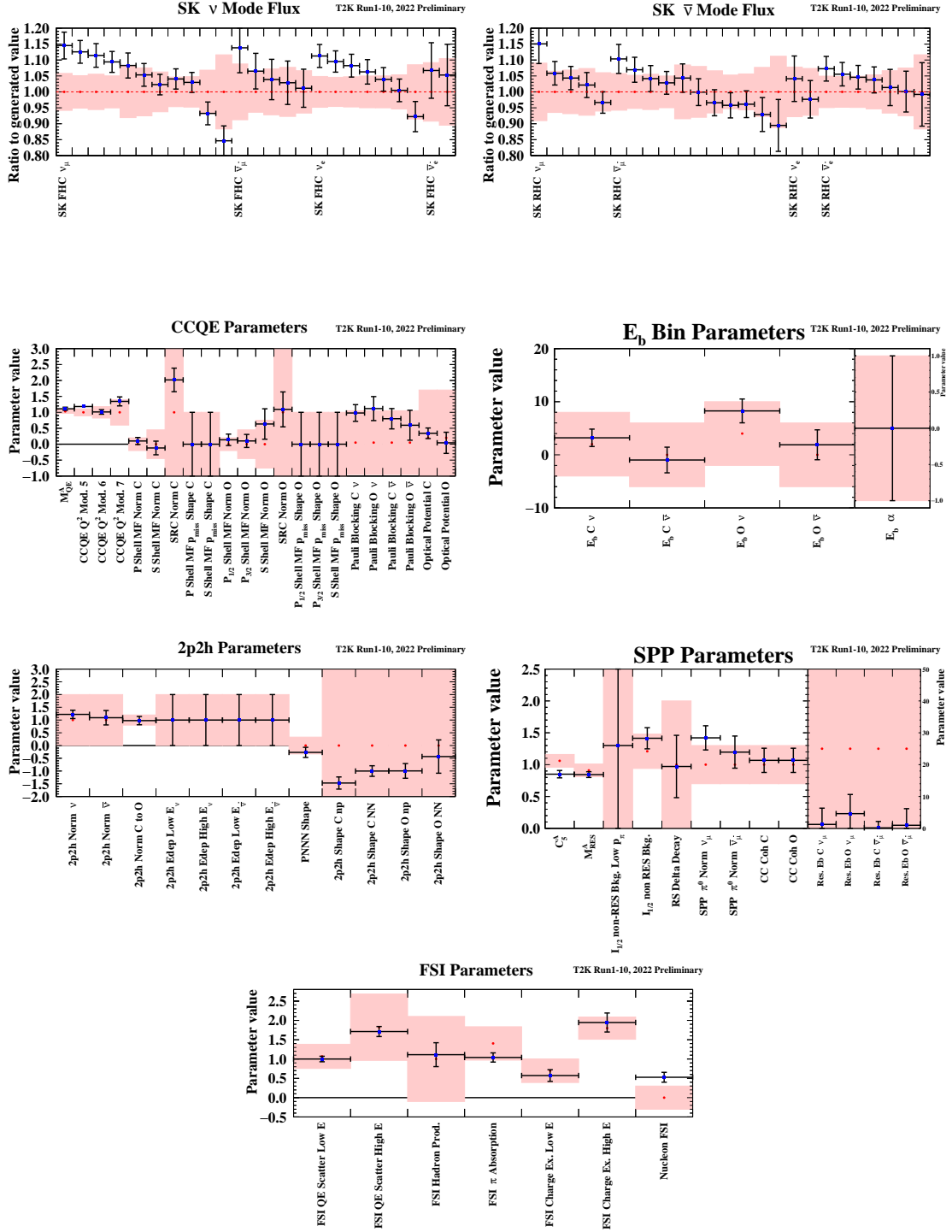


Figure 7.9: Prefit (red) and postfit (black) values and constraints on flux and cross-section parameters.



## Chapter 7. T2K oscillation analysis

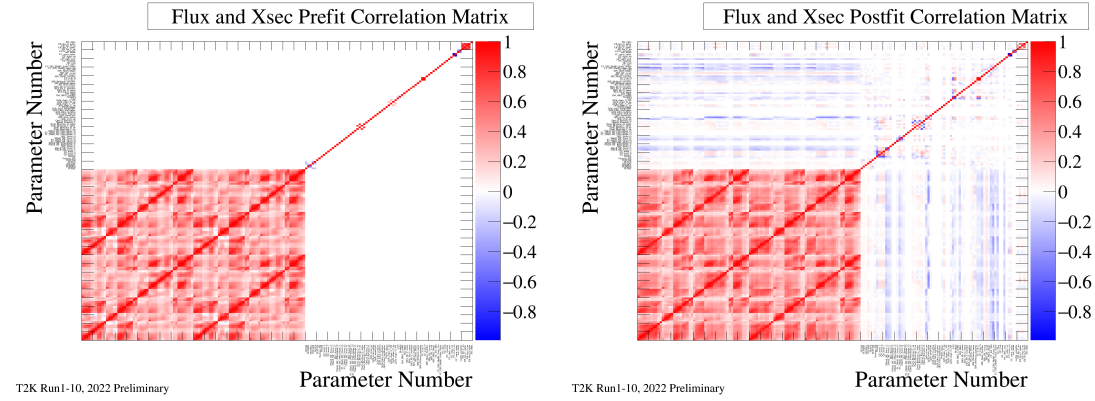


Figure 7.10: Prefit (left) and postfit (right) correlation matrices of the flux and cross-section parameters.

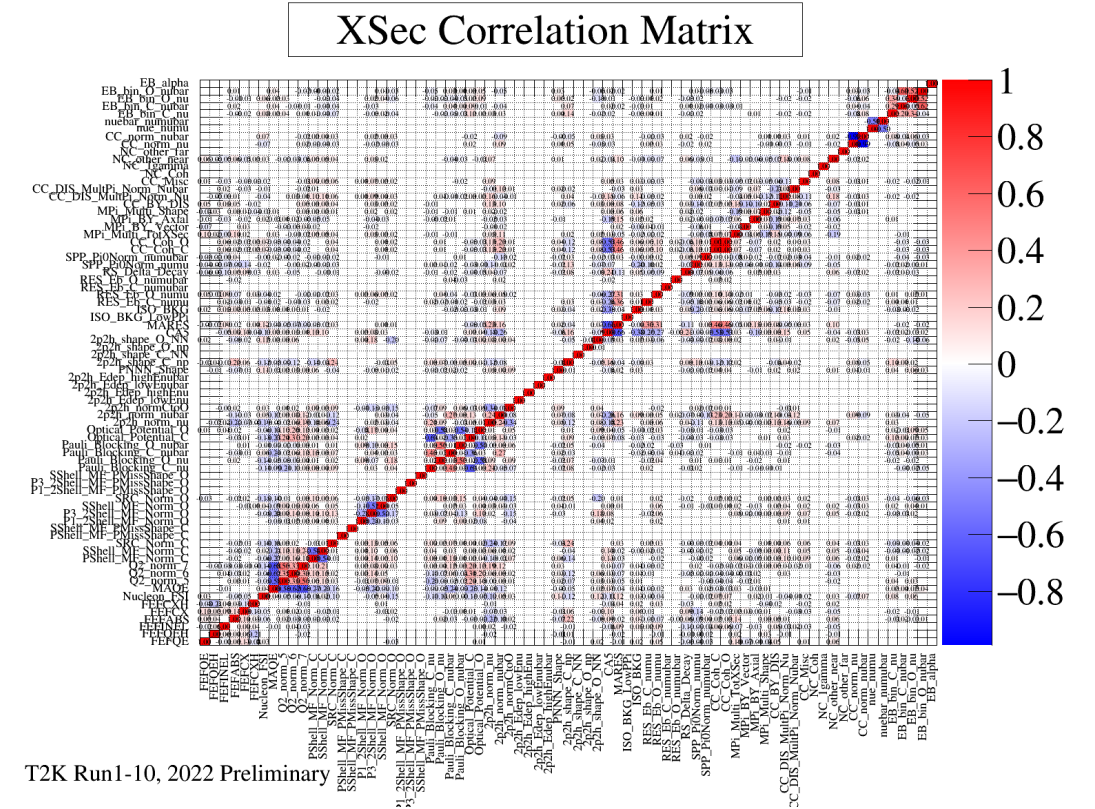


Figure 7.11: Postfit correlation matrix of the cross-section parameters.

The top panels of Figure 7.9 show the variations in the Super-Kamiokande flux parameters (which are strongly correlated with the ND280 ones as displayed in Figure 7.5). Most of the parameters are pulled by  $\sim 1 - 2\sigma$  from their prior values, where low-energy parameters are increased by up to  $\sim 15\%$ . Due to the prefit correlations, these strong pulls of the parameters do not mean a larger penalty from the  $-2\log\mathcal{L}_{\text{sys}}$  term. Nevertheless, these may indicate that the flux model does not allow us to fully describe the observed data, but they can also mean that mismodeled cross-section effects are absorbed within the flux uncertainties. The right panel of Figure 7.10 shows the (anti)correlations between them, where the most prominent ones involve the cross-section parameters that impact the normalization.

As for the cross-section uncertainties,  $M_A^{\text{QE}}$  is varied by  $2\sigma$  above its prior value. The normalizations of the carbon shells and the oxygen  $p_{1/2}$  and  $p_{3/2}$  shells are only slightly varied with respect to their prior values, while the SRC and the oxygen  $s$ -shell parameters are increased within their prior uncertainty and are also noticeably constrained. As discussed in Chapter 4, Pauli blocking and optical potential are expected to have a large impact when fitting the data since they affect the low energy transfer region where the impulse approximation used by the SF model does not hold and the disagreement with the data is important. We see here that the Pauli blocking parameters are strongly pulled above their prior for both targets and both neutrino types, whereas the optical potential remains closer to its prior.

The removal-energy shift parameters (referred to as  $E_b$ ) remain within their prior uncertainties but generally favor a higher removal energy, especially for  $\nu$ -oxygen interactions. Separate dedicated fits using the  $\alpha$  parameter (see Equation (7.3)) strongly favored the  $\alpha = 0$ , i.e. no  $|\vec{q}|$ -dependent correction to the removal energy. Consequently, it was decided to fix  $\alpha$  at this value to simplify the implementation in the far-detector fitters.

Furthermore, the 2p2h normalizations are strongly constrained while remaining close to their nominal values. The shape variations of this interaction channels are also well constrained. The PNNN shape parameter favors 2p2h interactions on  $NN$  pairs instead of  $np$  pairs, while the other 2p2h shape parameters show a preference for a more important  $\Delta$ -like contribution.

The CCRES, or single-pion production (SPP), interactions constitute a dominant fraction of the CC $1\pi$  interaction events in the ND280 selection. Consequently, the corresponding parameters are relatively well constrained as shown in Figure 7.9. The same observation can be made for the pion FSI parameters where all of them stay close to their prefit values except for the FSI pion absorption which is reduced.

### Compatibility with fits to cross-section data

Looking back at the fits to the cross-section measurements performed in Chapter 4, we can compare their results with those of the near-detector fit of the oscillation analysis. The most relevant cross-section studies to compare with are the fit to the joint T2K measurement of the muon kinematics on oxygen and carbon in the CC $0\pi$  presented in Reference [115] as well as

## Chapter 7. T2K oscillation analysis

---

the fits in the  $CC0\pi0p$  and  $CC0\pi Np$  topologies of Reference [93] since both use a subset of the near-detector data employed in the oscillation analysis. These comparisons are displayed in Figure 7.12, where the BANFF fit constraints (green) are overlaid on top of the results of Figures 4.17 and 4.22.

Let us first highlight the main differences between the near-detector analysis presented in this section and the cross-section fits of Chapter 4:

- the cross-section data are reported as a function of true kinematic variables, while the near-detector fit is performed in terms of the reconstructed kinematics,
- the events are Poisson-distributed at the near detector, while the cross sections are published with Gaussian errors on the bin content,
- the cross-section data errors include not only the statistical uncertainty, but also the possible variations due to the flux systematic uncertainties for instance and the fitted model uses as an input the averaged flux released by the experiment, while the near-detector analysis includes explicitly the flux uncertainties as fit parameters which can also serve as effective parameters to absorb cross-section-related mismodeling,
- the near-detector analysis features  $\sim 1000$   $CC0\pi$  bins in the neutrino mode (combined for FGD1 and FGD2, and split by proton and photon multiplicity) and also includes antineutrino samples, while the cross-section measurements of Chapter 4 have  $\sim 50 - 60$  bins in the neutrino mode only,
- even within the neutrino beam mode, the oscillation analysis uses roughly the double of the statistics (T2K runs 2 to 8) in comparison with these cross-section measurements (runs 2 to 4),
- the cross-section data in the  $CC0\pi Np$  topology is given in the transverse-momentum imbalance  $\delta p_T$ , while the oscillation analysis uses only the lepton kinematics in all the samples,
- the near-detector analysis uses additional samples to constrain non-CCQE interactions ( $CC1\pi$ ,  $CC\gamma$ , ...),
- the removal-energy shift parameters are not used in the cross-section fits,
- the missing-momentum shape uncertainties are fixed in the oscillation analysis (due to the lack of sensitivity when using the lepton kinematics only), but we fit them in the cross-section fits that use the nucleon information.

Other (less crucial) implementation-related differences that are not expected to be the cause of significant differences are summarized below:

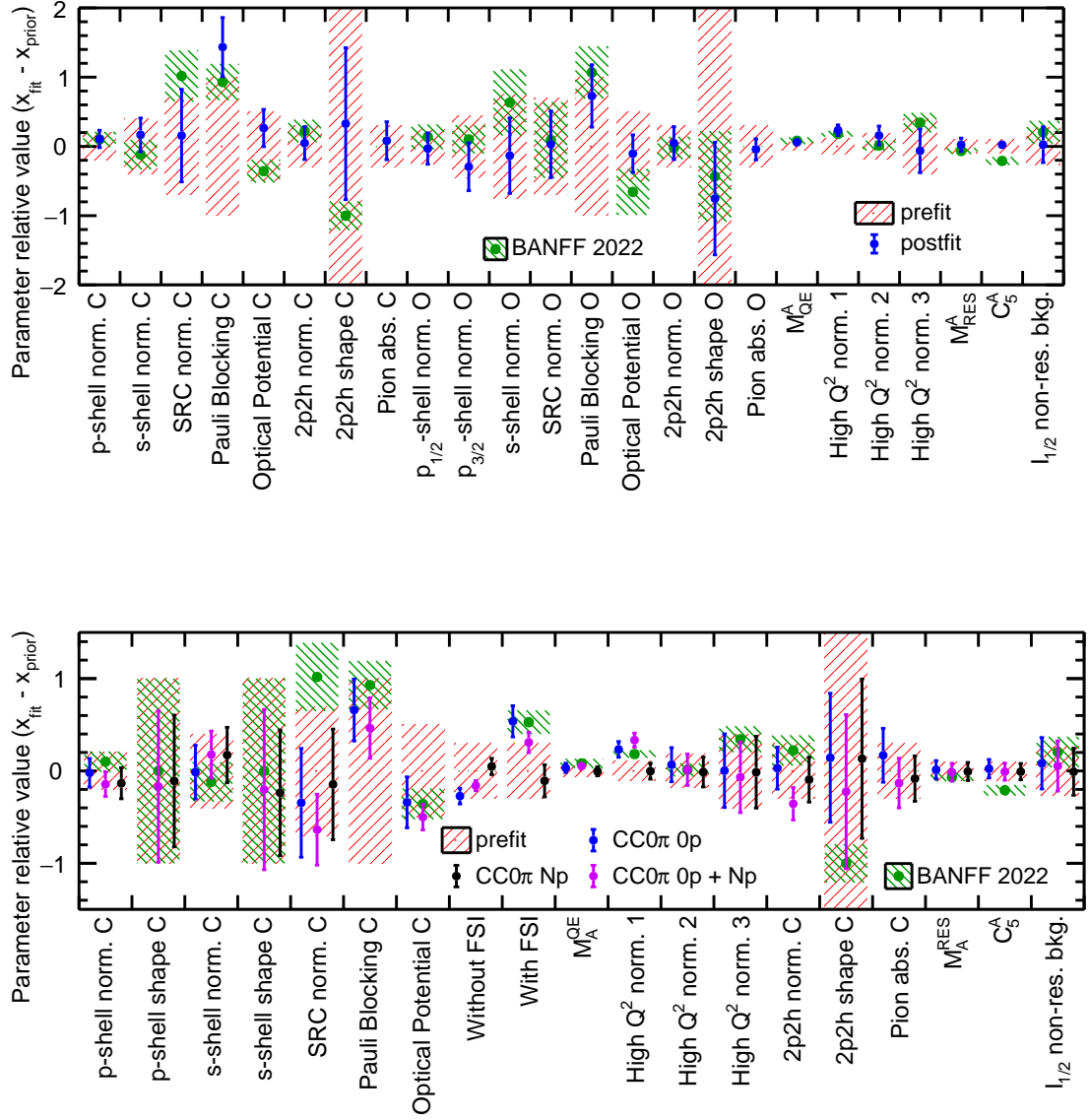


Figure 7.12: Comparison between the BANFF postfit and the results of fitting the joint T2K cross-section measurement on oxygen and carbon in the CC0 $\pi$  (top) and the T2K cross-section measurement on carbon in the CC0 $\pi$ 0 $p$  and the CC0 $\pi$ N $p$  topologies (bottom) as described in Chapter 4.

- the pion FSI dials are replaced by a simple normalization of the pion absorption for each target in the cross-section fits,
- Pauli blocking is implemented as a genuine variation in the pre-FSI nucleon in the studies of Chapter 4, while the oscillation analysis uses an effective reweighting treatment in the  $(q_0, |\vec{q}|)$  space when decreasing the Pauli blocking threshold below the nominal value,
- the prior on the optical potential correction uncertainty is of  $50\% \pm 50\%$  in the cross-section fits, while it corresponds to  $20\% \pm 100\%$  in the near-detector analysis, chosen to achieve stable fits in both cases,
- the nucleon FSI uncertainty is treated with a single parameter that varies simultaneously the FSI probability of the nucleon in the near-detector analysis, while the implementation in NUISANCE for the cross-section fits is done with two correlated uncertainties that scale the “With FSI” and “Without FSI” events,
- the 2p2h normalization is separated by target and the shape uncertainty is not separated for the  $nn$  and  $np$  pairs in the cross-section fits.

Consequently, we do not expect a perfect agreement between the two types of analysis, but the goal is to simply compare their broad compatibility.

First, as the T2K cross-section data is only in the  $CC0\pi$  topology, the CCRES uncertainties corresponding to the Rein – Sehgal model are not expected to vary significantly in comparison with the near-detector analysis as observed in Figure 7.12. On the other hand, the  $M_A^{QE}$  parameter is shifted in similar manners in the two analyses, accompanied by an increase in the first high- $Q^2$  uncertainty which suggests that the missing freedom for large energy transfers is seen in both analyses. When fitting only the  $CC0\pi0p$  cross section in  $\delta p_T$ , we do not observe any sensitivity to this parameter which is likely due to the coarse binning of the measurement yielding a disagreement with the near-detector fit. Additionally, the other high- $Q^2$  parameters, the Pauli blocking and optical potential uncertainties, and the normalizations of the carbon SRC and the oxygen  $s$ -shell exhibit varying degrees of differences between the cross-section data fits and the near-detector analysis. This could be explained by their significant impact on the CCQE event rate which implies their inevitable anticorrelations with the flux parameters in the near-detector fit. Besides, the cross-section fits show less sensitivity to the 2p2h shape uncertainties, which is due to the coarser binning and the missing statistics with respect to the oscillation analysis.

We can also observe similar trends in the correlation matrices from the two analyses. The Pauli blocking and optical potential are anticorrelated in Figure 7.11 for the near-detector analysis as expected. Pauli blocking is also anticorrelated with the nucleon FSI uncertainty because altering the probability of FSI impacts the low energy transfer events, which can be noticed in Figure 4.23. It is also correlated with the SRC and the 2p2h normalizations, which

further indicates that the data that we are using does not allow us to all the degeneracies in the neutrino interaction model. As discussed in Section 4.4, the addition of data samples in more sophisticated variables can allow us to separate the effects, particularly thanks to the ability of the single-transverse variables to disentangle the effects of the ground state and the multinucleon and FSI processes from the phase-space region corresponding to low energy transfers, which we will demonstrate in Chapter 9. Nevertheless, these comparisons show that, overall, the two analyses give broadly similar predictions even with the different frameworks and assumptions.

### ***p*-value**

In the near-detector analysis, one crucial study to confirm the ability of the model to reliably describe the data is by computing the corresponding *p*-value. It provides a metric to estimate how the data lies in the plausible model variations covered by the fit parameters with their prior uncertainties. This is conducted by fitting a large number of generated “pseudo-experiments”, each corresponding to the model prediction at a set of parameter values sampled from their prefit uncertainties and correlations. For the flux and the cross-section parameters, this is simply obtained from a Gaussian distribution defined by the parameters’ prefit central values and covariances. The ND280 response uncertainty samples on the other hand are generated by varying the fundamental underlying detector-response parameters in the reconstruction software, and not from the “ObsNorm” parameters. This ensures to cover the potential impact of non-Gaussian detector uncertainties, which is not captured by the effective “ObsNorm” parameters and their covariance. The (prefit) *p*-value is consequently defined as the probability of making an observation, according to the model, that is as extreme or more in comparison with the data fit given the nominal model predictions. The metric to evaluate how two models compare is simply their postfit negative log-likelihood. Consequently, the *p*-value is given by the fraction of the pseudo-experiments for which the postfit  $-2\log\mathcal{L}$  is larger than the data postfit negative log-likelihood  $-2\log\mathcal{L}_{\text{data}}$ . The chosen criterion to assert the compatibility of the data with the nominal model is  $p > 0.05$ .

To compute the *p*-value, around 1000 pseudo-experiments are generated with the described procedure and fitted with BANFF. The distribution of the pseudo-experiment postfit negative log-likelihoods (or  $\Delta\chi^2$ ) is shown in Figure 7.13. The obtained *p*-value is  $\sim 11\%$ , which is above the threshold and confirms the compatibility of the uncertainty model with the data.

### **7.5.2 Far-detector analysis**

#### **Overview**

The far-detector analysis presented here is performed with the P-Theta fitting framework. The goal is to constrain the four oscillation parameters that describe the  $\bar{\nu}_\mu$  disappearance and the  $\bar{\nu}_e$  appearance ( $\theta_{23}$ ,  $\Delta m_{32}^2$ ,  $\theta_{13}$  and  $\delta_{\text{CP}}$ ) as well as the mass ordering. The six Super-

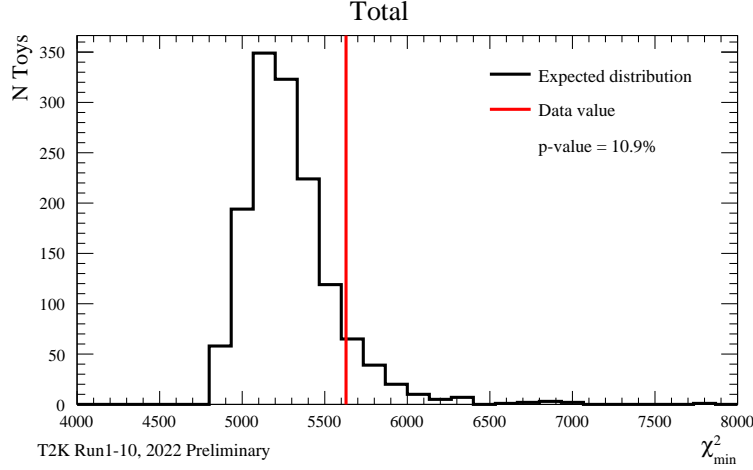


Figure 7.13: Distribution of the pseudo-experiment postfit negative log-likelihoods (or  $\Delta\chi^2$ ) compared to the data postfit negative log-likelihood (vertical red line). The fraction of the pseudo-experiments above the red line gives the  $p$ -value.

Kamiokande samples described in Section 7.2.3 are jointly fitted. All the  $e$ -like samples are binned in the reconstructed momentum  $p_l$  and angle  $\theta_l$  of the charged lepton, the single-ring muon samples are binned in the reconstructed neutrino energy (based on Equation (3.15)) and the charged-lepton angle, while the multi-ring muon-like sample (new addition of this year's analysis) is binned only in the reconstructed neutrino energy given by Equation (7.2).

The global best-fit point is obtained by profiling, i.e. minimizing the negative log-likelihood over all the systematic uncertainty parameters and the oscillation parameters using the gradient-descent algorithm of `Minuit2`. The sensitivity to the oscillation parameters and the confidence intervals (or contours) on the other hand are determined by marginalization as shown in Equation (7.8). In practice, it is difficult to simply visualize a three- or four-dimensional likelihood distribution, which is why these are often presented in one or two dimensions as we will see in this section. Consequently, in order to obtain the sensitivity for one or two oscillation parameters of interest, the other oscillation parameters are also marginalized in the same way as the systematic parameters. A large sample<sup>6</sup> of the systematic parameters is drawn from a Gaussian distribution given by the post-near-detector data fit for the flux and the cross-section uncertainties, as well as the Super-Kamiokande response covariance, while the marginalized oscillation parameters are uniformly sampled on an interval typically given by  $\pm 5\sigma$  from previous analyses. The exception to this uniform sampling of the marginalized oscillation parameters is  $\theta_{13}$  since, as discussed in Sections 1.4.4 and 1.4.5, reactor experiments are more sensitive to it and their constraints can be used. The results of the T2K oscillation analysis are always shown with and without reactor constraints: the former

<sup>6</sup>100,000 for one-dimensional marginal likelihoods, and 20,000 in two dimensions. These numbers are discussed and adjusted for the studies of Chapter 9

## 7.5 Results of the 2022 oscillation analysis

Parameter	Prior	
	Without reactor constraints	With reactor constraints
$\sin^2 2\theta_{13}$	$\mathcal{U}(a = 0.036, b = 0.187)$	$\mathcal{N}(\mu = 0.0861, \sigma = 0.0027)$
$\sin^2 \theta_{23}$	$\mathcal{U}(a = 0.38, b = 0.62)$	
$\delta_{\text{CP}}$	$\mathcal{U}(a = -\pi, b = \pi)$	
$\Delta m^2 [10^{-3} \text{ eV}^2/c^4]$	$\mathcal{U}(a = 2.25, b = 2.71)$	

Table 7.9: Sampling distributions used for the marginalized oscillation parameters.  $\Delta m^2$  refers to  $\Delta m_{32}^2$  in the normal mass ordering and to  $|\Delta m_{31}^2|$  in the inverted ordering.  $\mathcal{U}(a, b)$  denotes a uniform distribution over the interval  $[a, b]$ , while  $\mathcal{N}(\mu, \sigma)$  corresponds to a Gaussian distribution of mean  $\mu$  and variance  $\sigma^2$ .

Target coverage	Alternative name	1 parameter	2 parameters
68.3%	$1\sigma$	1	2.3
90%		2.71	4.61
95.45%	$2\sigma$	4	6.18
99.73%	$3\sigma$	9	11.62

Table 7.10: Fixed  $\Delta\chi^2$  values to define confidence intervals.

corresponds to a Gaussian sampling from the reactor constraints given by Reference [12] in the marginalization, while the latter means a uniform sampling similarly to the other marginalized oscillation parameters. The sampling distributions for the marginalized parameters are summarized in Table 7.9. The solar parameters  $(\Delta m_{21}^2, \theta_{12})$ , for which T2K has virtually no sensitivity, are fixed according to the best-fit values of Reference [12].

The sensitivity to one or two oscillation parameters, denoted by  $\vec{o}$ , is expressed as a chi-square difference given by the ratio of the marginalized likelihood  $\mathcal{L}_{\text{marg}}(\vec{o})$  as a function of  $\vec{o}$  over the maximum of the marginalized likelihood  $\mathcal{L}_{\text{marg}}^{\text{max}}$ :

$$\Delta\chi^2(\vec{o}) = -2\log\left(\frac{\mathcal{L}_{\text{marg}}(\vec{o})}{\mathcal{L}_{\text{marg}}^{\text{max}}}\right). \quad (7.9)$$

The marginal likelihood  $\mathcal{L}_{\text{marg}}(\vec{o})$  is evaluated on a grid defined on intervals in the oscillation parameter(s) of interest  $\vec{o}$  (i.e. grid search), and the fixed  $\Delta\chi^2$  confidence intervals are given by the region of oscillation parameters for which the value of  $\Delta\chi^2(\vec{o})$  is below the chosen confidence level determined by the target coverage as shown in Table 7.10.

This definition of the confidence intervals with this fixed  $\Delta\chi^2$ -method only holds under the conditions of Wilks' theorem [280], i.e. if the likelihood function is approximately Gaussian and its significant values are sufficiently far from the parameter boundaries. These condi-



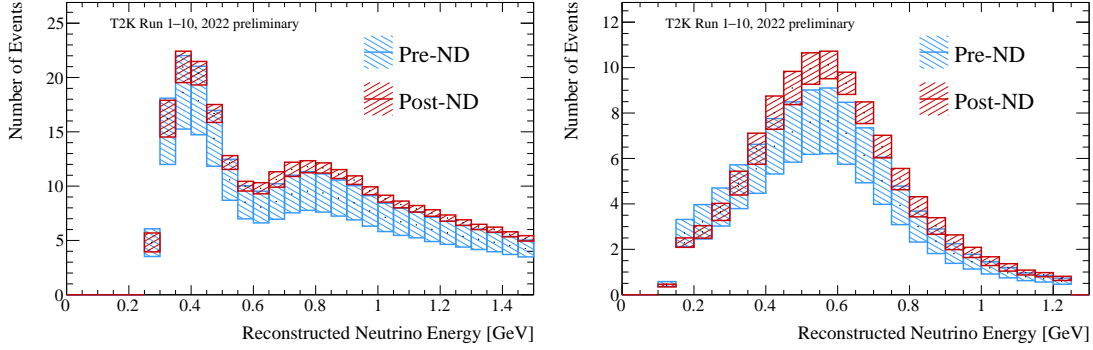


Figure 7.14: Impact of the near-detector tuning and constraints on the distribution the reconstructed neutrino energy in the FHC mode for the  $1R\mu$  (left) and the  $1Re$  samples. The oscillation parameters are evaluated close to the T2K best fit values from the previous analysis.

tions do not hold for some of the oscillation parameters, which consequently requires an alternative treatment to obtain intervals with the correct coverage such as the Feldman – Cousins method [281]. This method is used for the calculation of the one-dimensional confidence intervals for parameters that are known not to respect Wilks theorem conditions due to non-Gaussianities and boundary effects, namely  $\delta_{CP}$  and  $\sin^2 \theta_{23}$ .

### Impact of the near-detector constraints

As discussed in Sections 7.1 and 7.4.2, the oscillation analysis is designed so that the constraints from the near-detector data can be used to reduce the systematic uncertainties related to the flux and the neutrino interaction cross section. This is illustrated in Figure 7.14, where we can see the error bands on the distributions of the reconstructed neutrino energy when using only the prior knowledge on the systematic uncertainties (blue) compared to when the constraints from the near-detector fits are applied for the disappearance (left) and the appearance (right) oscillation channels. The total systematic uncertainties on the event rates are significantly reduced when using the near-detector constraints particularly in the single-ring samples from  $\sim 14 - 17\%$  down to  $\sim 3 - 6\%$ .

### Global best-fit values

Profiling over all the systematic uncertainty and oscillation parameters allows us to determine the global best-fit point for the four oscillation parameters ( $\theta_{23}$ ,  $\Delta m_{32}^2$ ,  $\theta_{13}$  and  $\delta_{CP}$ ) with and without reactor constraints of Reference [12] on  $\theta_{13}$ , and in the normal and inverted mass orderings as summarized in Table 7.11. The error on a given parameter is obtained by marginalizing over all the other parameters and calculating with this one-dimensional negative log-likelihood the difference between the parameter values for which  $\Delta\chi^2 = 1$  and the best-fit point. Table 7.11 also shows the value of  $-2\Delta\ln\mathcal{L}$  defined as the difference of the

negative log-likelihoods for the normal and inverted orderings.

At this global best-fit point, Table 7.12 shows the event rates in each Super-Kamiokande sample as predicted by the MC simulation when varying the  $\delta_{\text{CP}}$  parameter in comparison with the data. By comparing the variation of the event rates in the single-ring  $e$ -like samples in the FHC and RHC modes with the observed data rate, we can see a clear preference for the CP-violating value  $\delta_{\text{CP}} = -\pi/2$ . These are the samples that drive the sensitivity to CP violation, while the disappearance samples see their event rates almost unchanged when varying  $\delta_{\text{CP}}$ .

### Confidence contours

Figure 7.15 shows the fixed- $\Delta\chi^2$  two-dimensional confidence level contours in the atmospheric parameters  $\Delta m_{32}^2$  vs.  $\theta_{23}$  for normal (cyan) and inverted (magenta) ordering with (right) and without (left) reactor constraints. This shows the sensitivity to  $\Delta m_{32}^2$  and  $\theta_{23}$  of T2K to resolve the so-called octant degeneracy, i.e. to determine where the value of  $\theta_{23}$  lies with respect to  $\pi/4$ . The sensitivity is mainly driven by the  $\mu$ -like samples which give access to the disappearance probability as expressed in a simplified way in Equation (1.37). This expression shows that there is a symmetry around  $\sin^2 \theta_{23} \sim 0.5$  due to the term in  $\sin^2 2\theta_{23}$  which can be particularly seen in the result without the reactor constraints in the left panel of Figure 7.15. The slight asymmetry that is observed in this result is in fact due to the additional constraints coming from the  $e$ -like samples, since all the Super-Kamiokande samples are fitted simultaneously in the analysis. Indeed, the leading term of the appearance probability in Equation (1.46) is proportional to  $\sin^2 \theta_{23}$  (instead of  $\sin^2 2\theta_{23}$  in the disappearance probability) which can resolve this degeneracy, but only to a limited extent due to the other degeneracy with  $\theta_{13}$  in this leading term. Consequently, without reactor constraints, there is no clear preference to either octants. The addition of the constraints on  $\theta_{13}$  allows us to enhance the effect of the  $e$ -like sample on the octant sensitivity as it resolves the  $\theta_{13}$  vs.  $\theta_{23}$  ambiguities in Equation (1.46), and a stronger preference to the upper octant can be observed at the  $1\sigma$  level. Nevertheless, this preference is still weak and T2K data remains compatible with both octants. These constraints on the atmospheric parameters were also discussed and compared to other experiments in Section 1.4.3.

The impact of the constraints from reactor experiments on the sensitivity to  $\delta_{\text{CP}}$  was also discussed in Section 1.4.5 and illustrated in Figure 1.19. By strongly constraining the variations of the leading term in the appearance probability, T2K is more sensitive to the variations in the subleading terms which give access to the value of  $\delta_{\text{CP}}$ . Figure 7.16 shows the one-dimensional  $\Delta\chi^2$  as a function of  $\delta_{\text{CP}}$  using reactor constraints. The shaded regions indicate the different confidence levels computed with the Feldman – Cousins method. As expected from Table 7.12,  $\delta_{\text{CP}} \approx -\pi/2$  that maximally violates the CP symmetry is preferred by the data. A large region of  $\delta_{\text{CP}}$  is excluded at  $3\sigma$  C.L., including the CP conserving value  $\delta_{\text{CP}} = 0$ . The other CP-conserving value  $\delta_{\text{CP}} = \pi$ , and thus the CP-conservation hypothesis, is excluded at a  $2\sigma$  level. These conclusions are unchanged from the previous analyses [53, 263], although the constraints are slightly weaker, which is mainly due to the updated neutrino interaction model.

## Chapter 7. T2K oscillation analysis

Parameter	Best fit			
	T2K only		T2K + reactor	
	Normal	Inverted	Normal	Inverted
$\sin^2 2\theta_{13}$	0.103	0.114	0.0861	0.0865
$\delta_{\text{CP}}$	$-2.25^{+1.33}_{-0.74}$	$-1.25^{+0.66}_{-0.90}$	$-2.18^{+1.22}_{-0.47}$	$-1.37^{+0.52}_{-0.68}$
$\Delta m^2 [10^{-3} \text{ eV}^2/c^4]$	$2.506^{+0.048}_{-0.058}$	$2.474^{+0.050}_{-0.056}$	$2.506^{+0.047}_{-0.059}$	$2.473^{+0.051}_{-0.054}$
$\sin^2 \theta_{23}$	$0.466^{+0.107}_{-0.016}$	$0.465^{+0.100}_{-0.016}$	$0.559^{+0.018}_{-0.078}$	$0.560^{+0.019}_{-0.041}$
$-2\ln \mathcal{L}$	651.433	652.254	651.584	653.222
$-2\Delta\ln \mathcal{L}$	0	0.821	0	1.638

Table 7.11: Best fit values of the oscillation parameters in the normal and inverted ordering when using T2K data only and when combining it with the reactor constraints from Reference [12], along with the negative log-likelihood values.  $\Delta m^2$  refers to  $\Delta m_{32}^2$  in the normal mass ordering and to  $|\Delta m_{31}^2|$  in the inverted ordering.

Sample	$\delta_{\text{CP}} = -\pi/2$	$\delta_{\text{CP}} = 0$	$\delta_{\text{CP}} = \pi/2$	$\delta_{\text{CP}} = \pi$	Data
FHC 1R $\mu$	358.669	358.011	358.63	359.405	318
RHC 1R $\mu$	139.427	139.094	139.429	139.788	137
FHC 1Re	99.0567	83.5624	68.6139	84.1084	94
RHC 1Re	17.0154	19.3474	21.4265	19.0946	16
FHC 1Re1de	10.8521	9.44959	7.70161	9.10421	14
FHC multi-R $\mu$	118.527	118.017	118.501	119.02	134

Table 7.12: Predicted event rate in each of the far detector samples at the T2K best fit values of the systematic parameters as well as of the oscillation parameters shown in Table 7.11 for different values of the phase  $\delta_{\text{CP}}$ , compared to the measured event rate.

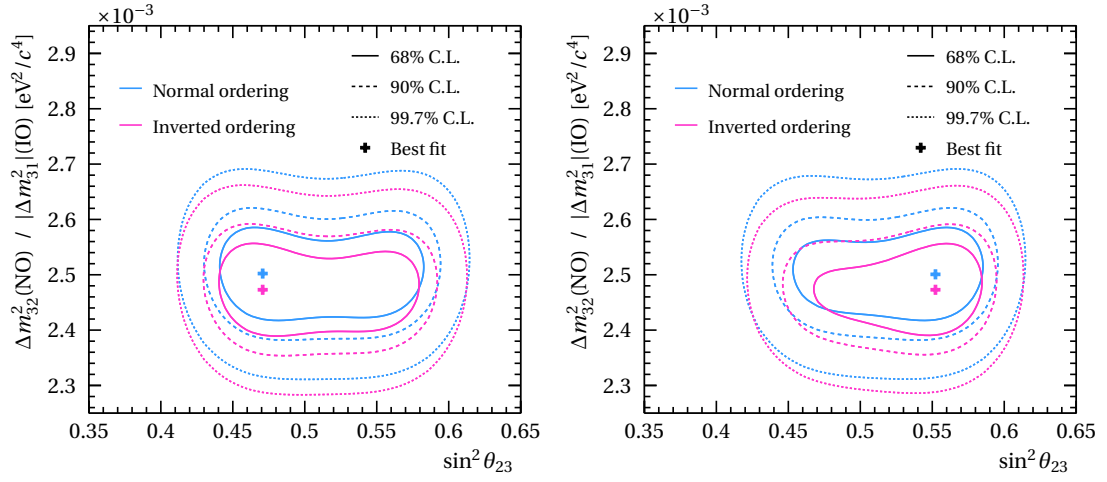


Figure 7.15: Fixed- $\Delta\chi^2$  two-dimensional confidence level contours in  $\Delta m_{32}^2$  ( $|\Delta m_{31}^2|$  for inverted ordering) vs.  $\sin^2 \theta_{23}$  for normal (cyan) and inverted (magenta) ordering with (right) and without (left) reactor constraints of Reference [12].

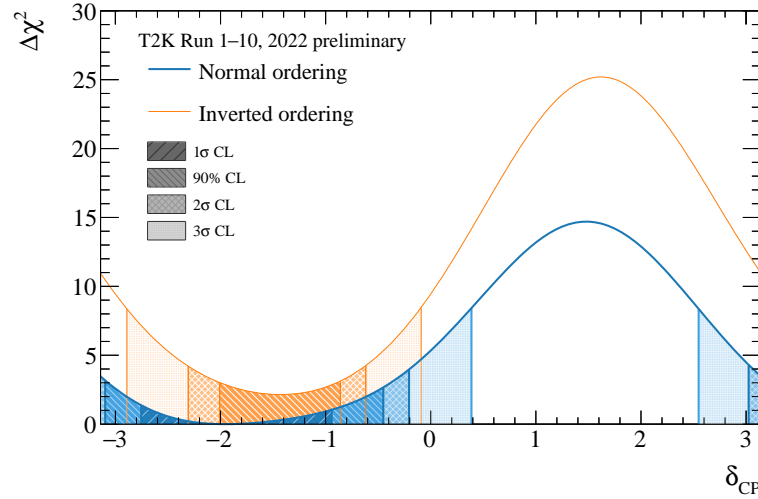


Figure 7.16: One-dimensional negative log-likelihood in  $\delta_{CP}$  for normal (blue) and inverted (orange) ordering using reactor constraints of Reference [12], and the shaded regions correspond to confidence levels obtained with the Feldman – Cousins method.

### 7.5.3 Impact of alternative neutrino interaction models

The uncertainty model of neutrino interactions described in Chapter 4 and Section 7.3.3 is designed to cover known and plausible variations, but it cannot account every possible differences especially when it comes to predictions from alternative models or data tunes from other experiments. A routine robustness test performed at each iteration of the oscillation analysis consists of fitting simulated data generated with alternative models. This allows us to gauge the ability of the current systematic uncertainty parametrization to offer enough model freedom to capture the effects of such models without biasing the results of the oscillation measurements. The typical steps for this study are the following:

1. The reference with which the results from the alternative-model simulated data fits are compared is generated. This corresponds to the so-called *Asimov* fits which are defined as fits for which the simulated data is taken exactly as the prediction of the nominal model. A near-detector Asimov fit is performed, and its constraints are used for far-detector Asimov fits. These far-detector fits use as data the nominal model prediction as well for chosen sets of oscillation parameter values.
2. A simulated data set is generated from the predictions of the alternative model or tune and fitted with BANFF/GUNDAM using the nominal uncertainty model.
3. The predictions from this alternative model are generated at the far detector in the form of a simulated data set as well, with the chosen values of the oscillation parameters, and this data is fitted with the nominal uncertainty model tuned and constrained with the results of the near-detector fit to the simulated data of the same alternative model.
4. The fixed- $\Delta\chi^2$  confidence intervals are determined for each oscillation parameter and compared to the ones obtained from the Asimov fits. If any biases are observed, then depending on their size, actions may be taken. These can vary from simply adding a smearing on the oscillation parameters to revisiting the uncertainty model altogether and adding appropriate freedoms to cover the observed variations.

In the 2022 analysis, more than ten different alternative models were tested following this procedure, and two simulated data sets caused noticeable biases on the  $\Delta m_{32}^2$  confidence intervals that warranted an action. The first one is an alternative ground-state model for CCQE interactions called the Hartree – Fock continuum random phase approximation (HF+CRPA) approach [282, 283], which has different shape predictions than the SF model particularly in the low energy transfer region. When fitting the corresponding simulated data, the uncertainty model of the analysis attempts to capture these differences by varying the Pauli blocking and optical potential uncertainties as shown in Figure 7.17. However, this appears to be insufficient as the far-detector fit of the simulated data exhibits a noticeable bias in the  $\Delta m_{32}^2$  contours. The second simulated data set that yielded a noticeable bias corresponds to a data-driven alteration to the model prediction, where the discrepancy between the nominal model and

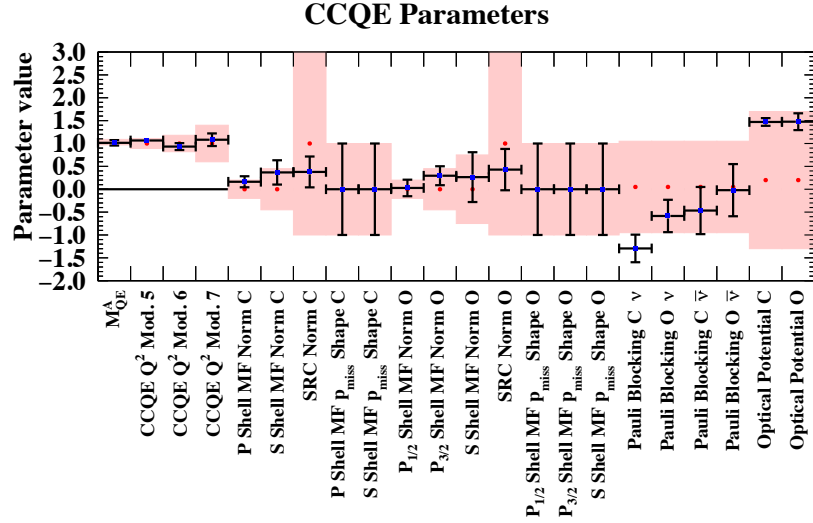


Figure 7.17: Postfit CCQE parameters from a near-detector fit with BANFF to the simulated data corresponding to the HF+CRPA model.

the ND280 data in the  $CC0\pi$  topology is corrected by rescaling the non-CCQE components of the  $CC0\pi$  events to match the data instead of varying the CCQE part. In total, these simulated data studies motivated an additional smearing of  $\sim 0.028 \times 10^{-3} \text{ eV}^2/c^4$  on the  $\Delta m_{32}^2$  obtained from the fit to Super-Kamiokande data.

These studies also indicate where the T2K collaboration needs to focus for further developments of the neutrino interaction model and the related uncertainties. In particular, while the low energy transfer uncertainties we introduced in Chapter 4 allow us to well describe the cross-section measurements and the ND280 data in the near-detector fit, they fail to cover more complex shape variations as the ones predicted by the HF+CRPA model. Consequently, an additional set of uncertainties is currently under development for the next iteration of the oscillation analysis.

## 7.6 Summary

In this chapter, we reviewed the full oscillation analysis pipeline from the selection of the near- and far-detector data and the definition of the uncertainty model, to the actual analyses to infer the oscillation parameters. We particularly focused on the neutrino interaction uncertainties introduced in Chapter 4 and how these were adapted for the oscillation-analysis framework and compared the results of the near-detector fits to the fits to the cross-section measurements discussed in Section 4.3. We found that these are broadly compatible and allow us to make similar physics conclusions on the nominal interaction model. We also described how the near-detector analysis is used with the far-detector fitters to extract the oscillation parameters and highlighted the importance of assessing out-of-model cross-section effects with

## Chapter 7. T2K oscillation analysis

---

simulated data studies, which can induce biases on the oscillation parameters. In Chapter 8, we reproduce the full oscillation-analysis pipeline presented here with an alternative fitter to BANFF, called GUNDAM, both for this iteration and the previous one. We particularly focus on the validation steps that are required to ensure that the fitters behave as expected before fitting data. In Chapter 9, we follow this same pipeline to estimate the future sensitivity to the oscillation parameters in the upcoming data-taking phase, with a focus on the potential impact of the upgraded near detector.

## 8 GUNDAM: a new fitting framework

The upcoming data from the near detector upgrade is expected to significantly increase the computational costs of the analyses. Indeed, it will be used to define multiple new samples with high statistics to explore previously-uncharted physics, which will undoubtedly require more sophisticated models and uncertainties beyond what was used in the studies of Chapters 4 and 7. Currently, with the analyses that use BANFF, a near-detector data fit can take multiple days to converge. With the larger data sets and more complex model parameters upcoming within the next few months, this is bound to become unbearable.

The development of a new fitting framework began with the purpose of overcoming this challenge. Its starting point was the `Super-xsl1hFitter` [284], a fitting tool developed within the T2K cross-section group to perform binned likelihood unfolding technique mentioned in Section 4.1.1, quite similar to the methods used in the near-detector fit. The focus of this new round of fitter developments was mainly the optimization of the performances and the improvement of the modularity, which led to a new software that we now call GUNDAM<sup>1</sup> [285].

This chapter focuses on describing the GUNDAM software. To start with, Section 8.1 gives an overview of its philosophy and capabilities. In order for it to become an official tool for T2K, it needs to be approved by the collaboration after passing rigorous validation tests. The ultimate goal is to reproduce results from previous analyses, which we present in Sections 8.2 and 8.3. Finally, Section 8.4 presents paths of further developments of this software.

### 8.1 Overview

GUNDAM is designed to be a multipurpose toolkit for a wide range of high-level data analyses, such as oscillation analyses and cross-section extraction, with the main goal of fitting multi-variate models to data. The main characteristic that allows us to achieve this is the modularity. In practice, this means that the software should be able to read any type of inputs, define any kind of samples with any sort of binning (e.g. non-uniform, multidimensional, ...) and with

---

<sup>1</sup>GUNDAM stands for *Generic fitter for Upgraded Near Detector Analysis Methods*.



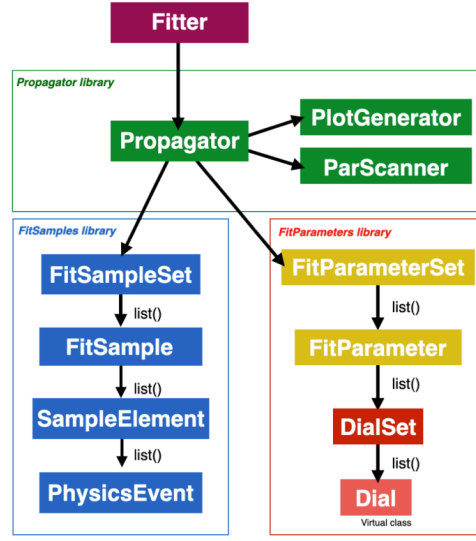


Figure 8.1: Simplified structure of GUNDAM. Credits: A. Blanchet.

any form of fit parameters, all in a user-friendly manner.

To this end, the source code built around a core structure shown in Figure 8.1. Each block in this structure is fully configurable with input YAML / JSON files. The propagation engine, referred to as the *Propagator*, is the heart of GUNDAM. It propagates the values of the user-defined fit parameters on the MC distributions in the specified samples. The *Fitter* engine calls the *Propagator* at each iteration of the minimization process by passing to it the updated values of the fit parameters, and the *Propagator* returns the value of the negative-log likelihood  $-2\log\mathcal{L}$  evaluated at this set of parameters. Since it is called a large number of times (typically  $\sim 500,000$  times), a special care was taken in optimizing and parallelizing the *Propagator*. It also embeds a set of plotting tools for debugging purposes.

The *Fitter* engine provides the interface between the *Propagator* and the minimization algorithm. The default implementation in GUNDAM is currently the *Minuit2* package of ROOT. The modularity of the GUNDAM code allows this *Fitter* engine to act as an interface with any C++-based minimization code, which opens the door to the implementation of more sophisticated fitting techniques.

To benchmark its performances, a comparison between BANFF and GUNDAM using the same computational resources (16 CPUs) showed that the speed of the minimization corresponds to  $\sim 1$  iteration/s for the former while the latter performs it at  $\sim 7$  iterations/s. Other ways to improve the convergence speed are implemented, such as a principal component analysis which reduces the dimensionality of the minimization problem.

## 8.2 Reproducing the 2020 oscillation analysis

When the validation of GUNDAM started, the latest available oscillation result was the 2020 oscillation analysis (OA2020) [263] which used a different parametrization of the cross-section uncertainties with respect to what we described in Chapter 7. In order for this tool to be approved by the collaboration, the goal was to fully reproduce this analysis and show its readiness for integration in the oscillation analysis pipeline. The criteria for a successful validation is to pass the same checks that are performed between BANFF and MaCh3, which correspond to the following comparisons:

1. predicted event rates at the prefit for each sample,
2. event rates per sample when varying each fit parameter individually,
3. likelihood scans for each fit parameter,
4. Asimov and data fits, including the propagated constraints on the oscillation parameters

### 8.2.1 Prefit event rates

Comparing the predicted event rates allows us to verify that the fitters select the same events in each sample, and that the prefit weights are applied correctly. This particularly permitted debugging the `Propagator` block of GUNDAM. There are multiple incremental stages in this comparison, as shown in Table 8.1:

- (a) Prefit with no weights: this verifies that the number of the “bare” MC events in each selected sample is the same in both fitters, which validates the definition of the sample and its binning in GUNDAM.
- (b) Prefit with POT weight: each event in the MC input is associated with a weight that scales it according to the collected POT. This comparison makes sure that this simple normalization weight is applied correctly in each sample.
- (c) Prefit with nominal flux weights: the flux tuning provides weights that are applied to events in bins of true neutrino energy, which is verified here.
- (d) Prefit with nominal “ObsNorm” weights: in this analysis, 574 “ObsNorm” parameters are used to account for the detector response, which correspond to bin normalizations tightly constrained by a covariance matrix as discussed in Section 7.3.2. Their prefit values are mostly  $\neq 1$ , and this check is a first test of the association between an event and simple normalization fit parameters in GUNDAM.
- (e) Prefit with nominal cross-section weights: at this stage, the weights from the prefit parameter values of the cross-section model are applied. The cross-section parameters

are the most complex ones in the analysis since they can be defined on an event-by-event or bin-by-bin basis with non-trivial variations of the weights. This check is a first test of the correct association between an event and such parameters.

- (f) Prefit with all weights: in this step, all the previous weights are applied simultaneously, which provides our prefit distributions of the MC.

Hard-coded conditions dating from many years ago deeply buried in the BANFF source code, and whose authors are often no longer part of the collaboration, complicated this task. In many cases, the disagreements we found were due to undocumented additional *ad hoc* conditions that were applied in BANFF. Furthermore, at the step (e), we discovered a bug in BANFF with a small but noticeable impact on the event rate due to the removal energy uncertainties discussed in Section 7.3.3. Unlike most other cross-section parameters, these are implemented on a bin-by-bin basis in the reconstructed lepton kinematics. A careful investigation of the BANFF source code allowed us to find that its loop that propagates this uncertainty always missed the last bin in the muon kinematics. This bug would have no major impact on the analysis result since the last bin is with very small statistics, but its effect was noticeable in this validation. At the end, the agreement of prefit event rates was reached for all the 18 samples of this analysis. Table 8.1 shows as an example four of them.

### 8.2.2 Varied event rates

In this step, each free parameter of the fit is varied, and the corresponding event rate in each sample is compared between BANFF and GUNDAM. The 2020 oscillation analysis featured a total number of 712 free fit parameters. In order to be able to reproduce the BANFF results, it is necessary to make sure that the parameters are well implemented and accurately produce the same effects on the MC distributions. This is tested by varying each of the 712 parameters individually at their  $-3\sigma$ ,  $-1\sigma$ ,  $1\sigma$  and  $3\sigma$  values, and comparing the corresponding event rate in each sample between the two fitters. Table 8.2 shows as an example the performed comparisons for the  $M_A^{\text{QE}}$  parameter.

This validation allowed us to discover other small code bugs present in BANFF, in addition to the missed bins in the propagation of the removal energy discussed in the previous section:

- NC $\gamma$  event weights were not correctly applied,
- Coulomb correction uncertainty (see Section 7.3.3) was not correctly enabled,
- The bin-by-bin weights of the removal energy shift were computed to be applied only on events with a true neutrino energy below 4 GeV, while in BANFF the threshold was set to 4000 GeV due to a unit conversion error.

These bugs only affect a negligible fraction of events and have no major impact on the final oscillation results, but their effect is noticeable in these comparisons as the goal of this

## 8.2 Reproducing the 2020 oscillation analysis

<b>FHC FGD1 <math>\nu_\mu</math> CC0<math>\pi</math></b>	BANFF	GUNDAM
Prefit with no weights	524093	524093
Prefit with POT weights	31077.7	31077.7
Prefit with nom. flux weights	33420.4	33420.4
Prefit with nom. “ObsNorm” weights	31036.7	31036.7
Prefit with nom. cross-section weights	26459.9	26459.9
Prefit with all weights	27951.8	27951.8
<b>FHC FGD2 <math>\nu_\mu</math> CC1<math>\pi</math></b>	BANFF	GUNDAM
Prefit with no weights	103305	103305
Prefit with POT weights	6106.46	6106.46
Prefit with nom. flux weights	7000.23	7000.23
Prefit with nom. “ObsNorm” weights	6071.81	6071.81
Prefit with nom. cross-section weights	6024.08	6024.08
Prefit with all weights	6723.79	6723.79
<b>RHC FGD2 <math>\bar{\nu}_\mu</math> CC Other</b>	BANFF	GUNDAM
Prefit with no weights	16111	16111
Prefit with POT weights	1167.71	1167.71
Prefit with nom. flux weights	1228.16	1228.16
Prefit with nom. “ObsNorm” weights	1161.1	1161.1
Prefit with nom. cross-section weights	1139.12	1139.12
Prefit with all weights	1176.53	1176.53
<b>RHC FGD2 <math>\nu_\mu</math> (bkg) CC Other</b>	BANFF	GUNDAM
Prefit with no weights	12363	12363
Prefit with POT weights	902.941	902.941
Prefit with nom. flux weights	1019.55	1019.55
Prefit with nom. “ObsNorm” weights	906.782	906.782
Prefit with nom. cross-section weights	894.095	894.095
Prefit with all weights	1000.39	1000.39

Table 8.1: Four examples of the 18 prefit event rate tables comparing BANFF and GUNDAM per sample, broken down by weight type.

Dial	Sample	$-3\sigma$		$-1\sigma$		$0\sigma$		$1\sigma$		$3\sigma$		(G-B)/G at $-1\sigma$
		BANFF	GUNDAM	BANFF	GUNDAM	BANFF	GUNDAM	BANFF	GUNDAM	BANFF	GUNDAM	
MAQE = $-0.14876 \pm 0.0495868$	FHC FGD1 $\nu_\mu$ CC0 $\pi$	25891	25891	27295.5	27295.5	27951.8	27951.8	28578.8	28578.8	29751.1	29751.1	-8.96746e-09
	FHC FGD1 $\nu_\mu$ CC1 $\pi$	8285.36	8285.36	8332.99	8332.99	8358.62	8358.62	8385.42	8385.42	8442.4	8442.4	1.46427e-07
	FHC FGD1 $\nu_\mu$ CC0th	6981.89	6981.89	7014.52	7014.52	7031.49	7031.49	7048.84	7048.84	7084.47	7084.47	-6.61261e-15
	FHC FGD2 $\nu_\mu$ CC0 $\pi$	25543.8	25543.8	26914.6	26914.6	27558.9	27558.9	28176.6	28176.6	29336.7	29336.7	7.43062e-08
	FHC FGD2 $\nu_\mu$ CC1 $\pi$	6664.27	6664.27	6702.65	6702.65	6723.79	6723.79	6746.17	6746.17	6794.48	6794.48	-9.59844e-08
	FHC FGD2 $\nu_\mu$ CC0th	6406.23	6406.23	6438.09	6438.09	6454.74	6454.75	6471.81	6471.81	6506.95	6506.95	2.8428e-07
	RHC FGD1 $\bar{\nu}_\mu$ CC0 $\pi$	6922.43	6922.43	7152	7152	7270.33	7270.33	7389.73	7389.73	7628.12	7628.12	1.66588e-14
	RHC FGD1 $\bar{\nu}_\mu$ CC1 $\pi$	689.842	689.842	692.63	692.63	694.322	694.322	696.207	696.207	700.529	700.529	1.3131e-15
	RHC FGD1 $\bar{\nu}_\mu$ CC0th	1270.13	1270.13	1280.9	1280.9	1286.79	1286.79	1292.99	1292.99	1306.26	1306.26	3.55023e-15
	RHC FGD2 $\bar{\nu}_\mu$ CC0 $\pi$	6713.22	6713.22	6925.52	6925.52	7036.5	7036.5	7149.31	7149.31	7376.67	7376.67	3.6771e-15
	RHC FGD2 $\bar{\nu}_\mu$ CC1 $\pi$	620.769	620.769	623.198	623.198	624.69	624.69	626.356	626.356	630.183	630.183	-2.9188e-15
	RHC FGD2 $\bar{\nu}_\mu$ CC0th	1163.4	1163.4	1171.83	1171.83	1176.53	1176.53	1181.54	1181.54	1192.43	1192.43	-1.7463e-15
	RHC FGD1 $\nu_\mu$ (bkg) CC0 $\pi$	2857.12	2857.12	2975.34	2975.34	3035.59	3035.59	3096.18	3096.18	3217.09	3217.09	7.18343e-15
	RHC FGD1 $\nu_\mu$ (bkg) CC1 $\pi$	1159.4	1159.4	1156.39	1156.39	1159.01	1159.01	1163.93	1163.93	1179.24	1179.24	-2.5561e-15
	RHC FGD1 $\nu_\mu$ (bkg) CC0th	1066	1066	1070.61	1070.61	1073.13	1073.13	1075.78	1075.78	1081.39	1081.39	-1.9114e-15
	RHC FGD2 $\nu_\mu$ (bkg) CC0 $\pi$	2856.93	2856.93	2957.66	2957.66	3012.4	3012.4	3069.4	3069.4	3188.3	3188.3	1.03014e-14
	RHC FGD2 $\nu_\mu$ (bkg) CC1 $\pi$	930.387	930.387	928.792	928.792	930.635	930.635	934.004	934.004	944.578	944.578	1.95845e-15
	RHC FGD2 $\nu_\mu$ (bkg) CC0th	994.118	994.118	998.171	998.171	1000.39	1000.39	1002.72	1002.72	1007.67	1007.67	-2.73348e-15

Table 8.2: One example of the 712 tables comparing the event rate in each sample at  $-3\sigma$ ,  $-1\sigma$ ,  $1\sigma$  and  $3\sigma$  for the  $M_A^{\text{QE}}$  parameter, as well as the relative difference in the last column at  $-1\sigma$ .

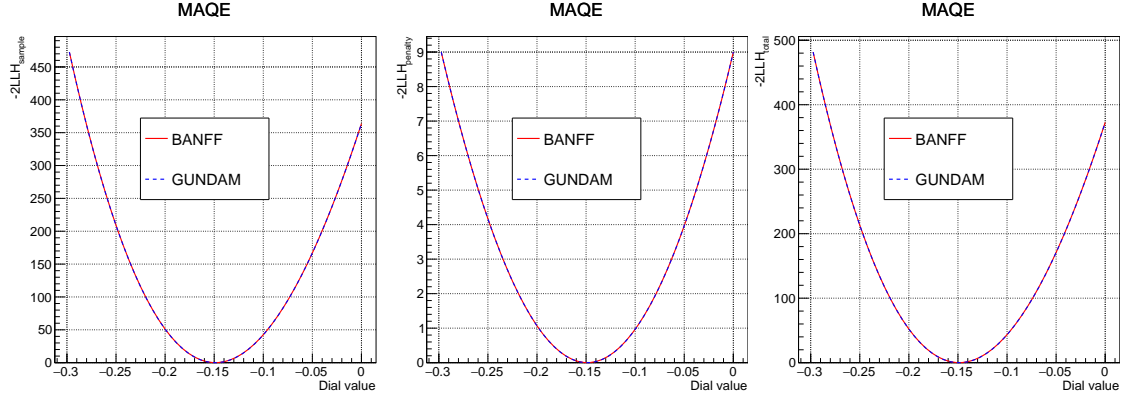


Figure 8.2: One example of the 712 likelihood scan comparisons of the statistical part  $-2\log \mathcal{L}_{\text{stat}}$  (left) and the penalty term  $-2\log \mathcal{L}_{\text{sys}}$  (center) separately, as well as the total likelihood  $-2\log \mathcal{L}_{\text{tot}}$  (right) for the  $M_A^{\text{QE}}$  parameter.

validation is to reproduce the BANFF event rates accurately in order to make sure that the GUNDAM code itself works properly. As shown in the last column of Table 8.2, the agreement is reached at machine-precision level between the two fitter when taking into account these implementation differences.

### 8.2.3 Likelihood scans

Once the prefit and varied event rates are validated, we can compare the response of the likelihood function to the variation of each of the fit parameters, which we call *likelihood scans*. The input configuration file of GUNDAM allow us to specify the type of the likelihood function to be applied. The 2020 oscillation analysis used the Barlow – Beeston likelihood, as discussed in Section 7.4.1 and Equation (7.6), which considers the Poisson distribution of the events corrected to account for the effects of the limited MC statistics.

The first iteration of this validation showed mismatches between the two fitters. It was found to be due to a GUNDAM bug in the implementation of the statistical errors in the MC samples which is used by this likelihood. In fact, the statistical error, while for a data bin is simply  $\sqrt{N}$  where  $N$  is the number of events in the bin, actually corresponds to  $\sqrt{\sum_i w_i^2}$  for a MC bin where the sum is over all the MC events of the bin, each with the corresponding weight  $w_i$ .

Once this was corrected, the comparison of the GUNDAM and BANFF likelihood scans were found to fully agree for all the 712 parameters. This consisted of comparing the statistical (i.e. Barlow – Beeston) part  $-2\log \mathcal{L}_{\text{stat}}$  and the penalty term  $-2\log \mathcal{L}_{\text{sys}}$  separately. The latter allows us to ensure that the prior uncertainties are consistent between the two fitters. Figure 8.2 shows an example of this verification for the  $M_A^{\text{QE}}$  parameter.

### 8.2.4 Fits

#### Asimov fit

The first fit to be performed is the so called *Asimov* fit. Such fits allow us to assess the bias of the fitter around a known set of parameters and evaluate the sensitivity to each fit parameter at the given statistics. In the near-detector fits, this is defined as a fit where the data simply corresponds to the predicted prefit MC spectra.

Since the responses of the likelihood are validated at this stage, this check allows us to identify any issues in the fitting engine. Both fitters use the `Minuit2` package, although with different `ROOT` versions which is not expected to cause important differences. The first attempt showed small discrepancies in the postfit constraints on some parameters, which was then found to be due to the different setting in the `Minuit2` tolerance in the two fitters. Finally, the postfit parameters were found to largely agree between the GUNDAM and BANFF as shown in Figures 8.3 and 8.4 for the flux and the cross-section parameters. The 574 “ObsNorm” parameters related to the uncertainty on the ND280 response (not shown here) are also in agreement.

#### Data fit

Before presenting the data fit results, let us described a problem specific to gradient-descent fitters. For a parameter  $\lambda$  defined on a bounded interval  $[a, b]$ , the gradient-descent fit may drive its value to one of the boundaries  $a$  and  $b$ . In this case, `Minuit2` struggles with the hessian estimation to determine the parameter errors and correlations. This is because `Minuit2` makes a non-linear transformation of its own to internally convert the bounded parameter  $\lambda$  into an unbounded parameter  $\lambda_{\text{int}} \in ]-\infty, +\infty[$ . This transformation writes as [232]:

$$\lambda_{\text{int}} = \arcsin\left(2\frac{\lambda - a}{b - a} - 1\right). \quad (8.1)$$

The `Minuit2`-internal parameter  $\lambda_{\text{int}}$  can now take any value. This non-linear transformation complicates the minimization process, and more importantly introduces numerical precision issues when  $\lambda \rightarrow a$  or  $b$  since it means that  $\partial\lambda/\partial\lambda_{\text{int}} \rightarrow \infty$  according to Equation (8.1). In this case, the minimization can get “stuck” in the boundary because the gradient of the likelihood is almost zero:

$$\frac{\partial(-2\log\mathcal{L})}{\partial\lambda_{\text{int}}} = \frac{\partial(-2\log\mathcal{L})}{\partial\lambda} \times \frac{\partial\lambda}{\partial\lambda_{\text{int}}} \rightarrow 0,$$

and the error estimation yields unphysical values.

To overcome this limitation in our `Minuit2`-based fits, bound parameters are *mirrored* around their boundaries  $a$  and  $b$ . This means that the weight function  $f(\lambda)$  for each event is extended beyond the  $[a, b]$  region by symmetry as shown in Figure 8.5 such that the new weight function

## 8.2 Reproducing the 2020 oscillation analysis

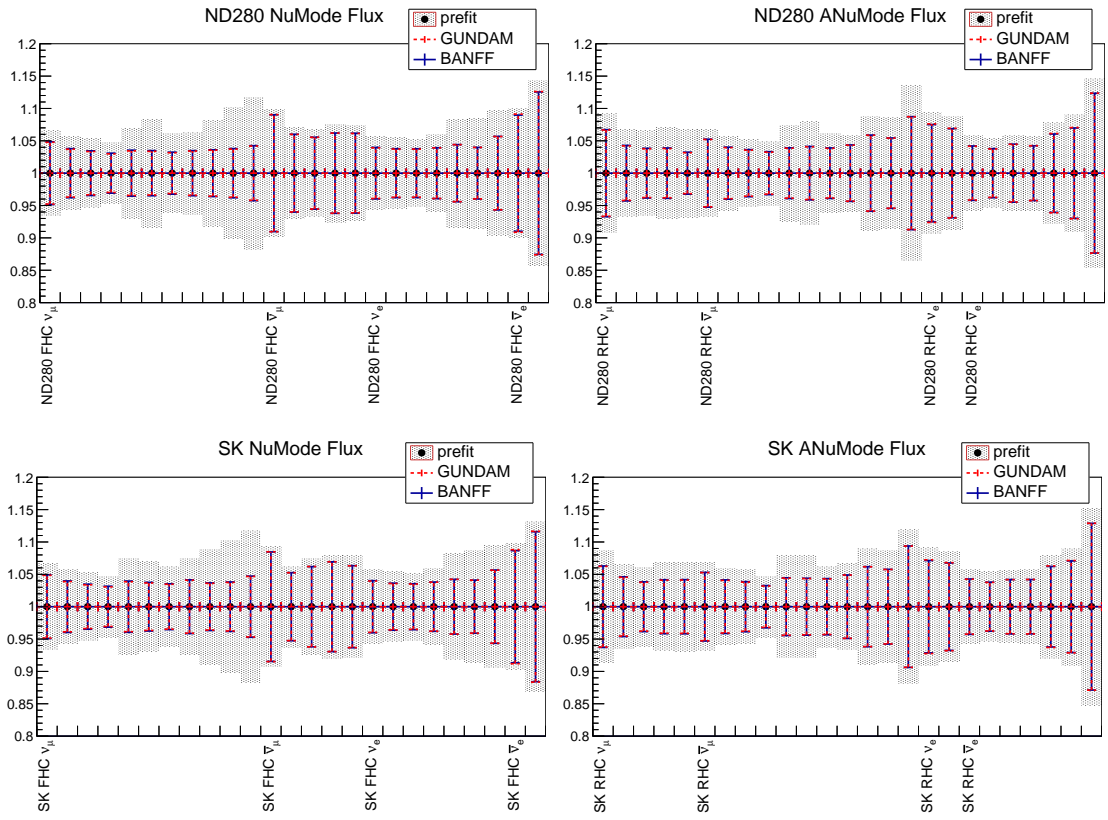


Figure 8.3: Flux parameters compared between BANFF and GUNDAM for the OA2020 Asimov fit.



## Chapter 8. GUNDAM: a new fitting framework

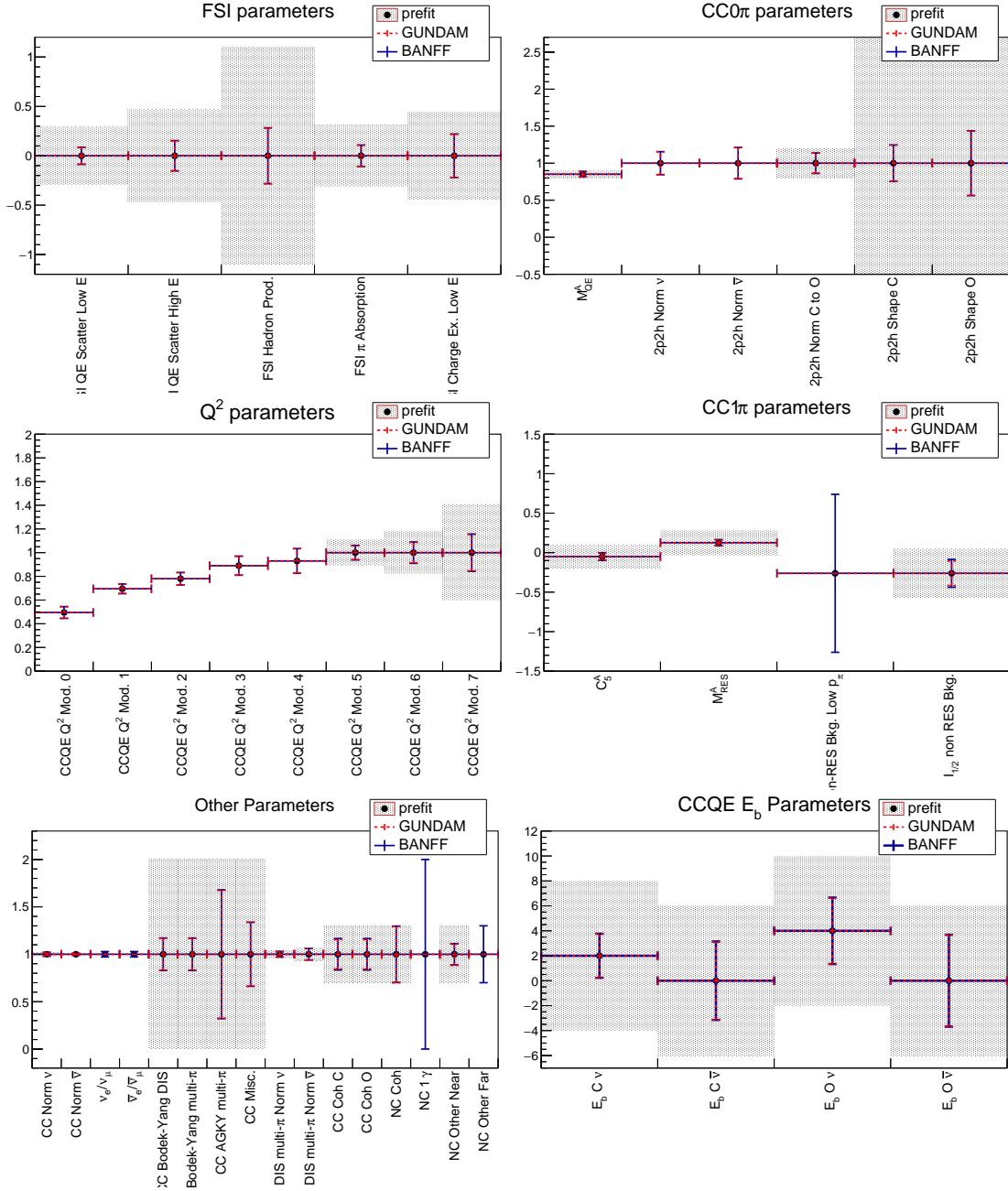


Figure 8.4: Cross-section parameters compared between BANFF and GUNDAM for the OA2020 Asimov fit. Parameters with no GUNDAM postfit errors are fixed in the fits.

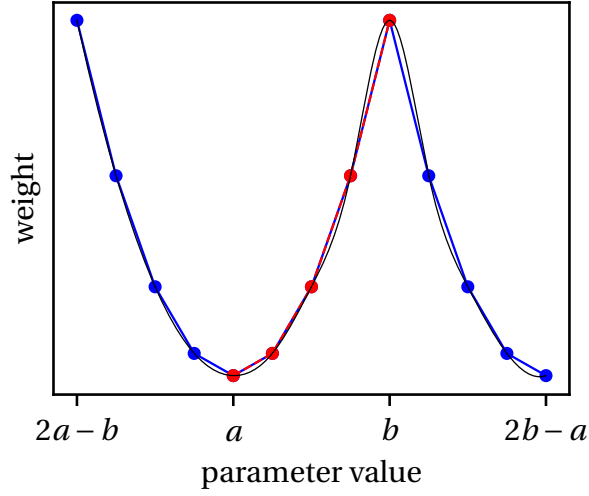


Figure 8.5: Illustration of extending a weight function  $f(\lambda)$  beyond its physical boundaries  $[a, b]$  (red) to  $f_{\text{mirr}}(\lambda)$  defined on a larger interval  $[2a - b, 2b - a]$  by mirroring as shown in Equation (8.2) (blue). The cubic spline interpolation used in the fit is also displayed (black).

$f_{\text{mirr}}(\lambda)$  is defined on the interval  $[a - (b - a), b + (b - a)] = [2a - b, 2b - a]$  by:

$$f_{\text{mirr}}(\lambda) = \begin{cases} f(2a - \lambda), & \text{if } \lambda \in [2a - b, a], \\ f(\lambda), & \text{if } \lambda \in [a, b], \\ f(2b - \lambda), & \text{if } \lambda \in [b, 2b - a]. \end{cases} \quad (8.2)$$

This mirroring ensures that the statistical likelihood response is symmetrical, while the corresponding penalty term (if any) disfavors large deviations of the parameters  $\lambda$  from its prior central value. This technique is only used in Minuit2-based fits, while the MCMC fitter does not require particular treatment of bounded parameters.

Let us now discuss the data fit results of the GUNDAM validation, which is the ultimate test to reproduce the oscillation analysis at the near detector. In fact, it gives the opportunity to test the performances of GUNDAM at a point in the fit parameter space that does not lie at the maximum likelihood as is the case in the Asimov fit. Figures 8.6 and 8.7 show a comparison between the GUNDAM and BANFF postfit values and constraints. Overall, there is an excellent agreement between most of the parameters. The small discrepancy in the constraint on the carbon 2p2h shape parameter, whose physical domain of definition  $[-1, 1]$  (see Section 4.2.3) is extended by mirroring as shown in Equation (8.2) and Figure 8.5, can be attributed to the fact that it converges to the mirroring point at 1. The parameter covariance  $\mathcal{C} = \text{Cov}[\{\lambda_i\}]$  is

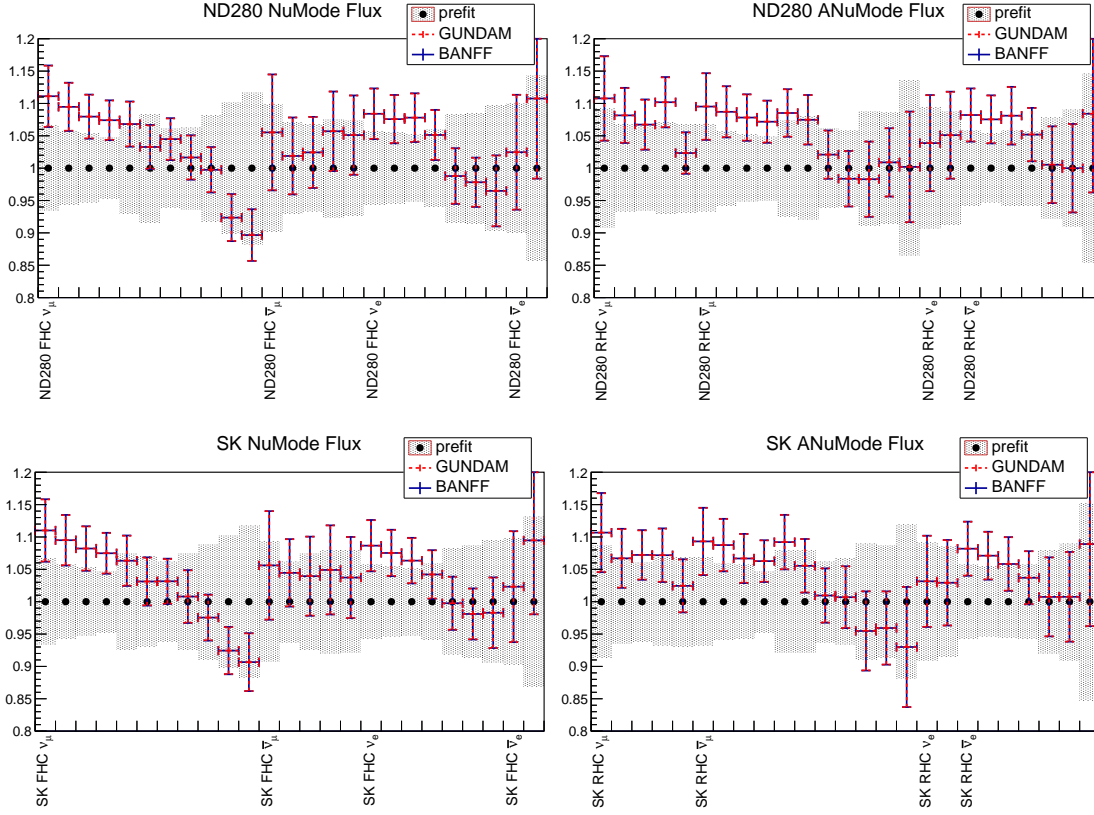


Figure 8.6: Flux parameters compared between BANFF and GUNDAM for the OA2020 data fit.

estimated by  $\mathcal{C} = \mathfrak{H}^{-1}$  where the  $\mathfrak{H}$  is the hessian of the likelihood function:

$$\mathfrak{H}_{i,j} = \frac{\partial^2 (-2 \log \mathcal{L})}{\partial \lambda_i \partial \lambda_j}. \quad (8.3)$$

The first derivative of the spline evaluation around the mirroring point is flat, as can be observed in Figure 8.5 at the point  $b$  for instance, which causes the second derivative to tend towards zero. This makes the covariance estimation, which involves the inversion of the hessian, prone to numerical instabilities. Consequently, some discrepancies can be expected in this case.

### Constraints on the oscillation parameters

In Chapter 7, we discussed how the constraints on the oscillation parameters are obtained using the results of the near-detector fits. P-Theta uses the postfit values and covariance of the parameters relevant to the analysis of Super-Kamiokande data. These include Super-Kamiokande flux uncertainties as well as nucleon-level and oxygen cross-section parameters. To show the readiness of the fitter for the integration in the T2K oscillation-analysis pipeline,

## 8.2 Reproducing the 2020 oscillation analysis

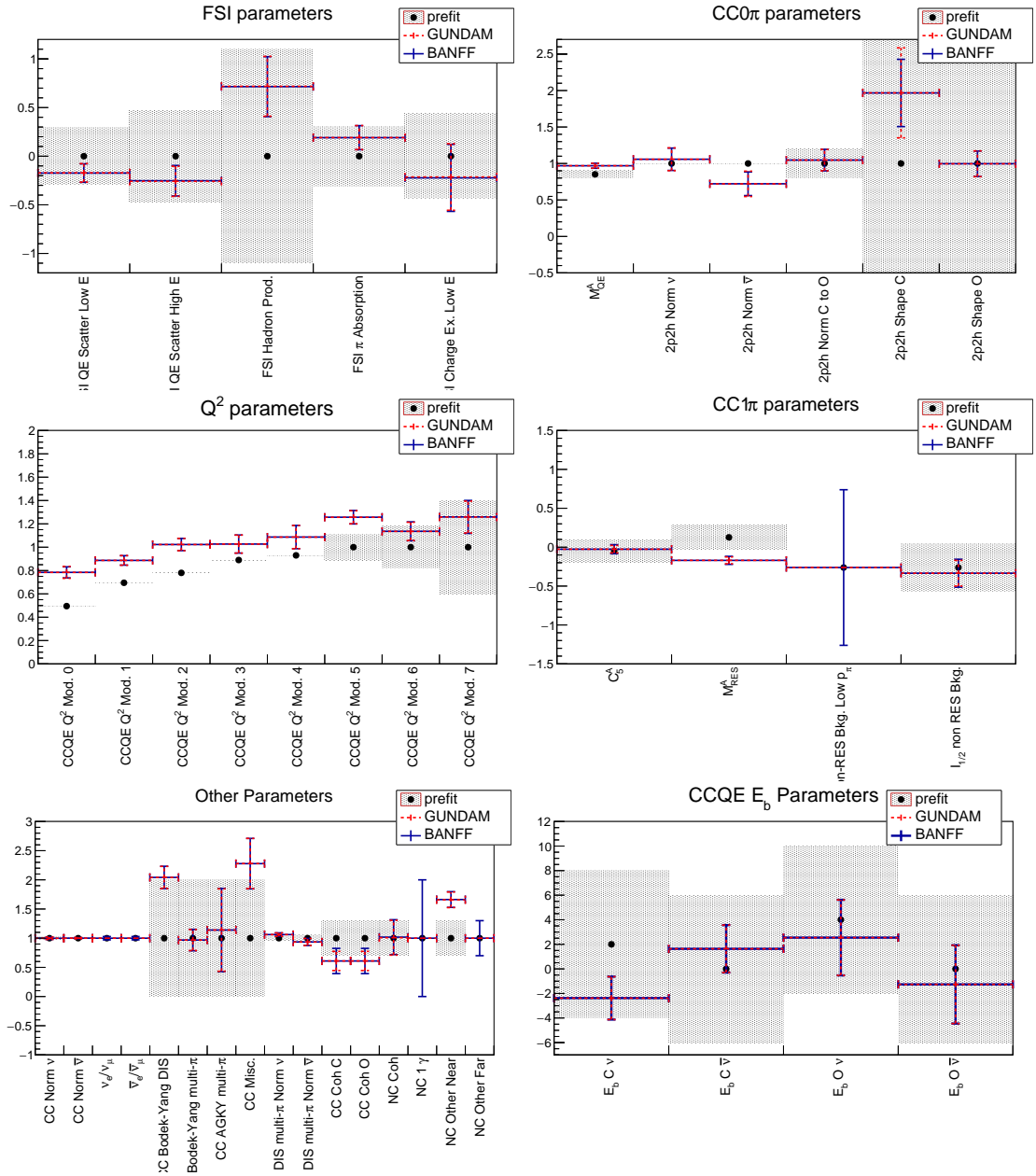


Figure 8.7: Cross-section parameters compared between BANFF and GUNDAM for the OA2020 data fit. Parameters with no GUNDAM postfit errors are fixed in the fits.

Parameters	Set A20
$\Delta m_{21}^2$	$7.53 \times 10^{-5} \text{eV}^2/c^4$
$\Delta m_{32}^2 \text{ (NO)} /  \Delta m_{31}^2  \text{ (IO)}$	$2.509 \times 10^{-3} \text{eV}^2/c^4$
$\sin^2 \theta_{23}$	0.528
$\sin^2 \theta_{12} (\sin^2 2\theta_{12})$	0.307 (0.851)
$\sin^2 \theta_{13} (\sin^2 2\theta_{13})$	0.0218 (0.0853)
$\delta_{\text{CP}}$ [rad]	-1.601
Mass ordering	Normal

Table 8.3: Reference A20 point of the oscillation parameters used in the Asimov fits with P-Theta to compare BANFF and GUNDAM.

we reproduce here the constraints on the oscillation parameters. This also validates the consistency of the covariance matrix produced by GUNDAM with the BANFF one.

This validation is performed with the far-detector Asimov Set A20 point, which is an Asimov fit where the oscillation parameters are set close to the best fit values of the previous analysis as shown in Table 8.3. Figures 8.8 to 8.10 show the constraints on the oscillation parameters with the near-detector constraints from BANFF and GUNDAM. Thanks to the very good agreement obtained in the near-detector data fit in the previous section, the oscillation parameter constraints are found to be almost indistinguishable as expected.

### Fits to alternative neutrino interaction models

Among the crucial robustness tests in the oscillation analysis is the assessment of the ability of the neutrino interaction uncertainty model to cover the effects of models different from the nominal ones in NEUT. This is achieved by creating a set of simulated data that we fit with our nominal model. We then use the output of the near-detector fit to evaluate the impact on the oscillation parameters at Super-Kamiokande with P-Theta as discussed in Section 7.5.3. Consequently, we reproduce this procedure using GUNDAM as the near-detector fitter. The goal of this validation step is not only to show that GUNDAM includes this functionality, but also to further test its performance at another point outside of the maximum likelihood in the fit parameter space.

One of the considered alternative models in the 2020 oscillation analysis is the Martini et al. model for 2p2h interactions. As discussed in Section 3.3, NEUT relies on the Nieves et al. description which predicts a significantly smaller cross-section as shown in Figure 3.11. The simulated data in this case simply consists of the nominal NEUT prediction where the 2p2h events are reweighted according to the ratio of the two models, while the other interaction modes are kept unchanged. Figure 8.11 shows the postfit result for a subset of the cross-section parameters. The fit captures the differences between the two models thanks to the

## 8.2 Reproducing the 2020 oscillation analysis

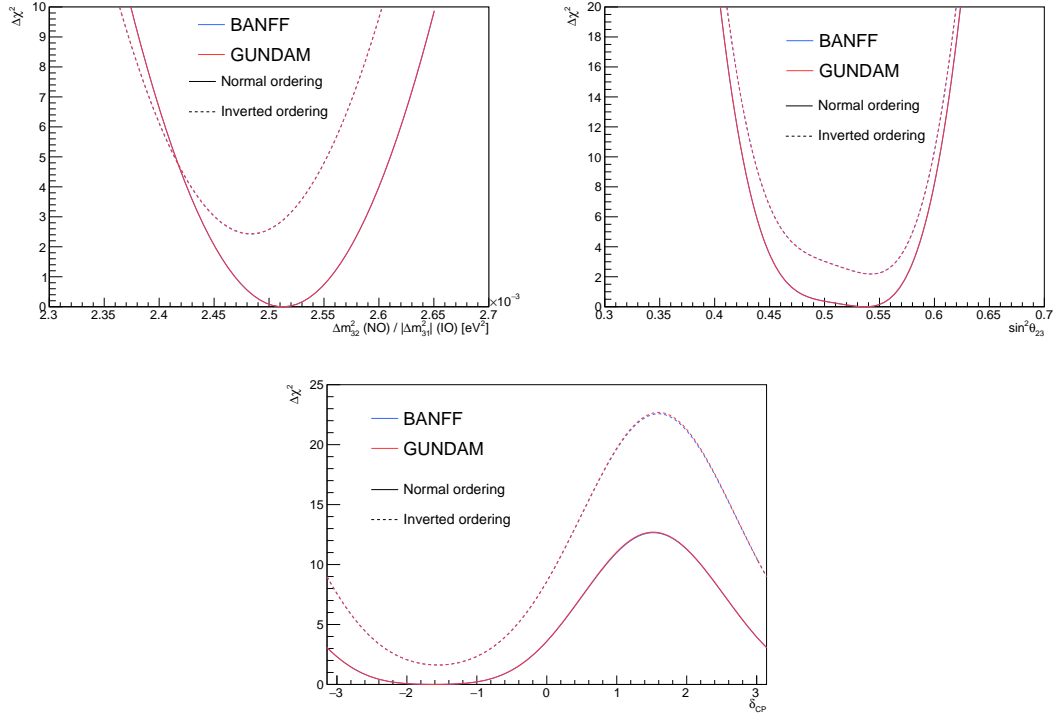


Figure 8.8: One-dimensional sensitivity  $\Delta\chi^2$  in  $\Delta m_{32}^2$  (top left),  $\sin^2 \theta_{23}$  (top right) and  $\delta_{\text{CP}}$  (bottom) for normal (full) and inverted (dashed) ordering at the Asimov Set A20 point compared between BANFF (blue) and GUNDAM (red) using the near-detector data fit constraints of OA2020.

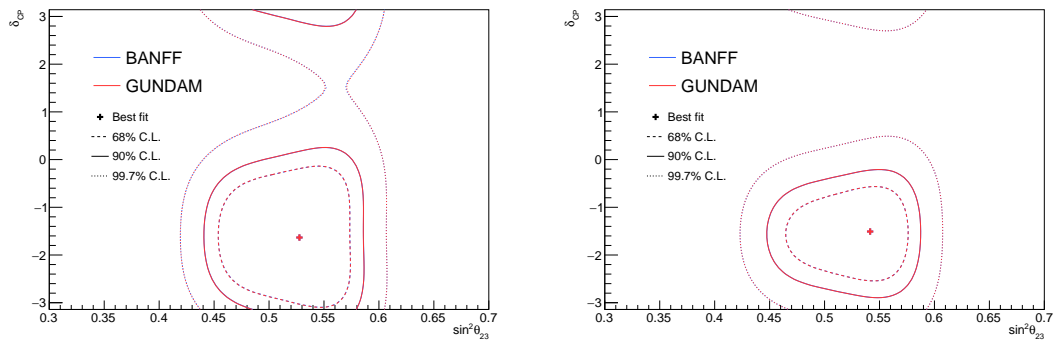


Figure 8.9: Two-dimensional sensitivity  $\Delta\chi^2$  in the disappearance oscillation parameters for normal (left) and inverted (right) ordering at Asimov Set A20 point compared between BANFF (blue) and GUNDAM (red) using the near-detector data fit constraints of OA2020.

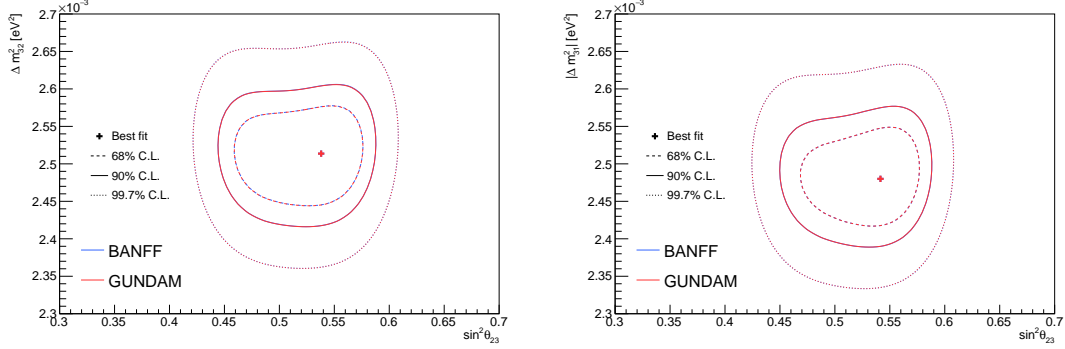


Figure 8.10: Two-dimensional sensitivity  $\Delta\chi^2$  in the appearance oscillation parameters for normal (left) and inverted (right) ordering at the Asimov Set A20 point compared between BANFF (blue) and GUNDAM (red) using the near-detector data fit constraints of OA2020.

2p2h normalization parameters separated for neutrinos and antineutrinos, while the other cross-section parameters of the fit remain at their prefit. It also shows that GUNDAM successfully captures the variations of the alternative model in the same way that BANFF does.

### 8.3 Reproducing the 2022 oscillation analysis

To further test GUNDAM, we attempt to reproduce the latest oscillation analysis (OA2022) presented in Chapter 7. The major changes in this analysis with respect to the 2020 one are the updated neutrino interaction uncertainty model, which now includes the SF model parameters introduced in Chapter 4, and the addition of new near-detector samples that separate the data sets according to whether protons and photons are detected or not, as discussed in Section 7.2.2.

The validations steps are the same as the ones discussed in Section 8.2. Since all of the debugging was already done at the stage of reproducing the 2020 results, the agreement in the prefit and varied event rates, the likelihood scans and the Asimov fit was found to be satisfactory (not shown here). The main discrepancies were observed in the data fits, where BANFF and GUNDAM particularly exhibit differences in the postfit values of the Pauli blocking and optical potential parameters displayed in Figure 8.12.

As suggested in the cross-section fits of Section 4.3, these two parameters are highly anticorrelated, which could explain these discrepancies. In fact, as can be seen in Figure 8.12, BANFF strongly pulls the oxygen Pauli blocking uncertainties while keeping the optical potential parameter of the same target around its prefit value, whereas GUNDAM rather prefers a milder pull of Pauli blocking accompanied with a  $\sim 30\%$  variation in optical potential. The postfit likelihood values are compared between BANFF and GUNDAM in Table 8.4. These values are very close, with the penalty term slightly smaller in the case of GUNDAM as expected from the difference in the preferred values of Pauli blocking and optical potential parameters.

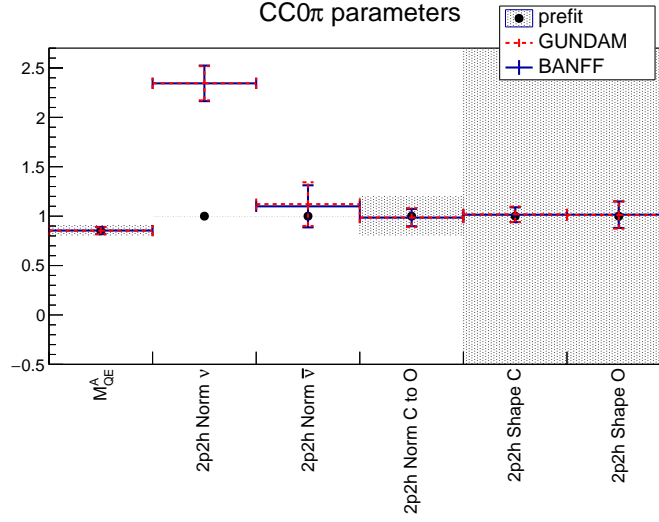


Figure 8.11: Subset of the cross-section parameters compared between BANFF (blue) and GUNDAM (red) for the OA2020 fit to the Martini et al. alternative model.

Fitter	$-2\log\mathcal{L}_{\text{stat}}$	$-2\log\mathcal{L}_{\text{syst}}$	$-2\log\mathcal{L}$
BANFF	5628.82	85.01	5713.83
GUNDAM	5626.93	84.28	5711.21

Table 8.4: Comparison of the postfit statistical, penalty and total likelihood  $-2\log\mathcal{L}$  between BANFF and GUNDAM.

To better visualize the correlations between the oxygen Pauli blocking and optical potential parameters, Figure 8.13 shows the distributions in these parameters of the MCMC steps from the MaCh3 fitter framework compared to the postfit values from BANFF and GUNDAM. These distributions do not include the first  $\sim 10\%$  steps that correspond to the “exploratory phase” of the MCMC draws (i.e. burn-in), and give the shape of the likelihood as estimated by MaCh3. First of all, since an 80% prefit correlation is imposed between the  $\nu$  and  $\bar{\nu}$  Pauli blocking uncertainties, Figure 8.13a shows that these two parameters are indeed positively correlated. Furthermore, the oxygen Pauli blocking  $\nu$  likelihood displays a double-peak structure: a prominent peak at  $0.2\sigma$  and another peak at  $1\sigma$ . When looking at the distribution of the Pauli blocking parameters vs. optical potential, Figures 8.13b and 8.13c both show a clear anticorrelation between them. The best fit points from GUNDAM and BANFF lay along these (anti)correlation lines, while it appears that their preferred values of Pauli blocking O  $\nu$  sit around the less prominent peak of the likelihood (although GUNDAM’s estimation is closer to the maximal likelihood of MaCh3). It is important to note that the gradient-descent algorithms are not expected to accurately find the behave well when the likelihood displays local optima (as is the case along the Pauli blocking O  $\nu$  parameter) in the same way that the MCMC-based MaCh3 fitter would, which could explain these differences.

To investigate the impact of these discrepancies, the results of this fit are propagated to the



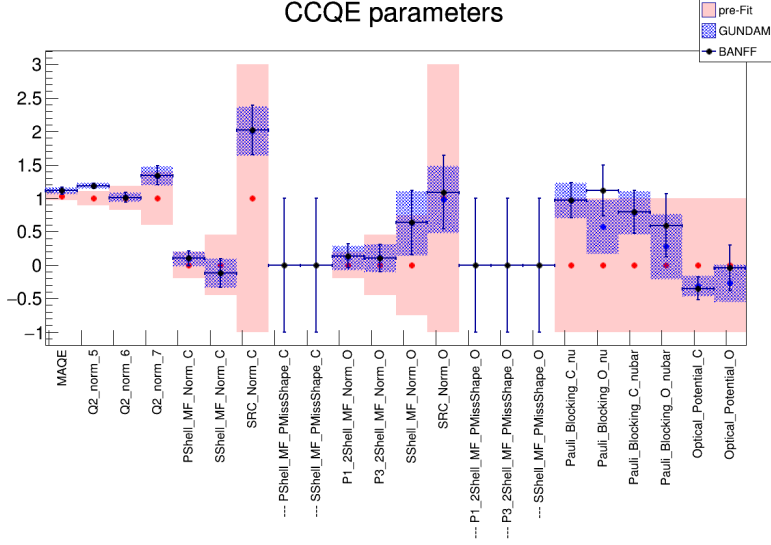


Figure 8.12: Cross-section parameters compared between BANFF and GUNDAM for the OA2020 data fit. Parameters with no GUNDAM postfit errors are fixed in the fits.

far detector using P-Theta at the Asimov Set A22 (see Table 9.5) point of the oscillation parameters. The obtained sensitivities are reported in Figure 8.14. While  $\delta_{\text{CP}}$  and  $\sin^2 \theta_{23}$  sensitivity contours are almost indistinguishable, the  $\Delta m_{32}^2$  one exhibits a shift of  $\sim 0.005 \times 10^{-3} \text{ eV}^2/c^4$ . Although this shift is significantly smaller than the smearing obtained in the bias studies of Section 7.5.3 of  $\sim 0.028 \times 10^{-3} \text{ eV}^2/c^4$ , it is still important to understand its origins.

First of all, a bug was identified in the BANFF covariance matrix related to the mirrored parameters. As previously discussed, Minuit2-based fits struggle with the boundaries of the fit parameters which is mitigated with a special treatment using the mirroring technique. P-Theta on the other hand rather relies on a grid search (see in Section 7.4.2), and thus does not employ this method. Therefore, when passing the BANFF or GUNDAM postfit parameters and their covariance to P-Theta, the mirrored parameters need to be “unmirrored”, i.e. converted back to their physical interval of definition. Using the notations of Equation (8.2), this means that if the fit parameter converges to a value  $\lambda_{\text{mirr}}$  outside of the physical region  $[a, b]$ , say in the interval  $[2a - b, a]$ , then the corresponding value  $\lambda$  in the physical region is simply given by  $\lambda_{\text{mirr}} = 2a - \lambda$ . Furthermore, the parameter-to-parameter correlations are related to the hessian of likelihood around the postfit point as given by Equation (8.3). Consequently, the correlation between two different parameters is given by the first (partial) derivative in each parameter. This implies that, for a mirrored parameter, in addition to converting it back to the physical region, the signs of its correlation with all of the non-mirrored parameters need to be flipped since:

$$\frac{\partial^2 (-2 \log \mathcal{L})}{\partial \lambda \partial \lambda'} = \frac{\partial^2 (-2 \log \mathcal{L})}{\partial \lambda_{\text{mirr}} \partial \lambda'} \times \frac{\partial \lambda_{\text{mirr}}}{\partial \lambda} = \frac{\partial^2 (-2 \log \mathcal{L})}{\partial \lambda_{\text{mirr}} \partial \lambda'} \times \frac{\partial (2a - \lambda)}{\partial \lambda} = - \frac{\partial^2 (-2 \log \mathcal{L})}{\partial \lambda_{\text{mirr}} \partial \lambda'},$$

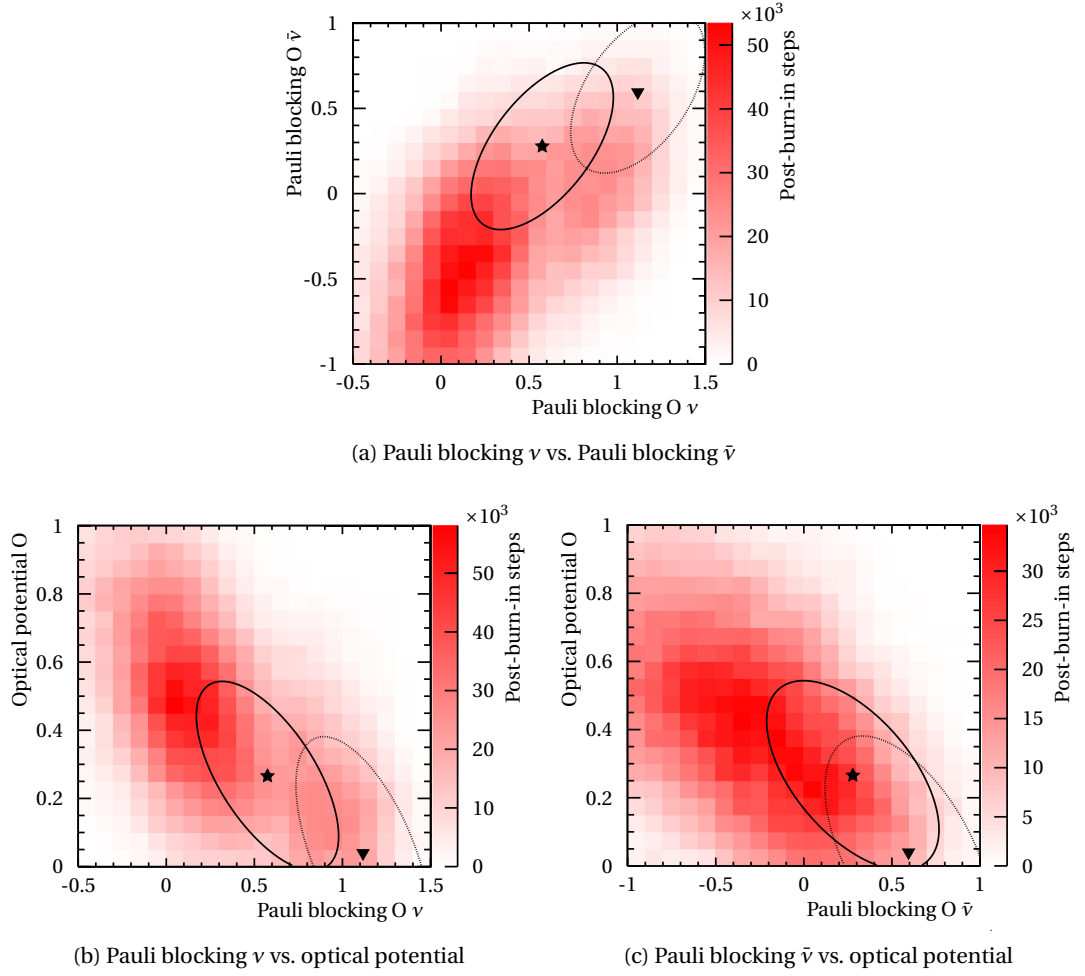


Figure 8.13: Two-dimensional distribution of the MCMC steps after burn-in in MaCh3 for the oxygen Pauli blocking  $\bar{\nu}$  (in  $1\sigma$  units) and optical potential, compared to the best fit points and the elliptical representation of the covariance found by BANFF (▼, dotted) and GUNDAM (★, full).

where  $\lambda'$  is a non-mirrored parameter different from  $\lambda$ . This can also be understood graphically from Figure 8.5: the sign of the gradient between a point in the physical region  $[a, b]$  and its mirrored counterpart is always inverted. The BANFF conversion only converted the value of the mirrored parameter and did not implement this sign flip for its correlations with the other parameters. This bug only concerns the oxygen optical potential parameter which is nominally defined in  $[0, 1]$  but it is mirrored beyond this interval, and the BANFF fit converges to  $\sim -0.3$  (see Figure 8.14). When correcting this bug in the BANFF matrix, a noticeable improvement in the agreement between the two fitters can be seen in Figure 8.15.

Finally, it is natural to think that the remaining disagreement is due to the different postfit values in the Pauli blocking and optical potential parameters. To test this intuition, we can replace the GUNDAM postfit values of these parameters with the BANFF ones, while keeping the

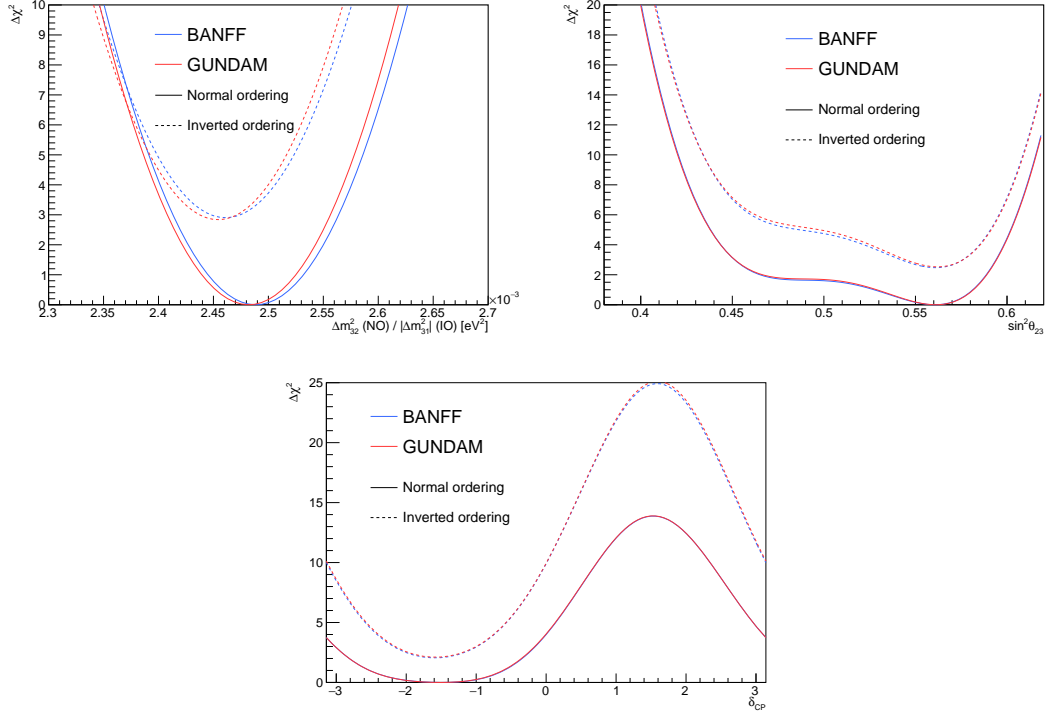


Figure 8.14: One-dimensional sensitivity  $\Delta\chi^2$  in  $\Delta m_{32}^2$  (top left),  $\sin^2 \theta_{23}$  (top right) and  $\delta_{\text{CP}}$  (bottom) for normal (full) and inverted (dashed) ordering at the Asimov Set A22 point compared between BANFF and GUNDAM using the near-detector data fit constraints of OA2022.

rest (i.e. the other parameters and the covariance) unchanged. Sure enough, Figure 8.16 shows that this results in a relatively improved agreement between the two fitters. This means that this difference is mostly due to the postfit values of these two parameters, and not necessarily because of differences in the covariance matrix.

It is important to note that this difference that we find in the postfit parameters does not mean that one fitter or the other is wrong. In fact, due to the strong anticorrelations between Pauli blocking and optical potential uncertainties, which was first highlighted in the cross-section fits of Section 4.3, the shape of the likelihood in this region is complex and a gradient-descent fitter may not be able to give the most stable results. Nevertheless, the postfit likelihood values shown in Table 8.4 suggest that the two results are quite consistent.

## 8.4 Ongoing developments and prospects

The remaining item for the GUNDAM validation is the ability to estimate the  $p$ -value of the result as discussed in Section 7.5.1. This consists of fitting a large number of model variations thrown from the prior knowledge of the near-detector systematic uncertainties, and the  $p$ -value is given as the fraction of the throws for which the postfit  $-2\log \mathcal{L}$  is larger than the data

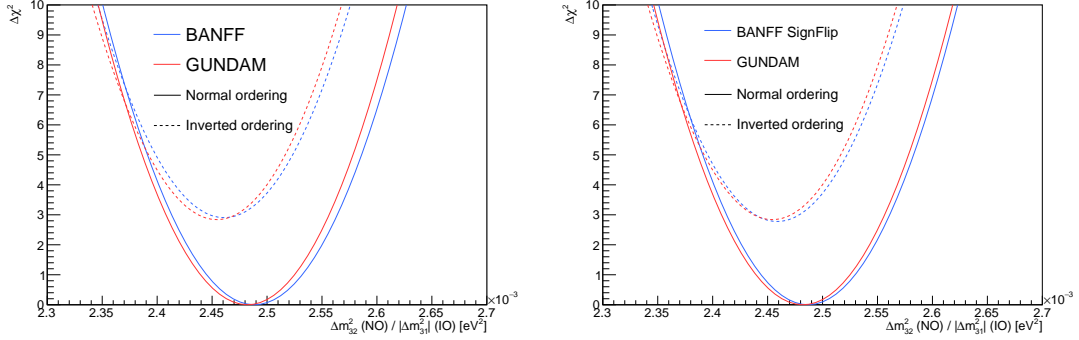


Figure 8.15: Left:  $\Delta m_{32}^2$  contour as shown in Figure 8.14, with the covariance matrix bug in BANFF. Right:  $\Delta m_{32}^2$  contours when the BANFF covariance matrix is corrected by flipping the sign of the correlations with the mirrored parameters.

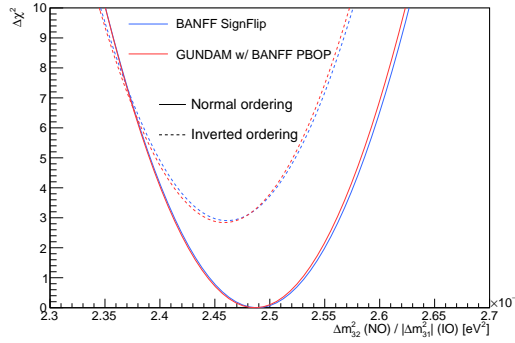


Figure 8.16: One-dimensional  $\Delta m_{32}^2$  contour with the covariance matrix bug fix for BANFF and where GUNDAM postfit values of oxygen Pauli blocking and optical potential parameters are replaced by the BANFF ones.

$-2 \log \mathcal{L}_{\text{data}}$ . The framework is already functional for these studies, and the final steps of the validation are ongoing.

The modularity of GUNDAM makes it suitable to perform a wide range of analyses, from near-detector fits as shown in this chapter, to cross-section extractions. This means that more people from different groups will be using it in the future, which provides more personpower for its development and maintenance. The validation of the cross-section fitting part is currently ongoing, and more functionalities are under developments. These include for instance the ability to run using GPUs which is estimated to increase up to 10 times the speed of the fit, and a MCMC minimization algorithm implement in the Fitter engine of GUNDAM. Alternative minimization programs, which could be more stable for complex likelihoods can also be considered. Other more technical developments are also of great interest, such as the optimization of the memory usage, which might become critical for near-future oscillation analyses.



## 9 T2K future sensitivity

Throughout the previous chapters of this thesis, we presented how the T2K experiment extracts the measurement of the oscillation parameters from its data. We particularly saw the importance of modeling neutrino-nucleus interactions to avoid biased oscillation measurements, and the various techniques to address the uncertainties related to them from the development of a parametrized uncertainty model in e.g. Sections 4.2 and 7.3.3 to the assessment of its robustness in Section 7.5.3. To further gauge the importance of the systematic uncertainties for future analyses, we dedicate this chapter to studying how the upcoming phase of data taking may improve the constraints on these uncertainties, especially with the upgraded near detector.

In Section 9.1, we introduce in the oscillation analysis presented in Chapter 7 new near-detector samples from the near-detector upgrade, whereas Section 9.2 studies their potential impact on constraining the systematic uncertainties in the near-detector fit with GUNDAM. Section 9.3 is split into two parts, the first part shows the expected sensitivity to constrain the oscillation parameters in the upcoming phase of data taking until 2027 without the upgraded near detector, while the second part discusses how to make most of the upgrade data to further constrain the systematic uncertainties relevant for the far-detector fit.

### 9.1 New samples with the upgraded near detector

#### 9.1.1 Simulating the upgrade

The full simulation of the upgraded near detector is currently under development within the collaboration, but preliminary estimations of the expected performances shown in Reference [240] were performed after the extensive studies of the Super-FGD and the HA-TPCs technologies with various prototypes and multiple beam tests as discussed in Section 5.3. Similarly to the oscillation analysis (see Section 7.2.1), we use NEUT as the base interaction model to simulate the scattering of neutrinos on the hydrocarbon of the Super-FGD, with the same models described in Section 3.3. Parametrized resolutions and efficiencies are applied

on the NEUT samples using a Gaussian smearing on the true momentum and angle of each outgoing particle from the neutrino interaction with a probability not to reconstruct it. The results of this simulation are displayed in Figures 5.21 and 5.22, and its details are described below.

The neutron resolutions and efficiencies are estimated using the method of Reference [255] as described in Section 5.4.3. The detector effects on the charged particles on the other hand are simulated within a preliminary reconstruction framework, where the energy depositions in the Super-FGD cubes are processed in form of tracks. The energy loss along each track, omitting a small region around the interaction vertex to avoid the impact of charge deposits from other short-range tracks, is used to identify the particle and estimate its momentum. Any tracks with ambiguous particle identification or undergoing important secondary interactions are discarded from this analysis. This particularly explains the important drop in the proton detection efficiency in the top right panel of Figure 5.21 for high momenta, as these are more likely to be deflected due to secondary interactions during their propagation in the Super-FGD. Recovering these tracks to increase the efficiency in this region is one of the ongoing efforts for the final reconstruction software. If a track is not fully contained in the Super-FGD and has a segment that enters a TPC (either a vertical TPC or a HA-TPC), this segment is reconstructed based on the well-known performances of the current TPCs of ND280. The performances of the HA-TPCs are considered to be the same as the vertical TPCs, and consequently their improved reconstruction are not accounted in this study.

It is important to note that this preliminary simulation does not consider many of the effects that a full reconstruction and event selection would. In particular, the possibility of misidentifying a particle is included. This limitation is only critical when looking at the reconstructed pions, which is the reason why we limit this study to the  $CC0\pi$  samples.

### 9.1.2 Observables

As discussed in Section 5.4, one of the main assets of the near-detector upgrade is its ability to reconstruct with unprecedented precision the hadronic products of neutrino interactions. In the following, we limit the study to  $CC0\pi$  events which we split into samples with and without a reconstructed nucleon. When a nucleon is reconstructed, the transverse momentum imbalance  $\delta p_T$  of Equation (4.2) and the visible energy  $E_{\text{vis}}$  of Equation (5.1) can be computed from the kinematics of the outgoing muon and nucleon. When no nucleon is reconstructed, the kinematics of the muons are the employed observables.

Figure 9.1 shows the two-dimensional  $(\delta p_T, E_{\text{vis}})$  distributions for  $CC0\pi$  events with a reconstructed proton in the FHC mode (left) or a reconstructed neutron in the RHC mode (right) within the Super-FGD, each assuming  $1.13 \times 10^{21}$  POT which roughly corresponds to one year of data taking in the beginning of the second phase of T2K as we will see in Table 9.1. The first, and most obvious, difference between the two distributions is how the RHC distribution is smeared in comparison with the FHC one. This is largely due to the lower resolution

## 9.1 New samples with the upgraded near detector

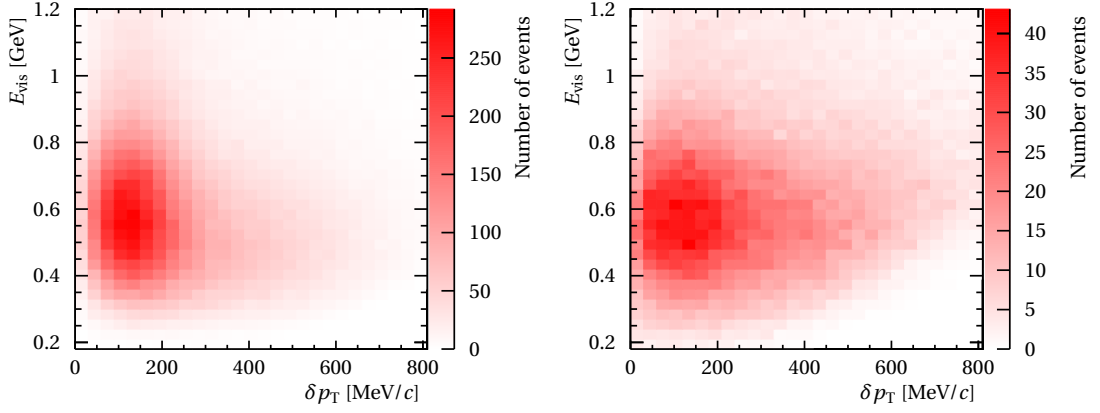


Figure 9.1: Two-dimensional distributions of the reconstructed  $(\delta p_T, E_{\text{vis}})$  in the  $\text{CC}0\pi$  samples with a reconstructed nucleon within the Super-FGD in the FHC (left) and RHC (right) beam mode, each with  $1.13 \times 10^{21}$  POT.

( $\sim 15 - 30\%$ ) in the reconstruction of the outgoing neutrons produced from antineutrino CCQE interactions as opposed to the protons ( $\leq 5\%$ ) as previously shown in Figure 5.22. Another discrepancy can be expected in the total event rates between the beam modes, which is mostly due to the differences between the  $\nu$  and the  $\bar{\nu}$  cross sections. Finally, as also shown in Figure 5.24, the lowest  $\delta p_T$  bins in the RHC mode contains more events compared to the FHC mode as they correspond to a region enriched with antineutrino interactions on hydrogen protons present in the plastic scintillator.

In total, four  $\text{CC}0\pi$  samples binned in two dimensions are considered depending on whether a proton (neutron) is reconstructed in the final state in the FHC (RHC) mode in addition to the muon:

- FHC SFGD  $\text{CC}0\pi 0p$ : no proton is reconstructed in the Super-FGD in the FHC mode,
- FHC SFGD  $\text{CC}0\pi Np$ : at least a proton is reconstructed in the Super-FGD in the FHC mode,
- RHC SFGD  $\text{CC}0\pi 0n$ : no neutron is reconstructed in the Super-FGD in the RHC mode,
- RHC SFGD  $\text{CC}0\pi Nn$ : at least a neutron is reconstructed in the Super-FGD in the RHC mode.

The samples with no reconstructed nucleon are always binned in the muon kinematics similarly to the existing ND280 samples, i.e. in  $(p_\mu, \cos\theta_\mu)$ . On the other hand, to demonstrate the impact of the additional hadronic information from the upgrade, we will compare the results of the analysis between binning the FHC SFGD  $\text{CC}0\pi Np$  and the RHC SFGD  $\text{CC}0\pi Nn$  samples in  $(p_\mu, \cos\theta_\mu)$  and in  $(\delta p_T, E_{\text{vis}})$ . These four samples are added to the existing 22 samples



currently used in the near-detector fit summarized in Table 7.2, yielding a total of 26 samples in an upgrade-era-like oscillation analysis.

Similarly to the analysis shown in Section 7.2.2, these new samples are binned in two dimensions. Ideally, to fully exploit the potential of the upgrade, the near-detector analysis would consist of a multidimensional fit in the kinematics of the muons, the hadrons, and their correlations. Such analysis is computationally expensive<sup>1</sup>, which is the reason why this study is limited to two-dimensional fits. The prospects of adding extra dimensions in this fit will be discussed in Section 9.4.

The choice of the observables  $(\delta p_T, E_{\text{vis}})$  is motivated by their sensitivity to the nuclear effects that impact the measurements of neutrino oscillations. As discussed in Section 5.4 and in Reference [240], other variables can also be considered. For instance, the transverse boosting angle  $\delta\alpha_T$  can allow to disentangle the multinucleon effects from FSI processes which are degenerate when using  $\delta p_T$  only. However,  $\delta\alpha_T$  by itself is not as sensitive to the other details of the nuclear ground state as  $\delta p_T$ . It could nevertheless serve as an interesting additional dimension by fitting in the  $(\delta p_T, \delta\alpha_T, E_{\text{vis}})$  space as we will highlight Section 9.4. An alternative observable that is more sensitive to nuclear effects in comparison to  $\delta p_T$  is the so-called *reconstructed initial-nucleon momentum*  $p_N$ , which includes the longitudinal component of the initial-state nucleon Fermi motion in contrast with the transverse momentum  $\delta p_T$  [286]. Employing this observable could yield improved sensitivities to the nuclear effects, but it should likely be accompanied by additional systematic uncertainties in the model. In fact, if the shape of  $\delta p_T$  is quite independent of the neutrino energy and nucleon-level physics [224], this is not necessarily the case for the variable  $p_N$ , which is the reason why we choose to employ the variable  $\delta p_T$  as a slightly more conservative approach.

### 9.1.3 Event rates

The upgrade of the near detector is accompanied with improvements to the beam power of the J-PARC accelerator. The maximum power that was reached in previous T2K runs is  $\sim 500$  kW, and it is expected to steadily increase over the upcoming years to reach the goal of 1.3 MW in 2027 before the start of the Hyper-Kamiokande era. This will result in an increased delivered POT for T2K as shown in Table 9.1 and Figure 9.2. In particular, within three years<sup>2</sup> of data taking, T2K will reach over the double of the POT collected so far since its start.

Along with this increase in the beam power, the near-detector upgrade will double the target mass for neutrino interactions at ND280 and reconstruct particles over a larger phase space. A significant increase in the event rates at the near detector is consequently expected. To illustrate this, we report in Table 9.2 (Table 9.3) the expected  $\text{CC}0\pi$  event rates in the current FGDs in comparison with the Super-FGD for  $1.13 \times 10^{21}$  POT (i.e.  $\sim 1$  year of data taking) in the FHC (RHC) beam mode.

---

<sup>1</sup>Although the improved performances of GUNDAM would make it more feasible.

<sup>2</sup>Each year consists of around four months of continuous data taking.

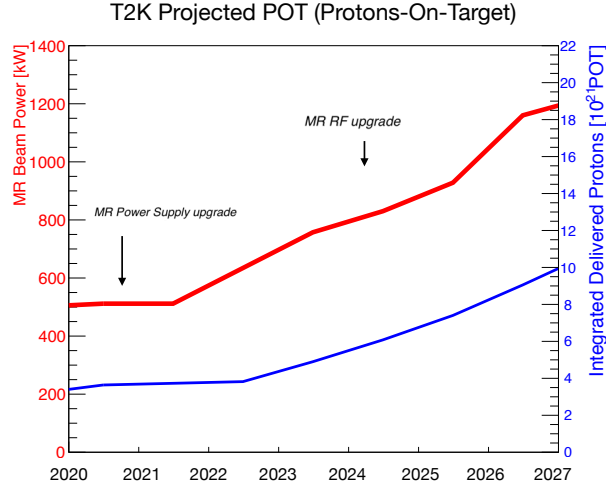


Figure 9.2: Projected beam power and delivered POT in the upcoming phase of T2K data taking.

In the FHC mode, a larger event rate is seen in the  $CC0\pi0p$  in the Super-FGD sample due to the improved and isotropic muon detection efficiency. A significantly increased rate can also be observed for the  $CC0\pi Np$  as well thanks to the lower tracking threshold and better detection efficiency of protons. In the RHC mode, a larger rate is obtained in the Super-FGD too. It is worth noting that the current FGDs do not have the ability to tag neutrons, and that the purity of the corresponding samples is  $\sim 60\%$ , while the expected purity in the Super-FGD samples is expected to be around  $\sim 85 - 90\%$ .

## 9.2 Impact on the near-detector fit

### 9.2.1 Assumptions

#### Running mode

The goal of this study is to evaluate the impact of adding the Super-FGD samples described in Section 9.1 to the near-detector fit. To do so, we use the projections shown in Table 9.1 and Figure 9.2 assuming a one-to-one ratio between the FHC and RHC beam modes. In other terms, 50% of the delivered POT is considered in the neutrino mode and 50% in the antineutrino mode.

#### Samples and observables

The starting point of this study is the 2022 oscillation analysis detailed in Chapter 7. Consequently, we consider the 22 samples summarized in Table 7.2 and compare three configurations using the additional Super-FGD samples:

Year	Power [kW]	POT/year	Accumulated POT
2022	–	0	$3.82 \times 10^{21}$
2023	757	$1.08 \times 10^{21}$	$4.90 \times 10^{21}$
2024	830	$1.18 \times 10^{21}$	$6.08 \times 10^{21}$
2025	928	$1.32 \times 10^{21}$	$7.40 \times 10^{21}$
2026	1160	$1.65 \times 10^{21}$	$9.06 \times 10^{21}$
2027	1226	$1.75 \times 10^{21}$	$1.08 \times 10^{22}$

Table 9.1: Summary of the projected POT delivered in the second phase of T2K data taking until 2027.

Sample	FGD1+2	Super-FGD
FHC CC0 $\pi$ 0 $p$	37111	52094
FHC CC0 $\pi$ $Np$	16193	48989

Table 9.2: Comparison between the expected event rates in the current FGDs and the Super-FGD for  $1.13 \times 10^{21}$  POT in the FHC mode.

Sample	FGD1+2	Super-FGD
RHC CC0 $\pi$ 0 $n$	20950	13401
RHC CC0 $\pi$ $Nn$		11483

Table 9.3: Comparison between the expected event rates in the current FGDs and the Super-FGD for  $1.13 \times 10^{21}$  POT in the RHC mode. Note that the FGDs do not have the ability to tag neutrons.

## 9.2 Impact on the near-detector fit

Sample	Super-FGD response uncertainty
FHC SFGD CC0 $\pi$ 0 $p$	2%
FHC SFGD CC0 $\pi$ $Np$	4%
RHC SFGD CC0 $\pi$ 0 $n$	2.5%
RHC SFGD CC0 $\pi$ $Nn$	5%

Table 9.4: Estimated uncertainty on the Super-FGD samples related to the detector response.

- FGD1+2 only: this corresponds to the 22 samples of Table 7.2 used in the current near-detector fit, binned in  $(p_\mu, \cos\theta_\mu)$ , without any additional samples.
- SFGD+FGD1+2  $\mu$  only: we add to these 22 samples the four Super-FGD CC0 $\pi$  samples shown in Section 9.1.2, all of them binned in  $(p_\mu, \cos\theta_\mu)$ .
- SFGD+FGD1+2  $\mu + N$ : the four additional Super-FGD samples are binned in  $(\delta p_T, E_{\text{vis}})$  when a nucleon is reconstructed, and  $(p_\mu, \cos\theta_\mu)$  when no nucleon is detected.

We perform Asimov near-detector fits at the expected POT for each year of data as shown in Table 9.1. This allows to quantitatively estimate the sensitivity to constrain the systematic uncertainties with the near-detector analysis in each of the three configurations.

### Uncertainty model

We use the full uncertainty model of the oscillation analysis as described in Section 7.3, including the neutrino cross section, the flux and the current ND280 response uncertainties. The only difference in the neutrino-interaction model is that the missing-momentum shape uncertainty is varied in this analysis (unlike the 2022 near-detector fit). Since the upgraded near detector is yet to be implemented in the ND280 reconstruction software, we do not use the same approach for the uncertainty on the Super-FGD response as the one described in Section 7.3.2. Instead, we use an uncorrelated and fixed uncertainty applied on each bin of the Super-FGD samples implemented within the Barlow – Beeston likelihood of Equation (7.6), where the Gaussian error due to the MC statistics  $\sigma_{\beta_i}$  is modified to account for the additional smearing due to the Super-FGD response in each of its four samples as given by Table 9.4. The detector uncertainties in the FHC SFGD CC0 $\pi$ 0 $p$ , FHC SFGD CC0 $\pi$  $Np$  and RHC SFGD CC0 $\pi$ 0 $n$  samples are estimated from the total uncertainties in the current FGDs (see e.g. Table 7.4) whose performances should be comparable to the Super-FGD, whereas the RHC SFGD CC0 $\pi$  $Nn$  uncertainty is broadly determined from the uncertainty on the neutron secondary interaction cross section with the measurements of Reference [287] on various targets.

The impact of including the detector smearing directly in the Barlow – Beeston likelihood for the Super-FGD samples is displayed in Figure 9.3 on a typical negative log-likelihood scan

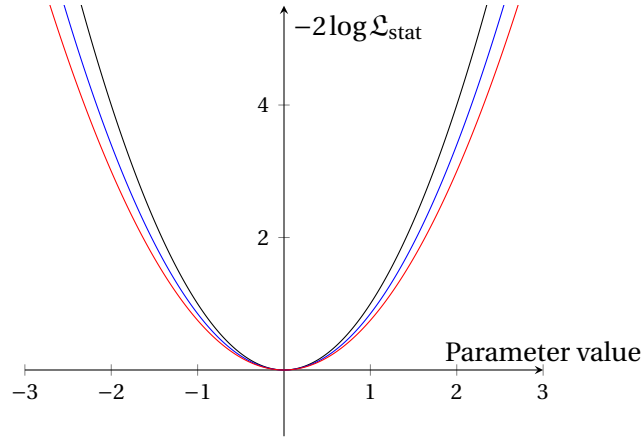


Figure 9.3: Statistical negative log-likelihood scan typically obtained for a parameter in an Asimov fit when using the Poisson likelihood (black) of Equation (7.5), the Barlow – Beeston likelihood (blue) of Equation (7.6), and the modified Barlow – Beeston likelihood to account for the detector smearing (red) used in this sensitivity study for the Super-FGD samples.

along a fit parameter around the best-fit point<sup>3</sup>. This simplified treatment of the uncertainty on the Super-FGD response is relatively conservative as it corresponds to an uncorrelated bin-by-bin smearing that is fixed in the fits. The actual detector uncertainties, as for the ones used for the current FGDs, have in general a strongly correlated effect on the bin content as shown in Figure 7.6 for the “ObsNorm” parameters applied to the ND280 samples.

### 9.2.2 Results

Figures 9.4 to 9.6 show the results of the postfit constraints  $\sigma_{\text{postfit}}$  relative to the prefit uncertainty  $\sigma_{\text{prefit}}$  as a function of the collected data in POT units for the main neutrino interaction and flux uncertainties, while the rest of the parameters are displayed in Appendix A. The first point in each panel (lowest POT) corresponds to the statistics used in the 2022 oscillation analysis, and the subsequent points are obtained with using the projected additional POT for each year as given by Table 9.1 in the three different configurations described in Section 9.2.1. This is obtained using Asimov fits, where the fitted data corresponds to the model prediction. An Asimov fit is one of the essential steps in validating the fitting framework as discussed in Chapter 8, but it also allows to estimate the sensitivity to constrain the systematic uncertainties at given statistics. In particular, the relative uncertainty at the 2022 statistics of Figures 9.4 to 9.6 for each parameter is actually quite similar to the constraints obtained from the real-data fit presented in Section 7.5.1 and shown in Figure 7.9.

## 9.2 Impact on the near-detector fit

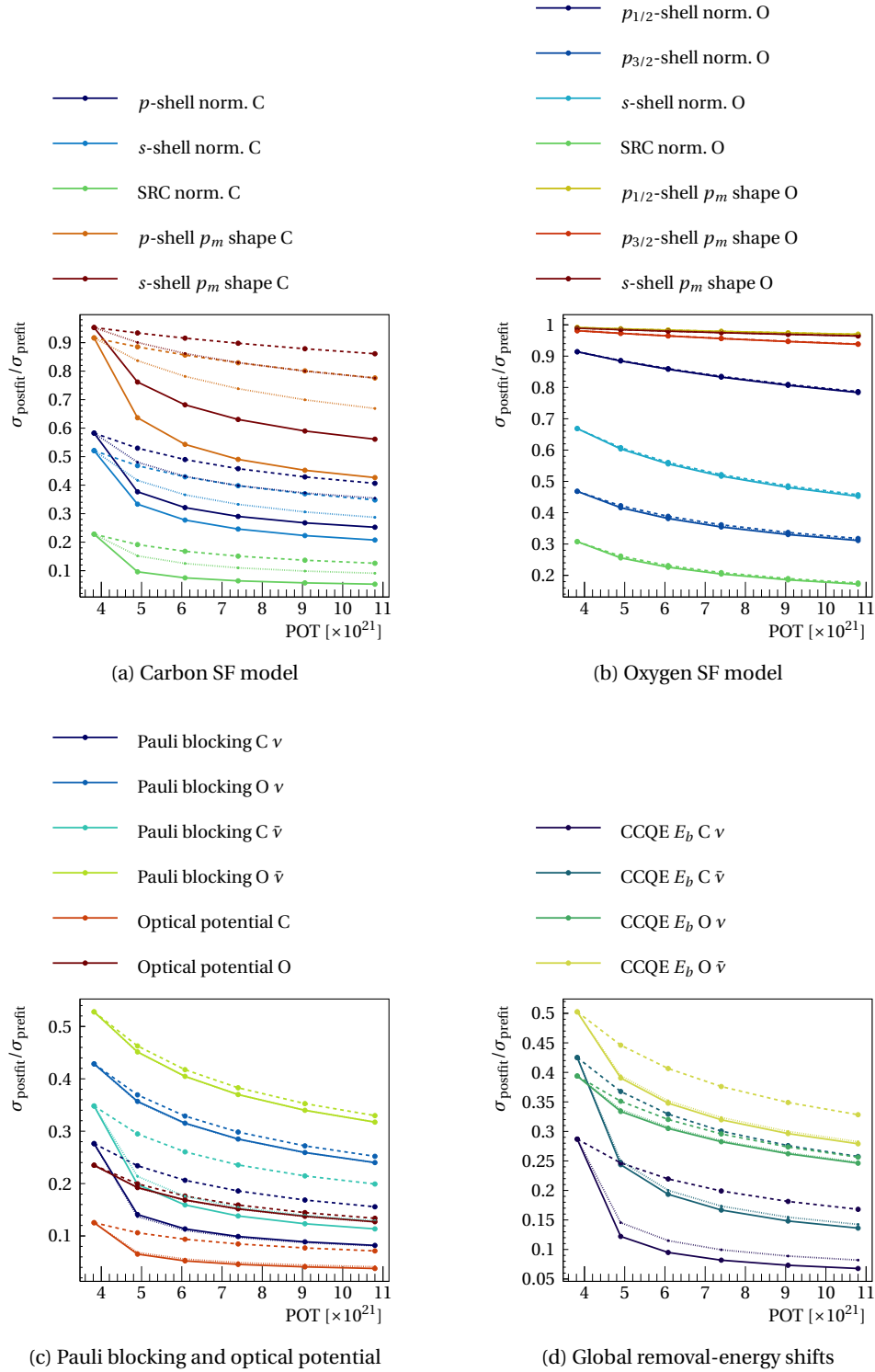


Figure 9.4: Expected constraints on CCQE-related uncertainties for the FGD1+2 only (dashed), SFGD+FGD1+2  $\mu$  only (dotted) and SFGD+FGD1+2  $\mu + N$  (full) configurations described in Section 9.2.1.

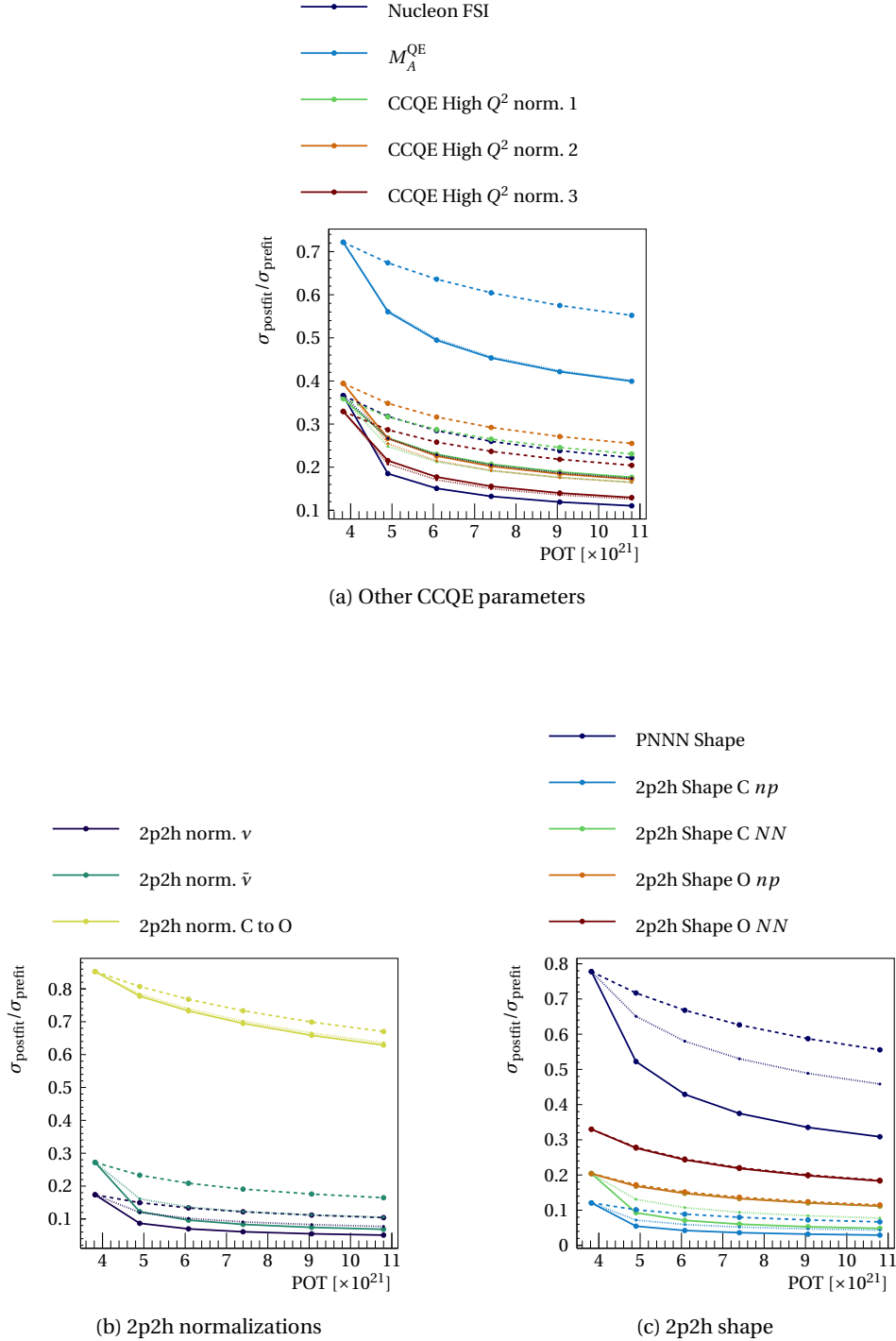


Figure 9.5: Expected constraints on CCQE- and 2p2h-related uncertainties for the FGD1+2 only (dashed), SFGD+FGD1+2  $\mu$  only (dotted) and SFGD+FGD1+2  $\mu$  +  $N$  (full) configurations described in Section 9.2.1.

### Neutrino interaction uncertainties

Since the added Super-FGD samples in this study contain only  $\text{CC}0\pi$  events, CCQE and 2p2h uncertainties are where we can expect to see the largest impact of the near-detector upgrade. This can be clearly noticed in Figures 9.4 and 9.5. In fact, this improvement is not only driven by the additional statistics from neutrino interactions in the Super-FGD, but also by the choice of the fit variables in the upgrade samples (dotted vs. full). As discussed in Chapter 4 and Section 5.4, the addition of the nucleon information in the  $E_{\text{vis}}$  and  $\delta p_T$  variables provides a more precise probe of the details of the nuclear effects.

In particular, Figure 9.4a shows that the uncertainties on the carbon SF model are drastically decreased as more data is gathered. The impact of the  $(\delta p_T, E_{\text{vis}})$  binning instead of  $(p_\mu, \cos\theta_\mu)$  for Super-FGD samples with a reconstructed nucleon is particularly clear for the missing-momentum shape parameters. As previously mentioned, these parameters are currently fixed in the current oscillation analysis due to its lack of sensitivity to their effect ( $\sim 100\%$  postfit relative uncertainty at the lowest POT value). Adding Super-FGD data in using the muon kinematics only marginally improves the sensitivity to these uncertainties, while considering the nucleon information in  $(\delta p_T, E_{\text{vis}})$  allows to remarkably reduce the relative uncertainty on e.g. the  $p$ -shell shape parameter down to below 60% in contrast with  $\sim 80\%$  when using the  $(p_\mu, \cos\theta_\mu)$  binning in the Super-FGD samples at the end of this new phase of data taking. In comparison, if there were no upgrade, this relative uncertainty would remain above 80%. On the other hand, the oxygen SF-model uncertainties in Figure 9.4b are constrained thanks to the interactions on the water modules of the FGD2, but there is virtually no improvement when adding the Super-FGD samples as the new target is made of hydrocarbon only. This is particularly due to the conservative approach of assuming independent models for each target without any correlations, which we will further discuss in Section 9.3.2.

The Pauli blocking and optical-potential correction parameters, which affect neutrino interactions with a low four-momentum transfer  $Q^2$ , are displayed in Figure 9.4c. The constraints on the carbon parameters are significantly improved when including the Super-FGD samples. This is particularly discernible in the sharp uncertainty drop within the first year of data taking. These uncertainties are almost unaffected by the change of the binning variables in the Super-FGD samples since most low energy transfer events end up in the FHC SFGD  $\text{CC}0\pi0p$  and the RHC SFGD  $\text{CC}0\pi0N$  samples with no nucleons in the final state that are always binned in  $(p_\mu, \cos\theta_\mu)$  in this analysis. Indeed, low- $Q^2$  interactions produce an outgoing nucleon with a momentum often below the detection threshold corresponding to  $\sim 300 \text{ MeV}/c$  in the Super-FGD. The oxygen parameters are only marginally improved with the addition of the Super-FGD samples in comparison with the FGD1+2-only case due to the absence of any extra water in the upgrade. The small improvement is mainly driven by the tighter constraints on the carbon uncertainties which allow a somewhat better constraint on oxygen parameters since the interactions on both targets are within the same FGD2 samples.

<sup>3</sup>The best-fit point is simply the prefit values for all the parameters as this study uses Asimov fits, i.e. where the fitted data is exactly the nominal model prediction.



We notice roughly the same trend with the global removal-energy shift uncertainties shown in Figure 9.4d, where the added samples significantly impact the constraints on the carbon parameters, and this is roughly similar whether we use the nucleon information or not in the fit variables as the muon kinematics are already sensitive to global variations in the removal-energy scale. The relatively better constraints on the oxygen uncertainties when including the Super-FGD samples is partly due to the prefit correlations assumed between the oxygen and carbon uncertainties (see Section 7.3.3).  $M_A^{\text{QE}}$  is also better constrained with the new samples regardless of the used binning variables, even with its tight prefit constraints ( $\pm 0.06 \text{ GeV}/c^2$ ). In fact, as previously mentioned and shown in Reference [224],  $\delta p_T$  is quite independent of the nucleon-level physics which means that this uncertainty is not particularly expected to be impacted by using it as a fit variable. The nucleon FSI parameter on the other hand is noticeably well constrained in the SFGD+FGD1+2  $\mu + N$  configuration as  $\delta p_T$  is sensitive to FSI effects unlike the muon kinematics. Its relative uncertainty is expected to decrease at the end of this phase of data taking from  $\sim 25\%$  with the FGD1+2-only samples to  $\sim 20\%$  when including the CC0 $\pi$  samples of the Super-FGD all binned in  $(p_\mu, \cos\theta_\mu)$ , down to almost 10% with the addition of the nucleon information with the observables  $(\delta p_T, E_{\text{vis}})$ .

Another channel where we can expect a large reduction of the uncertainties thanks to the new samples is the 2p2h interaction mode. These produce two nucleons at the primary neutrino interaction which often exit the nucleus in addition to the charged lepton and constitute an important fraction of CC0 $\pi$  events. As discussed in Section 7.2.2, the oscillation analysis of 2022 introduced proton tagging in the FHC CC0 $\pi$  samples with the goal to particularly increase the sensitivity to this interaction channel. Consequently, we also expect that the addition of new CC0 $\pi$  samples with additional nucleon information would only further improve this sensitivity. The corresponding uncertainties are shown in the bottom panels of Figure 9.5.

As  $\delta p_T$  allows to disentangle the multinucleon effects from the genuine CCQE interactions (see Figure 5.24), its use as a fit variable yields more constraints on the 2p2h uncertainties. For instance, this appears in the decreasing uncertainties of the  $\bar{\nu}$  normalizations displayed in Figure 9.5b in the SFGD+FGD1+2  $\mu + N$  configuration. Here again, as no additional interactions on water come with the near-detector upgrade samples, the uncertainty that scales the relative 2p2h contribution on oxygen with respect to carbon is almost unchanged. Similar observations can be made on the 2p2h shape uncertainties of Figure 9.5c. In particular, the PNNN Shape parameter, which alters the relative fraction of 2p2h interactions on nucleon pairs of the same or opposite isospin (see Section 7.3.3), sees its uncertainties more constrained with the  $(\delta p_T, E_{\text{vis}})$  binning in the Super-FGD samples with a reconstructed nucleon.

Even in a CC0 $\pi$  sample, CCRES or CCDIS neutrino interactions that produce pions may end up in this event selection if the outgoing pion is absorbed in the nucleus through FSI processes. This can amount up to 20% of the total CC0 $\pi$  event rate. As these would yield a larger imbalance in the transverse plane with respect to the incoming neutrino direction,  $\delta p_T$  is able to separate them from the CCQE interactions, although with some degeneracy with the multinucleon effects. We can clearly see the impact of using this observable on almost all

of the uncertainties in Figures A.1 and A.2. The difference with the FGD1+2-only fits is not very large as these parameters are only constrained with a background contribution in CC0 $\pi$  samples and no CC1 $\pi$  sample from the Super-FGD was considered in this study, lacking a reasonable simulation of the detector effects for pions.

### Flux uncertainties

The flux uncertainties are implemented as 100 normalization parameters applied in bins of true neutrino energy and split by beam mode, neutrino type and the considered detector as described in Section 7.3.1. These normalization parameters are tuned by fits to external data from the NA61/SHINE hadron-production experiment, which gives a prior uncertainty on each parameter as well as a correlation matrix (see e.g. Figure 7.5). The results of this sensitivity study on the constraints on the flux parameters related to  $\bar{\nu}_\mu$  at the near detector are shown for a subset of these parameters in Figure 9.6. The other Super-Kamiokande parameters as well as the  $\bar{\nu}_e$ -related uncertainties are displayed in Figures A.3 and A.4.

As normalization parameters, their constraints are expected to improve simply by increasing the statistics. This is particularly achieved by the addition of more neutrino interaction samples to the analysis from the Super-FGD. The choice of the fit variables also play a crucial role on constraining these uncertainties. In particular, when the nucleon information is available in the Super-FGD samples, the observable  $E_{\text{vis}}$  is a relatively accurate estimator of the true neutrino energy as shown in the right panel of Figure 5.25 since it uses the hadronic energy deposition in addition to the muon energy. This is well observed for instance in the constraints on the  $\nu_\mu$  component of the FHC beam in Figure 9.6a.

For the antineutrino uncertainties, an additional effect leads to even tighter constraints when using  $(\delta p_T, E_{\text{vis}})$  as fit variables with the Super-FGD samples. As shown in Figure 5.24, a significant fraction of the CCQE antineutrino interactions on the hydrocarbon that composes the Super-FGD occurs on the hydrogen protons. There is a nearly perfect transverse-momentum balance in such interactions since the target proton is free and no nuclear effects beyond the nucleon-level processes (e.g.  $M_A^{\text{QE}}$ ) are expected to impact the kinematics of the outgoing particles. This leads to a relatively larger reduction in the uncertainties on the  $\bar{\nu}_\mu$  flux uncertainties as shown for instance in Figures 9.6b and 9.6d in comparison with the  $\nu_\mu$  uncertainties.

Another effect of the additional statistics from the Super-FGD can be observed in the postfit covariance matrices shown in the Figure 9.7 where we see the impact of adding  $1 \times 10^{21}$  POT in the FGD1+2-only (left) and the SFGD+FGD1+2  $\mu + N$  (right) configurations. It can be noticed that there are less correlations when using the additional Super-FGD samples as they allow to better disentangle the effects of the flux normalization parameters particularly thanks to the  $E_{\text{vis}}$  fit variable. A simple analysis of the principal components of the two matrices, displayed in Figure 9.8 where we show the ordered eigenvalues for each *correlation* matrix, allows to gauge to which extent the parameters are independent. We see that a larger fraction of the principal components contribute to the overall flux variance in the SFGD+FGD1+2

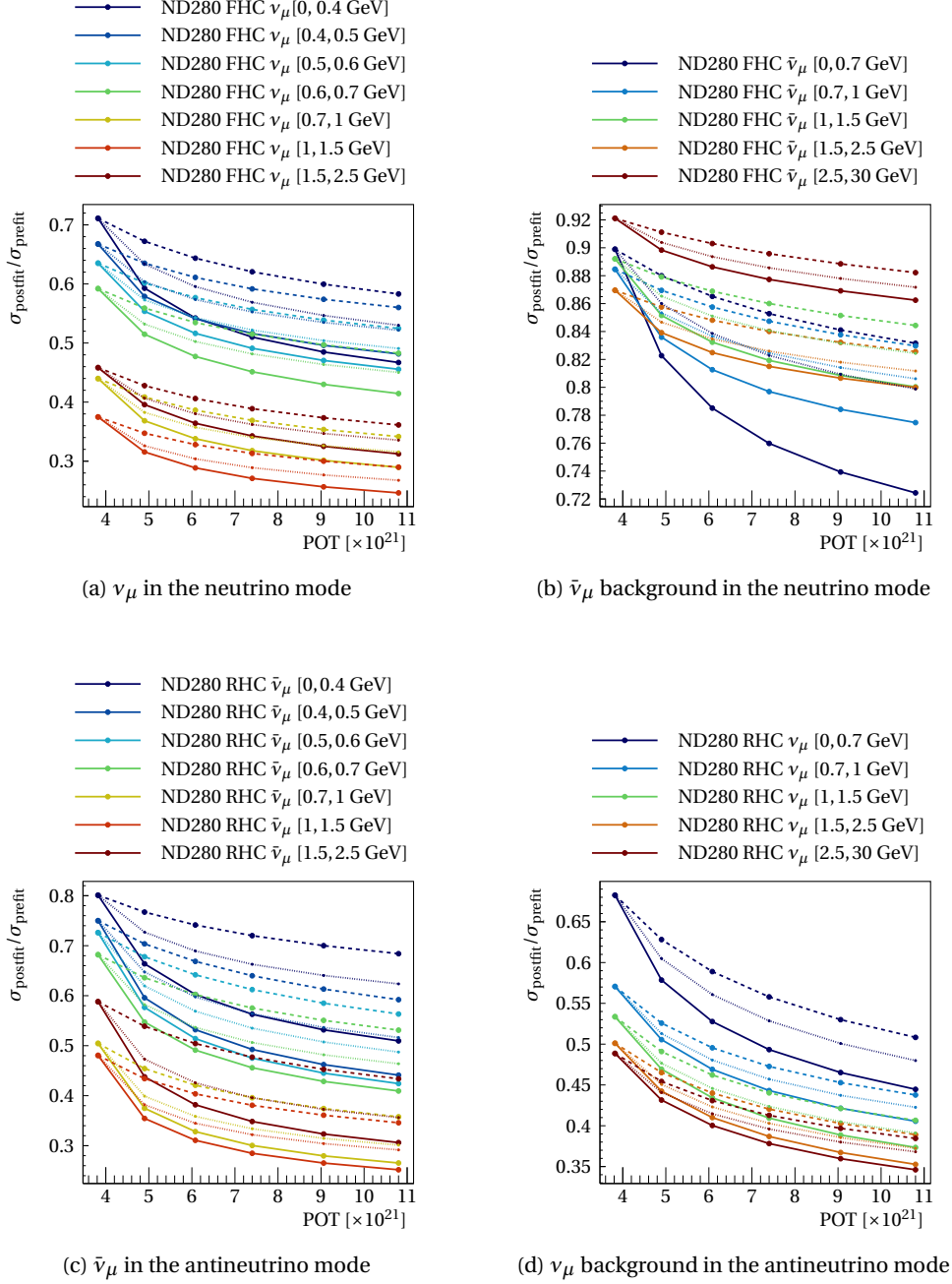


Figure 9.6: Expected constraints on ND280 flux uncertainties for the FGD1+2 only (dashed), SFGD+FGD1+2  $\mu$  only (dotted) and SFGD+FGD1+2  $\mu$  +  $N$  (full) configurations described in Section 9.2.1.

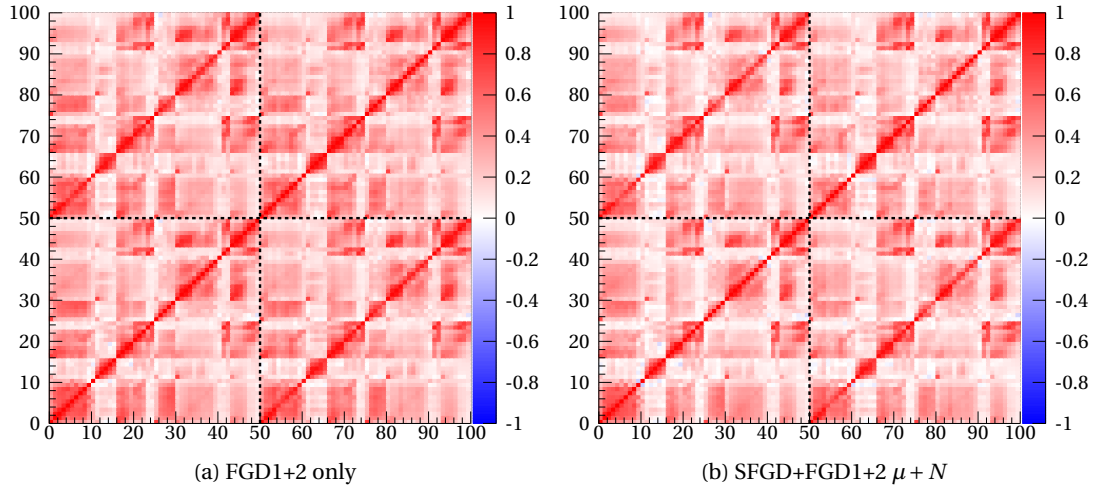


Figure 9.7: Postfit covariance matrix of the flux parameters when using in the FGD1+2-only (left) and the SFGD+FGD1+2 (right) configuration when the added POT is  $1 \times 10^{21}$ .

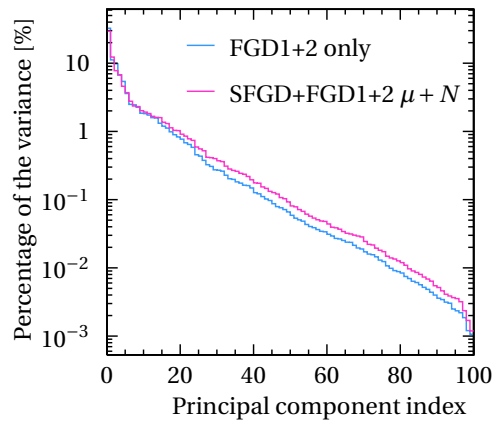


Figure 9.8: Principle components of the postfit flux correlation matrices shown in Figure 9.7.

$\mu + N$  configuration in comparison with the FGD1+2-only one, which means that the former encodes less correlations compared to the latter. Consequently, the added samples allow to further decorrelate the effect of the flux systematic uncertainties.

### 9.3 Sensitivity to constrain oscillation parameters

In the previous section, we discussed how the near-detector upgrade is expected to impact the constraints on the flux and the cross-section uncertainties in the oscillation analysis with additional CC0 $\pi$  samples. In particular, we saw how the choice of the fit variables can play a crucial role in disentangling the nuclear effects by comparing the constraints obtained when binning in  $(p_\mu, \cos\theta_\mu)$  or in  $(\delta p_T, E_{\text{vis}})$ . In this section, we evaluate the effect of the improved constraints from the near-detector fit on the oscillation parameters. As we noticed with the cross-section parameters related to the oxygen nucleus (e.g. Figures 9.4b and 9.4c), the upgraded near detector only marginally improves the corresponding sensitivity due to the absence of additional water material and the conservative approach of considering completely independent ground-state models between oxygen and carbon. Consequently, we split this study into two parts: a first part where we evaluate the sensitivity to the oscillation parameters over the upcoming data-taking phase using the FGD1+2-only configuration (Section 9.3.1), and a second part where we address the question of the carbon vs. oxygen correlations and discuss their potential impact on the oscillation analysis (Section 9.3.2). Similarly to the oscillation results presented in Chapter 7, we use the constraints obtained from the near-detector fits within the P-Theta fitting framework to obtain the sensitivity to the oscillation parameters.

The last detailed estimation of the sensitivity to constrain oscillation parameters were made back in 2016, with a now-obsolete NEUT model that for instance did not include 2p2h interactions [288]. It is consequently of great interest to update these studies with a more up-to-date flux and neutrino interaction models as well as with the latest projections of the expected POT. Reference [288] evaluated the sensitivity to constrain oscillation parameters assuming a total delivered POT of  $20 \times 10^{21}$ , i.e. nearly the double of data we now expect to collect by 2027 as shown in Table 9.1. It showed that the observation of CP violation, if maximal, is within reach at a  $3\sigma$  level with that amount of statistics. However, as we will see in Section 9.3.1 with the more realistic expectations of the beam time, it would now be only possible under multiple restrictive hypotheses.

#### 9.3.1 FGD1+2-only near-detector configuration

##### Near-detector constraints

In the study of this section, we *only* consider the constraints from the near-detector configuration corresponding to FGD1+2 only described in Section 9.2.1. For each value of the expected POT in Table 9.1, we use the constraints from the near-detector analysis obtained

### 9.3 Sensitivity to constrain oscillation parameters

with GUNDAM as shown in Figures 9.4 to 9.6 and A.1 to A.3 (dashed lines) at the far-detector fit with the P-Theta framework following the Frequentist stream of the oscillation analysis (see Section 7.4.2).

The increasing delivered POT over the upcoming years does not only mean tighter constraints on the systematic uncertainties from the near-detector fit, but also more neutrino interactions at Super-Kamiokande which directly impacts the sensitivity to the oscillation parameters. Indeed, T2K is currently a statistically limited experiment, and the sensitivity is mainly driven by the far-detector event rate. However, as we will see in this section, the higher statistics that we expect in this new phase of data taking will make the impact of the systematic errors more and more important. Therefore, in most of the results shown in this section, we will compare the sensitivity to the oscillation parameters between the ideal (and unrealistic) case of when there are no systematic uncertainties (referred to as stat. only), and when considering the systematic uncertainties used in the 2022 oscillation analysis (OA2022) constrained by the near-detector fit in the FGD1+2-only configuration.

#### Reference oscillation parameters

In this study, we will gauge the sensitivity to the oscillation parameters at two sets of reference points summarized in Table 9.5:

- **Set A22:** this is a point in the oscillation parameter space that is close to the T2K-preferred values, i.e. normal mass ordering, nearly maximal CP violation, and upper  $\theta_{23}$  octant.
- **Set B22:** this point is closer to the preferred values by the NOvA experiment, with a normal mass ordering, no CP violation, lower  $\theta_{23}$  octant, and a T2K-like  $\Delta m_{32}^2$  value.

When evaluating the sensitivity to the CP violation and the mass ordering, we will also test different true values of  $\theta_{23}$  and  $\delta_{\text{CP}}$  as the constraints heavily depend on these parameters. This will be explicitly stated in the legend and the caption of each presented result. Besides, in all of the following, we use the reactor constraints on  $\theta_{13}$  from Reference [12].

#### Event rates

Tables 9.6 and 9.7 show the predicted event rates in each of the six Super-Kamiokande samples considered in this analysis at the Set A22 and the Set B22 respectively for the considered additional POT from 2022 to 2027 summarized in Table 9.1. As assumed in Section 9.2.1, we consider that 50% of the delivered POT is used in the FHC mode and 50% in the RHC mode. Consequently, for each year, both FHC and RHC event rates increase.

Under this assumption, we can expect the number of one-ring  $\mu$ -like samples to almost triple at Super-Kamiokande by the end of this data-taking phase. At the Set A22, a larger difference

between the FHC and RHC number of events in one ring  $e$ -like samples can be observed in comparison with the Set B22, which reflects the assumption on the value of  $\delta_{CP}$ .

It is important to mention that, in this study, we use the Asimov near-detector constraints to generate the far-detector prediction, which explains the different predicted event rates between the ones in the 2022 column of Table 9.6 and the ones in Table 7.12. Indeed, the central values of the parameters in an *Asimov* near-detector fit simply correspond to their nominal values, while the near-detector *data* fit yields a change in the overall event rate normalization particularly due to the strong pulls on the flux parameters, which increases the event rates in Table 7.12 in comparison with the 2022 column of Table 9.6. This can also be seen in Figure 7.14, where the average post-near-detector predictions (red) correspond to a slightly higher normalization in comparison with the pre-near-detector predictions (blue).

### Marginalization effects

As mentioned in Section 7.4.2, P-Theta uses the marginalization approach over the nuisance and some of the oscillation parameters to reduce the dimensionality of the likelihood for the grid search. A large number  $N_{\text{marg}}$  of variations in the marginalized parameters is sampled from their prior distribution: the nuisance parameters are obtained from the Gaussian distribution defined by the central values and the covariance obtained from the near-detector fit, while the oscillation parameters are sampled from either a uniform or a normal distribution as summarized in Table 7.9.

The number of the generated variations of the marginalized parameters  $N_{\text{marg}}$  is finite, and random fluctuations may impact the marginalized likelihood and thus the sensitivity contours for given oscillation parameters. In particular, as the number of events increases, the statistical (Poisson) part of the negative log-likelihood increases roughly linearly with the delivered POT, and with it the size of the fluctuations due to the marginalization. Consequently, an important consistency check that is often performed in the analyses consists in generating multiple sets of variations with an increasing  $N_{\text{marg}}$  to check which value of  $N_{\text{marg}}$  ensures stable results.

In the 2022 analysis described in Chapter 7,  $N_{\text{marg}} = 100,000$  was found to be enough for the results to be reproducible. In this study, we evaluate the impact of the marginalization fluctuations at the largest expected POT, i.e. in 2027, by producing different sets of variations in the systematic uncertainty parameters and compare the sensitivity to  $\delta_{CP}$  contours at different values of  $N_{\text{marg}}$  as shown in Figure 9.9. We find that  $N_{\text{marg}} = 300,000$  (right) allows to mitigate the fluctuations observed when  $N_{\text{marg}} = 100,000$  (left).

As previously mentioned, the marginalization involves both systematic uncertainty and oscillation parameters, but the statistical fluctuations are mostly expected to come from the variations in the systematic uncertainties as their dimension is much higher than that of the marginalized oscillation parameters and would need a larger  $N_{\text{marg}}$  to well sample their distribution. Consequently, the sensitivities shown in Figure 9.9 are done by keeping the

### 9.3 Sensitivity to constrain oscillation parameters

Parameters	Set A22	Set B22
$\Delta m_{21}^2$	$7.53 \times 10^{-5} \text{eV}^2/c^4$	
$\Delta m_{32}^2$ (NO) / $ \Delta m_{31}^2 $ (IO)	$2.494 \times 10^{-3} \text{eV}^2/c^4$	
$\sin^2 \theta_{23}$	0.561	0.45
$\sin^2 \theta_{12} (\sin^2 2\theta_{12})$	0.307 (0.851)	
$\sin^2 \theta_{13} (\sin^2 2\theta_{13})$	0.0220 (0.0861)	
$\delta_{\text{CP}}$ [rad]	-1.601	0
Mass ordering	Normal	

Table 9.5: Reference points of the oscillation parameters used in the Asimov fits with P-Theta to evaluate the sensitivity.

Sample	2022	2023	2024	2025	2026	2027
FHC 1R $\mu$	301.18	383.89	474.26	575.35	701.71	837.26
RHC 1R $\mu$	124.68	165.86	210.86	261.20	324.13	391.63
FHC 1Re	79.53	101.37	125.24	151.93	185.30	221.09
RHC 1Re	15.47	20.58	26.17	32.42	40.23	48.60
FHC 1Re1de	10.87	13.85	17.11	20.76	25.32	30.21
FHC multi-R $\mu$	116.25	148.17	183.05	222.07	270.84	323.16

Table 9.6: Predicted event rate in each of the six far detector samples at the Asimov Set A22 with the additional POT per year as shown in Table 9.1.

Sample	2022	2023	2024	2025	2026	2027
FHC 1R $\mu$	305.92	389.93	481.72	584.39	712.74	850.42
RHC 1R $\mu$	125.49	166.95	212.25	262.92	326.26	394.20
FHC 1Re	57.97	73.89	91.28	110.74	135.06	161.15
RHC 1Re	15.42	20.52	26.08	32.31	40.09	48.44
FHC 1Re1de	8.12	10.34	12.78	15.50	18.91	22.56
FHC multi-R $\mu$	116.52	148.51	183.47	222.58	271.47	323.91

Table 9.7: Predicted event rate in each of the six far detector samples at the Asimov Set B22 with the additional POT per year as shown in Table 9.1.



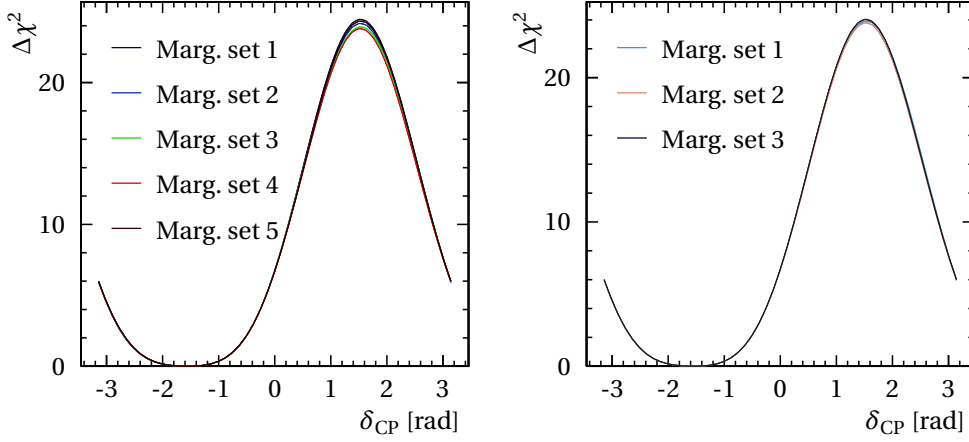


Figure 9.9: Impact of the statistical fluctuations in the marginalization using independently generated sets for the systematic parameters with  $N_{\text{marg}} = 100,000$  (left) and  $N_{\text{marg}} = 300,000$  (right) on the  $\delta_{\text{CP}}$  sensitivity at the Set A22 Asimov point using the expected statistics in 2027 (see Table 9.1).

	2023	2024	2025	2026	2027
$N_{\text{marg}}$	100,000	150,000	200,000	250,000	300,000

Table 9.8: Chosen  $N_{\text{marg}}$  for each value of the additional considered POT (see Table 9.1).

same set of varied oscillation parameters and changing only the variations of the systematic parameters. For the other lower values of delivered POT, we choose to incrementally increase the size  $N_{\text{marg}}$  of the generated variations as shown in Table 9.8. The limitation hindering the use of larger values of  $N_{\text{marg}}$  is simply computational as the required space for the storage of all the needed distributions for each of the six far-detector samples (in e.g.  $E_{\nu}^{\text{reco}}$ ,  $p_l$  and/or  $\theta_l$ ) with the values of Table 9.8 is already over 2 TB.

### Resolution on $\Delta m_{32}^2$

We start by evaluating the sensitivity to constrain the value of the squared-mass splitting  $\Delta m_{32}^2$ . As shown in Figure 7.2, its impact mainly appears in the disappearance channel, and particularly in the size of the oscillation dip in the neutrino energy. With the increased statistics in the  $\mu$ -like sample, the constraints are expected to become tighter. This is displayed in Figure 9.10, where we see how  $\Delta\chi^2$  evolves as a function of  $\Delta m_{32}^2$  in the normal ordering at the Set A22 for the different values of the delivered POT.

We can quantify this improvement by looking at the resolution on the  $\Delta m_{32}^2$  parameter, which we define as the half-width of the  $1\sigma$  interval highlighted in Figure 9.10 (dashed line). We particularly compare this resolution to the case where there are no systematic uncertainties in

the measurement in Figure 9.11 for the Set A22 (left) and the Set B22 (right) as a function of the delivered POT. The lowest POT value corresponds to the 2022 statistics used in the analysis presented in Chapter 7. The corresponding resolution with the systematic uncertainties is  $\sim 2\%$  at the Set A22, which is very close to the value obtained in the data analysis results of Table 7.11. It can be noticed that already at this level of the collected statistics, there is a non-negligible impact of the systematic uncertainties. This can be further observed in the noticeable gap between the statistics-only resolution and the resolution when taking into account the systematic uncertainties at both reference oscillation points. As the POT increases, the near-detector constraints are tighter which allows to maintain the impact of the systematic uncertainties relatively under control. The expected resolution on  $\Delta m_{32}^2$  by the end of this data-taking phase is  $\sim 1.2\%$  and  $\sim 1.3\%$  at the Set A22 and the Set B22 respectively. As a comparison, it corresponds to  $\sim 1.1\%$  in the case of no systematic uncertainties.

#### Resolution on $\sin^2 \theta_{23}$

The other disappearance parameter we consider is  $\theta_{23}$ , for which the main open question in oscillation physics is whether its true value is in the upper or the lower octant. Figure 9.12 shows the chi-square difference as a function of  $\sin^2 \theta_{23}$  at the Set A22 (left) and the Set B22 (right) for the expected POT up to 2027. In the case of the former, it can be seen that the octant degeneracy remains at the  $1\sigma$  level even with the highest expected statistics, while the latter shows a clearer preference for the true octant very close to the 90% C.L. ( $\Delta\chi^2 = 2.71$ ) at the 2027 POT.

Similarly to  $\Delta m_{32}^2$ , we can evaluate the resolution on  $\sin^2 \theta_{23}$ . However, unlike  $\Delta m_{32}^2$ , the likelihood as a function of  $\sin^2 \theta_{23}$  is not Gaussian and Wilks' theorem does not hold in this case. Nevertheless, we simply choose to report in Figure 9.13 the half-width of the  $1\sigma$  interval indicated by the dashed lines in Figure 9.12 using the fixed  $\Delta\chi^2$  method, compared between the cases of without (dotted) and with (full) systematic uncertainties. For the Set A22, the resolution at the lowest POT value when considering the systematic uncertainties is comparable with the one obtained in the data fit of the 2022 results shown in Table 7.11, which is 0.048. It is important to note that the confidence intervals on  $\sin^2 \theta_{23}$  in the published T2K oscillation analyses use the Feldman – Cousins method instead of the fixed  $\Delta\chi^2$ , which could explain the somewhat small difference. At both reference oscillation points, we clearly see that, even with the tighter constraints on the systematic uncertainties obtained from the near-detector fits, the resolution difference when using the systematic uncertainties steadily increases with respect to the statistics-only case.

#### Sensitivity to $(\sin^2 \theta_{23}, \Delta m_{32}^2)$

As shown in Figure 1.18, the constraints on the disappearance parameters are often displayed with the two-dimensional 90% confidence levels in  $(\sin^2 \theta_{23}, \Delta m_{32}^2)$ . Similarly, Figure 9.14 shows the contours at the Set A22 (left) and the Set B22 (right) for the statistics of 2022 (red),

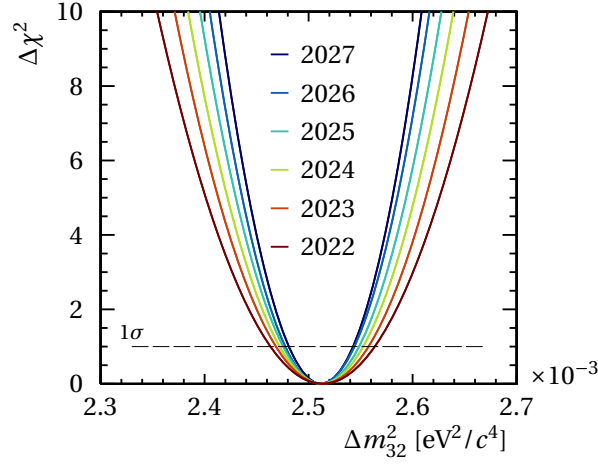


Figure 9.10: Evolution of the  $\Delta m_{32}^2$  contours in the normal ordering at the Asimov Set A22 for the projected POT shown in Table 9.1 using the systematic uncertainties of the 2022 oscillation analysis, constrained with the FGD1+2-only configuration at each value of the delivered POT. The dashed line indicate the  $1\sigma$  C.L. (i.e.  $\Delta\chi^2 = 1$ ) used to extract the resolution.

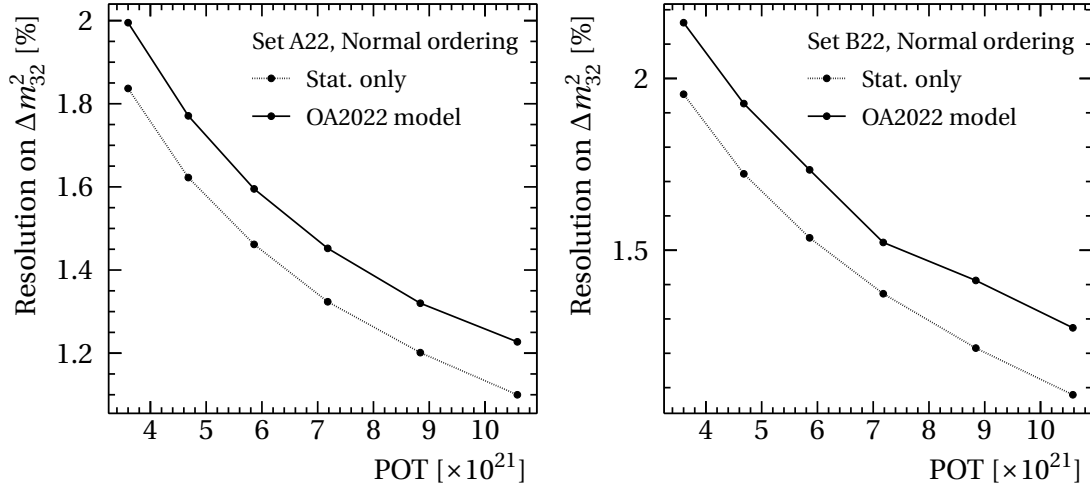


Figure 9.11: Resolution on  $\Delta m_{32}^2$  in the normal ordering at the Set A22 (left) and the Set B22 (right) for the projected POT shown in Table 9.1 compared between when considering only statistical uncertainties (dotted) and when using the systematic uncertainties of the 2022 oscillation analysis constrained with the FGD1+2-only configuration at each value of the delivered POT (full).

### 9.3 Sensitivity to constrain oscillation parameters

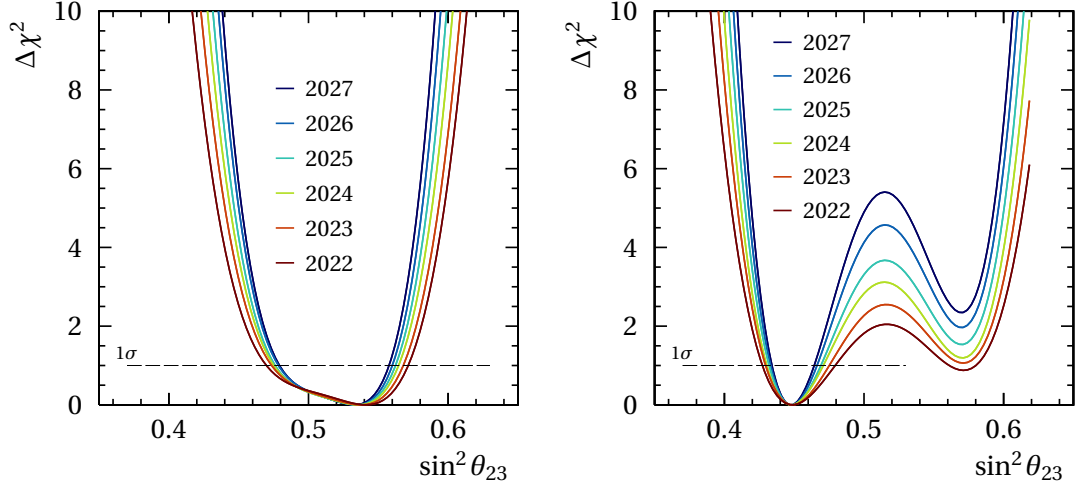


Figure 9.12: Evolution of the  $\sin^2 \theta_{23}$  contours in the normal ordering at the Set A22 (left) and the Set B22 (right) for the projected POT shown in Table 9.1 using the systematic uncertainties of the 2022 oscillation analysis, constrained with the FGD1+2-only configuration at each value of the delivered POT. The dashed line indicate the  $1\sigma$  C.L. (i.e.  $\Delta\chi^2 = 1$ ) used to extract the resolution.

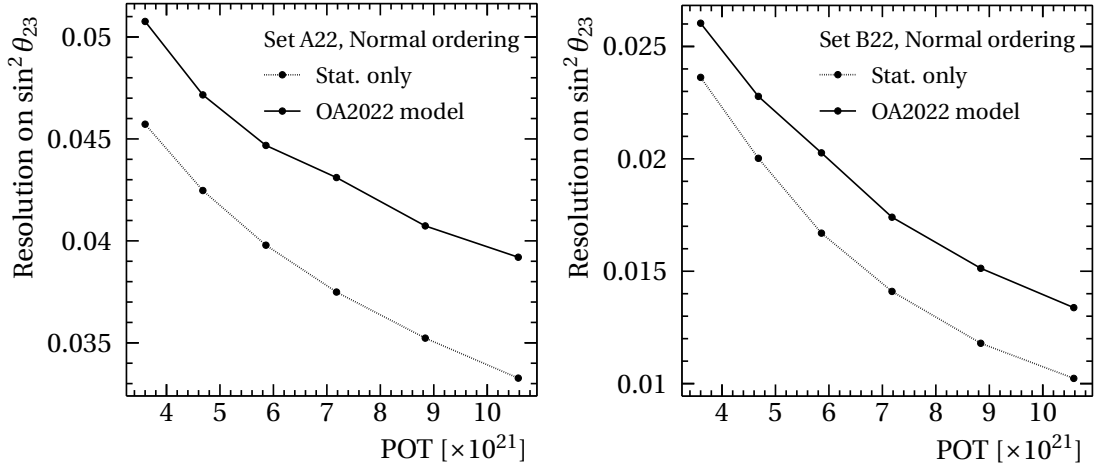


Figure 9.13: Resolution on  $\sin^2 \theta_{23}$  in the normal ordering at the Set A22 (left) and the Set B22 (right) for the projected POT shown in Table 9.1 compared between when considering only statistical uncertainties (dotted) and when using the systematic uncertainties of the 2022 oscillation analysis constrained with the FGD1+2-only configuration at each value of the delivered POT (full).

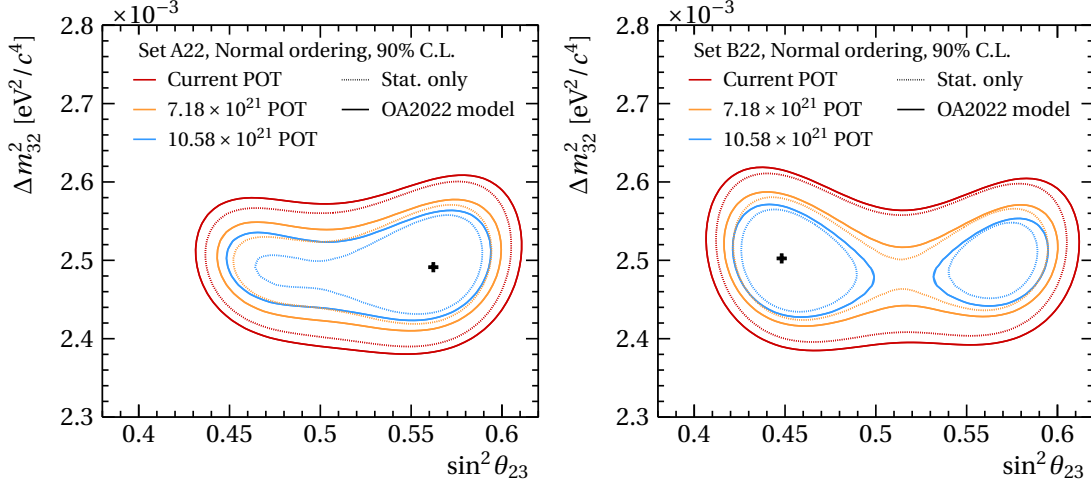


Figure 9.14: 90% C.L. contours in  $(\sin^2 \theta_{23}, \Delta m_{32}^2)$  in the normal ordering at the Set A22 (left) and the Set B22 (right) for the delivered POT in 2022 (red), 2025 (orange) and 2027 (cyan) as shown in Table 9.1 compared between when considering only statistical uncertainties (dotted) and when using the systematic uncertainties of the 2022 oscillation analysis constrained with the FGD1+2-only configuration at each value of the delivered POT (full).

2025 (orange) and 2027 (cyan). For the Set A22, and as seen with the one-dimensional  $\Delta\chi^2$  of Figure 9.12, the highest expected POT does not allow to exclude the wrong octant at the 90% C.L., but it is interesting to note the increasing discrepancy of the statistics-only contours and the ones with systematic uncertainties. For instance, the 2025 statistics-only C.L. contour appears to be comparable (if not better in certain regions) with the 2027 one including the systematic uncertainties. This shows the importance of the effort to improve constraints on the systematic uncertainties. For the Set B22, we can see at the end of this new phase of data taking two closed contours at the 90% C.L., one around the true value of  $\sin^2 \theta_{23}$ , and another (tighter) one in the region of the wrong octant.

### Sensitivity to CP violation

One of the main motivations behind this new phase of data taking is to further probe the possible CP violation in the lepton sector. As with the other oscillation parameters, we start by evaluating the sensitivity to the  $\delta_{\text{CP}}$  parameter as the statistics increase in the left panel of Figure 9.15 at the Set A22 in the normal ordering. This reference oscillation point corresponds to a maximal CP violation with  $\delta_{\text{CP}} \approx -\pi/2$ , and the sensitivity comes from the larger difference between the FHC and RHC  $e$ -like event rates as shown in Table 9.6 in comparison with Table 9.7. Naturally, as more data is collected, a larger region in  $\delta_{\text{CP}}$  is excluded.

The CP conserving values of  $\delta_{\text{CP}}$  are 0 and  $\pi$ , for which  $\sin \delta_{\text{CP}} = 0$  and the appearance probability of  $\nu_e$  and  $\bar{\nu}_e$  is the same up to the effects of propagation in matter in Equation (1.45). The sensitivity to reject CP conservation is given by the likelihood to exclude these two  $\delta_{\text{CP}}$

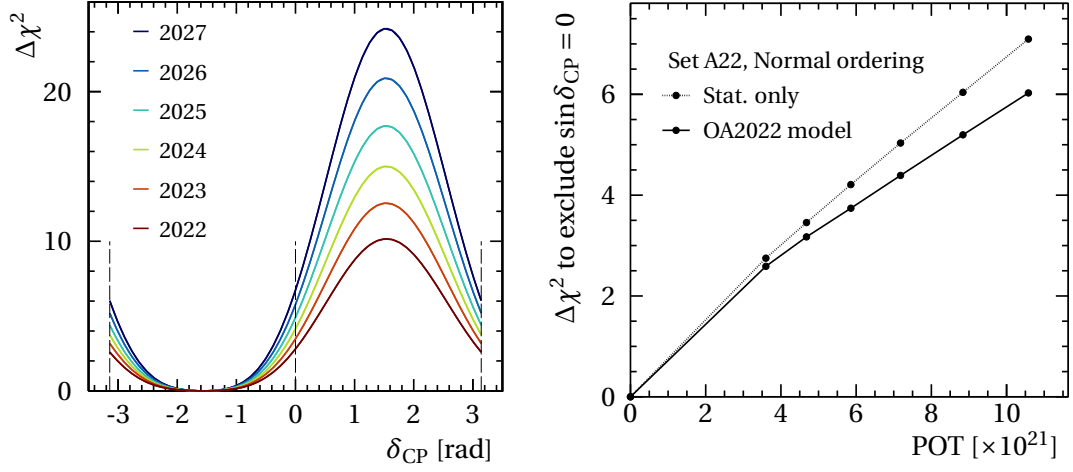


Figure 9.15: Left: evolution of the  $\delta_{CP}$  contours in the normal ordering at the Asimov Set A22 for the projected POT shown in Table 9.1 using the systematic uncertainties of the 2022 oscillation analysis constrained with the FGD1+2-only configuration at each value of the delivered POT, where the dashed line indicate the CP-conserving values of  $\delta_{CP}$ . Right:  $\Delta\chi^2$  to exclude CP violation as a function of the delivered POT when considering only statistical uncertainties (dotted) and when using the systematic uncertainties of the 2022 oscillation analysis constrained with the FGD1+2-only configuration at each value of the delivered POT (full).

values, which is obtained from the  $\Delta\chi^2$  as a function of  $\delta_{CP}$  by:

$$\min \left\{ \Delta\chi^2(\delta_{CP}), \delta_{CP} = 0, \pi \right\}.$$

This corresponds to the minimum of the  $\Delta\chi^2$  for the  $\delta_{CP}$  values indicated by the dashed lines in the left panel of Figure 9.15.

The right panel of Figure 9.15 shows how the sensitivity to exclude CP conservation evolves as a function of the delivered POT compared between the cases where the systematic uncertainties are included (full) or not (dotted). We can first notice that, at the 2022 statistics, the systematic uncertainties have a very limited impact on this sensitivity, which is also suggested by the small predicted event rate in the one-ring  $e$ -like samples of Table 9.6. However, the impact of the systematic uncertainties becomes increasingly visible as more data is collected. In particular, the statistics-only case is just short of a CP-conservation exclusion at a  $3\sigma$  C.L. ( $\Delta\chi^2 = 9$ ) for the 2027 POT, while it does not exceed  $\Delta\chi^2 = 6$  in the case of the constrained systematic uncertainties.

The sensitivity to  $\delta_{CP}$  heavily depends on the neutrino mass ordering and the value of  $\sin^2 \theta_{23}$  as shown in Equation (1.45). Consequently, we can evaluate how the CP-conservation exclusion evolves when these parameters vary. We choose three values for  $\sin^2 \theta_{23}$ : around the lower 90% C.L. boundary at 0.44, the maximal mixing at 0.5, and around the upper 90% C.L.

at 0.6. As for the mass ordering, we assume that it is normal<sup>4</sup> and that it is either known or unknown for the determination of the sensitivity to  $\delta_{\text{CP}}$ . With these choices, we can determine the sensitivity to exclude CP conservation as a function of the true value of  $\delta_{\text{CP}}$ . To do so, we generate at each considered POT and each value of  $\sin^2 \theta_{23}$  a set of simulated experiments in the normal ordering where the true  $\delta_{\text{CP}}$  spans the interval  $[-\pi, \pi]$  and fit each one of them. When we assume that the mass ordering is known, the chi-square difference to exclude CP conservation is obtained with:

$$\Delta\chi_{\text{NO}}^2(\bar{\delta}_{\text{CP}}) = \min \left\{ \chi^2(\delta_{\text{CP}}, \text{NO}) - \chi^2(\bar{\delta}_{\text{CP}}, \text{NO}), \delta_{\text{CP}} = 0, \pi \right\}$$

where  $\bar{\delta}_{\text{CP}}$  is the value of the true CP-violating phase at which the simulated experiment is generated, and  $\chi^2(\delta_{\text{CP}}, \text{MO})$  is the negative log-likelihood computed at  $\delta_{\text{CP}}$  for the mass ordering MO, which corresponds either to the normal ordering NO or the inverted ordering IO. When we assume that the mass ordering is unknown, we compute the chi-square difference as:

$$\Delta\chi_{\text{UO}}^2(\bar{\delta}_{\text{CP}}) = \min \left\{ \chi^2(\delta_{\text{CP}}, \text{MO}) - \chi^2(\bar{\delta}_{\text{CP}}, \text{NO}), \delta_{\text{CP}} = 0, \pi \text{ and MO} = \text{NO, IO} \right\}$$

where the minimum is over the CP-conserving values of  $\delta_{\text{CP}}$  and the mass ordering.

The results are displayed in Figure 9.16, where the left panels correspond to the assumption of a known normal mass ordering and the right panels to an unknown mass ordering. The top panels are obtained for  $\sin^2 \theta_{23} = 0.44$ , the middle ones for  $\sin^2 \theta_{23} = 0.5$  and the bottom ones for  $\sin^2 \theta_{23} = 0.6$ , all evaluated at the current statistics (red) and the highest expected POT (cyan).

The first striking observation is the significant degradation of the sensitivity to exclude CP conservation for  $\delta_{\text{CP}} \in [0, \pi]$  when the normal mass ordering is unknown. In fact, both the matter effects and the CP violation impact the neutrino and antineutrino appearance probabilities, and in this  $\delta_{\text{CP}}$  region, there is an ambiguity between the sign of  $\sin \delta_{\text{CP}}$  and the sign of  $\Delta m_{32}^2$  as can be seen in Equation (1.45). During the running period of this second phase of data taking with T2K, it is probable that other experiments would determine the mass ordering, such as JUNO [65] and KM3NeT/ORCA [66], which is the reason why we also provide the sensitivity to exclude CP violation in case the mass ordering is known. In this case, the sensitivity for  $\delta_{\text{CP}} \in [0, \pi]$  is recovered as there are no significant degeneracies of the CP violation with the matter effects in the appearance probability.

Furthermore, the sensitivity to exclude CP conservation heavily depends on the value of the mixing  $\sin^2 \theta_{23}$  as well. In case of the upper  $\theta_{23}$  octant (bottom row of Figure 9.16), the sensitivity to exclude  $\sin \delta_{\text{CP}} = 0$  is well below the  $3\sigma$  C.L. for all  $\delta_{\text{CP}}$  values, even with the assumption of a known mass ordering. We can clearly see the impact of the systematic uncertainties in this case, hinting at the possibility to improve their treatment for a closer result to the statistics-only sensitivity. This difference only appears at the highest expected POT, while the current POT sensitivity is almost unaffected by the systematic uncertainties.

<sup>4</sup>Assuming that the true ordering is inverted simply corresponds to changing the results of  $\delta_{\text{CP}}$  by  $-\delta_{\text{CP}}$ .

### 9.3 Sensitivity to constrain oscillation parameters

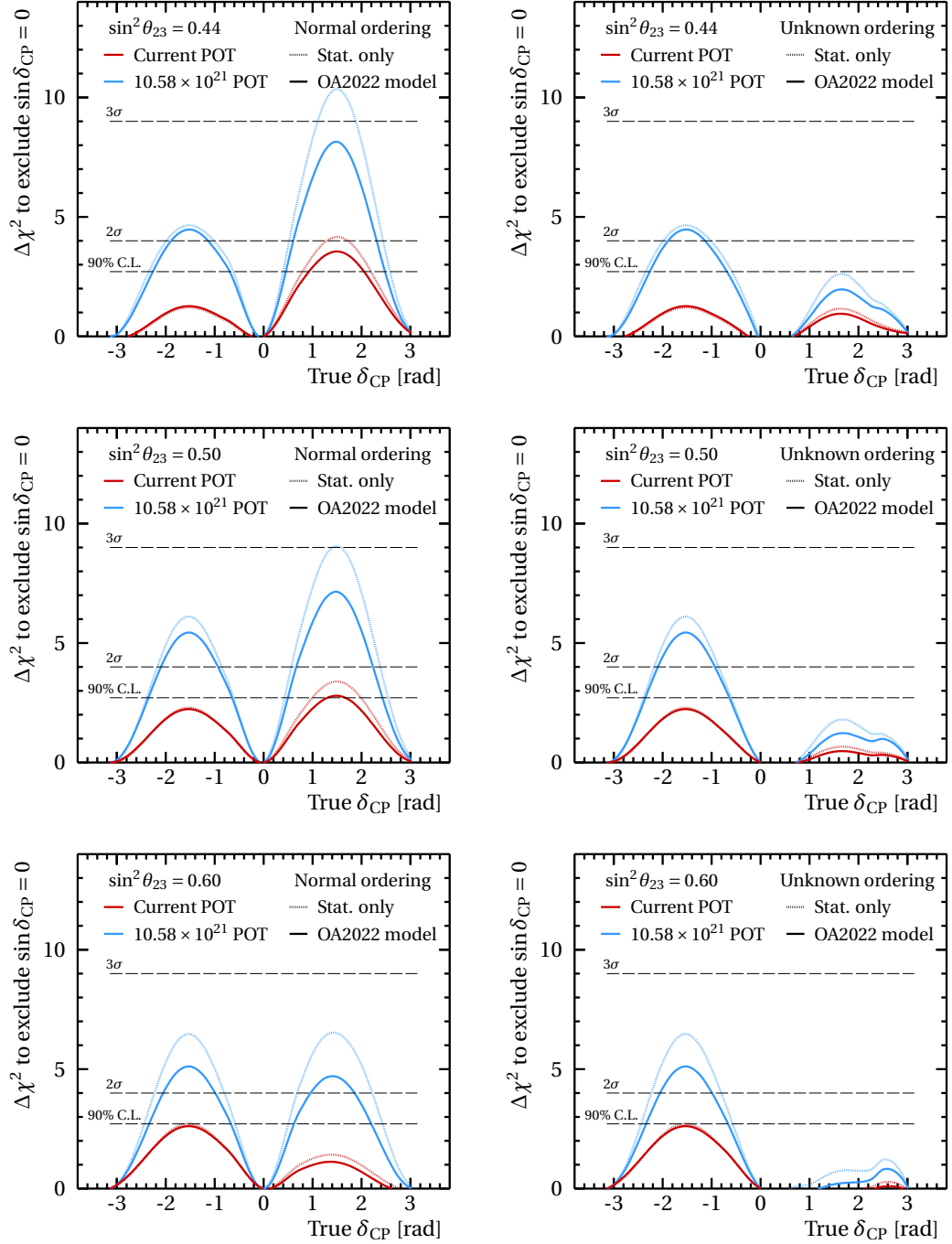


Figure 9.16: Sensitivity to exclude CP conservation as a function of the true value of  $\delta_{CP}$  when the true mass ordering is normal if it is *known* (left) or *unknown* (right) for the statistics-only case and for the systematic uncertainties of the 2022 oscillation analysis constrained with the FGD1+2-only configuration at the current (red) and the 2027 (cyan) values of the delivered POT. This is evaluated for three values of  $\sin^2 \theta_{23}$  from the current T2K 90% C.L. constraints: 0.44 (top), 0.5 (middle) and 0.6 (bottom).



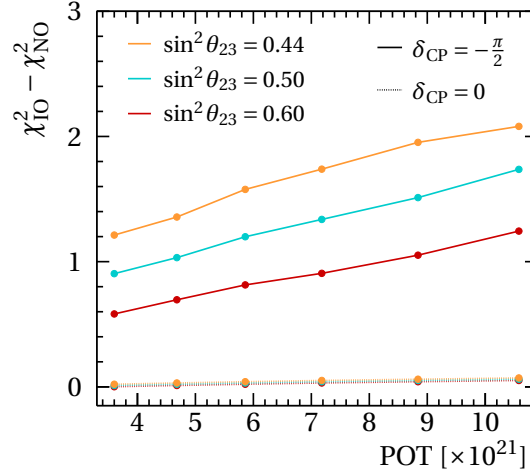


Figure 9.17: Sensitivity to exclude the inverted ordering assuming a true normal ordering as a function of the projected POT shown in Table 9.1 when using the systematic uncertainties of the 2022 oscillation analysis constrained with the FGD1+2-only configuration at each value of the delivered POT assuming a true value of  $\delta_{CP}$  at 0 (dotted) and  $-\pi/2$  (full) for three values of  $\sin^2 \theta_{23}$  from the current T2K 90% C.L. constraints: 0.44 (orange), 0.5 (cyan) and 0.6 (red).

When assuming a maximal  $\theta_{23}$  mixing (middle row of Figure 9.16), the sensitivity improves in the  $\delta_{CP} \in [0, \pi]$  region if the mass ordering is known and almost reaches the  $3\sigma$  significance for the highest expected POT in the statistics-only case for  $\delta_{CP} = \pi/2$ . Around this value, we can observe how the impact of the systematic uncertainties becomes more important. On the other hand, for the lower  $\theta_{23}$  octant (top row of Figure 9.16), the sensitivity to exclude CP conservation is further improved in this same  $\delta_{CP}$  region, where now almost 16% of the possible  $\delta_{CP}$  values allow a  $\sin \delta_{CP} = 0$  exclusion at  $3\sigma$  significance in the statistics-only case. The sensitivity when including the systematic uncertainties does not reach this significance for any  $\delta_{CP}$  value. This further confirms that better constraints on the systematic uncertainties could allow to reach this  $3\sigma$  sensitivity under these conditions.

### Sensitivity to the mass ordering

As previously mentioned, the T2K experiment has a limited sensitivity to determine the mass ordering due to its rather small baseline length in comparison with NOvA or even atmospheric neutrinos in Super-Kamiokande, where the longer neutrino travel distance through Earth allows the matter effects to have enough impact on the oscillation probabilities to distinguish the mass ordering. Nevertheless, we evaluate this weak T2K sensitivity in Figure 9.17. This is done by assuming that the true ordering is normal and computing the chi-square difference between the inverted ordering  $\chi_{IO}^2$  and the normal ordering  $\chi_{NO}^2$  when marginalizing over all the other parameters and fitting pseudo-experiments generated at different values of the  $\theta_{23}$  mixing and  $\delta_{CP}$ . We find that there is virtually no sensitivity to the mass ordering for the CP-conserving  $\delta_{CP} = 0$ , whereas when  $\delta_{CP} = -\pi/2$ , a weak sensitivity can be noticed

depending on the  $\theta_{23}$  mixing. The most favorable value to exclude the wrong mass ordering is  $\sin^2 \theta_{23} = 0.44$ , where the exclusion barely exceeds  $\Delta\chi^2 = 2$  at the highest expected POT. This sensitivity decreases as  $\sin^2 \theta_{23}$  increases, which can be understood from the appearance probability in Equation (1.45).

#### 9.3.2 Towards the use of constraints from the near-detector upgrade

All the sensitivities to the oscillation parameters presented in the previous section used the near-detector constraints coming from the FGD1+2-only configuration (dashed lines in Figures 9.4 to 9.6 and A.1 to A.3). In this section, we explore the potential impact on including the constraints from the Super-FGD samples shown in Section 9.2.

##### Limitations

As the additional target material in the upgrade is hydrocarbon while the far detector is composed of water, the measured neutrino interaction in the Super-FGD cannot be directly translated into constraints on the cross section for oxygen. The CCQE interactions rely on the SF model which is built independently for oxygen and carbon from electron scattering data and does not include any correlations between the two targets. However, as carbon and oxygen are quite similar nuclei with 12 and 16 nucleons respectively, it is only natural to assume that there should be some correlations between their models. Such correlations would allow to propagate (some of) the constraints on the cross-section model from the interactions measured on carbon in the Super-FGD to the neutrino interactions on water in Super-Kamiokande.

##### Carbon vs. oxygen correlations

Various ways can be employed to include correlations between the neutrino interaction models for the different targets. For instance, as seen in the fit to the T2K joint cross-section measurement on carbon and oxygen in Figure 4.18, some correlations can be obtained between the parametrized uncertainties of the two nuclei. However, as the measurement is rather coarse and statistically limited, these correlations are rather weak. More detailed cross-section measurements simultaneously on both targets would provide a strong probe for these effects. Alternatively, we could fit the SF model and its parameters to other available neutrino interaction models which has built-in correlations between the different nuclei.

In this study, we simply choose to introduce *ad-hoc* correlations between the SF-model parameters of oxygen and carbon to gauge the potential impact on the sensitivity to constrain the oscillation parameters. This is carried by modifying the prefit covariance matrix of the cross-section parameters that is used in the near-detector fit and introducing a one-to-one correlation  $\alpha$  between the CCQE parameters of oxygen and carbon, namely the *s*-shell and SRC normalizations, the Pauli blocking and the optical potential correction for the two targets.

Similarly, the carbon  $p$ -shell and the oxygen  $p_{1/2}$ - and  $p_{3/2}$ -shells, are also correlated with the same factor  $\alpha$ . By correlating separately the carbon  $p$ -shell with the oxygen  $p_{1/2}$ -shell, and the carbon  $p$ -shell with the oxygen  $p_{3/2}$ -shell, a constraint appears on the possible correlations between  $p_{1/2}$ - and  $p_{3/2}$ -shell parameters of oxygen in order for the covariance matrix to remain positive definite. This is detailed in Appendix B.

To evaluate the maximum impact we could expect from a nearly full correlation between the two nuclei, we take  $\alpha = 95\%$  and perform again the same near-detector fits presented in Section 9.2.2 where the prefit covariance matrix now includes the aforementioned correlations. The results for the parameters that are expected to change when including these correlations are shown in Figure 9.18. The oxygen parameters are significantly more constrained as we can expect, particularly for the SF-model shell normalizations in Figure 9.18b. The carbon parameters are also slightly more constrained since the interactions on the water layers of FGD2 constrain the carbon parameters through the introduced correlations.

### Impact on the event rates

In Table 9.9, we show the impact of the different systematic uncertainties on the event rates in the six Super-Kamiokande samples for different values of the delivered POT and configurations in the near-detector fit. In each configuration, the systematic uncertainties are broken down into three categories:

1. Near-detector-constrained (ND-constr.) flux+cross section uncertainties: these correspond to the flux and a large proportion of the neutrino interaction model parameters that are fitted in the near-detector analysis.
2. Near-detector-unconstrained (ND-unconstr.) uncertainties: these are neutrino interaction model parameters that are *not* fitted in the near-detector analysis due to the lack of the sensitivity at ND280 but relevant for Super-Kamiokande analyses, as indicated in the last column of Tables 7.6 and 7.7.
3. Super-Kamiokande response uncertainties: these correspond to the detector uncertainties which are naturally not used in the near-detector analysis and are assumed to remain the same throughout this new data-taking phase.

The total error from the systematic uncertainties is also quoted, and the shown statistical uncertainties for each sample are simply obtained using  $1/\sqrt{N}$  when  $N$  is the event rate in the sample at the Set A22 (see Table 9.6). This breakdown of the error sources is performed separately for the FGD1+2-only configuration at the POT of 2022 (Table 9.9a) and 2027 (Table 9.9b), as well as at the 2027 POT for the SF+FGD1+2  $\mu + N$  configuration without (Table 9.9c) and with (Table 9.9d) the strong prefit correlations between the oxygen and carbon SF-model parameters. The contribution to the uncertainty from each error source is evaluated with a sample of 100,000 Gaussian variations from the post-near-detector-fit covariance. The spread

### 9.3 Sensitivity to constrain oscillation parameters

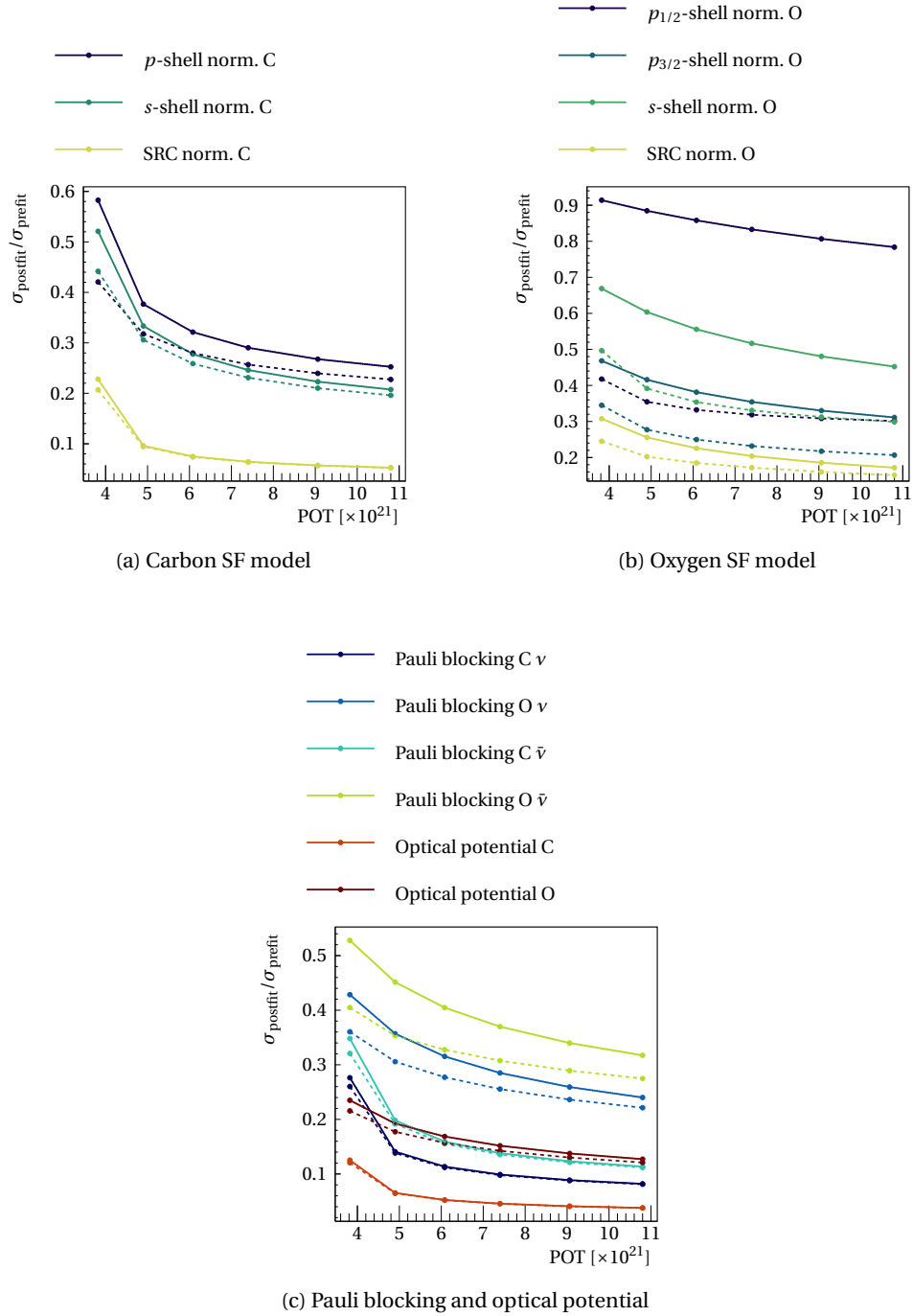


Figure 9.18: Expected constraints on CCQE-related uncertainties in the SFGD+FGD1+2  $\mu + N$  configuration without (full) and with (dashed) the carbon-oxygen correlations.

## Chapter 9. T2K future sensitivity

---

of the event rate in each sample at the Set A22 for each group of systematic uncertainties is calculated and reported in Table 9.9.

With just the FGD1+2 constraints, an important decrease of the near-detector-constrained systematic uncertainties between the first rows of Tables 9.9a and 9.9b. Adding the Super-FGD constraints to the near-detector fit in Table 9.9c only marginally improves the uncertainty on the event rates in the Super-Kamiokande samples, and leads to almost unchanged sensitivity contours in the oscillation parameters. This can be attributed to the conservative assumption of completely uncorrelated uncertainties between the carbon and oxygen targets in the CCQE model. Table 9.9c shows how introducing *ad-hoc* correlations can drastically decrease these near-detector-constrained uncertainties below the 2% level for all the six far-detector samples. Consequently, a more realistic model in which the similarities between the two nuclei are taken into account could play an important role in further reducing the systematic uncertainties. Overall, the statistical uncertainties remain relatively large even at the highest expected POT, but it becomes quite comparable with the impact of the systematic errors in most of the Super-Kamiokande samples.

### Other major sources of systematic uncertainties

Table 9.9 shows that there are other important sources of systematic uncertainties that are not constrained at the near detector. These are the cross-section uncertainties that the current ND280 has no sensitivity to probe, and the Super-Kamiokande response uncertainties. As such, their impact remains the same across the different POT values and near-detector-fit configurations as seen in the second row of Tables 9.9a to 9.9d. The breakdown of the most important unconstrained cross-section uncertainties is detailed in Table 9.10.

The non-resonant  $I_{1/2}$  background producing low-momentum pions in the Rein – Sehgal model has a strong impact on the single-ring samples in the RHC mode. The current ND280 is not sensitive to this contribution, but thanks to the Super-FGD and its lower tracking threshold for hadrons, it would be possible to include dedicated low-momentum pion samples in the near-detector fit in the future and constrain the corresponding uncertainty. This was not included in the study of Section 9.1 due to the lack of a reliable detector simulation as the particle identification of these pions is much more challenging.

The cross-section differences between  $\bar{\nu}_\mu/\bar{\nu}_e$  also play an important role in the  $e$ -like samples which directly impacts the sensitivity to the CP-violating phase  $\delta_{CP}$ . Here as well, the Super-FGD could allow the introduction of a  $\bar{\nu}_e$  selection in the near-detector analysis [289]. In fact, the  $\bar{\nu}_e$  background in the  $\bar{\nu}_\mu$  can be used to define a sample with relatively high statistics, but the main challenge is the background due to the  $\gamma$  electromagnetic showers.

### 9.3 Sensitivity to constrain oscillation parameters

Error source [%]	$\nu_e$ 1R	$\nu_\mu$ 1R	$\bar{\nu}_e$ 1R	$\bar{\nu}_\mu$ 1R	$\nu_e$ 1RD	$\nu_\mu$ CC1 $\pi$
ND-constr. flux+cross section	4.1	3.8	3.7	3.6	5.0	3.5
ND-unconstr. cross section	3.0	0.7	4.2	3.1	2.7	1.5
Super-Kamiokande response	3.5	2.6	4.1	2.2	13.7	4.1
All systematic uncertainties	6.1	4.6	7.0	5.5	14.9	5.6
Statistical uncertainties	11.2	5.8	25.4	9.0	30.3	9.3

(a) 2022 POT with FGD1+2-only constraints

Error source [%]	$\nu_e$ 1R	$\nu_\mu$ 1R	$\bar{\nu}_e$ 1R	$\bar{\nu}_\mu$ 1R	$\nu_e$ 1RD	$\nu_\mu$ CC1 $\pi$
ND-constr. flux+cross section	3.0	2.8	2.7	2.6	3.5	2.6
ND-unconstr. cross section	3.0	0.7	4.2	3.1	2.7	1.5
Super-Kamiokande response	3.5	2.6	4.1	2.2	13.7	4.0
All systematic uncertainties	5.5	3.9	6.5	4.8	14.5	5.1
Statistical uncertainties	6.7	3.5	14.3	5.1	18.2	5.6

(b) 2027 POT with FGD1+2-only constraints

Error source [%]	$\nu_e$ 1R	$\nu_\mu$ 1R	$\bar{\nu}_e$ 1R	$\bar{\nu}_\mu$ 1R	$\nu_e$ 1RD	$\nu_\mu$ CC1 $\pi$
ND-constr. flux+cross section	2.7	2.5	2.3	2.3	3.1	2.3
ND-unconstr. cross section	3.0	0.7	4.2	3.2	2.7	1.5
Super-Kamiokande response	3.5	2.6	4.1	2.2	13.8	4.1
All systematic uncertainties	5.3	3.7	6.4	4.6	14.4	4.9
Statistical uncertainties	6.7	3.5	14.3	5.1	18.2	5.6

(c) 2027 POT with SFGD+FGD1+2  $\mu + N$  constraints

Error source [%]	$\nu_e$ 1R	$\nu_\mu$ 1R	$\bar{\nu}_e$ 1R	$\bar{\nu}_\mu$ 1R	$\nu_e$ 1RD	$\nu_\mu$ CC1 $\pi$
ND-constr. flux+cross section	1.8	1.7	1.9	1.7	1.9	1.5
ND-unconstr. cross section	3.0	0.7	4.2	3.1	2.7	1.5
Super-Kamiokande response	3.5	2.6	4.1	2.2	13.7	4.1
All systematic uncertainties	5.0	3.2	6.2	4.3	14.1	4.6
Statistical uncertainties	6.7	3.5	14.3	5.1	18.2	5.6

(d) 2027 POT with SFGD+FGD1+2  $\mu + N$  constraints assuming carbon vs. oxygen correlations

Table 9.9: Impact of the systematic uncertainties on the event rates in the six Super-Kamiokande samples in % for the different POT and configurations in the near-detector fit, broken down by the uncertainties constrained and unconstrained with the near-detector data as well as the Super-Kamiokande detector response uncertainty. The statistical uncertainties evaluated with the event rates at the Set A22 (see Table 9.6) are also shown for reference.

## Chapter 9. T2K future sensitivity

Error source [%]	$\nu_e$ 1R	$\nu_\mu$ 1R	$\bar{\nu}_e$ 1R	$\bar{\nu}_\mu$ 1R	$\nu_e$ 1RD	$\nu_\mu$ CC1 $\pi$
2p2h $E_{\text{dep}}$	0.2	0.4	0.2	0.5	0.0	0.1
Non-res. $I_{1/2}$ bkg. low $p_\pi$	0.1	0.5	3.1	3.1	0.1	1.1
$\sigma(\nu_\mu)/\sigma(\nu_e)$ , $\sigma(\bar{\nu})/\sigma(\nu)$	2.6	0.0	1.5	0.0	2.6	0.0
NC1 $\gamma$	1.5	0.0	2.3	0.0	0.0	0.0
NC Other	0.2	0.3	0.4	0.2	0.7	1.0

Table 9.10: Impact of the near-detector-unconstrained systematic uncertainties on the event rates in the six Super-Kamiokande samples in %. Their values are the same across the different POT values and near-detector-fit configurations.

## 9.4 Prospects

In this chapter, we studied the potential impact of the upgrade presented in Chapter 5 to constrain the systematic uncertainties related to the flux and the neutrino interaction models in the near-detector analysis. This is performed by introducing new CC0 $\pi$  samples of interactions occurring in the Super-FGD with carefully chosen observables as fit variables. We then studied the sensitivity to constrain the oscillation parameters without this upgrade and evaluated the potential impact of including its tighter constraints on the far-detector samples. We showed that the conservative interaction model used in the current analyses which does not assume correlations between carbon and oxygen limits the potential impact of the Super-FGD on the sensitivity to the oscillation parameters. By introducing *ad-hoc* correlations between the corresponding uncertainties, we find that the impact on the errors in the far-detector samples can be sizable.

An alternative (or complementary) way to improve the constraints on the interactions on oxygen would simply be a larger sample of neutrino-water interactions at the near detector. The WAGSCI/BabyMIND detector (see Section 2.2.3) is also a recent addition to the T2K near-detector complex with water cells that could provide valuable additional samples of neutrino interactions on oxygen. Studies to develop new selections from this detector within the framework of the oscillation analysis are currently ongoing. On the longer term, Hyper-Kamiokande plans the construction of an additional detector  $\sim 2$  km away from the beam source, called the intermediate water Čerenkov detector (IWCD) [73], with performances similar to those of the far detector which would further address the oxygen-related systematic errors for the oscillation analysis.

The high statistics expected from the Super-FGD could allow to go beyond the simple two-dimensional binning in  $(p_\mu, \cos\theta_\mu)$  and  $(\delta p_T, E_{\text{vis}})$ . For instance, the addition of a third dimension in the samples with a reconstructed nucleon using the variable  $\delta\alpha_T$  could allow a further discrimination between the FSI and multinucleon effects. As such, the capabilities of GUNDAM can make additional dimensions possible, but the treatment of the systematic uncertainties with bin-by-bin normalization parameters means that the complexity increases exponentially

with the additional dimensions. This motivates the ongoing studies of finding new ways to implement the detector uncertainties in the near-detector analysis.

On the other hand, the reconstruction tools for the upgraded near detector are currently under development. The improvement of the proton detection efficiency, particularly at higher momenta, can allow to increase the statistics in the Super-FGD samples. The capabilities of the Super-FGD can also be exploited to define new samples targeting the currently unconstrained systematic uncertainties at the far detector such as those related to low-momentum pions and electron neutrinos.

The study presented in this chapter employed the current MC production as used in the 2022 oscillation analysis of Chapter 7. The operating current of the magnetic horns in the secondary beamline, which allow to select the right-sign hadrons to decay into neutrinos, is 250 kA in this analysis. This is planned to be increased up to 320 kA, which could yield an effective increase of the statistics by almost 10%. Including such improvement would naturally yield slightly better constraints on the oscillation parameters.

While the systematic uncertainties related to the neutrino interactions are one of the important uncertainties on the far-detector samples, the Super-Kamiokande response also plays a major role as shown in the third row of Tables 9.9a to 9.9d. By the end of this new phase of data taking, its impact may become the largest source of systematic uncertainty in the one-ring samples that drive the sensitivity to the oscillation parameters.





# Conclusion

In this thesis, we have explored various topics related to the ongoing work and upcoming challenges for the T2K experiment. As discussed in Chapter 1, neutrino oscillations offer a unique probe to physics beyond the Standard Model, and particularly to the violation of the CP symmetry in the lepton sector. Their measurement in accelerator-based experiments is however not straightforward because of the many sources of systematic uncertainties.

The oscillation probabilities depend on the neutrino energy (see Section 1.3), and as such, it is an important quantity to be well determined for a robust measurement of the oscillation parameters. In T2K, the neutrino beam is obtained from the in-flight decay of pions produced from accelerated 30-GeV protons impinging on a graphite target. As a result, the energy spectrum of the neutrino flux is quite broad, even when using the off-axis technique (see Section 2.1.3 and Figure 2.5). This is in great contrast with many other electron or hadron beams where the energy of the particles is known with great precision. Consequently, T2K needs to reconstruct the neutrino energy for each interaction event from the detected outgoing particles. In particular, the oscillation analysis with Super-Kamiokande only uses kinematics the charged lepton as the other produced particles are often below the Čerenkov detection threshold. This can lead to important biases in the neutrino energy estimation, notably due to neutrino interactions (see Figure 3.12).

Modeling neutrino interactions is a major challenge in this field, all the more so since various theoretical descriptions and approximations can lead to different results that do not always match the experimental measurements. This is why it is always important for the models to be accompanied with a suite of adapted systematic uncertainties that can cover plausible variations. Chapter 4 provided an example of such a study, where a set of uncertainty parameters was defined for the Benhar Spectral Function model, which has been recently adopted by the T2K collaboration as the baseline interaction model for charged-current quasielastic interactions. We found that the introduced parametrization is able to improve the agreement with the various cross-section data after tuning, but more detailed measurements of the hadron kinematics in the  $CC0\pi Np$  topology as the one by the MINERvA experiment likely require more model freedom. We also showed in Section 7.5.3 that, while this parametrization helps describing the cross-section measurements, it does not capture the shape variations that some other models predict, which opens the door to further developments of the systematic uncertainties.

## Conclusion

---

To further understand how neutrinos scatter on nuclei, the T2K collaboration is currently upgrading its near detector ND280 by adding a new set of subdetectors. This upgrade is centered around the Super-FGD, a highly segmented plastic scintillator detector with a quasi-3D readout, surrounded by two TPCs and a time-of-flight detectors. Its purpose is to overcome the limitations of the existing ND280, which are mainly the low acceptance for high-angle and backward tracks as well as the high-momentum detection threshold of protons. The upgraded ND280 will provide a more isotropic acceptance for all charged particles, similarly to Super-Kamiokande, and drastically improve the detection of the hadronic products of neutrino interactions as shown in Figure 5.21. This will pave the way to defining new observables that can precisely test our neutrino scattering models in novel ways.

As the Super-FGD is composed of almost two million cubes of plastic scintillator, each read in three orthogonal directions by optical fibers, the readout electronics of this system has naturally a complex architecture as detailed in Chapter 6. More than 220 front-end boards are going to be installed around the Super-FGD during the summer of 2023, each reading the light yield from up to 256 channels. First prototypes of these boards underwent thorough testing to confirm that their design satisfies the requirements. First, we checked the response to the signal from the same photosensors used in the Super-FGD setup and performed a basic charge calibration as will be done with the real setup. We also evaluated the linearity of the electronics response, and the electronic channel-to-channel cross talk which was found to be below  $\sim 0.4\%$ . We also tested the timing information that is recorded by the boards and assessed its accuracy. If the frequency of an input signal injected in a single channel can be obtained with great precision, these tests showed non-negligible timing delays between the channels that can go up to  $\sim 1$  ns. Indeed, the timing information is essential for the reconstruction of neutron kinematics using their time of flight as discussed in Section 5.4.3, and this test further highlights the need of a timing calibration of the detector.

This upgrade doubles the overall target mass for neutrino interactions at ND280, and with its high detection efficiency, a significantly larger amount of data is expected in the near-detector analyses. To cope with the associated computational challenges, we developed GUNDAM, a new multipurpose fitting framework for cross-section and oscillation analyses. Chapter 8 described its extensive validation to become an approved tool for the T2K collaboration by reproducing the T2K results of 2020 and 2022. Along with the code debugging, this validation also pointed out an important caveat in gradient-descent fitters when the likelihood function that is optimized is complicated and features local optima (see Figure 8.13), which can motivate the exploration of other optimization methods.

In parallel with these validations, we developed a near-detector analysis within GUNDAM that features new Super-FGD samples from the preliminary estimations of its performances, in addition to the existing samples from the current ND280 in the oscillation analysis. We demonstrated that the use of the nucleon kinematics in the  $CC0\pi Np$  samples of the Super-FGD can provide significantly improved constraints on the flux and the neutrino interaction models as shown for instance in Figures 9.4 and 9.6. As one may expect, since the nuclear

ground state model used in the analysis is built independently for oxygen and carbon, the additional constraints from the interactions in the Super-FGD cannot be directly translated into constraints on neutrino scattering on water, which is the most relevant uncertainty for the Super-Kamiokande analyses.

We also projected the expected improved constraints on the oscillation parameters in the far-detector fits, and showed how the sensitivity to these parameters is expected to evolve over the upcoming years. In particular, the uncertainty on  $\Delta m_{32}^2$  can reach below 1.3%, and the octant degeneracy can be more stringently constrained. The sensitivity to the CP-violating phase  $\delta_{\text{CP}}$  is expected to further improve with the larger statistics, but it is unlikely that a  $3\sigma$  exclusion of the CP conservation would be reached with the current estimated beam exposure until 2027. The top left panel of Figure 9.16 particularly shows that this could only be reached if the systematic uncertainties are further improved, and if the true  $\delta_{\text{CP}}$  is around  $\pi/2$ , the mass ordering is known, and the true octant is the lower one. We also explored how we can further utilize the constraints from the added Super-FGD samples using *ad-hoc* correlations between the carbon and oxygen uncertainties. Such correlations can be well motivated with cross-section data and/or other theoretical models. We found that, while these correlations could significantly impact the systematic uncertainties, other error sources will become dominant. These are related to the uncertainties that are unconstrained with the current near-detector analyses, such as those associated with the electron neutrino cross sections and the low-momentum pions, which could be addressed with new data selections in the Super-FGD. The systematic uncertainties related to the response of Super-Kamiokande will also start to become among the dominant ones in some of the far-detector samples.



## A Projected constraints on other flux and cross-section uncertainties

In this appendix, the constraints on the other parameters included in the near-detector oscillation analysis of Chapter 9 are shown. Figures A.1 and A.2 display the constraints on the cross-section uncertainties related to interactions that are not expected to see a significant improvement when adding the  $CC0\pi$  samples of the Super-FGD such as CCRES and CCDIS. We can still see some additional constraints especially with the  $(\delta p_T, E_{\text{vis}})$  binning (full) as  $CC0\pi$  samples include a background from such interactions that can be well separated by these observables. The constraints on the Super-Kamiokande flux uncertainties are also shown in Figure A.3 for the  $\bar{\nu}_\mu$  components of the flux. These are highly correlated with the ND280 flux parameters and thus their constraints is quite similar to Figure 9.6. Additionally, the constraints on the smaller fraction of  $\bar{\nu}_e$  events both at ND280 and Super-Kamiokande are displayed in Figure A.4.

## Appendix A. Projected constraints on other flux and cross-section uncertainties

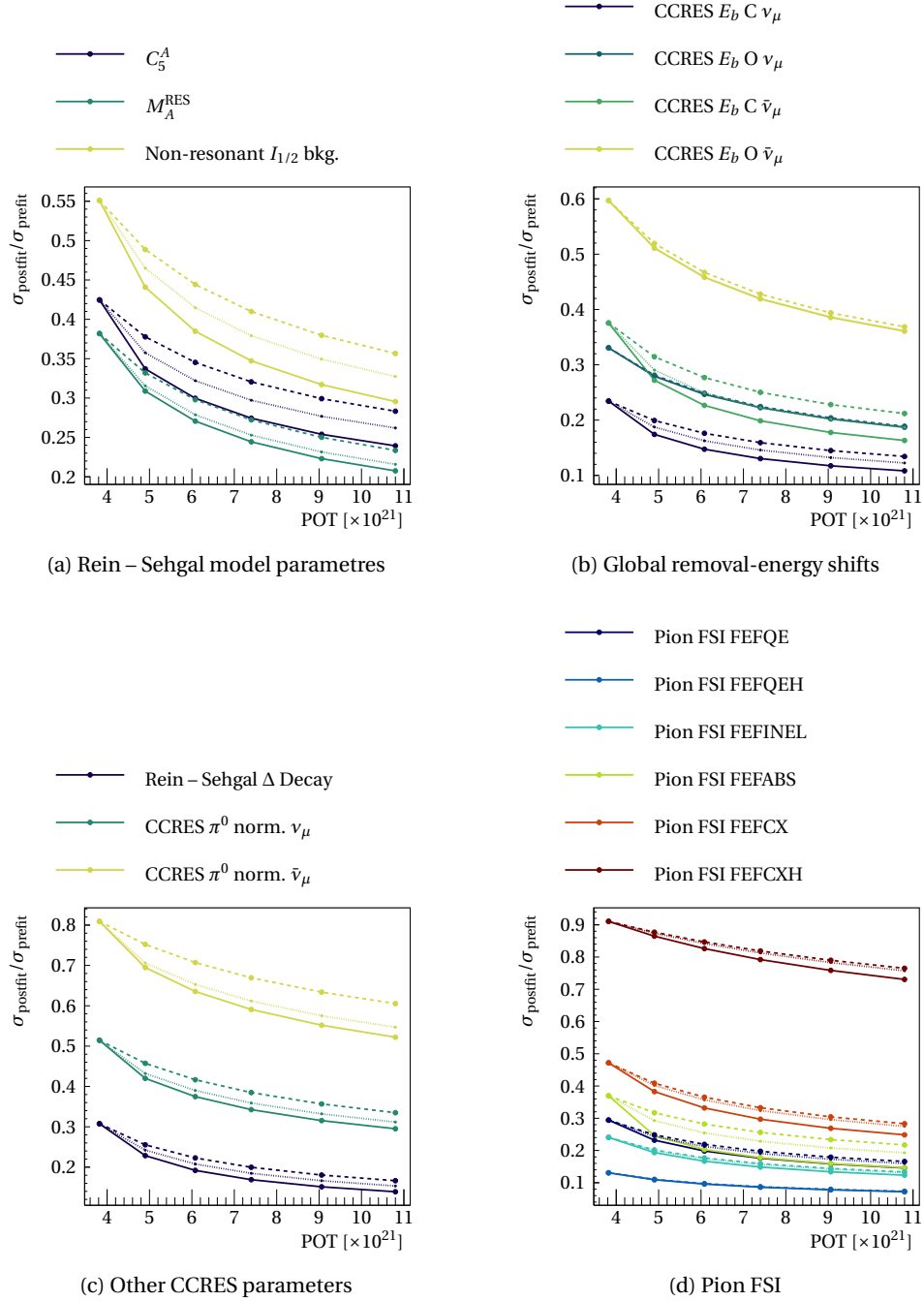


Figure A.1: Expected constraints on CCRES-related uncertainties for the FGD1+2 only (dashed), SFGD+FGD1+2  $\mu$  only (dotted) and SFGD+FGD1+2  $\mu$  + N (full) configurations described in Section 9.2.1.

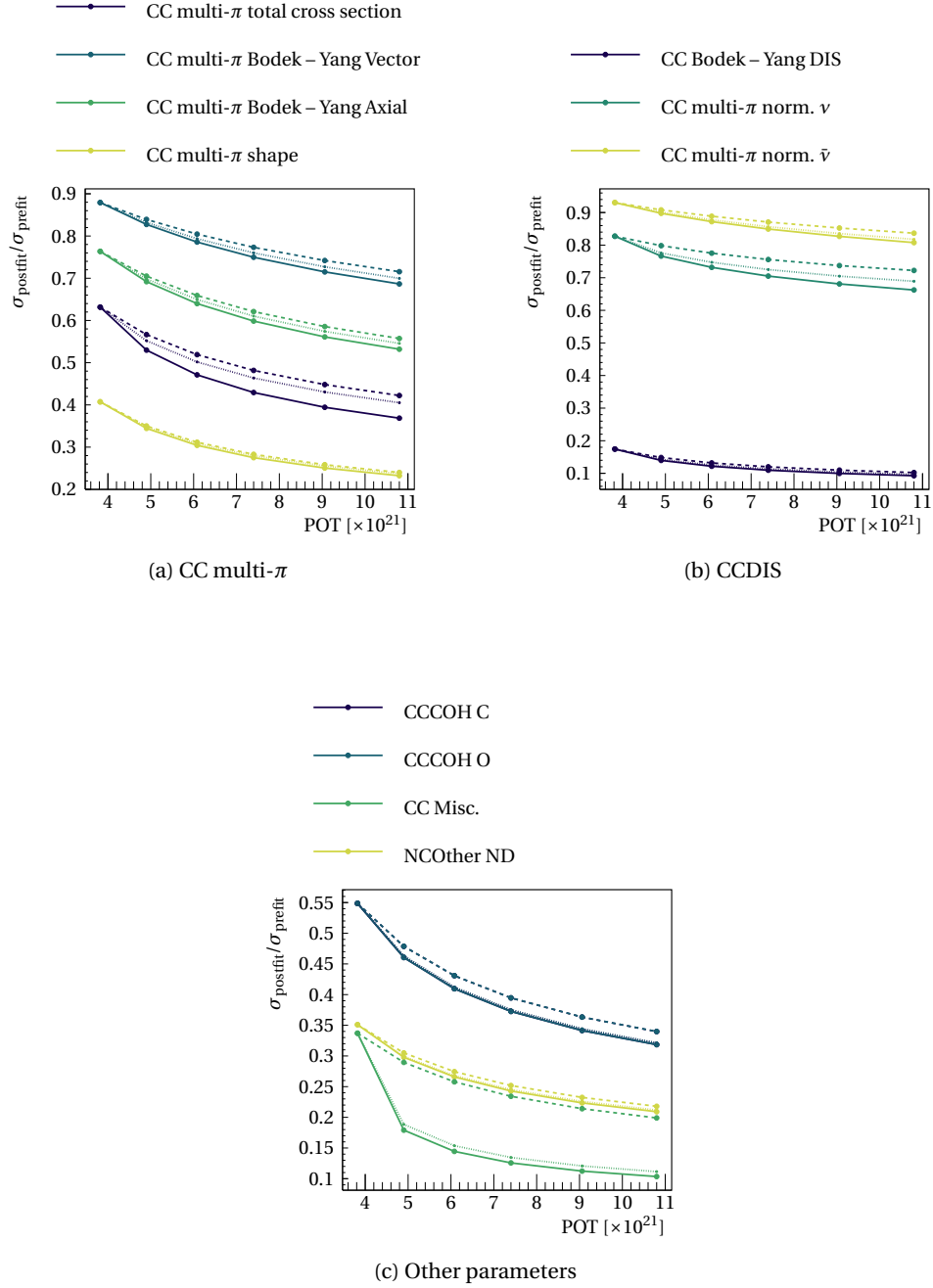


Figure A.2: Expected constraints on CCDIS-related and other uncertainties for the FGD1+2 only (dashed), SFGD+FGD1+2  $\mu$  only (dotted) and SFGD+FGD1+2  $\mu$  +  $N$  (full) configurations described in Section 9.2.1.



## Appendix A. Projected constraints on other flux and cross-section uncertainties

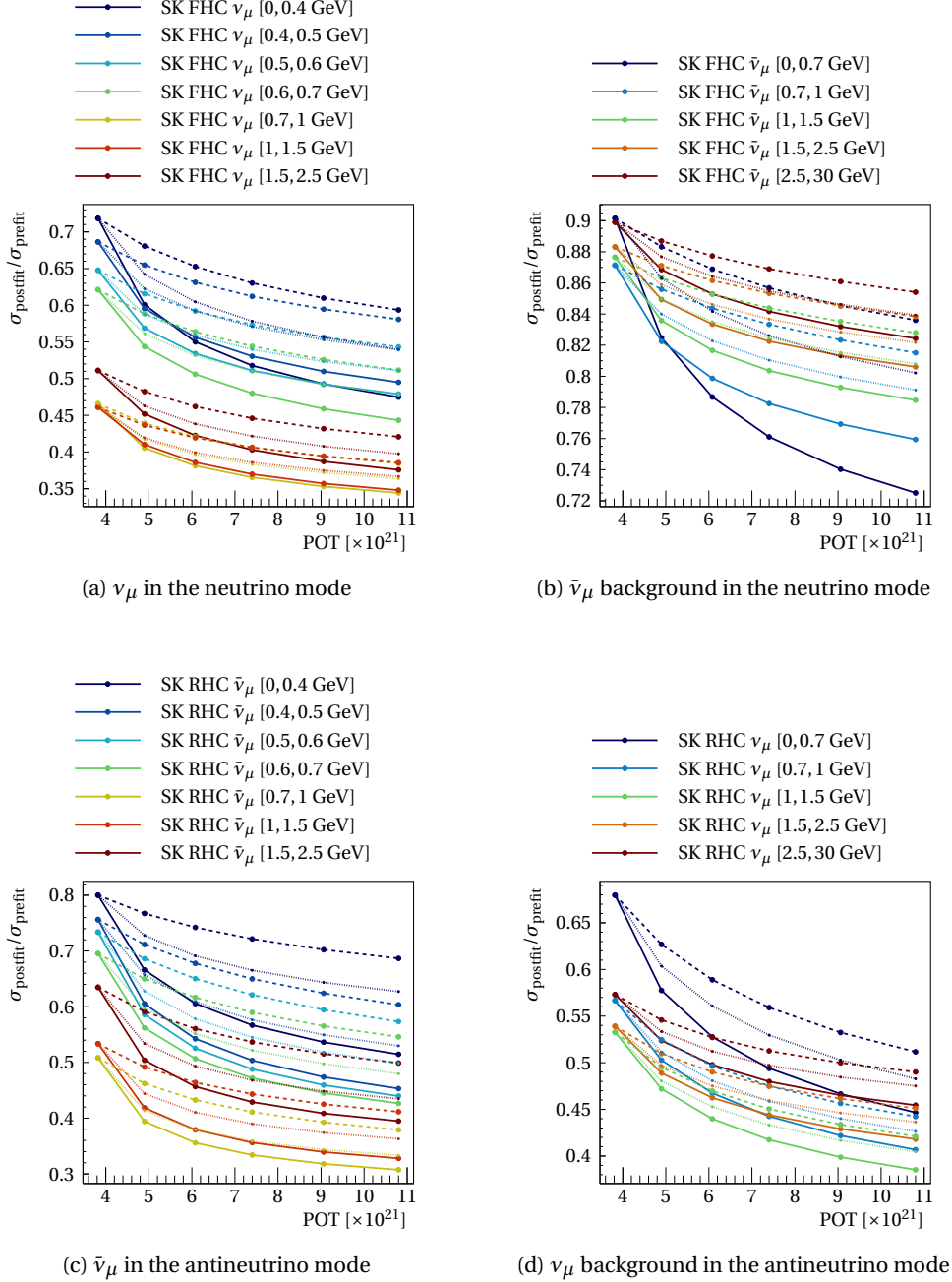


Figure A.3: Expected constraints on Super-Kamiokande flux uncertainties for the FGD1+2 only (dashed), SFGD+FGD1+2  $\mu$  only (dotted) and SFGD+FGD1+2  $\mu$  +  $N$  (full) configurations described in Section 9.2.1.

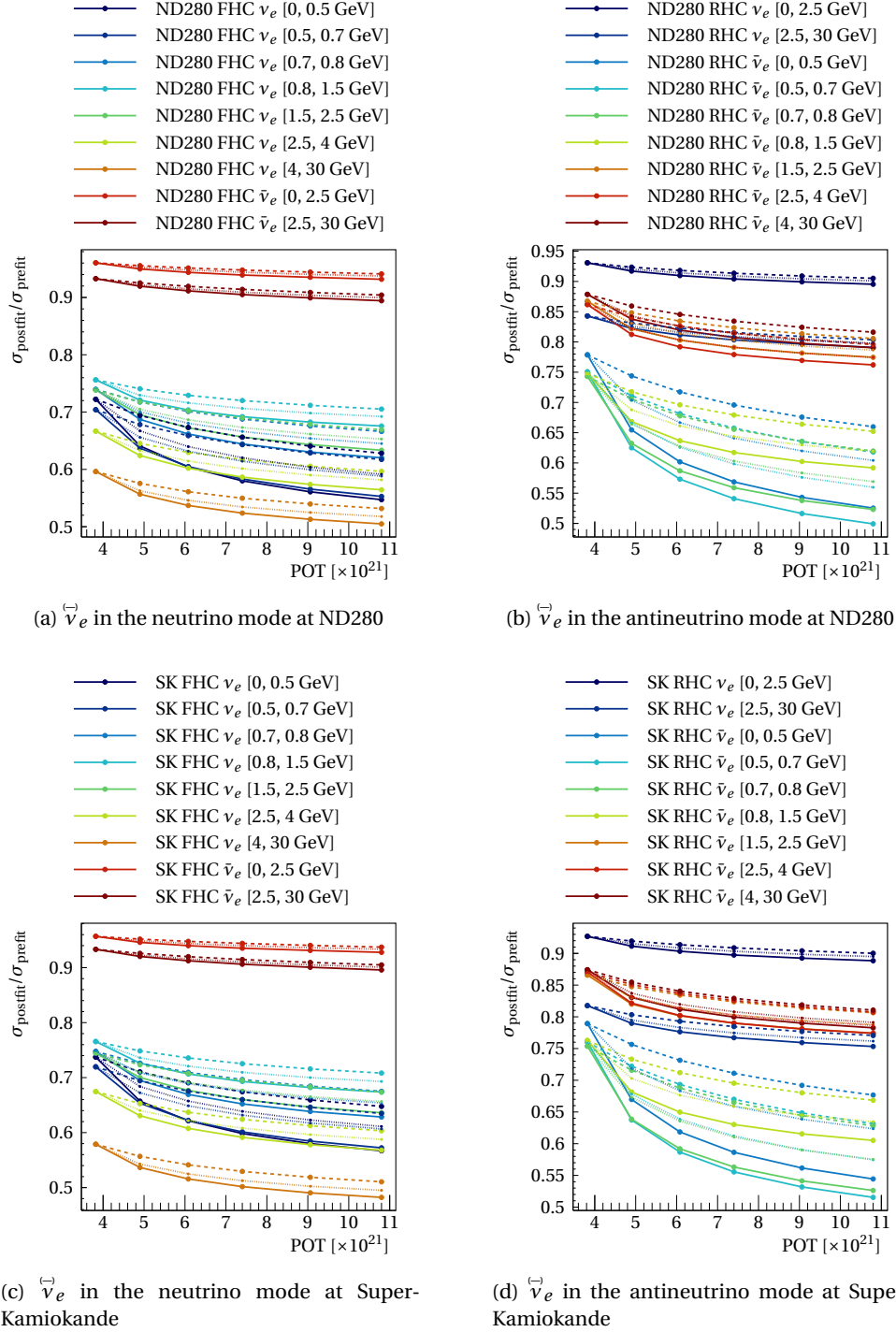


Figure A.4: Expected constraints on ND280 (top) and Super-Kamiokande (bottom) flux uncertainties for the FGD1+2 only (dashed), SFGD+FGD1+2  $\mu$  only (dotted) and SFGD+FGD1+2  $\mu$  +  $N$  (full) configurations described in Section 9.2.1.



## B Three-variable correlations

Let us consider three random variables  $X$ ,  $Y$  and  $Z$ , such that the correlation between  $X$  and  $Y$  is  $a$ , and the correlation between  $X$  and  $Z$  is  $b$ . What are the possible values of the correlation  $c$  between  $Y$  and  $Z$ ?

The correlation matrix  $M$  of the vector  $(X, Y, Z)$  is defined as:

$$M = \begin{pmatrix} 1 & a & b \\ a & 1 & c \\ b & c & 1 \end{pmatrix}.$$

As a correlation matrix, it is by definition positive semidefinite. This is satisfied if and only if the determinant of its leading principal minors are all positive [290]. The  $k$ th-order leading principal minor corresponds to the determinant of the upper left  $k \times k$  submatrix of  $M$ . The first-order and second-order leading principal minors of  $M$  are trivially positive as  $|a| \leq 1$ . Consequently,  $M$  is positive semidefinite if and only if  $\det M \geq 0$ .

This means that:

$$\begin{aligned} \det M &= \begin{vmatrix} 1 & a & b \\ a & 1 & c \\ b & c & 1 \end{vmatrix} \\ &= 1 \times \begin{vmatrix} 1 & c \\ c & 1 \end{vmatrix} - a \times \begin{vmatrix} a & b \\ c & 1 \end{vmatrix} + b \times \begin{vmatrix} a & b \\ 1 & c \end{vmatrix} \\ &= (1 - c^2) - a(a - bc) + b(ac - b) \\ &= 1 - a^2 - b^2 + 2abc - c^2 \\ &\geq 0. \end{aligned}$$

This is a second-order polynomial in  $c$ , and its discriminant is:

$$\Delta = (2ab)^2 - 4 \times (-1) \times (1 - a^2 - b^2) = 4(1 - a^2 - b^2 - a^2b^2) = 4(1 - a^2)(1 - b^2) \geq 0$$

## Appendix B. Three-variable correlations

---

since  $|a| \leq 1$  and  $|b| \leq 1$ . If  $\Delta = 0$ , then  $|a| = 1$  or  $|b| = 1$ . In such case, say for instance  $|a| = 1$ , the determinant  $\det M$  is positive if and only if  $c = ab$ . Otherwise,  $\Delta > 0$  and this second-order polynomial in  $c$  has two roots  $c_1$  and  $c_2$  such that  $c_1 < c_2$ . It is positive if and only if  $c_1 \leq c \leq c_2$ , where:

$$\begin{aligned} c_1 &= \frac{-2ab + \sqrt{\Delta}}{2 \times (-1)} = ab - \sqrt{(1-a^2)(1-b^2)}, \\ c_2 &= \frac{-2ab - \sqrt{\Delta}}{2 \times (-1)} = ab + \sqrt{(1-a^2)(1-b^2)}. \end{aligned}$$

Consequently, the possible values of the correlation  $c$  between  $Y$  and  $Z$  satisfy:

$$ab - \sqrt{(1-a^2)(1-b^2)} \leq c \leq ab + \sqrt{(1-a^2)(1-b^2)}, \quad (\text{B.1})$$

which trivially holds as well if  $\Delta = 0$ .

Let us apply this inequality to the correlations considered in Section 9.3.2. In that study, we have the following three uncertainties:

$$\begin{aligned} X &= p\text{-shell norm. C,} \\ Y &= p_{1/2}\text{-shell norm. O,} \\ Z &= p_{3/2}\text{-shell norm. O,} \end{aligned}$$

where we take  $a = b = 95\%$ . Using Equation (B.1), we conclude that the only possible values of the correlation  $c$  between  $Y$  and  $Z$  are between  $\sim 80\%$  and  $100\%$ . We consequently set it to a value slightly above  $80\%$  to ensure the positive-definiteness of the covariance matrix.

## References

- [1] W. Pauli. “Pauli letter collection: letter to Lise Meitner”. Typed copy. URL: <https://cds.cern.ch/record/83282>.
- [2] J. Chadwick. “Intensitätsverteilung im magnetischen Spectrum der  $\beta$ -Strahlen von radium B + C”. In: *Verhandlungen der deutschen physikalischen Gesellschaft* 16 (1914), pp. 383–391.
- [3] C. L. Cowan et al. “Detection of the free neutrino: A Confirmation”. In: *Science* 124 (1956), pp. 103–104. DOI: 10.1126/science.124.3212.103.
- [4] C. Cowan and F. Reines. “Pauli letter collection: telegram from Frederick Reines and Clyde Cowan”. URL: <http://cds.cern.ch/record/828311>.
- [5] G. Danby et al. “Observation of high-energy neutrino reactions and the existence of two kinds of neutrinos”. In: *Physical Review Letters* 9 (1962), pp. 36–44. DOI: 10.1103/PhysRevLett.9.36.
- [6] M. L. Perl et al. “Evidence for anomalous lepton production in  $e^+ - e^-$  annihilation”. In: *Physical Review Letters* 35 (1975), pp. 1489–1492. DOI: 10.1103/PhysRevLett.35.1489.
- [7] G. Abrams et al. “Measurements of Z-boson resonance parameters in  $e^+ e^-$  annihilation”. In: *Physical Review Letters* 63.20 (1989), p. 2173. DOI: 10.1103/PhysRevLett.63.2173.
- [8] K. Kodama et al. “Observation of tau neutrino interactions”. In: *Physics Letters B* 504.3 (Apr. 2001), pp. 218–224. DOI: 10.1016/S0370-2693(01)00307-0.
- [9] *Standard model of physics | TikZ example*. URL: <https://texample.net/tikz/examples/model-physics/> (visited on 06/02/2023).
- [10] G. Arnison et al. “Experimental observation of isolated large transverse energy electrons with associated missing energy at  $s=540$  GeV”. In: *Physics Letters B* 122.1 (1983), pp. 103–116. DOI: 10.1016/0370-2693(83)91177-2.
- [11] G. Arnison et al. “Experimental observation of lepton pairs of invariant mass around  $95 \text{ GeV}/c^2$  at the CERN SPS collider”. In: *Physics Letters B* 126 (1983), pp. 398–410. DOI: 10.1016/0370-2693(83)90188-0.
- [12] R. L. Workman et al. “Review of Particle Physics”. In: *PTEP* 2022 (2022), p. 083C01. DOI: 10.1093/ptep/ptac097.
- [13] F. Englert and R. Brout. “Broken Symmetry and the Mass of Gauge Vector Mesons”. In: *Phys. Rev. Lett.* 13 (9 Aug. 1964), pp. 321–323. DOI: 10.1103/PhysRevLett.13.321.
- [14] P. W. Higgs. “Broken Symmetries and the Masses of Gauge Bosons”. In: *Phys. Rev. Lett.* 13 (16 Oct. 1964), pp. 508–509. DOI: 10.1103/PhysRevLett.13.508.
- [15] T. D. Lee and C. N. Yang. “Parity Nonconservation and a Two-Component Theory of the Neutrino”. In: *Phys. Rev.* 105 (5 Mar. 1957), pp. 1671–1675. DOI: 10.1103/PhysRev.105.1671.

## References

---

- [16] C. S. Wu et al. “Experimental Test of Parity Conservation in Beta Decay”. In: *Phys. Rev.* 105 (4 Feb. 1957), pp. 1413–1415. DOI: 10.1103/PhysRev.105.1413.
- [17] The ALEPH Collaboration, the DELPHI Collaboration, the L3 Collaboration, the OPAL Collaboration, the SLD Collaboration, the LEP Electroweak Working Group, the SLD electroweak, heavy flavour groups. “Precision electroweak measurements on the Z resonance”. In: *Physics Reports* 427.5-6 (May 2006), pp. 257–454. DOI: 10.1016/j.physrep.2005.12.006.
- [18] N. Aghanim et al. “Planck 2018 results”. In: *Astronomy & Astrophysics* 641 (Sept. 2020), A6. DOI: 10.1051/0004-6361/201833910.
- [19] Y. Y. Wong. “Neutrino Mass in Cosmology: Status and Prospects”. In: *Annual Review of Nuclear and Particle Science* 61.1 (Nov. 2011), pp. 69–98. DOI: 10.1146/annurev-nucl-102010-130252.
- [20] E. Di Valentino, S. Gariazzo, and O. Mena. “Most constraining cosmological neutrino mass bounds”. In: *Phys. Rev. D* 104 (8 Oct. 2021), p. 083504. DOI: 10.1103/PhysRevD.104.083504.
- [21] M. Aker et al. “Direct neutrino-mass measurement with sub-electronvolt sensitivity”. In: *Nature Phys.* 18.2 (2022), pp. 160–166. arXiv: 2105.08533 [hep-ex]. DOI: 10.1038/s41567-021-01463-1.
- [22] J. N. Bahcall et al. “Standard solar models and the uncertainties in predicted capture rates of solar neutrinos”. In: *Rev. Mod. Phys.* 54 (3 July 1982), pp. 767–799. DOI: 10.1103/RevModPhys.54.767.
- [23] J. N. Bahcall and M. H. Pinsonneault. “What Do We (Not) Know Theoretically about Solar Neutrino Fluxes?” In: *Physical Review Letters* 92.12 (Mar. 2004). DOI: 10.1103/physrevlett.92.121301.
- [24] Q. R. Ahmad et al. “Direct Evidence for Neutrino Flavor Transformation from Neutral-Current Interactions in the Sudbury Neutrino Observatory”. In: *Physical Review Letters* 89.1 (June 2002). DOI: 10.1103/physrevlett.89.011301.
- [25] R. Davis Jr, D. Harmer, and K. Hoffman. “Search for neutrinos from the sun”. In: *Physical Review Letters* 20.21 (1968), p. 1205. DOI: 10.1103/PhysRevLett.20.1205.
- [26] J. Bahcall, N. Bahcall, and G. Shaviv. “Present status of the theoretical predictions for the Cl-36 solar neutrino experiment”. In: *Physical Review Letters* 20.21 (1968), p. 1209. DOI: 10.1103/PhysRevLett.20.1209.
- [27] K. Hirata et al. “Observation of B-8 solar neutrinos in the Kamiokande-II detector”. In: *Physical Review Letters* 63.1 (1989), p. 16. DOI: 10.1103/PhysRevLett.63.16.
- [28] A. Abazov et al. “Search for neutrinos from the sun using the reaction  $\text{Ga-71} (\nu_e e^-) \text{Ge-71}$ ”. In: *Physical Review Letters* 67.24 (1991), p. 3332. DOI: 10.1103/PhysRevLett.67.3332.
- [29] P. Anselmann et al. “GALLEX results from the first 30 solar neutrino runs”. In: *Physics Letters B* 327.3-4 (1994), pp. 377–385. DOI: 10.1016/0370-2693(94)90744-7.
- [30] B. Pontecorvo. “Inverse beta processes and nonconservation of lepton charge”. In: *Zh. Eksp. Teor. Fiz.* 34 (1957), p. 247.
- [31] Z. Maki, M. Nakagawa, and S. Sakata. “Remarks on the unified model of elementary particles”. In: *Progress of Theoretical Physics* 28 (1962), pp. 870–880. DOI: 10.1143/PTP.28.870.
- [32] K. Hirata et al. “Experimental study of the atmospheric neutrino flux”. In: *Physics Letters B* 205.1-2 (1988), p. 416. DOI: 10.1016/0370-2693(88)91690-5.
- [33] R. Becker-Szendy et al. “Electron-and muon-neutrino content of the atmospheric flux”. In: *Physical Review D* 46.9 (1992), p. 3720. DOI: 10.1103/PhysRevD.46.3720.

- 
- [34] T. Kajita et al. “Atmospheric neutrino results from Super-Kamiokande and Kamiokande - Evidence for  $\nu_\mu$  oscillations”. In: *Nuclear Physics B Proceedings Supplements* 77.1-3 (1999), pp. 123–132. DOI: 10.1016/S0920-5632(99)00407-7.
  - [35] *Super-Kamiokande Official Website - Physics*. URL: <https://www-sk.icrr.u-tokyo.ac.jp/en/sk/about/research/> (visited on 06/02/2023).
  - [36] K. Eguchi et al. “First Results from KamLAND: Evidence for Reactor Antineutrino Disappearance”. In: *Physical Review Letters* 90.2 (Jan. 2003). DOI: 10.1103/physrevlett.90.021802.
  - [37] S. Abe et al. “Precision Measurement of Neutrino Oscillation Parameters with KamLAND”. In: *Physical Review Letters* 100.22 (June 2008). DOI: 10.1103/physrevlett.100.221803.
  - [38] M. Decowski. “KamLAND’s precision neutrino oscillation measurements”. In: *Nuclear Physics B* 908 (2016). Neutrino Oscillations: Celebrating the Nobel Prize in Physics 2015, pp. 52–61. DOI: <https://doi.org/10.1016/j.nuclphysb.2016.04.014>.
  - [39] C. Giunti and C. W. Kim. *Fundamentals of Neutrino Physics and Astrophysics*. Oxford University Press, Mar. 2007. DOI: 10.1093/acprof:oso/9780198508717.001.0001.
  - [40] R. G. Winter. “NEUTRINO OSCILLATION KINEMATICS”. In: *Lett. Nuovo Cim.* 30 (1981), pp. 101–104. DOI: 10.1007/BF02817319.
  - [41] C. Giunti and C. W. Kim. “Quantum Mechanics of Neutrino Oscillations”. In: (2000). DOI: 10.48550/ARXIV.HEP-PH/0011074.
  - [42] B. Kayser and J. Kopp. *Testing the wave packet approach to neutrino oscillations in future experiments*. 2010. DOI: 10.48550/ARXIV.1005.4081.
  - [43] I. Esteban et al. “The fate of hints: updated global analysis of three-flavor neutrino oscillations”. In: *Journal of High Energy Physics* 2020.9 (Sept. 2020). DOI: 10.1007/jhep09(2020)178.
  - [44] C. Giganti, S. Lavignac, and M. Zito. “Neutrino oscillations: The rise of the PMNS paradigm”. In: *Progress in Particle and Nuclear Physics* 98 (Jan. 2018), pp. 1–54. DOI: 10.1016/j.pnpnp.2017.10.001.
  - [45] A. D. Sakharov. “Violation of CP Invariance, C asymmetry, and baryon asymmetry of the universe”. In: *Pisma Zh. Eksp. Teor. Fiz.* 5 (1967), pp. 32–35. DOI: 10.1070/PU1991v034n05ABEH002497.
  - [46] S. Khlebnikov and M. Shaposhnikov. “The statistical theory of anomalous fermion number non-conservation”. In: *Nuclear Physics B* 308.4 (1988), pp. 885–912. DOI: [https://doi.org/10.1016/0550-3213\(88\)90133-2](https://doi.org/10.1016/0550-3213(88)90133-2).
  - [47] M. Fukugita and T. Yanagida. “Baryogenesis without grand unification”. In: *Physics Letters B* 174.1 (1986), pp. 45–47. DOI: [https://doi.org/10.1016/0370-2693\(86\)91126-3](https://doi.org/10.1016/0370-2693(86)91126-3).
  - [48] L. Wolfenstein. “Neutrino oscillations in matter”. In: *Phys. Rev. D* 17 (9 May 1978), pp. 2369–2374. DOI: 10.1103/PhysRevD.17.2369.
  - [49] S. P. Mikheyev and A. Y. Smirnov. “Resonance Amplification of Oscillations in Matter and Spectroscopy of Solar Neutrinos”. In: *Sov. J. Nucl. Phys.* 42 (1985), pp. 913–917.
  - [50] A. Y. Smirnov. *The MSW effect and Solar Neutrinos*. 2003. DOI: 10.48550/ARXIV.HEP-PH/0305106.
  - [51] A. Cervera et al. “Golden measurements at a neutrino factory”. In: *Nuclear Physics B* 579.1-2 (July 2000), pp. 17–55. DOI: 10.1016/s0550-3213(00)00221-2.



## References

---

- [52] M. Freund. “Analytic approximations for three neutrino oscillation parameters and probabilities in matter”. In: *Physical Review D* 64.5 (July 2001). DOI: 10.1103/physrevd.64.053003.
- [53] and K. Abe et al. “Constraint on the matter–antimatter symmetry-violating phase in neutrino oscillations”. In: *Nature* 580.7803 (Apr. 2020), pp. 339–344. DOI: 10.1038/s41586-020-2177-0.
- [54] J. C. Pati and A. Salam. “Lepton number as the fourth “color””. In: *Phys. Rev. D* 10 (1 July 1974), pp. 275–289. DOI: 10.1103/PhysRevD.10.275.
- [55] Y. Suzuki. “Kamiokande solar neutrino results”. In: *Nuclear Physics B - Proceedings Supplements* 38.1 (1995). Neutrino 94, pp. 54–59. DOI: [https://doi.org/10.1016/0920-5632\(94\)00733-C](https://doi.org/10.1016/0920-5632(94)00733-C).
- [56] S. Fukuda et al. “The Super-Kamiokande detector”. In: *Nuclear Instruments and Methods in Physics Research Section A: Accelerators, Spectrometers, Detectors and Associated Equipment* 501.2 (2003), pp. 418–462. DOI: [https://doi.org/10.1016/S0168-9002\(03\)00425-X](https://doi.org/10.1016/S0168-9002(03)00425-X).
- [57] S. Appel et al. “Improved Measurement of Solar Neutrinos from the Carbon-Nitrogen-Oxygen Cycle by Borexino and Its Implications for the Standard Solar Model”. In: *Physical Review Letters* 129.25 (Dec. 2022). DOI: 10.1103/physrevlett.129.252701.
- [58] S. Adrián-Martínez et al. “Measurement of atmospheric neutrino oscillations with the ANTARES neutrino telescope”. In: *Physics Letters B* 714.2 (2012), pp. 224–230. DOI: <https://doi.org/10.1016/j.physletb.2012.07.002>.
- [59] M. G. Aartsen et al. “Determining neutrino oscillation parameters from atmospheric muon neutrino disappearance with three years of IceCube DeepCore data”. In: *Phys. Rev. D* 91 (7 Apr. 2015), p. 072004. DOI: 10.1103/PhysRevD.91.072004.
- [60] P. Adamson et al. “Precision Constraints for Three-Flavor Neutrino Oscillations from the Full MINOS+ and MINOS Dataset”. In: *Phys. Rev. Lett.* 125 (13 Sept. 2020), p. 131802. DOI: 10.1103/PhysRevLett.125.131802.
- [61] C. Bronner. *Accelerator Neutrino I\_Recent results from T2K*. June 2022. DOI: 10.5281/zenodo.6683821.
- [62] M. A. Acero et al. “Improved measurement of neutrino oscillation parameters by the NOvA experiment”. In: *Phys. Rev. D* 106 (3 Aug. 2022), p. 032004. DOI: 10.1103/PhysRevD.106.032004.
- [63] T. Wester. *Atmospheric Neutrino Oscillation Analysis with Super-Kamiokande*. June 2022. DOI: 10.5281/zenodo.6776294.
- [64] T. Stuttard. *Atmospheric Neutrino\_Particle physics with atmospheric neutrinos at IceCube*. June 2022. DOI: 10.5281/zenodo.6694972.
- [65] F. An et al. “Neutrino physics with JUNO”. In: *Journal of Physics G: Nuclear and Particle Physics* 43.3 (Feb. 2016), p. 030401. DOI: 10.1088/0954-3899/43/3/030401.
- [66] S. Aiello et al. “Determining the neutrino mass ordering and oscillation parameters with KM3NeT/ORCA”. In: *The European Physical Journal C* 82.1 (Jan. 2022). DOI: 10.1140/epjc/s10052-021-09893-0.
- [67] K. Abe et al. “Indication of Electron Neutrino Appearance from an Accelerator-Produced Off-Axis Muon Neutrino Beam”. In: *Phys. Rev. Lett.* 107 (4 July 2011), p. 041801. DOI: 10.1103/PhysRevLett.107.041801.
- [68] K. Abe et al. “Evidence of electron neutrino appearance in a muon neutrino beam”. In: *Phys. Rev. D* 88 (3 Aug. 2013), p. 032002. DOI: 10.1103/PhysRevD.88.032002.

- 
- [69] P. Adamson et al. “First Measurement of Electron Neutrino Appearance in NOvA”. In: *Phys. Rev. Lett.* 116 (15 Apr. 2016), p. 151806. DOI: 10.1103/PhysRevLett.116.151806.
- [70] D. Adey et al. “Measurement of the Electron Antineutrino Oscillation with 1958 Days of Operation at Daya Bay”. In: *Physical Review Letters* 121.24 (Dec. 2018). DOI: 10.1103/physrevlett.121.241805.
- [71] G. Bak et al. “Measurement of Reactor Antineutrino Oscillation Amplitude and Frequency at RENO”. In: *Physical Review Letters* 121.20 (Nov. 2018). DOI: 10.1103/physrevlett.121.201801.
- [72] H. de Kerret et al. “Double Chooz  $\theta_{13}$  measurement via total neutron capture detection”. In: *Nature Phys.* 16.5 (2020), pp. 558–564. arXiv: 1901.09445 [hep-ex]. DOI: 10.1038/s41567-020-0831-y.
- [73] H.-K. Proto-Collaboration, K. Abe, et al. “Physics potential of a long-baseline neutrino oscillation experiment using a J-PARC neutrino beam and Hyper-Kamiokande”. In: *Progress of Theoretical and Experimental Physics* 2015.5 (May 2015). 053C02. eprint: <https://academic.oup.com/ptep/article-pdf/2015/5/053C02/7697513/ptv061.pdf>. DOI: 10.1093/ptep/ptv061.
- [74] R. Acciarri et al. *Long-Baseline Neutrino Facility (LBNF) and Deep Underground Neutrino Experiment (DUNE) Conceptual Design Report Volume 1: The LBNF and DUNE Projects*. 2016. arXiv: 1601.05471 [physics.ins-det].
- [75] F. P. An et al. “Observation of electron-antineutrino disappearance at Daya Bay”. In: *Phys. Rev. Lett.* 108 (2012), p. 171803. arXiv: 1203.1669 [hep-ex]. DOI: 10.1103/PhysRevLett.108.171803.
- [76] K. Abe et al. “The T2K experiment”. In: *Nuclear Instruments and Methods in Physics Research Section A: Accelerators, Spectrometers, Detectors and Associated Equipment* 659.1 (2011), pp. 106–135. DOI: <https://doi.org/10.1016/j.nima.2011.06.067>.
- [77] K. Abe et al. “T2K neutrino flux prediction”. In: *Physical Review D* 87.1 (Jan. 2013). DOI: 10.1103/physrevd.87.012001.
- [78] L. Berns et al. “Flux Prediction and Uncertainty with NA61/SHINE 2010 Replica-Target Data”. T2K-TN-401 (T2K internal note). Mar. 2022. URL: <https://www.t2k.org/docs/technotes/401>.
- [79] D. Beavis et al. “Long baseline neutrino oscillation experiment at the AGS. Physics design report”. In: (Apr. 1995). DOI: 10.2172/52878.
- [80] G. Battistoni et al. “Overview of the FLUKA code”. In: *Annals of Nuclear Energy* 82 (2015). Joint International Conference on Supercomputing in Nuclear Applications and Monte Carlo 2013, SNA + MC 2013. Pluri- and Trans-disciplinarity, Towards New Modeling and Numerical Simulation Paradigms, pp. 10–18. DOI: <https://doi.org/10.1016/j.anucene.2014.11.007>.
- [81] R. Brun et al. *GEANT: Detector Description and Simulation Tool; Oct 1994*. CERN Program Library. Long Writeup W5013. Geneva: CERN, 1993. DOI: 10.17181/CERN.MUHEDMJ1.
- [82] C. Zeitnitz and T. Gabriel. “The GEANT-CALOR interface and benchmark calculations of ZEUS test calorimeters”. In: *Nuclear Instruments and Methods in Physics Research Section A: Accelerators, Spectrometers, Detectors and Associated Equipment* 349.1 (1994), pp. 106–111. DOI: [https://doi.org/10.1016/0168-9002\(94\)90613-0](https://doi.org/10.1016/0168-9002(94)90613-0).
- [83] N. Abgrall et al. “Measurements of cross sections and charged pion spectra in proton-carbon interactions at 31 GeV/c”. In: *Phys. Rev. C* 84 (3 Sept. 2011), p. 034604. DOI: 10.1103/PhysRevC.84.034604.

## References

---

- [84] N. Abgrall et al. “Measurement of production properties of positively charged kaons in proton-carbon interactions at 31 GeV/c”. In: *Phys. Rev. C* 85 (3 Mar. 2012), p. 035210. DOI: 10.1103/PhysRevC.85.035210.
- [85] N. Abgrall et al. “Measurements of  $\pi^\pm, K^\pm$  and proton double differential yields from the surface of the T2K replica target for incoming 31 GeV/c protons with the NA61/SHINE spectrometer at the CERN SPS”. In: *The European Physical Journal C* 79.2 (Jan. 2019). DOI: 10.1140/epjc/s10052-019-6583-0.
- [86] K. Abe et al. “The T2K experiment”. In: *Nuclear Instruments and Methods in Physics Research Section A: Accelerators, Spectrometers, Detectors and Associated Equipment* 659.1 (Dec. 2011), pp. 106–135. DOI: 10.1016/j.nima.2011.06.067.
- [87] S. Aoki et al. “The T2K Side Muon Range Detector (SMRD)”. In: *Nuclear Instruments and Methods in Physics Research Section A: Accelerators, Spectrometers, Detectors and Associated Equipment* 698 (Jan. 2013), pp. 135–146. DOI: 10.1016/j.nima.2012.10.001.
- [88] S. Assylbekov et al. “The T2K ND280 off-axis pi-zero detector”. In: *Nuclear Instruments and Methods in Physics Research Section A: Accelerators, Spectrometers, Detectors and Associated Equipment* 686 (Sept. 2012), pp. 48–63. DOI: 10.1016/j.nima.2012.05.028.
- [89] T. N. T. collaboration. *Time Projection Chambers for the T2K Near Detectors*. 2010. arXiv: 1012.0865 [physics.ins-det].
- [90] P.-A. Amaudruz et al. “The T2K fine-grained detectors”. In: *Nuclear Instruments and Methods in Physics Research Section A: Accelerators, Spectrometers, Detectors and Associated Equipment* 696 (Dec. 2012), pp. 1–31. DOI: 10.1016/j.nima.2012.08.020.
- [91] D. Allan et al. “The electromagnetic calorimeter for the T2K near detector ND280”. In: *Journal of Instrumentation* 8.10 (Oct. 2013), P10019–P10019. DOI: 10.1088/1748-0221/8/10/p10019.
- [92] K. Abe et al. “Measurement of the single  $\pi^0$  production rate in neutral current neutrino interactions on water”. In: *Physical Review D* 97.3 (Feb. 2018). DOI: 10.1103/physrevd.97.032002.
- [93] K. Abe et al. “First measurement of the  $\nu_\mu$  charged-current cross section on a water target without pions in the final state”. In: *Physical Review D* 97.1 (Jan. 2018). DOI: 10.1103/physrevd.97.012001.
- [94] K. Abe et al. “First measurement of the charged current  $\bar{\nu}_\mu$  double differential cross section on a water target without pions in the final state”. In: *Physical Review D* 102.1 (July 2020). DOI: 10.1103/physrevd.102.012007.
- [95] Y. Giomataris et al. “MICROMEGAS: a high-granularity position-sensitive gaseous detector for high particle-flux environments”. In: *Nuclear Instruments and Methods in Physics Research Section A: Accelerators, Spectrometers, Detectors and Associated Equipment* 376.1 (1996), pp. 29–35. DOI: [https://doi.org/10.1016/0168-9002\(96\)00175-1](https://doi.org/10.1016/0168-9002(96)00175-1).
- [96] I. Giomataris et al. “Micromegas in a bulk”. In: *Nuclear Instruments and Methods in Physics Research Section A: Accelerators, Spectrometers, Detectors and Associated Equipment* 560.2 (May 2006), pp. 405–408. DOI: 10.1016/j.nima.2005.12.222.
- [97] Y. Itow et al. *The JHF-Kamioka neutrino project*. 2001. arXiv: hep-ex/0106019 [hep-ex].
- [98] J. F. Beacom and M. R. Vagins. “Antineutrino Spectroscopy with Large Water Čerenkov Detectors”. In: *Physical Review Letters* 93.17 (Oct. 2004). DOI: 10.1103/physrevlett.93.171101.

- 
- [99] K. Abe et al. “Search for Lorentz and CPT violation using sidereal time dependence of neutrino flavor transitions over a short baseline”. In: *Physical Review D* 95.11 (June 2017). DOI: 10.1103/physrevd.95.111101.
  - [100] K. Abe et al. “Search for light sterile neutrinos with the T2K far detector Super-Kamiokande at a baseline of 295 km”. In: *Phys. Rev. D* 99 (7 Apr. 2019), p. 071103. DOI: 10.1103/PhysRevD.99.071103.
  - [101] K. Abe et al. “Search for heavy neutrinos with the T2K near detector ND280”. In: *Physical Review D* 100.5 (Sept. 2019). DOI: 10.1103/physrevd.100.052006.
  - [102] K. Abe et al. “Measurement of the inclusive  $\nu_\mu$  charged current cross section on carbon in the near detector of the T2K experiment”. In: *Physical Review D* 87.9 (May 2013). DOI: 10.1103/physrevd.87.092003.
  - [103] K. Abe et al. “Measurement of the inclusive  $\nu_\mu$  charged current cross section on iron and hydrocarbon in the T2K on-axis neutrino beam”. In: *Physical Review D* 90.5 (Sept. 2014). DOI: 10.1103/physrevd.90.052010.
  - [104] K. Abe et al. “Measurement of  $\bar{\nu}_\mu$  and  $\nu_\mu$  charged current inclusive cross sections and their ratio with the T2K off-axis near detector”. In: *Physical Review D* 96.5 (Sept. 2017). DOI: 10.1103/physrevd.96.052001.
  - [105] K. Abe et al. “Measurement of inclusive double-differential  $\nu_\mu$  charged-current cross section with improved acceptance in the T2K off-axis near detector”. In: *Physical Review D* 98.1 (July 2018). DOI: 10.1103/physrevd.98.012004.
  - [106] K. Abe et al. “Measurement of the muon neutrino charged-current cross sections on water, hydrocarbon and iron, and their ratios, with the T2K on-axis detectors”. In: *Progress of Theoretical and Experimental Physics* 2019.9 (Sept. 2019). DOI: 10.1093/ptep/ptz070.
  - [107] K. Abe et al. “Measurement of the Inclusive Electron Neutrino Charged Current Cross Section on Carbon with the T2K Near Detector”. In: *Physical Review Letters* 113.24 (Dec. 2014). DOI: 10.1103/physrevlett.113.241803.
  - [108] K. Abe et al. “Measurement of the electron neutrino charged-current interaction rate on water with the T2K ND280  $\pi^0$  detector”. In: *Physical Review D* 91.11 (June 2015). DOI: 10.1103/physrevd.91.112010.
  - [109] and K. Abe et al. “Measurement of the charged-current electron (anti-)neutrino inclusive cross-sections at the T2K off-axis near detector ND280”. In: *Journal of High Energy Physics* 2020.10 (Oct. 2020). DOI: 10.1007/jhep10(2020)114.
  - [110] K. Abe et al. “Measurement of the  $\nu_\mu$  charged-current quasielastic cross section on carbon with the ND280 detector at T2K”. In: *Physical Review D* 92.11 (Dec. 2015). DOI: 10.1103/physrevd.92.112003.
  - [111] K. Abe et al. “Measurement of the  $\nu_\mu$  charged current quasielastic cross section on carbon with the T2K on-axis neutrino beam”. In: *Physical Review D* 91.11 (June 2015). DOI: 10.1103/physrevd.91.112002.
  - [112] K. Abe et al. “Measurement of double-differential muon neutrino charged-current interactions on  $C_8H_8$  without pions in the final state using the T2K off-axis beam”. In: *Physical Review D* 93.11 (June 2016). DOI: 10.1103/physrevd.93.112012.
  - [113] K. Abe et al. “Characterization of nuclear effects in muon-neutrino scattering on hydrocarbon with a measurement of final-state kinematics and correlations in charged-current pionless interactions at T2K”. In: *Physical Review D* 98.3 (Aug. 2018). DOI: 10.1103/physrevd.98.032003.

## References

---

- [114] K. Abe et al. “First combined measurement of the muon neutrino and antineutrino charged-current cross section without pions in the final state at T2K”. In: *Physical Review D* 101.11 (June 2020). DOI: 10.1103/physrevd.101.112001.
- [115] K. Abe et al. “Simultaneous measurement of the muon neutrino charged-current cross section on oxygen and carbon without pions in the final state at T2K”. In: *Physical Review D* 101.11 (June 2020). DOI: 10.1103/physrevd.101.112004.
- [116] K. Abe et al. “Measurements of  $\nu_\mu$  and  $\nu_\mu + \bar{\nu}_\mu$  charged-current cross-sections without detected pions or protons on water and hydrocarbon at a mean anti-neutrino energy of 0.86 GeV”. In: *Progress of Theoretical and Experimental Physics* 2021.4 (Mar. 2021). DOI: 10.1093/ptep/ptab014.
- [117] K. Abe et al. “Measurement of Coherent  $\pi^+$  Production in Low Energy Neutrino-Carbon Scattering”. In: *Physical Review Letters* 117.19 (Nov. 2016). DOI: 10.1103/physrevlett.117.192501.
- [118] K. Abe et al. “First measurement of the muon neutrino charged current single pion production cross section on water with the T2K near detector”. In: *Physical Review D* 95.1 (Jan. 2017). DOI: 10.1103/physrevd.95.012010.
- [119] K. Abe et al. “Measurement of the muon neutrino charged-current single  $\pi^+$  production on hydrocarbon using the T2K off-axis near detector ND280”. In: *Physical Review D* 101.1 (Jan. 2020). DOI: 10.1103/physrevd.101.012007.
- [120] K. Abe et al. “First T2K measurement of transverse kinematic imbalance in the muon-neutrino charged-current single- $\pi^+$  production channel containing at least one proton”. In: *Physical Review D* 103.11 (June 2021). DOI: 10.1103/physrevd.103.112009.
- [121] K. Abe et al. “Measurement of the neutrino-oxygen neutral-current interaction cross section by observing nuclear deexcitation  $\gamma$  rays”. In: *Physical Review D* 90.7 (Oct. 2014). DOI: 10.1103/physrevd.90.072012.
- [122] K. Abe et al. “Measurement of neutrino and antineutrino neutral-current quasielasticlike interactions on oxygen by detecting nuclear deexcitation  $\gamma$  rays”. In: *Physical Review D* 100.11 (Dec. 2019). DOI: 10.1103/physrevd.100.112009.
- [123] C. H. Llewellyn Smith. “Neutrino Reactions at Accelerator Energies”. In: *Phys. Rept.* 3 (1972), pp. 261–379. DOI: 10.1016/0370-1573(72)90010-5.
- [124] F. Halzen and A. D. Martin. *QUARKS AND LEPTONS: AN INTRODUCTORY COURSE IN MODERN PARTICLE PHYSICS*. 1984.
- [125] K. Borah et al. “Parametrization and applications of the low- $Q^2$  nucleon vector form factors”. In: *Phys. Rev. D* 102 (7 Oct. 2020), p. 074012. DOI: 10.1103/PhysRevD.102.074012.
- [126] C. Patrignani. “Review of Particle Physics”. In: *Chinese Physics C* 40.10 (Oct. 2016), p. 100001. DOI: 10.1088/1674-1137/40/10/100001.
- [127] N. J. Baker et al. “Quasielastic neutrino scattering: A measurement of the weak nucleon axial-vector form factor”. In: *Phys. Rev. D* 23 (11 June 1981), pp. 2499–2505. DOI: 10.1103/PhysRevD.23.2499.
- [128] T. Kitagaki et al. “Study of  $\nu d \rightarrow \mu^- pp_s$  and  $\nu d \rightarrow \mu^- \Delta^{++}(1232)n_s$  using the BNL 7-foot deuterium-filled bubble chamber”. In: *Phys. Rev. D* 42 (5 Sept. 1990), pp. 1331–1338. DOI: 10.1103/PhysRevD.42.1331.
- [129] W. A. Mann et al. “Study of the Reaction  $\nu + n \rightarrow \mu^- + p$ ”. In: *Phys. Rev. Lett.* 31 (13 Sept. 1973), pp. 844–847. DOI: 10.1103/PhysRevLett.31.844.

- 
- [130] T. Kitagaki et al. “High-energy quasielastic  $\nu_\mu n \rightarrow \mu^- p$  scattering in deuterium”. In: *Phys. Rev. D* 28 (3 Aug. 1983), pp. 436–442. DOI: 10.1103/PhysRevD.28.436.
  - [131] S. J. Barish et al. “Study of neutrino interactions in hydrogen and deuterium: Description of the experiment and study of the reaction  $\nu + d \rightarrow \mu^- + p + p_s$ ”. In: *Phys. Rev. D* 16 (11 Dec. 1977), pp. 3103–3121. DOI: 10.1103/PhysRevD.16.3103.
  - [132] D. Allasia et al. “Investigation of exclusive channels in neutrino / anti-neutrino deuteron charged current interactions”. In: *Nucl. Phys. B* 343 (1990), pp. 285–309. DOI: 10.1016/0550-3213(90)90472-P.
  - [133] K. L. Miller et al. “Study of the reaction  $\nu_\mu d \rightarrow \mu^- pp_s$ ”. In: *Phys. Rev. D* 26 (3 Aug. 1982), pp. 537–542. DOI: 10.1103/PhysRevD.26.537.
  - [134] A. Bodek et al. “Vector and axial nucleon form factors: A duality constrained parameterization”. In: *The European Physical Journal C* 53.3 (Dec. 2007), pp. 349–354. DOI: 10.1140/epjc/s10052-007-0491-4.
  - [135] T. Cai et al. “Measurement of the axial vector form factor from antineutrino–proton scattering”. In: *Nature* 614.7946 (2023), pp. 48–53. DOI: 10.1038/s41586-022-05478-3.
  - [136] A. W. Thomas and W. Weise. *The Structure of the Nucleon*. Germany: Wiley, 2001. DOI: 10.1002/352760314X.
  - [137] E. Hernández, J. Nieves, and M. Valverde. “Weak pion production off the nucleon”. In: *Physical Review D* 76.3 (Aug. 2007). DOI: 10.1103/physrevd.76.033005.
  - [138] L. Tiator et al. “Electroproduction of nucleon resonances”. In: *The European Physical Journal A* 19.S1 (Feb. 2004), pp. 55–60. DOI: 10.1140/epjad/s2004-03-009-9.
  - [139] I. G. Aznauryan et al. “Electroexcitation of the P(33)(1232), P(11)(1440), D(13)(1520), S(11)(1535) at  $Q^2 = 0.4$  and  $0.65$  (GeV/c) $^2$ ”. In: *Phys. Rev. C* 71 (2005), p. 015201. arXiv: nucl-th/0407021. DOI: 10.1103/PhysRevC.71.015201.
  - [140] V. D. Burkert and T. S. H. Lee. “Electromagnetic meson production in the nucleon resonance region”. In: *Int. J. Mod. Phys. E* 13 (2004), pp. 1035–1112. arXiv: nucl-ex/0407020. DOI: 10.1142/S0218301304002545.
  - [141] V. D. Burkert et al. “Single quark transition model analysis of electromagnetic nucleon resonance transitions in the  $[70,1^-]$  supermultiplet”. In: *Phys. Rev. C* 67 (2003), p. 035204. arXiv: hep-ph/0212108. DOI: 10.1103/PhysRevC.67.035204.
  - [142] C. H. Albright and L. S. Liu. “Test of SU(6) Predictions in Weak  $N^*$  Production”. In: *Phys. Rev. Lett.* 14 (9 Mar. 1965), pp. 324–326. DOI: 10.1103/PhysRevLett.14.324.
  - [143] O. Lalakulich and E. A. Paschos. “Resonance production by neutrinos:  $J = 3/2$  resonances”. In: *Phys. Rev. D* 71 (7 Apr. 2005), p. 074003. DOI: 10.1103/PhysRevD.71.074003.
  - [144] S. L. Adler. “Photo-, electro-, and weak single-pion production in the (3,3) resonance region”. In: *Annals of Physics* 50.2 (Nov. 1968), pp. 189–311. DOI: 10.1016/0003-4916(68)90278-9.
  - [145] G. M. Radecky et al. “Study of single-pion production by weak charged currents in low-energy  $\nu d$  interactions”. In: *Phys. Rev. D* 25 (5 Mar. 1982), pp. 1161–1173. DOI: 10.1103/PhysRevD.25.1161.
  - [146] T. Kitagaki et al. “Charged-current exclusive pion production in neutrino-deuteron interactions”. In: *Phys. Rev. D* 34 (9 Nov. 1986), pp. 2554–2565. DOI: 10.1103/PhysRevD.34.2554.

## References

---

- [147] D. Rein and L. M. Sehgal. “Neutrino-excitation of baryon resonances and single pion production”. In: *Annals of Physics* 133.1 (1981), pp. 79–153. DOI: [https://doi.org/10.1016/0003-4916\(81\)90242-6](https://doi.org/10.1016/0003-4916(81)90242-6).
- [148] C. Berger and L. M. Sehgal. “Lepton mass effects in single pion production by neutrinos”. In: *Phys. Rev. D* 76 (11 Dec. 2007), p. 113004. DOI: 10.1103/PhysRevD.76.113004.
- [149] K. S. Kuzmin, V. V. Lyubushkin, and V. A. Naumov. “Extended Rein–Sehgal model for tau lepton production”. In: *Nuclear Physics B - Proceedings Supplements* 139 (Feb. 2005), pp. 158–161. DOI: 10.1016/j.nuclphysbps.2004.11.213.
- [150] K. M. Graczyk and J. T. Sobczyk. “Lepton mass effects in weak charged current single pion production”. In: *Physical Review D* 77.5 (Mar. 2008). DOI: 10.1103/physrevd.77.053003.
- [151] M. Kabirnezhad. “Single pion production in neutrino-nucleon interactions”. In: *Physical Review D* 97.1 (Jan. 2018). DOI: 10.1103/physrevd.97.013002.
- [152] J. A. Formaggio and G. P. Zeller. “From eV to EeV: Neutrino cross sections across energy scales”. In: *Rev. Mod. Phys.* 84 (3 Sept. 2012), pp. 1307–1341. DOI: 10.1103/RevModPhys.84.1307.
- [153] A. M. Ankowski and O. Benhar. “Electroweak nuclear response at moderate momentum transfer”. In: *Phys. Rev. C* 83 (5 May 2011), p. 054616. DOI: 10.1103/PhysRevC.83.054616.
- [154] O. Benhar et al. “Electron- and neutrino-nucleus scattering in the impulse approximation regime”. In: *Phys. Rev. D* 72 (5 Sept. 2005), p. 053005. DOI: 10.1103/PhysRevD.72.053005.
- [155] A. M. Ankowski, O. Benhar, and N. Farina. “Analysis of the  $Q^2$  dependence of charged-current quasielastic processes in neutrino-nucleus interactions”. In: *Phys. Rev. D* 82 (1 July 2010), p. 013002. DOI: 10.1103/PhysRevD.82.013002.
- [156] H. Meier-Hajduk et al. “Quasi-elastic electron scattering from  $^3\text{He}$ ”. In: *Nuclear Physics A* 395.2 (1983), pp. 332–348. DOI: [https://doi.org/10.1016/0375-9474\(83\)90047-7](https://doi.org/10.1016/0375-9474(83)90047-7).
- [157] C. C. d. Atti et al. “Realistic nucleon-nucleon interactions and the three-body electrodisintegration of  $^3\text{H}$ ”. In: *Phys. Rev. C* 21 (3 Mar. 1980), pp. 805–815. DOI: 10.1103/PhysRevC.21.805.
- [158] C. Ciofi degli Atti et al. “Nucleon spectral function in complex nuclei and nuclear matter and inclusive quasielastic electron scattering”. In: *Phys. Rev. C* 41 (6 June 1990), R2474–R2478. DOI: 10.1103/PhysRevC.41.R2474.
- [159] S. Kulagin and R. Petti. “Global study of nuclear structure functions”. In: *Nuclear Physics A* 765.1-2 (Jan. 2006), pp. 126–187. DOI: 10.1016/j.nuclphysa.2005.10.011.
- [160] O. Benhar and A. Fabrocini. “Two-nucleon spectral function in infinite nuclear matter”. In: *Physical Review C* 62.3 (Aug. 2000). DOI: 10.1103/physrevc.62.034304.
- [161] E. J. Moniz et al. “Nuclear Fermi Momenta from Quasielastic Electron Scattering”. In: *Phys. Rev. Lett.* 26 (8 Feb. 1971), pp. 445–448. DOI: 10.1103/PhysRevLett.26.445.
- [162] M. Leuschner et al. “Quasielastic proton knockout from  $^{16}\text{O}$ ”. In: *Physical review C: Nuclear physics* 49 (Mar. 1994), pp. 955–967. DOI: 10.1103/PhysRevC.49.955.
- [163] D. Dutta et al. “Quasielastic ( $e, e'p$ ) reaction on  $^{12}\text{C}$ ,  $^{56}\text{Fe}$ , and  $^{197}\text{Au}$ ”. In: *Phys. Rev. C* 68 (6 Dec. 2003), p. 064603. DOI: 10.1103/PhysRevC.68.064603.
- [164] L. Jiang et al. “Determination of the argon spectral function from ( $e, e'p$ ) data”. In: *Phys. Rev. D* 105 (11 June 2022), p. 112002. DOI: 10.1103/PhysRevD.105.112002.

- 
- [165] R. Subedi et al. “Probing Cold Dense Nuclear Matter”. In: *Science* 320.5882 (June 2008), pp. 1476–1478. DOI: 10.1126/science.1156675.
  - [166] O. Benhar et al. “Spectral function of finite nuclei and scattering of GeV electrons”. In: *Nuclear Physics A* 579.3 (1994), pp. 493–517. DOI: [https://doi.org/10.1016/0375-9474\(94\)90920-2](https://doi.org/10.1016/0375-9474(94)90920-2).
  - [167] A. M. Ankowski, O. Benhar, and M. Sakuda. “Improving the accuracy of neutrino energy reconstruction in charged-current quasielastic scattering off nuclear targets”. In: *Phys. Rev. D* 91 (3 Feb. 2015), p. 033005. DOI: 10.1103/PhysRevD.91.033005.
  - [168] O. Benhar, D. Day, and I. Sick. “Inclusive quasielastic electron-nucleus scattering”. In: *Rev. Mod. Phys.* 80 (1 Jan. 2008), pp. 189–224. DOI: 10.1103/RevModPhys.80.189.
  - [169] D. Rohe et al. “Nuclear transparency from quasielastic  $^{12}\text{C}(e, e' p)$ ”. In: *Phys. Rev. C* 72 (5 Nov. 2005), p. 054602. DOI: 10.1103/PhysRevC.72.054602.
  - [170] A. A. Aguilar-Arevalo et al. “First measurement of the muon neutrino charged current quasielastic double differential cross section”. In: *Phys. Rev. D* 81 (9 May 2010), p. 092005. DOI: 10.1103/PhysRevD.81.092005.
  - [171] U. Mosel. “Neutrino Interactions with Nucleons and Nuclei: Importance for Long-Baseline Experiments”. In: *Annual Review of Nuclear and Particle Science* 66.1 (2016), pp. 171–195. eprint: <https://doi.org/10.1146/annurev-nucl-102115-044720>. DOI: 10.1146/annurev-nucl-102115-044720.
  - [172] M. B. Barbaro, A. D. Pace, and L. Fiume. *The SuSA model for neutrino oscillation experiments: from quasielastic scattering to the resonance region*. 2021. arXiv: 2104.10472 [hep-ph].
  - [173] A. Liesenfeld et al. “A Measurement of the axial form-factor of the nucleon by the  $p(e, e'\text{-prime } \pi^+)n$  reaction at  $W = 1125\text{-MeV}$ ”. In: *Phys. Lett. B* 468 (1999), p. 20. arXiv: nucl-ex/9911003. DOI: 10.1016/S0370-2693(99)01204-6.
  - [174] M. Martini et al. “Unified approach for nucleon knock-out and coherent and incoherent pion production in neutrino interactions with nuclei”. In: *Phys. Rev. C* 80 (6 Dec. 2009), p. 065501. DOI: 10.1103/PhysRevC.80.065501.
  - [175] K. Abe et al. “Measurement of neutrino and antineutrino oscillations by the T2K experiment including a new additional sample of  $\nu_e$  interactions at the far detector”. In: *Phys. Rev. D* 96 (9 Nov. 2017), p. 092006. DOI: 10.1103/PhysRevD.96.092006.
  - [176] J. Nieves, I. R. Simo, and M. J. V. Vacas. “Inclusive charged-current neutrino-nucleus reactions”. In: *Physical Review C* 83.4 (Apr. 2011). DOI: 10.1103/physrevc.83.045501.
  - [177] J. Nieves, I. R. Simo, and M. V. Vacas. “The nucleon axial mass and the MiniBooNE quasielastic neutrino-nucleus scattering problem”. In: *Physics Letters B* 707.1 (Jan. 2012), pp. 72–75. DOI: 10.1016/j.physletb.2011.11.061.
  - [178] J. Nieves et al. “Neutrino energy reconstruction and the shape of the charged current quasielastic-like total cross section”. In: *Physical Review D* 85.11 (June 2012). DOI: 10.1103/physrevd.85.113008.
  - [179] J. Nieves, I. R. Simo, and M. V. Vacas. “Two particle-hole excitations in charged current quasielastic antineutrino-nucleus scattering”. In: *Physics Letters B* 721.1-3 (Apr. 2013), pp. 90–93. DOI: 10.1016/j.physletb.2013.03.002.
  - [180] R. Gran et al. “Neutrino-nucleus quasi-elastic and 2p2h interactions up to 10 GeV”. In: *Physical Review D* 88.11 (Dec. 2013). DOI: 10.1103/physrevd.88.113007.



## References

---

- [181] M. Martini et al. “Neutrino and antineutrino quasielastic interactions with nuclei”. In: *Physical Review C* 81.4 (Apr. 2010). DOI: 10.1103/physrevc.81.045502.
- [182] M. Martini, M. Ericson, and G. Chanfray. “Neutrino quasielastic interaction and nuclear dynamics”. In: *Physical Review C* 84.5 (Nov. 2011). DOI: 10.1103/physrevc.84.055502.
- [183] M. Martini, M. Ericson, and G. Chanfray. “Neutrino energy reconstruction problems and neutrino oscillations”. In: *Physical Review D* 85.9 (May 2012). DOI: 10.1103/physrevd.85.093012.
- [184] M. Martini and M. Ericson. “Quasielastic and multinucleon excitations in antineutrino-nucleus interactions”. In: *Physical Review C* 87.6 (June 2013). DOI: 10.1103/physrevc.87.065501.
- [185] M. Martini, M. Ericson, and G. Chanfray. “Energy reconstruction effects in neutrino oscillation experiments and implications for the analysis”. In: *Physical Review D* 87.1 (Jan. 2013). DOI: 10.1103/physrevd.87.013009.
- [186] M. Martini and M. Ericson. “Inclusive and pion production neutrino-nucleus cross sections”. In: *Physical Review C* 90.2 (Aug. 2014). DOI: 10.1103/physrevc.90.025501.
- [187] M. Ericson and M. Martini. “Neutrino versus antineutrino cross sections and CP violation”. In: *Physical Review C* 91.3 (Mar. 2015). DOI: 10.1103/physrevc.91.035501.
- [188] M. Martini et al. “Electron-neutrino scattering off nuclei from two different theoretical perspectives”. In: *Physical Review C* 94.1 (July 2016). DOI: 10.1103/physrevc.94.015501.
- [189] J. Amaro et al. “Meson-exchange currents and quasielastic neutrino cross sections in the superscaling approximation model”. In: *Physics Letters B* 696.1-2 (Jan. 2011), pp. 151–155. DOI: 10.1016/j.physletb.2010.12.007.
- [190] J. E. Amaro et al. “Relativistic analyses of quasielastic neutrino cross sections at MiniBooNE kinematics”. In: *Physical Review D* 84.3 (Aug. 2011). DOI: 10.1103/physrevd.84.033004.
- [191] J. E. Amaro et al. “Meson-Exchange Currents and Quasielastic Antineutrino Cross Sections in the Superscaling Approximation”. In: *Physical Review Letters* 108.15 (Apr. 2012). DOI: 10.1103/physrevlett.108.152501.
- [192] I. R. Simo et al. “Relativistic effects in two-particle emission for electron and neutrino reactions”. In: *Physical Review D* 90.3 (Aug. 2014). DOI: 10.1103/physrevd.90.033012.
- [193] I. R. Simo et al. “Angular distribution in two-particle emission induced by neutrinos and electrons”. In: *Physical Review D* 90.5 (Sept. 2014). DOI: 10.1103/physrevd.90.053010.
- [194] G. Megias et al. “Meson-exchange currents and quasielastic predictions for charged-current neutrino- $^{12}\text{C}$  scattering in the superscaling approach”. In: *Physical Review D* 91.7 (Apr. 2015). DOI: 10.1103/physrevd.91.073004.
- [195] M. V. Ivanov et al. “Charged-current inclusive neutrino cross sections in the superscaling model including quasielastic, pion production and meson-exchange contributions”. In: *Journal of Physics G: Nuclear and Particle Physics* 43.4 (Feb. 2016), p. 045101. DOI: 10.1088/0954-3899/43/4/045101.
- [196] I. R. Simo et al. “Relativistic model of 2p-2h meson exchange currents in (anti)neutrino scattering”. In: *Journal of Physics G: Nuclear and Particle Physics* 44.6 (Apr. 2017), p. 065105. DOI: 10.1088/1361-6471/aa6a06.
- [197] I. R. Simo et al. “Emission of neutron-proton and proton-proton pairs in neutrino scattering”. In: *Physics Letters B* 762 (Nov. 2016), pp. 124–130. DOI: 10.1016/j.physletb.2016.09.021.

- 
- [198] G. Megias et al. “Charged-current neutrino-nucleus reactions within the superscaling meson-exchange current approach”. In: *Physical Review D* 94.9 (Nov. 2016). DOI: 10.1103/physrevd.94.093004.
  - [199] A. De Pace et al. “The 2p - 2h electromagnetic response in the quasielastic peak and beyond”. In: *Nucl. Phys. A* 726 (2003), pp. 303–326. arXiv: nucl-th/0304084. DOI: 10.1016/S0375-9474(03)01625-7.
  - [200] Y. Hayato and L. Pickering. “The NEUT neutrino interaction simulation program library”. In: *The European Physical Journal Special Topics* 230.24 (Oct. 2021), pp. 4469–4481. DOI: 10.1140/epjs/s11734-021-00287-7.
  - [201] C. Andreopoulos et al. “The GENIE neutrino Monte Carlo generator”. In: *Nuclear Instruments and Methods in Physics Research Section A: Accelerators, Spectrometers, Detectors and Associated Equipment* 614.1 (2010), pp. 87–104. DOI: <https://doi.org/10.1016/j.nima.2009.12.009>.
  - [202] T. Golan, C. Juszczak, and J. T. Sobczyk. “Effects of final-state interactions in neutrino-nucleus interactions”. In: *Phys. Rev. C* 86 (1 July 2012), p. 015505. DOI: 10.1103/PhysRevC.86.015505.
  - [203] T. Leitner et al. “Electron- and neutrino-nucleus scattering from the quasielastic to the resonance region”. In: *Phys. Rev. C* 79 (3 Mar. 2009), p. 034601. DOI: 10.1103/PhysRevC.79.034601.
  - [204] R. Bradford et al. “A New Parameterization of the Nucleon Elastic Form Factors”. In: *Nuclear Physics B - Proceedings Supplements* 159 (Sept. 2006), pp. 127–132. DOI: 10.1016/j.nuclphysbps.2006.08.028.
  - [205] K. M. Graczyk and J. T. Sobczyk. “Form factors in the quark resonance model”. In: *Phys. Rev. D* 77 (5 Mar. 2008), p. 053001. DOI: 10.1103/PhysRevD.77.053001.
  - [206] K. M. Graczyk, J. Żmuda, and J. T. Sobczyk. “Electroweak form factors of the  $\Delta(1232)$  resonance”. In: *Phys. Rev. D* 90 (9 Nov. 2014), p. 093001. DOI: 10.1103/PhysRevD.90.093001.
  - [207] M. Glück, E. Reya, and A. Vogt. “Dynamical parton distributions revisited”. In: *The European Physical Journal C* 5.3 (Sept. 1998), pp. 461–470. DOI: 10.1007/s100529800978.
  - [208] A. Bodek and U. K. Yang. “Modeling neutrino and electron scattering cross-sections in the few GeV region with effective LO PDFs”. In: *AIP Conf. Proc.* 670.1 (2003). Ed. by U. Cotti, M. Mondragon, and G. Tavares-Velasco, pp. 110–117. arXiv: hep-ex/0301036. DOI: 10.1063/1.1594324.
  - [209] A. Bodek and U.-k. Yang. “A Unified model for inelastic e - N and  $\nu$  - N cross-sections at all  $Q^2$ ”. In: *AIP Conf. Proc.* 792.1 (2005). Ed. by W. H. Smith and S. R. Dasu, pp. 257–260. arXiv: hep-ph/0508007. DOI: 10.1063/1.2122031.
  - [210] Z. Koba, H. B. Nielsen, and P. Olesen. “Scaling of multiplicity distributions in high-energy hadron collisions”. In: *Nucl. Phys. B* 40 (1972), pp. 317–334. DOI: 10.1016/0550-3213(72)90551-2.
  - [211] T. Sjostrand. “High-energy physics event generation with PYTHIA 5.7 and JETSET 7.4”. In: *Comput. Phys. Commun.* 82 (1994), pp. 74–90. DOI: 10.1016/0010-4655(94)90132-5.
  - [212] E. Oset and L. L. Salcedo. “ $\Delta$  Selfenergy in Nuclear Matter”. In: *Nucl. Phys. A* 468 (1987), pp. 631–652. DOI: 10.1016/0375-9474(87)90185-0.
  - [213] L. L. Salcedo et al. “Computer Simulation of Inclusive Pion Nuclear Reactions”. In: *Nucl. Phys. A* 484 (1988), pp. 557–592. DOI: 10.1016/0375-9474(88)90310-7.

## References

---

- [214] E. S. P. Guerra et al. “Using world  $\pi^\pm$ -nucleus scattering data to constrain an intranuclear cascade model”. In: *Phys. Rev. D* 99 (5 Mar. 2019), p. 052007. DOI: 10.1103/PhysRevD.99.052007.
- [215] P. A. Machado, O. Palamara, and D. W. Schmitz. “The Short-Baseline Neutrino Program at Fermilab”. In: *Ann. Rev. Nucl. Part. Sci.* 69 (2019), pp. 363–387. arXiv: 1903.04608 [hep-ex]. DOI: 10.1146/annurev-nucl-101917-020949.
- [216] G. D’Agostini. “A multidimensional unfolding method based on Bayes theorem”. In: *Nuclear Instruments and Methods in Physics Research Section A: Accelerators, Spectrometers, Detectors and Associated Equipment* 362.2 (Aug. 1995), pp. 487–498. DOI: 10.1016/0168-9002(95)00274-X.
- [217] A. A. Aguilar-Arevalo et al. “The MiniBooNE Detector”. In: *Nucl. Instrum. Meth. A* 599 (2009), pp. 28–46. arXiv: 0806.4201 [hep-ex]. DOI: 10.1016/j.nima.2008.10.028.
- [218] R. Acciarri et al. “Design and Construction of the MicroBooNE Detector”. In: *JINST* 12.02 (2017), P02017. arXiv: 1612.05824 [physics.ins-det]. DOI: 10.1088/1748-0221/12/02/P02017.
- [219] L. Aliaga et al. “Design, Calibration, and Performance of the MINERvA Detector”. In: *Nucl. Instrum. Meth. A* 743 (2014), pp. 130–159. arXiv: 1305.5199 [physics.ins-det]. DOI: 10.1016/j.nima.2013.12.053.
- [220] X. G. Lu et al. “Measurement of final-state correlations in neutrino muon-proton mesonless production on hydrocarbon at  $E_\nu \sim 3$  GeV”. In: *Phys. Rev. Lett.* 121.2 (2018), p. 022504. arXiv: 1805.05486 [hep-ex]. DOI: 10.1103/PhysRevLett.121.022504.
- [221] A. Gil, J. Nieves, and E. Oset. “Many body approach to the inclusive (e, e-prime) reaction from the quasielastic to the Delta excitation region”. In: *Nucl. Phys. A* 627 (1997), pp. 543–598. arXiv: nucl-th/9711009. DOI: 10.1016/S0375-9474(97)00513-7.
- [222] J. Nieves, J. E. Amaro, and M. Valverde. “Inclusive quasi-elastic neutrino reactions”. In: *Phys. Rev. C* 70 (2004). [Erratum: *Phys. Rev. C* 72, 019902 (2005)], p. 055503. arXiv: nucl-th/0408005. DOI: 10.1103/PhysRevC.70.055503.
- [223] J. Nieves, M. Valverde, and M. J. Vicente Vacas. “Inclusive nucleon emission induced by quasi-elastic neutrino-nucleus interactions”. In: *Phys. Rev. C* 73 (2006), p. 025504. arXiv: hep-ph/0511204. DOI: 10.1103/PhysRevC.73.025504.
- [224] X. G. Lu et al. “Measurement of nuclear effects in neutrino interactions with minimal dependence on neutrino energy”. In: *Phys. Rev. C* 94.1 (2016), p. 015503. arXiv: 1512.05748 [nucl-th]. DOI: 10.1103/PhysRevC.94.015503.
- [225] P. Stowell et al. “NUISANCE: a neutrino cross-section generator tuning and comparison framework”. In: *JINST* 12.01 (2017), P01016. arXiv: 1612.07393 [hep-ex]. DOI: 10.1088/1748-0221/12/01/P01016.
- [226] D. Dutta et al. “A Study of the quasielastic (e,e-prime p) reaction on C-12, Fe-56 and Au-97”. In: *Phys. Rev. C* 68 (2003), p. 064603. arXiv: nucl-ex/0303011. DOI: 10.1103/PhysRevC.68.064603.
- [227] C. Maieron, T. W. Donnelly, and I. Sick. “Extended superscaling of electron scattering from nuclei”. In: *Phys. Rev. C* 65 (2 Jan. 2002), p. 025502. DOI: 10.1103/PhysRevC.65.025502.
- [228] S. K. Singh. “The Effect of final state interactions and deuteron binding in neutrino  $d \rightarrow \mu^- p$ ”. In: *Nucl. Phys. B* 36 (1972), pp. 419–435. DOI: 10.1016/0550-3213(72)90227-1.
- [229] V. Bernard, L. Elouadrhiri, and U.-G. Meissner. “Axial structure of the nucleon: Topical Review”. In: *J. Phys. G* 28 (2002), R1–R35. arXiv: hep-ph/0107088. DOI: 10.1088/0954-3899/28/1/201.

- [230] B. Bhattacharya, R. J. Hill, and G. Paz. “Model independent determination of the axial mass parameter in quasielastic neutrino-nucleon scattering”. In: *Phys. Rev. D* 84 (2011), p. 073006. arXiv: 1108.0423 [hep-ph]. DOI: 10.1103/PhysRevD.84.073006.
- [231] K. Abe et al. “Measurement of neutrino and antineutrino oscillations by the T2K experiment including a new additional sample of  $\nu_e$  interactions at the far detector”. In: *Phys. Rev. D* 96.9 (2017). [Erratum: *Phys.Rev.D* 98, 019902 (2018)], p. 092006. arXiv: 1707.01048 [hep-ex]. DOI: 10.1103/PhysRevD.96.092006.
- [232] *Minuit 2*. URL: <https://root.cern/root/html/doc/guides/minuit2/Minuit2.html> (visited on 04/23/2023).
- [233] K. M. Hanson, T. Kawano, and P. Talou. “Probabilistic Interpretation of Peelle’s Pertinent Puzzle and its Resolution”. In: *AIP Conference Proceedings* 769.1 (May 2005), pp. 304–307. eprint: [https://pubs.aip.org/aip/acp/article-pdf/769/1/304/11897773/304\\_1\\_online.pdf](https://pubs.aip.org/aip/acp/article-pdf/769/1/304/11897773/304_1_online.pdf). DOI: 10.1063/1.1945011.
- [234] T. Bonus et al. “Data-based two-body current contribution to the neutrino-nucleus cross section”. In: *Phys. Rev. C* 102 (1 July 2020), p. 015502. DOI: 10.1103/PhysRevC.102.015502.
- [235] A. A. Aguilar-Arevalo et al. “First measurement of the muon antineutrino double-differential charged-current quasielastic cross section”. In: *Phys. Rev. D* 88 (3 Aug. 2013), p. 032001. DOI: 10.1103/PhysRevD.88.032001.
- [236] G. D’Agostini. “On the use of the covariance matrix to fit correlated data”. In: *Nucl. Instrum. Meth. A* 346 (1994), pp. 306–311. DOI: 10.1016/0168-9002(94)90719-6.
- [237] J. Chakrani, M. Buizza Avanzini, and S. Dolan. “Parametrising CCQE uncertainties in the Spectral Function model for neutrino oscillation analyses”. In: *PoS NuFact2021* (2022), p. 235. arXiv: 2202.03219 [hep-ph]. DOI: 10.22323/1.402.0235.
- [238] J. Tena-Vidal et al. “Neutrino-nucleus  $CC0\pi$  cross-section tuning in GENIE v3”. In: *Phys. Rev. D* 106.11 (2022), p. 112001. arXiv: 2206.11050 [hep-ph]. DOI: 10.1103/PhysRevD.106.112001.
- [239] P. Abratenko et al. “New  $CC0\pi$  GENIE model tune for MicroBooNE”. In: *Phys. Rev. D* 105.7 (2022), p. 072001. arXiv: 2110.14028 [hep-ex]. DOI: 10.1103/PhysRevD.105.072001.
- [240] S. Dolan et al. “Sensitivity of the upgraded T2K Near Detector to constrain neutrino and antineutrino interactions with no mesons in the final state by exploiting nucleon-lepton correlations”. In: *Phys. Rev. D* 105.3 (2022), p. 032010. arXiv: 2108.11779 [hep-ex]. DOI: 10.1103/PhysRevD.105.032010.
- [241] S. Alonso-Monsalve et al. “Graph neural network for 3D classification of ambiguities and optical crosstalk in scintillator-based neutrino detectors”. In: *Phys. Rev. D* 103.3 (2021), p. 032005. arXiv: 2009.00688 [physics.data-an]. DOI: 10.1103/PhysRevD.103.032005.
- [242] D. Douqa. “The SuperFGD for the T2K near detector upgrade”. In: *J. Phys. Conf. Ser.* 1690.1 (2020). Ed. by P. Teterin, p. 012070. DOI: 10.1088/1742-6596/1690/1/012070.
- [243] K. Abe et al. “T2K ND280 Upgrade - Technical Design Report”. In: (Jan. 2019). arXiv: 1901.03750 [physics.ins-det].
- [244] J. Kvasnicka and I. Polak. “LED Calibration Systems for CALICE Hadron Calorimeter”. In: *Physics Procedia*. Proceedings of the 2nd International Conference on Technology and Instrumentation in Particle Physics (TIPP 2011) 37 (Jan. 2012), pp. 402–409. DOI: 10.1016/j.phpro.2012.02.379.

## References

---

- [245] *MPPC S13360-1325PE* | *Hamamatsu Photonics*. URL: [https://www.hamamatsu.com/eu/en/product/optical-sensors/mppc/mppc\\_mppc-array/S13360-1325PE.html](https://www.hamamatsu.com/eu/en/product/optical-sensors/mppc/mppc_mppc-array/S13360-1325PE.html) (visited on 04/23/2023).
- [246] E. Delagnes et al. “The SAMPIC Waveform and Time to Digital Converter”. In: *2014 IEEE Nuclear Science Symposium and Medical Imaging Conference (2014 NSS/MIC), and 21st Symposium on Room-Temperature Semiconductor X-Ray and Gamma-Ray Detectors*. See Electronique. Seattle, United States, Nov. 2014. URL: <https://hal.in2p3.fr/in2p3-01082061>.
- [247] A. Korzenev et al. “A 4 $\pi$  time-of-flight detector for the ND280/T2K upgrade”. In: *JINST* 17.01 (2022), P01016. arXiv: 2109.03078 [physics.ins-det]. DOI: 10.1088/1748-0221/17/01/P01016.
- [248] O. Mineev et al. “Beam test results of 3D fine-grained scintillator detector prototype for a T2K ND280 neutrino active target”. In: *Nucl. Instrum. Meth. A* 923 (2019), pp. 134–138. arXiv: 1808.08829 [physics.ins-det]. DOI: 10.1016/j.nima.2019.01.080.
- [249] A. Blondel et al. “The SuperFGD Prototype Charged Particle Beam Tests”. In: *JINST* 15.12 (2020), P12003. arXiv: 2008.08861 [physics.ins-det]. DOI: 10.1088/1748-0221/15/12/P12003.
- [250] I. Alekseev et al. “SuperFGD prototype time resolution studies”. In: *JINST* 18.01 (2023), P01012. arXiv: 2206.10507 [physics.ins-det]. DOI: 10.1088/1748-0221/18/01/P01012.
- [251] A. Agarwal et al. “Total neutron cross-section measurement on CH with a novel 3D-projection scintillator detector”. In: *Phys. Lett. B* 840 (2023), p. 137843. arXiv: 2207.02685 [physics.ins-det]. DOI: 10.1016/j.physletb.2023.137843.
- [252] D. Attié et al. “Performances of a resistive Micromegas module for the Time Projection Chambers of the T2K Near Detector upgrade”. In: *Nucl. Instrum. Meth. A* 957 (2020), p. 163286. arXiv: 1907.07060 [physics.ins-det]. DOI: 10.1016/j.nima.2019.163286.
- [253] D. Attié et al. “Characterization of resistive Micromegas detectors for the upgrade of the T2K Near Detector Time Projection Chambers”. In: *Nucl. Instrum. Meth. A* 1025 (2022), p. 166109. arXiv: 2106.12634 [physics.ins-det]. DOI: 10.1016/j.nima.2021.166109.
- [254] U. Yevarouskaya. “The T2K Near Detector Upgrade”. In: *PoS ICHEP2022* (Nov. 2022), p. 618. DOI: 10.22323/1.414.0618.
- [255] L. Munteanu et al. “New method for an improved antineutrino energy reconstruction with charged-current interactions in next-generation detectors”. In: *Phys. Rev. D* 101.9 (2020), p. 092003. arXiv: 1912.01511 [physics.ins-det]. DOI: 10.1103/PhysRevD.101.092003.
- [256] *Citiroc 1A*. URL: <https://www.weeroc.com/products/sipm-read-out/citiroc-1a> (visited on 04/23/2023).
- [257] M. Antonova et al. “Baby MIND: a magnetized segmented neutrino detector for the WAGASCI experiment”. In: *Journal of Instrumentation* 12.07 (July 2017), pp. C07028–C07028. DOI: 10.1088/1748-0221/12/07/c07028.
- [258] K. Kotera, W. Choi, and T. Takeshita. *Describing the response of saturated SiPMs*. 2016. arXiv: 1510.01102 [physics.ins-det].
- [259] *Micro Coax Products* | *Samtec*. URL: <https://www.samtec.com/picturesearch/high-speed-cable/micro-coax> (visited on 04/23/2023).
- [260] J. B. Birks. “Scintillations from Organic Crystals: Specific Fluorescence and Relative Response to Different Radiations”. In: *Proc. Phys. Soc. A* 64 (1951), pp. 874–877. DOI: 10.1088/0370-1298/64/10/303.

- 
- [261] ADG3247 Datasheet and Product Info | Analog Devices. URL: <https://www.analog.com/en/products/adg3247.html> (visited on 04/25/2023).
  - [262] L. Alvarez-Ruso et al. “NuSTEC White Paper: Status and challenges of neutrino–nucleus scattering”. In: *Prog. Part. Nucl. Phys.* 100 (2018), pp. 1–68. arXiv: 1706.03621 [hep-ph]. DOI: 10.1016/j.pnpnp.2018.01.006.
  - [263] K. Abe et al. “Measurements of neutrino oscillation parameters from the T2K experiment using  $3.6 \times 10^{21}$  protons on target”. In: (Mar. 2023). arXiv: 2303.03222 [hep-ex].
  - [264] S. Agostinelli et al. “GEANT4—a simulation toolkit”. In: *Nucl. Instrum. Meth. A* 506 (2003), pp. 250–303. DOI: 10.1016/S0168-9002(03)01368-8.
  - [265] Y. Fukuda et al. “The Super-Kamiokande detector”. In: *Nucl. Instrum. Meth. A* 501 (2003). Ed. by V. A. Ilyin, V. V. Korenkov, and D. Perret-Gallix, pp. 418–462. DOI: 10.1016/S0168-9002(03)00425-X.
  - [266] M. Harada. *Geant4 based Simulation Study for Super-Kamiokande*. Feb. 2020. DOI: 10.1088/1742-6596/1468/1/012255.
  - [267] M. Jiang et al. “Atmospheric neutrino oscillation analysis with improved event reconstruction in Super-Kamiokande IV”. In: *Progress of Theoretical and Experimental Physics* 2019.5 (May 2019), 053F01. DOI: 10.1093/ptep/ptp015.
  - [268] T. Doyle. “Development of New Off-Axis Near Detector Samples for the T2K Oscillation Analysis”. PhD thesis. Lancaster University, 2022. DOI: 10.17635/lancaster/thesis/1655.
  - [269] A. Bodek and T. Cai. “Removal Energies and Final State Interaction in Lepton Nucleus Scattering”. In: *Eur. Phys. J. C* 79.4 (2019), p. 293. arXiv: 1801.07975 [nucl-th]. DOI: 10.1140/epjc/s10052-019-6750-3.
  - [270] S. Dolan et al. “Electron-nucleus scattering in the NEUT event generator”. In: *23rd International Workshop on Neutrinos from Accelerators*. Jan. 2023. arXiv: 2301.09195 [hep-ex].
  - [271] A. Bodek and U.-k. Yang. “Axial and Vector Structure Functions for Electron- and Neutrino-Nucleon Scattering Cross Sections at all  $Q^2$  using Effective Leading order Parton Distribution Functions”. In: (Nov. 2010). arXiv: 1011.6592 [hep-ph].
  - [272] T. Yang et al. “A Hadronization Model for Few-GeV Neutrino Interactions”. In: *Eur. Phys. J. C* 63 (2009), pp. 1–10. arXiv: 0904.4043 [hep-ph]. DOI: 10.1140/epjc/s10052-009-1094-z.
  - [273] P. Guèye et al. “Coulomb distortion measurements by comparing electron and positron quasielastic scattering off  $^{12}\text{C}$  and  $^{208}\text{Pb}$ ”. In: *Phys. Rev. C* 60 (4 Sept. 1999), p. 044308. DOI: 10.1103/PhysRevC.60.044308.
  - [274] K. S. Kim and M. K. Cheoun. “Final state interaction and Coulomb effect for neutrino-nucleus scattering in the quasielastic region”. In: *AIP Conference Proceedings* 1189.1 (Nov. 2009), pp. 163–168. eprint: [https://pubs.aip.org/aip/acp/article-pdf/1189/1/163/11982267/163\1\\\_online.pdf](https://pubs.aip.org/aip/acp/article-pdf/1189/1/163/11982267/163\1\_online.pdf). DOI: 10.1063/1.3274148.
  - [275] R. Barlow and C. Beeston. “Fitting using finite Monte Carlo samples”. In: *Computer Physics Communications* 77.2 (1993), pp. 219–228. DOI: [https://doi.org/10.1016/0010-4655\(93\)90005-W](https://doi.org/10.1016/0010-4655(93)90005-W).
  - [276] J. Conway. “Incorporating Nuisance Parameters in Likelihoods for Multisource Spectra”. In: (2011). Comments: Presented at PHYSTAT 2011, CERN, Geneva, Switzerland, January 2011, to be published in a CERN Yellow Report, pp. 115–120. arXiv: 1103.0354. DOI: 10.5170/CERN-2011-006.115.

## References

---

- [277] C. A. Argüelles, A. Schneider, and T. Yuan. “A binned likelihood for stochastic models”. In: *JHEP* 06 (2019), p. 030. arXiv: 1901.04645 [physics.data-an]. DOI: 10.1007/JHEP06(2019)030.
- [278] N. Metropolis et al. “Equation of State Calculations by Fast Computing Machines”. In: *The Journal of Chemical Physics* 21.6 (Dec. 2004), pp. 1087–1092. DOI: 10.1063/1.1699114.
- [279] W. K. Hastings. “Monte Carlo sampling methods using Markov chains and their applications”. In: *Biometrika* 57.1 (Apr. 1970), pp. 97–109. DOI: 10.1093/biomet/57.1.97.
- [280] S. Algeri et al. “Searching for new phenomena with profile likelihood ratio tests”. In: *Nature Rev. Phys.* 2.5 (2020), pp. 245–252. arXiv: 1911.10237 [physics.data-an]. DOI: 10.1038/s42254-020-0169-5.
- [281] G. J. Feldman and R. D. Cousins. “A Unified approach to the classical statistical analysis of small signals”. In: *Phys. Rev. D* 57 (1998), pp. 3873–3889. arXiv: physics/9711021. DOI: 10.1103/PhysRevD.57.3873.
- [282] N. Jachowicz et al. “Continuum random phase approximation approach to charged-current neutrino-nucleus scattering”. In: *Phys. Rev. C* 65 (2 Jan. 2002), p. 025501. DOI: 10.1103/PhysRevC.65.025501.
- [283] V. Pandey et al. “Low-energy excitations and quasielastic contribution to electron-nucleus and neutrino-nucleus scattering in the continuum random-phase approximation”. In: *Phys. Rev. C* 92.2 (2015), p. 024606. arXiv: 1412.4624 [nucl-th]. DOI: 10.1103/PhysRevC.92.024606.
- [284] *Andrew / xsLLhFitter · GitLab*. Feb. 2021. URL: <https://gitlab.com/cuddandr/xsLLhFitter> (visited on 04/21/2023).
- [285] *GUNDAM*. Feb. 2023. URL: <https://github.com/gundam-organization/gundam> (visited on 04/21/2023).
- [286] A. P. Furmanski and J. T. Sobczyk. “Neutrino energy reconstruction from one muon and one proton events”. In: *Phys. Rev. C* 95.6 (2017), p. 065501. arXiv: 1609.03530 [hep-ex]. DOI: 10.1103/PhysRevC.95.065501.
- [287] W. P. Abfalterer et al. “Measurement of neutron total cross sections up to 560 MeV”. In: *Phys. Rev. C* 63 (4 Mar. 2001), p. 044608. DOI: 10.1103/PhysRevC.63.044608.
- [288] K. Abe et al. “Sensitivity of the T2K accelerator-based neutrino experiment with an Extended run to  $20 \times 10^{21}$  POT”. In: (July 2016). arXiv: 1607.08004 [hep-ex].
- [289] A. Eguchi. *EM shower reconstruction and electron neutrino selection with the T2K SuperFGD detector*. June 2022. DOI: 10.5281/zenodo.6768535.
- [290] *Definite matrix*. Page Version ID: 1156011000. May 2023. URL: [https://en.wikipedia.org/w/index.php?title=Definite\\_matrix&oldid=1156011000#Other\\_characterizations](https://en.wikipedia.org/w/index.php?title=Definite_matrix&oldid=1156011000#Other_characterizations) (visited on 05/22/2023).

**Titre :** Vers une compréhension complète des interactions neutrino-noyau avec l'upgrade du détecteur proche de T2K

**Mots clés :** neutrino, oscillation, interaction, T2K, Super-FGD

**Résumé :** L'expérience T2K mesure les oscillations des neutrinos pour mesurer les paramètres de mélange avec un faisceau de neutrinos produit à J-PARC. Elle peut ainsi étudier la violation de la symétrie charge-parité (CP) dans le secteur leptonique, ce qui pourrait éclaircir la question de l'asymétrie matière-antimatière dans l'Univers.

Plusieurs sources d'incertitudes empêchent la mesure précise des oscillations des neutrinos comme celles liées au flux et à l'interaction avec les noyaux. Une grande partie de ces erreurs peut être contrainte à travers des détecteurs proches comme ND280. L'augmentation d'exposition au faisceau attendue demande un meilleur contrôle sur ces systématiques, ce qui a motivé la mise à niveau de ND280. Cette thèse discute cette mise à niveau, ainsi que les différents défis qui l'accompagnent.

Un nouveau modèle d'interaction neutrino-noyau a été introduit dans les analyses d'oscillation de T2K en préparation aux données des nouveaux détecteurs.

Nous avons défini une paramétrisation des incertitudes liées à ce modèle et démontré comment elle permet une meilleure description de diverses mesures de section efficace.

La statistique élevée attendue avec cette mise à niveau requiert un logiciel d'ajustement optimisé. Cette thèse décrit le logiciel GUNDAM et se focalise sur sa validation. Nous y concevons une analyse des données du ND280 mis à niveau en ajoutant de nouveaux échantillons avec les performances attendues et discutons l'impact de nouvelles observables pour contraindre les erreurs systématiques. L'effet de ces contraintes améliorées est aussi projeté sur les paramètres d'oscillation, et particulièrement sur la sensibilité à exclure la conservation de la symétrie CP ainsi que la résolution sur les autres paramètres.

L'architecture de l'électronique du Super-FGD, la nouvelle cible active du ND280, est aussi décrite, avec les tests extensifs de ses cartes pour valider leur performances.

**Title :** Towards a complete understanding of neutrino-nucleus interactions with the upgraded T2K near detector

**Keywords :** neutrino, oscillation, interaction, T2K, Super-FGD

**Abstract :** The T2K experiment measures neutrino oscillations to constrain the mixing parameters using a neutrino beam produced at J-PARC. With this, it can probe the conservation of the charge-parity (CP) symmetry in the lepton sector, as its violation could shed light on the origins of the matter-antimatter asymmetry in the Universe.

The accurate measurement of oscillations with accelerator neutrinos is hindered by multiple sources of systematic uncertainties like those related to the flux spectrum and how neutrinos interact with nuclei. Many of these errors can actually be constrained with the so-called near detectors like ND280. The increasing beam exposure requires more control over these error sources, which motivates the ongoing upgrade of ND280. It will enable the measurement of the products of neutrino interactions with unprecedented precision. This thesis discusses this near-detector upgrade and various challenges associated with its addition to the T2K experiment.

A new neutrino interaction model was introduced in the T2K oscillation analyses to cope with the upcoming detailed measurements of the upgraded ND280, and with it a novel set of parametrized systematic un-

certainties was defined. This parametrization allows us to tune this model and improve its agreement with multiple existing cross-section measurements.

The higher statistics that come with this upgrade will require an optimized fitting software that can handle the larger samples and high-dimensional problems. This thesis describes a new framework called GUNDAM and focuses on its validations. We develop within it a near-detector analysis using the samples with the expected performances of the ND280 upgrade and discuss the impact of new observables on constraining flux and neutrino interaction uncertainties.

This thesis also studies the potential impact on constraining the oscillation parameters over the new T2K phase of data taking until 2027. The sensitivity to exclude the CP violation is discussed in detail under different hypotheses and the resolution on the other mixing parameters is also evaluated.

On the hardware side, the architecture of the electronics of the Super-FGD, the new active and highly granular target of the upgrade, is described. We also present the exhaustive tests of its front-end boards and assess their performance before their installation.